

**Waste Form Characteristics Report  
Revision 1**

**Editors:**

**Ray B. Stout  
Herman R. Leider**

**Issued: July 1998  
Published:**



This is an informal report intended primarily for internal or limited external distribution. The opinions and conclusions stated are those of the author and may or may not be those of the Laboratory. Work performed under the auspices of the Department of Energy by the Lawrence Livermore National Laboratory under Contract W-7405-Eng-48.

98  
9811250078 981120  
PDR WASTE  
WM-11 PDR

### Preface to Version 1.3

This version incorporates changes to 10 sections of the *Waste Form Characteristics Report*. Those sections changed are 2.1.3.1 Cladding Degradation; 2.1.3.2 UO<sub>2</sub> Oxidation in Fuel; 2.1.3.5 Dissolution Release from UO<sub>2</sub>; 2.2.1.5 Fracture/Fragmentation Studies of Glass; 2.2.2.2 Dissolution Radionuclide Release from Glass; 2.2.2.3 Soluble-Precipitated/Colloidal Species from Glass; 3.2.2 Spent-Fuel Oxidation Models; 3.4.2 Spent-Fuel Dissolution Models; 3.5.1 Glass-Dissolution Experimental Parameters; and 3.5.2 Glass-Dissolution Models.

Eric Siegmann (CRWMS M&O) furnished section 2.1.3.1, and Brady Hanson (PNNL) provided section 2.1.3.2. William Bourcier was responsible for updating the glass properties and dissolution sections 2.2.1.5, 2.2.2.2, 2.2.2.3, 3.5.1, and 3.5.2. Edward J. Kansa updated section 3.2.2, which covers spent fuel-oxidation models. Steven A. Steward had the responsibility for the spent-fuel dissolution sections on data (2.1.3.5) and modeling (3.4.2). Ananda Wijesinghe provided the unsaturated test release modeling in section 3.4.2.

The evaluation of parameters for the models is based on test data obtained from previous and ongoing testing activities at Argonne National Laboratory, Chicago, Illinois; Lawrence Livermore National Laboratory, Livermore, California; and Pacific Northwest National Laboratories, Richland, Washington.

Sincere appreciation is extended to Steven A. Steward, who edited this update of the *Waste Form Characteristics Report*; to James C. Cunnane and J. Kevin McCoy, who technically reviewed it; and to Karen L. Lew, who edited the update and prepared it for submission and publication.

Ray B. Stout

June 1998

## Preface to Version 1.2

This version incorporates changes to several sections of the *Waste Form Characteristics Report*. Those sections changed are 2.1.3.5 Dissolution Release from  $UO_2$ ; 3.2.2 Spent-Fuel Oxidation Models; 3.4.2 Spent-Fuel Dissolution Models; 3.5.1 Glass-Dissolution Experimental Parameters; and 3.5.2 Glass-Dissolution Models. These sections were also updated in Version 1.1 of the report (August 1996).

William Bourcier was responsible for updating the glass-dissolution sections 3.5.1 and 3.5.2. Edward J. Kansa updated section 3.2.2, which covers spent-fuel oxidation models. Steven A. Steward had the responsibility for the spent-fuel dissolution sections on data (2.1.3.5) and modeling (3.4.2).

The evaluation of parameters for the models is based on test data obtained from previous and ongoing testing activities at Argonne National Laboratory, Chicago, Illinois; Lawrence Livermore National Laboratory, Livermore, California; and Pacific Northwest National Laboratories, Richland, Washington.

Ray B. Stout

April 1997

## Preface to Version 1.0

Over the past several decades, sophisticated techniques have been developed to characterize the physical, thermal, chemical, mechanical, and radiological properties of nuclear radioactive waste form(s). (Here, "waste form" means the radioactive waste materials and any encapsulating or stabilizing matrix and is the definition provided by U.S. Nuclear Regulatory Commission in its regulation of Title 10 CFR 60.) Much of the early characterization was for design, operational efficiency, and safety of nuclear power plants. More recently, characterization activities have been directed at the design problem of safely emplacing radioactive waste form(s) in a suitable geological repository. The emplacement problem entails the teamwork of people from different technical disciplines, and the data exchange interfaces among the different technical personnel is of the utmost importance for an effective, efficient, and safe repository design.

With this need in mind, a preliminary data source of waste form characteristics has been assembled. Most of the data was taken from the open literature. The remaining data were summarized, in a preliminary form, from early results of ongoing waste-form-testing and model-development activities. In assembling the data, the intention has been to address waste-form-related informational needs for the wide variety of technical specialists that are part of a repository-design team. Care has been taken not to impose any limits or restrictions on waste-form response before the repository-design process because only an overall design analysis or performance assessment of the waste repository system can optimize the potential design trade-off options that satisfy requirements of a geologic repository containing radioactive waste form(s).

Because this is the first version of this waste form characteristics report, comments are expected and welcomed and other input from users, potential users, and others who are interested in waste form information is requested. In this way, the waste-form informational needs of the different technical specialists performing the design tasks for a repository can be met. It is anticipated that this report will be updated annually with new results from testing and model-development activities as well as with responses to the additional informational needs noted by users. Some deficiencies in data form and data needs have been identified and will be addressed in future revisions.

The accumulation of data was greatly facilitated because of the cooperation, interest, and esprit de corps of the following individuals, all of whom are graciously acknowledged and thanked: Karl Notz, Robert Einziger, Charles Wilson, Walter Gray, Harry Smith, Steve Marschman, Andrew Luksic, George Mellinger, John Bates, Les Jardine, Son Nguyen, Homer Weed, Knud Pedersen, Gregory Gdowski, Richard Van Konynenburg, William Bourcier, Carol Bruton, Stan Prussin, Andrew Zolnay, David Stahl, Richard Morissette, and Diane Harrison-Giesler. In addition, we extend a special thanks to William O'Connell for his helpful and meaningful review; Robert Day for his relentless pursuance of numerous corrections and resolution of review comments; and finally, to Sue Garber, for the fantastic job, performed with a smile, of putting the pieces together (again and again).

Ray B. Stout

Herman R. Leider

October 1991

## Contents

Preface .....	i
Abbreviations and Acronyms .....	ix
Executive Summary .....	xi
1. Introduction .....	(V 1.0, 14 p)
1.1 Overview .....	1-1
1.2 Technical Objectives .....	1-1
1.3 Quality Objectives .....	1-3
1.4 Types of Waste Forms .....	1-4
1.5 Spent Fuel Waste Forms .....	1-4
1.6 Physical Inventory .....	1-5
1.7 Radionuclides .....	1-6
1.8 Decay Heat and Criticality .....	1-7
1.9 Radiation Field .....	1-10
1.10 Hardware .....	1-13
1.11 Modeling .....	1-13
1.12 Burnup Models .....	1-14
1.13 Glass Modeling Status .....	1-14
2. Design Data for Waste Forms .....	(V 1.0, 1 p)
2.1 Spent Fuel Waste Form .....	(V 1.0, 0 p)
2.1.1 Radionuclide Content .....	(V 1.0, 1 p)
2.1.1.1 Present Inventory .....	(V 1.0, 24 p)
2.1.1.2 Projected Inventory .....	(V 1.0, 19 p)
2.1.1.3 Radionuclide Activity vs. History .....	(V 1.0, 17 p)
2.1.1.4 Decay Heat vs. Time .....	(V 1.0, 17 p)
2.1.1.5 Fission Gas Release Distribution .....	(V 1.0, 18 p)
2.1.2 Structural Characteristics and Dimension .....	(V 1.0, 1 p)
2.1.2.1 Fuel Assemblies .....	(V 1.0, 15 p)

2.1.2.2	PWR Fuel.....	(V 1.0, 9 p)
2.1.2.3	BWR Fuel.....	(V 1.0, 8 p)
2.1.2.4	Non-Zircaloy™ Clad Fuel.....	(V 1.0, 1 p)
2.1.2.5	Hardware .....	(V 1.0, 13 p)
2.1.3	Repository Response.....	(V 1.0, 0 p)
2.1.3.1	Cladding Degradation.....	(V 1.3, 24 p)
2.1.3.2	UO <sub>2</sub> Oxidation in Fuel.....	(V 1.3, 37 p)
2.1.3.3	Gaseous Radionuclide Release from Cladding.....	(V 1.0, 2 p)
2.1.3.4	Gaseous Radionuclide Release from UO <sub>2</sub> Fuel.....	(V 1.0, 5 p)
2.1.3.5	Dissolution-Radionuclide Release from UO <sub>2</sub> Fuel.....	(V 1.3, 84 p)
2.1.3.6	Soluble-Precipitated/Colloidal Species .....	(V 1.0, 25 p)
2.1.3.7	Radionuclide Release from Hardware.....	(V 1.0, 26 p)
2.2	Glass Waste Form.....	(V 1.0, 1 p)
2.2.1	Radionuclide Content.....	(V 1.0, 0 p)
2.2.1.1	Present Inventory .....	(V 1.0, 6 p)
2.2.1.2	Projected Inventory.....	(V 1.0, 8 p)
2.2.1.3	Radioactivity and Decay Heat vs. Time.....	(V 1.0, 9 p)
2.2.1.4	Glass Species Composition Statistics.....	(V 1.0, 17 p)
2.2.1.5	Fracture/Fragmentation Statistics.....	(V 1.3, 4 p)
2.2.2	Repository Response.....	(V 1.0, 0 p)
2.2.2.1	Gaseous Release from Glass .....	(V 1.0, 1 p)
2.2.2.2	Dissolution Radionuclide Release from Glass .....	(V 1.3, 14 p)
2.2.2.3	Soluble-Precipitated/Colloidal Species.....	(V 1.3, 2 p)
2.3	Special Cases Waste Forms.....	(V 1.0, 1 p)
2.3.1	Damaged Spent Fuel.....	(V 1.0, 2 p)
2.3.2	Non-LWR Spent Fuel.....	(V 1.0, 9 p)
3.	Scientific Basis for Predictive Model Development.....	(V 1.0, 0 p)
3.1	Spent Fuel Cladding Failure.....	(V 1.0, 5 p)

3.1.1	Experimental Parameters for Failure Models.....	(V 1.0, 7 p)
3.1.2	Failure Models.....	(V 1.0, 1 p)
3.2	Spent Fuel Oxidation.....	(V 1.0, 3 p)
3.2.1	Experimental Parameters for Oxidation Models.....	(V 1.0, 21 p)
3.2.2	Oxidation Models.....	(V 1.3, 65 p)
3.3	Spent Fuel Fission Gas Release.....	(V 1.0, 0 p)
3.3.1	Experimental Parameters for Fission Gas Release.....	(V 1.0, 6 p)
3.3.2	Release Models.....	(V 1.0, 3 p)
3.4	Spent Fuel Dissolution.....	(V 1.0, 2 p)
3.4.1	Experimental Parameters for Dissolution.....	(V 1.0, 3 p)
3.4.1.1	Dissolution Rates.....	(V 1.0, 6 p)
3.4.1.2	Solubility Limits.....	(V 1.0, 2 p)
3.4.1.3	Solubility Limiting Phases.....	(V 1.0, 4 p)
3.4.2	Spent Fuel Dissolution Models.....	(V 1.3, 57 p)
3.5	Glass Dissolution.....	(V 1.0, 1 p)
3.5.1	Experimental Parameters for Glass Dissolution.....	(V 1.3, 32 p)
3.5.2	Glass Dissolution Models.....	(V 1.3, 28 p)
3.6	Other Release Sources of Radionuclides.....	(V 1.0, 0 p)
3.6.1	Crud.....	(V 1.0, 2 p)
3.6.2	Hardware.....	(V 1.0, 1 p)
3.6.3	Cladding.....	(V 1.0, 3 p)
	Bibliography.....	(V 1.0, 4 p)
	Appendix A. Quality Assurance Information.....	(V. 1.3, 7 p)
	Appendix B. Technical Data Submissions.....	(V. 1.3, 4 p)

## Abbreviations and Acronyms

AEM	analytical electron microscopy
ASTM	American Society for Testing and Materials
BET	Brunauer-Emmett-Teller
BWR	boiling-water reactor
DHC	delayed hydride cracking
DIW	deionized distilled water
DTN	data-tracking number
DWPF	defense waste-processing facility
EDS	energy-dispersive spectroscopy
EELS	electron-energy-loss spectroscopy
EF	error factor
HBR	H. B. Robinson
HLW	high-level waste
LWR	light-water reactor
MWd	megawatt day
NIST	National Institute of Standards and Technology
NMR	nuclear magnetic resonance
NNWSI	Nevada Nuclear Waste Site Investigations
NRC	Nuclear Regulatory Commission
ODB	oven drybath
O/M	oxygen-to-metal
PA	performance assessment
PNNL	Pacific Northwest National Laboratory
PWR	pressurized-water reactor
QA	quality assurance
RMS	root mean square
SIMS	secondary ion mass spectroscopy
S/V	surface/volume
SA/V	surface area/volume
SCCTP	substantially complete containment time period
SEM	scanning electron microscopy

<b>SNF</b>	spent nuclear fuel
<b>SPFT</b>	single-path, flow-through
<b>SRM</b>	standard reference material
<b>SS</b>	stainless steel
<b>TDMS</b>	Technical Data Management System
<b>TGA</b>	thermal gravimetric analysis
<b>TP</b>	Turkey Point
<b>TSPA</b>	total system performance assessments
<b>TSPA-VA</b>	total system performance assessment–viability assessment
<b>WFCR</b>	<i>Waste Form Characteristics Report</i>
<b>WP</b>	waste package
<b>WPA</b>	waste-package assemblage
<b>WPDD</b>	Waste Package Development Department
<b>XRD</b>	X-ray powder diffraction
<b>XRF</b>	X-ray florescence
<b>YMP</b>	Yucca Mountain Site Characterization Project

## Executive Summary

This *Waste Form Characteristics Report (WFCR)* update, Version 1.3, incorporates substantial additions and changes to following 10 sections of the WFCR:

- 2.1.3.1 Cladding Degradation
- 2.1.3.2 UO<sub>2</sub> Oxidation in Fuel
- 2.1.3.5 Dissolution Release from UO<sub>2</sub>
- 2.2.1.5 Fracture /Fragmentation Studies of Glass
- 2.2.2.2 Dissolution Radionuclide Release from Glass
- 2.2.2.3 Soluble-Precipitated/Colloidal Species from Glass
- 3.2.2 Spent-Fuel Oxidation Models
- 3.4.2 Spent-Fuel Dissolution Models
- 3.5.1 Glass Dissolution Experimental Parameters
- 3.5.2 Glass Dissolution Models

Section 2.1 includes accumulated data for spent-fuel waste forms. Section 2.1.3.1 on cladding failure describes process models for strain failure, delayed hydride cracking, and mechanical failure from rock drops. Also included is a discussion of as-received fuel with deteriorated cladding or fuel that is made with stainless-steel cladding that is expected to fail soon after the waste package (WP) fails. This section is considered preliminary and has been reproduced with minor modifications from Section 2.7.2 of the *Waste Form Degradation and Radionuclide Mobilization Preliminary Total System Performance Assessment*. Additional experimental and model-development efforts are necessary to substantiate the use of Zircaloy™ cladding as a barrier.

Experimental results of the thermogravimetric analysis (TGA) and oxidation drybath (ODB) spent-fuel-oxidation studies are in Section 2.1.3.2. These data provide the results of the oxidation studies, including the burnup and post-oxidation analyses performed. Detailed oxidation curves (oxygen-to-metal ratio as a function of time at operating temperature) for individual samples are included.

Spent-fuel dissolution and subsequent transport processes in groundwater are generally considered to be the main routes by which radionuclides could be released from a geological repository. Laboratory testing of the behavior of spent fuel under the conditions expected in a repository provides the information necessary to determine the magnitude of the potential radionuclide source term at the boundary of the fuel's cladding. Dissolution (leach) and release-rate tests of spent fuel and uranium dioxide (UO<sub>2</sub>) are the most important aqueous data-collection activities in spent-fuel waste-form testing. Section 2.1.3.5 summarizes the available Yucca Mountain Site Characterization

Project (YMP) spent-fuel and unirradiated-uranium-oxide dissolution and release data. The three dissolution activities (i.e., saturated [semi-static], flow-through, and unsaturated [drip] tests) have been separated, based on the different technical techniques involved in conducting each type of experiment. The intrinsic  $UO_2$  dissolution rate sets an upper bound on the aqueous radionuclide release rate, even if the fuel is substantially degraded by other processes such as oxidation. Dissolution responses are provided, based on limited data, for spent fuel that is substantially degraded to other oxidation states. In scenarios for the potential geological repository, it is assumed that the cladding has failed, and water as vapor or liquid contacts the fuel. Drip tests that simulate the unsaturated and oxidizing conditions expected at the proposed repository site have provided data to evaluate the long-term behavior of spent nuclear fuel.

Section 2.2 includes accumulated data for glass waste forms. Section 2.2.1.5 documents the recommended values of glass surface area to be used in estimating glass-alteration rates in the total system performance—viability assessment (TSPA-VA) modeling work. Unsaturated (drip) tests have been in progress since the mid-1980s. The tests using actinide- and technetium-doped Savannah River Site 165 glass are termed the N2 Test Series. Tests with a West Valley Demonstration Project former reference glass (ATM-10) are termed the N3 Test Series. Drip tests are designed to replicate the synergistic interactions among waste glass, repository groundwater, water vapor, and sensitized 304L stainless steel in the proposed geological repository. The information provided in Section 2.2.2.2 includes long-term data relevant to glass reaction under conditions anticipated for an unsaturated repository. Measurements obtained from each test series include the following:

- Rate of glass reaction and radionuclide release as a function of time
- Description of the distribution of radionuclides in solution (i.e., dissolved in solution, associated with colloidal material, or sorbed onto metal components of the test)
- Monitoring of the interactions among the various components in the test

Ultimately, the results from these tests will be used to formulate and validate source terms of models used in WP performance assessment codes. Section 2.2.2.3 includes a brief description of the colloidal particle analysis of data from the unsaturated tests on waste glass reported in Section 2.2.2.2.

Section 3 contains descriptions of models for the responses of spent fuel and glass waste forms. Section 3.2.2 comprises a discussion of the oxidation-response model that was developed for the two phase-transitions  $UO_2 \rightarrow U_4O_9$  and  $U_4O_9 \rightarrow U_3O_8$ , and for the model predictions for the geological repository. Because of the higher potential risk associated with the  $U_3O_8$  phase, its modeling-phase transformation is emphasized. Arrhenius kinetic parameters for both phase transformations were obtained from a set of thermogravimetric analysis (TGA) experiments. The two phase-formation models gave reasonable responses when compared with an independent set of experimental

data. The oxidation history of the oven drybath (ODB) experiments could be explained by an envelope of various sizes of  $\text{UO}_2$  grains. There is a focus on new material concerning the formation of  $\text{U}_3\text{O}_8$ . Although it has been predicted that burnup would be a very important property in spent-fuel oxidation, only recently has experimental evidence been obtained verifying this theoretical prediction. In the model, the activation energy for the phase transformation  $\text{U}_4\text{O}_9 \rightarrow \text{U}_3\text{O}_8$ , varies linearly with burnup. Experimental evidence shows that, for burnups greater than  $\sim 40$  MWd/kgU,  $\text{UO}_2$  grains undergo major restructuring to a much finer and more porous structure in the rim region of spent-fuel pellets.

Modeling of the aqueous dissolution- and release-rate responses of uranium oxide spent-fuel waste forms is described in Section 3.4.2. The derivation of dissolution-rate function forms is in Section 3.4.2.2. The previous nonequilibrium, thermodynamic model for dissolution rate (WFCR, Version 1.2) has been extended to include surface chemisorption effects. The surface chemisorption phenomenon is represented by the well-known Tempkin isotherm. This extension provides the theoretical basis for function forms used to regress the existing experimental data. Additional model development for radiolysis effects is in progress, but is not included at this revision. In Section 3.4.2.3, numerical regression analyses, using various dissolution-rate functions are discussed. The incorporation of available new data has not changed the previous model significantly. The regression of the existing data to a dissolution-rate model suggested by outside experts has a small R-square-value ( $R^2$ ) measure relative to the  $R^2$  of the nonequilibrium, thermodynamic model. In Section 3.4.2.4, the aqueous release-rate modeling approach has not been changed. It has, however, been used as a basis to evaluate film concentrations of radionuclides in the alteration layers with data from the unsaturated drip tests. This film analysis and values of the film concentrations are discussed in Section 3.4.2.5.

The topic of Section 3.5.1 is experimental parameters and data as a basis for glass waste-form-dissolution models. These parameters include exposed glass surface area; solution chemistry, including pH and dissolved iron; temperature; and glass radionuclide content. To provide a context with which to place the parameters, a succinct summary of the fundamental rate equations in the model is included. More information on the model and its development is presented in Section 3.5.2 on dissolution models.

A chemical model of glass corrosion is used in Section 3.5.2 to predict the rates of release of radionuclides from borosilicate glass waste forms in a geological repository. The model is employed to calculate the rate of degradation of the glass and also to predict the effects of chemical interactions between the glass and repository materials (e.g., spent fuel, canister and container materials, backfill, cements, grouts). Coupling between the degradation processes affecting all these materials is expected.

## Section 2.1.3.1 Contents

2.1.3.1	Cladding Degradation .....	2.1.3.1-1
2.1.3.1.1	Introduction.....	2.1.3.1-1
2.1.3.1.2	Cladding-Failure Process Models .....	2.1.3.1-1
2.1.3.1.3	Juvenile Cladding Failures and Stainless Steel Cladding..	2.1.3.1-1
2.1.3.1.4	Creep (Strain) Failures.....	2.1.3.1-1
2.1.3.1.4.1	Pin Temperatures .....	2.1.3.1-2
2.1.3.1.4.2	Pin Stress.....	2.1.3.1-3
2.1.3.1.4.3	Pin Strain and Failure Limit.....	2.1.3.1-3
2.1.3.1.4.4	Zircaloy™ Dry Oxidation.....	2.1.3.1-7
2.1.3.1.4.5	Cladding Unzipping.....	2.1.3.1-7
2.1.3.1.5	Delayed Hydride Cracking.....	2.1.3.1-8
2.1.3.1.6	Mechanical Failure.....	2.1.3.1-9
2.1.3.1.7	Details of Cladding Mechanical Failure Process Model.....	2.1.3.1-9
2.1.3.1.7.1	Abstraction of Model.....	2.1.3.1-17
2.1.3.1.7.2	Recommended Model.....	2.1.3.1-17
2.1.3.1.8	Zircaloy™ Corrosion.....	2.1.3.1-18
2.1.3.1.9	Clad Unzipping.....	2.1.3.1-19
2.1.3.1.10	References.....	2.1.3.1-21

## **Section 2.1.3.1: Cladding Degradation**

**Version 1.3  
July 23, 1998**

### **2.1.3.1.1 Introduction**

This section on cladding degradation has been taken from the Waste Form Degradation and Radionuclide Mobilization Preliminary Total System Performance Assessment, Section 2.7.2 (Siegmann, 1998).

### **2.1.3.1.2 Cladding-Failure Process Models**

Process models for cladding failure were developed from strain failure, delayed hydride cracking, and mechanical failure from rock drops. In addition, some fuel is received with failed cladding or is made with stainless steel cladding, which is expected to fail soon after the waste package (WP) fails.

### **2.1.3.1.3 Juvenile Cladding Failures and Stainless Steel Cladding**

In this analysis, it is assumed that a small fraction of the fuel (0.1%, median, range 0.01 to 3%) will be received with failed cladding (juvenile cladding failures). A recent survey (Yang, 1997) shows that today's fuel has a pin failure rate of approximately 0.01%, but the historic failure rate is higher (0.1%). Rothman (1984) suggests much less than 0.1% of all fuel that will be accepted will be failed. There have been a few reactor cores with manufacturing defects having failure rates as high as 3%, but these have been rare.

Some early cores were designed with stainless-steel (SS) cladding. This represents about 1.15% of the spent fuel (CRWMS M&O, 1997a). Because the SS cladding has a much higher corrosion rate than does the Zircaloy™ cladding, no credit is taken for SS cladding, and it is assumed to fail when the WP fails, exposing the complete pin to the environment. No range was assigned to the SS fraction.

### **2.1.3.1.4 Creep (Strain) Failures**

A Monte Carlo model was developed to estimate the fraction of spent fuel cladding that becomes perforated from creep (strain). The model analyzes the performance of eight groups of pins, distributed across the WP, as a function of time. It calculates the time in which the pin becomes perforated and the time in which the cladding unzips. The pin properties, initial conditions, and performance correlations are assumed to be described using log-normal distributions. This analysis is repeated 5200 times, and the statistics are collected. The analysis is performed for two groups of WPs: one operating at the average temperature and power and one operating at a hot (design-basis) temperature and power. Both

Rothman 1984) and Pescatore (1989; 1994) reviewed other cladding failure mechanisms and concluded that strain failure was the dominant failure mechanism during dry storage.

#### 2.1.3.1.4.1 Pin Temperatures

Pin temperatures were radially distributed across the WP, and time histories were taken from a detailed analysis conducted by the Waste Package Development Department (WPDD) (Bahney, 1995). Temperatures for the average and design-basis WP are both used. The average WP contains 21 assemblies at 445 W/assembly, and the hot (design-basis) WP contains 21 assemblies at 850 W/assembly. In the Monte Carlo analysis, the temperature of an individual pin is sampled by assuming that the pin temperature is log normally distributed about a median temperature. The error factor (EF) is the ratio of the median to 95% quantile. For this analysis, an error factor of 1.25 was used, based on the difference in predicted temperatures for the WPs in different locations in the repository. The median peak temperature of the cladding in the center of the design-basis WP is 327°C (see Figure 2.1.3.1-1).

When considering the temperature uncertainties, the extreme (5%) pins could have a peak temperature as hot as 408°C and could possibly fail from creep. The use of temperatures that are continuously distributed produces this temperature maximum in the tail of the log-normal distribution. These high temperatures are a product of the Monte Carlo simulation and may exceed the design analysis, which has no pins (hottest pin in hottest WP) exceeding the 350°C limit. The average pin in the design-basis (hot) WP has a peak temperature of 289°C. In the design-basis WP, the median pins do not undergo creep failure. The average WP operates at much cooler temperature, with a median peak center pin temperature of only 237°C (see Figure 2.1.3.1-1). The average pin in the average WP has a peak temperature of 220°C. No creep failures are observed with this group. It is assumed that the repository contents comprises 95% average WPs and 5% design-basis WPs.

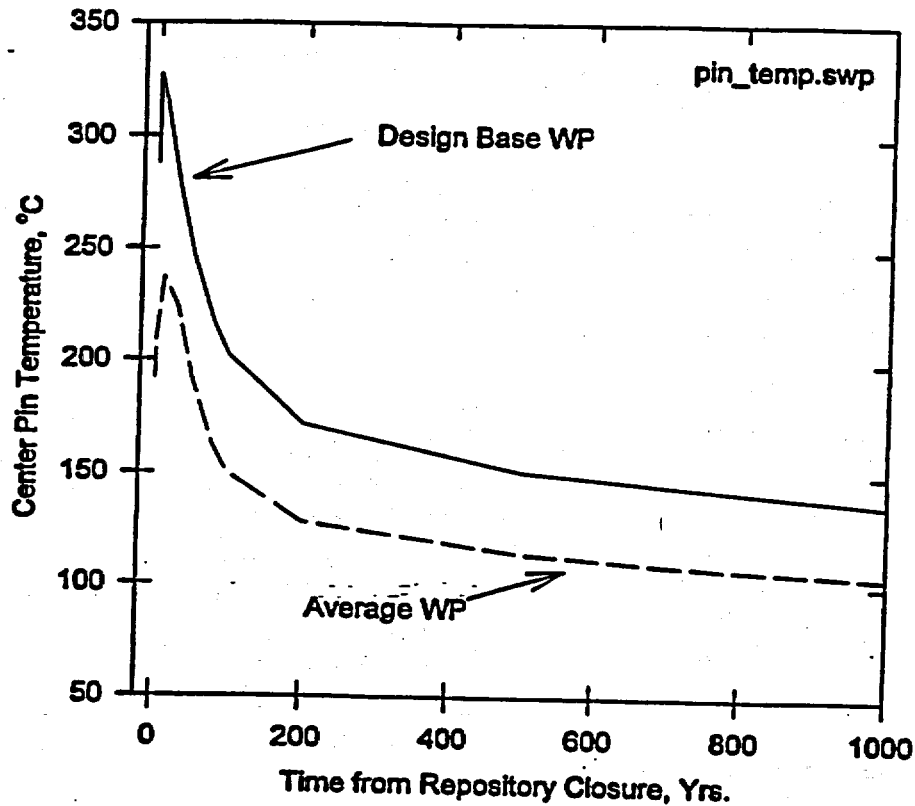


Figure 2.1.3.1-1 Center fuel pin temperature distribution

#### 2.1.3.1.4.2 Pin Stress

For this analysis, the median stress for a Westinghouse 17 x 17 (W1717WL) assembly of 32 MPa room temperature (Pescatore, 1994) was used. A log-normal distribution is assumed with an EF (ratio of the median to 95% quantile) of 1.4. This represents the observed range for fission gas release reported by Manzel (1997). Fission gas is the principal source of internal pressure. The stress at any time is calculated using the ideal gas law and the current temperature. In addition, the stress is reduced by adjusting the free volume inside the cladding from the strain that has expanded it outward.

#### 2.1.3.1.4.3 Pin Strain and Failure Limit

The model assumes that the cladding creeps as a function of stress, temperature, and time using the creep correlation developed by Matsuo (1987). Figure 2.1.3.1-2 gives the strain for pins operating at a constant temperature for 10 yr. This figure shows that creep failures might be expected if the cladding operated in a repository for long periods of time at temperatures great than 350°C, the cladding temperature design limit. At the temperatures observed in the average WP, little or no creep is expected. The model presented here assumes that the strain is log-normal distributed with the median value from Matsuo's correlation and an EF (ratio of the

median to 95% quantile) of 2.0. This error factor is derived by comparing Matsuo's correlation with experimentally measured strains. The 95% quantile strain is two times greater than the median, as predicted by Matsuo's correlation.

Earlier modeling used creep correlation from Peehs and Fleisch (1986). This model predicted slightly higher creep rates below 300°C and slightly lower creep rates above that temperature. The results are very similar to those using Matsuo's (1987) correlation, and neither model predicts any creep failures for the average WP because of the low cladding temperatures.

Cladding was assumed to become perforated when a strain limit of 4% was reached. This is the median and mean value of 55 experiments summarized in Table 2.1.3.1-1. The 4% strain failure criteria is also assumed to be a median value for the failure strain, and an EF (ratio of the median to 95% quantile) of 10.0 was used. This error factor was selected to cover all but one of the experimental values. It permits 5% of the pins to fail with strains less than 0.4%. The 4% strain limit could be conservative. Lowry et al, (1981, p. 219), reports the strength and ductility of spent fuel cladding from three different pressurized water reactors (PWRs). The tests were expanding mandrel tests performed at 371°C. This is a possible temperature for creep failure because the pins that fail in the design-basis WP have temperatures greater than the median. The measured, uniform strains were about 15%, and the ultimate stress was typically above 250 MPa, again higher than expected in the WP.

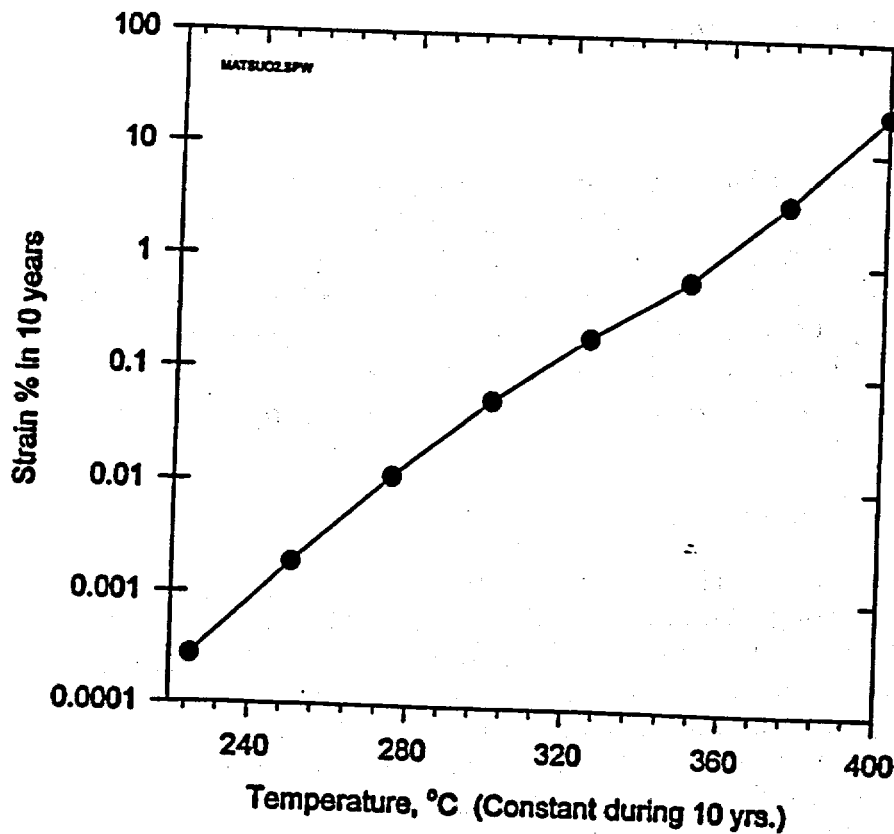


Figure 2.1.3.1-2 Cladding strain vs. temperature

**Table 2.1.3.1-1 Strain limit observed in testing**

Source	Stress Temp. (°C)	Ult. Tens Stress (MPa)	Unif. Elong. Strain (%)	Number of Tests	Notes
VanSwam, 1997	25	910	1.50	1	Irrad
VanSwam, 1997	25	775-883	2.00	2	Irrad
VanSwam, 1997	25	660-856	4.00	3	Irrad
VanSwam, 1997	25	710-878	5.00	3	Irrad
VanSwam, 1997	25	840	6.00	1	Irrad
VanSwam, 1997	350	602	3.00	1	Irrad
VanSwam, 1997	350	686-666	4.00	6	Irrad
VanSwam, 1997	350	376-417	4.50	2	Irrad
Puls, 1988	25	625-1079	4.10	3	Unirr, hydrides added
Puls, 1988	-25	659-689	4.70	5	Unirr, hydrides added
Puls, 1988	25	698-730	6.00	3	Unirr, hydrides added
Einzigler et al., 1982	482	43*	1.70	2	Irrad, no failure
Einzigler et al., 1982	510	39*	3.40	5	Irrad, no failure
Einzigler et al., 1982	571	23-50*	5.00	3	Irrad, no failure
Einzigler et al., 1982	571	33-39*	7.00	5	Irrad, no failure
Chung et al. 1987	325	337	0.40	1	Irrad
Chung et al. 1987	325	344	0.80	1	Irrad
Chung et al. 1987	325	384-498	1.00	3	Irrad
Chung et al. 1987	325	469-545	2.00	2	Irrad
Chung et al. 1987	325	552	11.00	1	Irrad
Yagee et al., 1980	325	275	0.01	1	Irrad
Yagee et al., 1979	360	200	0.40	1	Irrad
Number of Tests				55	
Mean Strain %			4.0		
Median Strain %			4.0		
Standard Deviation			2.1		
Variance			4.2		

\*Stress at which creep test was performed.

At a strain of 4%, the cladding is assumed to fail by developing a perforation, relieving the internal pressure and stress. The cladding perforation then permits UO<sub>2</sub> oxidation and cladding unzipping if oxygen is present (i.e., if the WP has been breached). For perforated cladding, it is assumed that the hole developed is 2 mm<sup>2</sup>, the observed hole size reported in pin burst tests (Lorenz, 1980).

For the design-basis (hot) WPs, 3% of the pins become perforated by creep strain. No pins in the average WP fail because of the low temperatures in that group of WPs. Assuming that 5% of the WPs operate at the design conditions, 0.15% of the pins are expected to become perforated by strain failure. The range was selected from 0.01%, (representing current pin failure rates) to 1.5% (representing one order of magnitude increase from the median). Figure 2.1.3.1-3 gives the percentage of pins that are simulated to perforate as a function of WP surface temperature for the average WP and for the design-basis WP. WP surface temperatures are affected by location in the repository and by water ingress rates. For the average WP, the figure shows (labeled base case) that the current WP surface temperature is almost 100°C, from where cladding perforation would increase dramatically. The design-basis WP represents a very hot WP, being loaded with 21 assemblies, all of which have the maximum power. It is seen that, for the base case, perforation could increase if the WP surface temperature were increased.

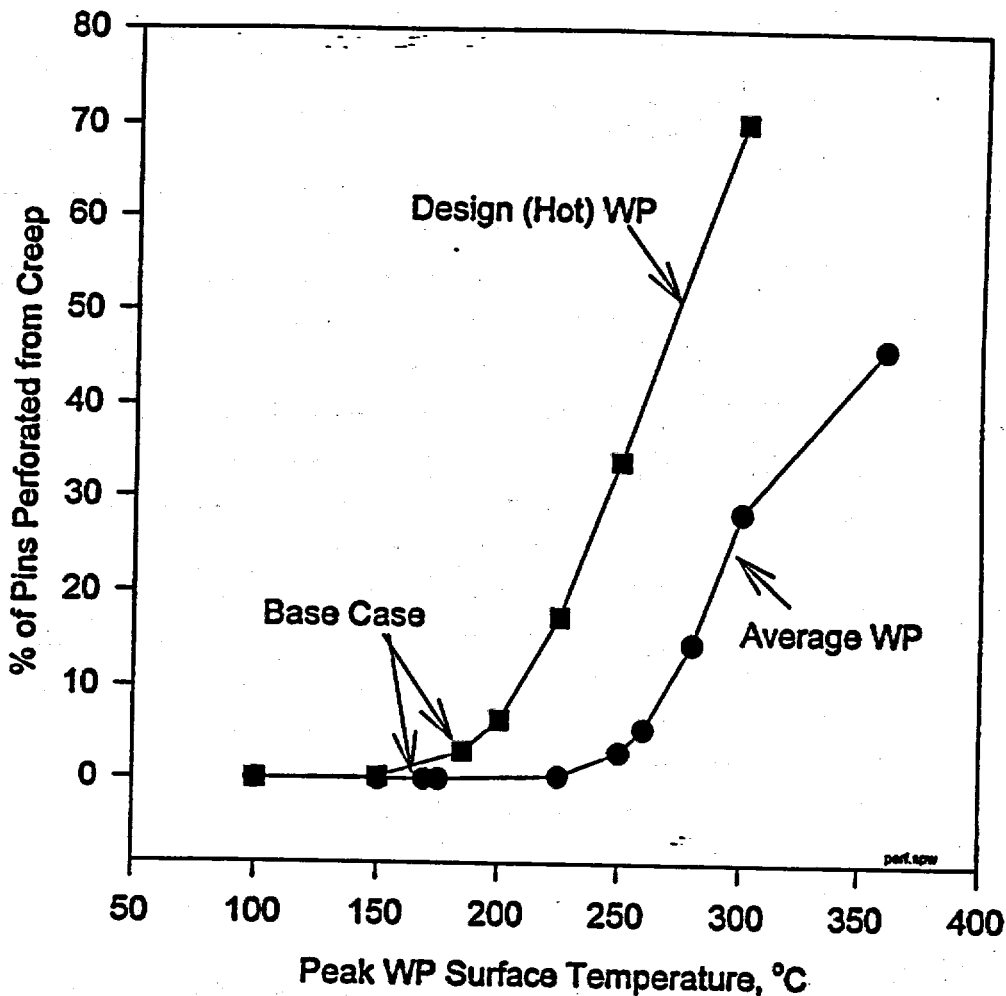


Figure 2.1.3.1-3 Percent cladding perforation due to creep vs WP surface temperature

#### 2.1.3.1.4.4 Zircaloy™ Dry Oxidation

For fuel rods in failed WPs, Zircaloy™ oxidation was modeled using the equations developed by Einziger (1994). The oxidation has the effect of thinning the clad. The thinning is small and increases the stress slightly but has a very small effect on strain failure. The second effect is direct cladding failure. However, no fuel rods were observed to fail directly by dry oxidation through the cladding thickness in these analyses. This is consistent with earlier analysis that showed that this mechanism's unzipping is about four orders of magnitude slower than cladding unzipping and requires 10,000 yr at temperatures greater than 250°C to fail the cladding by this mechanism (CRWMS M&O, 1995). If the cladding were wet, the wet Zircaloy™ oxidation rates would be slightly slower than the dry Zircaloy™ oxidation rates and make little change on the effects of cladding oxidation.

#### 2.1.3.1.4.5 Cladding Unzipping

If both the cladding and WP are penetrated, the  $UO_2$  fuel can oxidize to  $U_3O_8$ , increasing the fuel volume and tearing the clad. The model used for cladding unzipping was developed by Einziger (1994). The cladding unzips in two phases: an incubation phase and an unzipping phase. In the incubation phase, the oxidized spent fuel phase builds up just inside the perforation until tearing starts. The time required for crack propagation is small compared with the incubation time and can be ignored.

Figure 2.1.3.1-4 shows the fraction of perforated pins that might unzip using the Einziger model. For the design-basis (hot) WP, all perforated pins would unzip in a juvenile failed WP (open to air at time = 0). If the WP were not breached for 200 yr, very few perforated pins would unzip. For the average WP, only 56% of the perforated pins in a juvenile failed WP would unzip. If the WP were to stay sealed for 50 yr, very few perforated pins would unzip. This analysis shows that cladding unzipping is unlikely for the YMP-designed WPs, which have expected lifetimes of thousands of years.

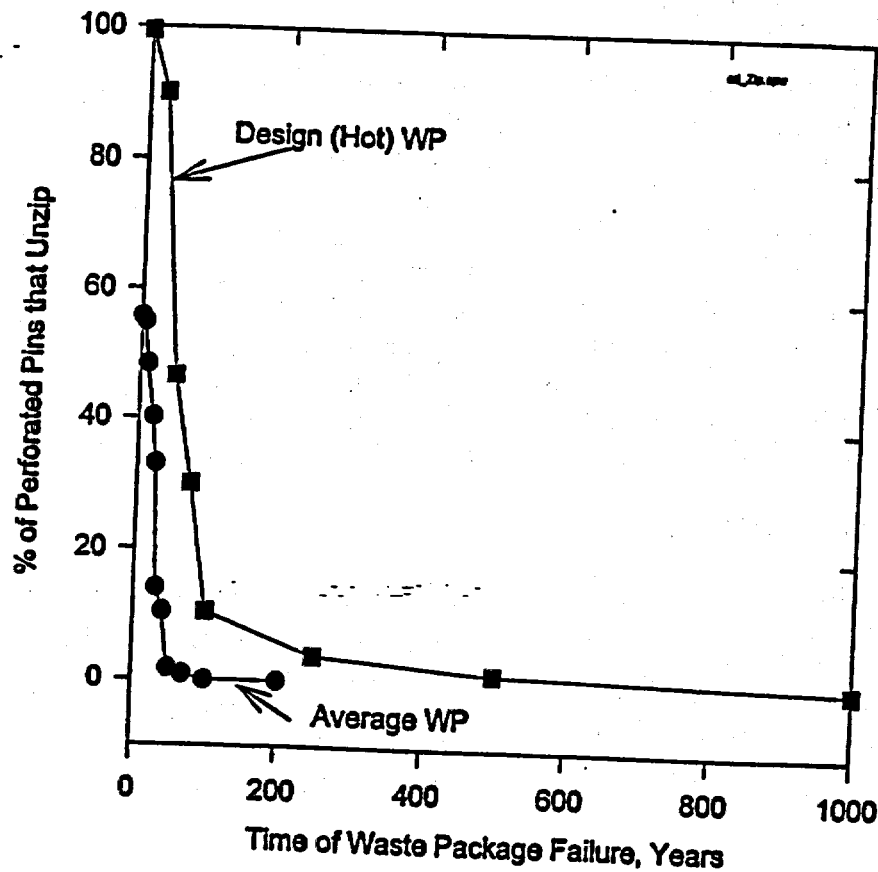


Figure 2.1.3.1-4 Clad unzipping vs WP failure time

### 2.1.3.1.5 Delayed Hydride Cracking

Delayed hydride cracking (DHC) under repository conditions is another cladding failure mode to consider. A separate analysis was performed and showed that only a very small percentage (< 0.01%) of cladding would fail by this mechanism; therefore, DHC was not incorporated into the cladding Monte Carlo analysis.

At repository closure, the design-basis spent-fuel cladding heats to a maximum of 330°C and then slowly cools over many years (to about 200°C at 100 yr). For DHC, the predicted threshold stress intensity factor for the onset of crack propagation is compared with the stress intensity factor. It is assumed that, if crack propagation starts, there is sufficient time to propagate across the cladding.

Using a model for threshold stress intensity factor ( $K_{IH}$ ) (Shi, 1994), crack propagation would be expected if the stress intensity reached a threshold level of 6.7 MPa·m<sup>0.5</sup>. Stresses for Westinghouse W1717WL fuel are predicted to increase from 66 MPa to 100 MPa as burnup increases from 40 to 60 MWd/kgU (median crack depth, at a peak repository cladding temperature of 350°C). This produces a stress intensity factor of 0.28 to 0.40 MPa·m<sup>0.5</sup>. This stress intensity is a factor of 17 to 24 smaller than the threshold stress intensity limits. Cracks at the largest possible size

for surviving reactor operation (28% of wall thickness, probability =  $6.8E-5$ /pin) produce stress intensity factors of 1.39 to 2.00  $\text{MPa}\cdot\text{m}^{0.5}$ , a factor of 2 to 5 smaller than the threshold range. In light of these differences, a statistical model for DHC was not developed because only a very small fraction of pins would fail.

A mapping of the temperature and stress field, where hydride reorientation has been observed, and comparison with expected stresses and temperatures suggests that hydride reorientation is not expected under repository conditions. Strain experiments by Puls (1988) using reoriented hydrides suggest that, even if hydride reorientation did occur, the cladding strength would be only marginally affected.

#### 2.1.3.1.6 Mechanical Failure

A preliminary model has been developed for the fraction of fuel rods broken, and fuel exposed, because of mechanical failure of cladding. The repository drifts are assumed to collapse at some time a few hundred years after emplacement, as rubble blocks pile on the intact containers and then crush the containers at some later time when the containers have degraded to the point of losing their mechanical integrity. The sizes of the rubble blocks are derived from information on rock-joint spacings and angles, and the height from which the blocks fall is determined from the design of the WP.

The number of fuel rods that break from the impact of a rubble block is limited by the available energy: breakage stops when the energy of the falling block is consumed. The energy necessary to break a single fuel rod is calculated by using beam theory and an elastic-plastic-stress-strain relation. An approximate method is developed for treating the effects of load sharing when one fuel rod contacts another.

Predicting the loading on the fuel rods is difficult because rubble blocks have irregular bottom faces. As an approximation, the blocks are modeled as having protrusions or "punches" on their bottom faces. Two types of punches are considered: one simulates the vertex of a block, and the other simulates an edge. All of the energy of the falling block is concentrated on the rods under the punches. To estimate the exposure of fuel, the length of each broken rod that lies under the punch is assumed to have its cladding entirely removed.

Previous total system performance assessments (TSPAs) have treated cladding by simply assuming a certain level of cladding performance. This model is the first attempt to quantify the effect of mechanical loading on cladding performance.

#### 2.1.3.1.7 Details of Cladding Mechanical Failure Process Model

Over long times, the WP containment barriers may degrade to the point that they can no longer provide mechanical protection to the spent fuel inside them. The following sequence of events is considered: The ground support for the emplacement drifts is designed to last only until the repository is closed; thus, the

emplacement drifts will collapse and be filled with rubble blocks. Some of these blocks will lie on the waste containers. When the containers become sufficiently weak, the blocks will crush the container and impact the fuel assemblies inside it. The blocks will accumulate kinetic energy as they fall, then dissipate the energy in bending and breaking the fuel rods. Breakage stops when all the kinetic energy is dissipated.

The fuel cladding and spacer grids of nuclear fuel are typically made of zirconium alloy and are, thus, extremely resistant to corrosion. Because of this corrosion resistance, the fuel assemblies should maintain their geometry even when the disposal containers are breached. However, when the disposal containers lose their mechanical integrity, blocks of rock can fall on the assemblies and break them.

Because the fuel rods are long and slender, they act as simple beams with supports at the spacer grids. A span of cladding from one spacer grid to the next is taken to be a simple elastic-plastic beam with clamped ends. The spacer grids in fact allow some rotation at the ends of the span, but the use of clamped ends simplifies the treatment and conservatively reduces the amount of energy the beam can absorb. The cladding is treated as a thin-walled tube with a radius equal to the arithmetic mean of the inner and outer radii. Although the uranium dioxide fuel has negligible flexural strength by itself, it nevertheless contributes to the stiffness of the fuel rod. Because irradiated fuel is in the form of discrete pellets or fragments, the fuel resists compression but can be readily extended. As a result, the neutral axis moves toward the compressive surface of the fuel rod. In this treatment, the neutral axis is taken to lie at the surface of the fuel rod. Note that the neutral axis is on the bottom of the fuel rod near the supports and on the top near the load. This treatment is conservative in that it gives the smallest energy absorption.

The failure behavior of the cladding depends on the stress-strain properties of the cladding. Two types of fuel, with different mechanical properties, were considered. The properties were chosen to simulate typical and high-burnup fuel assemblies. Mechanical failure of fuel rods will occur only long after emplacement, when temperatures in the repository will be low. Accordingly, room-temperature mechanical properties were used. For typical fuel, the yield strength of the cladding is 780 MPa, the ultimate tensile strength is 925 MPa, and the uniform tensile elongation is 3.5% (Lowry et al., 1981, p. 219). For high-burnup fuel, the uniform tensile elongation is 0.15% (Garde, 1986). The elongations listed previously are taken to include the plastic portion only. For both types of fuel, the elastic modulus of the cladding is 99 GPa. For the calculations, the tensile portion of the stress-strain curve is taken to be composed of two line segments; these connect the origin, the tensile yield stress and strain, and the ultimate tensile stress and uniform tensile elongation (elastic plus plastic), respectively. The stress-strain curve is determined by properties for typical fuel. To simplify the treatment, the curve for high-burnup fuel is taken to coincide with that for typical fuel, but it is truncated at a smaller strain.

As is discussed subsequently, the external load from a rubble block is taken to be a point load at midspan. The loading, the geometry of the cladding, and the stress-strain curve of the cladding have been used with standard elastic-plastic beam theory to calculate the midspan displacement as a function of applied force. This model, however, requires substantial amounts of computation. For efficiency, it is replaced by the following empirical force-displacement function (CRWMS M&O, 1997a):

$$D(F) = F \frac{D_y}{F_y} \text{ if } 0 \leq F < F_y \quad (2.1.3.1-1)$$

$$D(F) = F \frac{D_y}{F_y} + \left( D_{ut} - F_y \frac{D_y}{F_y} \right) \left( \frac{F - F_y}{F_{ut} - F_y} \right)^{3.468} \text{ if } F_y \leq F < F_{ut} \quad (2.1.3.1-2)$$

In Equations 2.1.3.1-1 and 2.1.3.1-2,  $F$  and  $D$  are the current force and displacement, respectively.  $F_y$  and  $D_y$  are the force and displacement at the onset of yielding (i.e., when the maximum fiber stress reaches the yield stress), and  $F_{ut}$  and  $D_{ut}$  are the force and displacement when the maximum fiber strain reaches the uniform elongation for typical fuel. Note that positive forces and displacements are downward. For a given assembly design,  $F_y$ ,  $D_y$ ,  $F_{ut}$ , and  $D_{ut}$  are constants. They are calculated with the equations

$$F_y = 2.941 \cdot 10^{10} \frac{tR^2}{l}, \quad (2.1.3.1-3)$$

$$D_y = 1.636 \cdot 10^{-4} \frac{l^2}{R}. \quad (2.1.3.1-4)$$

$$F_{ut} = 4.374 \cdot 10^{10} \frac{tR^2}{l}, \text{ and} \quad (2.1.3.1-5)$$

$$D_{ut} = 4.016 \cdot 10^{-4} \frac{l^2}{R}, \quad (2.1.3.1-6)$$

where  $t$  is the thickness of the cladding wall,  $R$  is the mean cladding radius, and  $l$  is the distance between supports. For high-burnup fuel, Equations 2.1.3.1-1 and 2.1.3.1-2 still apply, but the force-displacement curve is truncated at smaller forces and displacements; the force and displacement at failure,  $F_{uh}$  and  $D_{uh}$ , respectively, are

$$F_{uh} = 3.262 \cdot 10^{10} \frac{tR^2}{l} \text{ and} \quad (2.1.3.1-7)$$

$$D_{uh} = 1.829 \cdot 10^{-4} \frac{f^2}{R}$$

(2.1.3.1-8)

Equations 2.1.3.1-1 and 2.1.3.1-2 agree with the beam-theory calculation to within 0.22% of  $D_{ut}$  for all applicable values of  $F$ .

Data on fuel-assembly design were obtained from qualified references. Data of interest include rod diameter, rod pitch, number of rods per side, cladding thickness, rod length, and maximum distance between spacer grids (CRWMS M&O, 1997a). Numbers of assemblies discharged were also obtained (DOE, 1996). Only pressurized-water reactor (PWR) fuel assemblies were considered because the fuel cladding of boiling-water reactor assemblies is normally protected by the flow channels. Complete data were available for 20 fuel types. These account for 31,931 of the 44,598 PWR fuel assemblies discharged through 1994 and were taken to be representative of all PWR fuel assemblies. No attempt was made to estimate the performance of the remaining assemblies.

A fuel assembly is an array of rods rather than an individual rod. Because the details of loading for individual rods are not known, forces from an impacting block are calculated in a one-dimensional continuum approximation. In this approximation, the array of rods is replaced by a continuum that has the force-displacement behavior that would result if the rods were smeared over space and the continuum responds to the impact by being displaced only in the direction of block motion. As a falling block of rock penetrates an assembly, the fuel rods will be compacted from their original density to a substantially higher density. The compacted region will accumulate ahead of the block. At the same time, the deformed but unbroken fuel rods will exert a retarding force on the block. At first, the force on the block increases as additional rods take up more of the load. At larger penetrations, however, the force becomes constant as rods begin to break and new rods take the place of the broken rods. The one-dimensional-continuum model is used to calculate the energy absorbed before rods begin to break and to calculate the additional energy per rod needed to break rods.

In developing the one-dimensional-continuum approximation, the block is approximated as a rigid body. Because the rods are light, their mass is neglected. The density of rods in the compacted region is taken to be 90% of the density for closely packed rods with a hexagonal pattern. Although not all fuel-rod positions are fueled, the number of fuel-rod positions is taken to be equal to the square of the number of fuel rods per side.

The standard disposal container for PWR fuel has a capacity of 21 assemblies; these are arranged in three columns of five assemblies and two columns of three assemblies. This arrangement is approximated in the continuum model by a uniform arrangement of assemblies in which each column is 21/5 assemblies tall. Edge effects and end effects are neglected. This is appropriate because blocks that fall near the edge of a WP are expected to strike rubble as well as fuel.

The external loading may be described in terms of the types and sizes of blocks that fall onto the assemblies, the exposure of assemblies to falling blocks, and the response of the assemblies upon impact. Each of these is discussed in the following text.

A distribution of block sizes for the repository rock has been developed from information on joint spacings and angles for the geologic member that would contain the potential repository (CRWMS M&O, 1997b). The block size distribution has been applied in the following way: Blocks are assumed to fall so that they cover the area of the fuel assemblies exactly once. The shape of the blocks is taken to be a right circular cylinder, and the height and diameter are taken to be equal. The axes of the blocks are taken to be vertical, and the blocks are assumed to fall freely onto the fuel assemblies.

In the standard disposal container, a component called a basket side cover, shaped as a segment of a circle, fills the space between the fuel assemblies and the curved wall of the container. Because the basket degrades before the containment barriers fail mechanically, the bottom layer of fuel assemblies can settle into the space originally occupied by the bottom basket side covers, and the overlying assemblies can also settle. Accordingly, the drop height was taken to be twice the height of a basket side cover. For the standard disposal container, the basket side cover is a segment of a circle with radius 711.7 mm and chord length 733 mm. From these dimensions, the height of the side cover is calculated to be 101.6 mm.

If the bottom surface of a falling block is flat, the energy of the block would be spread over as many rods as were exposed to the impact (e.g., the diameter of the block divided by the rod pitch). Because the blocks are irregular, however, this description is not realistic. To provide greater realism, two geometries were considered; both are intended to simulate the effects of irregular block surfaces. In these geometries, the bottom surface of the block is taken to have a rigid, massless protrusion called a punch. The entire energy of the falling block is concentrated onto the rods that lie under the punch. The punch is taken to be sufficiently long that only the punch contacts the fuel; the rods that lie under the remainder of the area of the block are not loaded. For purposes of calculating the amount of fuel exposed, the cladding is taken to be completely removed from the portion of a broken fuel rod that lies under the punch.

Two types of punches are considered: circular and linear. With the circular punch, the ratio of the diameter of the punch to the diameter of the block is called the focusing parameter. To provide maximum energy transfer, the punch may be considered to be coaxial with the block. The second type is a linear punch. Two parallel chords of equal length and the two arcs that connect them define the outline of a linear punch. A linear punch is defined by two variables: the focusing parameter and the angle. The focusing parameter is the ratio of the distance between the two chords to the block diameter. The angle is simply the angle between a chord and the fuel rods. For both punch types, a focusing parameter of one corresponds to

a flat-bottomed block. Focusing parameters near zero describe a block with either a slender pin (circular punch) or a blade (linear punch) on the bottom. The circular and linear punches are intended to simulate blocks that fall on their vertices or their edges, respectively.

When a block strikes the fuel, the number of rod breaks can vary from zero (if there is not enough energy to begin breaking rods) to the number of rods under the punch. The number of breaks is determined as a weighted average over the number of assemblies of each type and the distribution of block sizes.

The number of breaks is calculated by considering the energy of the falling block. The block accumulates kinetic energy as it falls freely toward the fuel rods. It releases additional potential energy as it deforms the fuel rods; at the same time, the deformation of the rods consumes energy. If the block has sufficient energy, it breaks fuel rods. After the first layer of rods is broken, the energy consumed for each additional layer is constant. Again, there is an additional release of potential energy as the block continues to fall. After the number of breaks is determined, the number of broken rods is calculated by a probabilistic approach. These two quantities can differ because a single rod can be broken in several places.

It was mentioned previously that two types of fuel were considered: typical and high-burnup. Burnup is significant because cladding tends to become brittle at high burnups. Because there is a long-term trend toward higher burnups as experience with reactor operations increases, what constitutes high burnup depends on when the fuel was irradiated. However, the continued demand by utilities for good fuel performance should ensure that the strength and ductility of typical fuel assemblies are maintained even though "typical" burnups are increasing.

The typical fuel was taken to represent 95% of the inventory, and the high-burnup fuel was taken to represent 5% of the inventory. The mechanical properties of high-burnup fuel are those for a sample, discharged no later than 1986, with a local burnup of 59.0 GWd/MTU. This is an exceptionally high burnup for fuel that was discharged that early; of the 19,968 PWR fuel assemblies discharged through 1986, only 200 had assembly average burnups of greater than 40.0 GWd/MTU (DOE, 1996).

The fraction of fuel rods broken and the fraction of fuel exposed were calculated for both circular and linear punches with several values, ranging from 1 to 0.01, of the focusing parameter. The results are documented in Tables 2.1.3.1-2 and 2.1.3.1-3. The results of most interest are those in columns labeled "95% typ + 5% hi-burn," which contain arithmetically weighted means for a repository that contains 95% typical fuel and 5% high-burnup fuel. All of the results in the tables account for the block size distribution and the number of assemblies of each type.

Results for blocks with a circular punch are shown in Table 2.1.3.1-2. The number of breaks per rod and the fraction of fuel rods broken increase as the focusing parameter decreases. A smaller punch apparently makes the block more

effective in breaking rods. The largest reported values of the number of breaks per rod and the fraction of rods broken are 0.2845 and 0.2341, respectively. Both of these values are reached at a focusing parameter of 0.1. In contrast to these results, the amount of fuel exposed is nearly independent of the focusing parameter over the range 1.0 to 0.4, then decreases at smaller values of the focusing parameter. The maximum fraction of fuel exposed per waste package is 0.0114 at a focusing parameter of 0.6.

**Table 2.1.3.1-2 Amount of fuel damage as a function of the focusing parameter for fuel struck by blocks with a circular punch**

Focus Param.	Average Number of Breaks per Rod			Fraction of Rods Broken			Fraction of Fuel Exposed			Punch Aspect Ratio	
	Typical	Hi-Burn	95% Typ +5% Hi-Burn	Typical	Hi-Burn	95% Typ +5% Hi-Burn	Typical	Hi-Burn	95% Typ +5% Hi-Burn	Typical	Hi-Burn
1.0	0.0325	0.6145	0.0616	0.0142	0.1799	0.0225	0.0060	0.1055	0.0110	0.006	0.045
0.9	0.0386	0.6466	0.0689	0.0175	0.2050	0.0268	0.0064	0.0997	0.0111	0.008	0.058
0.8	0.0463	0.6831	0.0782	0.0217	0.2383	0.0325	0.0068	0.0941	0.0112	0.010	0.077
0.7	0.0568	0.7339	0.0906	0.0273	0.2830	0.0401	0.0073	0.0886	0.0113	0.013	0.106
0.6	0.0700	0.8073	0.1069	0.0345	0.3481	0.0501	0.0076	0.0839	0.0114	0.020	0.156
0.5	0.0853	0.9058	0.1263	0.0441	0.4343	0.0636	0.0076	0.0785	0.0112	0.033	0.248
0.4	0.1032	1.0390	0.1500	0.0576	0.5490	0.0822	0.0073	0.0716	0.0105	0.059	0.440
0.3	0.1264	1.1410	0.1771	0.0784	0.6482	0.1069	0.0067	0.0576	0.0092	0.122	0.868
0.2	0.1650	0.9978	0.2066	0.1174	0.6276	0.1429	0.0058	0.0323	0.0071	0.329	1.770
0.1	0.2682	0.5934	0.2845	0.2229	0.4467	0.2341	0.0046	0.0090	0.0049	1.920	4.620

Another result of interest for calculations with a circular punch is the punch-aspect ratio. This is the ratio of the depth of penetration of the punch to the width of the punch. Here "depth of penetration" is defined as the number of layers of rods broken times the effective rod pitch. Different combinations of block size and assembly type yield different punch-aspect ratios. The values reported in Table 2.1.3.1-2 are arithmetic means for blocks that break rods. (For blocks that do not break rods, the punch-aspect ratio is zero.) Because it is improbable that a block has a very long, slender protrusion on its bottom surface, large punch-aspect ratios indicate an unrealistic focusing of energy onto a few rods. It is seen from Table 2.1.3.1-3 that the punch-aspect ratio increases as the focusing parameter decreases. Because the punch-aspect ratios are fairly large for a focusing parameter of 0.1, it is expected that the actual number of breaks per rod and fraction of rods broken will be smaller than the values reported above.

**Table 2.1.3.1-3**

**Amount of fuel damage as a function of the focusing parameter for fuel struck by blocks with a linear punch (composite of eight punch orientations)**

Focus Param	Average Number of Breaks per Rod			Fraction of Rods Broken			Fraction of Fuel Exposed		
	Typical	Hi-Burn	95% Typ +5% Hi-Burn	Typical	Hi-Burn	95% Typ +5% Hi-Burn	Typical	Hi-Burn	95% Typ. +5% Hi-Burn
1.0	0.0325	0.8145	0.0618	0.0142	0.1799	0.0225	0.0060	0.1055	0.0110
0.9	0.0348	0.6258	0.0643	0.0154	0.1893	0.0241	0.0062	0.1032	0.0110
0.8	0.0377	0.6402	0.0678	0.0170	0.2018	0.0262	0.0063	0.0990	0.0109
0.7	0.0418	0.6593	0.0725	0.0191	0.2186	0.0291	0.0064	0.0940	0.0108
0.6	0.0467	0.6875	0.0787	0.0219	0.2436	0.0329	0.0065	0.0892	0.0108
0.5	0.0528	0.7281	0.0864	0.0257	0.2773	0.0382	0.0068	0.0845	0.0105
0.4	0.0600	0.7787	0.0959	0.0310	0.3225	0.0456	0.0087	0.0797	0.0103
0.3	0.0695	0.8209	0.1071	0.0392	0.3630	0.0554	0.0068	0.0713	0.0100
0.2	0.0852	0.7731	0.1198	0.0545	0.3603	0.0698	0.0072	0.0526	0.0095
0.1	0.1255	0.6296	0.1507	0.0950	0.2995	0.1052	0.0092	0.0267	0.0101

For a linear punch, the results depend on the angle between the punch and the rods. The rubble blocks in a drift are randomly oriented. As a discrete approximation of a random orientation, the fraction of rods broken and the fraction of fuel exposed were calculated for 8 orientations (0, 22.5, . . . 157.5), and the arithmetic mean was taken. The results for this composite orientation are shown in Table 2.1.3.1-3. As is the case with a circular punch, the number of breaks per rod and the fraction of rods broken both increase as the focusing parameter decreases from 1 to 0.1. The largest reported values are 0.1507 and 0.1052, respectively. However, the dependence on the focusing parameter is much weaker than it is with a circular punch. The fraction of fuel exposed has a more complicated dependence on the focusing parameter, with a maximum at 1, a minimum near 0.2, and a second maximum at 0.1. The maximum fraction of fuel exposed is 0.0110 at focusing parameters of 0.9 and 1.0.

The two models provide substantially different results for the fraction of rods broken. With a linear punch (Table 2.1.3.1-3), the largest reported value is 0.1052 for a focusing parameter of 0.1; with a circular punch (Table 2.1.3.1-2), the largest reported value is 0.2341, again for a focusing parameter of 0.1. The two models agree more closely at larger focusing parameters. However, it may be that the circular punch simply represents a more severe loading configuration as regards the number of rods broken.

With respect to the amount of fuel exposed per waste package, the agreement between results for a circular punch and a linear punch is much closer. With a linear punch, the maximum fraction of fuel exposed per waste package is 0.0114;

with a circular punch, 0.0110 is exposed. These values are reached at fairly large values of the focusing parameter, 0.6 and 0.9 to 1.0, respectively. These results indicate that only a small fraction of fuel will be exposed by mechanical failure.

Energies for breaking fuel rods of boiling-water reactor (BWR) assemblies have not been calculated. For most of these, the fuel rods are protected by the flow channels from impacts and static loads. It would be conservative to assume that the number of breaks per rod and the fraction of fuel exposed are the same for PWR and BWR fuels.

#### 2.1.3.1.7.1 Abstraction of Model

The development of the model is its own abstraction. An elastic-plastic beam theory is used to calculate the force-displacement behavior of a fuel rod. A curve is fitted to those results to provide an empirical force-displacement equation. That equation, in turn, is used to develop a one-dimensional continuum model for the energy absorbed in breaking rods. Finally, the fraction of fuel exposed is calculated by accounting for the distribution of block sizes and the number of fuel assemblies of each type.

#### 2.1.3.1.7.2 Recommended Model

For the geometries considered in this analysis, the maximum fraction of fuel exposed by mechanical loading is 0.0114 per waste package. The uncertainty range for this value has not yet been defined. It is recommended that this value be used for all Zircaloy™-clad, commercial spent nuclear fuel that does not fail by other mechanisms.

The model does not predict the time at which mechanical failure of the container (and thus cladding failure) occurs. If this time cannot be derived from other models, it is recommended that the time of container breach be used as the time of mechanical failure.

The model of dynamic loading contains the following conservatisms:

- The block fall height is essentially an upper limit; there is no accounting for possible deformation of the containment barriers before complete collapse.
- Blocks are assumed to fall freely; there is no accounting for blocks that encounter friction or are partially supported.
- There is no accounting for energy absorbed in deforming the remnants of the containment barriers.
- There is no reduction of block size to account for breakage when the blocks fall onto the intact disposal container or other rubble.

- There is no accounting for energy absorption by crushing of the spacer grids; that process would also increase the flexibility of the rods and thus increase the energy they could absorb before breaking.
- Falling blocks are assumed to cover the entire exposed area of the assemblies.
- Rod breakage is likely to cause only a few guillotine breaks in the cladding, but the amount of fuel exposed is assumed to be that in the entire length of the rod under the block.
- The neutral axis is taken to be at the surface of the rod; this location minimizes energy absorption.
- No credit is taken for the protection of BWR fuel rods by their flow channels.

Because of these conservatisms, the reported values of the number of breaks per rod and the fraction of fuel exposed are believed to be conservative.

#### 2.1.3.1.8 Zircaloy™ Corrosion

The current cladding model accounts for Zircaloy™ cladding failure from strain, oxidation, and mechanical failures. It does not address failure from corrosion. Uhlig, (1985) and Schweitzer (1996) summarized the susceptibility of zirconium to corrosion by common chemicals. They concluded that the material is resistant to corrosion by most basic chemicals but is corroded by ferric chloride and a few other compounds. Cragolino (Cragolino and Galvele, 1977) measured anodic behavior of Zircaloy™ in Cl solutions and showed that a pitting potential exists. Maguire's experiments (1984) show that FeCl<sub>3</sub> corrosion potentials exist.

In an experiment, Barkatt (1983) showed that gamma radiolysis of 6.2E4 grays (6.2E6 rads) over 3 days at 25°C could produce:

Acid	Concentration	Comment on Formation
Nitric	78E-6 M	pH must be below 4, formed in gas phase.
Formic	46E-6 M	Formed by dissolved CO <sub>2</sub> in liquid phase, pH at or below 4.
Oxalic	30E-6 M	Formed by dissolved CO <sub>2</sub> in liquid phase, pH at or below 4.
H <sub>2</sub> O <sub>2</sub>	16E-6 M	Formed in liquid phase.

Van Konynenburg (Van Konynenburg and Curtis, 1996) performed accelerated corrosion tests with Zircadyne-702, an unalloyed metal. The test solution contained 0.01M each of sodium formate (NaCOOH), nitric acid (HNO<sub>3</sub>), NaCl, H<sub>2</sub>O<sub>2</sub>, and 0.02M sodium oxalate (Na<sub>2</sub>C<sub>2</sub>O<sub>4</sub>). The temperature was 90°C, and the duration was 96 hr. The corrosion rate measured was 0.06 mm/yr (a rate fast enough to be

through cladding in 10 yr). The initial pH was 4.06, and final pH was 4.26. The solutions used were three orders of magnitude more concentrated than the acids observed in Barkatt's tests.

Water does not contact the cladding until the WPs have failed. Current analysis predicts that this will not occur for thousands of years. At that time, the gamma dose will have decreased by about three orders of magnitude. Alpha and beta radiation is inside the cladding and will not contribute to the radiolysis on the cladding outer surface. Near-field chemical analysis suggests that the water will be modified by the concrete and will be basic (or at worst, near neutral) for tens of thousands of years. This incoming water should neutralize the production of radiolytic acids. Until the chemical analysis is performed to predict radiolysis, pH,  $\text{HCO}_3^-$ , and  $\text{FeCl}_3$  in solution, and the composition of the water contacting the cladding, it is assumed that the cladding is not damaged by radiolytically produced acids because the incoming solution is basic from the effects of the concrete. Thus, corrosion of Zircaloy™ is not expected to contribute to significant failures.

#### 2.1.3.1.9 Clad Unzipping

If there is a pinhole crack in the cladding and air is present, the spent fuel inside can oxidize, eventually to  $\text{U}_3\text{O}_8$ , which expands and exerts pressure in its confined space. The pinhole can then be transformed into a longitudinal crack. Because of data variability, it is difficult to put a value on the radius at crack initiation. Rather, model the phenomenon is modeled in net-result form closely following the parameters measured in the experiments. Later, a radius is estimated at cracking, but that is a check on reasonableness rather than a link in the model. The crack eventually extends along the length of the cladding. The crack propagation velocity depends on the oxidation of additional  $\text{U}_3\text{O}_8$  along the rod.

Einzigler and Strain (1986) have done experiments at 255°C and above on fuel rod sections and on exposed fuel fragments, both from the same batch of spent fuel. They report the oxidation progress curves, the initiation of spalling in the exposed fragments, and the initiation and propagation of cracks in the fuel-rod sections. For the time to initiation of spalling, they find an activation energy of 46.4 kcal/mole. They use this activation energy for the temperature dependence and use an adjustable multiplier to form a lower-bound curve for the initiation-of-rod-splitting data. In both free fragment spalling and rod cracking, sections from near the ends of the rods reach these changes at earlier times, with the difference averaging approximately a factor of five. The data on crack initiation for rod center pieces seem to have a lesser slope with temperature, closer to the activation energy found previously from a number of different experiments. The data on crack initiation for rod end pieces are fewer and do not give much additional information on the temperature dependence. To extrapolate to lower temperatures than the data range covers and to cover end as well as center locations of initial pinholes or pinhole cracks, a  $Q_0$  and a curve anchored in the 283°C data are recommended. The equation for time to initiation of rod splitting is then

$$t_0 = c_{50} \cdot \exp(+Q_{50} / RT) \quad (2.1.3.1-9)$$

where  $c_0 = 3.04 \text{ e-}13 \text{ hr}$  with a multiplicative standard deviation of a factor of 5 (i.e.,  $c_0$  has a log-normal distribution, and 3.04 e-13 hours is the median) and  $Q_0 = (38.4 \pm 3) \text{ kcal/mol}$ , as previously. (This gives  $t_0 = 385 \text{ hr}$  at  $T = 283^\circ\text{C}$  using the central values of the parameters.)

The subsequent crack propagation velocity has a lower activation energy (i.e., less change with temperature), but the full-rod extension time is fairly short compared with the initiation time. The crack propagation velocity depends on the oxidation of additional  $\text{U}_3\text{O}_8$ . Presumably there is some early fraction oxidized along the interior during the initiation period; hence, the temperature-dependence of the crack extension is not as strong overall as it is for the initiation. Because of the short overall crack extension time, this part of the phenomenon can be considered instantaneous in the model; the time to cracking is the main time in the process.

The reported experiments were done on one series of spent fuel. The activation energy used in the fit is global for  $\text{U}_3\text{O}_8$ ; the leading multiplying factor for the crack initiation time should depend on grain size. The uncertainty of a factor of five is large enough to encompass a good fraction of this source of variability.

One can compare (Figure 2.1.3.1-5) the time to initiation of splitting at  $255^\circ\text{C}$  (5000 to 10,000 in the data of Einziger and Strain (1986) or 2000 to 10,000 hr using a fit to the data for rod center sections only) to the  $\text{U}_3\text{O}_8$  oxidation rate data of Einziger et al., reported in 1995 and reproduced in Figures 3.2.2-5 through 3.2.2-8 of this report (*Waste Form Characterization Report [WFCR]*). At 5000 to 10,000 hr, the WFCR data show that the  $\Delta(\text{O/M})$  is on the order of one-seventh of the way between  $\text{U}_4\text{O}_9$  and  $\text{U}_3\text{O}_8$ . The time values in this set of experiments vary with a multiplicative standard deviation of approximately a factor of five. The  $\Delta(\text{O/M})$  parallels the change in mass of U oxidized to a higher state and, thus, to the change in volume. A one-seventh change from a base volume to a 30%-increased volume means a 4.3% increase in volume, or a 1.4% increase in radius (assuming that the initial oxidized mass can expand longitudinally in the fuel rod, pushing other spent fuel along the rod and radially pushing on the cladding). The fuel-cladding gap is essentially gone in spent fuel because of expansion of the matrix during irradiation; hence, the expansion means an expansion (strain) of the cladding circumference of about 1.4%. This seems to be about the right order of magnitude to initiate unzipping, given that there is an initial crack or pinhole to provide an initial crack tip or stress riser. Thus, the time-to-initiation data and the oxidation-rate data at  $255^\circ\text{C}$  are plausibly consistent, at least using an order-of-magnitude comparative rationale.

Thus, the final model recommended for the time delay in generating a large breach in cladding from a small pinhole breach, when exposed to air, is given by the time to initiation of longitudinal cracking, given by Eq. 2.1.3.1-3. Extrapolating the model to  $T = 100^\circ\text{C}$  gives the following time  $t_0$ , depending on the values of the parameters within their distributions. It gives  $t_0 = 9.9\text{e} + 9 \text{ hr}$ , or  $1.1\text{e} + 6 \text{ yr}$  using



### 2.1.3.1.10 References

- Bahney, R. H. (1995). *Thermal Calculations in Support of the Thermal Loading Study*. LV.WP.RHB.12/95-392. [MOL.19960611.0506; 237199]
- Barkatt, A., A. Barkatt, and W. Sousanpour (1983). "Gamma Radiolysis of Aqueous Media and its Effects on the Leaching Processes of Nuclear Waste Disposal Materials." *Nucl. Technol.* 60(2):218-227. [NNA.19891101.0002]
- Chung, H. M., F. L. Yagee, and T. F. Kassner (1987). "Fracture Behavior and Microstructural Characteristics of Irradiated Zircaloy Cladding." *Zirconium in the Nuclear Industry*. (ASTM STP 939) American Society for Testing and Materials.
- Cragolino, G. A., and J. R. Galvele (1977). "Anodic behavior and pitting of zirconium and Zircaloy-4 in aqueous solutions of sodium chloride." *Passivity of Metals*. R. P. Frankenthal and J. Kruger (eds.). Princeton, NJ: The Electrochemical Society. (pp. 1053-1057) [237155]
- CRWMS M&O (1995). *Updated Report on RIP/YMIM Analysis of Designs*. (BBA000000-01717-5705-00002, Rev. 02) Las Vegas, NV: Civilian Radioactive Waste Management System Management and Operating Contractor, TRW Environmental Safety Systems, Inc., for the U.S. Department of Energy.
- CRWMS M&O (1997a). *Design Basis Cladding Analysis*. (BBA000000-01717-0200-00054, Rev. 00) Las Vegas, NV: Civilian Radioactive Waste Management System Management and Operating Contractor, TRW Environmental Safety Systems, Inc., for the U.S. Department of Energy. [MOL.19971121.0750]
- CRWMS M&O (1997b). *Waste Quantity, Mix and Throughput Study Report*. (B00000000-01717-5705-00059, Rev. 01) Las Vegas, NV: Civilian Radioactive Waste Management System Management and Operating Contractor, TRW Environmental Safety Systems, Inc., for the U.S. Department of Energy. [MOL.19971210.0628]
- DOE (1996). *Spent Nuclear Fuel Discharges from U.S. Reactors 1994*. (SR/CNEAF/96-01) Washington, DC: U. S. Department of Energy, Energy Information Administration. [232923]
- Einzigler, R. E., S. D. Atkin, D. E. Stellrecht, and V. Pasupathi (1982). "High-Temperature Post-Irradiation Materials Performance of Spent Pressurized Water-Reactor Fuel-Rods under Dry Storage-Conditions" *Nucl. Technol.* 57(1):65-80.
- Einzigler, R. E. (1994). "Preliminary Spent LWR Fuel Oxidation Source Term Model," in proceedings from High Level Radioactive Waste Management International Conference. Las Vegas, NV: May 1994. pp. 554. [MOL.19950517.0141; 233158]

- Einzigler, R. E., L. E. Thomas, and B. D. Hanson (1995). *Oxidation of Spent LWR Fuel, FY 95 Year end Report*. (MOL212 and MOL213 combined interim report). Richland, WA: Pacific Northwest National Laboratory. [MOL.19960611.0215]
- Einzigler, R. E., and R. V. Strain (1986). "Behavior of Breached Pressurized Water-Reactor Spent-Fuel Rods in an Air Atmosphere Between 250°C and 360°C." *Nucl. Technol.* 75(1):82-95.
- Garde, A. M. (1986). *Hot Cell Examination of Extended Burnup Fuel from Fort Calhoun*. DOE/ET/34030-11, CEND-427, Combustion Engineering. [NNA.19911017.0103; 237128]
- Lorenz, R. A., J. L. Collins, R. L. Towns, A. P. Malinauskas, and O. L. Kirkland (1980). *Fission Product Release for Highly Irradiated LWR Fuel*. (NUREG/CR-0722) Oak Ridge, TN: Oak Ridge National Laboratory. [NNA.19891109.0121; 211434]
- Lowry, L. M. A., J. Markworth, J. S. Perrin, and M. P. Landow (1981). *Evaluating Strength and Ductility of Irradiated Zircaloy, Task 5*. (NUREG/CR-1729) Washington, DC: Nuclear Regulatory Commission. [237180]
- Maguire, M. (1984). "The Pitting Susceptibility of Zirconium in Aqueous Cl<sup>-</sup>, Br<sup>-</sup>, and I<sup>-</sup> solutions." In proceedings from *Industrial Applications of Titanium and Zirconium: Third Conference*. American Society for Testing and Materials. 830:175-189. [237161]
- Manzel, R., and M. Coquerelle (1997). "Fission gas release and pellet structure at extended burnup." In proceedings from *International Topical Meeting on LWR Fuel Performance*. Portland, OR: March 2-6, 1997. pp. 463-470. [237134]
- Matsuo, Y. (1987). "Thermal Creep of Zircaloy-4 Cladding Under Internal Pressure," *J. Nucl. Sci. and Technol.* 24:111-119. [237137]
- Peehs, M., and J. Fleisch (1986). "LWR Spent Fuel Storage Behavior," *J. Nucl. Mat.* 137:190. [235595]
- Pescatore, C., M. G. Cowgill, and T. M. Sullivan (1989). *Zircaloy Cladding Performance Under Spent Fuel Disposal Conditions*. (BNL 52235) Upton, NY: Brookhaven National Laboratory. [NNA.19900710.0055; 200475]
- Pescatore, C., and M. Cowgill (1994). *Temperature Limit Determination for the Inert Dry Storage of Spent Nuclear Fuel*. (EPRI TR-103949) Upton, NY: Brookhaven National Laboratory. [102933]
- Puls, M. P. (1988). "The influence of hydride size and matrix strength on fracture initiation at hydrides in zirconium alloys." *Met. Trans. A.* 19(6):1507-1522. [237143]
- Rothman, A. J. (1984). *Potential Corrosion and Degradation Mechanisms for Zircaloy Cladding on Spent Nuclear Fuel in a Tuff Repository*. (UCID-20172.) Livermore, CA: Lawrence Livermore National Laboratory. [209058]

- Schweitzer, P. A. (1996). *Corrosion Engineering Handbook*. New York, NY: Marcel Dekker, Inc.
- Shi, S. -Q., M. P. Puls, (1994). "Criteria for fracture initiation at hydrides in zirconium alloys. 1. Sharp crack-tip." *J. Nucl. Mat.* 208(3)232-242. [237135]
- Siegmann, E. (1998). *Waste Form Degradation and Radionuclide Mobilization Preliminary TSPA, Section 2.7*. Las Vegas, NV: Civilian Radioactive Waste Management System, Management and Operating Contractor. (B00000000-01717-2200-0199)
- Uhlig, H. H., and R. W. Revie (1985). *Corrosion and Corrosion Control*. (Third Edition) New York, NY: John Wiley & Sons.
- Van Konynenburg, R. A. and P. G. Curtis (1996). *Corrosion test on candidate waste package basket materials for the Yucca Mountain Project*. (UCRL-JC-123236) Livermore, CA: Lawrence Livermore National Laboratory. [MOL.19960417.0256; 237230]
- VanSwam, I. I. (1997). "Behavior of Zircaloy-4 and zirconium liner Zircaloy-4 cladding at high burnup." In proceedings from International Topical Meeting on LWR Fuel Performance. Portland, OR: March 2-6, 1997. pp. 421-431.
- Yagee, F. L., R. F. Mattas, and L. A. Neimark (1979). *Characterization of Irradiated Zircalloys: Susceptibility to Stress Corrosion Cracking*. (EPRI NP-1155) Argonne, IL: Argonne National Laboratory.
- Yagee, F. L., R. F. Mattas, and L. A. Neimark (1980). *Characterization of Irradiated Zircalloys: Susceptibility to Stress Corrosion Cracking*. (EPRI NP-1557) Argonne, IL: Argonne National Laboratory.
- Yang, R. L. (1997). "Meeting the Challenge of Managing Nuclear Fuel in a Competitive Environment." In proceedings from International Topical Meeting on LWR Fuel Performance. Portland, OR: March 2-6, 1997. p. 3. [237148]

## Section 2.1.3.2 Contents

2.1.3.2	UO <sub>2</sub> Oxidation in Fuel.....	2.1.3.2-1
2.1.3.2.1	Thermal Gravimetric Analysis Oxidation Results .....	2.1.3.2-1
2.1.3.2.1.1	Doped Fuel.....	2.1.3.2-2
2.1.3.2.1.2	ATM-105 Tests.....	2.1.3.2-2
2.1.3.2.1.3	283°C Tests .....	2.1.3.2-6
2.1.3.2.1.4	ATM-104 Tests.....	2.1.3.2-12
2.1.3.2.1.5	ATM-108 Tests.....	2.1.3.2-13
2.1.3.2.2	Burnup Analyses.....	2.1.3.2-15
2.1.3.2.2.1	<sup>148</sup> Nd Isotope-Dilution Method .....	2.1.3.2-15
2.1.3.2.2.2	Gamma Spectrum Analysis .....	2.1.3.2-16
2.1.3.2.3	Dry-Bath Oxidation Results.....	2.1.3.2-18
2.1.3.2.3.1	175°C Tests .....	2.1.3.2-18
2.1.3.2.3.2	195°C Tests .....	2.1.3.2-19
2.1.3.2.3.3	255°C Test.....	2.1.3.2-20
2.1.3.2.4	Quantitative XRD Results.....	2.1.3.2-24
2.1.3.2.5	References.....	2.1.3.2-25

## Section 2.1.3.2: UO<sub>2</sub> Oxidation in Fuel

Version 1.3  
July 23, 1998

This section has been reproduced essentially intact from Chapter 3 of Hanson (1998). It details the results of the present oxidation studies, including the burnup and post-oxidation analyses performed. Detailed oxidation curves (oxygen-to-metal ratio as a function of time at operating temperature) for individual samples are presented in Appendix 2.1.3.2-A.

### 2.1.3.2.1 Thermal Gravimetric Analysis Oxidation Results

A summary of the experimental conditions and measured parameters for the thermal gravimetric analysis (TGA) tests is presented in Table 2.1.3.2-1. All oxygen-to-metal (O/M) ratios were calculated using Eq. 2.1.3.2-1:

$$\Delta(O/M) = (270/16) \cdot (\Delta M/M_0) \quad 2.1.3.2-1$$

where 270 represents the atomic mass of UO<sub>2</sub> (the mass difference due to fission of U and substitution of fission products and higher actinides is ignored), 16 represents the atomic mass of the oxygen taken up by the sample (i.e., assumes that the only mechanism for mass increase is oxygen uptake), DM is the increase in mass, and M<sub>0</sub> is the original mass of the specimen.

The O/M ratios were calculated directly from the mass increase of a sample, neglecting any effects due to substitution of two fission products for each fission in the specimen or replacement of a uranium atom by a higher actinide. Further, it was assumed that all specimens had an initial O/M ratio of 2.00. The uncertainty in the calculated O/M ratios is estimated as ±0.01.

Table 2.1.3.2-1 Summary of experimental conditions and measured parameters

Sample ID#	Oxidation Temperature (°C)	Final O/M Ratio	XRD results	Sample Burnup (MWd/kgM)	
				<sup>137</sup> Cs <sup>(a)</sup>	<sup>148</sup> Nd <sup>(b)</sup>
105-01	283	2.78	U <sub>3</sub> O <sub>8</sub>	c	c
105-02	325	2.73	U <sub>3</sub> O <sub>8</sub>	c	c
105-03	305	2.75	U <sub>3</sub> O <sub>8</sub>	c	28.1
105-04	270	2.59	c	c	27.5
105-05	255	2.41	U <sub>4</sub> O <sub>9</sub>	c	29.2
105-06	283	2.49	U <sub>3</sub> O <sub>8</sub> /U <sub>4</sub> O <sub>9</sub>	c	31.5
105-07	283	2.62	U <sub>3</sub> O <sub>8</sub> /U <sub>4</sub> O <sub>9</sub>	c	27.6
105-08	283	2.47	U <sub>3</sub> O <sub>8</sub> /U <sub>4</sub> O <sub>9</sub>	c	32.5

Sample ID#	Oxidation Temperature (°C)	Final O/M Ratio	XRD results	Sample Burnup (MWd/kgM)	
105-09	305	2.43	c	c	c
105-10	305	2.65 <sup>(a)</sup>	c	c	29.8
105-11	305	2.70	c	25.9	29.6
105-12	305	2.73	c	27.9	c
105-13	305	2.71	c	28.3	c
105-14	305	2.73	c	28.1	c
105-15	305	2.73	c	19.1	18.6
105-16	305	2.71	c	18.3	c
105-17	305	2.70	c	16.7	c
105-18	305	2.69	c	16.8	c
104-01	305	2.51	c	42.3	c
104-02	305	2.42	c	42.4	c
108-01	305	2.48	c	17.6	c
108-02	305	2.45	c	34.8	c

- (a) Measured by  $\gamma$ -ray energy analysis prior to oxidation  
(b) Measured by destructive analysis after oxidation  
(c) Measurement/analysis not performed

#### 2.1.3.2.1.1 Doped Fuel

The TGA systems had not been used for two to three years prior to the present tests. New, calibrated pressure transducers were installed, and the sample temperature thermocouples were checked by comparing them with a calibrated thermocouple. The balances and the data-acquisition system were also calibrated. All calibrated standards are traceable to National Institute of Standards and Technology (NIST) standards.

To test one of the TGA systems, a 268.50 mg disk of  $UO_2$  doped with 8 wt%  $Gd_2O_3$  was cut from an unirradiated pellet. The specimen was oxidized in TGA#2 for 454 hr at 283°C. As seen in Figure 2.1.3.2-A-1, the sample reached a plateau at an O/M ratio of approximately 2.35 within about 250 hr. Upon unloading, the disk broke into smaller pieces, which were found to be quite friable. A subsample was taken and analyzed via X-ray powder diffractometry (XRD). The XRD analysis revealed that the sample was entirely converted to a phase that most closely matches  $U_4O_9$ , even though the O/M ratio was significantly higher than the nominal value of 2.25 for  $U_4O_9$ . No other analyses were performed, and the systems were deemed ready for experimental use.

### 2.1.3.2.1.2 ATM-105 Tests

To minimize the possible influence of factors associated with fuel variability, each fuel specimen (except where noted for samples 105-15 through 105-18) consisted of a single fragment of ATM-105 fuel that came from a 56 cm axial segment from the high-burnup region of the characterized rod ADD2974. The bulk average burnup of this segment, as calculated by correlating the measured  $^{137}\text{Cs}$   $\gamma$ -ray activity with  $^{148}\text{Nd}$  analyses (Guenther et al., 1991a), ranged from 28.5 to 31.5 MWd/kgM. A radial distribution in burnup was also expected. The fuel had been removed from the clad, and fragments were taken for earlier TGA studies and for the dry-bath tests. The remaining fragments (approximately 90 g from the original 687 g of fuel in this segment) had been placed in a capped storage tube and kept in the hot cell where the dry-baths were located. When a fragment was needed for a test, the tube was opened, and fragments were poured into a petri dish. Once a fragment of ~200 mg was found, it was placed in a glass vial and transported to the TGA laboratory. The remaining fragments were returned to the storage tube. Thus, the exact radial and axial location of these specimens within the irradiated rod is not known.

#### *Scoping Tests*

The first five oxidation tests were run as scoping tests to help determine the time required to oxidize the spent fuel samples to  $\text{U}_3\text{O}_8$  (i.e., a second plateau at an O/M ratio of approximately 2.75) as a function of temperature. These results, plotted as the O/M ratio as a function of time (Figure 2.1.3.2-1), were to be used to establish the test matrix to determine the oxidation kinetics and to assist in the development of the mechanism of oxidation of spent fuel to  $\text{U}_3\text{O}_8$ . The temperatures were chosen to compare the data from the present studies with the previous oxidation data of Einziger and Strain (1986).

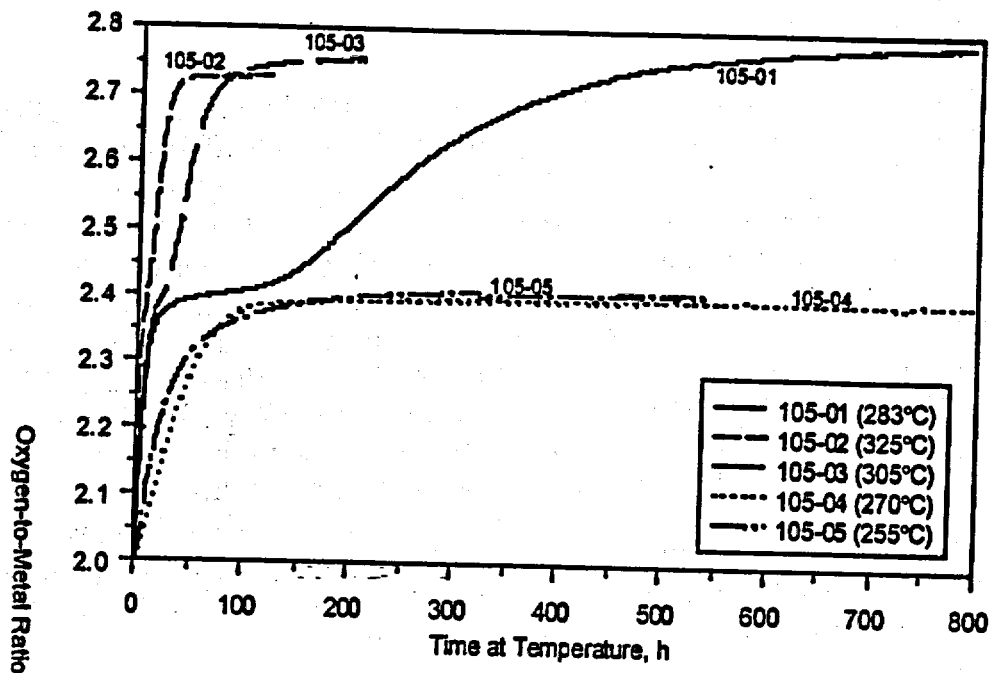


Figure 2.1.3.2-1 Oxygen-to-metal ratio as a function of time for ATM-105 fragments oxidized at various temperatures

Sample 105-01 (i.e., ATM-105 sample #1) consisted of a 184.63 mg fragment; it was oxidized for 793 hr at 283°C. The first plateau at an O/M ratio of about 2.4 was reached after approximately 55 hr, and a short plateau (although not of zero slope) was observed before the onset of more rapid mass increase resumed. A final bulk O/M ratio of 2.78 was achieved. XRD analysis revealed the sample was converted to  $U_3O_8$  with minor amounts of  $U_4O_9$  remaining. Scanning electron microscopy (SEM) revealed that the sample had disintegrated into small clusters of individual grains with a great deal of inter- and intragranular cracking.

Sample 105-02 was a 193.73 mg fragment oxidized at 325°C to a final bulk O/M ratio of approximately 2.73. An O/M ratio of approximately 2.4 was reached after only 8 hr, and no truly identifiable plateau existed, although there was an obvious change in the rate-of-increase in O/M ratio after this point (see Figure 2.1.3.2-A-3). The only phase detected by XRD was  $U_3O_8$ . SEM revealed even more intragranular cracking than was observed with the first sample; this is consistent with the higher stresses experienced because of the rapid oxidation at higher temperatures.

The third sample, 105-03, consisted of a single 207.11 mg fragment, which was oxidized at 305°C to a final bulk O/M of 2.75. An O/M ratio of 2.4 was reached after approximately 23 hr. Again, a plateau with zero slope did not exist, although there was clearly a different rate of change in O/M ratio after a ratio of approximately 2.39 was reached. XRD of the resultant powder detected only  $U_3O_8$ .

Sample 105-04 was oxidized for 2375 hr at 270°C. This 203.39 mg fragment was the first in this series to exhibit a plateau with zero slope, as seen in Figure 2.1.3.2-A-5. The duration of the plateau was between 700 and 800 hr; mass increase then began again. An eventual final bulk average O/M of 2.59 was reached before the test was terminated. This sample was converted to powder, but no XRD analysis was performed because of the loss of the subsample taken for this purpose. Twice during oxidation of this sample, at 1076 and 1870 hr, power fluctuations caused relays to the furnace to reset, resulting in loss of power to the furnace. Each time, the sample cooled to room temperature before the test was restarted.

Sample 105-05 was oxidized at 255°C to compare with sample 105F-100, which was being oxidized in a dry-bath also operating at 255°C. As can be seen in Figure 2.1.3.2-2, the two oxidation curves agree fairly well over the first 400 hr. A computer malfunction after 322 hr at operating temperature resulted in the sample cooling to room temperature before being reheated to 255°C. Because the data of Einziger and Strain (1986) suggested that the duration of the plateau would be on the order of  $10^4$  hr, this TGA test was halted after only 544 hr when a bulk O/M ratio of 2.41 had been reached. The sample appeared to be an intact fragment when it was unloaded, and XRD analysis revealed that  $U_4O_9$  was the only phase present.

Originally, spent fuel fragments were to be oxidized to progressively larger O/M ratios between the plateau (~2.4) and final completion (~2.75) at a fixed temperature. Post-oxidation analyses would then be used to determine the amount of each phase present and to determine the mechanism and kinetics of the transition from  $UO_{2.4}$  to  $U_3O_8$ . The tests would then be repeated at different temperatures to determine the temperature dependence of oxidation. From the scoping tests, it was clear that, to perform enough tests to adequately study this transition, the temperatures would need to be in the range of 275° to 305°C. At temperatures less than 275°C, the duration of the plateau was expected to be  $\geq 800$  hr; at temperatures greater than 305°C, the plateau is not well defined and oxidation occurs rapidly. It was decided that the first series of tests would be performed at 283°C.

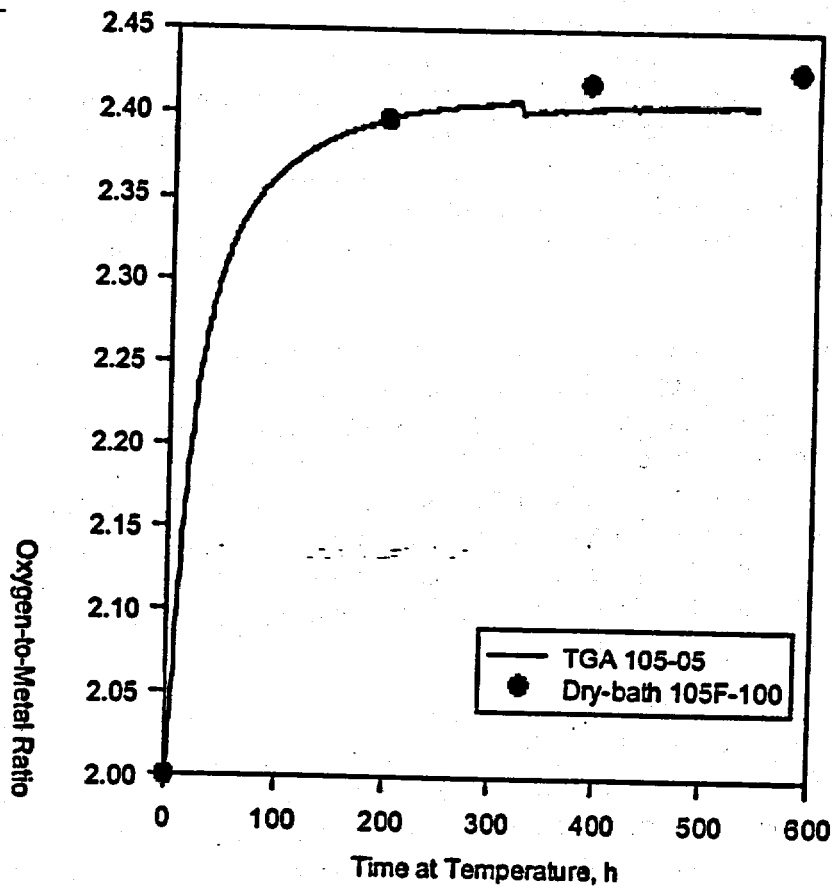


Figure 2.1.3.2-2 Oxidation behavior of ATM-105 fragments in a TGA and dry-bath at 255°C

### 2.1.3.2.1.3 283°C Tests

As reported in Section 2.1.3.2.1.2, sample 105-01 had been oxidized at 283°C. Based on the behavior of this sample and the earlier samples of Einziger and Strain (1986), it was expected that a short plateau with non-zero slope would exist for each sample at this temperature. Sample 105-06 was then oxidized at 283°C. It is clearly seen in Figure 2.1.3.2-3 that the oxidation behaviors of samples 105-01 and 105-06 were quite different. Although the time to reach an O/M ratio of 2.4 was similar, and neither specimen exhibited a plateau of zero slope, the time rate of change in O/M for sample 105-06 was much smaller than it was for the previous sample. This 214.06 mg fragment was oxidized for 1125 hr to a final bulk O/M ratio of 2.49. This sample consisted of powder and of a remaining fragment when unloaded from the TGA. XRD was performed, and both  $U_3O_8$  and  $U_4O_9$  were detected in the powder; the fragment consisted solely of  $U_4O_9$ . The only known difference between samples 105-01 and 105-06 was that the latter experienced two intermittent power losses to the furnace (at 21 and 816 hr) during which the sample cooled to room temperature before the test was resumed.

Sample 105-07 was then oxidized at 283°C for 743 hr. The oxidation behavior of this 167.37 mg fragment was intermediate to the previous two samples oxidized under identical conditions. The initial rate of O/M increase was less than that of the other samples (Figure 2.1.3.2-3); however, the time to reach an O/M ratio of 2.4 was about the same for all specimens. This sample then exhibited a plateau with near zero slope; once mass increase resumed, it was at a rate intermediate to that of the previous samples. The test was halted when a final bulk O/M ratio of 2.62 was reached. The sample consisted of only powder, which XRD identified as a mixture of  $U_3O_8$  and  $U_4O_9$ . During oxidation of this specimen, a power outage resulted in the sample cooling to room temperature after 314 hr at operating temperature. A computer malfunction resulted in the loss of data from 356–434 hr, although no other impact on the test was observed.

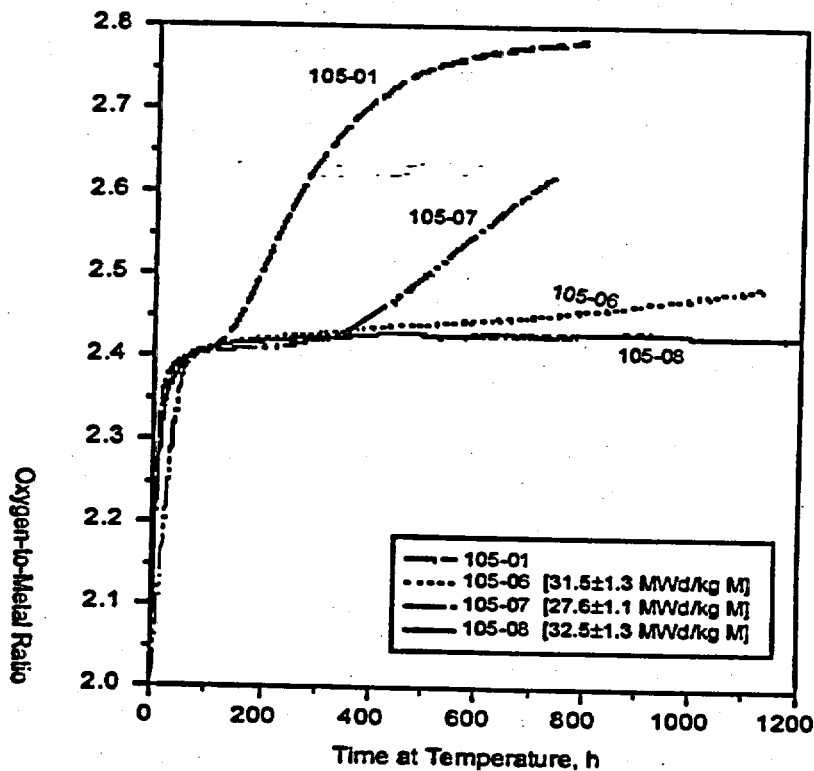


Figure 2.1.3.2-3 Oxidation behavior of ATM-105 fragments oxidized at 283°C

Both TGA systems were then thoroughly checked using NIST-traceable standards to ensure their proper calibration. Copper wire was oxidized in each TGA to determine if the tare and/or calibration of the balance drifted as a function of time or temperature. No problems were found with the balances or with the calibrated data-acquisition systems. Thus, the observed difference in oxidation behavior for the first three samples oxidized at 283°C was determined to be real and not due to equipment problems. The furnace-control relays were reconfigured so that power fluctuations or power outages lasting less than 2 min would not cause the relays to reset.

Sample 105-08 was a 195.63 mg fragment that was oxidized at 283°C. Three weeks after this test was initiated, the building where the TGA laboratory is located was placed under a radiologic work stoppage. No entry was allowed to the laboratory, so this system ran virtually unattended for months. Although the system appeared to have operated normally, there are large gaps in the data because no data were recorded once the data disk was full. Still, it is clear that a plateau with zero slope persisted for well over 1000 hr and likely closer to 3000 hr, as observed in Figure 2.1.3.2-A-9. Once mass increase began after this plateau, it was at a very slow rate. This experiment was halted after 5375 hr at constant temperature, and the final bulk average O/M ratio was 2.47. The sample consisted of powder and a remaining fragment. As with earlier samples, XRD detected a mixture of  $U_3O_8$  and  $U_4O_9$  in the powder, whereas only  $U_4O_9$  was detected in the fragment. While the oxidation behavior to an O/M ratio of ~2.4 was rather consistent with earlier observations (Einzig et al. 1992), the duration of the plateau and oxidation behavior to  $U_3O_8$  varied widely among the samples tested.

#### *305°C Tests*

A second series of samples from the high-burnup region of the ATM-105 fuel rod was oxidized at 305°C to determine if the variable oxidation behavior after reaching an O/M ratio of ~2.4 persisted at higher temperatures. Sample 105-09 (185.42 mg) was oxidized for about 122 hr, at which time the bulk O/M ratio was 2.43. This sample oxidized at a much slower rate than did sample 105-03, the scoping test specimen also oxidized at 305°C. Oxidation of sample 105-09 was halted because of this marked difference. When unloaded, the sample consisted of powder and a remaining fragment. XRD of the sample is planned for future work.

Sample 105-10 was then oxidized under identical conditions of temperature and ambient atmosphere in the same TGA system that had been used for the oxidation of sample 105-09. As seen in Figure 2.1.3.2-4, the oxidation behavior of this 181.36 mg fragment was intermediate to those of the samples previously oxidized at 305°C. This sample oxidized for 287 hr; however a problem with the balance resulted in no mass data being recorded for the last 60 hr. Prior to this failure, the O/M ratio was calculated as 2.65. It is clear that the variability in oxidation behavior persisted at 305°C.

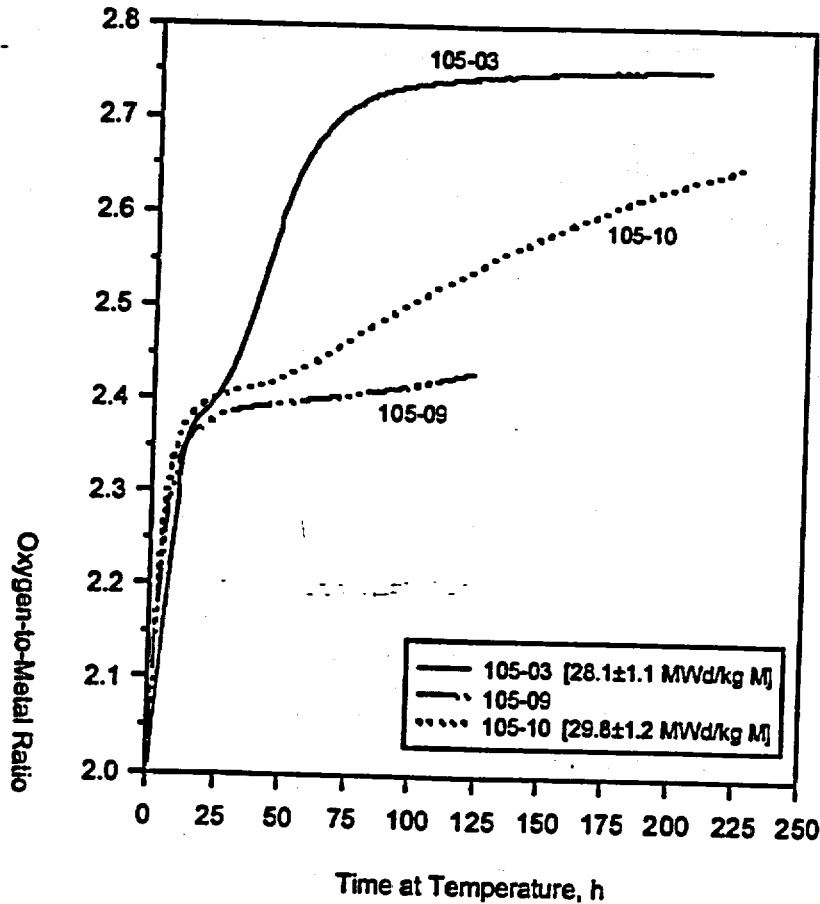
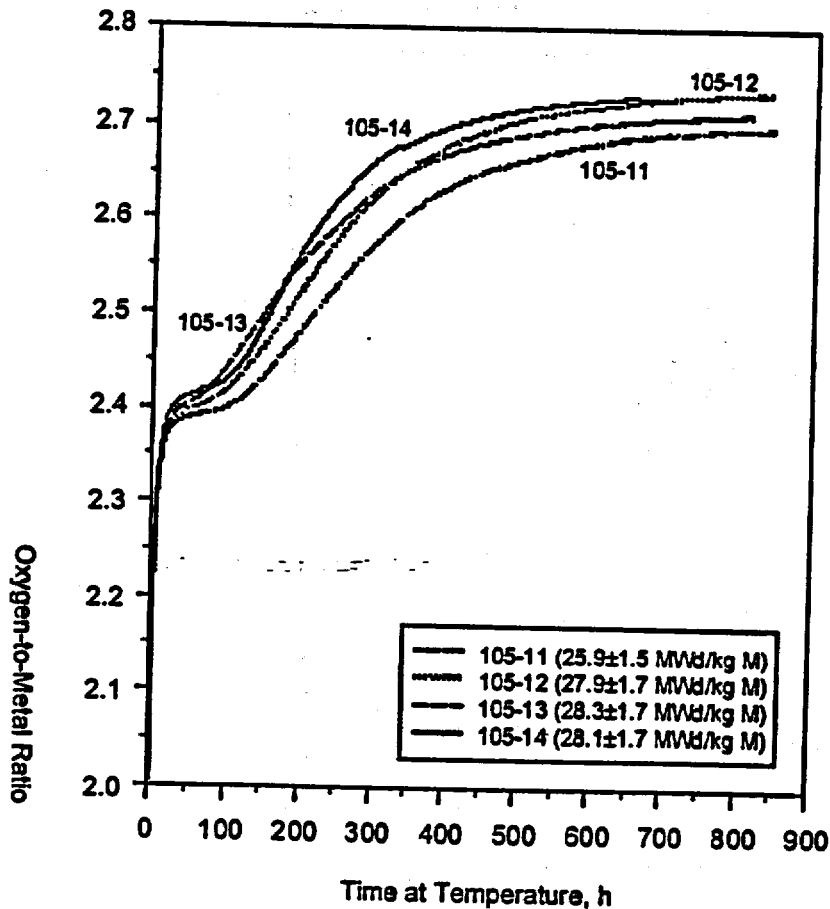


Figure 2.1.3.2-4 Oxidation behavior of ATM-105 fragments oxidized at 305°C

The only known differences among the first 10 samples oxidized were specimen-to-specimen variations and the intermittent cooling of some specimens to room temperature as a result of power fluctuations or computer failure. To test the effect of these variables, one large fragment from the high-burnup region of the ATM-105 fuel was broken into four smaller fragments. All four (samples 105-11 through 105-14) were oxidized individually at 305°C; the time dependence of their oxidation is shown in Figure 2.1.3.2-5.



**Figure 2.1.3.2-5** Oxidation behavior of four samples broken from the same fragment of ATM-105 fuel oxidized at 305°C

Sample 105-11 (143.37 mg) was oxidized for 843.5 hr to a final bulk O/M ratio of 2.70. Concurrently, sample 105-12 (188.27 mg) was oxidized for 840.5 hr to a final bulk O/M ratio of 2.73. Although some variability in the oxidation kinetics is evident (see Figure 2.1.3.2-5), it is much less than seen in Figure 2.1.3.2-4 for fragments with random locations within the same fuel segment.

Sample 105-13 (238.26 mg) was then oxidized under identical conditions. The furnace was turned off after 170 hr when the O/M ratio was 2.53. A subsequent problem with the balance required that the sample remain at room temperature for one month before testing could be resumed. It was necessary to open the system to temporarily add weight to the tare side of the balance. The system was then sealed, evacuated, and filled with dry air. During this procedure, some of the sample fell from the quartz crucible to the bottom of the reaction tube. This was confirmed by the very high activity measured in this location with a Geiger-Mueller detector. Comparison of the mass before and after this incident indicated that about 22.58 mg of the sample fell from the crucible. Because the entire sample had gained only 7.54 mg, it was assumed

that the sample lost included both  $\text{UO}_{24}$  and  $\text{U}_3\text{O}_8$  and that the remaining sample had an O/M ratio of 2.53. The test was restarted and continued for a total oxidation time of 819.5 hr, when a final bulk average O/M ratio of 2.71 was achieved.

Sample 105-14 (241.21 mg) was also oxidized at 305°C. For the first 50 hr, the behavior of this sample was nearly identical to that of sample 105-12. Power to the furnace was turned off after 68 hr when the bulk O/M ratio was 2.42. The sample remained at room temperature for one week before being reheated to 305°C. Oxidation continued for a total of 656 hr, at which time the relay for the temperature controller failed, resulting in a slight rise in the sample temperature; this, in turn, resulted in an automatic loss of power to the furnace. The final bulk O/M ratio was 2.73.

Again, Figure 2.1.3.2-5 clearly illustrates some variability in the oxidation kinetics for these four samples broken from the same larger parent fragment; however, the variability is much less than that observed previously for fragments that were probably located at random locations within the segment of the fuel rod taken for study. Based on the comparison of the results of the oxidation of samples 105-11 through 105-14, and on dry-bath data where the samples are intermittently cooled for periodic weighings, it was concluded that temperature cycling had a relatively small or negligible effect on the characteristics of the fuel oxidation and was not the cause of the variability observed.

It is clear that specimen-to-specimen variability is the major cause of the different oxidation behaviors observed. The small sample size (~200 mg) mandated by radiologic dose control ensures that an individual specimen is much too small to sample across the entire fuel radius. The small sample size, coupled with the axial and radial burnup variations in the fuel, was suspected as the cause of the wide variation found in the oxidation kinetics of  $\text{UO}_{24}$  to  $\text{U}_3\text{O}_8$ . To test this hypothesis, two large fragments of ATM-105 fuel from the low-burnup upper-end of the same fuel rod were each broken into two smaller fragments (samples 105-15 through 105-18) and oxidized at 305°C (Guenther et al., 1991a). The bulk average burnup reported for this segment ranged from 13.5 to 17.5 MWd/kgM.

The variation in the O/M ratio dependence on time for samples 105-15 through 105-18 is shown in Figure 2.1.3.2-6. Samples 105-15 (213.20 mg) and 105-16 (138.68 mg) both oxidized rapidly, achieving an O/M ratio of 2.4 within 16 hr. The plateaus at this lower burnup were merely an inflection in the O/M curve. Sample 105-15 reached an O/M of 2.73 in 78.5 hr and remained at this O/M until the test was terminated after 121 hr. Similarly, sample 105-16 obtained an O/M ratio of 2.71 within approximately 100 hr and remained there until the test was terminated after 142 hr. Samples 105-17 (210.49 mg) and 105-18 (161.97 mg) oxidized even faster and reached bulk O/M ratios of 2.70 and 2.69, respectively, within 50 hr. Clearly, the transformation from  $\text{UO}_{24}$  to  $\text{U}_3\text{O}_8$  occurred much earlier than for the fragments from the high-burnup region.

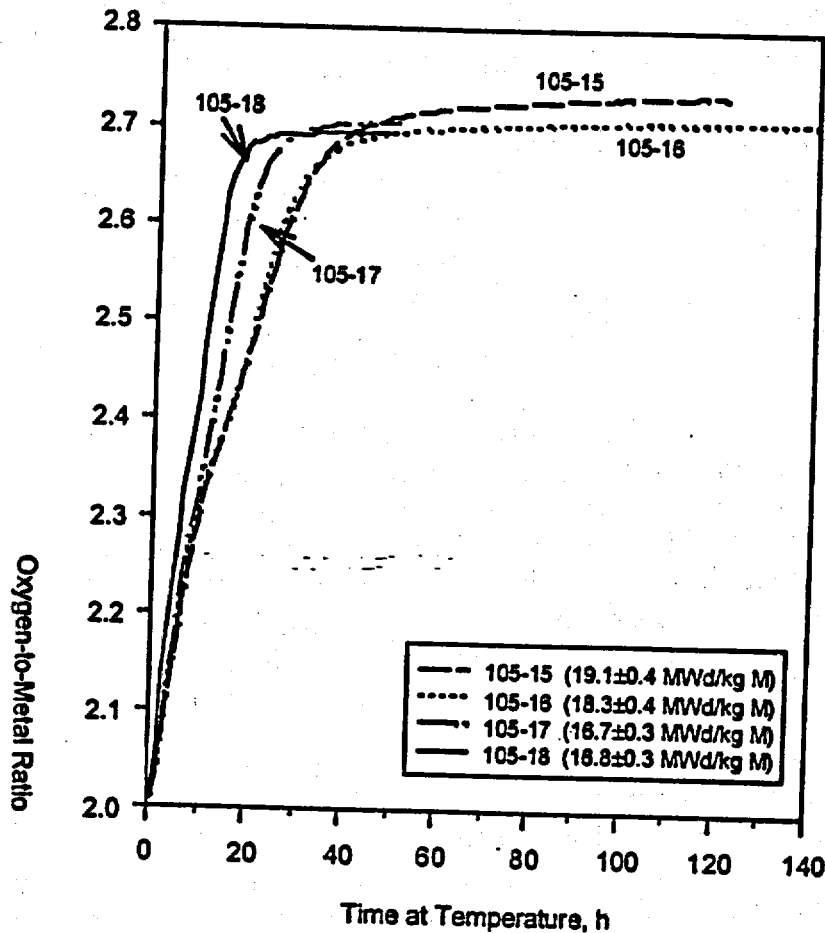


Figure 2.1.3.2-6 Oxidation behavior of low burnup ATM-105 fragments oxidized at 305°C

#### 2.1.3.2.1.4 ATM-104 Tests

To support the burnup dependence on oxidation rate inferred from measurements on fuel fragments that were randomly distributed axially and radially throughout the ATM-105 (boiling-water reactor [BWR]) fuel segments studied, fuel specimens were taken from a specially cut segment of ATM-104 (pressurized-water reactor [PWR]) fuel in which the fuel had not separated from the cladding.

With a low-speed saw, two fragments were taken from near the centerline of a segment from the high-burnup region of the ATM-104 fuel rod (MKP-109), thus reducing the likelihood that the sample would contain the large burnup gradients and highly restructured microstructure found near the fuel surface. The fuel in this region had an estimated bulk average burnup of 44 MWd/kgM (Guenther et al., 1991b). These two fragments, 104-01 and 104-02, were oxidized individually at 305°C (see Figure 2.1.3.2-7). Sample 104-01 (184.53 mg) was oxidized to an O/M ratio of approximately 2.41 within 100 hr and exhibited a plateau with zero slope for approximately 400 hr before mass increase resumed. The test was terminated after 1201 hr and gave a final

O/M ratio of 2.51. Sample 104-02 (213.90 mg) oxidized to an O/M ratio of about 2.40 within 120 hr and remained on this plateau with no mass increase for more than 500 hr before mass increase resumed, albeit at a much slower rate than with sample 104-01. A final bulk average O/M ratio of 2.42 was reached before the test was terminated after 1200 hr.

Oxidation of these PWR fragments clearly demonstrated much longer plateaus than those observed in oxidation of the lower burnup ATM-105 (BWR) fragments at the same temperature and under similar atmosphere. While further testing should be performed to rule out the possible dependence of the stabilization effect (plateau behavior of the transition from  $UO_2$  to  $U_3O_8$ ) on reactor type, the data obtained in these measurements strongly suggest similar burnup dependencies for BWR and PWR fuels.

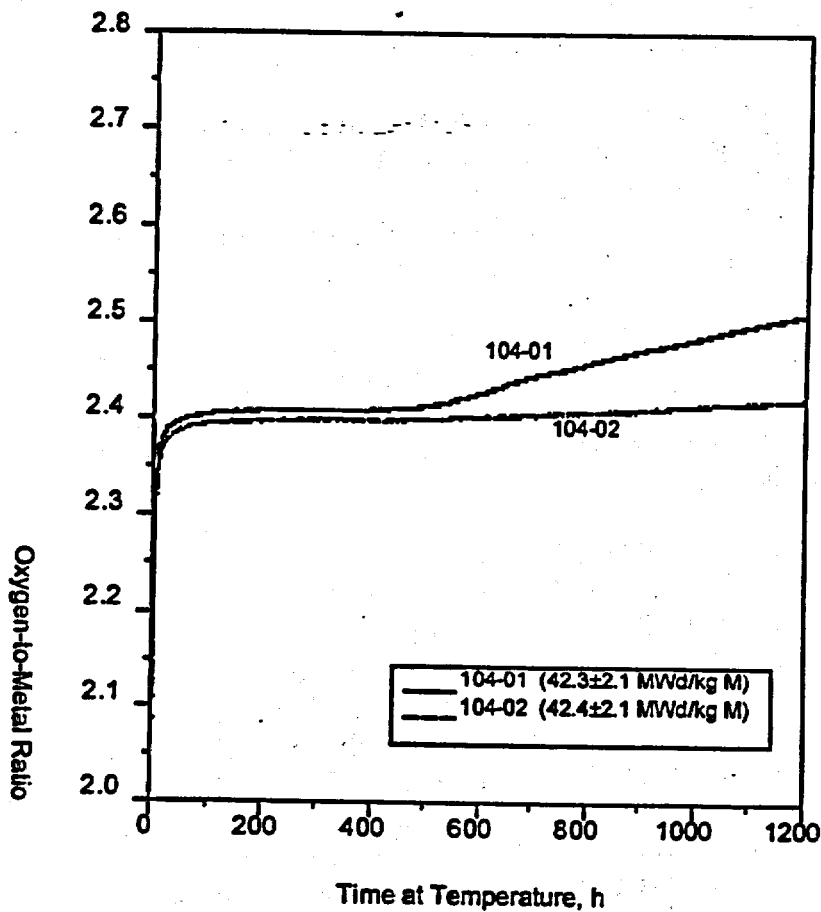


Figure 2.1.3.2-7 Oxidation behavior of ATM-104 fragments at 305°C

#### 2.1.3.2.1.5 ATM-108 Tests

In this final test, two fragments of fuel from the high-burnup region of ATM-108 were obtained in a manner similar to that for the ATM-104 samples. One fragment (108-01) was cut from near the centerline of a pellet, and a second fragment (108-02) was cut from the pellet surface. ATM-108 is a group of fuel rods from the same assembly as ATM-105; however, the rods making up ATM-108 contained an initial doping of  $Gd_2O_3$  to serve as a burnable poison for reactivity control. The rod (ADN0206) from which these samples were cut contained 3 wt%  $Gd_2O_3$  and the same initial enrichment (2.93 wt%) of  $^{235}U$  as did the ATM-105 rod from which the previous samples were obtained. The burnup of the ATM-108 fuel in this region was expected to be approximately 26-28 MWd/kgM (Guenther et al., 1994), slightly lower than the 28.5 to 31.5 MWd/kgM expected for the ATM-105 high-burnup region (Guenther et al., 1991a).

The initial Gd in the fuel undergoes neutron capture during reactor operations and remains as Gd, although of higher atomic mass number. Both the substitution of U with fission products and actinides and the Gd-doping were expected to stabilize the  $UO_{2.4}$  with respect to oxidation to  $U_3O_8$ . The actual distribution of  $Gd_2O_3$  within the fuel is not known; however, the homogeneity of these early fuels is questionable.

Sample 108-01 (171.01 mg) was cut from near the centerline of the fuel pellet and was oxidized at 305°C for more than 2400 hr. As seen in Figure 2.1.3.2-8, this sample did not exhibit a plateau with zero slope, but exhibited a very slow, continuous increase in the O/M ratio. The time required to oxidize this sample from an O/M of about 2.475 to 2.481 was approximately 1000 hr.

On the other hand, sample 108-02 (232.23 mg) was taken from the higher burnup fuel pellet surface and has exhibited two different plateau behaviors. The first plateau, at an O/M ratio of approximately 2.38, was reached after about 40 hr and had a duration of less than 50 hr before more rapid mass increase resumed. A second plateau at an O/M ratio of 2.45 was reached after about 475 hr and then exhibited a plateau with zero slope for more than 2000 hr. It is believed that those portions of the specimen with lower burnup or lower Gd content have oxidized to  $U_3O_8$ , while the portions with higher substitutional impurities remained at  $UO_{2.4}$ . This would explain the second plateau at such a low O/M ratio. Post-oxidation analyses are planned to determine the quantity of each phase present. Clearly, these irradiated samples doped with  $Gd_2O_3$  have exhibited much slower overall oxidation behavior than have any other specimen oxidized at 305°C.

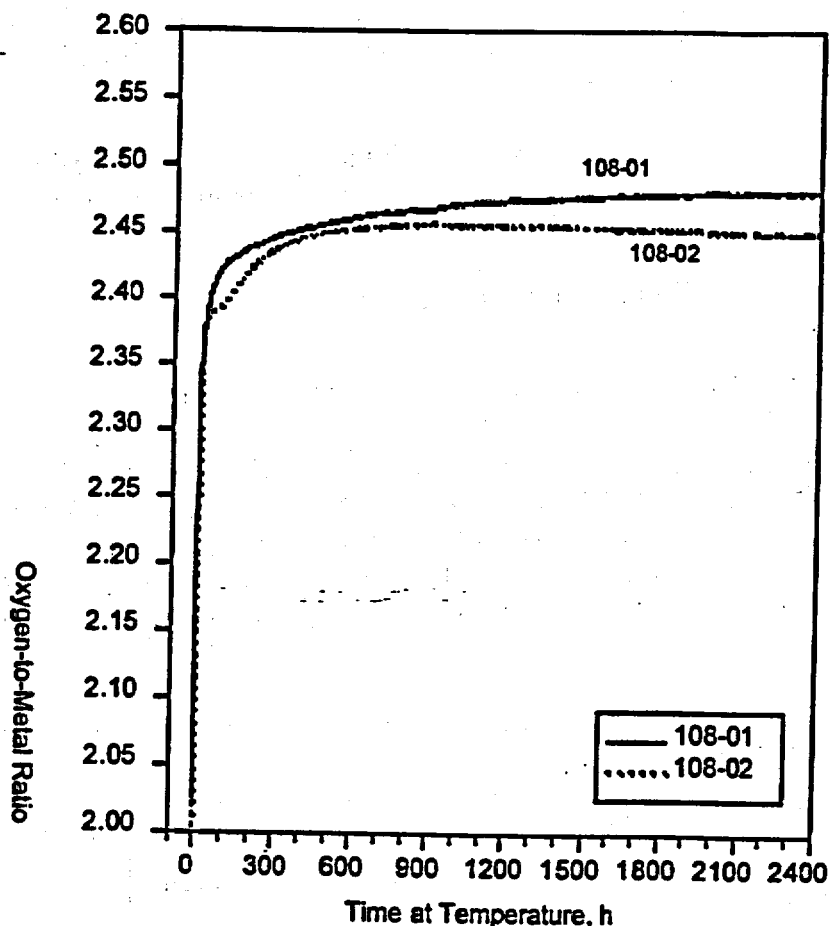


Figure 2.1.3.2-8 Oxidation behavior of ATM-108 fragments at 305°C

### 2.1.3.2.2 Burnup Analyses

#### 2.1.3.2.2.1 <sup>148</sup>Nd Isotope-Dilution Method

At the end of 1996, authorization and funding were obtained to perform an analysis of the burnup of some of the individual specimens that had been oxidized previously. Nine of the 18 samples oxidized prior to that time were chosen. Samples 105-01 and 105-02 had been disposed of and were unavailable for any further testing. The remaining specimens from the scoping tests (105-03 through 105-05), the 283°C tests (105-6 through 105-08), and three of the 305°C tests (105-10, 105-11, and 105-15), including one of the known low-burnup specimens, were analyzed for burnup using the method essentially equivalent to American Society for Testing and Materials (ASTM) procedure E321 (ASTM, 1990). The results of this analysis are found in Table 2.1.3.2-1 and are identified on the appropriate oxidation curves in square brackets. The

uncertainty of  $\pm 4\%$  accounts for experimental uncertainty and the reported uncertainty in converting atom percent burnup to burnup in units of MWd/kgM (ASTM, 1990). Analysis of other specimens will be performed is planned.

Table 2.1.3.2-2 lists the number of fissions and the total number of uranium and plutonium atoms normalized to the mass of the specimen in the one-tenth mL aliquots analyzed. The atom percent burnup is calculated using

$$\text{atom\% burnup} = \text{Fissions} / (\text{U} + \text{Pu} + \text{Fissions})$$

2.1.3.2-2

Also included is the fraction of  $^{242}\text{Pu}$  in the total Pu, as determined by thermal ionization mass spectrometry. The amount of  $^{242}\text{Pu}$  can be used to qualitatively order the samples with respect to possible higher actinide content. The atom densities reported for sample 105-11 appear very low with respect to the other samples; however, additional calculations (comparing the ratios of the atom densities of this sample to samples of similar burnup) seem to indicate that the burnup results are correct. It is suspected that either the reported mass was incorrect (too large) or that not all of the sample dissolved.

Table 2.1.3.2-2 Atom densities found by mass spectrometry normalized to sample mass

Sample	Atom Density U	Atom Density Pu	Atom Density Fissions	Percent $^{242}\text{Pu}$
105-03	$8.107 \times 10^{18}$	$5.583 \times 10^{18}$	$2.458 \times 10^{17}$	8.03
105-04	$8.247 \times 10^{18}$	$5.629 \times 10^{18}$	$2.445 \times 10^{17}$	7.56
105-05	$8.234 \times 10^{18}$	$7.209 \times 10^{18}$	$2.610 \times 10^{17}$	7.79
105-06	$8.033 \times 10^{18}$	$7.104 \times 10^{18}$	$2.753 \times 10^{17}$	9.01
105-07	$8.109 \times 10^{18}$	$5.610 \times 10^{18}$	$2.414 \times 10^{17}$	7.84
105-08	$8.069 \times 10^{18}$	$7.206 \times 10^{18}$	$2.851 \times 10^{17}$	10.44
105-10	$7.933 \times 10^{18}$	$6.548 \times 10^{18}$	$2.559 \times 10^{17}$	8.19
105-11	$6.386 \times 10^{18}$	$5.157 \times 10^{18}$	$2.048 \times 10^{17}$	8.46
105-15	$8.343 \times 10^{18}$	$4.169 \times 10^{18}$	$1.653 \times 10^{17}$	3.17

#### 2.1.3.2.2.2 Gamma Spectrum Analysis

The burnup of all specimens starting with sample 105-11 was determined prior to oxidation by correlating the specific activity of  $^{137}\text{Cs}$  with ORIGEN2 predictions. The specific activity for each sample, the uncertainty associated with the combined effects of the  $\gamma$ -ray self-absorption and statistical and calibration uncertainties, and the corresponding burnup range are listed in Table 2.1.3.2-3. Burnups calculated by comparing the measured  $^{137}\text{Cs}$  specific activity with ORIGEN2 predictions are also included in parentheses in the corresponding oxidation curves. Included in Table 2.1.3.2-3 are the specific activities for  $^{241}\text{Am}$  and the rather large uncertainties associated

with this isotope. Although the activity of  $^{241}\text{Am}$  is not a good measure of burnup, it is the only higher actinide detected by this method and is the only means of qualitatively determining the relative higher actinide content of samples. Samples from near the pellet surface will have not only higher burnup, but larger concentrations of higher actinides due to the resonance absorption in  $^{238}\text{U}$ .

Table 2.1.3.2-3 Burnup as a function of  $^{137}\text{Cs}$  specific activity

Sample	Specific activity of $^{137}\text{Cs}$ ( $\mu\text{Ci}/\text{mg}$ )	Burnup (MWd/kgM)	Specific activity of $^{241}\text{Am}$ ( $\mu\text{Ci}/\text{mg}$ )
105-11	48.3±2.9	25.9±1.5 (3.9)	1.6±0.5
105-12	52.1±3.1	27.9±1.7 (4.2)	1.9±0.6
105-13	52.8±3.2	28.3±1.7 (4.2)	1.1±0.3
105-14	52.5±3.2	28.1±1.7 (4.2)	2.0±0.6
105-15	34.9±0.7	19.1±0.4 (2.9)	1.4±0.4
105-16	33.3±0.7	18.3±0.4 (2.7)	0.8±0.2
105-17	30.3±0.6	16.7±0.3 (2.5)	0.7±0.2
105-18	30.6±0.6	16.8±0.3 (2.5)	1.1±0.3
104-01	80.8±4.0	42.3±2.1 (6.3)	1.8±0.5
104-02	81.1±4.1	42.4±2.1 (6.4)	2.0±0.6
108-01 <sup>a</sup>	31.3±3.1	17.6±1.8 (2.6)	Not detected
108-02 <sup>a</sup>	63.0±3.2	34.8±1.9 (5.2)	18.0±6.7

<sup>a</sup> ORIGEN2 runs were performed using the same input parameters as for the ATM-105 samples (i.e.,  $\text{Gd}_2\text{O}_3$  doping was ignored).

In the present tests, two samples had burnup determined by both the  $^{148}\text{Nd}$  and  $^{137}\text{Cs}$  methods. ORIGEN2 was run for the burnups found by the  $^{148}\text{Nd}$  method for these two samples, and the specific activity of  $^{137}\text{Cs}$  predicted by ORIGEN2 was compared with the measured value. Sample 105-15 had a burnup of  $18.6\pm0.7$  MWd/kgM measured using the isotope-dilution method. The  $^{137}\text{Cs}$  activity predicted for a BWR sample with this burnup was within 3% of the value measured by the  $\gamma$ -ray energy analysis.

Similarly, sample 105-11 had a measured burnup of  $29.6\pm1.2$  MWd/kgM. ORIGEN2 predicted a specific activity of  $55.5 \mu\text{Ci}/\text{mg}$ , which is 13% larger than the experimentally measured value of  $48.3 \mu\text{Ci}/\text{mg}$ . The deviation of the predicted value from the measured value ranged from 8% (at  $+1\sigma$  of the measured value) to 18% (at  $-1\sigma$ ). With the estimated uncertainty of about 4% for the  $^{148}\text{Nd}$  analysis and an average difference between the ORIGEN2 burnup prediction for  $^{137}\text{Cs}$  activity and experimental values of 13%, it is reasonable to assume an uncertainty in the burnup estimates obtained through  $\gamma$ -ray spectroscopy of approximately  $\pm 15\%$ . This 15% uncertainty is expressed in parentheses for the burnups reported in Table 2.1.3.2-3. The smaller uncertainties are those associated with the uncertainty in the specific activity only. It is

important to note the marked difference in  $^{137}\text{Cs}$  activity and the corresponding difference in local burnup between sample 108-02, which was taken from the pellet surface, and sample 108-01, which was taken from the pellet centerline.

### 2.1.3.2.3 Dry-Bath Oxidation Results

During the past 10 yr, more than 100 different samples have been oxidized at various temperatures in the dry-baths. A large fraction of the samples has been oxidized at temperatures less than  $150^{\circ}\text{C}$ ; even though they had operated for almost 50,000 hr, the bulk average O/M ratios were less than 2.2. For the purpose of this study, the primary focus was on samples that consisted of fragments (as opposed to fragments crushed to powders) and were oxidized in dry air to an O/M ratio near the plateau. As with the TGA studies, the precise axial and radial location of the fuel samples in the fuel rod segments is not known.

#### 2.1.3.2.3.1 $175^{\circ}\text{C}$ Tests

Multiple samples of each of the fuels have been oxidized at  $175^{\circ}\text{C}$  in two separate dry-baths using a dry-air atmosphere. Overall agreement of the samples for each fuel type has been excellent, with the largest difference in the O/M ratio between samples at any given time being approximately 0.04. Each sample had an initial mass of approximately 10 g; however, the number of fragments required to make up this sample varied greatly. For example, the three different ATM-105 samples contained 15, 22, and 28 fragments, respectively. The number of fragments for a 10 g sample of Turkey Point fuel ranged from 31 to 34, while the range was from 15 to 40 and 35 to 101 for ATM-104 and ATM-106, respectively.

The corresponding variation in surface area exposed to the oxidant is thought to be one reason for the minor differences in the initial mass increase among samples of the same fuel type. Also, fragments from near the pellet surface will have a high concentration of fine fission gas bubbles on the grain boundaries, promoting more rapid oxidation than promoted for the fuel near the center where the bubbles are larger and fewer in number. This hypothesis is substantiated by the fact that the differences among samples decreased with increasing time such that the O/M ratios for samples of each fuel type varied by no more than 0.02 at the end of these experiments. The temperature difference between the two blocks of dry-bath #1 was roughly  $7^{\circ}\text{C}$ , which also contributed to the more rapid mass increase for some of the samples. Figure 2.1.3.2-9 shows the change in the O/M ratio as a function of time for one sample of each of the four fuel types. For each fuel, with the possible exception of ATM-106, it appears that a plateau at an O/M of about 2.4 had been reached, and mass increase was continuing to occur at the end of the measurements.

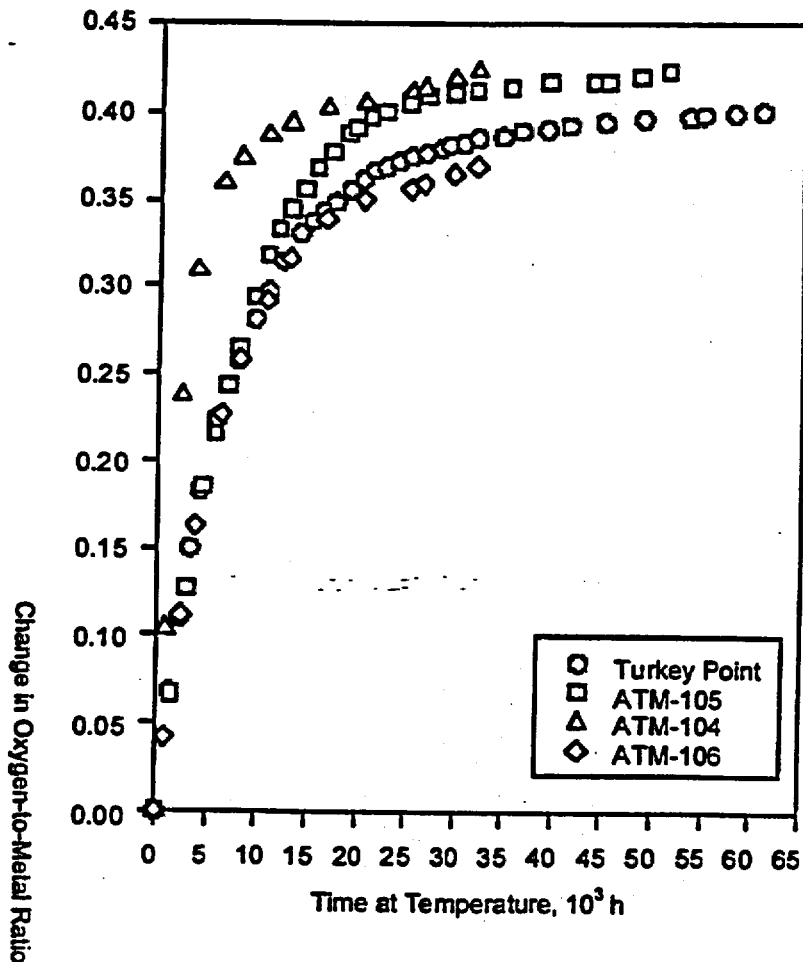


Figure 2.1.3.2-9 Oxidation behavior of light-water reactor (LWR) spent-fuel fragments oxidized in a 175°C dry-bath

#### 2.1.3.2.3.2 195°C Tests

One sample of each of the four fuel types was oxidized in a dry-air atmosphere at 195°C. In each case, the sample consisted of fragments that had been crushed and sieved to a Tyler mesh size of -12/+24 (roughly 0.7 to 1.7 mm). Figure 2.1.3.2-10 shows the change in the O/M ratio as a function of time for these four samples. With the exception of the Turkey Point fuel, which had been previously oxidized for 28,868 hr at 110°C to a bulk O/M of 2.009, all of the samples were as-irradiated and assumed to have an O/M of 2.00. The ATM-105 sample was freshly crushed for this test; the ATM-104 and ATM-106 samples were from powder stored for 3 yr prior to the start of this test. Again, it appears that a plateau in the range of O/M 2.35 to 2.40 had been reached, and mass increase was continuing to occur at the end of the measurements.

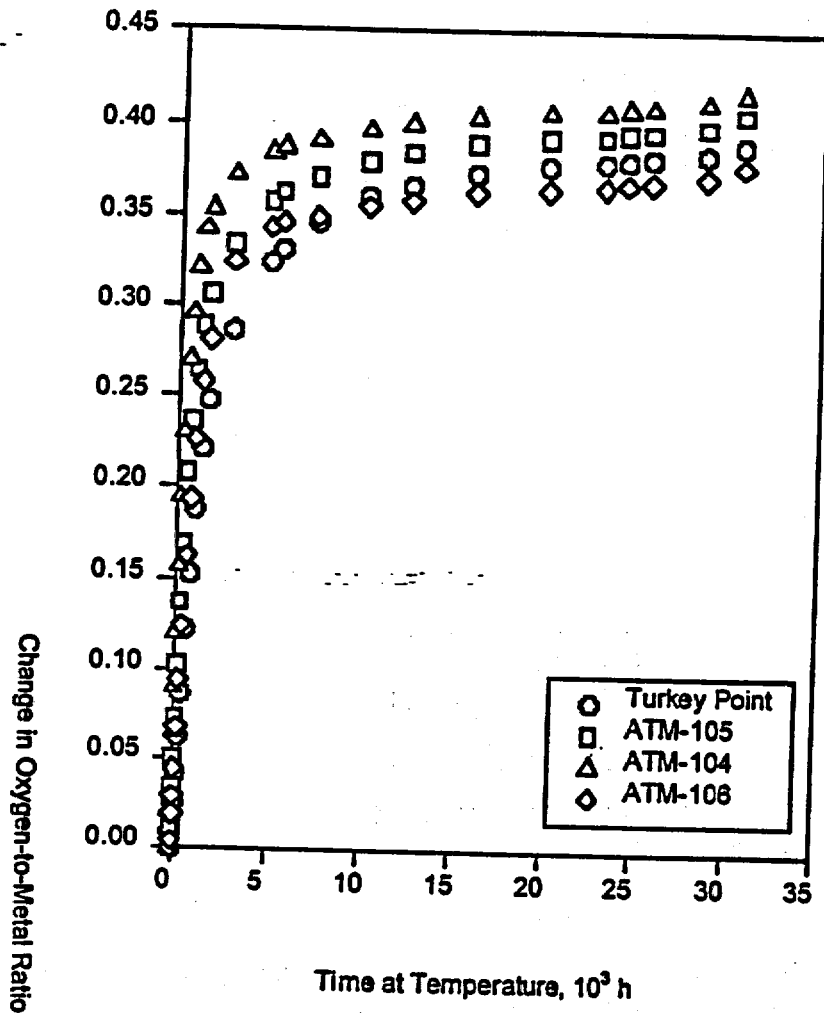


Figure 2.1.3.2-10 Oxidation behavior of crushed LWR spent-fuel fragments in a 195°C dry-bath

### 2.1.3.2.3.3 255°C Test

In 1993, a dry-bath test at 255°C was initiated. This test contained 11 samples, 7 of which each consisted of approximately 5 g of spent fuel fragments, with the remaining 4 samples consisting of approximately 5 g each of crushed fuel fragments. The seven samples were as follows:

- One sample each of ATM-104 and ATM-105 from as-irradiated (no prior oxidation) fuel fragments
- One each of Turkey Point (110°C for 28,868 hr to O/M ~2.004) and ATM-106 (110°C for 525 hr to O/M ~2.000) that had been very slightly oxidized at low temperature

- One each of Turkey Point (175°C for 43,945 hr to O/M ~2.395), ATM-105 (175°C for 34,420 hr to O/M ~2.422), and ATM-104 (176°C for 15,671 hr to O/M ~2.395) from fragments that had been oxidized to an O/M ratio near the plateau at 175°C

Figure 2.1.3.2-11 is a plot of the oxidation curves for the as-irradiated and slightly pre-oxidized samples. Unlike the previous data of Einziger and Strain (1986), in which the plateau at 250°C existed for almost 10,000 hr, none of these samples exhibited the typical plateau behavior. The lack of an observable plateau for these samples, which started with an O/M <2.005, is in marked contrast to the behavior of the Turkey Point and ATM-105 samples that had been pre-oxidized to an O/M ratio near the plateau at lower temperatures before being oxidized at 255°C.

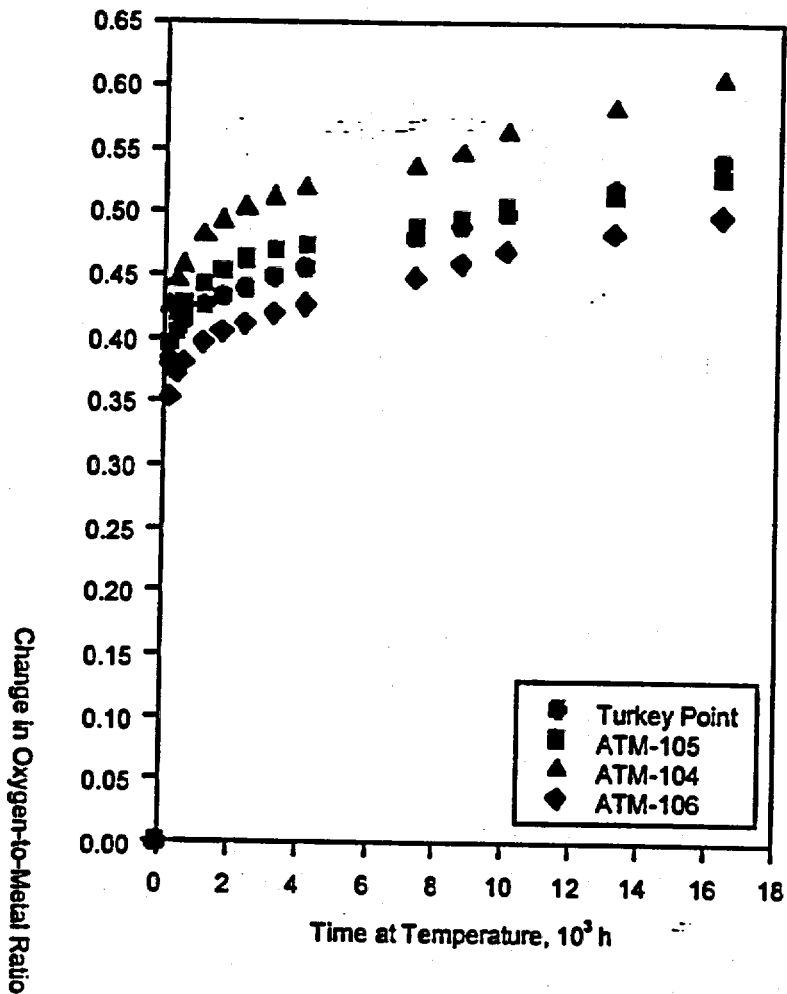


Figure 2.1.3.2-11 Oxidation behavior of as-irradiated LWR spent-fuel fragments in a 255°C dry-bath

The open symbols in Figure 2.1.3.2-12 represent the samples that had been pre-oxidized. The previously oxidized samples of Turkey Point and ATM-105 fuel clearly exhibited plateau behavior, although the duration was much less than that expected based on the previous Einziger data (Einziger and Strain, 1986).

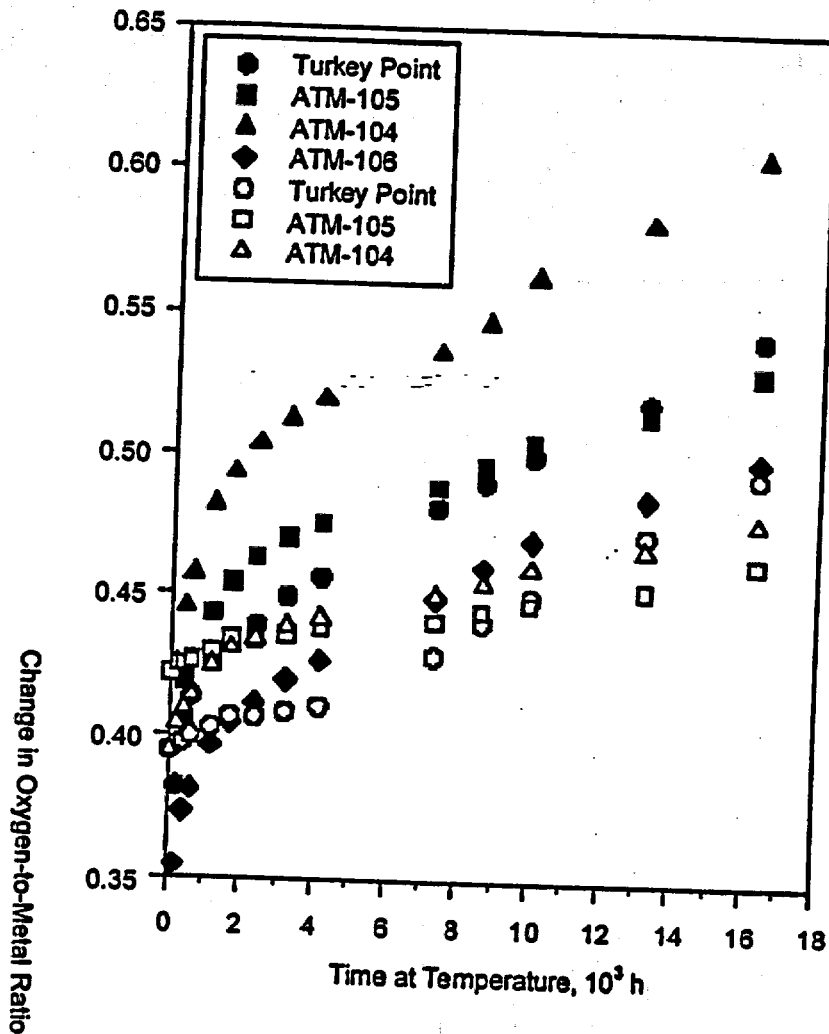


Figure 2.1.3.2-12 Oxidation behavior of as-irradiated and pre-oxidized (open symbols) LWR spent-fuel fragments in a 255°C dry-air bath

The ATM-104 pre-oxidized sample, on the other hand, had no observable plateau. All samples did, however, begin to oxidize at about the same rate of change in O/M ratio after approximately 4000 hr. (No interim weighings to determine mass increase were performed between 4095 and 7281 hr). Figure 2.1.3.2-13 is a plot of the oxidation curves for the four different Turkey Point fuels oxidized in the 255°C dry-bath test. Again, it is clear that the sample oxidized at a lower temperature to an O/M ratio of about 2.4 prior to oxidation at 255°C exhibited a plateau (open circles), whereas the as-

irradiated or only slightly pre-oxidized samples (closed symbols) exhibited no plateau. It is also clear that the crushed fragments increased in mass much more quickly than did the intact fragments because of the much larger surface area exposed.

XRD of the samples oxidized in the 255°C dry-bath with an O/M ratio as high as 2.56 has detected  $U_4O_9$ , with only minor  $U_3O_8$  formation, even though the two Turkey Point samples and one of the ATM-105 samples had formed significant amounts of powder. A Turkey Point sample of crushed fragments also oxidized at 255°C had obtained a bulk O/M ratio of 2.62; still the only phase identified by XRD was  $U_4O_9$ . The lack of observable  $U_3O_8$  at these relatively high O/M ratios is in contrast to the TGA studies in which  $U_3O_8$  has been identified in samples oxidized at 283°C to an O/M as low as 2.49.

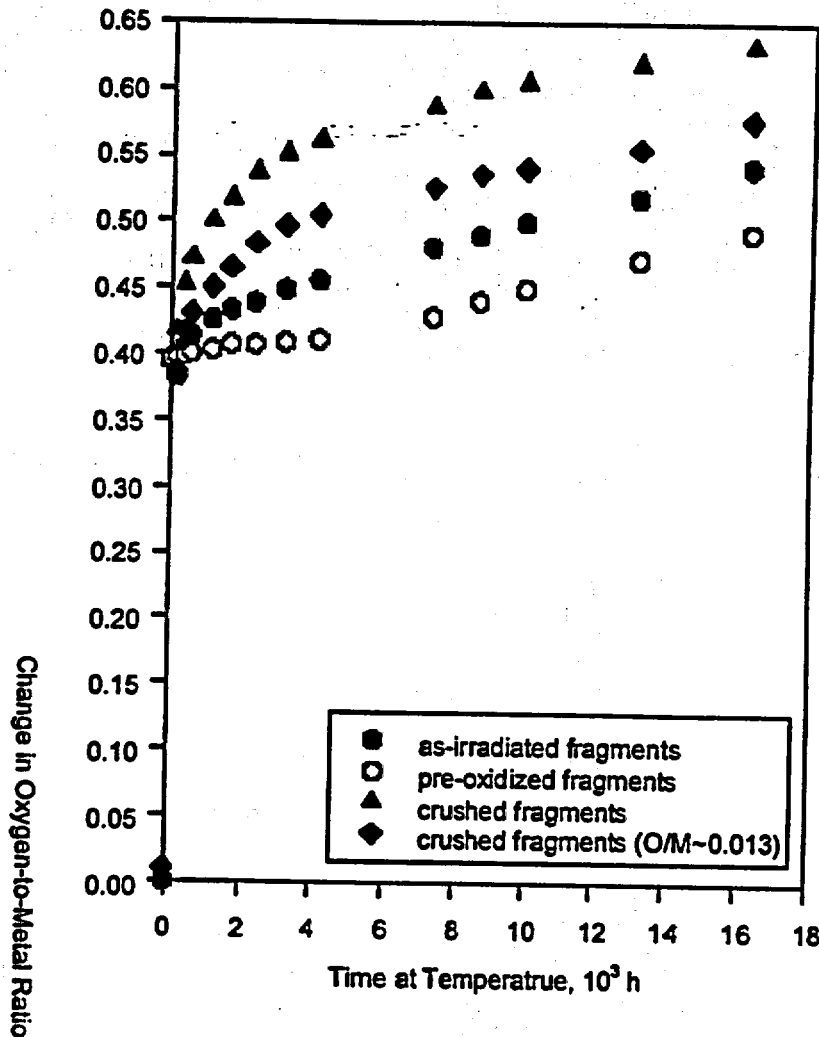


Figure 2.1.3.2-13 Oxidation behavior of Turkey Point fuel in a 255°C dry-bath

### 2.1.3.2.4 Quantitative XRD Results

A quantitative XRD analysis of spent-fuel samples oxidized in the dry-baths and having average O/M ratios ranging from 2.40 to 2.61 was conducted by Larry Thomas of Pacific Northwest National Laboratory (PNNL) (Einziger et al., 1995) by combining known quantities of fuel and a reference material (in this case,  $\text{Al}_2\text{O}_3$ ). Using the integrated peak intensities, with the knowledge of the amount of material present, it was possible to determine the weight fractions of each phase present.

Figure 2.1.3.2-14 is a plot of the peak intensity of the  $\text{U}_4\text{O}_9$  ( $\text{UO}_{2.4}$ ) peak when normalized to the  $\text{Al}_2\text{O}_3$  standard and corrected for the fuel to  $\text{Al}_2\text{O}_3$  weight ratio of each sample. It is clear that, as the O/M ratio increases, the amount of  $\text{UO}_{2.4}$  present decreases. There is also a corresponding broadening of the X-ray peak. Because no other phases are present, it is clear that the  $\text{UO}_{2.4}$  is being transformed into a phase that is amorphous to XRD, meaning it is either a nanocrystalline phase or is truly amorphous. Analysis of 10 oxidized samples resulted in an average O/M of  $2.70 \pm 0.08$  for this "amorphous" phase. A truly amorphous phase would not be expected to have such a constant O/M. Because the calculated O/M ratio is very similar to that of  $\text{U}_3\text{O}_8$ , it is believed that oxidation of spent fuel beyond  $\text{UO}_{2.4}$  at temperatures  $\leq 255^\circ\text{C}$  results in  $\text{U}_3\text{O}_8$  formation, but in a nanocrystalline state that is not readily detected by XRD. This is in agreement with the findings of Hoekstra et al. (1961), who have shown that  $\text{U}_3\text{O}_8$  formed below about  $250^\circ\text{C}$  may be poorly crystalline.

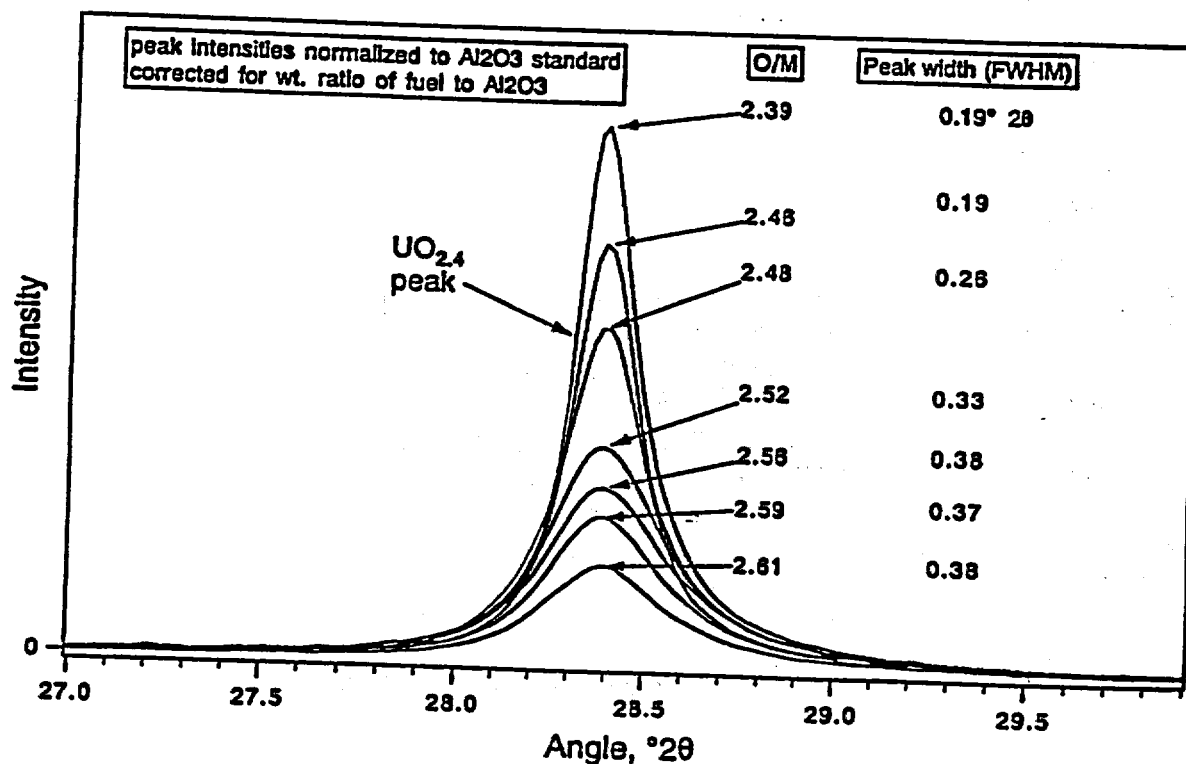


Figure 2.1.3.2-14 Quantitative XRD analysis of oxidized LWR spent fuel  
Version 1.3  
2.1.3.2-24

### 2.1.3.2.5 References

- ASTM (1990). "Standard Test Method for Atom Percent Fission in Uranium and Plutonium Fuel (Neodymium-148 Method)" (Standard E 321) *Annual Book of ASTM Standards*, Vol. 12.02. Philadelphia, PA: American Society for Testing and Materials.
- Einzigler, R. E., and R. V. Strain (1986). "Behavior of Breached Pressurized Water-Reactor Spent-Fuel Rods in an Air Atmosphere Between 250°C and 360°C." *Nucl. Technol.* 75(1):82-95.
- Einzigler, R. E., L.E. Thomas, and B. D. Hanson (1995). *Oxidation of Spent LWR Fuel, FY 95 Year end Report*. (MOL212 and MOL213 combined interim report). Richland, WA: Pacific Northwest National Laboratory. [MOL.19960611.0215]
- Einzigler, R. E., L. E. Thomas, H. C. Buchanan, and R. B. Stout (1992). "Oxidation of Spent Fuel in Air at 175 to 195°C," *J. Nucl. Mat.* 190:53-60. [MOL.19980213.0585]
- Guenther, R. J., D. E. Blahnik, T. K. Campbell, U. P. Jenquin, J. E. Mendel, L. E. Thomas, and C. K. Thornhill (1991a). *Characterization of Spent Fuel Approved Testing Material-ATM-105*. (PNL-5109-105) Richland, WA: Pacific Northwest National Laboratory. [NNA.19911217.0014]
- Guenther, R. J., D. E. Blahnik, U. P. Jenquin, J. E. Mendel, L. E. Thomas, and C. K. Thornhill (1991b). *Characterization of Spent Fuel Approved Testing Material- ATM-104*. (PNL-5109-104) Richland, WA: Pacific Northwest National Laboratory. [NNA.19911218.0073]
- Guenther, R. J., D. E. Blahnik, and N. J. Wildung (1994). *Radiochemical Analyses of Several Spent Fuel Approved Testing Materials*. (PNL-10113) Richland, WA: Pacific Northwest Laboratory.
- Hanson, B. D. (1998). *The Burnup Dependence of Light Water Reactor Spent Fuel Oxidation*. (Report No. 98-XX, modified from the dissertation of Brady D. Hanson submitted for the degree of Ph.D. in Engineering-Nuclear Engineering at the University of California, Berkeley) Richland, WA: Pacific Northwest National Laboratory.
- Hoekstra, H. R., A. Santoro, and S. Siegel (1961). "The Low Temperature Oxidation of  $UO_2$  and  $U_4O_9$ ," *J. Inorg. Nucl. Chem.* 18:166-178.

Section 2.1.3.2, Appendix A

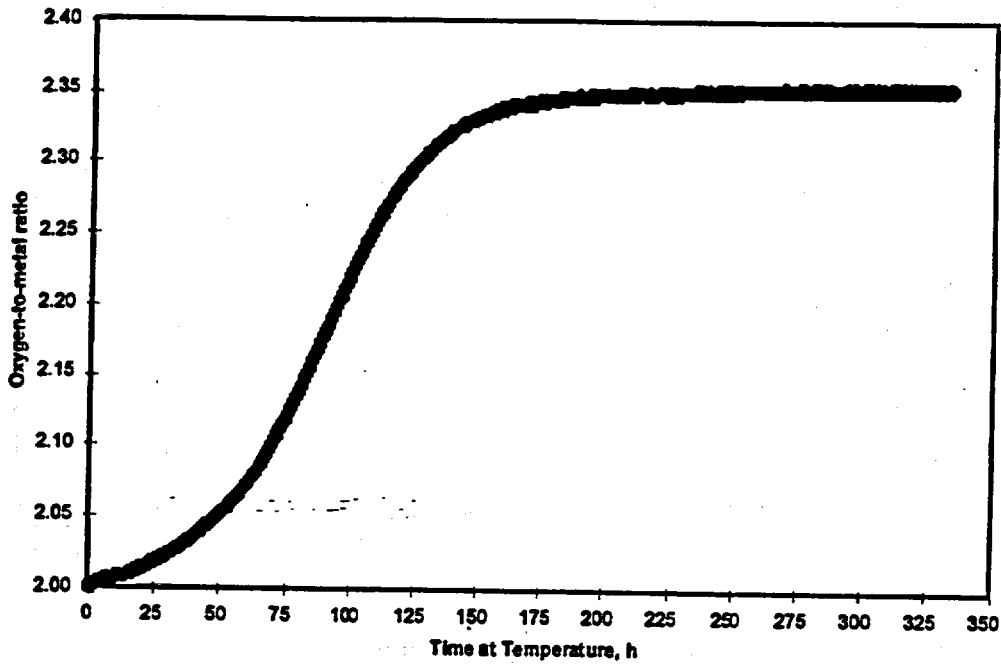


Figure 2.1.3.2-A-1 Sample of unirradiated UO<sub>2</sub> with 8 wt% Gd<sup>203</sup> oxidized at 283°C

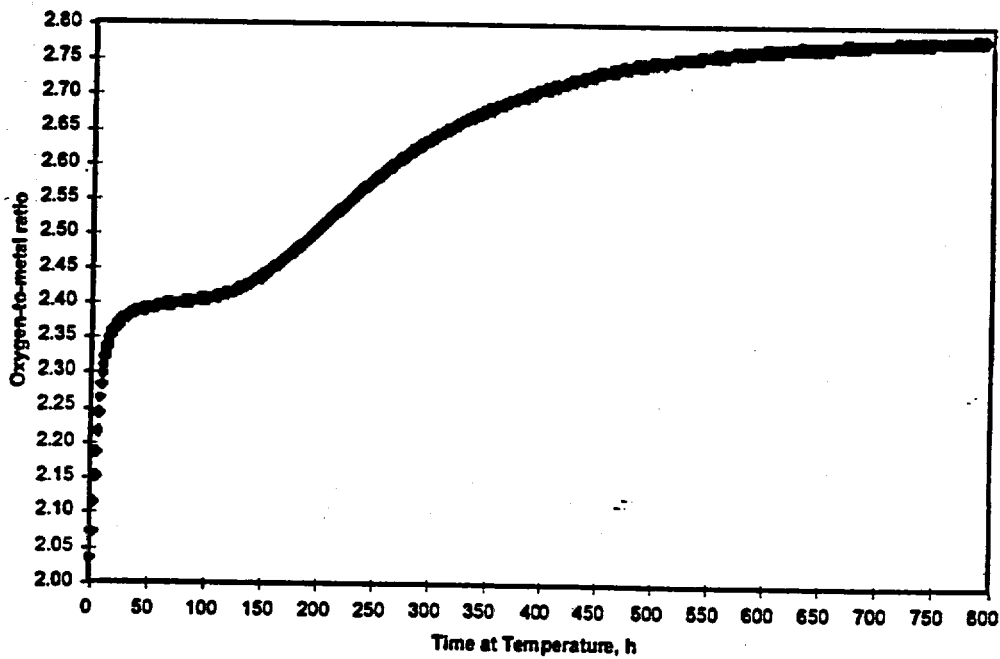


Figure 2.1.3.2-A-2 Sample of 105-01 oxidized at 283°C

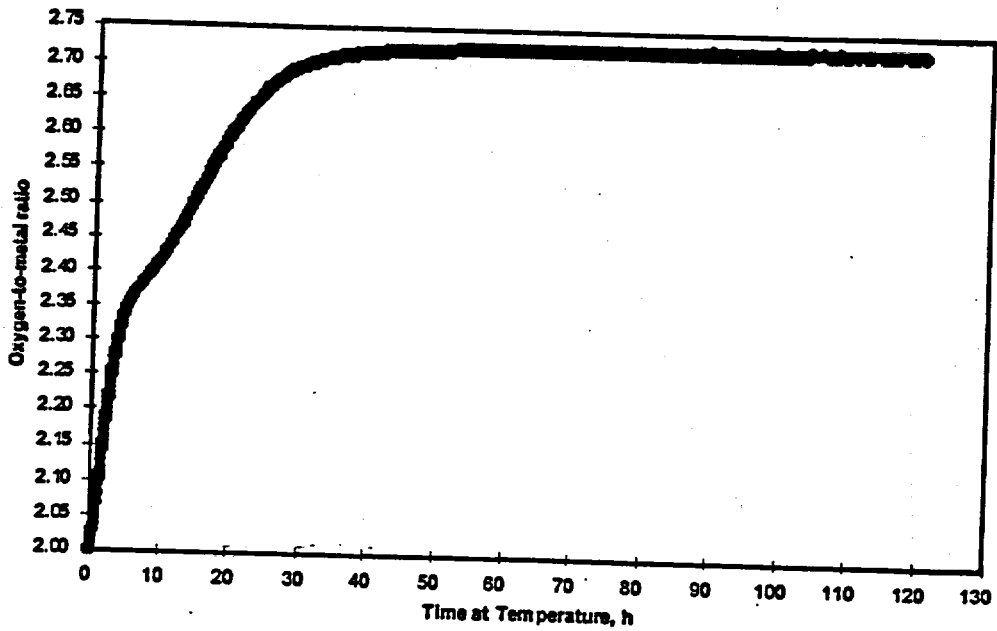


Figure 2.1.3.2-A-3 Sample 105-02 oxidized at 325°C

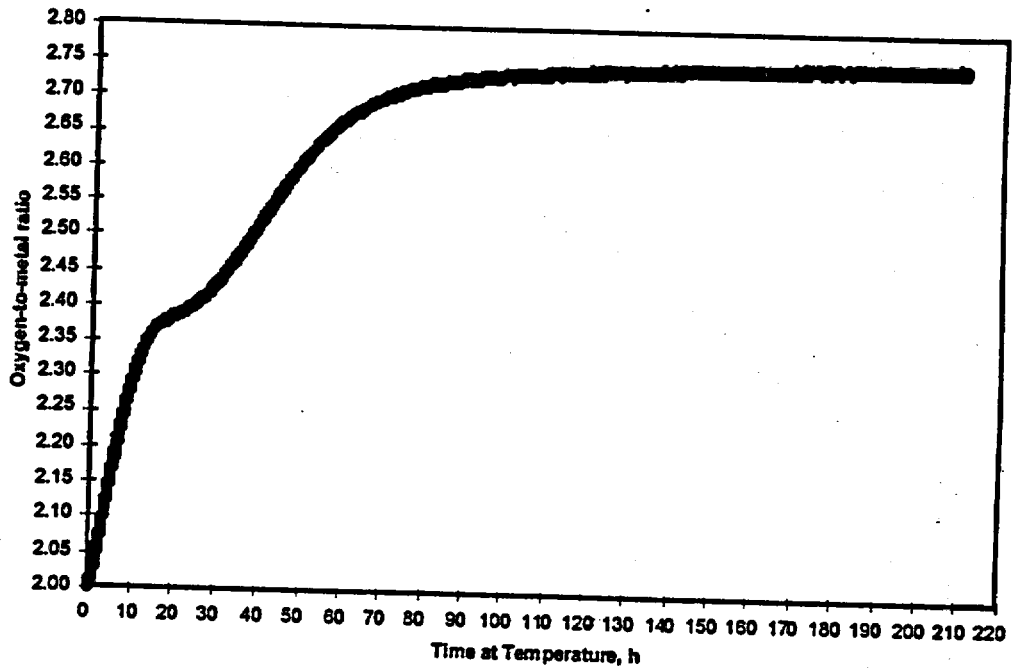


Figure 2.1.3.2-A-4 Sample 105-03 oxidized at 305°C

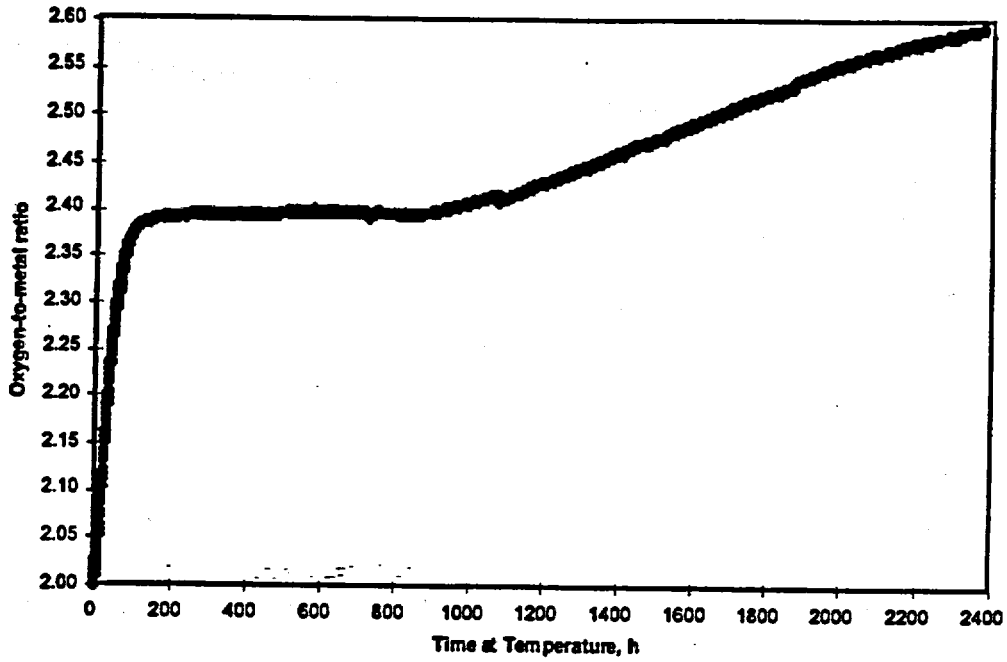


Figure 2.1.3.2-A-5 Sample 105-04 oxidized at 270°C

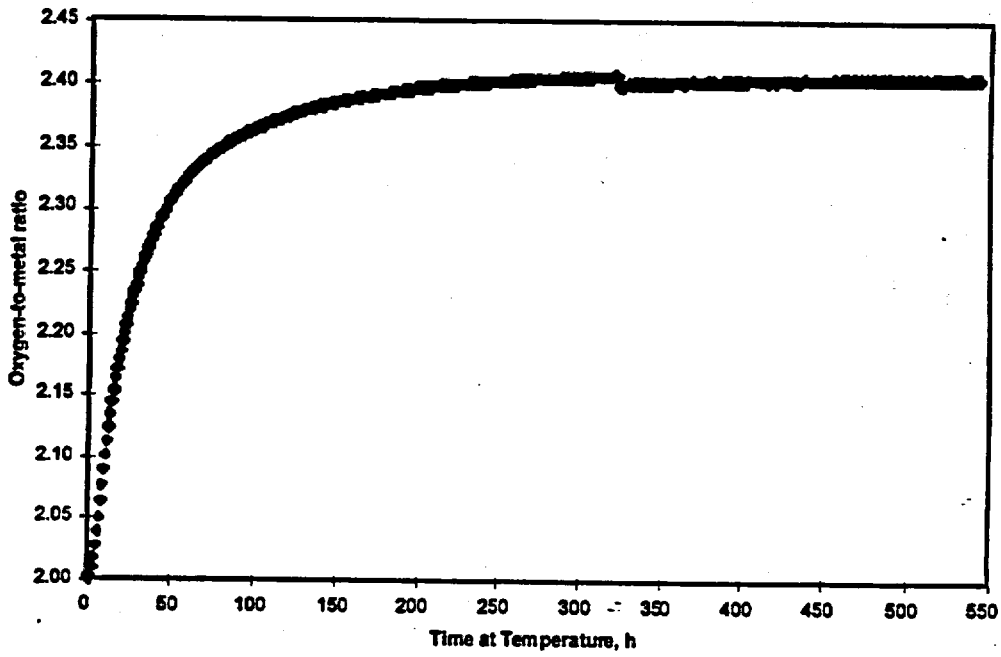


Figure 2.1.3.2-A-6 Sample 105-05 oxidized at 255°C

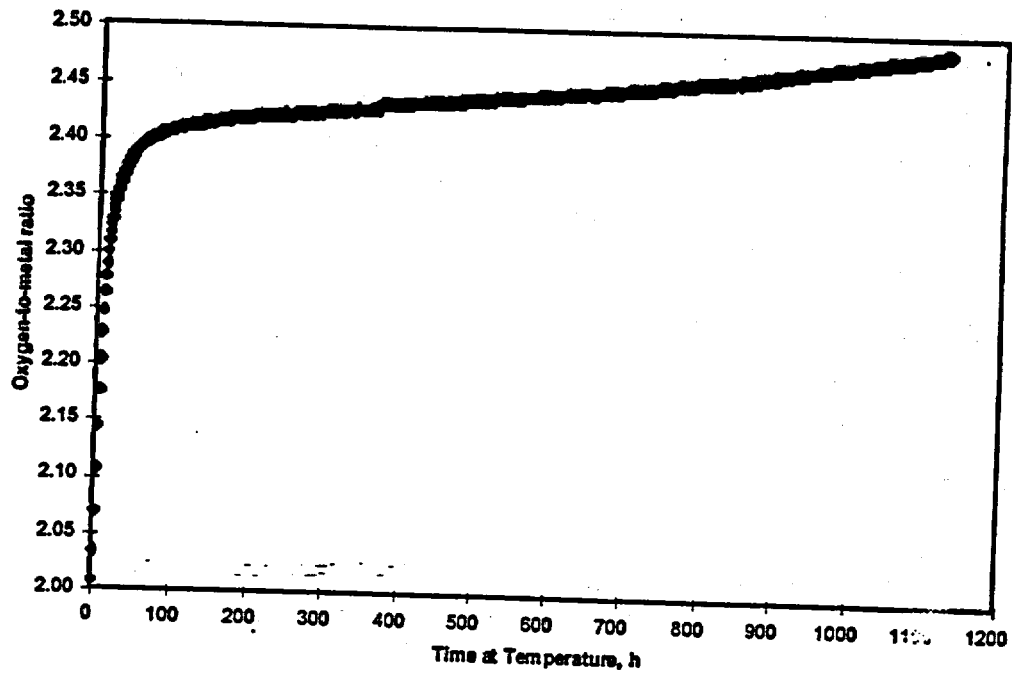


Figure 2.1.3.2-A-7 Sample 105-06 oxidized at 283°C

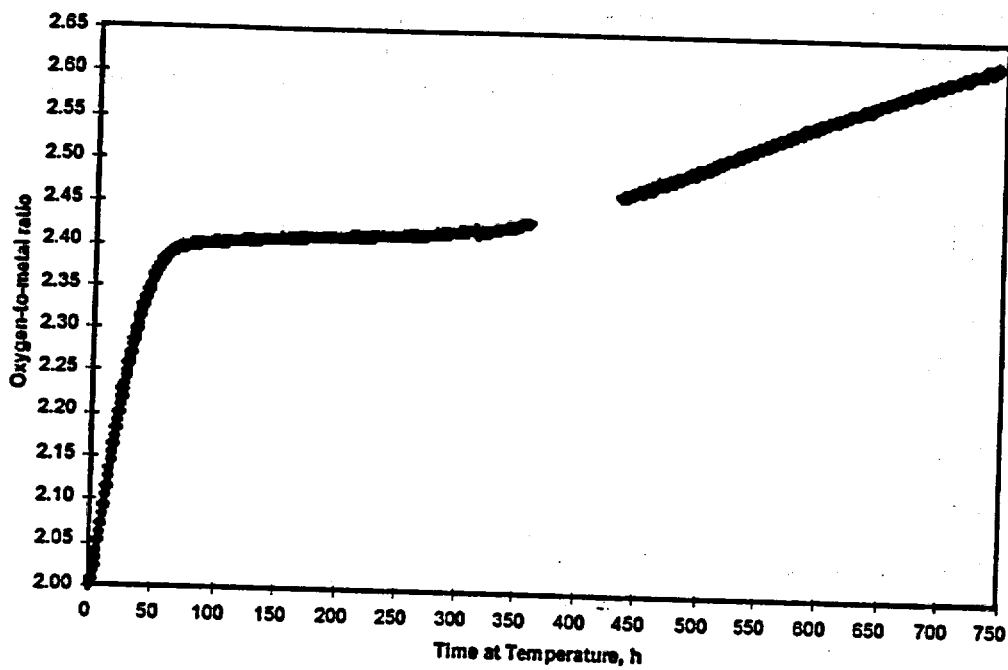


Figure 2.1.3.2-A-8 Sample 105-07 oxidized at 283°C

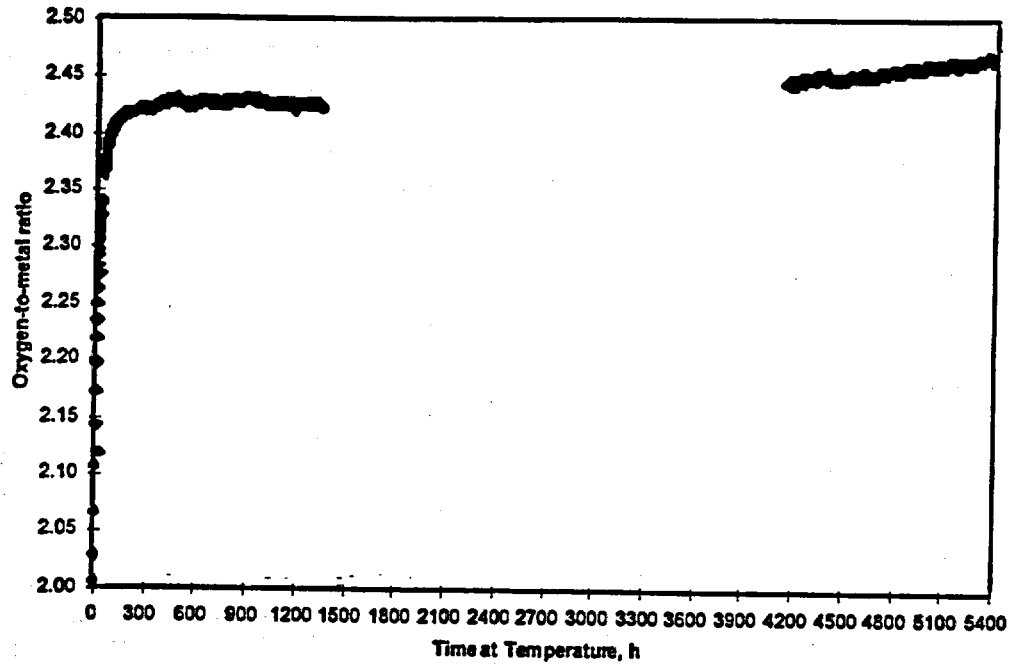


Figure 2.1.3.2-A-9 Sample 105-08 oxidized at 283°C

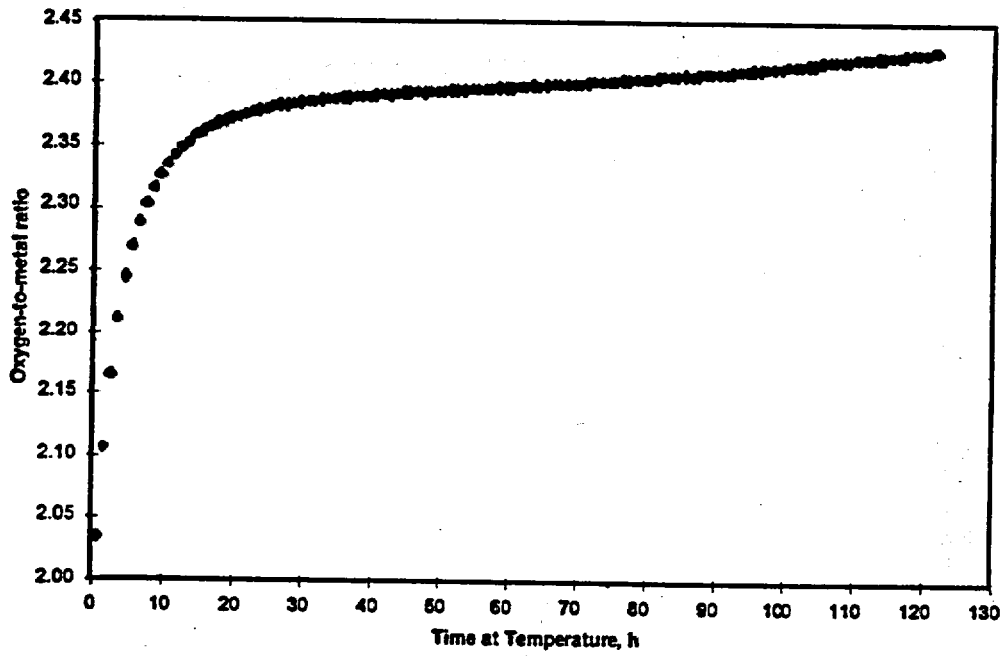


Figure 2.1.3.2-A-10 Sample 105-09 oxidized at 305°C

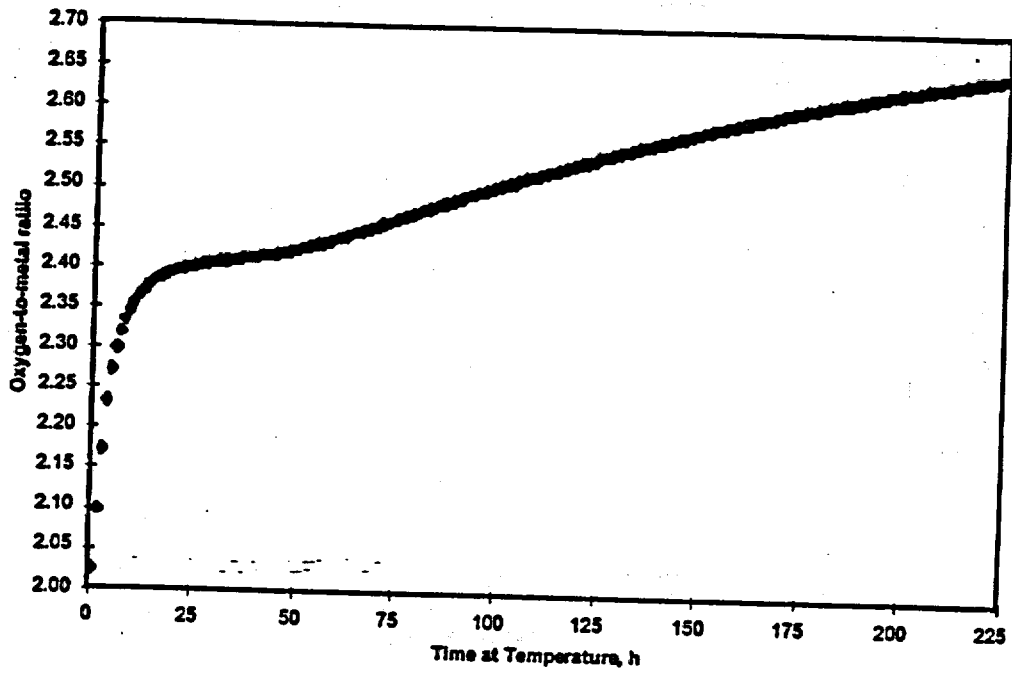


Figure 2.1.3.2-A-11 Sample 105-10 oxidized at 305°C

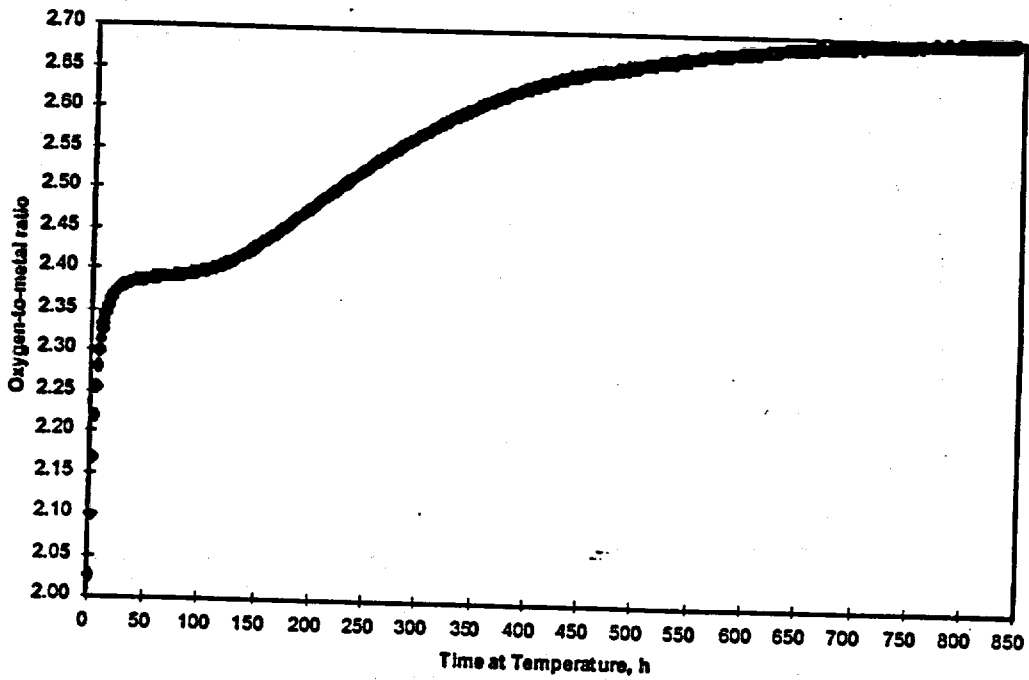


Figure 2.1.3.2-A-12 Sample 105-11 oxidized at 305°C

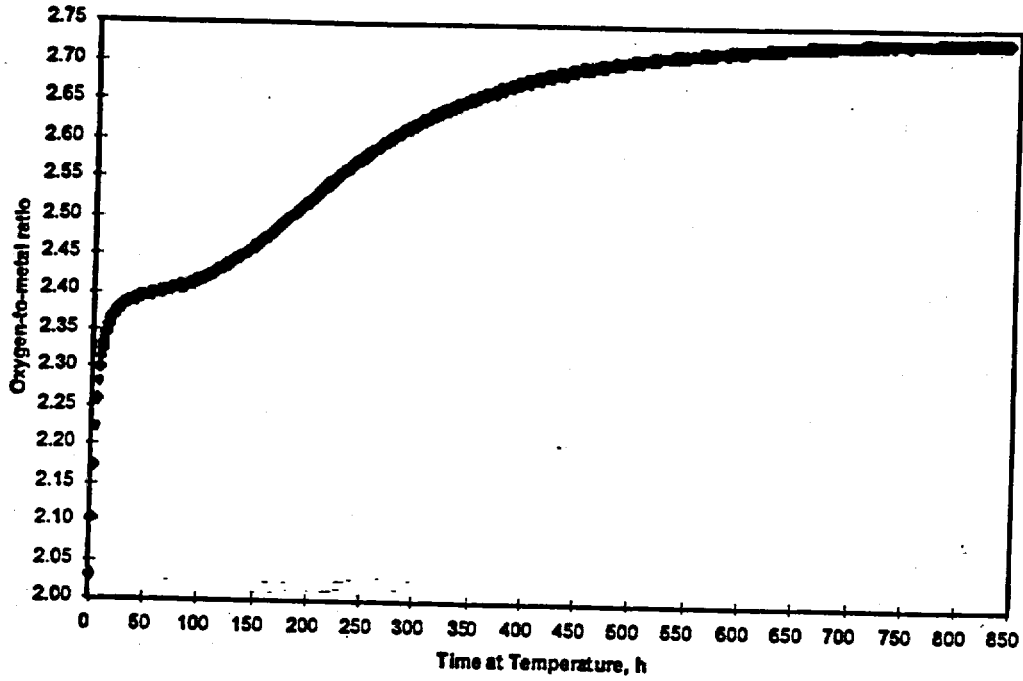


Figure 2.1.3.2-A-13 Sample 105-12 oxidized at 305°C

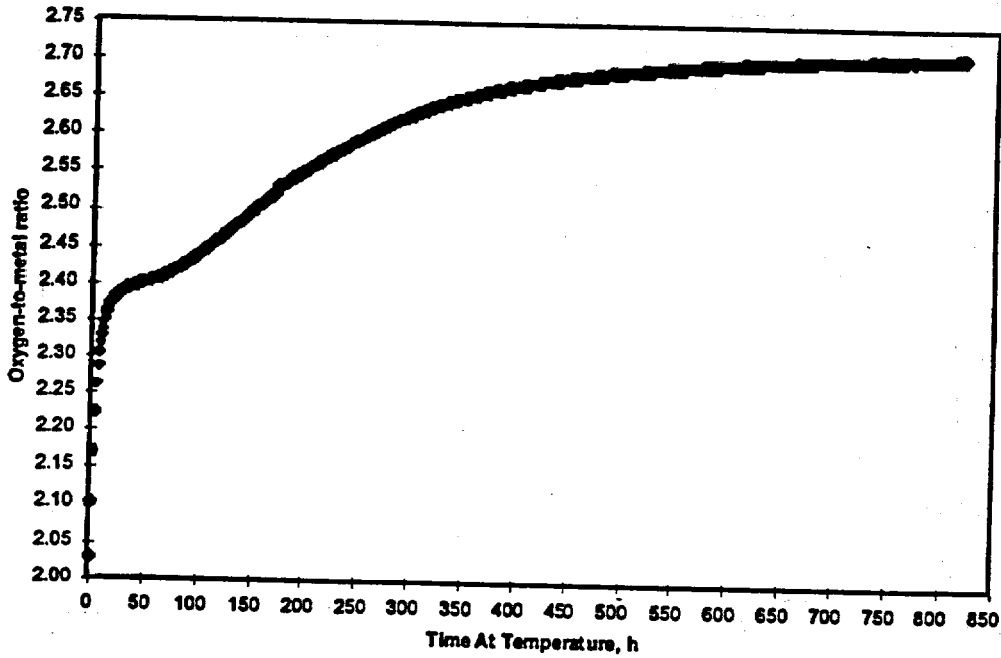


Figure 2.1.3.2-A-14 Sample 105-13 oxidized at 305°C

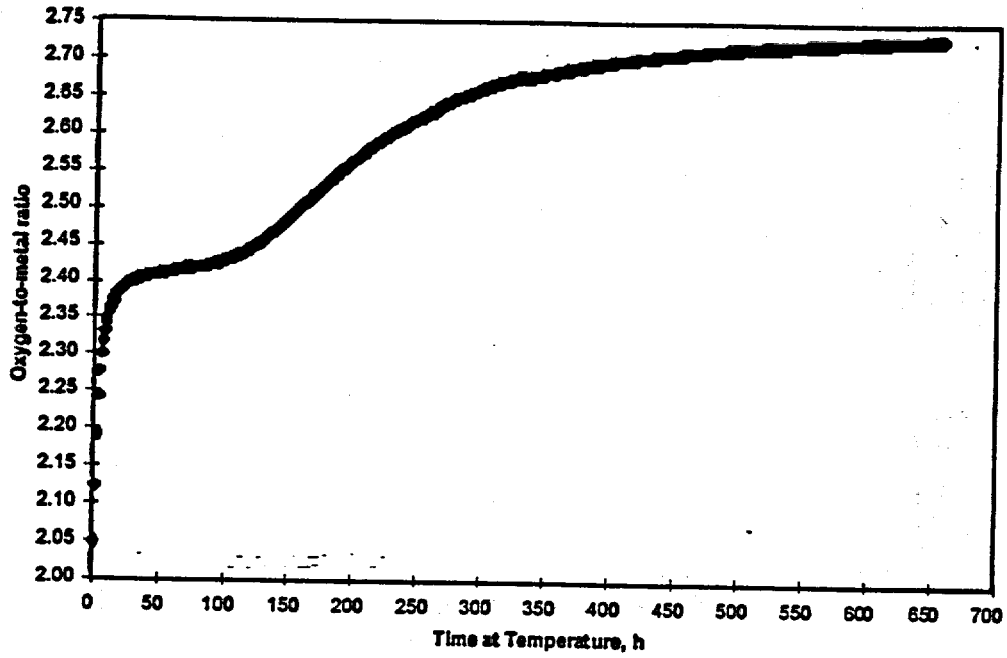


Figure 2.1.3.2-A-15 Sample 105-14 oxidized at 305°C

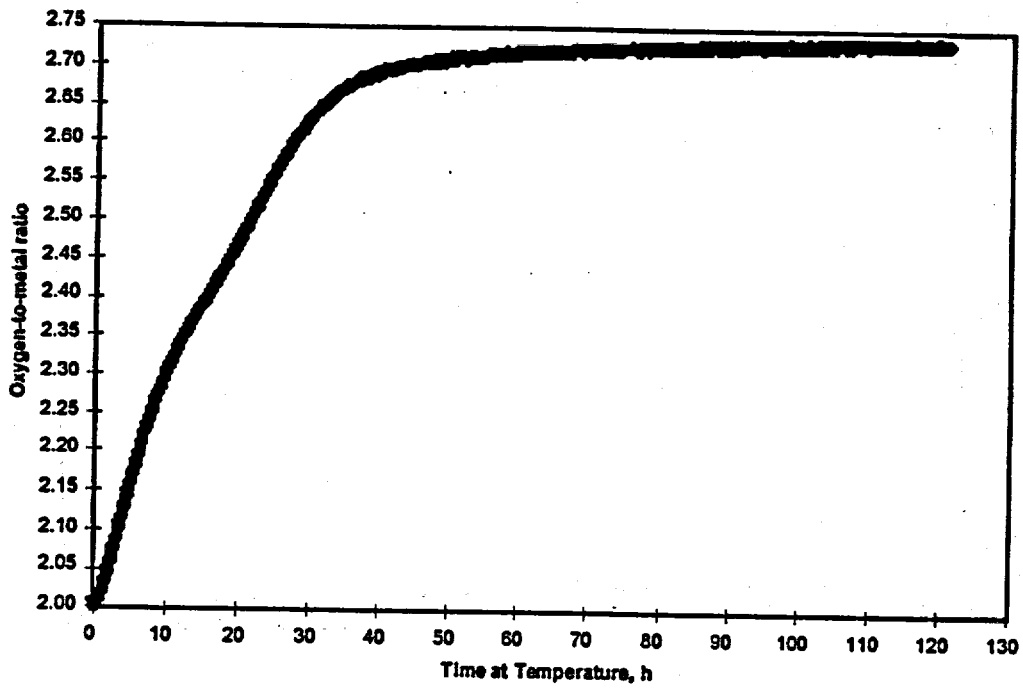


Figure 2.1.3.2-A-16 Sample 105-15 oxidized at 305°C

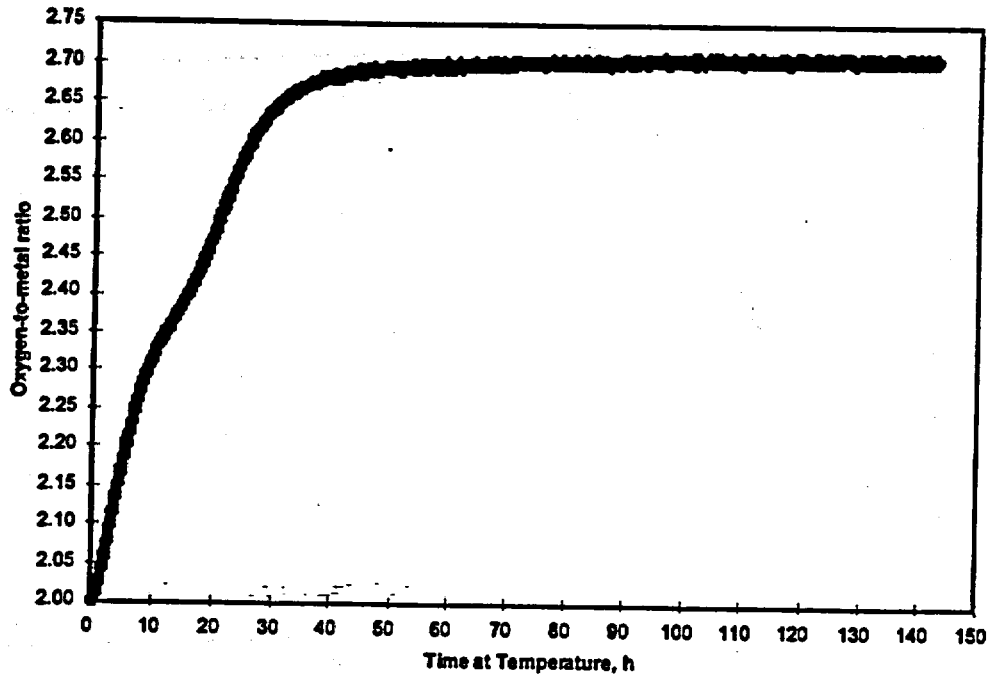


Figure 2.1.3.2-A-17 Sample 105-16 oxidized at 305°C

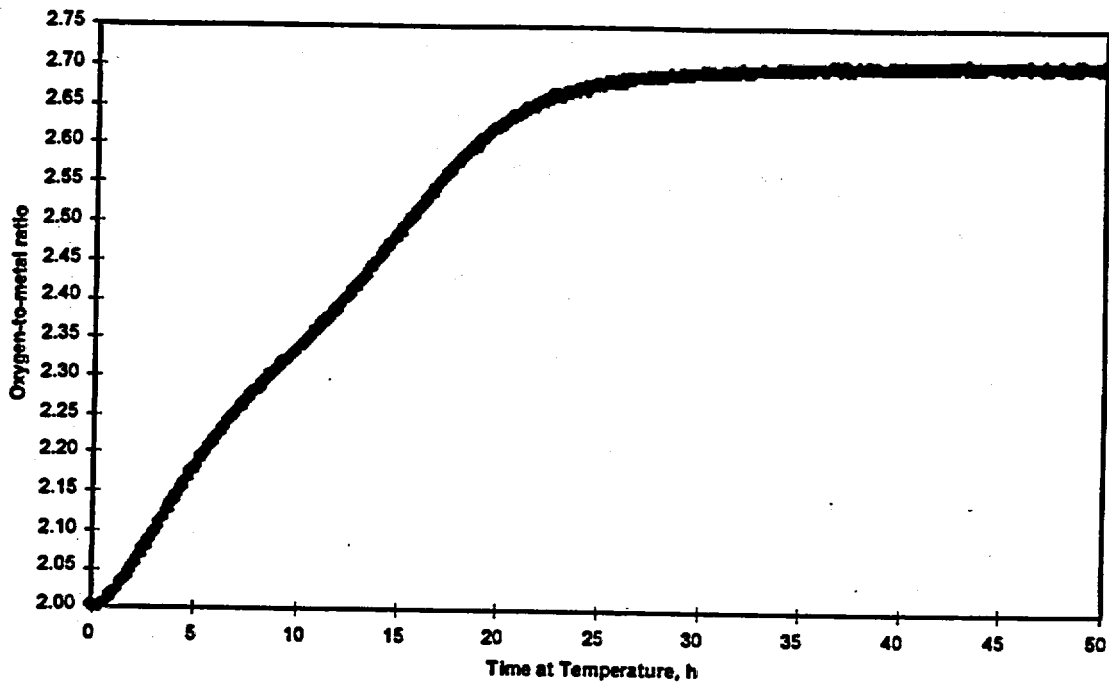


Figure 2.1.3.2-A-18 Sample 105-17 oxidized at 305°C

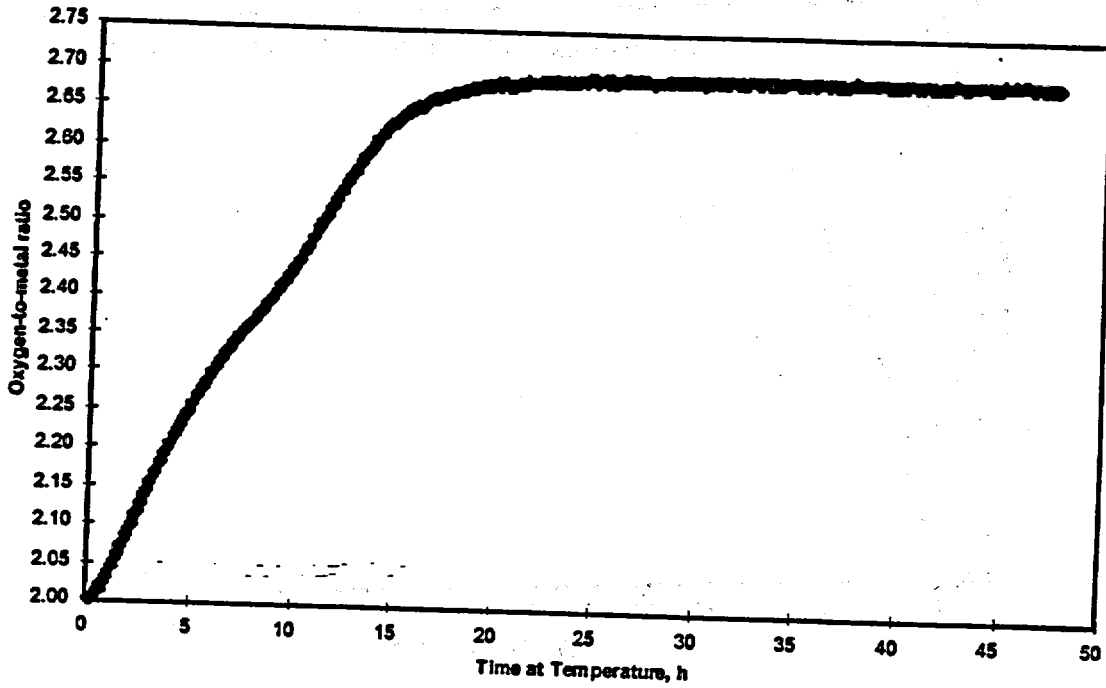


Figure 2.1.3.2-A-19 Sample 105-18 oxidized at 305°C

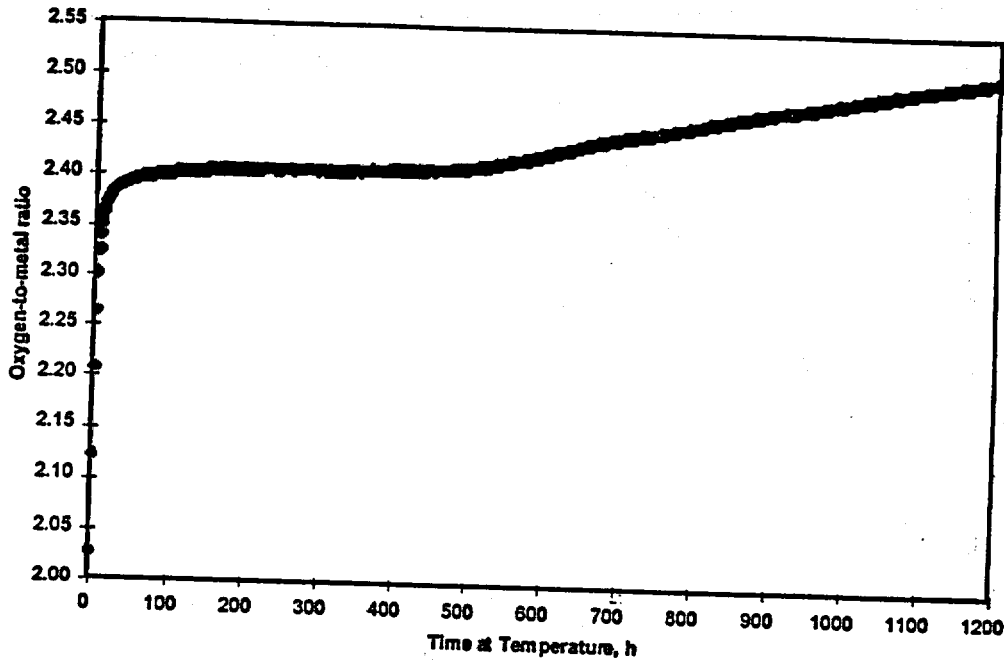


Figure 2.1.3.2-A-20 Sample 104-01 oxidized at 305°C

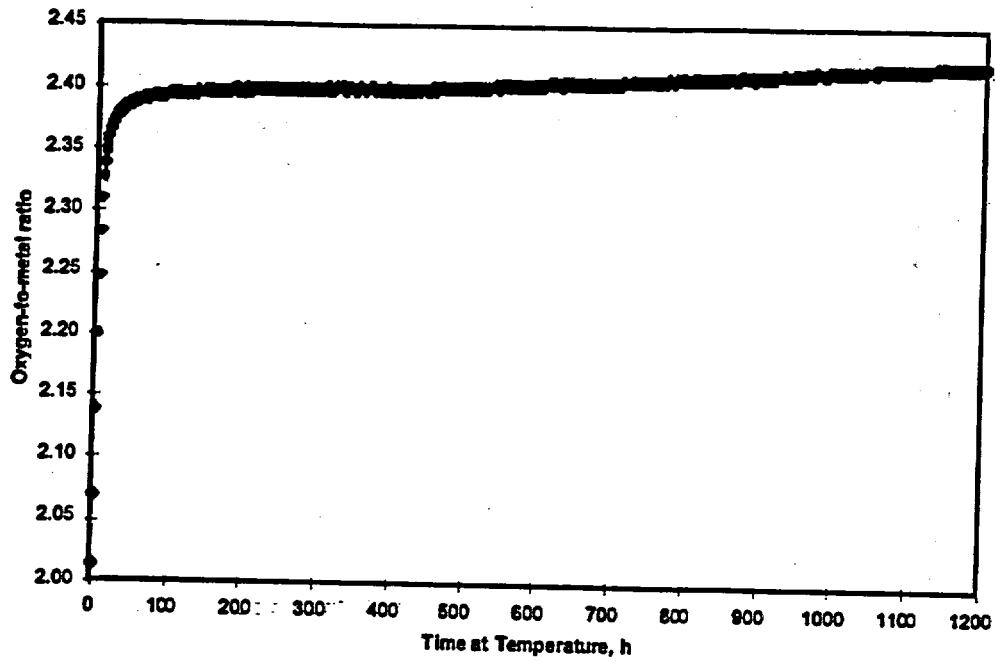


Figure 2.1.3.2-A-21 Sample 104-02 oxidized at 305°C

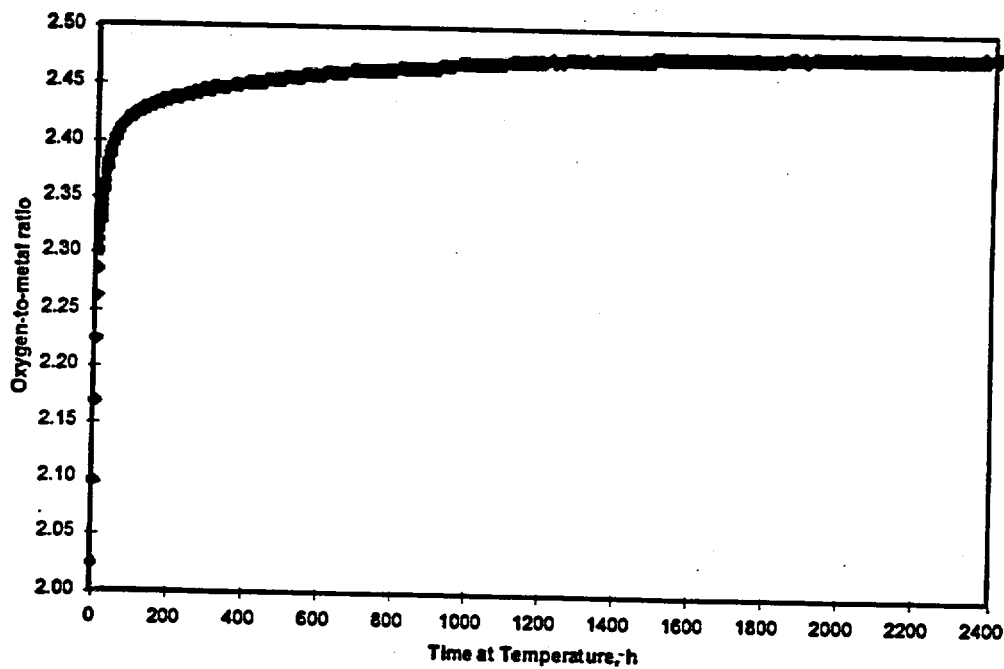


Figure 2.1.3.2-A-22 Sample 108-01 oxidized at 3-5°C

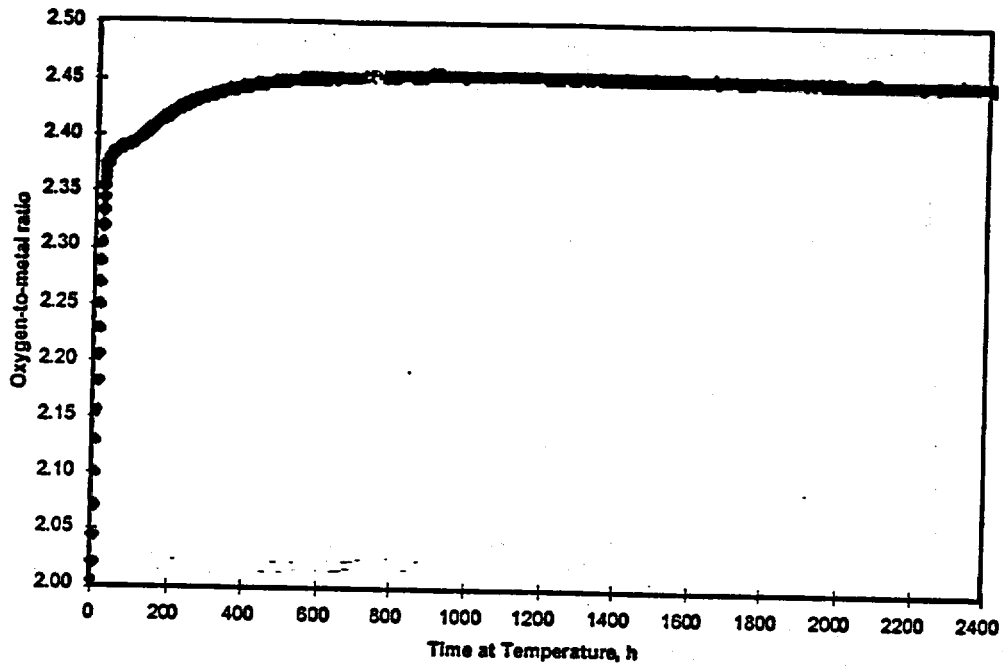


Figure 2.1.3.2-A-23 Sample 108-02 oxidized at 305°C

## Section 2.1.3.5 Contents

2.1.3.5	Dissolution Radionuclide Release from UO <sub>2</sub> Fuel.....	2.1.3.5-1
2.1.3.5.1	Introduction.....	2.1.3.5-1
2.1.3.5.2	Saturated (Static) Dissolution Tests.....	2.1.3.5-2
2.1.3.5.2.1	Series 1 Summary.....	2.1.3.5-3
2.1.3.5.2.2	Series 2 Summary.....	2.1.3.5-5
2.1.3.5.2.3	Series 3 Summary.....	2.1.3.5-7
2.1.3.5.2.4	Summary of "Semi-Static" Unsaturated Tests and Geochemical Modeling.....	2.1.3.5-10
2.1.3.5.3	Flow-Through Dissolution Tests.....	2.1.3.5-12
2.1.3.5.3.1	Flow-Through Test Results.....	2.1.3.5-14
2.1.3.5.3.2	Dissolution Rates of Oxidized Spent Fuel and Additional Tests With Unirradiated Uranium Oxides.....	2.1.3.5-18
2.1.3.5.3.3	Flow-through Studies of Dissolution Rates of Unirradiated Uranium Oxides and Spent Fuel Performed Outside the Yucca Mountain Site Characterization Project.....	2.1.3.5-21
2.1.3.5.4	Unsaturated Dissolution Tests.....	2.1.3.5-21
2.1.3.5.4.1	UO <sub>2</sub> Reactions Through 12 Years of Testing.....	2.1.3.5-22
2.1.3.5.4.2	Spent Nuclear Fuel Reactions After 3.7 Years.....	2.1.3.5-31
2.1.3.5.4.3	Discussion.....	2.1.3.5-47
2.1.3.5.4.4	Summary.....	2.1.3.5-50
2.1.3.5.5	References.....	2.1.3.5-50

## Section 2.1.3.5: Dissolution Radionuclide Release from $\text{UO}_2$ Fuel

Version 1.3  
July 23, 1998

### 2.1.3.5.1 Introduction

The long-term effects of the interactions between spent fuel, as a radioactive waste form, and groundwaters must be anticipated to safely dispose of spent fuel in an underground repository. Spent-fuel dissolution and subsequent transport processes in groundwater are generally considered to be the main routes by which radionuclides could be released from a geological repository. Laboratory testing of the behavior of spent fuel under the conditions expected in a repository provides the information necessary to determine the magnitude of the potential radionuclide source term at the boundary of the fuel's cladding. Dissolution (leach) and solubility tests of spent fuel and uranium dioxide ( $\text{UO}_2$ ) are the most important data-collection activities in spent-fuel waste-form testing. All work in these activities is done within the controls of an approved quality assurance (QA) program.

The testing is done under conditions identified by modeling Activity D-20-50 as most important in calculating release rates. Any scenarios to be used as the basis for long-term modeling are being tested to the extent possible on a laboratory scale. Spent fuel with characteristics spanning the ranges identified in Activity D-20-50 will be tested. In addition, oxidized fuel produced under Activity D-20-45 will be tested. The three dissolution activities have been separated, based on the different technical techniques involved in conducting saturated (semi-static), flow-through and unsaturated (drip) tests. The solubility tests with actinide isotopes will provide concentration limits, speciation, and potential colloidal formation for a range of compositions of groundwater that may contact the waste forms at various temperatures. The key outputs from these activities are the dissolution rate of irradiated fuel, the release rates of radionuclides from spent fuel, and the solution chemistry of water in contact with spent fuel.

Because  $\text{UO}_2$  is the primary constituent of spent nuclear fuel, the dissolution of the  $\text{UO}_2$  spent-fuel matrix is regarded as a necessary first step for release of about 98% of the radioactive fission products contained within the  $\text{UO}_2$  matrix. The intrinsic  $\text{UO}_2$  dissolution rate sets an upper bound on the aqueous radionuclide release rate, even if the fuel is substantially degraded by other processes such as oxidation. If the fuel is substantially degraded to other oxidation states, the fuels' dissolution responses also must be provided. The release rate is reduced for the solubility-limited actinides (U, Np, Pu, and Am), which account for most of the long-lived radioactivity in spent fuel when colloids are not present. In scenarios for the potential Yucca Mountain repository, it is assumed that the cladding has failed, and water as vapor or liquid contacts the fuel. Drip tests that simulate the unsaturated and oxidizing conditions expected at Yucca Mountain are in progress to evaluate the long-term behavior of spent nuclear fuel.

There have been many investigations of the dissolution of  $\text{UO}_2$ , spent fuel, and uraninite (a naturally occurring  $\text{UO}_2$  mineral) in aqueous solutions, under both reducing and oxidizing conditions and as a function of various other environmental variables. Several reviews have been written, the most recent being by Grambow (1989) and McKenzie (1992). Important variables considered in the reviewed investigations included pH, temperature, oxygen fugacity, carbonate/bicarbonate concentrations, and fuel attributes. The data vary because of the differences in experimental purpose and methods, the diverse history of the fuel samples, the formation of secondary phases during the tests, the complexity of the solution and the surface chemistry of  $\text{UO}_2$ , and the surface area measurements of the test specimens.

The following material summarizes the available Yucca Mountain Site Characterization Project (YMP) spent-fuel and unirradiated-uranium-oxide dissolution data.

#### 2.1.3.5.2 Saturated (Static) Dissolution Tests

The Series 1 tests described (Wilson, 1984) were the first of several tests planned at Pacific Northwest National Laboratory (PNNL) to characterize potential radionuclide release from and behavior of spent fuel stored under YMP-proposed conditions. In the Series 1 tests, specimens prepared from Turkey Point Reactor Unit 3 fuel were tested in deionized distilled water in unsealed, fused silica vessels under ambient hot-cell air and temperature<sup>1</sup> conditions. Four specimen configurations were tested:

1. Undefected fuel-rod segments with watertight end fittings
2. Fuel-rod segments containing small (~200  $\mu\text{m}$  diameter) laser-drilled holes through the cladding and with watertight end fittings
3. Fuel-rod segments with machined slits through the cladding and watertight end fittings
4. Bare fuel particles removed from the cladding plus the cladding hulls

A "semi-static" test procedure was developed in which periodic solution samples were taken with the sample volume replenished with fresh deionized distilled water. Cycle 1 of the Series 1 tests was started during July 1983 and was 240 days in duration. At the end of the first cycle, the tests were sampled, the vessels stripped in 8 M  $\text{HNO}_3$ , and the specimens restarted in fresh deionized distilled water for a second cycle. Cycle 2 of the Series 1 tests was terminated at 128 days in July 1984. A cycle is a testing period in which samples are taken at its conclusion and the test vessels are stripped and cleaned or replaced. Samples may have also been cleaned before starting another cycle.

---

<sup>1</sup> Hot cell temperature range is approximately 21°C to 28°C, depending on time of year and time of day. An average value of 25°C was assumed for these ambient temperature tests (Wilson, 1990a).

The Series 2 tests (Wilson, 1990b) were similar to the Series 1 tests except for the following:

- The Series 2 tests were run in YMP (Nevada Nuclear Waste Site Investigations [NNWSI]) reference J-13 well water.
- Each of the four specimen configurations was duplicated using both the Turkey Point Reactor and H. B. Robinson Reactor pressurized-water reactor (PWR) spent fuels.
- A vessel and specimen rinse procedure was added to the cycle termination procedures.

Filtration of the collected rinse solution provided solids residues that were later examined for secondary-phase formation. Cycle 1 of the Series 2 tests was started in June 1984. All eight Series 2 specimens were run for a second cycle. The 2 bare fuel specimens were continued for Cycles 3, 4, and 5. Cycle 5 of the Series 2 bare fuel tests was terminated in June 1987 for a total 5-cycle testing time of ~34 mos.

The Series 3 tests (Wilson, 1990b) were run for three cycles during the same approximate time period as were Cycles 3, 4, and 5 of the Series 2 tests. The Series 3 tests were run in sealed, stainless-steel vessels and used the same four-specimen configurations used in Series 1 and Series 2 Cycles 1 and 2. Five specimens: one each of the four configurations using H. B. Robinson (HBR) reactor fuel (plus an additional bare-fuel specimen using Turkey Point (TP) reactor fuel) were tested at 85°C; a sixth specimen (HBR bare fuel) was run at 25°C. Two additional scoping tests using preoxidized bare fuel specimens in Series-2-type silica vessels were started in August 1986. The Series 1 and 2 tests were originally entitled "Cladding Containment Credit Tests." All of the test series were later referred to as "Spent-Fuel Dissolution Tests."

#### 2.1.3.5.2.1 Series 1 Summary

Measured releases were compared to the 10 CFR 60 inventory maximum annual release rate requirement of  $10^{-5}$  of 1000-yr inventory per year. Total measured release and total measured release as a fraction of inventory  $\times 10^5$  are summarized in Table 2.1.3.5-1. The principal observations and conclusions from these spent-fuel leaching tests are summarized as follows:

- Within the probable accuracy of total release measurements and specimen inventory calculations, the actinides U, Pu, Am, and Cm appear to have been released congruently.
- Limited data suggest that  $^{237}\text{Np}$  may have been preferentially released rather than being congruently released with other actinides as expected. However, these data are too limited to be conclusive. Inaccuracies in ORIGEN-2 - calculated  $^{237}\text{Np}$  inventory and radiochemical analysis could also account for those results.

- A fractional release of cesium on the order of the fractional fission-gas release was observed for the bare-fuel, slit-defect, and holes-defect tests. Additional preferential cesium release, possibly from grain boundary inventory, was also noted in the second run (cycle) on these specimens.
- Observed fractional <sup>99</sup>Tc release ranged from one order of magnitude greater relative to the actinides in the bare-fuel test to almost three orders of magnitude greater fractional release relative to the actinides in the holes-defect test.
- For the actinides U, Pu, Am, and Cm, approximately two orders of magnitude less total fractional release was measured in the slit-defect test relative to the bare-fuel test. An additional approximate one order of magnitude reduction in actinide release was observed in the holes-defect test relative to the slit-defect test.
- Apparent uranium saturation occurred at ~1 ppb in all tests. Uranium in excess of a few ppb was removed by 18 Å filtration. Most of the U, Am, and Cm in solution samples from the bare-fuel test was removed by filtration.
- Grain-boundary dissolution appeared to be a major source of release. Preferential release of <sup>99</sup>Tc is likely a result of its segregation to the grain boundaries. Grain boundaries in the spent fuel are relatively wide and easily resolved by scanning electron microscopy (SEM). Grain boundaries in unirradiated UO<sub>2</sub> are tight and not resolvable on a fracture surface by SEM.
- Spent-fuel leaching behavior, as well as other chemical and mechanical behavior, is influenced by microstructural phenomena such as localized segregation of some elements to the grain boundaries. The extent of localized radionuclide segregation is influenced by irradiation temperature and may be correlated to fission-gas release. Additional segregation of radionuclides into more easily leached phases could possibly occur if the fuel structure is degraded by oxidation during long-term repository storage.

**Table 2.1.3.5-1 Total measured release as a fraction of inventory ( $\times 10^3$ )<sup>a</sup> for Series 1**

Component	Bare Fuel	Slit Defect	Holes Defect	Undeformed
Uranium ( $\mu\text{g}$ )	28.0 (9510)	0.078 (28)	<0.041 (<14)	<0.018 (<6.6)
<sup>239-240</sup> Pu (nCi)	28.0 (7940)	0.341 (104)	0.069 (20)	0.027 (8)
<sup>241</sup> Am (nCi)	21.7 (12,604)	0.208 (130)	<0.030 (<18.6)	<0.011 (<6.4)
<sup>244</sup> Cm (nCi)	30.0 (13,300)	0.76 (362)	0.039 (18.1)	0.008 (<3.9)

Component	Bare Fuel	Slit Defect	Holes Defect	Undefected
<sup>237</sup> Np <sup>b</sup> (nCi)	54 (4.73)	2.2 (0.2)	— —	— —
<sup>137</sup> Cs (nCi)	300 <sup>c</sup> (1.94x10 <sup>6</sup> )	142.1 (3.94x10 <sup>6</sup> )	85.6 (2.33x10 <sup>6</sup> )	0.041 (1.1x10 <sup>3</sup> )
<sup>99</sup> Tc <sup>d</sup> (nCi)	230 (900)	12.1 (51)	<6.7 (<28)	— —

- Total measured release given in parentheses; sum of both cycles.
- <sup>237</sup>Np includes only vessel strip from initial and second runs (cycles) and final solution from second run (cycle).
- Estimate based on maximum <sup>137</sup>Cs activities measured in solution.
- <sup>99</sup>Tc includes only final solution in a vessel strip from initial and second runs (cycle).

### 2.1.3.5.2.2 Series 2 Summary

Radionuclide releases were measured from PWR spent-fuel specimens tested in YMP (NNWSI) J-13 well water (see Table 2.1.3.5-2) in unsealed, fused silica vessels under ambient hot-cell air conditions (~25°C). Two bare-fuel specimens were tested: one prepared from a rod irradiated in the HBR Unit 2 reactor and the other from a rod irradiated in the TP Unit 3 reactor. Both fuels were low-gas release and moderate burnup. The specimen particle size range (2 to 3 mm) was that which occurs in the fuel as a result of thermal cracking. A semi-static test method was used in which the specimens were tested for multiple cycles starting in fresh J-13 water. Periodic water samples were taken during each cycle with the sample volume (~10% of test solution) being replenished with fresh J-13 water. The specimens were tested for 5 cycles for a total time of 34 months.

Table 2.1.3.5-2 J-13 well-water analysis

Component	Concentration (µg/ml)	Component	Concentration (µg/ml)
Li	0.042	Si	27.0
Na	43.9	F	2.2
K	5.11	Cl	6.9
Ca	12.5	NO <sub>3</sub>	9.6
Mg	1.92	SO <sub>4</sub>	18.7
Sr	0.035	HCO <sub>3</sub>	125.3
Al	0.012	—	—
Fe	0.006	pH	7.6

- Series 2 actinide concentrations appeared to rapidly reach steady-state levels during each test cycle. Concentrations of Pu, Am, and Cm were dependent on filtration, with Am and Cm concentrations being affected the most by filtration; this suggests that these elements may have formed colloids. Approximate steady-state concentrations of actinide elements indicated in 0.4-µm-filtered-solution samples are as follows:

U —  $4 \times 10^{-6}$  to  $8 \times 10^{-6}$  M (1 to 2 ppm)

Pu —  $8.8 \times 10^{-10}$  to  $4.4 \times 10^{-9}$  M (20 to 100 pCi/mL  $^{239+240}\text{Pu}$ )

Am —  $\sim 1.5 \times 10^{-10}$  M ( $\sim 100$  pCi/mL  $^{241}\text{Am}$ )

Cm —  $\sim 2.6 \times 10^{-12}$  M ( $\sim 50$  pCi/mL  $^{244}\text{Cm}$ )

Np —  $2.4 \times 10^{-9}$  M (0.4 pCi/mL  $^{237}\text{Np}$ )

- Actinide releases as a result of water transport should be several orders of magnitude lower than the NRC 10 CFR 60.113 release limits ( $10^{-5}$  of 1000-yr inventory per year) if actinide concentrations (true solution plus colloids) in the repository do not greatly exceed the steady-state concentrations measured in 0.4- $\mu\text{m}$  filtered samples. Assuming a water flux through the repository of 20 L per yr per waste package containing 3140 kg of spent-fuel saturates at the actinide elemental concentrations given previously, the following annual fractional releases are calculated based on 1000-yr inventories for 33 megawatt days/kgM burnup PWR fuel:

U — ( $8 \times 10^{-6}$  M),  $1.4 \times 10^{-8}$  per yr

Pu — ( $4 \times 10^{-9}$  M),  $\sim 1 \times 10^{-9}$  per yr

Am —  $\sim 8 \times 10^{-10}$  per yr

Cm —  $\sim 1 \times 10^{-8}$  per yr

Np —  $\sim 3 \times 10^{-9}$  per yr

- Gap inventory  $^{137}\text{Cs}$  releases of about 0.7% of inventory in the HBR test and about 0.2% of inventory in the TP test were measured at the start of Cycle 1. Smaller initial Cycle 1 releases on the order of  $10^{-4}$  of inventory were measured for  $^{129}\text{I}$  and  $^{99}\text{Tc}$ .
- Fission product nuclides  $^{137}\text{Cs}$ ,  $^{90}\text{Sr}$ ,  $^{99}\text{Tc}$ , and  $^{129}\text{I}$  were continuously released with time and did not reach saturation in solution. The continuous-release rates of these soluble nuclides were relatively constant during Cycles 3, 4, and 5. During Cycle 5, the release rate for both  $^{90}\text{Sr}$  and  $^{129}\text{I}$  was about  $5.5 \times 10^{-5}$  of inventory per yr in both HBR and TP tests. Marginally higher continuous-release rates on the order of  $1 \times 10^{-4}$  of inventory per yr were measured for  $^{137}\text{Cs}$  and  $^{99}\text{Tc}$ .

- The degree to which the soluble nuclides ( $^{137}\text{Cs}$ ,  $^{90}\text{Sr}$ ,  $^{99}\text{Tc}$ , and  $^{129}\text{I}$ ) were preferentially released relative to the amount of congruent dissolution of the  $\text{UO}_2$  matrix phase was not quantitatively measured. However, the near-congruent release of soluble nuclides in later test cycles and the inventory ratios of these nuclides to that of uranium in initial solution samples from the later cycles (a ratio of about 2.5 for  $^{137}\text{Cs}$ ) suggest that the fractional-release rates for these nuclides may not have greatly exceeded the matrix dissolution rate. Based on these data, a matrix dissolution rate of about  $4 \times 10^{-5}$  per yr appears to be a reasonable estimate for the 2- to 3-mm fuel particles tested.
- The present data suggesting fuel-matrix dissolution rates greater than  $10^{-5}$  per yr imply that demonstrating 10 CFR 60.113 compliance for soluble nuclides will involve considerations other than the durability of the spent-fuel waste form—e.g., scenarios for low-probability water contact, a distribution of cladding/container failures over time, or very low migration rates. In time, fuel degradation resulting from oxidation and grain-boundary dissolution (increasing surface area) may increase the matrix-dissolution rate. Upper limits for degraded-fuel matrix-dissolution rates are yet to be determined.
- Comparison to the Series 3 tests (sealed vessels) indicated that most of the  $^{14}\text{C}$  released in the Series 2 tests was lost to the atmosphere as  $\text{CO}_2$ , and not measured. The  $^{14}\text{C}$  was preferentially released in the Series 3 tests at about 1% of its measured inventory in HBR fuel samples. As an activation product derived partially from nitrogen impurities, evaluation of  $^{14}\text{C}$  release relative to 10 CFR 60.113 is complicated because its inventory and distribution in fuel are not well characterized.
- The quantities of precipitated, secondary-phase material observed in filter residues were significantly less than those observed in the  $85^\circ\text{C}$  Series 3 tests.  $\text{UO}_2$  and calcite were the only phases confirmed by X-ray powder diffractometry (XRD) examination of a cycle-termination rinse filter, with a tentative indication of haiweeite based on a single line in the XRD pattern. Amorphous-appearing, silicon-containing phases were also observed by SEM on the rinse filters, and silicon-containing flocs were observed on filters used to filter solution samples. With the possible exception of haiweeite for uranium, phases controlling the solubility of actinide nuclides were not identified.

#### 2.1.3.5.2.3 Series 3 Summary

Specimens prepared from PWR fuel rod segments were tested in sealed, stainless-steel vessels in Nevada Test Site J-13 well water at  $85^\circ\text{C}$  and  $25^\circ\text{C}$ . The test matrix included three specimens of bare-fuel particles plus cladding hulls, two fuel-rod segments with artificially defected cladding and watertight end fittings, and an undefected fuel-rod section with watertight end fittings. Periodic solution samples were taken during test cycles with the sample volumes replenished with fresh J-13 water. Test cycles were periodically terminated and the specimens restarted in fresh J-13 water. The specimens were run for 3 cycles for a total test duration of 15 mos.

Actinide concentrations (U, Pu, Am, Cm, and Np) peaked early in Cycle 1 of the bare-fuel tests and then declined to steady-state levels. Isotopes of Pu and Am account for approximately 98% of the activity in spent fuel at 1000 yr. Actinide concentrations rapidly reached stable steady-state values during Cycles 2 and 3. Steady-state activities on the order of 100 pCi/mL were measured for  $^{239+240}\text{Pu}$ ,  $^{241}\text{Am}$ , and  $^{244}\text{Cm}$  at 25°C, and much lower activities on the order of 1 pCi/mL were measured for these radionuclides at 85°C. Even using the higher 25°C values, the steady-state concentrations indicated for all of the actinide elements were at least three orders of magnitude below those required to meet the Nuclear Regulatory Commission (NRC) 10 CFR 60.113 controlled-release requirements for any realistic water-flow rate through the repository. Calcium-uranium-silicate phases that may have contributed to the control of U concentrations were identified in the 85°C tests. Secondary phases controlling Np, Pu, Am, and Cm concentrations were not identified.

Concentrations of the more soluble fission-product and activation-product radionuclides generally tended to increase continuously with time. An exception was  $^{90}\text{Sr}$ , which tended to reach maximum concentrations in the 85°C tests. Continuous release rates measured for  $^{99}\text{Tc}$ ,  $^{137}\text{Cs}$ , and  $^{129}\text{I}$  were generally in the range of  $10^{-4}$  to  $10^{-3}$  of inventory per yr, but the rate for  $^{129}\text{I}$  was lower at 25°C. Preferential release of  $^{14}\text{C}$  continued through all three test cycles for a total release of about 1% of the  $^{14}\text{C}$  specimen inventory. Comparison of  $^{14}\text{C}$  releases in tests conducted in sealed and unsealed vessels indicated that  $^{14}\text{C}$  was released to the atmosphere, most likely as  $\text{CO}_2$ . Although soluble radionuclides were released at rates in excess of the NRC limit of  $10^{-5}$  of inventory per yr in the current tests, additional data are needed to predict long-term release rates.

The following conclusions and observations are made based on the results of the YMP (NNWSI) Series 3 Spent-Fuel Dissolution Tests:

- Actinide concentrations (U, Pu, Am, Cm, and Np) generally appeared to reach steady-state levels in all three test cycles of the bare-fuel tests. Control of actinide concentrations at stable levels in solution was attributed to the achievement of a steady-state between fuel dissolution and secondary-phase formation or other mechanisms such as sorption.
- Uranium-bearing secondary phases were found in significant amounts in filter (18 Angstrom) residues from the 85°C bare-fuel tests. Formation of the calcium-uranium-silicate phase uranophane was confirmed, and haiweeite was tentatively identified. A possible indication of soddyite formation was also found in one of the filter residues. Secondary phases controlling Pu, Am, Cm, and Np concentrations were not identified.
- Pu, Am, and Cm activities measured in solution samples from the 85°C bare-fuel tests were from two to three orders of magnitude lower than those measured in unfiltered and 0.4  $\mu\text{m}$  filtered samples from the 25°C test. Slightly lower U concentrations were also measured at 85°C in Cycles 2 and 3. Lower

actinide concentrations at 85°C are attributed to faster kinetics for formation of solubility-limiting secondary phases at the higher 85°C temperature. Np activities showed no significant dependence on temperature or filtration.

- Pu, Am, and Cm activities measured in 18Å filtered samples from the 25°C bare-fuel test were less than those measured in unfiltered and 0.4-µm filtered samples; this suggests that these elements were present as colloids in this test. The effects of filtration were generally greater for Am and Cm than for Pu. Notable reductions in Am and Cm activities also occurred with 0.4 µm filtration in the 85°C bare-fuel tests.
- Steady-state actinide concentrations measured in 0.4-µm filtered samples from the 25°C bare-fuel test were at least three orders of magnitude below those necessary to meet the NRC 10 CFR 60.113 controlled-release requirements, based on reasonable assumed water-flow rates through a repository. This result is of particular significance because Pu and Am isotopes account for ~98% of the activity in spent fuel at 1000 yr, and eventual Pu and Am concentrations may be lower than those measured in 0.4-µm filtered samples from the 25°C tests.
- Measured U concentrations were consistent with those predicted by the EQ3/6 geochemical modeling code for precipitation of soddyite. Good agreement between measured and predicted concentration was obtained for Np, based on equilibration with NpO<sub>2</sub> at 25°C when the oxygen fugacity in the simulation was set at 10<sup>-12</sup> bars. A broad range of concentrations that bracketed the measured values was predicted for Pu, depending on the assumed oxygen fugacity and concentration-controlling phase. Measured Am concentrations were less than predicted, based on data for equilibration with Am(OH)CO<sub>3</sub> or Am(OH)<sub>3</sub>.
- Actinide fractional releases from the bare-fuel tests were much greater than in the slit-defect or hole-defects tests. Actinide releases from the slit-defect test were somewhat greater than in the hole-defects test, with most of the difference accounted for in the Cycle 1 acid strip samples. Actinide releases in the hole-defects test were not significantly different than those measured in the undefected test.
- The radionuclides <sup>137</sup>Cs, <sup>90</sup>Sr, <sup>99</sup>Tc, <sup>129</sup>I, and <sup>14</sup>C were continuously released in the bare-fuel tests at rates exceeding 10<sup>-5</sup> of inventory per yr. Of these radionuclides, only <sup>90</sup>Sr showed significant indications that its concentration was limited by solubility. Cesium-137 showed the greatest fractional release during Cycle 1, while <sup>14</sup>C showed the greatest fractional release during Cycles 2 and 3.

- Iodine-129 release was much greater at 85°C than at 25°C. Comparison of the Series 3 test results to those from the Series 2 tests gave no indication that  $^{129}\text{I}$  had been lost as  $\text{I}_2$  from the unsealed, Series 2 vessels. The  $^{129}\text{I}$  release in the slit-defect test was equivalent to that in the bare-fuel test, but  $^{129}\text{I}$  released in the hole-defects test was not significantly greater than that in the undefected test.
- Comparison of  $^{14}\text{C}$  solution activity data measured in the sealed, Series 3 tests to that measured in the unsealed, Series 2 tests indicated that most of the  $^{14}\text{C}$  released in the Series 2 tests was probably lost to the atmosphere as  $^{14}\text{CO}_2$ . The TP fuel appeared to have a much greater  $^{14}\text{C}$  inventory (or gap inventory) than did the HBR fuel on which fuel and cladding  $^{14}\text{C}$  inventory was radiochemically determined.
- Long-term release rates for soluble nuclides were uncertain. The relative contributions of fuel-matrix dissolution, versus preferential release from locations such as grain boundaries where soluble nuclides may be concentrated, was not determined. Preferential release would likely decrease as the inventory of soluble nuclides on exposed grain boundaries is depleted.
- A vessel-corrosion anomaly occurred during Cycle 1 of the 85°C HBR bare-fuel test. The most significant effects associated with the apparent vessel corrosion were 1) U concentration dropped to about 10 ppb, and 2)  $^{99}\text{Tc}$  activity dropped to less than detectable. These effects are attributed to removal of U and Tc by coprecipitation with or sorption on iron-bearing precipitates or to reduction of the soluble  $\text{UO}_2^{2+}$  and  $\text{TcO}_4^-$  species as a result of redox coupling with  $\text{Fe}^0$  to  $\text{Fe}^{2+}/\text{Fe}^{3+}$  reactions.
- Ca, Mg, Si, and  $\text{HCO}_3^-$  precipitated from solution during all 85°C tests cycles, while the chemistry of the starting J-13 well water remained essentially unchanged during the 25°C test. In addition to the calcium-uranium-silicate phases observed in the two 85°C bare-fuel tests, scale formation was observed at the waterline in all of the 85°C tests. The SEM-energy-dispersive spectrometry (EDS) examinations suggest that calcite,  $\text{SiO}_2$  (possibly as a gel), and possibly dolomite were formed during the 85°C tests. A portion of the released  $^{14}\text{C}$  is likely to be incorporated in the carbonate phases. A portion of the released  $^{90}\text{Sr}$  is also likely to be incorporated in secondary phases, possibly as a partial substitute for Ca.

#### 2.1.3.5.2.4 Summary of "Semi-Static" Unsaturated Tests and Geochemical Modeling

The following summary was extracted from Wilson and Bruton (1989). The full text of that paper is attached to this section as Addendum 1. Laboratory testing and geochemical simulation of the dissolution of spent fuel under conditions selected for relevance to the proposed Yucca Mountain repository have resulted in the following conclusions:

- Radionuclides of interest in spent fuel appear to fall into three categories of potential release mechanisms: 1) radionuclides whose release appears to be controlled by concentration-limiting mechanisms, 2) more highly soluble radionuclides, and 3) radionuclides that are released in the vapor phase (principally C-14).
- The principal radionuclides whose releases appear to be controlled by concentration-limiting mechanisms are the actinides U, Np, Pu, Am, and Cm. Steady-state concentrations measured for these actinide elements are at least three orders of magnitude lower than those required to meet NRC release limits, based on conservative estimates of water fluxes through the repository. This result is of particular significance because isotopes of Pu and Am account for about 98% of the activity in spent fuel at 1000 yr. However, results from geochemical modeling suggest that steady-state concentrations may vary significantly with time because of changes in solution composition and the identity of precipitating phases.
- Good agreement between measured and predicted concentrations was obtained for Np based on equilibration with  $\text{NpO}_2$  at 25°C when the oxygen fugacity in the simulation was set at  $10^{-12}$  bars. A broad range of solubilities that bracketed the measured values was predicted for Pu depending on the assumed oxygen fugacity and solubility-controlling phase. Measured Am concentrations were less than predicted, based on data for equilibration with  $\text{Am}(\text{OH})\text{CO}_3$  and  $\text{Am}(\text{OH})_3$ .
- Dissolution rates for soluble radionuclides ( $^{137}\text{Cs}$ ,  $^{90}\text{Sr}$ ,  $^{99}\text{Tc}$  and  $^{129}\text{I}$ ) exceeding  $10^{-5}$  of specimen inventory per year were measured during the laboratory tests. The implications of these data relative to long-term release of soluble radionuclides from a failed waste package (WP) are uncertain. The degree to which these radionuclides were preferentially released from grain boundaries where they may have concentrated during irradiation was not determined. Preferential release could be expected to provide a lesser contribution overtime as exposed grain boundary inventories are depleted. However, physical degradation of the fuel over time from exposure to the oxidizing repository environment may result in accelerated release of soluble nuclides.
- Additional work is required to identify solid phases that control actinide concentrations and to acquire reliable thermodynamic data on these phases for use in geochemical modeling. In this regard, identification of any stable, suspended phases that can be transported by water movement is also important. In addition, there is a need for a better understanding of the potential release of soluble and volatile radionuclides, which may initially depend on preferential release from gap and grain boundary inventories, but may ultimately depend on the rate of fuel degradation by oxidation or other processes in the postcontainment repository environment.

### 2.1.3.5.3 Flow-Through Dissolution Tests

The purpose of the work reported here is to examine the systematic effect of temperature and important water-chemistry variables on the dissolution rates of the  $\text{UO}_2$  matrix phase in both unirradiated  $\text{UO}_2$  and spent fuel. The dissolution rates of the higher oxidation states of uranium,  $\text{U}_4\text{O}_{9+x}$ ,  $\text{U}_3\text{O}_8$ , and  $\text{UO}_3 \cdot x\text{H}_2\text{O}$  are also reported because of their likely presence in spent fuel placed in a repository. Unirradiated  $\text{UO}_{2+x}$  represents reactor fuel with no burnup. The data sets obtained at equivalent conditions allow a direct comparison of  $\text{UO}_{2+x}$  and spent-fuel dissolution rates and provide insight into the effect of fuel burnup. Additional data at higher spent-fuel burnup are needed to model the effect of burnup over the range of spent-fuel inventory.

The exact chemistry of groundwater in an underground repository is not certain, but groundwater has typical constituents such as carbonates, sulfates, chlorides, silicates, and calcium. Water taken from wells near Yucca Mountain contains all of these ions and has a pH near 8. Of the anions commonly found in groundwater, carbonate is considered to be the most aggressive towards  $\text{UO}_2$  and, as such, is a conservative surrogate for all anions in groundwater.

As mentioned in Section 2.1.3.5.1., there have been many investigations of the dissolution of  $\text{UO}_2$ , spent fuel, and uraninite in aqueous solutions under both reducing and oxidizing conditions and as a function of various other environmental variables (Grambow, 1989). Important variables considered in the investigations included pH, temperature, oxygen fugacity, carbonate/bicarbonate concentrations, and fuel attributes. These same variables were used in the flow-through experiments reported here.

The data obtained from the tests described here can be used to 1) identify important parameters that control the dissolution rates of the  $\text{UO}_2$ -matrix phase of spent fuel, 2) estimate bounding values for  $\text{UO}_2$  and spent-fuel matrix dissolution rates, and 3) develop a release model for radionuclides from spent fuel that will be used in waste-package design and in performance assessment.

The intrinsic dissolution rates of  $\text{UO}_{2+x}$  and spent fuel were determined by using a single-pass, flow-through method that was used successfully in the study of the dissolution kinetics of glass and other minerals (Knauss et al., 1989; 1990). The advantage of the single-pass, flow-through technique is that flow rates and specimen size can be controlled so that the  $\text{UO}_2$  dissolves under conditions that are far from solution saturation (no precipitation of dissolved products). Under such conditions, the steady-state dissolution rates are directly proportional to the effective surface area of the specimen. Thus, the dependence of  $\text{UO}_2$  dissolution kinetics on pH, temperature, oxygen, and carbonate/bicarbonate concentrations can be evaluated.

To test for nonlinear effects of the four variables on the uranium dissolution rate from  $\text{UO}_2$  and spent fuel, experiments at three different values of each variable were required. The chosen settings were pH = 8, 9, 10; temperatures of 25°, 50°, and 75°C; oxygen partial pressures of 0.002, 0.02, and 0.2 atm; and total carbonate concentrations

of 0.2, 2, and 20 millimol/L. Because carbonate solutions are natural pH buffers, total carbonate concentration and pH could be tested independently by varying the carbonate/bicarbonate and CO<sub>2</sub> gas ratios. A statistical experimental-design approach was used to select the experiments to be performed and to reduce the number of required experiments. A model including nonlinear effects and interactions of all 4 variables has at least 15 terms, thus requiring a minimum design of 17 experiments with 2 degrees of freedom or redundancy.

A set of experiments was selected to examine systematically the effects of temperature (25–75°C), dissolved oxygen (0.002–0.2 atm overpressure), pH (8–10), and carbonate concentrations (0.2–20 millimol/L) on UO<sub>2</sub> and spent-fuel dissolution (Steward and Gray, 1994). Similar sets of experiments at atmospheric oxygen partial pressure were conducted on U<sub>3</sub>O<sub>8</sub> and UO<sub>3</sub>·xH<sub>2</sub>O to measure the effect of higher oxidation states on dissolution. The high temperature in all experiments was limited to 75°C, because temperatures nearer to 100°C induce experimental difficulties in an aqueous, flow-through system. The carbonate concentrations bracketed the typical groundwater concentration of about 1–2 millimol/L. The oxygen pressure represented the atmospheric value and down two orders of magnitude to a minimally oxidizing atmosphere. The pH covered a value typical of groundwaters (pH = 8) to very alkaline conditions. In the basic region, carbon dioxide dissolved in water, CO<sub>2</sub> (aq), occurs mostly as carbonate/bicarbonate species. Therefore, carbonate/bicarbonate concentrations were fixed by adding sodium carbonate and bicarbonate to those basic buffer solutions, and the partial pressure of CO<sub>2</sub> in the gas phase above them was kept at the values calculated for stability. The spent fuel used in the PNNL tests was ATM-103, a PWR fuel with a burnup of 30 MWd/kgM and a fission gas release of 0.25%. The UO<sub>2</sub> specimens used at Lawrence Livermore National Laboratory (LLNL) were about 1 cm across and consisted of large crystallites containing dislocation substructures (i.e., low-angle grain boundaries).

Table 2.1.3.5-3 provides a list of the spent fuels used in the flow-through dissolution and other tests.

**Table 2.1.3.5-3 Spent-fuel test materials**

Reactor Type	Fuel	Rod	Peak Burnup (MWd/kgM)	Fission Gas Release (%)
PWR	ATM-103	MLA-098	30	0.25
PWR	ATM-104	MKP-109	44	1.1
BWR	ATM-105	ADD-2974	31	0.59
BWR	ATM-105	ADD-2966	34	7.9
PWR	ATM-106	NBD-095	43	7.4
PWR	ATM-106	NBD-107	46	1
PWR	ATM-106	NBD-131	50	18

### 2.1.3.5.3.1 Flow-Through Test Results

The results of the combined uranium dioxide and ATM-103 spent-fuel test matrices (Steward and Gray, 1994) are given in Table 2.1.3.5-4. Two different averages of the ATM-103 spent fuel and  $UO_2$  data were calculated. The first was for 20% oxygen (air), and the second was for all tests where the conditions were nominally identical. For both averages, the  $UO_2$  rates were about three times higher than the spent fuel rates. There is a clear difference in the way the two materials responded to changes in oxygen concentration, which may be a result of radiolysis-produced oxidants. Uranium dioxide dissolves significantly faster at the aggressive condition of high temperature, oxygen, and carbonate. Aside from oxygen concentration, both spent-fuel and  $UO_2$  dissolution rates were most dependent on temperature, with a lesser dependence on carbonate concentration. Changes in pH had the least effect on the dissolution rates of both materials.

Additional spent-fuel data are available for specific fuels and conditions (Gray and Wilson, 1995; Gray, 1996; Gray, 1998). These 11 dissolution rates of unoxidized high-burnup fuels are listed in Table 2.1.3.5-4a. The combined 53 dissolution rates from Tables 2.1.3.5-4 and 4a are used in the most recent intrinsic dissolution model of Section 3.4.2.

Table 2.1.3.5-4 Test parameters and results for spent fuel (ATM-103) and  $UO_2$  dissolution tests<sup>a</sup>

Run No.	Temp. (°C)	Carbonate <sup>b</sup> (mmol/L)	Oxygen <sup>c</sup> %	pH <sup>d</sup>	U Dissolution Rate (mgU/m <sup>2</sup> ·day)	
					Spent Fuel (ATM-103)	$UO_2$
1	50	2	20	9.0	6.34	
2	50	2	20	9.0	7.05	
3	50		20	9.0	5.07	
4	22/25	2	20	8.0/8.7	3.45	2.42
5	74/75	20	20	10.0/10.3	14.2	77.4
6	74/75	0.2	20	8.0/9.1	8.60	10.9
7	21/25	0.2	20	10.0/9.0	0.63	2.55
8	22/25	20	20	9.0/9.4	2.83	6.72
9	22/25	2	20	10.0/9.3	2.04	9.34
10	27/26	0.2	2	8.0/7.8	1.79	0.12
11	78/75	0.2	2	10.0/9.7	1.49	9.21
12	25/26	20	2	10.0/10.1	2.05	1.87
13	77/75	20	2	8.0/8.5	2.89	5.11
14	23/25	20	0.3/0.2	8.0/8.0	2.83	0.22
15	74/75	20	0.3/0.2	10.0/9.8	0.69	5.61

Run No.	Temp. (°C)	Carbonate <sup>b</sup> (mmol/L)	Oxygen <sup>c</sup> %	pH <sup>d</sup>	U Dissolution Rate (mgU/m <sup>2</sup> ·day)	
					Spent Fuel (ATM-103)	UO <sub>2</sub>
16	78/75	0.2	0.3/0.2	8.0/8.7	1.98	0.51
17	19/26	0.2	0.3/0.2	10.0/9.3	0.51	0.23
18	50/50	20	0.3/0.2	10.0/9.9	1.04	4.60
19	21/26	2	0.3/0.2	9.0/9.0	1.87	1.52
20	75	20	2	10.0	4.75	
21	50	2	2	8.9		12.3
22	50	2	2	8.8		7.96
23	50	2	2	8.9		10.4
24	75	0.2	20	9.5		6.48
25	75	2	20	9.6		23.3
26	75	20	20	8.5		54.0
Average	Runs 4-9				5.29	18.2
Average	Runs 4-19				3.08	8.57

- Numbers separated by a "/" are data for spent fuel and UO<sub>2</sub>, respectively (SF/UO<sub>2</sub>)
- Made up using appropriate amounts of Na<sub>2</sub>CO<sub>3</sub> and NaHCO<sub>3</sub>
- Percent of oxygen in sparge gas
- Measured at room temperature. For spent fuel, the measured values were within ±0.1 unit of the nominal values listed.

**Table 2.1.3.5-4a Additional spent-fuel flow-through dissolution tests at atmospheric oxygen (20%)**

Fuel	Rod	Burnup (MWd/kgM)	Intrinsic Dissolution Rates [mgU/(m <sup>2</sup> ·day)]				
			pH = 8 2 × 10 <sup>-2</sup> M Total Carbonate		pH = 8 2 × 10 <sup>-4</sup> M Total Carbonate		pH = 9 2 × 10 <sup>-3</sup> M Total Carbonate
			25°C	75°C	25°C	75°C	50°C
ATM-104	MKP-109	44	3.5 <sup>a</sup>				
ATM-105	ADD-2974	31	4.0 <sup>a</sup>	9.1 <sup>a</sup>	2.6 <sup>a</sup>	11 <sup>b</sup>	6.6 <sup>b</sup>
ATM-106	NBD-131	50	1.5				
ATM-106	NBD-131	50	3.8 <sup>c</sup>	6.9 <sup>c</sup>	2.9 <sup>c</sup>	9.5 <sup>c</sup>	

- These values were revised in Gray, 1998.
- These values from Gray, 1996.
- These values were added in Gray, 1998.

The dependence of  $\text{UO}_{2,x}$  dissolution kinetics on pH, temperature, time, and carbon dioxide/carbonate/bicarbonate concentrations was also investigated (Steward and Mones, 1997). All experiments in this higher-oxide test series were run at 20% oxygen buffer solution overpressure or 8 ppm dissolved oxygen. The flow-through tests were carried out in basic buffer solutions (pH of 8–10). The chemical composition of the solutions provided concentrations and dissolution-rate data useful in developing kinetic models for  $\text{UO}_2$  matrix dissolution of spent fuel and for use in the waste-package design. The intrinsic dissolution rate obtained from these data is expected to be an upper-bound dissolution response for high pH water chemistries. Again, in order to test for nonlinear effects, experiments at three different values of each quantitative or continuous variable were required. Tests were done at three temperatures (25°, 50°, and 75°C), three carbonate/bicarbonate concentrations ( $2 \times 10^{-4}$  to  $2 \times 10^{-2}$  mol/L), and three pH values (8, 9, and 10) using an arbitrary flow rate (>100 mL/day) for the two compounds  $\text{U}_3\text{O}_8$  and  $\text{UO}_3 \cdot x\text{H}_2\text{O}$ .

Dehydrated schoepite,  $\text{UO}_3 \cdot x\text{H}_2\text{O}$ , was used in the  $\text{UO}_3$  runs. It is easy to produce and is more stable than either the dihydrate or anhydrous form of uranium trioxide. Approximately 20 grams of  $\text{UO}_3 \cdot x\text{H}_2\text{O}$  were prepared via an aqueous hydrolysis of uranyl acetate,  $\text{UO}_2(\text{Ac})_2$ , a procedure that took place over several days. The  $\text{U}_3\text{O}_8$  in use is National Bureau of Standards (NBS) Standard Reference Material (SRM) 750b. It can also be produced by heating the dehydrated schoepite in air. Both  $\text{U}_3\text{O}_8$  and  $\text{UO}_3 \cdot x\text{H}_2\text{O}$  samples were powders because of the synthetic routes available for each. The  $\text{U}_3\text{O}_8$  powders were NBS or National Institute of Standards and Technology (NIST) SR 750(b).  $\text{U}_3\text{O}_8$  is the most stable of the uranium oxides and is easily produced by the well-known method of heating a uranium compound,  $\text{UO}_2$  in this case, to several hundred degrees centigrade in air. Surface areas of both materials were measured via the traditional Brunauer–Emmett–Teller (BET) method using xenon gas. The resulting surface area for the  $\text{U}_3\text{O}_8$  is  $0.18 \pm 0.02 \text{ m}^2/\text{g}$  and  $0.31 \pm 0.04 \text{ m}^2/\text{g}$  for the  $\text{UO}_3 \cdot x\text{H}_2\text{O}$ . Particle-size distributions were also determined by means of sedimentation techniques. The median particle size for the  $\text{U}_3\text{O}_8$  powder was  $2.1 \text{ }\mu\text{m}$  with a 25–75 percentile range of 1.0 to  $2.8 \text{ }\mu\text{m}$ . The median particle size for the  $\text{UO}_3 \cdot x\text{H}_2\text{O}$  powder was  $4.1 \text{ }\mu\text{m}$  with a 25–75 percentile range of 2.5 to  $5.5 \text{ }\mu\text{m}$ .

Table 2.1.3.5-5 lists the uranium dissolution rates for the three oxides  $\text{UO}_2$ ,  $\text{U}_3\text{O}_8$ , and  $\text{UO}_3 \cdot x\text{H}_2\text{O}$  that were measured at LLNL under atmospheric oxygen conditions. The two new, room-temperature  $\text{UO}_2$  results were measured at a pH of 10 and  $2 \times 10^{-4}$  molar total carbonate and a pH of 10 at  $2 \times 10^{-2}$  molar total carbonate. These were recently acquired so that there would be a full set of eight measurements at the extreme conditions (a full-factorial linear experimental design) for each oxide. Previously obtained results for spent fuel (ATM-103) are listed at equivalent conditions. To facilitate comparisons of the dissolution rates and variable effects, the results for the eight experimental conditions at the high and low values of each variable are grouped together at the beginning of the table (Part 1). They are grouped first by pH, then by carbonate concentration, and finally by temperature. The results at intermediate conditions are listed last as Part 2 in Table 2.1.3.5-5, using the same grouping scheme.

As shown in Table 2.1.3.5-5, Part 1, the oxide state had, by far, the strongest effect on the uranium-dissolution rate. The rate increased significantly in going from  $UO_2$  to  $U_3O_8$  and dramatically from  $U_3O_8$  to  $UO_3 \cdot xH_2O$ . Increasing carbonate concentrations increased the dissolution rates of  $U_3O_8$  and  $UO_3 \cdot xH_2O$ , as shown previously with  $UO_2$ . An increase in  $U_3O_8$  dissolution rate with increasing temperature was also seen. A similar temperature effect on  $UO_3 \cdot xH_2O$  was not apparent, which may be due to the rapid  $UO_3 \cdot xH_2O$  dissolution. Raising the temperature to 75°C from room temperature increased the dissolution rate by a factor of 2 to 4 for the two higher oxides. As with the  $UO_2$  results, alkaline pH did not have a significant role in changing the dissolution rate of the higher oxides. However, the detailed dependence on temperature and carbonate concentrations was not visually well demonstrated. Because pH shows little correlation, a surface plot for dissolution rate in three dimensions would better depict the effects of carbonate concentration and temperature.

The data in Table 2.1.3.5-5 indicate that, with the higher oxides, unlike  $UO_2$ , carbonate seems to affect the dissolution rate to a greater extent than does temperature. The enhancement is particularly strong at the highest carbonate concentration.

Because  $U_3O_8$  has both U(IV) and U(VI) valence states, its dissolution rates might be expected to be between that of  $UO_2$  and  $UO_3 \cdot xH_2O$ , particularly as carbonate concentrations increase. That does not seem to be the case with the present data. The data indicate that alkaline pH is the least significant factor in dissolution of spent fuel or any of the uranium oxides under the alkaline conditions of these experiments. Changes in alkaline pH produced almost random changes in dissolution rates in this and previous data sets.

Table 2.1.3.5-5, Part 1 Comparison of dissolution rates at bounding conditions

pH	Carbonate (mol/L)	Oxygen (atm)	Temp (°C)	Dissolution Rate (mgU/(m <sup>2</sup> ·day))			
				ATM-103 Spent Fuel	$UO_2$	$U_3O_8$	$UO_3 \cdot xH_2O$
8	0.0002	0.2	25		3.87	-5	-100
8	0.0002	0.2	50		5.4		
8	0.0002	0.2	75	8.6	10.9	-6	>200
8	0.02	0.2	25	3.45	2.42	18.8	-700
8	0.02	0.2	50		38.3		
8	0.02	0.2	75		54	-150	>1500
10	0.0002	0.2	25	0.63	2.55	0.8	>100
10	0.0002	0.2	50		3.1		
10	0.0002	0.2	75		6.48	-3	>150
10	0.02	0.2	25		20.1	21.1	-200
10	0.02	0.2	50		25.8		
10	0.02	0.2	75	14.2	77.4	-200	>1000

Table 2.1.3.5-5, Part 2 Comparison of dissolution rates at intermediate conditions

pH	Carbonate (mol/L)	Oxygen (atm)	Temp (°C)	Dissolution Rate (mgU/(m <sup>2</sup> ·day))			
				ATM-103 Spent Fuel	UO <sub>2</sub>	U <sub>3</sub> O <sub>8</sub>	UO <sub>2</sub> ·xH <sub>2</sub> O
8	0.002	0.2	25			-10	
8	0.002	0.2	50			-10	
9	0.0002	0.2	25			1.26	
9	0.0002	0.2	75			-4	
9	0.002	0.2	25				-120
9	0.002	0.2	50	6.1	11.7		
9	0.002	0.2	75		23.3		>20
9	0.02	0.2	25	2.83	6.72	8.33	>1500
9	0.02	0.2	50			>100	
10	0.002	0.2	25	2.04	9.34		

2.1.3.5.3.2 Dissolution Rates of Oxidized Spent Fuel and Additional Tests With Unirradiated Uranium Oxides

Uranium dissolution rates were measured on crushed, unirradiated UO<sub>2</sub> fuel pellet samples under oxidizing conditions using the flow-through test method (Wilson and Gray, 1990). Water compositions included J-13 well water, deionized distilled water (DIW), and variations on the J-13 water composition selected to measure the effects of various J-13 water components on UO<sub>2</sub> dissolution rates. Dissolution rates at 25°C in air-equilibrated DIW were 1–2 mgU/(m<sup>2</sup>·day). Calcium (15 µg/ml as CaCl<sub>2</sub> and CaNO<sub>3</sub>) and silicon (30 µg/ml as silicic acid) were sequentially added to the DIW, resulting in an order of magnitude decrease in uranium dissolution rate. Adding NaHCO<sub>3</sub> in concentrations similar to J-13 water (170 µg/ml) to this calcium- and silicon-containing DIW increased the uranium dissolution rate by almost two orders of magnitude.

Results from flow-through dissolution tests with oxidized specimens of spent fuel and unirradiated U<sub>3</sub>O<sub>8</sub> and U<sub>3</sub>O<sub>7</sub> have been published (Gray and Thomas, 1992; Gray et al., 1993; and Gray and Thomas, 1994). Therefore, only highlights are discussed here, together with some details that were not included in these publications (Gray and Wilson, 1995).

Dissolution rates of spent fuels oxidized to U<sub>4</sub>O<sub>9,x</sub> currently have been measured for three spent fuels; ATM-104, ATM-105, and ATM-106. The surface-area normalized-dissolution rate of oxidized fuel grains was little or no higher than unoxidized (UO<sub>2</sub>) grains for ATM-105. Oxidized ATM-106 fuel grains dissolved somewhat faster than did unoxidized grains, but the difference still was a factor of only about five.

Note that the test conditions for ATM-105 were different from those used with the ATM-104 and ATM-106 fuels (see Table 2.1.3.5-6). This precludes a direct comparison between ATM-105 and the other two fuels. However, the purpose of the tests in each case was to compare results for oxidized versus unoxidized specimens, not for comparisons among different fuels. The tests with ATM-105 were conducted first, and a decision was made after that to change the conditions for future tests. This test condition ( $2 \times 10^{-2}$  M total carbonate, pH =8, 25°C, atmospheric oxygen partial pressure), which will be included in most future testing to allow a wider variety of direct comparisons among different fuels, was used for the oxidized and unoxidized specimens of ATM-104 and ATM-106 fuels.

Oxidation has the potential to change spent-fuel dissolution rates in two ways: it could change the intrinsic dissolution rates; it could increase the dissolution rate of fuel particles by making the grain boundaries more accessible to the water, thereby increasing the effective surface area.

Table 2.1.3.5-6 shows that the intrinsic dissolution rates of ATM-104 and ATM-105 (data obtained using grain specimens) were not significantly affected by oxidation, but there was a modest increase in the intrinsic dissolution rate of ATM-106 fuel grains. Secondly, oxidation left the dissolution rate of ATM-105 particles unchanged, which implies that the depth of water penetration into the grain boundaries was unchanged by the oxidation.

**Table 2.1.3.5-6** Dissolution rate ( $\text{mgU}\cdot\text{m}^{-2}\cdot\text{d}^{-1}$ ) and estimated grain boundary penetration of unoxidized ( $\text{UO}_2$ ) and oxidized ( $\text{U}_4\text{O}_{9,x}$ ) spent fuel

Fuel	Rod	Unoxidized			Oxidized		
		Grains	Particles	GBP <sup>a</sup>	Grains	Particles	GBP <sup>a</sup>
ATM-104 <sup>b</sup>	MKP-109	3.4	33	4-6	3.5	166	-100
ATM-106 <sup>b</sup>	NBD-131	1.5	25	6-9	8.2	241	12-18
ATM-105 <sup>c</sup>	ADD-2974	6.6	25	2-3	7.4	28	2-3

<sup>a</sup> Grain boundary penetration: estimate of depth of water penetration into the grain boundaries (number of grain layers)

<sup>b</sup>  $2 \times 10^{-2}$  M total carbonate, pH =8, 25°C, atmospheric oxygen partial pressure

<sup>c</sup>  $2 \times 10^{-3}$  M total carbonate, pH =9, 50°C, atmospheric oxygen partial pressure

In contrast to its effect on the ATM-105 particles, oxidation had a marked effect on the dissolution rates of ATM-104 and ATM-106 particles. This effect can be attributed to opening of the grain boundaries by the oxidation, which allows greater water penetration, thereby increasing the effective surface area available for reaction with the water. So great was this effect with ATM-104 that the water appears to have penetrated the entire volume of grain boundaries throughout the particles. This is evident from the estimated depth of water penetration (~100 grain layers) multiplied by the grain size (~12  $\mu\text{m}$ ), which leads to a penetration depth that is well over half the particle diameters (700 to 1700  $\mu\text{m}$ ).

Because replicate tests have not been run, it is not possible to say whether the three different fuels in Table 2.1.3.5-6 really respond differently to oxidation and subsequent reaction with water or if the observed differences were simply sample-to-sample variations. However, the data do suggest that oxidation up to the  $U_4O_{9+x}$  stage does not have a large effect on intrinsic dissolution rates (the largest increase was a factor of <6). Data for some of the particle specimens also suggest that this degree of oxidation may markedly increase dissolution rates of relatively intact fuel rods by opening the grain boundaries and thereby increasing the effective surface area that is available for contact by water. From a disposal viewpoint, this is the more important consideration.

When ATM-106 fuel was oxidized to  $U_3O_8$ , its surface-area normalized-dissolution rate was about 10 times faster than unoxidized ATM-106 fuel grains and about twice as fast as ATM-106 fuel grains oxidized to  $U_4O_{9+x}$ . A more important effect of oxidation to  $U_3O_8$  was the very large increase in surface area compared to the particles used to prepare the  $U_3O_8$ . This resulted in a fractional dissolution rate (rate per unit specimen weight) of  $U_3O_8$  equal to 150 times that of the unoxidized particles.

At atmospheric  $O_2$  overpressure, the intrinsic dissolution rate of unirradiated  $U_3O_7$  (~3 mgU/(m<sup>2</sup>·day)) was similar to  $UO_2$  (~2.5 mgU/(m<sup>2</sup>·day)), and the intrinsic dissolution rate of unirradiated  $U_3O_8$  (~10-15 mgU/(m<sup>2</sup>·day)) was about three to five times that of  $UO_2$ . At an  $O_2$  overpressure of 0.003 atm, the intrinsic dissolution rate of the  $U_3O_7$  was two to three times that of  $UO_2$  (0.5-1 mgU/(m<sup>2</sup>·day)). These estimates are based on single experiments with each oxide at each condition.

In summary, for each test conducted with oxidized spent fuel or unirradiated  $U_3O_7$  or  $U_3O_8$ , the intrinsic dissolution rate of the oxidized material was only moderately higher than that of the unoxidized ( $UO_2$ ) material. The largest difference was a factor of 10 with spent fuel  $U_3O_8$ . This difference seems relatively small when one considers that the surface of  $UO_2$  must first oxidize to a stoichiometry equivalent to approximately  $UO_{2.33}$  before significant dissolution of U, as U(VI) species, can occur. These observations suggest that initial surface oxidation is not involved in a rate-limiting step of the  $UO_2$  oxidation/dissolution mechanism.

A major reason for conducting dissolution tests with spent fuel oxidized to  $U_3O_8$  was to determine whether the inter- and intragranular cracks produced by the oxidation would lead to high initial dissolution rates of soluble radionuclides. Therefore, 100% of the test-column effluent was collected and analyzed for each of the first two days. During the first day (29 h), 16.2% of the total <sup>137</sup>Cs inventory dissolved compared with 4.5% of the U; thus the excess of <sup>137</sup>Cs over U was about 12%, which represents the amount exposed by oxidation-induced cracking and grain-boundary opening. Nearly congruent dissolution of <sup>137</sup>Cs and U was observed during the second and subsequent days.

Because the fuel particles were washed before they were oxidized to  $U_3O_8$ , the <sup>137</sup>Cs associated with the gap inventory would have been removed. Also, the <sup>137</sup>Cs inventory associated with grain boundaries of this fuel was only about 1% of the total <sup>137</sup>Cs inventory. Therefore, of the 12% excess of <sup>137</sup>Cs over U cited previously, only 1% could

have come from oxidation-induced opening of the grain boundaries. The remaining 11% had to originate from oxidation-induced cracking of the grain interiors. This confirms speculation that oxidation to  $U_3O_8$  might expose a relatively large fraction of the  $^{137}Cs$  inventory to water where it could be readily dissolved, at least for this one type of spent fuel (ATM-106).

#### 2.1.3.5.3 Flow-through Studies of Dissolution Rates of Unirradiated Uranium Oxides and Spent Fuel Performed Outside the Yucca Mountain Site Characterization Project (Non-Qualified Studies)

There are a number of uranium oxide and spent fuel dissolution studies in the literature. Grambow (1989) and McKenzie (1992) provide reviews of the literature prior to 1992. There are three more recent reports of particular interest for flow-through dissolution data. De Pablo (1997) performed flow-through studies of  $UO_2$  dissolution in brine solutions as a function of both temperature and carbonate concentration at atmospheric oxygen. Tait and Luht (1997) recently published a report summarizing  $UO_2$  and spent-fuel flow-through dissolution studies performed over an extended period of time at Atomic Energy of Canada, Limited, Whiteshell Laboratories. Acidic and alkaline dissolution of  $UO_2$  under reducing conditions at room temperature were reported by Bruno et al. (1991). These data can be used for comparison with dissolution models developed for performance assessment.

#### 2.1.3.5.4 Unsaturated Dissolution Tests

This section summarizes work reported in Bates et al. (1995) and Finn et al. (1997). In scenarios for the potential Yucca Mountain repository, it is assumed that the cladding has failed, and water as vapor or liquid has contacted the fuel. Drip tests that simulate the unsaturated and oxidizing conditions expected at Yucca Mountain are in progress to evaluate the long-term behavior of spent nuclear fuel. The purpose of the experiments is to determine if the rate of fuel alteration affects the release rate<sup>2</sup> of different radionuclides under unsaturated conditions. The results from the drip tests are used to monitor the reaction rate of the fuel, the formation of alteration phases, the corresponding release rates for individual radionuclides, and the solution chemistry. The information from these tests can be used to estimate the magnitude of the potential radionuclide source term at the exterior of the fuel cladding and the changes that can be expected in water chemistry due to groundwater interaction with the spent fuel.

The reaction of  $UO_2$  and spent nuclear fuel samples was examined in unsaturated drip tests that simulate an environment that may be expected for spent fuel in the unsaturated/oxidizing environment of the potential Yucca Mountain nuclear waste repository. The reaction of both  $UO_2$  and spent fuel in these tests, results in the formation of alteration phases similar to minerals observed during the oxidative

---

<sup>2</sup> In these unsaturated tests, radionuclide release means the quantity of those elements that go into solution as dissolved or colloidal species or precipitate on the container walls. The quantity of sample that initially dissolves and reprecipitates on the sample or sampleholders is not measured or included in the mass-release totals.

dissolution of uraninite in natural geologic systems. Overall reaction pathways for both  $\text{UO}_2$  and spent fuel appear to be controlled by a combination of sample corrosion, precipitation kinetics of alteration phases, and leachant composition.

#### 2.1.3.5.4.1 $\text{UO}_2$ Reactions Through 12 Years of Testing

The present unsaturated drip tests are being conducted with unirradiated  $\text{UO}_2$ , as a surrogate for spent fuel, using EJ-13 water at 90°C. Direct testing of spent fuel is difficult because of its high level of radioactivity. While these experiments cannot mimic spent-fuel behavior completely, the reaction processes operating during the corrosion of spent fuel and  $\text{UO}_2$  should be similar because spent fuel contains >95%  $\text{UO}_2$ . The gross corrosion processes in the  $\text{UO}_2$  experiments should be relevant to spent-fuel behavior, especially with respect to the identification of secondary alteration products and modes of waste-form degradation. More specifically, these tests examine the dissolution behavior of the  $\text{UO}_2$  pellets, identify long-term mineral paragenesis in the alteration phases, identify parameters that control the release of uranium from the  $\text{UO}_2$  pellets, and serve as a pilot study for similar tests with spent nuclear fuel.

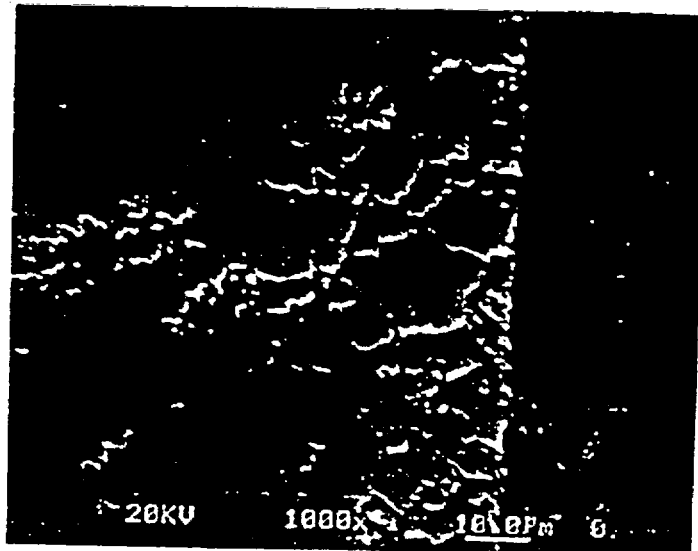
The experimental apparatus and materials used to conduct these tests have been described previously (Wronkiewicz et al., 1991; 1992) and are only briefly summarized here. The samples were fabricated and pressed sintered from a uranium oxide powder with a natural isotopic abundance of uranium and an oxygen/metal ratio of  $2.000 \pm 0.002$ . An analysis of the samples indicated <70 ppm total contaminants, of which Cl (10 ppm), Th (15 ppm), and Fe (20 ppm) were the major contributors.

The  $\text{UO}_2$  samples were placed into 0.38-mm-thick Zircaloy™-4 metal tubes that had been cut to accommodate the lengths of the various sample configurations. Pellets were exposed on their upper and lower surfaces, with their sides enclosed by the Zircaloy™. Several sample configurations were used to assess the effect of surface/volume (S/V) ratios on the dissolution of  $\text{UO}_2$  (Table 2.1.3.5-7). These configurations included the following:

1. A stack of eleven 13.9 mm-diameter by 1.8 mm-thick wafered pellets (experiments 1 and 2)
2. Crushed -60- to +80-mesh grains sandwiched between an upper and lower wafer of the dimensions of the first assembly (experiments 3 and 4)
3. A stack of three 13.9 mm-diameter by 10 mm-thick pellets (experiments 5 through 8)

Uranium release from the  $\text{UO}_2$  samples, listed in Table 2.1.3.5-7 and Table 2.1.3.5-8, was rapid from 1 to 2 yr of testing, followed by relatively low rates of release over the 2- to 10-yr period (Wronkiewicz et al., 1996). The rapid release period could be correlated with an episode of preferential corrosion along  $\text{UO}_2$  grain boundaries and subsequent spallation of micrometer-to-submicrometer-sized  $\text{UO}_{2+x}$  particles (where  $0 \leq x \leq 0.25$ ) from the sample surfaces. Electron microscopy and optical examinations of the altered samples revealed a reaction front that penetrated into the  $\text{UO}_2$  samples an average of 2 to 4 grains (~10 to 20  $\mu\text{m}$ ) ahead of the exposed external sample surface, but varied from

regions with little visible corrosion to regions where penetration occurred to a depth of approximately 10 grains. This corrosion occurred preferentially along the grain boundaries between the original press-sintered granules making up the  $\text{UO}_2$  pellets (Figure 2.1.3.5-1a). The formation of a dense mat of alteration phases in the longer-term tests enveloped the loosened  $\text{UO}_2$  grains (Figure 2.1.3.5-1b), reducing particulate spallation and lowering uranium-release rates.



(a)



(b)

**Figure 2.1.3.5-1** Scanning electron photomicrographs of cross-sectioned corroded  $\text{UO}_2$  pellet samples: (a) Open porosity resulting from penetrative intergranular corrosion along pellet sides from the 3.5-yr sample. Surface phase (gray color) is dehydrated schoepite. (b) Precipitation of compreignacide on top surface of the 8-yr sample. Note the continuation of crystal delamination planes into the open porous region of the sample and the encapsulation of the residual  $\text{UO}_{2+x}$  surface grains by the alteration phases.

Uranium-release rates vary, as determined using unfiltered solutions from the 2- to 10-yr period, but were generally between 0.1 and 0.3 mg/m<sup>2</sup>-day. An analysis of the size-fractionated release patterns during this period indicates that the majority (86 to 97%) of the released uranium was sorbed or precipitated on the walls of the stainless-steel test vessel and the Teflon™ support stand. Between 1 and 12% (U) was present as >5 nm-sized particles suspended in the leachate, whereas less than 2% of the total uranium passed through a filter with a 5-nm pore size. This latter fraction corresponds to a uranium concentration of  $4 \times 10^{-6}$  M in the leachate at the bottom of the test vessel.

An SEM examination of the cross-sectioned samples indicated that the vast majority of the uranium released from the dissolving samples was deposited on the surface of the UO<sub>2</sub> pellets and Zircaloy™ cladding as alteration phases. The quantity of uranium incorporated in these phases was calculated by estimating the volume of material precipitated on the sample surface, the relative proportions of each alteration phase, and the molar proportion of uranium contained in each alteration phase and multiplying the calculated volume of each alteration phase by its respective density. Preliminary calculations for sample PMP8U-2 (Table 2.1.3.5-9), which reacted for 8 yr, indicate that ~80 mg of uranium was incorporated into the alteration phases deposited on the sample or Zircaloy™ surfaces, an amount that far exceeds the 5 mg released (as recovered in the acid strip component).

**Table 2.1.3.5-7 Total uranium release in unsaturated tests with UO<sub>2</sub> samples<sup>a</sup>**

Elapsed Time (wks)	Sample #1			Sample #2			Sample #3			Sample #4		
	Sol. Vol. (mL)	U Release (µg)	Cum. U Release (µg)	Sol. Vol. (mL)	U Release (µg)	Cum. U Release (µg)	Sol. Vol. (mL)	U Release (µg)	Cum. U Release (µg)	Sol. Vol. (mL)	U Release (µg)	Cum. U Release (µg)
8.0	0.84	26.2	26.2	0.81	11	11	0.78	0.28	0.28	0.81	2.7	2.7
13.0	0.19	21.6	47.8	0.64	25.7	36.7	0.58	5.88	6.16	0.64	7.7	10.4
19.6	0.77	449	497	1.01	388	425	0.79	71.9	77.5	0.83	9.2	19.6
26.0	0.78	264	761	0.93	201	626	0.78	126	204	0.81	9.7	29.3
32.6	0.67	129	890	0.81	56.2	682	0.75	88.8	293	0.75	193	222
39.0	0.64	74.5	965	0.83	38.3	721	0.82	31.1	324	0.81	113	336
45.6	0.66	1001	1966	0.66	46.9	768	0.85	195	518	0.83	624	959
52.0	0.74	2159	4125	0.80	1446	2214	0.83	131	649	0.25	867	1927
78.0	3.21	274	4398	2.63	1494	3708	3.42	266	915	1.57	1401	3328
105	3.03	168	4566	3.40	105	3812	3.31	139	1053			
134	3.29	145	4711	3.65	69.6	3882	3.52	50.8	1104			
157	2.58	124	4838	3.22	174	4056	3.06	287	1391			
183	2.77	164	4999	3.41	73.9	4130	3.28	172	1563			
211				2.09	193	4323	3.32	250	1813			
238				1.87	71.6	4394	2.38	97.7	1911			
291				5.43	38.1	4432	6.14	106	2017			
358				6.70	266	4698	6.15	424	2441			
417				4.47	325	5023	5.88	301	2742			
469							4.24	298	3040			
521							3.54	288	3328			
				Terminated after 417 weeks			Ongoing					
Drip Rate	0.075 mL/3.5 days			0.075 mL/3.5 days			0.075 mL/3.5 days			0.075 mL/3.5 days		
Configuration	11 disks			11 disks			Crushed UO <sub>2</sub>			Crushed UO <sub>2</sub>		
Sample Wt (g)	29.52			29.17			19.86			18.26		
Sample SA (m <sup>2</sup> )	40.7			40.6			486			467		
Sample Vol. (m <sup>3</sup> )	2.83			2.80			2.21			2.14		

Terminated after 78 weeks

Elapsed Time (wks)	Sample #1			Sample #2			Sample #3			Sample #4		
	Sol. Vol. (mL)	U Release (µg)	Cum. U Release (µg)	Sol. Vol. (mL)	U Release (µg)	Cum. U Release (µg)	Sol. Vol. (mL)	U Release (µg)	Cum. U Release (µg)	Sol. Vol. (mL)	U Release (µg)	Cum. U Release (µg)
8.0	0.75	2.85	2.85	0.87	2.61	2.61						
13.0	0.58	1.22	4.07	0.66	2.95	5.56	0.30	1.06	1.06	0.35	0.88	0.88
19.6	0.85	109	113	0.78	30.4	38.0						
26.0	0.76	36.1	150	0.77	41.9	77.9	0.67	302	303	0.51	525	526
32.6	0.77	33.8	183	0.70	799	876						
39.0	0.77	19.4	203	0.76	1391	2267		95.3	398	0.34	247	772
45.6	1.07	322	524	0.43	55.7	2323						
52.0	0.92	72.7	597	0.22	593	2916	0.39	665	1063	0.63	264	1036
78.0	3.62	103	700	2.95	3710	6626	0.72	1075	2138	0.78	5948	6984
105	3.41	47.8	748	3.14	389	7015	0.52	225	2363	0.37	2107	9091
134	3.35	69.3	817				0.13	79.3	2442	0.51	10324	19415
157	1.54	58.2	876	6.52	450	7465	0.64	113	2555			
183	1.24	31.1	907	3.48	85.0	7550	1.05	106	2661			
211				1.16	424	7974	2.53	110	2771			
238				2.37	58.0	8030	0.61	11.9	2783			
291				6.09	78.2	8106	1.50	14.4	2797			
358				7.79	97.0	8203	2.28	42.8	2840			
417				5.98	162.0	8365	1.88	58.8	2897			
469				4.80	198.0	8562	1.58	159.0	3056			
521				4.06	358	8918	1.31	57.6	3114			
				Ongoing			Ongoing					
Drip Rate	0.075 mL/3.5 days			0.075 mL/3.5 days			0.0375 mL/7 days			0.0375 mL/7 days		
Configuration	3 Pellets			3 Pellets			3 Pellets			3 Pellets		
Sample Wt (g)	47.96			48.36			47.60			47.77		
Sample SA (m <sup>2</sup> )	22.1			22.2			21.9			22.1		
Sample Vol. (m <sup>3</sup> )	4.54			4.58			4.48			4.54		

Terminated after  
117 Weeks

\* Values represent total uranium released from sample, excluding portion that reprecipitates on the UO<sub>2</sub>-Zircaloy™ assembly. Solution volumes determined by weight differences measured between the beginning and the end of each sampling period. Terminated and ongoing tests are indicated. Blanks indicate no analysis performed. Horizontal bars separate per annum intervals. Water-injection schedule and sample configuration explained in the text. All experiments were conducted at 90°C. Uranium determinations made from collected and acid strip solution of the test vessels.

**Table 2.1.3.5-8 Normalized release rate for UO<sub>2</sub> samples in unsaturated tests**

	Pellet Surface Area (m <sup>2</sup> )	Normalized Periodic Release (mg/m <sup>2</sup> /day)	Sampling Period (weeks)	Normalized Cumulative Release (mg/m <sup>2</sup> /day)	Elapsed Time (weeks)		Pellet Surface Area (m <sup>2</sup> )	Normalized Periodic Release (mg/m <sup>2</sup> /day)	Sampling Period (weeks)	Normalized Cumulative Release (mg/m <sup>2</sup> /day)	Elapsed Time (weeks)
PMP8U-1	0.00407	0.11515	8.0	0.11515	8.0	PMP8U-3	0.0486	0.00010	8.0	0.00010	8.0
		0.15133	5.0	0.12907	13.0			0.00345	5.0	0.00139	13.0
		2.39978	6.6	0.89150	19.6			0.03190	6.6	0.01163	19.6
		1.43989	6.4	1.02704	26.0			0.05775	6.4	0.02304	26.0
		0.89075	6.6	0.95919	32.6			0.03974	6.6	0.02641	32.6
		0.40672	6.4	0.86812	39.0			0.01424	6.4	0.02440	39.0
		5.34723	6.6	1.51401	45.6			0.08706	6.6	0.03344	45.6
		11.79066	6.4	2.78448	52.0			0.05976	6.4	0.03669	52.0
		0.36943	26.0	1.97946	78.0			0.03005	26.0	0.03488	78.0
		0.22085	26.7	1.53081	104.7			0.01525	26.7	0.02957	104.7
		0.17635	28.9	1.23819	133.6			0.00518	28.9	0.02430	133.6
		0.18940	23.0	1.08413	156.6			0.03672	23.0	0.02613	156.6
		0.22096	26.0	0.98120	182.6			0.01940	26.0	0.02517	182.6
								0.02624	28.0	0.02531	210.6
PMP8U-2	0.00406	0.04848	8.0	0.04848	8.0			0.01064	27.0	0.02364	237.6
		0.18103	5.0	0.09946	13.0			0.00588	53.0	0.02040	290.6
		2.07823	6.6	0.76386	19.6			0.01852	67.4	0.02005	357.9
		1.10180	6.4	0.84742	26.0			0.01490	59.6	0.01932	417.3
		0.30067	6.6	0.73711	32.6			0.01683	52.0	0.01904	469.3
		0.20958	6.4	0.65016	39.0			0.01627	52.0	0.01877	521.6
		0.25122	6.6	0.59263	45.6						
		7.91338	6.4	1.49767	52.0	PMP8U-4	0.0467	0.00103	8.0	0.00103	8.0
		2.02146	26.0	1.67227	78.0			0.00472	5.0	0.00245	13.0
		0.13801	26.7	1.28085	104.7			0.00428	6.6	0.00306	19.6
		0.08484	28.9	1.02246	133.6			0.00460	6.4	0.00344	26.0
		0.26617	23.0	0.91136	156.6			0.08988	6.6	0.02088	32.6
		0.10003	26.0	0.79582	182.6			0.05387	6.4	0.02632	39.0
		0.24244	28.0	0.72224	210.6			0.29037	6.6	0.06440	45.6

Pellet Surface Area (m <sup>2</sup> )	Normalized Periodic Release (mg/m <sup>2</sup> /day)	Sampling Period (weeks)	Normalized Cumulative Release (mg/m <sup>2</sup> /day)	Elapsed Time (weeks)	Pellet Surface Area (m <sup>2</sup> )	Normalized Periodic Release (mg/m <sup>2</sup> /day)	Sampling Period (weeks)	Normalized Cumulative Release (mg/m <sup>2</sup> /day)	Elapsed Time (weeks)
PMP8U-5	0.00221	0.09331	27.0	0.65076	237.6	PMP8U-7	0.00219	0.46036	6.4
		0.02532	53.0	0.53668	290.6			0.11335	52.0
		0.13910	67.4	0.46191	357.9			0.16478	26.0
		0.19262	59.6	0.42358	417.3				
		0.02300	8.0	0.02300	8.0			0.00531	13.0
		0.01579	5.0	0.02023	13.0			1.51479	13.0
		1.07652	6.6	0.37480	19.6			0.47826	13.0
		0.36278	6.4	0.37190	26.0			3.33593	13.0
		0.33216	6.6	0.36388	32.6			2.69632	26.0
		0.19498	6.4	0.33604	39.0			0.54993	26.7
		3.16443	6.6	0.74389	45.6			0.17935	28.9
		0.73091	6.4	0.74229	52.0			0.32024	23.0
		0.25635	26.0	0.58031	78.0			0.26570	26.0
		0.11571	26.7	0.46178	104.7			0.25592	28.0
		0.15513	28.9	0.39553	133.6			0.02882	27.0
0.16365	23.0	0.36147	156.6	0.01768	53.0				
0.07739	26.0	0.32101	182.6	0.04146	67.4				
PMP8U-6	0.00222	0.02097	8.0	0.02097	8.0	PMP8U-8	0.00221	0.00435	13.0
		0.03793	5.0	0.02749	13.0			2.61075	13.0
		0.29806	6.6	0.11834	19.6			1.22607	13.0
		0.41986	6.4	0.19289	26.0			1.31096	13.0
		7.81982	6.6	1.73166	32.6			14.78857	26.0
		13.92192	6.4	3.74104	39.0			5.09921	26.7
		0.54592	6.6	3.28030	45.6			56.28545	11.9
		5.93649	6.4	3.60868	52.0				
		9.18176	26.0	5.46637	78.0				
		0.93702	26.7	4.31086	104.7				
0.55796	51.9	3.06788	156.6						

Pellet Surface Area (m <sup>2</sup> )	Normalized Periodic Release (mg/m <sup>2</sup> /day)	Sampling Period (weeks)	Normalized Cumulative Release (mg/m <sup>2</sup> /day)	Elapsed Time (weeks)	Pellet Surface Area (m <sup>2</sup> )	Normalized Periodic Release (mg/m <sup>2</sup> /day)	Sampling Period (weeks)	Normalized Cumulative Release (mg/m <sup>2</sup> /day)	Elapsed Time (weeks)
	0.21048	26.0	2.66096	182.6					
	0.97387	28.0	2.43663	210.6					
	0.13339	27.0	2.17486	237.6					
	0.09252	53.0	1.79505	290.6					
	0.09274	67.4	1.47492	357.9					
	0.17528	59.6	1.28991	417.3					
	0.24509	52.0	1.17413	469.3					
	0.44016	52.0	1.10091	521.6					

Pellet surface area determined by geometric calculation.

**Table 2.1.3.5-9 Fractional distribution of uranium from unsaturated drip tests with  $UO_2$  and spent fuel (values in mg and total percentage in parentheses)**

Test	Acid Strip	Alteration Phases	Grain Boundary Corroded	Unaffected Region	Initial Sample Weight
8-yr $UO_2$	5.0 (0.02%)	80 (0.3%)	780 (3.0%)	24,844 (96.6%)	25,709
Spent fuel <sup>a</sup>	ND <sup>c</sup>	180 (2.3%)	All visible	None	8,000
Spent Fuel <sup>b</sup>	250 (acid strip + alteration phases) (3.1%)		ND	ND	8,000

<sup>a</sup> Fractions determined from measured cross-sections of alteration layers

<sup>b</sup> Fractions determined from Tc release

<sup>c</sup> ND = not determined

Reaction of  $UO_2$  pellets occurs primarily along boundaries between the original press-sintered  $UO_2$  grains. Most of the dissolved uranium reprecipitated into alteration products on the sample surfaces. A significant portion of the uranium was released as particulate matter. Both colloidal-sized uranyl silicates and  $UO_{2+x}$  particles were observed in the filtered residues from the tests. The observed alteration-phase paragenesis mimics that of natural uraninite alteration under oxidizing conditions (e.g., the Nopal I deposit in Mexico). Both the natural and experimental systems display the following mineral paragenetic sequence:

$UO_2 \Rightarrow$  uranyl oxide hydrates  $\Rightarrow$  alkali- and alkaline-earth uranyl oxide hydrates  $\Rightarrow$  uranyl silicates  $\Rightarrow$  alkali- and alkaline-earth uranyl silicates + palygorskite clay (Table 2.1.3.5-10).

The alkali- and alkaline-earth uranyl silicates appear to be the long-term solubility-limiting phases for uranium in the  $UO_2$  tests and the uranium deposits at Nopal. This similarity suggests that the present experiments and the analogous reactions at Nopal may simulate the long-term reaction progress of spent  $UO_2$  fuel following disposal at the proposed Yucca Mountain repository.

**Table 2.1.3.5-10 Summary of UO<sub>2</sub> alteration phases**

---

<b>Uranyl-Oxide Hydrates</b>	
Schoepite (meta-schoepite)	UO <sub>3</sub> ·2H <sub>2</sub> O
Dehydrated Schoepite	UO <sub>3</sub> ·(0.8-1.0H <sub>2</sub> O)
Compreignacite	(Na,K) <sub>2</sub> [(UO <sub>2</sub> ) <sub>6</sub> O <sub>4</sub> (OH) <sub>6</sub> ]·8H <sub>2</sub> O
Becquerelite	Ca[(UO <sub>2</sub> ) <sub>6</sub> O <sub>4</sub> (OH) <sub>6</sub> ]·8H <sub>2</sub> O
<b>Uranyl Silicate Hydrate</b>	
Soddyite	(UO <sub>2</sub> ) <sub>2</sub> SiO <sub>4</sub> ·2H <sub>2</sub> O
<b>Uranyl Alkaline Silicate Hydrates</b>	
β-Uranophane	Ca(UO <sub>2</sub> ) <sub>2</sub> (SiO <sub>3</sub> OH) <sub>2</sub> (H <sub>2</sub> O) <sub>5</sub>
Boltwoodite	K <sub>2</sub> (UO <sub>2</sub> )(SiO <sub>3</sub> OH)(H <sub>2</sub> O)
Na-Boltwoodite	(Na,K)(UO <sub>2</sub> )(SiO <sub>3</sub> OH)(H <sub>2</sub> O)
Skodowskite	Mg(UO <sub>2</sub> ) <sub>2</sub> (SiO <sub>3</sub> OH)(H <sub>2</sub> O) <sub>4</sub>
<b>Non-Uranyl Phases</b>	
Palygorskite	(Mg,Al <sub>0.12-0.66</sub> ) <sub>5</sub> (Si,Al <sub>0.12-0.66</sub> ) <sub>8</sub> O <sub>20</sub> (OH) <sub>5</sub> ·4H <sub>2</sub> O
Fe-Oxides	
Ti-Oxides	
Amorphouse Silica	

---

#### 2.1.3.5.4.2 Spent Nuclear Fuel Reactions After 3.7 Years

##### *Radionuclide Release from Spent Fuel*

Samples of two pressurized-water-reactor fuels, ATM-103 (Guenther et al., 1988a) and ATM-106 (Guenther, 1988b), with burnups of 30 and 45 MWd/kg U, respectively, are used in these ongoing unsaturated drip tests with EJ-13 water at 90°C. See Finn et al. (1994) and Bates et al. (1995) for a detailed description of the experimental apparatus and conditions of the unsaturated drip tests. Alteration of the spent fuel was noted on a microscopic scale after 60 days of reaction and on a macroscopic scale after 748 days of reaction. During the almost three years of testing, concurrent release of radionuclides was also noted. The magnitude of the radionuclide release in these tests was a function of several parameters, including time. The following preliminary conclusions are drawn from release results for the first 581 days of reaction.

Congruent release of the radionuclides with <sup>238</sup>U was not noted during the first 581 days of reaction. An exception was the release of the transuranics <sup>239</sup>Pu, <sup>237</sup>Np, and <sup>241</sup>Am from the ATM-106 fuel. The <sup>238</sup>U release fractions were much lower than those for <sup>99</sup>Tc, <sup>129</sup>I, <sup>90</sup>Sr, and <sup>137</sup>Cs. Because there was, after 748 days of reaction, macroscopic evidence for the formation of alteration products, the release results may indicate that the fuel matrix dissolved congruently under the conditions of the test; however, because of the low water inventory in the drip tests, many of the radionuclides were reprecipitated on

the fuel or on the Zircaloy™ fuel holder. Only those isotopes with very high solubilities in acidic solutions (the pHs in these tests) were found in the leachate collected in the test vessel.

The different release fractions observed for the different radioisotopes suggest that the four fission products (Cs, Sr, Tc, and I) were affected differently by the conditions in these tests. The possible parameters included water chemistry (e.g., acidic pH). The cumulative and 581-day-interval <sup>90</sup>Sr release fractions were comparable to the <sup>137</sup>Cs release fractions for both fuels. For the ATM-103 fuel, the <sup>99</sup>Tc release fractions were two orders of magnitude larger than the <sup>137</sup>Cs release fractions. These large <sup>99</sup>Tc release fractions may be associated with rapid aqueous oxidation and dissolution of this fuel. The cumulative <sup>129</sup>I release fractions were two orders of magnitude larger than the <sup>137</sup>Cs release fractions for both fuels. Release in the earlier reaction intervals, which had the highest <sup>129</sup>I release fractions, may be dominated by release from the gap and grain boundaries. Later release fractions may be dominated by release from the UO<sub>2</sub> matrix. The large fractional releases for <sup>99</sup>Tc may then reflect actual matrix dissolution under the conditions present in the unsaturated tests. These results would suggest that uranium release fractions do not reflect matrix dissolution for low water-volume flow rates, which are typical of unsaturated testing conditions, nor the release fraction of highly soluble species. This observation may impact some of the assumptions made concerning the magnitude of the source term in performance assessment studies.

Colloidal species containing americium and plutonium have been found in the leachate of the drip tests. These results suggest that significant quantities of colloids can form and may provide a mode of transport for the transuranics. Therefore, the incorporation of colloidal transport in performance assessment models is needed to ensure that the models have conservative transport limits.

The total extent of the spent-fuel reaction is difficult to determine because the amount of material incorporated into precipitated alteration products or adsorbed on the Zircaloy™ holder or on the spent-fuel fragments has not been measured. However, the following terms are defined to aid in comparing and interpreting the data:

- "Interval release fraction" is the ratio of the sum for each test interval of the amount of radionuclide in the leachate and in the acid strip divided by the amount of radionuclide in the spent fuel sample.
- The "cumulative release fraction" is the sum of the individual interval release fractions.
- "Release rate" is the ratio of an interval release fraction divided by the days in the interval. (This definition assumes that all of the fuel surface area has reacted in a given time interval.)

The fractional release behavior of the radionuclides for high-drip rate, low-drip rate and vapor tests are listed in Tables 2.1.3.5-11 through 2.1.3.5-13 (Finn et al., 1996). Table 2.1.3.5-11 lists the interval-release fractions for the high-drip rate tests. Table 2.1.3.5-12

lists the cumulative release fractions after 1.6, 2.5, and 3.1 yr of reaction for the high-drip rate tests. Table 2.1.3.5-13 compares the cumulative release fractions for the high-drip, low-drip, and vapor tests at 1.6 and 2.5 yr, respectively, and the cumulative release fraction for a "semistatic" saturated test.

These tables are similar to the later tables 2.1.3.5-16, 2.1.3.5-17, 2.1.3.5-19, and 2.1.3.5-20, which focus only on the release of the  $\epsilon$ -phase constituents.

**Table 2.1.3.5-11 Interval-release fractions for the high-drip-rate tests**

Time (yr)	I-129	Tc-99	Mo-97	Sr-90	Cs-137	U-238	Pu-239
<b>ATM-103</b>							
0.2	8E-3	2E-3	1E-5	2E-3	5E-4	3E-5	4E-6
0.3	4E-3	3E-3	2E-4	7E-4	8E-4	2E-5	2E-6
0.7	7E-3	2E-3	9E-5	5E-5	2E-4	5E-6	1E-6
1.3	3E-4	7E-3	2E-4	1E-4	9E-5	9E-6	2E-6
1.6	3E-4	8E-3	1E-3	3E-5	2E-4	2E-5	3E-7
2.0	1E-4	1E-3	4E-4	4E-6	1E-4	2E-6	2E-8
2.5	2E-4	2E-3	3E-4	2E-5	1E-4	8E-7	1E-8
3.1	3E-4	5E-3	1E-2	1E-5	2E-3	3E-6	6E-7
<b>ATM-106</b>							
0.2	2E-3	0	0	9E-8	3E-8	1E-9	3E-10
0.3	1E-2	1E-5	6E-6	5E-5	4E-5	2E-5	2E-5
0.7	2E-2	1E-4	6E-4	4E-4	2E-3	2E-4	1E-4
1.3	2E-4	6E-5	9E-6	1E-5	1E-3	8E-6	8E-6
1.6	6E-4	1E-3	3E-4	3E-5	1E-4	1E-6	3E-8
2.0	4E-4	4E-3	9E-5	9E-6	3E-4	1E-7	8E-9
2.5	8E-4	4E-3	9E-5	8E-6	2E-4	3E-7	4E-8
3.1	6E-4	8E-3	8E-4	5E-6	6E-4	3E-7	2E-8

**Table 2.1.3.5-12 Comparison of cumulative release fractions after 1.6, 2.5, and 3.1 yr reaction—high-drip-rate tests**

	I-129	Tc-99	Mo-97	Sr-90	Cs-137U-238	Pu-239
<b>1.6 Yr Reaction</b>						
ATM-103	2e-2	2e-2	2e-3	3e-3	2e-3	1E-5
ATM-106	4E-2	2e-3	8e-4	5e-4	3e-3	1E-4
<b>2.5 Yr Reaction</b>						
ATM-103	2e-2	2e-2	3e-3	3e-3	2e-3	1E-5
ATM-106	4e-2	1e-2	1e-3	5e-4	3e-3	1E-4
<b>3.1 Yr Reaction</b>						
ATM-103	2e-2	3e-2	1e-2	3e-3	4e-3	1E-5
ATM-106	4e-2	2e-2	2e-3	5e-4	4e-3	1E-4

**Table 2.1.3.5-13 Comparison of cumulative release fractions\* for high-drip, low-drip, and vapor tests after 1.6 and 2.5 years of reaction and those for "semistatic" tests**

	High Drip		Low Drip		Vapor		Semistatic*	
<b>Reaction Time: 1.6 yr<sup>b</sup></b>								
Fuel ATM#	103	106	103	106	103	106	TP	101
<sup>99</sup> Tc	2E-2	2E-3	9E-5	9E-5	2E-6	8E-7	5E-4	2E-4
<sup>137</sup> Cs	2E-3	3E-3	2E-5	1E-6	1E-7	4E-6	5E-3	1E-2
<sup>238</sup> U	9E-5	2E-4	4E-6	2E-5	6E-8	4E-7	1E-4	1E-4
<sup>239</sup> Pu	1E-5	1E-4	2E-5	2E-5	2E-7	3E-7	1E-4	1E-4
<sup>237</sup> Np	1E-3	1E-4	4E-5	5E-5	7E-7	5E-7	1E-4	1E-4
<sup>241</sup> Am	3E-3	3E-4	4E-4	1E-4	3E-6	6E-7	1E-4	2E-4
<b>Reaction Time: 2.5 yr</b>								
Fuel	103	106	103	106	103	106		
<sup>99</sup> Tc	2E-2	1E-2	1E-4	1E-4	6E-5	2E-6		
<sup>137</sup> Cs	2E-3	3E-3	2E-5	3E-6	1E-6	4E-6		
<sup>238</sup> U	9E-5	2E-4	4E-6	2E-5	5E-7	4E-7		
<sup>239</sup> Pu	1E-5	1E-4	2E-5	2E-5	9E-7	3E-7		
<sup>237</sup> Np	1E-3	1E-4	4E-5	5E-5	1E-6	5E-7		
<sup>241</sup> Am	3E-3	3E-4	4E-4	1E-4	4E-6	6E-7		

\* The error bars for <sup>137</sup>Cs are ± 0.5% and are ± 50% for the actinides.  
 b A reaction time of 1.6 yr is comparable to the total length of Wilson's tests.  
 c Three cycles (460 d) at 85°C for Turkey Point (TP) fuel, 27 (MWd)/kg U, and a fission gas release of 0.3%; and two cycles (360 d) for ATM-101 fuel, 30 (MWd)/kg U, and a fission gas release of 0.2% (Wilson and Gray, 1990)

### *Corrosion of the $\epsilon$ -Phase*

Particles of corroded spent fuel from the ATM-103 test were selected for analysis with electron microscopy (Finn et al., 1997). Several interesting features were observed in this sample. Particles of a molybdenum-technetium-ruthenium (Mo-Tc-Ru) phase ( $\epsilon$ -phase) were found within the spent-fuel grain. The particles were extremely small: approximately 20–50 nm in diameter. Some appeared weathered; on the whole, however, they appeared uniform. The composition of many of the particles did not match that reported by Thomas et al. (Thomas and Guenther, 1989; Thomas and Charlot, 1990; Thomas et al., 1992) during analytical electron microscopy (AEM) characterization of the ATM-103. Quantitative analysis by Thomas et al. (Thomas and Guenther, 1989; Thomas and Charlot, 1990; Thomas et al., 1992) of the transition metals in the  $\epsilon$ -particles agreed with the fission product ratio for these elements in ATM-103. This result supports the contention that all the transition metals partition to the  $\epsilon$ -phases. The Tc and Mo appeared suppressed relative to Ru and Pd, suggesting that the phases may have reacted.

Two types of  $\epsilon$ -ruthenium phase were found in the fuel; this, again, is consistent with the work of Thomas et al. (Thomas and Guenther 1989; Thomas and Charlot, 1990; Thomas et al., 1992) (see Table 2.1.3.5-14); however, the palladium (Pd)-rich phase may be described as  $\alpha$ -Pd(Ru,Rh) phase based on tertiary plots by (Kleykamp et al., 1985). The  $\epsilon$ -ruthenium phase is the accepted transition metal phase described by Thomas and Guenther (1989). The ratio of Mo/(Ru+Pd) has been used to allow comparison of all particles observed. This ratio is one in uncorroded ATM-103 calculated using the ORIGEN-2 code. Thomas and Guenther have also obtained this value in their analyses. In the particles found in the vapor test exposed to a corroding environment for 49 mos, this ratio was found to be much lower for many of the analyzed particles. However, in comparison to the particles found in the ATM-103 high-drip test,  $\epsilon$ -ruthenium phases retained more Mo in the vapor tests (see Table 2.1.3.5-18). This indicates that the 4d-metal phases examined exhibited preferential removal of Mo during the corrosion tests. This partial corrosion of the  $\epsilon$ -phases may provide some insight into the local oxidative conditions. The observed behavior is in agreement with the relative nobility of the 4d metals.

For comparison of quantification methods, results from Thomas and Charlot (1990) and from the ATM-103 high-drip test fuel fragments are shown in Table 2.1.3.5-15. Thomas and Charlot (1990) performed semi-quantitative energy-dispersive spectroscopy (EDS) analyses of transition metals in the  $\epsilon$ -phases. Table 2.1.3.5-15 also presents recent quantification of  $\epsilon$ -phases with electron-energy-loss spectroscopy (EELS) and EDS. In the high-drip sample, it was more difficult to find evidence of corrosion of  $\epsilon$ -ruthenium phases because all appeared to be equally modified from the more typical composition. The "Pu-rich region" in Table 2.1.3.5-15 refers to a region in the ATM-103 fuel that had higher levels of Pu than did most other portions of the fuel.

Evidence for the partial corrosion of the  $\epsilon$ -phase supports the use of Tc as a marker element for spent-fuel dissolution. However, there are still questions regarding the role of intra- and intergranular  $\epsilon$ -particles. Further analysis of thin sections of corroded fuel will be necessary to understand the possible differences.

**Table 2.1.3.5-14** Composition of  $\epsilon$ -phase (elements in wt%) ATM-103 vapor hydration results

Element	Calculated <sup>a</sup>	<i>Pd-rich Particles</i>			
		Mo	44	29	30
Tc	11	9	12	11	
Ru	28	40	30	30	
Rh	—	—	—	—	—
Pd	17	22	28	28	-100
Mo/(Ru+Pd)	0.98	0.47	0.51	0.52	—
		<i>Ru-rich Particles</i>			
Mo		29	26	33	27
Tc		17	15	12	0
Ru		33	42	55	73
Rh		—	—	—	—
Pd		22	17	—	—
Mo/(Ru+Pd)		0.53	0.44	0.60	0.36

<sup>a</sup> Calculated from Guenther et al. (1989) in ATM-103 and normalized without Rh  
<sup>b</sup> Pd not analyzed in this case.

**Table 2.1.3.5-15** Composition of  $\epsilon$ -phase (elements in wt%) ATM-103 high-drip results

Element	Calculated <sup>a</sup>	Unreacted Phase <sup>b</sup>	Edge Region	Pit Region	Pu-Rich Region <sup>c</sup>
Mo	41.2	40	12.3	16.6	15.2
Tc	9.6	10	5.0	10.1	3.9
Ru	27.5	25	41.7	44.8	45.1
Rh	5.5	10	7.5	17.6	9.8
Pd	16.0	15	32.6	10.8	26.1
Mo/(Pd+Ru)	0.95	1.0	0.16	0.30	0.21

<sup>a</sup> Calculated from Guenther et al. (1989) from ORIGEN2 code for 30 MWd/kgM at 15 yr  
<sup>b</sup> Semiquantitative EDS analysis by Thomas and Charlot (1990)  
<sup>c</sup> Quantification of EELS was performed using a 100 eV window and the oscillator strength values calculated from a Dirac-Foch model by Ahn et al. (1989).

This section examines the reaction of the  $\epsilon$ -phase in high-drip-rate tests in the leachate for the first 3.1 yr of reaction. Table 2.1.3.5-16 provides a summary of the release behavior of the five elements in the  $\epsilon$ -phase (Tc, Mo, Ru, Rh, and Pd) for tests with ATM-103 for successive reaction intervals. Similar information for the ATM-106 test is shown in Table 2.1.3.5-17. The information includes the following:

- Released mass ( $\mu\text{g}$ ) for the isotope of each element with minimal interference from other elements
- Total released mass of each element, based on the isotope measured and the element's isotopic distribution
- Calculated mass of elements from the  $\epsilon$ -phases that reacted, based on the  $^{99}\text{Tc}$  release and the distribution of each element in the  $\epsilon$ -phase
- Amount of each element that was not released, based on the difference between the material released (column 2) and that calculated to have reacted (column 3)

The isotope  $^{99}\text{Tc}$  was the dominant element released from ATM-103 and ATM-106 at each reaction interval. Ten percent of the Mo and only trace amounts of Rh, Ru, and Pd were detected in the leachate.

Microtomed samples of reacted fuel were examined to determine if  $\epsilon$ -phase particles (Ru-Mo-Tc-Rh-Pd) were being oxidized as proposed (Finn et al., 1996). Table 2.1.3.5-18, as a superset of Table 2.1.3.5-15, shows the distribution of the five elements in unreacted fuel and the ratio Mo/(Ru+Pd), which can range from 0.9 to 1.5, depending on fission yield or the (Guenther et al., 1988a) distribution found in unreacted fuel (Guenther, 1988b). To determine if the  $\epsilon$ -phase particles had reacted in both the ATM-103 high-drip-rate and the vapor tests, the Mo/(Ru+Pd) mass ratio was measured in reacted particles, as was the change in the relative masses of the five elements in the  $\epsilon$ -phase particles.

In Table 2.1.3.5-19, the cumulative release fractions for  $^{99}\text{Tc}$ ,  $^{238}\text{U}$ , and  $^{239}\text{Pu}$ , as well as for  $^{137}\text{Cs}$  and  $^{97}\text{Mo}$ , are shown for several cumulative reaction times. Table 2.1.3.5-19 illustrates the following points:

- After 3.7 yr of reaction, the cumulative  $^{99}\text{Tc}$  release fractions for the two fuels are similar: 3% of the total inventory for ATM-103 and 2% for ATM-106.
- For the ATM-103 fuel, the  $^{97}\text{Mo}$  cumulative release fraction after 3.7 yr of reaction is similar to the  $^{99}\text{Tc}$  cumulative release fraction; however, for the ATM-106 fuel, the  $^{97}\text{Mo}$  release fraction is only 10% of the  $^{99}\text{Tc}$  release fraction. Thus, some of the Mo appears to be held up in the ATM-106 test; however, at 4.1 yr of reaction, the Mo and Tc release fractions appear comparable (data analysis is still in progress).

- The  $^{137}\text{Cs}$  cumulative release fractions for the two fuels are similar, but are only 10-20% of the cumulative  $^{99}\text{Tc}$  release fraction. It appears that most  $^{137}\text{Cs}$  is held up. An alteration product that can incorporate both Cs and Mo is  $(\text{Cs}_{0.9}\text{Ba}_{0.53})[(\text{UO}_2)_5(\text{MoO}_2)_4(\text{OH})_6] \cdot 6\text{H}_2\text{O}$  (Buck et al., 1997). The formation of this alteration product could account for the hold up of  $^{137}\text{Cs}$  and Mo relative to  $^{99}\text{Tc}$ , especially in the ATM-106 test prior to 4.1 yr of reaction.
- Prior to the first 1.6 yr of reaction, both fuels had a large  $^{238}\text{U}$  release fraction; thereafter, most (99.9%) of the reacted uranium remained on the fuel surface in alteration products based on the difference in release fractions between  $^{99}\text{Tc}$  and U, the visual appearance of the fuel, and the weight gain measured.
- Prior to the first 1.6 yr of reaction, both fuels had a  $^{239}\text{Pu}$  release fraction that was equivalent to 10-40% of the U release fraction. At longer reaction times, most of the Pu was held up.

The reaction suggested by the leachate data for both fuels is one in which there is a continuous release of  $^{99}\text{Tc}$  over 4 yr of reaction, which consists of at least 0.3% of the total inventory in each 6-mo interval. The U release effectively ceases after about a year, but uranium is incorporated into alteration products that form on the surface of the fuel. Alteration-phase formation increases after 1.6 yr of reaction, but the  $^{99}\text{Tc}$  release does not increase. The  $^{99}\text{Tc}$  release fraction can be used to calculate the uranium release fraction and, thus, the mass of uranium that has reacted. This value can be compared to the amount of sodium and silicon removed from the dripped EJ-13 water. In addition, the mass gain for the reacted spent fuel can be compared to the expected increase in mass due to the formation of alteration products. These data are summarized in Table 2.1.3.5-20 for the two fuels after 3.1 yr of reaction. (Units of moles are used for simplicity in comparing the different elements.)

In Table 2.1.3.5-21, the cumulative release fractions for  $^{99}\text{Tc}$ ,  $^{97}\text{Mo}$ ,  $^{137}\text{Cs}$ ,  $^{238}\text{U}$ , and  $^{239}\text{Pu}$  for the ATM-106 low-drip-rate test after 2.5 yr of reaction and 3.1 yr of reaction are compared. At the longer time, the fuel fragments were immersed in EJ-13 for 10 min to determine if reaction had occurred but insufficient liquid were present for transport of the released radionuclides. After immersion, the  $^{99}\text{Tc}$  release fraction increased two orders of magnitude, yielding a total release of ~1%, which is comparable to the cumulative release in the high-drip-rate test after 3.7 yr of 3%. Nearly all of the  $^{99}\text{Tc}$  release after immersion (93%) is in the leachate, as is most of the  $^{97}\text{Mo}$  release. From 90 to 100% of the  $^{137}\text{Cs}$ ,  $^{238}\text{U}$ , and  $^{239}\text{Pu}$  release in the 3.1-yr interval is sorbed on the stainless steel. The sorption behavior on stainless steel is not surprising for the actinides, but was not expected for cesium.

The large fractional release after a short immersion in EJ-13 suggests that the fraction of fuel reacted is underrepresented by the  $^{99}\text{Tc}$  release in the low-drip-rate tests and that most of the reacted radionuclides are present on the fuel surface. If this hypothesis is true, a potential exists for large radionuclide bursts during episodic water

flow if fracture flow occurs after a large portion of the spent fuel has reacted with low volumes of standing water or with water vapor for extended periods. This is different than with the normal steady-state film flow.

The fission product Tc, owing to its high solubility and general tendency not to become incorporated into alteration phases, is being used as a marker element for calculating the corrosion rate of spent nuclear fuel in the ongoing drip tests. Based on the preceding discussion, the Tc marker may be appropriate, at least for low-burnup fuels. However, previous studies have suggested that the  $\epsilon$ -phase is highly insoluble and that, therefore, the observed leached Tc must originate from grain-boundary regions in the fuel.

Fission product segregation and precipitation in low burnup light-water reactor (LWR) fuels can only be effectively studied with AEM because these features, which are characteristic of these types of spent nuclear fuel, can only be probed with a high-spatial-resolution instrument. As limited transport of fission products occurred in the fuel, the features observed in one series of spent nuclear fuel grains are most likely representative of the entire material.

Table 2.1.3.5-16 Disposition of elements in  $\epsilon$ -phase for selected reactive intervals—ATM-103 high-drip-rate test

Isotope	Measured <sup>a</sup> Released Element <sup>b</sup> (μg)	Calculated Released Element <sup>c</sup> (μg)	Calculated Amount Reacted (μg)	Element <sup>d</sup> Retained (mass %)
<b>0.3-Yr Reaction</b>				
<sup>99</sup> Tc	20	20	20	—
<sup>97</sup> Mo	0.9	4	50	93
<sup>101</sup> Ru	0.02	0.07	50	100
<sup>103</sup> Rh	0.6	0.6	7	92
<sup>105</sup> Pd	0.04	0.1	0.5	75
<b>0.8-Yr Reaction</b>				
<sup>99</sup> Tc	10	10	10	—
<sup>97</sup> Mo	0.05	2	30	94
<sup>101</sup> Ru	6E-5	2E-4	40	100
<sup>103</sup> Rh	0.06	0.06	5	99
<sup>105</sup> Pd	ND <sup>e</sup>	ND	0.3	100
<b>1.6-Yr Reaction</b>				
<sup>99</sup> Tc	40	40	40	—
<sup>97</sup> Mo	8	30	100	77
<sup>101</sup> Ru	2E-3	7E-3	200	100
<sup>103</sup> Rh	0.02	0.02	20	100

Isotope	Measured <sup>a</sup> Released Element <sup>b</sup> (μg)	Calculated Released Element <sup>c</sup> (μg)	Calculated Amount Reacted (μg)	Element <sup>d</sup> Retained (mass %)
<sup>105</sup> Pd	2E-3	9E-3	1	100
<b>2.1-Yr Reaction</b>				
<sup>99</sup> Tc	5	5	5	—
<sup>97</sup> Mo	2	10	20	44
<sup>101</sup> Ru	8E-5	2E-4	20	100
<sup>103</sup> Rh	7E-3	7E-3	3	100
<sup>105</sup> Pd	8E-3	0.03	0.2	83
<b>2.5-Yr Reaction</b>				
<sup>99</sup> Tc	10	10	10	—
<sup>97</sup> Mo	1	6	30	82
<sup>101</sup> Ru	6E-4	2E-3	30	100
<sup>103</sup> Rh	0.02	0.02	5	100
<sup>105</sup> Pd	5E-3	0.02	0.3	94

- <sup>a</sup> Measured mass in leachate. Values were rounded to one significant figure.
- <sup>b</sup> The isotopic distribution for each element and the mass of the measured isotope were used to determine the total mass released.
- <sup>c</sup> For ATM-103, the wt% in the ε-phase are (Guenther, 1998a): Tc(11.8); Mo(39.9); Ru(42.3); Rh(5.6); Pd(0.4). The released <sup>99</sup>Tc was the basis for the reacted amount of a given element.
- <sup>d</sup> This is the minimum amount retained and is based on <sup>99</sup>Tc and its wt% in the ε-phase.
- ND = not detected

**Table 2.1.3.5-17 Disposition of elements in ε-phase for selected reactive intervals—ATM-106 high-drip-rate test**

Isotope	Measured <sup>a</sup> Released Element <sup>b</sup> (μg)	Calculated Released Element <sup>c</sup> (μg)	Calculated Amount Reacted (μg)	Element <sup>d</sup> Retained (mass %)
<b>0.3 Yr Reaction</b>				
<sup>99</sup> Tc	0.07	0.07	0.07	—
<sup>97</sup> Mo	0.05	0.2	0.2	4
<sup>101</sup> Ru	0.03	0.1	0.2	50
<sup>103</sup> Rh	0.1	0.1	0.04	Xs <sup>e</sup>
<sup>105</sup> Pd	0.04	0.2	0.1	XS
<b>0.8 Yr Reaction</b>				
<sup>99</sup> Tc	0.9	0.9	0.9	—
<sup>97</sup> Mo	4	20	3	XS
<sup>101</sup> Ru	0.02	0.05	3	83
<sup>103</sup> Rh	0.02	0.02	0.4	50
<sup>105</sup> Pd	ND <sup>f</sup>	ND	2	100

Isotope	Measured <sup>a</sup> Released Element <sup>b</sup> ( $\mu\text{g}$ )	Calculated Released Element <sup>c</sup> ( $\mu\text{g}$ )	Calculated Amount Reacted ( $\mu\text{g}$ )	Element <sup>d</sup> Retained (mass %)
<b>1.3 Yr Reaction</b>				
<sup>99</sup> Tc	0.4	0.4	0.4	—
<sup>97</sup> Mo	0.08	0.3	1	70
<sup>101</sup> Ru	8E-3	0.03	1	97
<sup>103</sup> Rh	0.03	0.03	0.2	85
<sup>105</sup> Pd	0.03	0.1	0.8	87
<b>1.6 Yr Reaction</b>				
<sup>99</sup> Tc	10	10	10	—
<sup>97</sup> Mo	2	9	40	77
<sup>101</sup> Ru	6E-4	2E-3	30	100
<sup>103</sup> Rh	4E-3	4E-3	5	100
<sup>105</sup> Pd	ND	ND	20	100
<b>2.1 Yr Reaction</b>				
<sup>99</sup> Tc	30	30	30	—
<sup>97</sup> Mo	0.07	3	105	97
<sup>101</sup> Ru	1E-3	3E-3	90	100
<sup>103</sup> Rh	6E-3	6E-3	15	100
<sup>105</sup> Pd	3E-3	0.01	60	100
<b>2.5 Yr Reaction</b>				
<sup>99</sup> Tc	30	30	30	—
<sup>97</sup> Mo	0.07	3	105	100
<sup>101</sup> Ru	1E-4	3E-4	90	100
<sup>103</sup> Rh	0.01	0.01	15	100
<sup>105</sup> Pd	5E-3	0.02	60	100

- <sup>a</sup> Measured mass in leachate. Values were rounded to one significant figure.
- <sup>b</sup> The isotopic distribution for each element and the mass of the isotope that was measured were used to determine the total mass released.
- <sup>c</sup> The wt% for ATM-106 (Thomas et al., 1992) for the  $\epsilon$ -phase were: Tc(10); Mo(35); Ru(30); Rh(5); Pd(20). The released <sup>99</sup>Tc mass was the basis for the amount of a given element that reacted.
- <sup>d</sup> This is the minimum amount retained and is based on <sup>99</sup>Tc and its wt% in the  $\epsilon$ -phase.
- <sup>e</sup> XS = excess measured
- <sup>f</sup> ND = not detected

**Table 2.1.3.5-18**      **Composition of reacted  $\epsilon$ -phase particles in ATM-103 tests**  
**(elements in wt%)**

Unreacted Particles					
Element	Fission Yield	Grain Boundary (Guenther et al., 1988b)	Grain (I-1) (Guenther et al., 1988b)		
Mo	40	39.9	52		
Tc	10	11.8	8		
Ru	30	42.3	23		
Rh	5	5.6	6		
Pd	15	0.4	12		
Mo/(Ru+Pd)	0.9	0.9	1.5		
High-Drip-Rate Test after 3.7 Years of Reaction					
Element	Edge Region	Pit Region	Pu-Rich <sup>b</sup> Region		
Mo	12	17	15		
Tc	5	10	4		
Ru	42	45	45		
Rh	8	18	10		
Pd	33	11	26		
Mo/(Ru+Pd)	0.2	0.3	0.2		
Vapor Test after 4.1 Years of Reaction					
Element	Sample 1	Sample 2	Sample 3	Sample 4	Sample 5
Mo	29	30	30	29	26
Tc	9	12	11	17	15
Ru	40	30	30	33	42
Rh	—	—	—	—	—
Pd	22	28	28	22	17
Mo/(Ru+Pd)	0.5	0.5	0.5	0.5	0.4

<sup>a</sup> This is the average distribution in the fuel.

<sup>b</sup> Quantification of EELS was done using a 100 eV window and the oscillator strength values calculated from a Dirac-Foch model.

**Table 2.1.3.5-19 Cumulative release fractions<sup>a</sup> for the high-drip-rate tests**

Time (yr)	<sup>99</sup> Tc	<sup>97</sup> Mo	<sup>137</sup> Cs	<sup>238</sup> U	<sup>239</sup> Pu
<b>1.6 Yr of Reaction</b>					
ATM-103	2.1E-2 <sup>b</sup>	1.9E-3	1.8E-3	8.6E-5	9.8E-6
ATM-106	1.6E-3	8.5E-4	3.0E-3	1.8E-4	1.4E-4
<b>2.5 Yr of Reaction</b>					
ATM-103	2.4E-2	2.6E-3	2.0E-3	9.0E-5	9.9E-6
ATM-106	9.6E-3	1.0E-3	3.4E-3	1.8E-4	1.4E-4
<b>3.1 Yr of Reaction</b>					
ATM-103	2.9E-2	1.4E-2	3.7E-3	9.2E-5	1.0E-5
ATM-106	1.7E-2	8.E-3	4.0E-3	1.8E-4	1.4E-4
<b>3.7 Yr of Reaction</b>					
ATM-103	3.0E-2	1.6E-2	4.7E-3	9.3E-5	1.0E-5
ATM-106	2.0E-2	2.1E-3	5.0E-3	1.8E-4	1.4E-4

<sup>a</sup> Cumulative release fractions have been rounded to two significant figures.  
<sup>b</sup> The unit E-2 is  $1 \times 10^{-2}$ .

**Table 2.1.3.5-20 High-drip-rate tests—alteration products after 3.1 yr of reaction**

Species	Na-Boltwoodite <sup>c</sup> (mol)	Dehydrated Schoepite <sup>d</sup> (mol)	Excess <sup>e</sup> (mol)	Total (mol)	Calculated <sup>a</sup> Weight-UO <sub>2</sub> (g)	Measured <sup>b</sup> Weight Gain (g)
ATM-106					0.07	0.06
U	2.9E-4	6E-5	1E-4	4.5E-4		
Si	2.9E-4	—	—	2.9E-4		
Na	2.9E-4	—	6E-4	8.9E-4		
ATM-103					0.07	0.05
U	2.7E-4	2E-4	2.9E-4	8E-4		
Si	2.7E-4	—	—	2.7E-4		
Na	2.7E-4	—	5E-5	3.2E-4		

<sup>a</sup> Difference between sum of masses of alteration products and the original fuel's UO<sub>2</sub>  
<sup>b</sup> Difference between original fuel weight and that after 3.1 yr of reaction. The weight gain for the interval between 2.5 and 3.1 yr was estimated as the average over the previous 2.5 yr: 0.01 g/0.5 yr for ATM-106 and 0.007 g/0.5 yr for ATM-103. Weights when water was retained were not used.  
<sup>c</sup> Formula: Na[(UO<sub>2</sub>)<sub>2</sub>(SiO<sub>2</sub>OH)] · H<sub>2</sub>O. This was the major alteration product from XRD; the silicon was assumed to be primarily in this product. The total moles of U are based on the <sup>99</sup>Tc release fraction.  
<sup>d</sup> Formula: UO<sub>2</sub> · 0.8 H<sub>2</sub>O. This was identified in the vapor test.  
<sup>e</sup> The moles listed are the differences from the total moles. The excess may result from uncertainty in the analyses of Na and U in solution and U unaccounted for during solids analysis

**Table 2.1.3.5-21** Release fractions for the ATM-106 low-drip-rate test after 3.1 yr of reaction and immersion for 10 min in EJ-13

Radionuclide	Cumulative Interval		
	2.5 yr	3.1 yr	3.1 yr
<sup>99</sup> Tc	1.0E-4	9.4E-3	9.4E-3
<sup>97</sup> Mo	1.2E-4	1.1E-3	9.7E-4
<sup>137</sup> Cs	3.3E-6	4.9E-4	4.9E-4
<sup>238</sup> U	1.8E-5	1.6E-4	1.4E-4
<sup>239</sup> Pu	2.4E-5	2.0E-4	1.8E-4

#### *Evidence for Plutonium Segregation*

During the AEM examination of corroded ATM-103 from both the vapor and high-drip tests, regions were found that possessed anomalously high concentrations of plutonium. The plutonium enrichment levels in these regions far exceeded those reported in the uncorroded fuels (Thomas and Guenther, 1989; Thomas and Charlot, 1990; Thomas et al., 1992). EDS indicated significant levels of Zr and Ru in this region. Zirconium is a fission product, and the fuel cladding is a zirconium alloy. Zirconium is also the major component in the sample retainer of the test apparatus. It is possible that reaction might occur at the fuel's edge where pellets are in contact with the Zr-bearing cladding. However, the levels of Pu in these regions are generally suppressed, owing to the high burnup. Also, these regions exhibit high levels of fission products such as rare earths. The EELS analysis indicated anomalously low concentrations of rare earths. Therefore, the enriched Pu regions are most likely produced during oxidative corrosion. This may also suggest that Pu is not readily incorporated into uranyl phases. Burns et al. (1997) speculate that substitution of Pu<sup>6+</sup> and Pu<sup>4+</sup> for U<sup>6+</sup> may occur in uranyl oxide hydrates and uranyl silicates.

#### *Alteration Phases*

Combined optical, SEM, EDS, and XRD examinations of samples taken from tests being performed on the two ATM fuels indicated that the rate at which groundwater contacts the fuel samples may be the most important single factor determining the alteration-phases that form as spent UO<sub>2</sub> fuel corrodes in a humid, oxidizing environment (Finn et al., 1997). The three tests (high-drip-rate, low-drip-rate, and vapor) show several similarities, including corroded grain boundaries, dissolution of fuel grains, and precipitation of U<sup>6+</sup>-phases (Table 2.1.3.5-22). The vapor tests display the simplest assemblage of alteration products; only U and the radionuclides in the fuel dissolve into the thin film of water in contact with the fuel surfaces. The most abundant phase identified in the vapor tests is probably dehydrated schoepite, (UO<sub>2</sub>)O<sub>0.25-x</sub>(OH)<sub>1.5+2x</sub> (0 ≤ x ≤ 0.15).

The drip tests display more chemically complex alteration phases, owing to the interaction of the fuel with EJ-13 water (rather than water vapor only). The most abundant elements in EJ-13 water are Na and S; not surprisingly, the most abundant alteration products in the high-drip-rate tests are Na- and Si-bearing  $U^{6+}$  phases. Other  $U^{6+}$  phases are also present, including metaschoepite and  $\beta$ -uranophane, indicating the importance of additional minor phases and elements to the overall corrosion process.

An important observation at this stage is that the time-dependent evolution of the alteration-phase assemblage appears to be strongly dependent on the rate at which the EJ-13 water contacts the spent fuel. Fuel samples exposed to the higher drip-rates (nominally 10 times higher than that of the low-drip-rate tests) display a comparatively simple phase assemblage consisting of two uranophane-group silicates,  $\beta$ -uranophane and Na-boltwoodite (Table 2.1.3.5-22). In contrast, the sample from the low-drip-rate test displays a more complex alteration-phase assemblage, with four or five phases identified (Table 2.1.3.5-22). It is likely that the simpler phase assemblage in the high-drip-rate tests reflects higher overall reaction progress for the spent fuel in these tests. Also, samples from the first sampling periods were not taken, and it is possible that the early phases formed but were not detected.

Another important observation concerns the identification of uranyl oxyhydroxides in the vapor-hydration tests. The precipitation of dehydrated schoepite and metaschoepite in these tests indicates that the film of water that forms on the fuel surface is sufficiently corrosive to dissolve the fuel and form a thin corrosion rind of alteration products. Such a water film is likely present in the drip tests as well during those intervals that EJ-13 water is not being dripped onto the fuel. It seems likely that the corrosion processes important in the vapor tests remain important in the drip tests. Dehydrated schoepite and/or metaschoepite may continue to form in the drip tests between water injections. If these phases are present when contacted by EJ-13 water, they may be at least as susceptible to dissolution and/or replacement as the unoxidized fuel. The degree to which this may be important is unknown at this time.

The mechanism by which the fuel has reacted during these tests is important, although there is only limited information available at this time. Most striking is that the fuel in the high-drip-rate test on sample ATM-103 has dissolved along a uniform front that has penetrated from the outer surface into the spent-fuel fragments. This "through-fragment" dissolution has proceeded without regard to existing grain boundaries. The replacement of the fuel by Na-boltwoodite at the fuel surface may also be self-accelerating. Through-fragment dissolution appears to be an important mechanism by which the fuel is reacting in the high-drip-rate tests. Of course, the dissolution of the fuel along grain boundaries is also important in the high-drip-rate tests. This is especially evident from the extent to which the grain boundaries in one fragment of ATM-103 had been opened, resulting in a friable fragment that decomposed during sample handling.

Additional grains and fragments of reacted fuel are being examined to understand more fully the corrosion and alteration processes, including grain-boundary penetration by water, changes in the reactive surface area, and the distribution of radionuclides between the alteration phases and the EJ-13 water.

**Table 2.1.3.5-22 Alteration Phases Identified by SEM or XRD from ATM Test Samples**

Phase	Formula	Test
metaschoepite (?)	$UO_3 \cdot 2H_2O$ (?)	ATM-103 (LDR) ATM-103 (vapor) ATM-106 (vapor)
dehydrated schoepite	$(UO_2)_{0.25-x}(OH)_{1.5+2x}$ ( $0 \leq x \leq 0.15$ )	ATM-103 (LDR) (?) ATM-103 (vapor) ATM-106 (vapor)
unidentified Na-UOH	$(Na,K)[(UO_2)_3O_2(OH)_3](H_2O)$ (?)	ATM-103 (LDR)
soddyite	$(UO_2)_2SiO_4(H_2O)_2$	ATM-103 (LDR)
$\beta$ -uranophane	$Ca(UO_2)_2(SiO_3OH)_2(H_2O)_5$	ATM-103 (HDR)
Na-boltwoodite	$(Na,K)(UO_2)(SiO_3OH)(H_2O)$	ATM-103 (LDR) ATM-103 (HDR) ATM-106 (HDR)

(?) indicates a tentative identification or an uncertain formula  
LDR = low-drip-rate test; HDR = high-drip-rate test

Two fragments of reacted spent fuel were examined by SEM: ATM-103 and ATM-106. Based on crystal morphology, chemical composition as determined by EDS and XRD, the most abundant alteration product of spent fuel after 3.7 yr of reaction is Na-boltwoodite,  $(Na,K)(UO_2)(SiO_3OH)(H_2O)$ . Additional minor phases have been detected by AEM and XRD analyses, the most abundant of which is  $\beta$ -uranophane,  $Ca(UO_2)_2(SiO_3OH)_2(H_2O)_5$  (~10 vol.%); however, Na-boltwoodite makes up more than ~80 vol.% of the alteration products identified (a Cs-Mo-uranyl phase was found on the Zircaloy™ stand removed from the test vessel at 1.8 yr).

Figure 2.1.3.5-2 shows a cross-section through a fragment of the ATM-103 fuel. This is the only fragment studied as of July 1997, and final conclusions must be based on a representative number of fragments. Nevertheless, the SEM image shows the fuel (brightest region), in which the grain boundaries are readily visible. Gaps of approximately 0.5  $\mu$ m or less are visible between the fuel grains. No alteration phases between the grain boundaries have been detected, and Si is not evident from EDS analyses at the grain boundaries; this indicates that dissolved Si is depleted in fluids penetrating the grain boundaries, possibly due to the formation of uranyl silicates on the outer surface of the fuel.

Surrounding the fuel is an alteration layer consisting of predominantly Na-boltwoodite. The thickness of the layer varies but is approximately 20–40  $\mu$ m. This Na-boltwoodite layer consists of two regions that differ in appearance: a dense layer, approximately 10  $\mu$ m thick closest to the fuel surface, and a much less dense outer layer,

10–30  $\mu\text{m}$  thick. No difference in composition is evident between the two layers using EDS. Near the outer edge of the denser (inner) layer is an interface (arrow, Figure 2.1.3.5-2b) defined by a gap (dark band) that lies approximately 10  $\mu\text{m}$  above the fuel surface and 2–3  $\mu\text{m}$  below the outer edge of the dense layer. Just below this interface, crystals of Na-boltwoodite have formed more or less perpendicular to the fuel surface; whereas, above this interface, Na-boltwoodite forms a dense mat of crystals subparallel to the fuel surface. Above these flat-lying crystals is the low-density outer layer. The inner, dense layer may represent a region where the spent fuel has been replaced isovolumetrically by the Na-boltwoodite, but this hypothesis requires verification. The different densities of the two layers are manifested as different colors under optical examination: the inner layer is dark yellow, and the outer layer is pale yellow to white. The inner layer is attached strongly to the adjacent fuel grains, whereas the outer layer is not.

#### *Neptunium Incorporation in Alteration Phases*

AEM analysis of the dehydrated schoepite with EELS indicates the presence of Np. Examinations of cross-sections of the corroded fuel grains and alteration products indicate that it is unlikely that the occurrence of Np is due to sorption on the dehydrated schoepite; however, this mechanism cannot be totally excluded for retention of Np in an alteration phase.

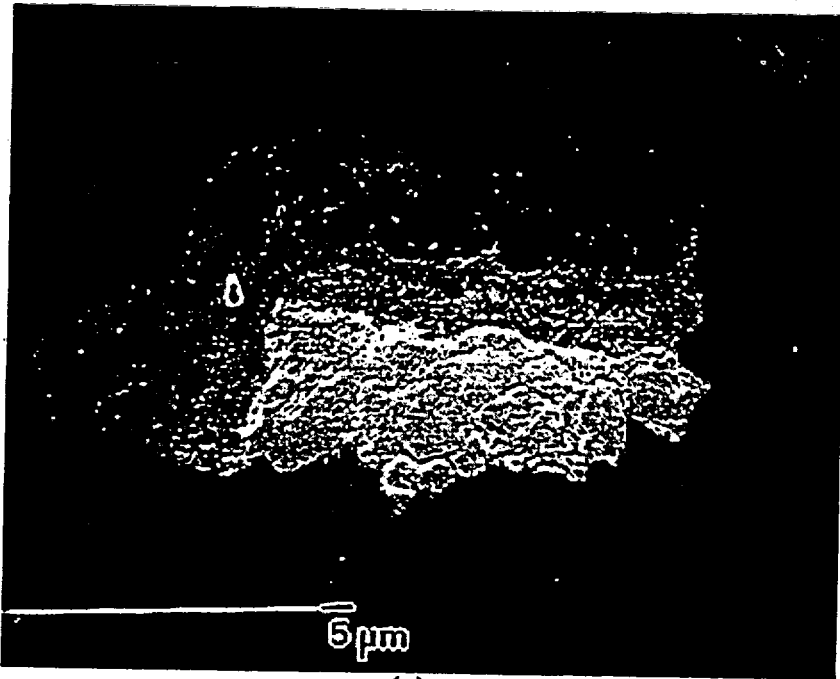
Np was observed with EELS in three samples of dehydrated schoepite that were taken from different regions of the corroded fuel pellets. The U:Np ratio was estimated to be between 1:0.003 and 1:0.006, based on 5 analyses. In the dehydrated schoepite ( $\text{UO}_3 \cdot 0.8\text{H}_2\text{O}$ ), where Np was detected, this ratio corresponds to one Np atom for every 250 unit cells of  $\text{UO}_3 \cdot 0.8\text{H}_2\text{O}$  or about 550 ppm. The U:Np ratio in the ATM-103 fuel is 1:0.0005, taken from calculated values reported by Guenther et al. (Guenther, 1988b) for ATM 103 at 35 MWd/kgM after 15 yr. The estimated U:Np ratio in the alteration phase indicates that a large proportion of the Np has entered into the phase. Owing to the scarcity of water on the fuel surface in the vapor tests, only a small amount of water was able to flow into the steel collection vessel positioned at the bottom of the test apparatus. Under these conditions, it might be expected that the highly soluble elements would become concentrated enough in the thin film of water to precipitate secondary phases. The absence of Pu and Am in the dehydrated schoepite supports the contention that mainly Np and U were mobilized during the corrosion process and were incorporated into a secondary phase. There may be a suggestion of some Np in a uranyl silicate phase; however, the levels are at, or below, the detection limits for the instrument.

#### 2.1.3.5.4.3 Discussion

The interface indicated in Figure 2.1.3.5-2b is interpreted as corresponding to the position of the surface of the original fuel fragment. Na-boltwoodite precipitated on the fuel surface, forming a mat of flat-lying crystals; as the fuel dissolved, Na-boltwoodite replaced the fuel as the surface dissolved. There is approximately a four-fold volume

increase between cubic  $\text{UO}_2$  and monoclinic Na-boltwoodite, so that (at most) one-quarter of the U in the replaced outer fuel layer is incorporated in the Na-boltwoodite within the replacement layer. The remaining three-quarters of the U was transported out of the replaced region, where much of it precipitated as Na-boltwoodite making up the outer, less-dense layer. However, Na-boltwoodite is not sufficiently dense to contain all the U that was lost from the reacted layer. Based on an estimate of the density of the Na-boltwoodite depicted in Figure 2.1.3.5-2a, the outer layer probably contains only about one-half of the U lost from the reacted layer (i.e., ~38% of the reacted uranium). Some U is adsorbed on the vessel walls and is associated with the retainer, and there may be a build-up of alteration phases elsewhere in the test vessel.

There appears to have been extensive dissolution along grain boundaries, as evident from the friable nature of the fuel fragment when removed from the test vessel and from the wide gaps between grains (Figure 2.1.3.5-2) (the expansion of the gaps between grains is enhanced by the oxidation of  $\text{UO}_2$  to  $\text{UO}_{2.25}$ , but this cannot account fully for the observed widths of the gaps). However, dissolution along grain boundaries appears to be limited compared to the "through-fragment" dissolution of the  $\text{UO}_2$  fragments, as indicated by the lack of embayment at grain-boundaries (Figure 2.1.3.5-2). The replacement of the fuel proceeded uniformly inward from the original outer surface (arrow in Figure 2.1.3.5-2b) without regard to grain boundaries. Thus, the through-fragment dissolution of the  $\text{UO}_2$  fuel matrix may predominate over grain-boundary-enhanced dissolution at this stage of reaction and has resulted in the replacement of spent fuel by (predominantly) Na-boltwoodite. Note, however, that the volume of fuel reacted along grain boundaries within the fuel grains may be quite large compared to a uniform ~10  $\mu\text{m}$ -thick replacement layer (see subsequent text).



(a)



(b)

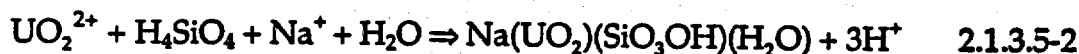
Fig. 2.1.3.5-2

ATM-103 sample (high-drip-rate, 3.7 reaction) SEM micrographs of polished section through the contact between fuel grains and corrosion rind: (a) Particle showing both corrosion layers and the adjacent fuel grains; (b) magnified view of particle shown in (a), illustrating details of the dense inner layer of Na-boltwoodite.

The (simplified) reaction for the oxidative dissolution of the  $\text{UO}_2$  fuel can be written as



The precipitation of Na-boltwoodite is



Thus the *net* reaction for the replacement of the  $\text{UO}_2$  fuel by Na-boltwoodite is



The last reaction (which is not an equilibrium expression) shows that, as Na- and Si-rich EJ-13 water is added to the system (i.e., to react with the  $\text{UO}_2^{2+}$  and/or  $\text{H}^+$  is removed (due to flowing water and/or reaction with fuel via the first reaction), the replacement reaction proceeds to the right, provided that a sufficient supply of oxidants is available. In fact, an abundant supply of oxidants is likely available because of the effects of radiolysis and  $\text{O}_2$  in the reaction vessel atmosphere.

#### 2.1.3.5.4.4 Summary

The retention of fission products and actinides cannot be predicted quantitatively at this time without further examination of additional grains and fragments of reacted fuel to obtain a better understanding of the grain-boundary penetration and the increase of surface area and the distribution of radionuclides between reacted phases and solution. While these studies suggest that the alteration phases will incorporate a large proportion of the radionuclides that have been released from dissolved spent fuel and that such a process may act as a significant mechanism for retarding the migration of radionuclides from the WP, synergistic effects among the waste form, and parameters affecting its corrosion, and other components of the repository must be taken into account before using the present data in predicting the fate of radionuclides in a repository.

#### 2.1.3.5.5 References

- Ahn, C. C., D. H. Pearson, P. Rez, and B. Fultz (1989). "EELS white line intensities calculated for the 3d and 4d metals." In proceedings from 47th Annual Meeting of Electron Microscopy Society of America. G. W. Bailey (Ed.). pp. 388-389.
- Bates, J. K., J. A. Fortner, P. A. Finn, D. J. Wronkiewicz, J. C. Hoh, J. W. Emery, E. C. Buck, and S. F. Wolf (1995). Yucca Mountain Project—Argonne National Laboratory, Annual Progress Report, FY 1995. (ANL-95/xx; YMP Milestone 209) Argonne, IL: Argonne National Laboratory [MOL.19960620.0123]

- Bruno, J., I. Casas, and I. Puigdomenech (1991). "The Kinetics of Dissolution of  $UO_2$  Under Reducing Conditions and the Influence of an Oxidized Surface Layer ( $UO_{2,x}$ ): Application of a Continuous Flow-Through Reactor." *Geochim. Cosmochim. Acta* 55(3):647-658. [NNA.19910821.0004]
- Buck, E. C., D. J. Wronkiewicz, P. A. Finn, and J. K. Bates (1997) "A New Uranyl Oxide Hydrate Alteration Phase Derived from Spent Fuel Corrosion." *J. Nucl. Mater.* 249:70. [MOL.19980107.0446]
- Burns, P. C., R. C. Ewing, and M. L. Miller (1997). "Incorporation Mechanisms of Actinide Elements into the Structures of  $U^{6+}$  phases formed during the Oxidation of Spent Nuclear Fuel." *J. Nucl. Mater.* 245:1. [235501]
- de Pablo, J., I. Casas, J. Giménez, M. Molera, and M. E. Torrero (1997). "Effect of Temperature and Bicarbonate Concentration on the Kinetics of  $UO_2(s)$  Dissolution Under Oxidizing Conditions." In proceedings from Material Research Society Symposia. 465:535-542.
- Finn, P. A., J. C. Hoh, S. F. Wolf, S. A. Slater, and J. K. Bates (1994). "The Release of Uranium, Plutonium, Cesium, Strontium, Technetium, and Iodine from Spent Fuel Under Unsaturated Conditions." *Radiochim. Acta* 66/67:189.
- Finn, P. A., J. C. Hoh, S. F. Wolf, M. T. Surchik, E. C. Buck, and J. K. Bates (1996). Spent fuel reaction: The behavior of the  $\epsilon$ -phase over 3.1 years." In proceedings from *Mater. Res. Soc. Symp.* 465:527-534.
- Finn, P. A., D. J. Wronkiewicz, R. J. Finch, J. C. Hoh, J. W. Emery, E. C. Buck, J. A. Fortner, S. F. Wolf, L. A. Neimark, and J. K. Bates (1997). *Yucca Mountain Project—Argonne National Laboratory, Annual Progress Report, FY 1997*. (ANL-98/12) Argonne, IL: Argonne National Laboratory.
- Grambow, B. (1989). *Spent Fuel Dissolution and Oxidation. An Evaluation of Literature Data*. (SKB Technical Report 89-13) Stockholm, Sweden: Swedish Nuclear Fuel and Waste Management Co. [NNA.18981013.0094]
- Gray, W. J., and L. E. Thomas (1992). "Dissolution Rates of As-Received and Partially Oxidized Spent Fuel." In proceedings from Third International High-Level Radioactive Waste Management Conference. La Grange Park, IL: American Nuclear Society, Inc. pp. 1458-1464. [NNA.19920204.0037]
- Gray, W. J., L. E. Thomas, and R. E. Einziger (1993). "Effects of Air Oxidation on the Dissolution Rate of LWR Spent Fuel." In proceedings from Scientific Basis for Nuclear Waste Management XVI. C. G. Interrante and R. T. Pabalan 294 [Eds.]. Pittsburgh, PA: Materials Research Society. pp. 47-54. [236035]
- Gray, W. J., and L. E. Thomas (1994). "Initial Results from Dissolution Testing of Various Air-Oxidized Spent Fuels." In proceedings from Scientific Basis for Nuclear Waste Management XVII. Barkatt and R. A. Van Konynenburg (Eds.) Pittsburgh, PA: Materials Research Society 333A:391-398. [NNA.19940204.0108]

- Gray, W. J., and C. N. Wilson (1995). *Spent Fuel Dissolution Studies FY1991 to 1994*. (PNL-10540) Richland, WA: Pacific Northwest National Laboratory. [MOL.19960802.0045]
- Gray, W. J. (1996). *FY 1996 Letter Report on Spent Fuel Dissolution Studies*. (Informal YMP Status Report) Richland, WA: Pacific Northwest National Laboratory. [MOL.19970114.0282]
- Gray, W. J. (1998). *Letter Report on Spent Fuel Dissolution Rates as a Function of Burnup and Water Chemistry*. (Informal YMP Status Report, PNNL-11895) Richland, WA: Pacific Northwest National Laboratory.
- Guenther, R. J., D. E. Blattnik, T. K. Campbell, U. P. Jenquin, J. E. Mendel, L. E. Thomas, and C. K. Thornhill (1988a). *Characterization of Spent Fuel Approved Testing Material—ATM-103*. (PNL-5109-103) Richland, WA: Pacific Northwest Laboratory. [NNA.19911017.0104]
- Guenther, R. J., D. E. Blattnik, T. K. Campbell, U. P. Jenquin, J. E. Mendel, L. E. Thomas, and C. K. Thornhill (1988b). *Characterization of Spent Fuel Approved Testing Material—ATM-106*. (PNL-5109-106) Richland, WA: Pacific Northwest Laboratory. [NNA.19911017.0105]
- Kleykamp, H., J. O. Paschoal, R. Pejsa, and F. Thommler (1985). "Composition and Structure of Fission Product Precipitates in Irradiated Oxide Fuels: Correlation with Phase Studies in the Mo-Ru-Rh-Pd and BaO<sub>2</sub>-UO<sub>2</sub>-ZrO<sub>2</sub>-MoO<sub>2</sub> Systems," *J. Nucl. Mater.* 130:426–433.
- Knauss, K. G., and T. J. Wolery (1989). Muscovite dissolution kinetics as a function of pH and time at 70°C." *Geochim. Cosmochim. Acta.* 53(7):1493–1501.
- Knauss, K. G., W. L. Bourcier, K. D. McKeegan, C. I. Merabacher, S. N. Nguyen, F. J. Ryerson, D. K. Smith, H. C. Weed, and L. Newton (1990). "Dissolution kinetics of a simple analogue nuclear waste glass as a function of pH, time, and temperature." In proceedings from Materials Research Society: Scientific Basis for Nuclear Waste Management XIII. 176:371.
- McKenzie, W. F. (1992). *UO<sub>2</sub> Dissolution Rates: A Review*. (UCRL-ID-111663) Livermore, CA: Lawrence Livermore National Laboratory.
- Steward, S. A., and W. J. Gray (1994). "Comparison of Uranium Dissolution Rates from Spent Fuel and Uranium Dioxide." In proceedings from Fifth Annual Intl. High-Level Radionuclide Waste Management Conference. Las Vegas, NV: May 22–26, 1994. 4:2602–2608. (Also UCRL-JC-115355 for Lawrence Livermore National Laboratory, Livermore, CA). [210933]
- Steward, S. A., and E. T. Mones (1997). "Comparison and Modeling of Aqueous Dissolution Rates of Various Uranium Oxides." In proceedings from Materials Research Society Fall Meeting: Scientific Basis for Nuclear Waste Management XX. W. J. Gray and I. R. Triay (Eds.). Boston, MA: December 2–6, 1996. 465 557–564. Also UCRL-JC-124602 (1996) for Lawrence Livermore National Laboratory, Livermore, CA. [MOL.19971210.0278]

Tait, J. C., and J. L. Luht (1997). *Dissolution Rates of Uranium from Unirradiated and Uranium and Radionuclides from Used CANDU Fuel Using the Single-Pass Flow-Through Apparatus*. (06819-REP-01200-0006 R00) Atomic Energy of Canada, Ltd., Whiteshell Laboratories, and Ontario Hydro.

Thomas, L. E., and R. J. Guenther (1989). "Characterization of low-gas-release LWR fuels by transmission electron microscopy." In proceedings from Mater. Res. Soc. 127:293-300.

Thomas, L. E., and L. A. Charlot (1990). "Analytical Electron Microscopy of Light-Water Reactor Fuels." *Ceram. Trans.* 9:397-407.

Thomas, L. E., C. E. Beyer, and L. A. Charlot (1992). "Microstructural analysis of LWR spent fuels at high burnup." *J. Nucl. Mater.* 188:80-89.

Wilson, C. N. (1984). *Results from NNWSI Series 1 Spent Fuel Leach Tests*. (HEDL-TME 84-30) Richland, WA: Hanford Engineering Development Laboratory. [NNA.900216.0070]

Wilson, C. N. (1990a). *Results from NNWSI Series 2 Spent Fuel Dissolution Tests*. (PNL-7169) Richland, WA: Pacific Northwest National Laboratory. [200816]

Wilson, C. N. (1990b). *Results from NNWSI Series 3 Spent Fuel Dissolution Tests*. (PNL-7170) Richland, WA: Pacific Northwest National Laboratory. [NNA.199000814.0048]

Wilson, C. N., and C. J. Bruton (1989). "Studies on Spent Fuel Dissolution Behavior Under Yucca Mountain Repository Conditions." *Ceramic Transactions*. In proceedings from Nuclear Waste Mgt. III. G. B. Mellinger (Ed.) Westerville, OH. 9:423-442. [NNA.19891106.0260]

Wilson, C. N., and W. J. Gray (1990). "Effects of Water Composition on the Dissolution Rate of  $UO_2$  Under Oxidizing Conditions." In proceedings from First International High-Level Radioactive Waste Management Topical Meeting. La Grange Park, IL: American Nuclear Society, Inc. pp. 1431-1436. [MOL.19980324.0145]

Wronkiewicz, D. J., J. K. Bates, T. J. Gerding, E. Veleckis, and B. S. Tani (1991). *Leaching action of EJ-13 water on unirradiated  $UO_2$  surfaces under unsaturated conditions at 90°C: Interim Report*. (ANL-91/11) Argonne, IL: Argonne National Laboratory. [NNA.19910314.0091]

Wronkiewicz, D. J., J. K. Bates, T. J. Gerding, E. Veleckis, and B. S. Tani (1992). "Uranium Release and Secondary Phase Formation During Unsaturated Testing of  $UO_2$  at 90°C." *J. Nucl. Mater.* 190: 107-127. [MOL.19980314.0091]

Wronkiewicz, D. J., J. K. Bates, S. F. Wolf, and E. C. Buck (1996). "Ten-Year Results From Unsaturated Drip Tests With  $UO_2$  at 90°C: Implications for the Corrosion of Spent Nuclear Fuel." *J. Nucl. Mater.* 238: 78-95. [MOL.19971218.0965]

# STUDIES ON SPENT FUEL DISSOLUTION BEHAVIOR\* UNDER YUCCA MOUNTAIN REPOSITORY CONDITIONS

C. N. Wilson  
Pacific Northwest Laboratory

C. J. Bruton  
Lawrence Livermore National Laboratory

## ABSTRACT

Nuclide concentrations measured in laboratory tests with PWR spent fuel specimens in Nevada Test Site J-13 well water are compared to equilibrium concentrations calculated using the EQ3/6 geochemical modeling code. Actinide concentrations in the laboratory tests reach steady-state values lower than those required to meet Nuclear Regulatory Commission (NRC) release limits. Differences between measured and calculated actinide concentrations are discussed in terms of the effects of temperature (25°C to 90°C), sample filtration, oxygen fugacity, secondary phase precipitation, and the thermodynamic data in use. The concentrations of fission product radionuclides in the laboratory tests tend to increase continuously with time, in contrast to the behavior of the actinides.

## 1.0 INTRODUCTION

The Yucca Mountain Project of the U. S. Department of Energy is studying the potential dissolution and radionuclide release behavior of spent fuel in a candidate repository site at Yucca Mountain, Nevada. The repository horizon under study lies in the unsaturated zone 200 to 400 meters above the water table. With the exception of C-14, which may migrate in a vapor phase,<sup>1</sup> and possibly I-129, the majority of long-lived radionuclides present in spent nuclear fuel will be transported from a failed waste package in the repository via dissolution or suspension in water in the absence of a major geological event such as volcanism.

\*This material also is important in understanding Section 3.4.

<sup>1</sup>Published in Ceramic Transactions, V-9, pp. 423-442. Nuclear Waste Mgt. III, G. B. Mellinger, ed. Westerville, Ohio, 1990.

Spent fuel will not be contacted by liquid water infiltrating the rock until several hundred years after disposal when the repository has cooled to below the 95°C boiling temperature of water at the repository elevation. The potential dissolution behavior of spent fuel during the repository post-thermal period is being studied using geochemical models and laboratory tests with actual spent fuel specimens.\* Selected initial results from these studies are discussed in the present paper.

## 2.0 LABORATORY TESTS

Three spent fuel dissolution test series have been conducted in laboratory hot cells using spent fuel specimens of various configurations. Results from the Series 2 and Series 3 tests with bare fuel particles are discussed in the present paper. The Series 2 tests used unsealed fused silica test vellels and were run for five cycles in air at ambient hot cell temperature (25°C). The Series 3 tests used sealed stainless steel vessels and were run for three cycles at 25°C and 85°C. Each test cycle was started in fresh Nevada Test Site J-13 well water and was about six months in duration. Periodic solution samples were taken during each test cycle and the sample volume was replenished with fresh J-13 water. Five bare fuel specimens tested in these two tests series are identified in Table 1 and the test configurations are shown in Figure 1. Additional information on the laboratory tests is provided in references 3 and 4.

### 2.1 Actinide Results

Actinide concentrations (U, Np, Pu, Am and Cm) measured in solution samples rapidly reached maximum levels during the first test cycle and then generally dropped to lower steady-state levels in later test cycles. The concentrations of uranium and the activities of Pu-239+240 and Am-241 measured in 0.4 mm filtered solution samples are plotted in Figure 2. The initial concentration peaks are attributed to dissolution of more readily soluble  $UO_{2+x}$  oxidized phases present initially of the fuel particle surfaces, and to kinetic factors limiting the nucleation and growth of secondary phases that may ultimately control actinide concentrations at lower levels.

---

\* This work was performed under the auspices of the U. S. Department of Energy (DOE) by Lawrence Livermore National Laboratory under Contract No. W-7405-Eng-48, and by Pacific Northwest Laboratory operated for the DOE by Battelle Memorial Institute under Contract No. DE-AC06-76RLO-1830

**Table 1. Bare Fuel Test Identification**

<u>identification</u>	<u>Description</u>	<u>Starting Fuel Wt. (g)</u>
HBR-2-25	Series 2, H.B. Robinson Fuel, 25°C	83.10
TP-2-25	Series 2, Turkey Point Fuel, 25°C	27.21
HBR-3-25	Series 3, H.B. Robinson Fuel, 25°C	80.70
HBR-3-85	Series 3, H.B. Robinson Fuel, 85°C	85.55
TP-3-85	Series 3, Turkey Point Fuel, 85°C	86.17

Uranium (U) concentrations at 25°C were lower in the Series 3 tests than in the Series 2 tests, and with the exception of the Cycle 1 data, U concentrations in the 85°C Series 3 tests were lower than those in the 25°C tests. The very low U concentrations measured during Cycle 1 of the HBR-3-85 test were attributed to a vessel corrosion anomaly. In the later cycles of the Series 2 tests, U concentrations tended to stabilize at steady-state levels of about 1 to 2 µg/ml. In Cycles 2 and 3 of the Series 3 tests, U concentrations stabilized at about 0.3 µg/ml at 25°C and about 0.15 µg/ml at 85°C. Precipitated crystals of the calcium-uranium-silicates, uranophane (Figure 3) and haiweeite, and possibly the uranium-silicate soddyite, were found on filters used to filter cycle termination rinse solutions from both 85°C tests. Phase identifications were based on examinations by X-ray diffraction and microanalysis in the SEM.<sup>4</sup> Secondary phases controlling actinide concentrations other than U were not found.

The 0.4 µm filtered Pu-239+240 solution activities measured in Cycles 2 through 5 of the TP-2-25 test generally ranged from about 100 to 200 pCi/ml (Figure 2). Activities as low as about 20 pCi/ml were measured in the HBR-2-25 test. During Cycles 2 and 3 of the HBR-3-25 test, activities varied from about 60 to 100 pCi/ml. A value of 100 pCi/ml, which corresponds to a Pu concentration of about  $4.4 \times 10^{-9}$  M (M = molarity), would appear to be a reasonable estimate of steady-state Pu-239+240 activities in 0.4 µm filtered solutions in the 25°C. Significantly lower activities on the order of 1 pCi/ml were measured in the 85°C tests. The lower activities at 85°C may result from enhanced nucleation and growth of secondary phases at the higher temperature that limit pU concentration.

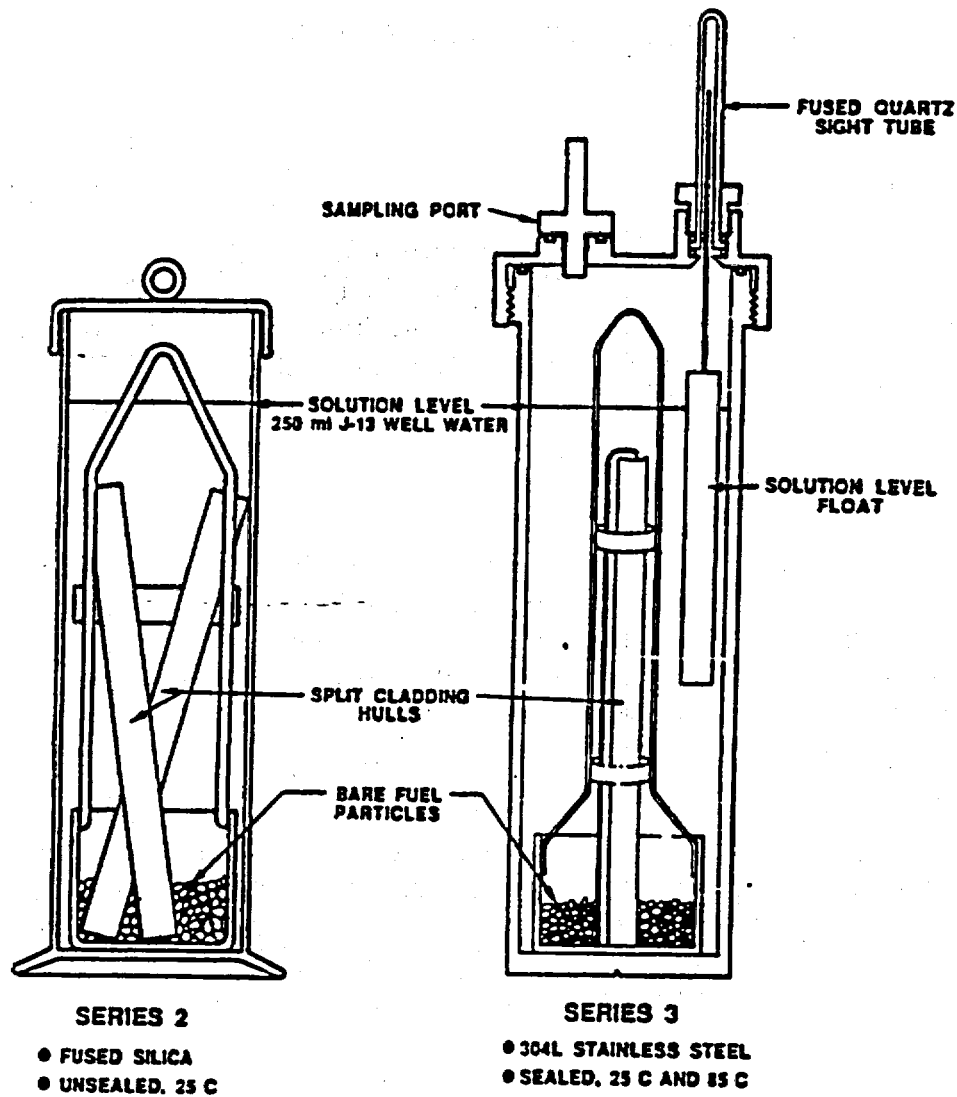


Figure 1. Test Configurations for the Series 2 and Series 3 Bare Fuel Dissolution Tests.

Selected solution samples were centrifuged through membrane filters that provide an estimated filtration size of approximately 2 nm.\* Filtering to 2 nm caused Pu-239+240 activities to decrease by about 20 to 40%. No significant differences between 0.4 µm filtered sample data are considered the most significant relative to radionuclide release because larger particles probably would not be transported by water, whereas colloidal particles greater than 2 nm may remain in stable suspension and be transported by water movement.

Table 2. J-13 Well Water Analysis<sup>2</sup>

Component	Concentration (µg/ml)	Component	Concentration (µg/ml)
Li	0.042	Si	27.0
Na	43.9	F	2.2
K	5.11	Cl	6.9
Ca	12.5	NO <sub>3</sub>	9.6
Mg	1.92	SO <sub>4</sub>	18.7
Sr	0.035	HCO <sub>3</sub>	125.3
Al	0.012		
Fe	0.006	pH	7.6

Steady-state Am-241 activities on the order of 100 pCi/ml, corresponding to Am concentrations of about  $1.5 \times 10^{-10}$  M, were measured in 0.4 µm filtered samples during cycles 2 and 3 of the TP-2-25 and HBR-3-25 tests. The 100 pCi/ml value would appear to be a conservative estimate for Am-241 activity at steady-state and 25°C considering that activities on the order of 10 pCi/ml were measured during Cycles 2, 4 and 5 of the HBR-2-25 test. Much lower 0.4 µm filtered Am-241 activities of about 0.3 pCi/ml were measured during Cycles 2 and 3 of the two 85°C tests. The effects of both 0.4 µm and 2 nm filtration were in general greater for Am-241 than for Pu-239+240. Association of Am with an apparent suspended phase is suggested by unfiltered data from the 85°C tests plotted as dashed lines in Figure 2, and by a relatively large fraction of 0.4 µm filtered Am-241 activity removed by 2 nm filtration (not shown). Cm-244 activity measured in most samples was similar to that measured for Am-241 in each of the tests. However, Cm-244 alpha decays with an 18-year half-life to Pu-240 and will not be present during the repository post-thermal period.

Measured Np-237 activities in most samples were generally not much greater than the detection limit of 0.1 pCi/ml and were below detection limits in several samples. Measured Np-237 activities showed very little dependence on temperature, vessel type or sample filtration. Following initially higher values at the beginning of Cycle 1, Np-237 activities generally ranged from 0.1 to 0.5 pCi/ml.

\*Amicon Corporation Model CF-25 centrifuge membrane cone filter

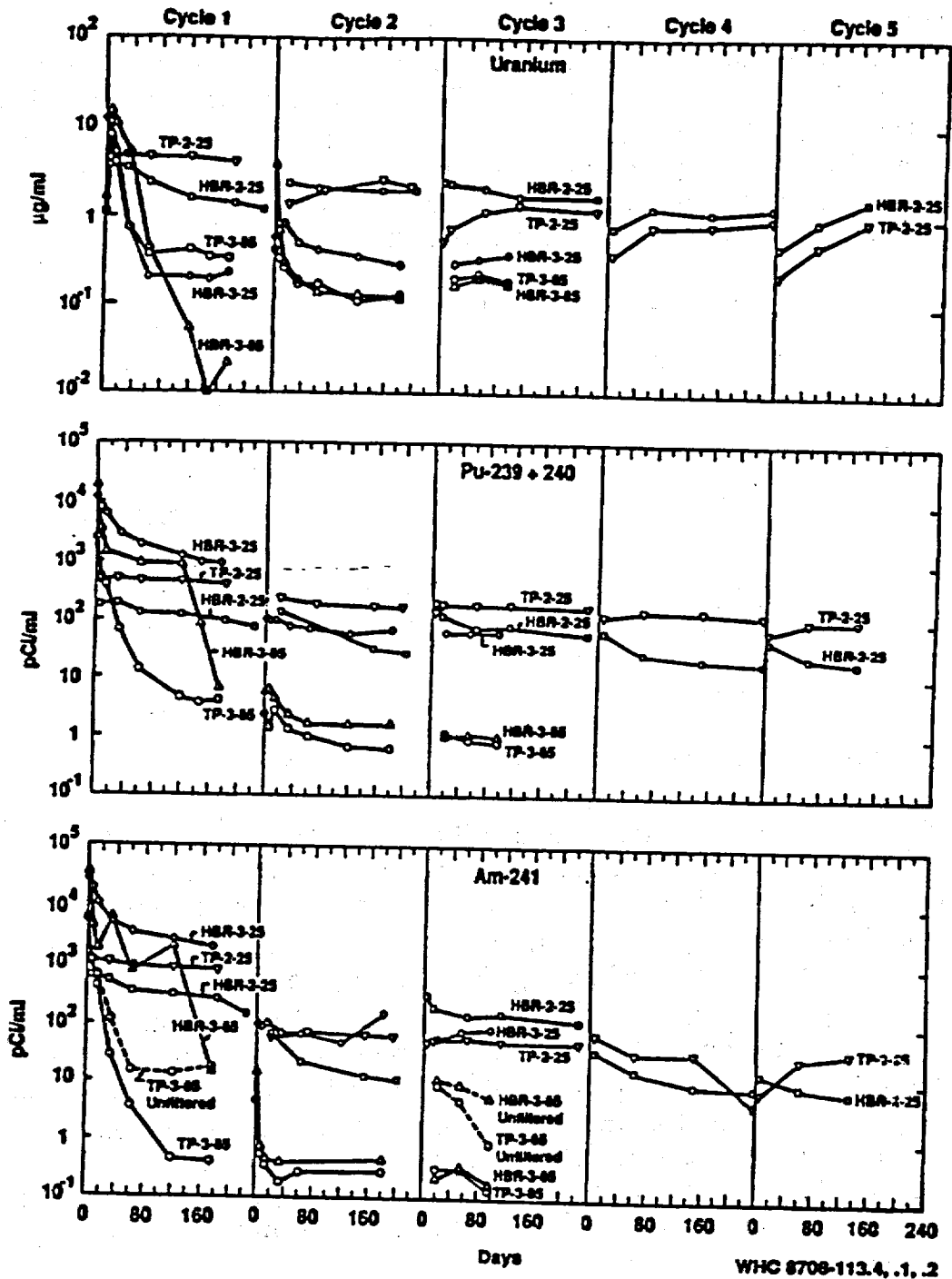


Figure 2. Uranium Concentrations (top), Pu-239+240 Activities (center), and Am-241 Activities (bottom); Measured in 0.4  $\mu\text{m}$  Filtered Solution Samples.

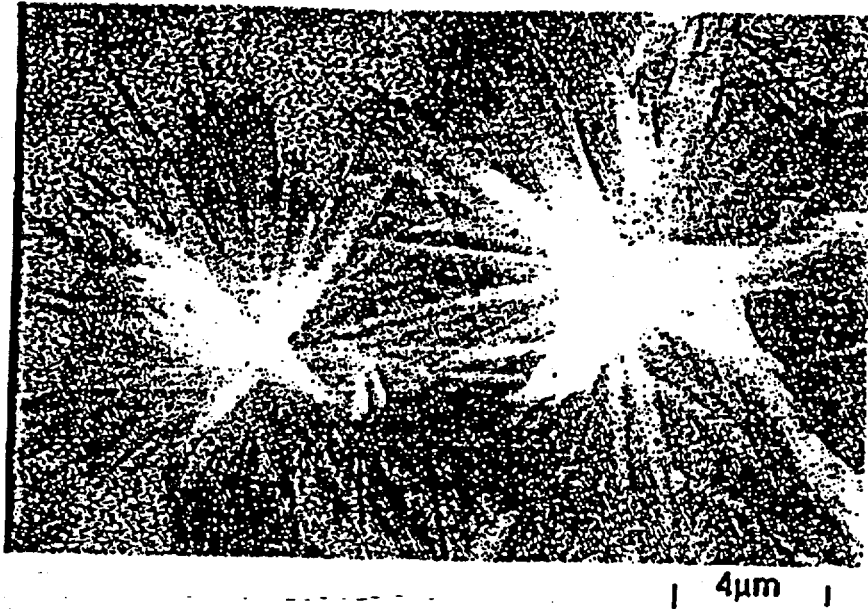


Figure 3. Acicular crystals of Uranophane formed on spent fuel grains in the 85°Series 3 tests.

## 2.2 Fission Product Results

Specimen inventory fractions of the fission product radionuclides Cs-137, Sr-90, Tc-99, and I-129 measured in solution are plotted in Figure 4 for the HBR-2-25 and HBR-3-85 tests. Each data point represents the fraction of the ORIGEN-2 calculated specimen inventory in solution on the sample data plus the inventory fraction calculated to have been removed in previous samples from the test cycle. During Cycle 1 of the HBR-3-85 test, Tc-99 fell to below detectable levels as a result of the corrosion anomaly that occurred in this test. Cycle 1 Cs-137 gap inventory release was about 0.7% from the HBR fuel and is therefore off-scale in Figure 4. Sr-90 was not measured during Cycle 1 of the Series 2 tests, and appeared to be limited by association with an unknown precipitated phase in the 85°C tests.

The inventory fractions of Cs-137, Sr-90, Tc-99 and I-129 in solution increased continuously with time, with the exception of the anomalous precipitation of Tc-99 in Cycle 1 of the HBR-3-85 test and the limit on Sr-90 activity in solution at 85°C. The continuous release rates of the fission products in units of inventory fraction per year are given in Figure 4 for the final cycle of the two tests. Because the actual quantity of fuel matrix dissolution and precipitation of actinides was not measured, it is not known to what degree the continuous fission product release resulted from preferential leaching of grain boundaries where fission products were thought to concentrate during irradiation. Whether as a result of increased matrix dissolution or increased grain boundary leaching, the soluble fission product release rate is greater in the later test cycles at the higher temperature.

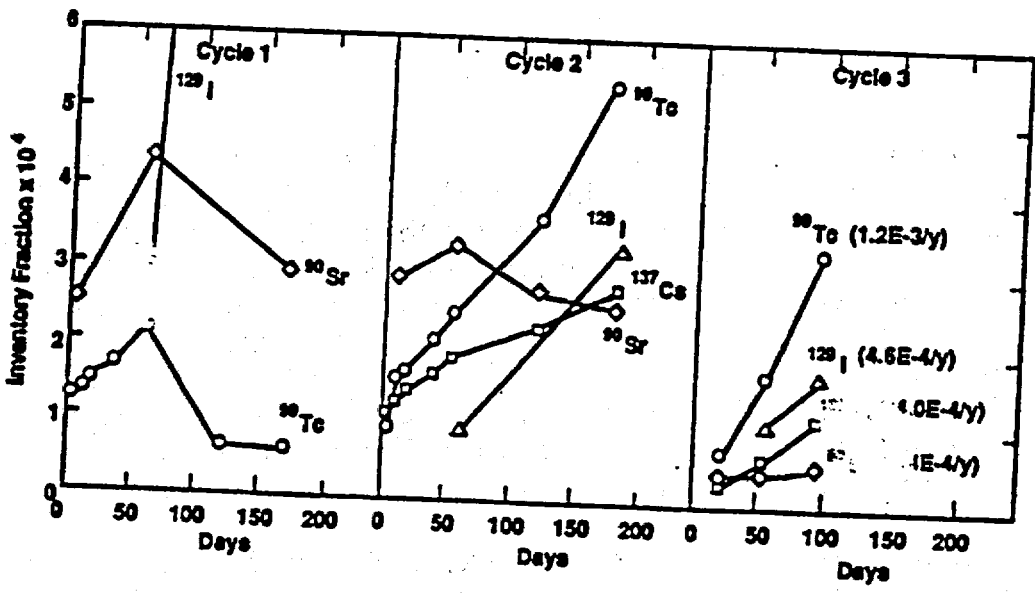
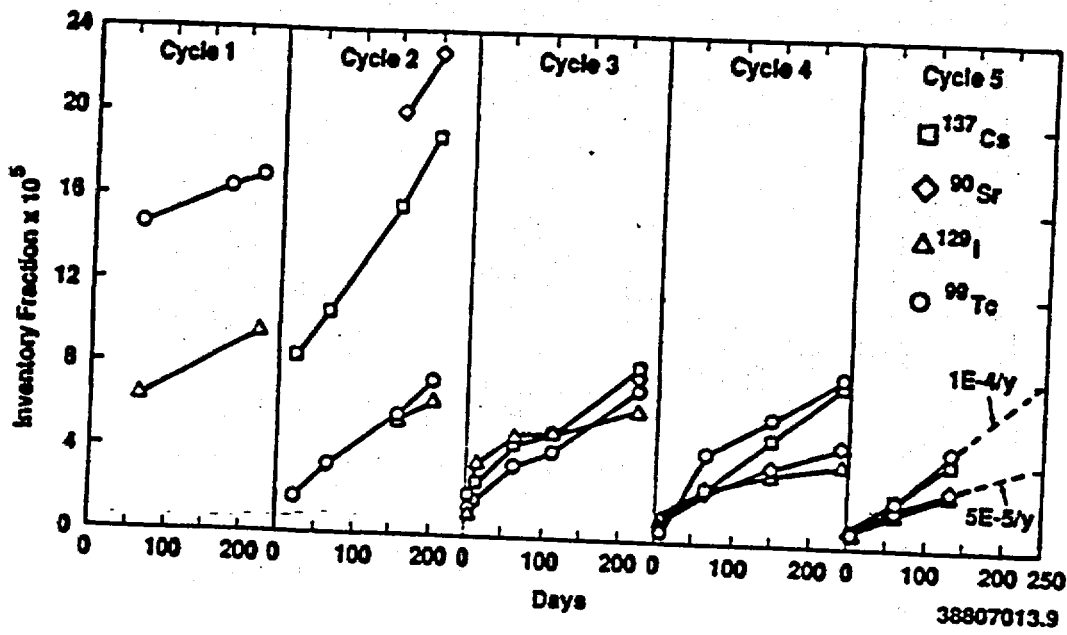


Figure 4. Inventory Fractions of Cs-137, Sr-90, Tc-99 and I-129 Measured in Solution in the HBR-2-25 Test (top) and in the HBR-3-85 Test (bottom). Approximate annual fractional release rates are listed for each nuclide during the last cycle plotted.

### 3.0 GEOCHEMICAL MODELING

#### 3.1 Actinide Concentrations in Solution

Spent fuel dissolution in J-13 well water was simulated using the geochemical modeling code EQ3/6<sup>5</sup> to determine whether steady-state actinide concentrations measured in the tests could be related to the precipitation of actinide-bearing solids. Version 3245 of the EQ3/6 code and version 327OR13 of the supporting thermodynamic database were used to simulate spent fuel dissolution at 25°C and 90°C assuming atmospheric CO<sub>2</sub> gas fugacity and two different O<sub>2</sub> gas fugacities of 10<sup>-07</sup> (atmospheric) and 10<sup>-12</sup> bars (see later discussion). The simulation process is described in more detail elsewhere.<sup>6</sup> The computer simulations yield: 1) the sequence of solids that precipitate and sequester elements released during spent fuel dissolution, and 2) the corresponding elemental concentrations in solution. Approximate steady-state actinide concentrations measured at 25°C and 85°C in the Series 3 laboratory tests were compared in Table 3 to concentrations of actinides in equilibrium with the listed solids as calculated in the EQ3/6 simulations. Comparisons of simulation results with experimental results are being used to determine the adequacy of the thermodynamic database and to identify additional aqueous species and minerals for which data are needed.

**Table 3. Comparison of Measured and Predicted Actinide Concentrations (log M)**  
(New runs have not been completed) May 22, 1993 RBS)

Actinide	Measured <sup>(a)</sup>		EQ3/6 <sup>(b)</sup>				Phase
	-25°C	85°C	25°C		90°C		
			-0.7	-12.0	-0.7	-12.0	
U	-5.9	-6.2	-7.2/-7.0*	-7.1/6.9	-8.8.-7.6	-8.5/-7.5	H
			-7.0/-6.9	-6.9/-6/8	-7/6	-7.5	H + S
			-6.9/-4.3	-6.8/-4.2	-7.6/-6.0	-7.5/-5.9	S
			-4.3	-4.2	-6.0	-5.9	S + Sch
			-4.2	-4.1	-6.0/-5.8	-5.8/-5.6	Sch
Np	-8.9	-9.1	-6.2	-9.0	-5.2	-8.0	NpO <sub>2</sub>
Pu	-8.4	-10.4	-12.4	-13.8	-11.9	-14.6	PuO <sub>2</sub>
			-4.3	-5.7	-4.2	-6.9	Pu(OH) <sub>4</sub>
Am	-9.8	-12.3	-8.3	-8.3	-	-	Am(OH)CO <sub>3</sub>
			-	-	-8.4	-8.4	Am(OH) <sub>3</sub>
Cm	-11.3	-14.3	Cm not in thermodynamic data base				

(a) Series 3 tests, 0.4 μm filtered.

(b) At oxygen fugacities log f<sub>O2</sub> = -0.7 (atmospheric) and log f<sub>O2</sub> = -12.0 with solubility control by precipitated secondary phases as listed. H = haiweeite; S = soddyite; Sch = schospite. All phases are in crystalline state except Pu(OH)<sub>4</sub> which is amorphous.

\*-7.2/-7.0- refers to a range in concentration from -7.2 to -7.0.

Uranium (U) concentrations in the simulations vary as a function of the secondary U-bearing precipitates. The following sequence of mineral assemblages are predicted to precipitate and sequester U as increasing amounts of spent fuel dissolve: haiweeite, haiweeite plus soddyite, soddyite, soddyite plus schoepite, and schoepite. The relative compositions of these phases and of U-bearing phases that were observed in residues from the 85°C laboratory tests are shown in Figure 5. Unique, and steadily increasing, concentrations of U in solution are related to each mineral assemblage. The concentration of U varies not only as the precipitates vary, but also during the precipitation of a single mineral, such as soddyite, because of changes in the pH and overall chemical characteristics of the fluid. As previously discussed, uranophane, haiweeite, and possibly soddyite were found in the 85°C Series 3 tests. Unfortunately, reliable thermodynamic data for uranophane were not available, which complicates comparison of the laboratory test results to the calculated solubility limits. Haiweeite, a Ca-U-silicate like uranophane, is predicted to precipitate at U concentrations that are lower than the measured steady-state values. In the absence of data for uranophane, the experimental concentrations of U would appear to be consistent with the precipitation of soddyite at both 25°C and 90°C in the simulations.

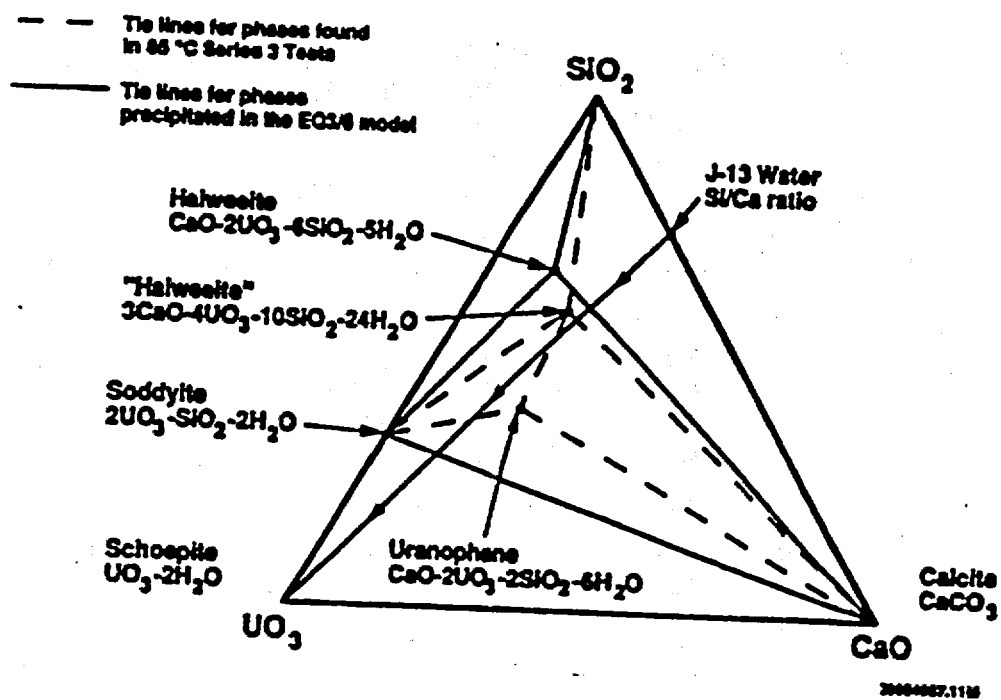


Figure 5. Relative Compositions (mole %) of U-bearing Phases Indicated as Controlling U Concentration in the EQ3/6 Simulation and for which Indications were Observed in the 85°C Series 3 Tests.

Neptunium concentration is controlled by equilibrium with  $\text{NpO}_2$  in the simulations. However, the predicted concentration of Np is highly dependent on solution Eh and pH.<sup>7</sup> The  $\text{O}_2$  fugacity in the simulations was reduced from  $10^{-0.7}$  bars to  $10^{-12}$  bars in order to produce good agreement between the measured and predicted concentrations of Np at 25°C. An  $\text{O}_2$  fugacity of  $10^{-12}$  bars may correspond to conditions at the fuel surface in an otherwise oxygenated system (i.e., contains an air cap) that is poorly buffered. Eh was not measured during the laboratory tests, and redox equilibrium may not have been established among the various species and phases within the sealed stainless steel vessels. An oxygen fugacity of  $10^{-12}$  bars overestimates Np concentration at 90°C, however, because the experimental data do not reflect predicted increases in Np concentration with temperature. The thermodynamic data for Np and other actinides must, consequently, be critically evaluated at elevated temperature.

Significant differences exist between measured and predicted Pu and Am concentrations in Table 3. Measured Am concentrations may have been lower than those predicted because of Am removal from solution by phases such as lanthanide precipitates that were not accounted for in the E03/6 simulations. Another possible mechanism controlling Am concentration not accounted for in the simulation may have been sorption. Although  $\text{Am}(\text{OH})\text{CO}_3$  is predicted to control Am concentration at 25°C and  $\text{Am}(\text{OH})_3$  precipitates at 90°C, the Am concentration in equilibrium with both phases is about the same.

Predicted Pu concentrations in equilibrium with crystalline  $\text{PuO}_2$  at both temperatures and oxygen fugacities are much lower than those measured. Pu concentrations measured at 25°C are similar to those reported by Rai and Ryan,<sup>8</sup> who measured the solubility of  $\text{PuO}_2$  and hydrous  $\text{PuO}_2 \cdot x\text{H}_2\text{O}$  in water for periods of up to 1300 days at 25°C. At a pH of 8, which was the extrapolated lower limit of their data and the approximate pH in the Series 2 and 3 tests, they reported that Pu concentrations ranged from about  $10^{-7.4}$  M, where amorphous  $\text{PuO}_2 \cdot x\text{H}_2\text{O}$  was thought to control concentration, down to about  $10^{-9}$  M where aging of the amorphous material produced a more (but incompletely) crystalline  $\text{PuO}_2$  that was thought to control concentration. Concentrations of Pu in equilibrium with amorphous  $\text{Pu}(\text{OH})_4$  calculated in recognition of the fact that an amorphous or less crystalline phase is more likely to precipitate than crystalline  $\text{PuO}_2$ , are listed in Table 3. Measured Pu concentrations would be expected to fall between the equilibrium concentrations for  $\text{PuO}_2$  and  $\text{Pu}(\text{OH})_4$ , becoming closer to  $\text{PuO}_2$  with aging. Equilibrium with amorphous  $\text{Pu}(\text{OH})_4$  and crystalline  $\text{PuO}_2$  at  $\text{O}_2$  fugacities of  $10^{-0.7}$  and  $10^{-12}$  bars yields predicted Pu concentrations that bracket measured results at both 25°C and 85°C.

### 3.2 Sources of Discrepancy Between Measured and Predicted Results

Discrepancies between measured and predicted concentrations are to be expected considering database limitations and uncertainty in the interpretation of measured apparent steady-state actinide concentrations. Care must be taken in interpreting the 90°C simulation results because insufficient data exist to accurately calculate the temperature-dependence of the thermodynamic properties of many radionuclide-bearing solids and solution species. The 3270 thermodynamic data basis constantly updated through inclusion of new and revised thermodynamic data and the selection of a consistent set of aqueous complexes for each chemical element. Puigdomenech and Bruno<sup>9</sup> have constructed a thermodynamic database for U minerals and aqueous species that they showed to be in reasonable agreement with available experimental solubility data in systems in which U is complexed by OH<sup>-</sup> and CO<sub>3</sub>. The 3270 database contains many of the same aqueous species and minerals, but Puigdomenech and Bruno have included recent data for aqueous uranyl hydroxides from Lemire<sup>10</sup> which are not yet in the EQ3/6 database. Future plans include a critical evaluation of simulations of spent fuel dissolution made using the Puigdomenech and Bruno U database, and comparison with simulations made using the latest version of the EQ3/6 database. Inclusion of standard Nuclear Energy Agency (NEA) data for U minerals and species will also help to standardize future databases.

Until the U database is better established, calculated U concentrations must be recognized as preliminary and speculative. Simulation results can be used as a vehicle for identifying geochemical trends and studying the interactions between solid precipitation and elemental concentrations in solution. Seemingly small changes in the thermodynamic database can have potentially large impacts on predictions. For example, U concentrations calculated to be in equilibrium with schoepite using version 3270 of the EQ3/6 database are radically lower than those predicted in 1987<sup>6</sup> using an older database. The species (U<sub>2</sub>)<sub>3</sub>(OH)<sub>7</sub> - and (UO<sub>2</sub>)<sub>2</sub>(OH)<sub>3</sub>CO<sub>3</sub> - were omitted from version 3270 of the EQ3/6 database because their validity was questioned. UO<sub>2</sub>(CO<sub>3</sub>)<sub>2</sub><sup>-2</sup> and UO<sub>2</sub>(CO<sub>3</sub>)<sub>3</sub><sup>-4</sup> were left as the only dominant U species in solution throughout the EQ3/6 simulations. U concentrations accordingly remain lower during U mineral precipitation. Future work must address the sensitivity of the results to variations in thermodynamic data and the choice of a self-consistent set of aqueous species for elements of interest.

Comparisons between experimental results and predictions in Table 3 are predicated on the assumption that the listed solid phases precipitate from solution and control the solution composition. Except for some U-bearing minerals, no minerals containing radionuclides have been identified in the laboratory tests. Detection and characterization of actinide-bearing secondary phases may be difficult because of the extremely small masses of these actinides involved. Precipitates limiting actinide concentrations in the laboratory tests may also be

amorphous, colloidal, or in some other less-than-perfect crystalline state. For instance, Rai and Ryan<sup>2</sup> observed that early Pu precipitates tend to be hydrated oxides which undergo aging to more crystalline solids. The concentrations of the affected actinides would, therefore, gradually decrease as aging progresses.

The chemistry of trivalent Am and Cm can be expected to be almost identical to that of the light lanthanide fission product elements which are present in much greater concentrations in spent fuel than are Am and Cm. Am and Cm may, therefore, be present in dilute solid solution with secondary phases formed by the lanthanides, which would result in lower measured solution concentrations than predicted for Am based on equilibration with  $\text{Am}(\text{OH})\text{CO}_3$  or  $\text{Am}(\text{OH})_3$ . Pu and Np, and possibly Am and Cm, may also have been incorporated at low concentrations in solid solution with the U-bearing precipitates or other secondary phases. Efforts are planned to separate crystals of uranophane from test residues and to perform radiochemical analyses of these crystals to check for incorporation of other radionuclides. Sorption of actinides on colloids or other surfaces such as the fuel or test hardware may also control solution concentrations, but the impact or sorption was not considered in the simulations. Other factors, such as local variations in redox potential, may also contribute to differences between measured and predicted solubilities.

As it is not currently reasonable to expect a geochemical model to predict accurately the effects of all potential concentration-controlling processes over thousands of years, we hope to use modeling predictions to establish upper limits, or conservative estimates, of radionuclide concentrations over time. Lower limits to radionuclide concentrations imposed by solid precipitation are also of interest, however, as a baseline for further calculations, and because radionuclide concentrations may be expected to approach the lower limits over extended time periods. Accordingly, we assume in this paper that the actinide concentrations are controlled by the most stable and insoluble precipitates for which data are available. The consequences of precipitation of progressively less stable precipitates will be explored in future calculations, and upper limits of radionuclide concentrations controlled by solid precipitation will be estimated. In the case of Pu, for example, we have begun to explore the upper limits to Pu concentration as controlled by the precipitation of amorphous  $\text{Pu}(\text{OH})_4$ . Comparison of modeling results with experimental results helps to identify phenomena which may revise our estimates of concentration limits. Processes such as sorption and aging of solids to forms of increasing crystallinity tend to lower element concentrations in solution, and increase the conservative nature of our estimates. However, consideration of colloid formation and colloid migration with the fluid phase may lead to an increase in our estimates of mobile concentrations over those made considering precipitation phenomena alone.

#### 4.0 RADIONUCLIDE RELEASES

Annual actinide releases per failed waste package were calculated assuming that water flowing at a rate of 20 l/yr per waste package transports the actinides at the approximate concentrations measured at steady-state in Cycles 2 and 3 of the HBR-3-25 test. Each waste package was assumed to contain 3140 kg of fuel with an average burnup of approximately 33,000 MWd/MTM. The logarithms of the waste package 1000-year inventory fractions transported annually for each actinide under such conditions is given in Table 4. These releases are at least three orders of magnitude lower than the Nuclear Regulatory Commission (NRC) requirement in 10 CRF 60.113<sup>11</sup> that annual radionuclide releases during the post-containment period shall not exceed one part in 100,000 of the 1000-year inventories. The calculated annual release results would appear to be particularly encouraging for Pu and Am because isotopes of these two actinide elements account for about 98% of the total activity present in spent fuel at 1000 years. These values may be conservative in that they are based on the higher steady-state Pu and Am concentrations measured at 25°C and assume a conservative (high) estimate of the water flux through the repository. The calculated releases do, however, assume maintenance of steady values for actinide concentrations over time, whereas the geochemical simulations suggest that actinide concentrations, and U concentrations in particular, may vary with time. Confidence in such release predictions will be greatly increased when the chemical mechanisms of solubility control are identified and successfully modeled.

Table 4. Annual Actinide Releases as a Fraction of the 1000-Year Inventories Based on HBR-3-25 Test Date

<u>Actinide</u>	<u>Concentration Log(M)</u>	<u>Log (Release)*</u>
U	-5.9	-8.6
Np	-8.9	-8.8
Pu	-8.4	-9.0
Am	-9.8	-9.1

-----  
\*Assumes water flow rate of 20 l/yr per waste package transporting actinides at the indicated concentrations. Each waste package is assumed to contain 3140 kg of 33,000 MWd/MTM burnup PWR fuel.

Measured activities of the more soluble fission product radionuclides Cs-137, Sr-90, Tc-99 and I-129 continuously increase in solution at rates generally corresponding to annual release rates in the range of  $10^{-4}$  to  $10^{-3}$  of specimen inventory per year (Figure 4). These release rates imply a problem in meeting the NRC  $10^{-5}$  annual fractional release limit for the more soluble radionuclides if the waste form alone is expecting to carry the burden of compliance in the unanticipated case of large quantities of water contacting the waste. However, there are two factors that make these release rates uncertain. First, the degree to which these radionuclides are preferentially released from grain boundaries where they may be concentrated during irradiation has not yet been determined. Preferential release could be expected to provide a lesser contribution over time as exposed grain boundary inventories are depleted and release rates approach the congruent fuel matrix dissolution rate. A second factor is the extent to which the fuel may be degraded over time by exposure to the repository environment. Degradation of the fuel as a result of oxidation to higher oxygen stoichiometries such as  $U_3O_8$ , or as a result of preferential grain boundary dissolution, may cause increases in surface area and increased rates of nuclide dissolution from grain boundaries and from the fuel matrix over time.

Flow-through tests in which uranium minerals do not precipitate are being developed to measure the degree to which soluble nuclides are preferentially released during the initial phases of fuel dissolution. Dissolution tests using spent fuel specimens that have been degraded by slow, low-temperature oxidation are also planned. Results from these tests should provide a better understanding of potential long-term releases of the soluble and volatile radionuclides. Additional characterization of potential release of C-14 is important because it is soluble as bicarbonate and could also be released in the vapor phase as  $CO_2$ .

## 5.0 CONCLUSIONS

Laboratory testing and geochemical simulation of the dissolution of spent fuel under conditions selected for relevance to the proposed Yucca Mountain repository have resulted in the following conclusions.

1. Radionuclides of interest in spent fuel appear to fall into three categories of potential release mechanisms: 1) radionuclides whose release appears to be controlled by concentration-limiting mechanisms, 2) more highly soluble radionuclides, and 3) radionuclides that are released in the vapor phase (principally C-14).
2. The principal radionuclides whose releases appear to be controlled by concentration-limiting mechanisms are the actinides U, Np, Pu, Am and Cm.

Steady-state concentrations measured for these actinide elements are at least three orders of magnitude lower than those required to meet NRC release limits based on conservative estimates of water fluxes through the repository. This result is of particular significance because isotopes of Pu and Am account for about 98% of the activity in spent fuel at 1000 years. However, results from geochemical modeling suggest that steady-state concentrations may vary significantly with time because of changes in solution composition and the identity of precipitating phases.

3. Good agreement between measured and predicted concentrations was obtained for Np based on equilibration with  $\text{NpO}_2$  at 25°C when the oxygen fugacity in the simulation was set at  $10^{-12}$  bars. A broad range of solubilities that bracketed the measured values were predicted for Pu depending upon the assumed oxygen fugacity and solubility-controlling phase. Measured Am concentrations were less than predicted based on data for equilibration with  $\text{Am}(\text{OH})\text{CO}_3$  and  $\text{Am}(\text{OH})_3$ .
4. Dissolution rates for soluble radionuclides (Cs-137, Sr-90, Tc-99 and I-129) exceeding  $10^{-5}$  of specimen inventory per year were measured during the laboratory tests. The implications of these data relative to long-term release of soluble radionuclides from a failed waste package are uncertain. The degree to which these radionuclides were preferentially released from grain boundaries where they may have concentrated during irradiation was not determined. Preferential release could be expected to provide a lesser contribution overtime as exposed grain boundary inventories are depleted. However, physical degradation of the fuel over time from exposure to the oxidizing repository environment may result in accelerated release of soluble nuclides.
5. Additional work is required to identify solid phases that control actinide concentrations, and to acquire reliable thermodynamic data on these phases for use in geochemical modeling. In this regard, identification of any stable suspended phases that can be transported by water movement is also important. In addition, we must better understand the potential release of soluble and volatile radionuclides, which may initially depend on preferential release from gap and grain boundary inventories, but may ultimately depend on the rate of fuel degradation by oxidation or other processes in the postcontainment repository environment.

## REFERENCES

1. R. A. Van Konynenburg, C. F. Smith, H. W. Culham and C. H. Otto Jr., "Behavior of Carbon-14 in Waste Packages for Spent Fuel in a Repository in Tuff," *Scientific Basis for Nuclear Waste Management VIII*, C. M. Jantzen, J. A. Stone and R. C. Ewing, eds., Materials Research Soc., Pittsburgh, PA, 44:405-412 (1985).
2. J. M. Delany, Reaction of Topopah Spring Tuff with J-13 Water: A Geochemical Modeling Approach Using the EQ3/6 Reaction Path Code, Lawrence Livermore National Laboratory, UCRL-53631 (1985).
3. C. N. Wilson, Results from Cycles 1 and 2 of NNWSI Series 2 Spent Fuel Dissolution Tests, Hanford Engineering Development Laboratory, HEDL-TME 85-22 (1987).
4. C. N. Wilson, "Summary Results from the Series 2 and Series 3 NNWSI Bare Fuel Dissolution Tests," *Scientific Basis for Nuclear Waste Management IX*, M. J. Apted and R. E. Westerman, eds. Materials Research Soc., Pittsburgh, PA, 112:473-483 (1987).
5. T. J. Wolery, Calculation of Chemical Equilibrium Between Aqueous Solution and Minerals: The EQ3/6 Software Package, Lawrence Livermore National Laboratory, UCRL-52658 (1979).
6. C. J. Bruton and H. F. Shaw, "Geochemical Simulation of Reaction Between Spent Fuel Waste Form and J-13 Water at 25°C and 90°C," *Scientific Basis for Nuclear Waste Management IX*, M. J. Apted and R. E. Westerman, eds. Materials Research Soc., Pittsburgh, PA, 112:485-494 (1987).
7. R. J. Lemire, An Assessment of the Thermodynamic Behavior of Neptunium in Water and Model Groundwater from 25°C to 150°C, Atomic Energy of Canada Limited, Whiteshell Nucl. Res. Estbl. AECL-7817 (1984).
8. D. Rai and J. L. Ryan "Crystallinity and Solubility of PU(IV) Oxide and Hydrous Oxide in Aged Aqueous Suspensions," *Radiochem. Acta*, 30:213--216 (1982).
9. I. Puigdomenech and J. Bruno, Modelling Uranium Solubilities in Aqueous Solutions: Validation of Thermodynamic Data Base for the EQ3/6 Geochemical Codes, SKB technical report 88-21 (1988).
10. R. J. Lemire, Effects of High Ionic Strength Groundwaters on Calculated Equilibrium Concentrations in the Uranium-Water System, Atomic Energy of Canada Limited, Whiteshell Nucl. Res. Estbi. AECL-9549 (1988).
11. Code of Federal Regulations, "Disposal of High-Level Radioactive Wastes in Geological Repositories - Licensing Procedures, Title 10, Ch. 1, Pt. 60, Sec. 60.113 (1983).

# LAWRENCE LIVERMORE NATIONAL LABORATORY

LLYMP9101029  
January 22, 1991

WBS 1.2.2.3.1.1  
QA

SEPDB Administrator  
Sandia National Laboratory  
Organization 6310  
P.O. Box 5800  
Albuquerque NM 87185

Subject: Submission of Data to the SEPDB

Attached are a Technical Data Information Form (TDIF) and associated data for inclusion in the SEPDB. These data are taken from two reports:

- 1) C.N. Wilson, "Results from Cycles 1 and 2 of NNWSI Series 2 Dissolution Tests." HEDLTME85-22, May 1987.
- 2) C.N. Wilson, "Results from the NNWSI Series 3 Spent Fuel Dissolution Tests," PNL-7170, June 1990.

The pertinent solubility data taken after "steady-state" was reached are given in Table 1. In cases where several values from different samples with different geometries and different burnup histories were shown, the most conservative upper value is indicated. Since we don't know the cause of the scatter, it is prudent to assume the worst case, pending a better understanding of the spread in the steady-state solubilities. Where filtered and unfiltered values were available, the filtered data were used because solubility is the information desired.

Table 2 indicates the specific source for each data value.

For slow flow of water over the spent fuel, the solubility can be used to determine the mass of each radionuclide dissolved as a function of time. Given solubilities,  $C$ , a flow rate of water contacting the spent fuel,  $\Phi$ , and a time,  $t$ , over which dissolution occurs, the total amount of any nuclide,  $i$ , dissolved and transported,  $M_i$ , is given by

$$M_i = C_i \Phi t$$

Please contact Mike Revelli of my staff at FTS 532-1982 for further information.

L. J. Jardine  
LLNL Technical Project Officer  
for the Yucca Mountain Project

LJJ/JB.jw

Attachments

c: C. Newbury, YMPO

Table 1. Solubility Data, Ci

<u>Species</u>	<u>Upper Limit Steady-State Concentration (ug/ml)</u>	
	<u>25°C</u>	<u>85°C</u>
U	≤ 5	≤ 0.5
<sup>239+240</sup> Pu	≤ 5 × 10 <sup>-3</sup>	≤ 6 × 10 <sup>-5</sup>
<sup>241</sup> Am	≤ 3 × 10 <sup>-4</sup>	≤ 1.5 × 10 <sup>-7</sup>
<sup>244</sup> CM	≤ 1.2 × 10 <sup>-4</sup>	≤ 2.4 × 10 <sup>-9</sup>
<sup>237</sup> Np	≤ 4 × 10 <sup>-4</sup>	≤ 1.4 × 10 <sup>-3</sup>

Only data for the solubility limited species are listed in the above table.

Table 2. Solubility Data Sources

Species	References	
	25°C	85°C
U	Ref. 1, Fig. 5	Ref. 2, Fig. 3.1
<sup>239+240</sup> Pu	Ref. 1, Fig. 6	Ref. 2, Fig. 3.12
<sup>241</sup> Am	Ref. 1, Fig. 7	Ref. 2, Fig. 3.15
<sup>244</sup> Cm	Ref. 1, Fig. 8	Ref. 2, Fig. 3.18
<sup>237</sup> Np	Ref. 2, Fig. 3.20	Ref. 2, Fig. 3.20

Conversion factors from pCi to µg taken from Ref. 2, Table A.1.

The following describes data and an analysis procedure to obtain the release rate time response for a fully wetted mass of spent fuel dissolving without solubility limitations in water. The description is from an LLNL report UCRL-ID-107289 published in December, 1991.

Waste package analysts and designers have to understand the long term dissolution of waste form in groundwater to safely dispose of high level nuclear waste in an underground repository. The dissolution and transport processes in groundwater flow are generally considered to be the main route by which radionuclides could be released to the biosphere from a geological repository.

Many researchers have investigated the dissolution of  $UO_2$ , spent fuel and uraninite (a naturally occurring  $UO_2$  mineral) in aqueous solutions, under either reducing or oxidizing conditions, and as a function of various other environmental variables. Experimental data on the dissolution rates of  $UO_2$ , spent fuel and uraninite have been reviewed by Arnell and Langmuir,<sup>1</sup> Parks and Pohl,<sup>2</sup> Bruno et al.,<sup>3</sup> and most recently by Grambow.<sup>4</sup>

Important variables considered in the many investigations were pH, temperature, oxygen fugacity, carbonate/bicarbonate concentrations and other reacting media. The dissolution data are very scattered, and vary as much as six orders of magnitudes.<sup>4</sup> The dependence of the dissolution rates of  $UO_2$ , spent fuel and uraninite on these variables is not clear because of uncertainties regarding redox chemistry of uranium in solutions and in solid phases, secondary-phase formation, and surface area measurement. In addition, the previous studies were conducted under experimental conditions which were either inadequately controlled or which simulated complex repositiorial conditions. The results of such studies are difficult to interpret. Several of these researchers have developed equations to correlate dissolution rates as a function of relevant variables.<sup>5-8</sup> However, none of the rate laws is universal, and inconsistencies or incompatibilities among the proposed laws are common.

Data indicate that  $UO_2$  is easily oxidized to  $U_4O_9$  and  $U_3O_7$  in an air<sup>9,10</sup> and can be further oxidized to either  $U_4O_8$ <sup>9,10,11</sup> or schoepite,  $UO_3 \cdot 2H_2O$ .<sup>12</sup> The  $UO_2$  surface oxidation may lead to higher leach rates because of possibly higher dissolution rates of  $U_3O_7$ ,  $U_4O_8$  or schoepite relative to that of  $UO_2$ <sup>4</sup> because of the increase of surface area of the fuels due to surface cracking.

## Discussion

We are estimating a source term for liberation of radionuclides from spent fuel dissolving under conditions of temperature and water composition related to those anticipated for a potential repository at Yucca Mountain. This is done in the same spirit as estimates that have been made for repositories in Germany<sup>13</sup> and Sweden.<sup>14</sup> It is implicit in the following treatment that fission products are dissolved congruently with the  $UO_2$  fuel matrix, except for those volatile species that have partially vaporized and that fraction that has migrated to near-surface grain boundaries and are possibly dissolved independent of the matrix dissolution. Most fission products and higher actinides are distributed throughout the  $UO_2$  matrix, however.

Recent measurements on  $UO_2$ <sup>15</sup> and spent fuel (SF)<sup>16</sup> under comparable conditions have provided dissolution rates for  $UO_2$  between 25°C and 85°C in waters of various composition and for SF in deionized water (DIW) at 25°C. These experiments were done in contact with air. The results are shown in Figures 1 and 2. The rate of dissolution of SF in DIW at 25°C is  $1.2-1.7 \times 10^{-12} \text{ g cm}^{-2} \text{ sec}^{-1}$ . This is similar to the rate for  $UO_2$  in DIW at 25°C at  $5 \times 10^{-12} \text{ g cm}^{-2} \text{ sec}^{-1}$ . Given the great variability in other reported values<sup>4</sup> this is reasonable agreement. In fact, the observed dissolution rate for SF at 25°C is about the same as that of  $UO_2$  in (DIW + Ca + Si), a simulation of ground water.<sup>14</sup>

A model for dissolution is used in which the dissolution front propagates linearly in time, much like a recently published model for the advance of the oxidation front during oxidation of  $UO_2$  and spent fuel.<sup>16-19</sup> This implies that the particle geometry is retained. We can describe the change in characteristic dimension of a SF particle (a sort of "radius"),  $X$  as follows:

$$X(t) = X_0 - \left( \frac{Q}{\rho} \right) t, \quad (1)$$

where

- $X(t)$  = the characteristic dimension as a function of time
- $X_0$  = the original dimension (half of the actual size)
- $t$  = time
- $Q$  = dissolution rate per unit area
- $\rho$  = density

## Conclusions

These times are calculated for the case of bare fuel immersed in unlimited quantities of flowing water at flow rates sufficient to prevent any species from forming a saturated solution. Nonetheless, this estimate provides a "core" value on which to apply "credits" corresponding to features of realistic repository performance such as frequency of cladding and container failure, actual amounts of ground water and various transport rates, etc. Of course, this "core" estimate is based on only one particular dissolution rate, as is discussed above. Future measurements of dissolution rate may change this value considerably. The estimates presented here ignore the possibility that grain boundary dissolution behaves differently than bulk SF dissolution.

Dissolution tests are now under way that are designed to define the mechanism of the dissolution process of  $UO_2$  and SF in terms of oxidizing potential, temperature, pH and other water composition variables generally appropriate to a potential repository at Yucca Mountain. When these tests are completed, considerably more realistic estimates will be possible. These tests will also clarify the contribution of radionuclides from grain boundaries to the total dissolution rate.<sup>16</sup>

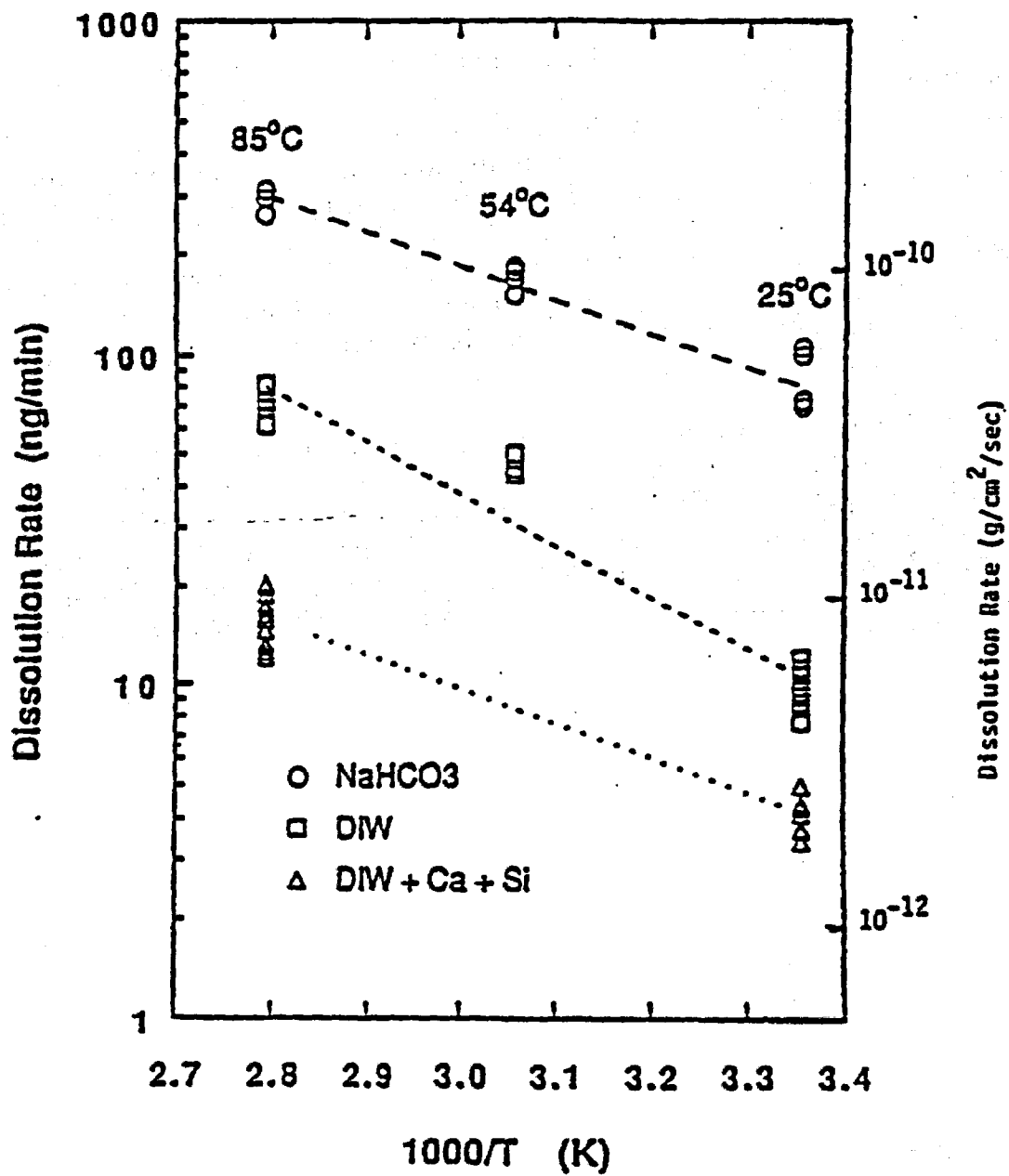


Figure 1. Arrhenius plots of the dissolution rate of  $UO_2$  in waters of various composition.

The time for complete dissolution of a particle of original size  $X_0$  is then

$$t_{\infty} = \frac{X_0 r}{Q} \quad (2)$$

This dissolution time is proportional to size, of course, and for an ensemble of particles of different sizes,  $t_{\infty}$  for the ensemble is that for the largest particle.

Some data are available on the size distribution of spent fuel fragments. These data are given for two different fuels but the distributions are quite similar. The aggregate of these two sets of data can be adequately described by the simplified distribution shown in Table I.

Table I

Approximate Size (cm) ( $2X_0$ )	Weight (Volume Fraction)
0.15	.02
0.25	.14
0.35	.29
0.50	.38
0.70	.17

Using the relationship of equation (1), we can calculate the time to dissolve a given weight (volume) fraction of an amount of SF as a function of time. For generality, we treat time as the dimensionless quantity  $t/t_{\infty}$  with  $t_{\infty}$  defined above. This is shown in Figure 3 for the size distribution given in Table I\*, and also for a single size with  $X_0 = 0.35$  cm. Here  $V_0$  and  $V(t)$  are the original volume of a particle and its volume at arbitrary time, respectively. The volume is proportional to the characteristic dimension

$$V_0 = kX_0^3 \text{ and } V(t) = kX^3(t)$$

where  $k$  is a constant depending on shape. Since geometry is retained, as noted above,

---

\*Each size was calculated separately and the time responses were added together.

$$\frac{V(t)}{V_0} = \left(\frac{X(t)}{X_0}\right)^3 = 1 - 3\left(\frac{Q}{X_0\rho}\right)t + 3\left(\frac{Q}{X_0\rho}\right)^2 t^2 - \left(\frac{Q}{X_0\rho}\right)^3 t^3, \quad (3)$$

$$\frac{d\left(\frac{V(t)}{V_0}\right)}{dt}$$

and the dissolution rate is -

Initially, i.e.,  $t \rightarrow 0$

$$\text{Rate } (t=0) = 3 \left(\frac{Q}{X_0\rho}\right)$$

and the extrapolated time for total dissolution is

$$t_{\infty} = \frac{X_0\rho}{3Q}$$

In Figure 4 we show that the rate of dissolution relative to the initial rate varies with time for both the system with  $X_0 = 0.35$  cm and for the distribution of Table I.

The measured dissolution rate for  $UO_2$ <sup>15</sup> and spent fuel<sup>16</sup> allow us to calculate actual times for dissolution. As is evident from Figure 3, the overall dissolution rate is greatest at early time and approaches zero as  $t_{\infty}$  is approached; therefore, as a conservative approximation, we have also calculated the total dissolution time extrapolated from the initial rate,  $t_{\infty}$ . These times calculated for the size distribution in Table I are given in Table II. The actual dissolution rates are derived from the bottom curve in Figure 1. We chose this curve as most representative of the expected ground water. The rate equation used is

$$Q(t)(\text{gcm}^{-2} \text{sec}^{-1}) = 6.43 \times 10^{-9} \exp\left(-\frac{4740}{RT(\text{K})}\right) \quad (\text{R is in cal/mole K}) \quad (5)$$

Table II

Temperature (°C) $t_{\infty}$	Dissolution Time (years) $t_{\infty}$
$258.0 \times 10^3$	$5.5 \times 10^4$
$852.2 \times 10^3$	$1.5 \times 10^4$

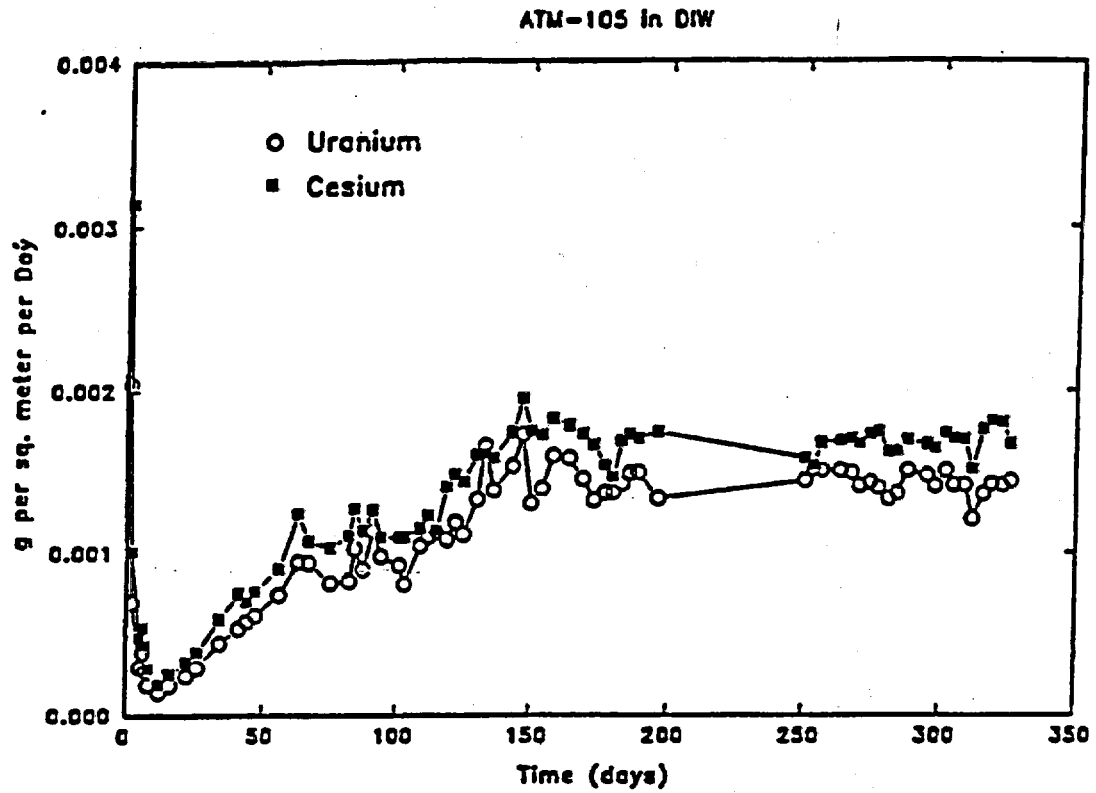


Figure 2. The approach to steady-state of the dissolution rate of two spent fuel samples. Experiments were done at 25°C using deionized water (DIW).

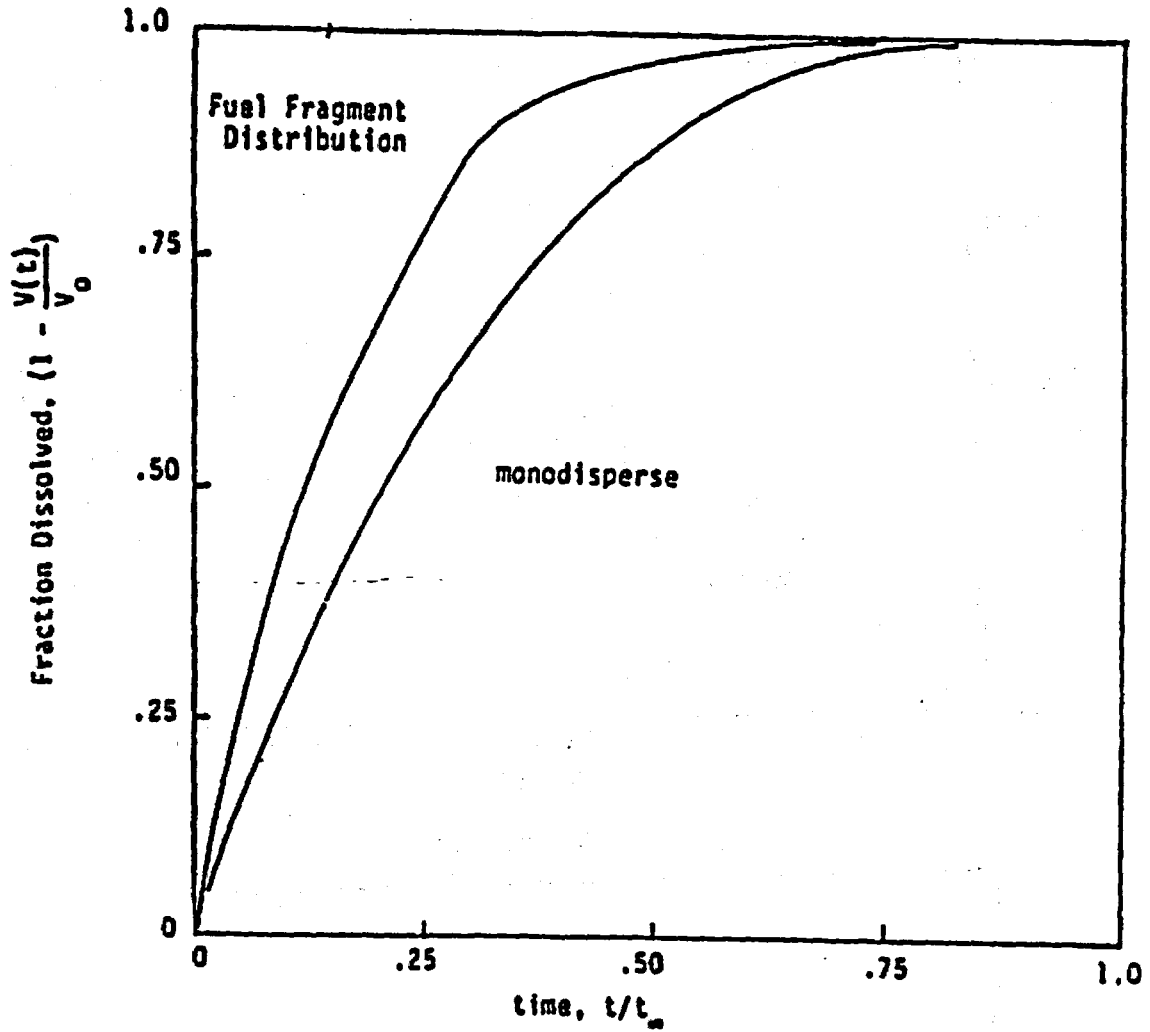


Figure 3. Calculation of the fractional dissolution in terms of dimensionless time, according to equation (3). Monodisperse refers to a single particle size.

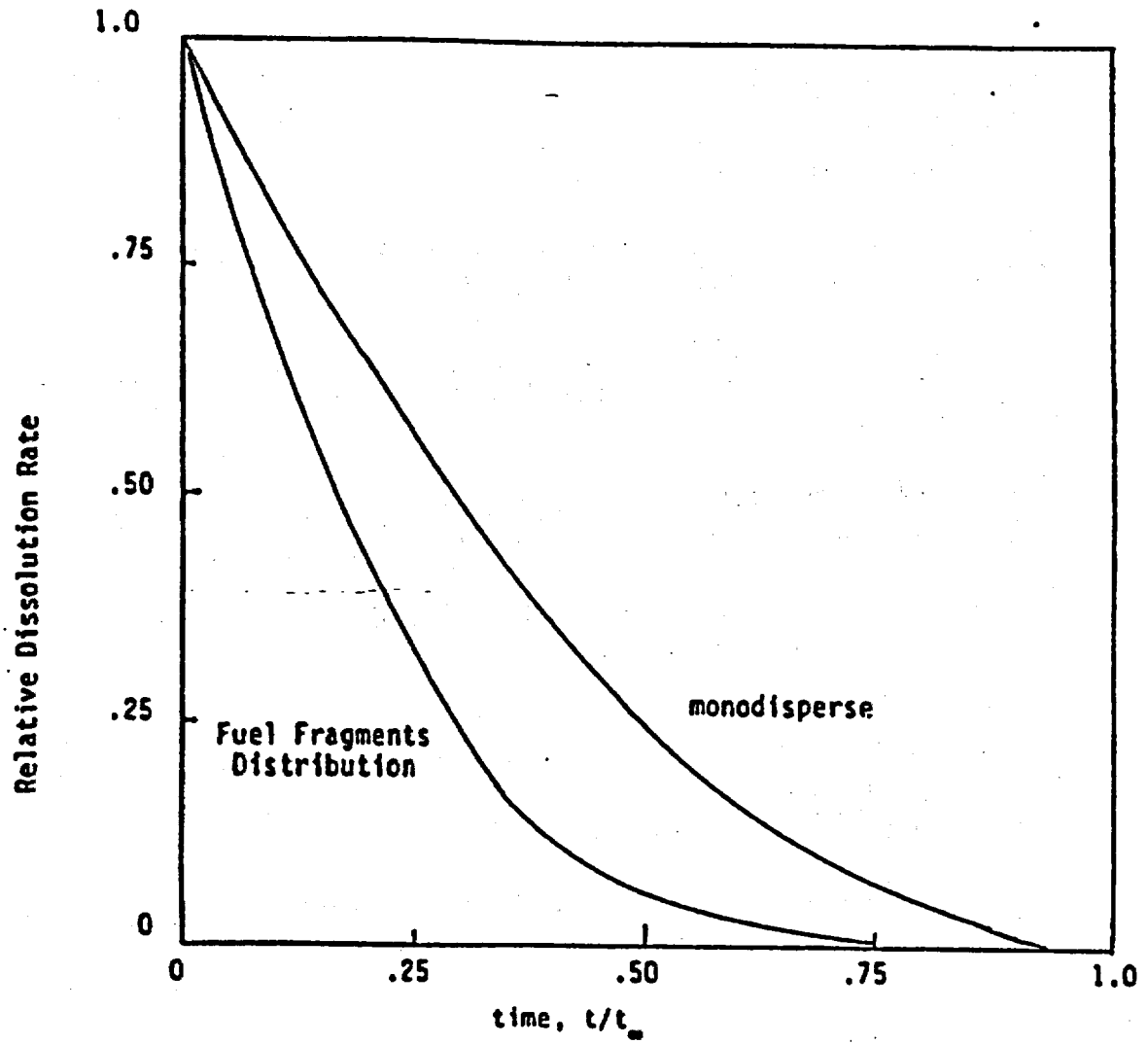


Figure 4. Evolution of the normalized dissolution rate with time as the particle size decreases, according to equation (3).

## References

1. Amell, A. R., and Langmuir, D., "Factors Influencing the Solution Rate of Uranium Dioxide Under Conditions Applicable to in-Situ Leaching", Bureau of Mines Open File Report 84-79, U.S. Department of the Interior - Bureau of Mines, (1978). (Readily Available)
2. Parks, G. A., and Pohl, D. C., "Hydrothermal Solubility of Uraninite", *Geochim. Cosmochim. Acta* 52 863 (1988). NNA.910821.0003
3. Bruno, J., Casas, I., and Puigdomenech, I., "The Kinetics of Dissolution of  $UO_2(s)$  Under Reducing Conditions", *Radiochimica Acta* 44/45, 11 (1988). NNA.910821.0004
4. Grambow, B., "Spent Fuel Dissolution and Oxidation. An Evaluation of Literature Data", SKB Technical Report 89-13 (1989). NNA.891013.0094
5. Grandstaff, D. E., "A Kinetic Study of the Dissolution of Uraninite", *Econ. Geo.* Z1 1493, (1976). NNA.911025.0061
6. Schortmann, W. E. and De Sesa, M. A., "Kinetics of the Dissolution of Uranium Dioxide in Carbonate-Bicarbonate Solutions", *Proc. 2nd International United Nations Conference Peaceful Uses of Atomic Energy, United Nations, Geneva*, 3, 333 (1958). NNA.910821.0005
7. Pearson, R. L., and Wadsworth, M. E., "A Kinetic Study of the Dissolution of  $UO_2$  in Carbonate Solution", *Trans. Metal Sor. AIME* 212, 294 (1958). NNA.910821.0006
8. Habashi, F., and Thurston, G. A., "Kinetics and Mechanisms of the Dissolution of Uranium Dioxide", *Energ. Nucl.* 14. 238 (1967). NNA.910821.0007
9. Aronson, S., "Oxidation and Corrosion of Uranium Dioxide in Uranium Dioxide: Properties and Nuclear Applications", J. Belle, ed., United States Atomic Energy Commission, 377 (1961). NNA.9110234.0060
10. Einziger, R. E., "Test Plan for Long-Term, Low-Temperature Oxidation of BWR Spent Fuel", PNL-6427, Pacific Northwest Laboratory, (1988). NNA.890224.0045

11. Aronson, S., "Oxidation of  $UO_2$  in Water Containing Oxygen", Bettis Tech. Rev., Westinghouse Atomic Power Div., Report WAPD-BT-10, 93 (1958).  
NNA.91IM5.0062
12. Wadsten, T., "The Oxidation of Polycrystalline Uranium Dioxide in Air at Room Temperature", T. Nucl. Mat. 64, 315 (1977). (Readily Available)
13. Wvertz, R. and Ellinger, M., "Source Term for the Activity Release from a Repository for Spent LWR Fuel", Mat. Res. Soc. Symp. Proc 50, 393 (1985). (Readily Available).
14. Gray, W. and Wilson, C., "Effects of Water Composition and Temperature on the Dissolution Rate of  $UO_2$ ", presented at 1990 Spent Fuel Workshop, Gull Harbor, Manitoba, Canada (1990). NNA.910821.0008
15. Gray, W., and Strachan, D., "Spent Fuel Grain Boundary Inventory and Testing the Congruency of  $UO_2$  Matrix Dissolution of Spent Fuel", presented at the 1990 Spent Fuel Workshop, Gull Harbor, Manitoba, Canada (1990).  
NNA.910821.0009
16. Stout, R. B, Shaw, H. F. and Einziger, R. E., "Statistical Model for Grain Boundary and Grain Volume Oxidation Kinetics in  $UO_2$  Spent Fuel", Lawrence Livermore National Laboratory UCRL-100859, September 1989.  
NNA.891031.0015
17. Stout, R. B., Kansa, E., Buchanan, H. C., Einziger, R. E. and Thomas, L. E., "Spent Fuel Waste Form Characteristics: Grain and Fragment Size Statistical Dependence for Oxidation Studies", Lawrence Livermore National Laboratory, UCRL-104932, December 1990. (Readily Available)
18. Stout, R. B. et al, "Spent Fuel Waste Form Characteristics: Grain and Fragment Size Statistical Dependence for Dissolution Response", Lawrence Livermore National Laboratory Report UCRL-104931, December 1990. (Readily Available)
19. Van Luik, A. E, et al, "Spent Nuclear Fuel as a Waste Form for Geologic Disposal: Assessment and Recommendations on Data and Modeling Needs, Pacific Northwest Laboratory Report, PNL-6329 (UC-70), September 1987. (Readily Available)

## Section 2.2.1.5 Contents

2.2.1.5	Fracture/Fragmentation Studies.....	2.2.1.5-1
2.2.1.5.1	Summary of Effects of Fracturing on Reactive Surface Area of Borosilicate Glass Waste Form.....	2.2.1.5-1
2.2.1.5.1.1	Background .....	2.2.1.5-1
2.2.1.5.1.2	Recommendation.....	2.2.1.5-3
2.2.1.5.1.3	References.....	2.2.1.5-3

## Section 2.2.1.5: Fracture/Fragmentation Studies

Version 1.3  
July 23, 1998

### 2.2.1.5.1 Summary of Effects of Fracturing on Reactive Surface Area of Borosilicate Glass Waste Form

This section documents the recommended values of glass surface area to be used in estimating glass alteration rates in the total system performance assessment-viability assessment (TSPA-VA) modeling work.

#### 2.2.1.5.1.1 Background

The reactive surface area of glass in a defense waste processing facility (DWPF) pour canister is increased above its simple geometric value through two processes (Wicks, 1985):

- **Thermal Fracturing**—As the waste glass cools after pouring, thermal gradients induce stresses that cause the glass to crack. Figure 2.2.1.5-1 shows the relative increase in actual surface area over the geometric surface area as a function of cooling rate. The faster the glass cools, the larger the surface area due to cracking. For typical cooling rates for the DWPF, the factor is approximately 10 to 15 (Smith and Baxter, 1981; Baxter, 1983). The glass area also is increased a minor amount due to production of fines generated during thermal cracking. These fines do not appear to contribute significantly to total surface area and, based on leaching studies of cracked glasses (Perez and Westsik, 1980) and on measurements of fines generated (Ross and Mendel, 1979), these fines can be ignored.
- **Impact Cracking**—If the glass canister is impacted by being dropped or experiencing a collision, the glass will crack (Smith and Ross, 1975). Figure 2.1.1.5-2 shows the increase in surface area, again expressed as a fraction of initial (geometric) surface area, as a function of collision velocity. At an impact velocity of 117 ft per sec (80 mph), the glass surface area is increased by a factor of about 40.

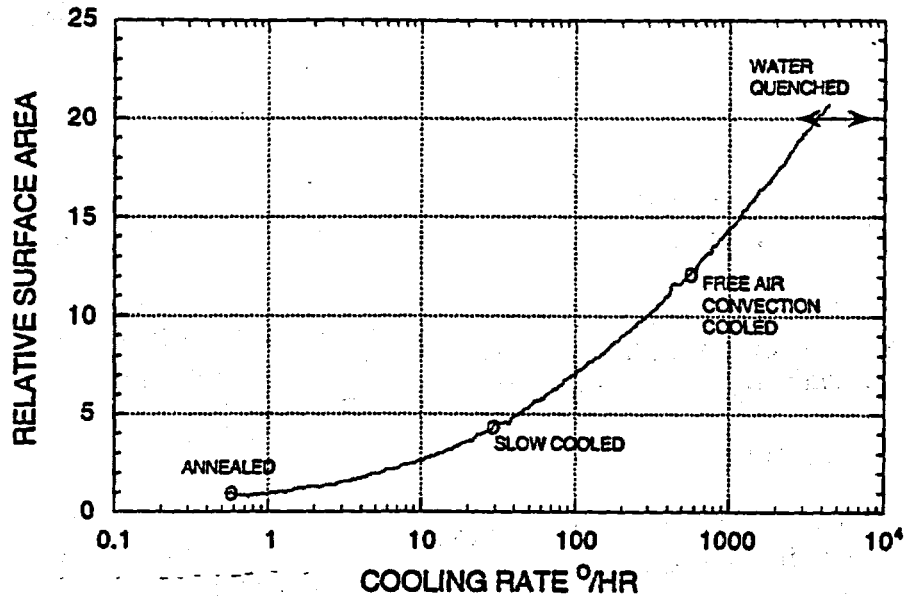


**Figure 2.2.1.5-1** Area increase of thermally shocked, simulated nuclear waste glass; values are relative to geometric area of glass cylinder with no surface roughness (data from Ross and Mendel, 1979)

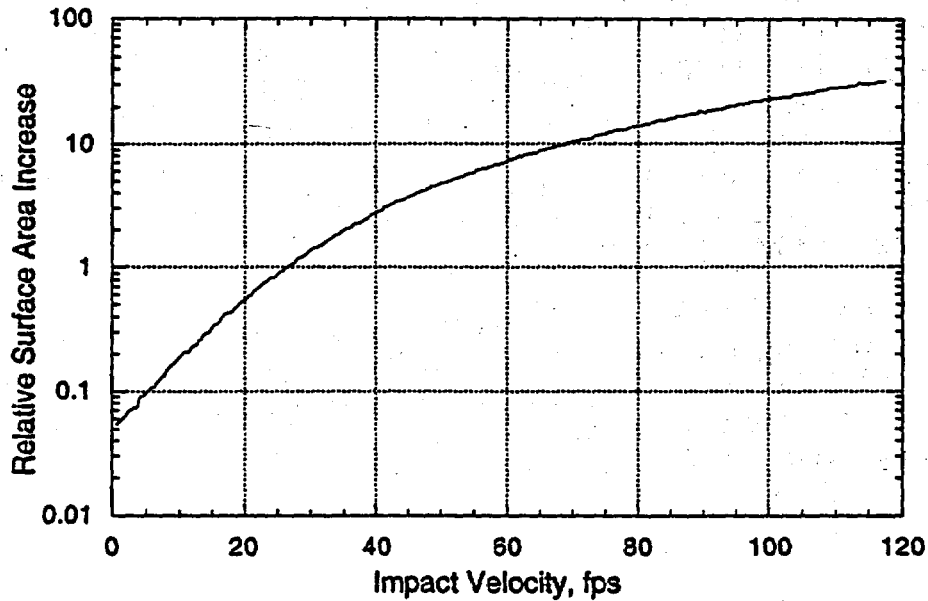


**Figure 2.2.1.5-2** Impact effects on surface area for simulated commercial waste glass (from Smith and Ross, 1975)

For both types of cracking, the actual increase in glass reaction rate is actually less than proportional to the increase in surface area (Perez and Westsik, 1980). Presumably this is due to a combination of restricted water mobility through tight

cracks, solution saturation effects, and swelling due to precipitation of hydrous alteration phases. Generally, a factor of 10 increase in surface area gives only a factor of 3 to 5 times faster reaction rate in a static leach test (Wicks, 1985).

#### 2.2.1.5.1.2 Recommendation

Based on these data, a conservative surface area value of roughly 21 times geometric area for typical DWPF glass, which is approximately 20% smaller than the value used in calculations in Section 3.5.1 of this report, is recommended. To obtain this value, one assumes 1% of all canisters suffer severe damage during transit so that their surface areas are increased a factor of 40 times above the normal value of air-cooled glass. For every 100 canisters, the one damaged canister has a surface area of  $40 \times 15 = 600$  times geometric, and the other 99 have surface areas of 15 times geometric. The total surface area is

$$40 \times 15 \times 1 \text{ (damaged)} + 15 \times 99 \text{ (undamaged)} = 2085/100 = 20.85 \text{ times}$$

No credit is given for the lack of scaling between observed increase in surface area and a lesser increase in glass reaction rate.

A typical, filled canister of SRL-202 glass has approximately 1680 kg of glass with a density of  $2.7 \text{ g/cm}^3$ . The volume of the glass log is therefore  $1,680,000/2.7 = 622,000 \text{ cm}^3$ . The inside diameter of the canister is approximately 60 cm. Therefore the glass cylinder has a height of

$$\pi r^2 \times \text{height} = \text{volume}$$

$$\text{height} = 622,000 \text{ cm}^3 / \pi 900 \text{ cm}^2 = 220 \text{ cm}$$

with total surface area

$$2 \pi r^2 + 2 \pi r \times \text{length} = 5,655 + 41,469 = 47,124 \text{ cm}^2 = 4.7 \text{ m}^2$$

Therefore an average DWPF glass canister has a surface area of  $21 \times 4.7 = 99 \text{ m}^2$ .

#### 2.2.1.5.1.3 References

Baxter, R. G. (1983). Description of Defense Waste Processing Facility Reference Waste Form and Container. Aiken, SC: Savannah River Site. [210286]

Perez, J. M., and J. H. Westsik (1980). "Effects of Cracks on Glass Leaching." In proceedings from ORNL Conference on Leachability of Radioactive Solids. Oak Ridge, TN: Oak Ridge National Laboratory. p. 35.

Ross, W. A., and J. E. Mendel (1979). *Annual Report on the Development and Characterization of Solidified Waste Forms for High-Level Wastes*. Richland, WA: Pacific Northwest National Laboratory.

Smith, P. K., and C. A. Baxter (1981). *Fracture During Cooling of Cast Borosilicate Glass Containing Nuclear Wastes*. Aiken, SC: Savannah River Laboratory.

Smith, T. H., and W. A. Ross (1975). *Impact Testing of Simulated High-Level Waste Glass in Canisters*. Richland, WA: Pacific Northwest National Laboratory.

Wicks, G. (1985). "Nuclear waste glasses." *Treatise on Materials Science and Technology*. 26:57-117. New York, NY: Academic Press.

## Section 2.2.2.2 Contents

2.2.2.2	Dissolution Radionuclide Release from Glass.....	2.2.2.2-1
2.2.2.2.1	Radionuclide Release Data From Unsaturated Tests.....	2.2.2.2-1
2.2.2.2.1.1	Data Description.....	2.2.2.2-1
2.2.2.2.2	Results.....	2.2.2.2-4
2.2.2.2.2.1	Solution Cation Analyses.....	2.2.2.2-4
2.2.2.2.2.2	Elements in the N2 Solution.....	2.2.2.2-4
2.2.2.2.2.3	Elements in the N3 solution.....	2.2.2.2-10
2.2.2.2.3	References.....	2.2.2.2-13

## **Section 2.2.2.2: Dissolution Radionuclide Release from Glass**

**Version 1.3  
July 23, 1998**

### **2.2.2.2.1 Radionuclide Release Data From Unsaturated Tests**

#### **2.2.2.2.1.1 Data Description**

The N2 and N3 unsaturated (drip) tests have been in progress at Argonne National Laboratory since February 1986 and July 1987, respectively. Drip tests are designed to replicate the synergistic interactions between waste glass, repository groundwater, water vapor, and sensitized 304L stainless steel in the proposed Yucca Mountain repository.

The tests using actinide- and technetium-doped Savannah River Laboratory (SRL) 165 glass, are termed the N2 Test Series. Tests with a West Valley Demonstration Project former reference glass (ATM-10) have been in progress and are termed the N3 Test Series. The information provided here includes long-term data relevant to glass reaction under conditions anticipated for an unsaturated repository. While SRL-165 glass is no longer the reference glass to be used for the defense waste-processing facility (DWPF), it does represent a glass within the production envelope, and the tests provide information that can be used for the following:

- Model validation
- Investigation of reaction mechanisms
- Evaluation of synergistic effects
- Form of radionuclide release
- Glass reaction rates over long time periods under repository service conditions

Measurements obtained from each test series include the rate of glass reaction and radionuclide release as a function of time, a description of the distribution of radionuclides in solution (i.e., dissolved in solution, associated with colloidal material, or sorbed onto metal components of the test), and monitoring of the interactions among the various components in the test. Ultimately, the Yucca Mountain Site Characterization Project (YMP) plans to use the results from these tests to validate source terms of models used in waste-package-performance assessment codes.

In the unsaturated tests, 0.075 mL (about 3 drops) of tuff-equilibrated groundwater from the J-13 well near Yucca Mountain (termed EJ-13 water) is dripped every 3.5 days onto the simulated waste package (WP) in a sealed stainless-steel test vessel. Additional air is injected into the test vessel with the water. The simulated waste-package assemblage (WPA) used in the tests consists of a cylindrical monolith of waste glass, approximately 16 mm diameter and 20 mm high, contacted on the top and bottom by two perforated retainer plates made from sensitized 304L stainless steel; these are held in place by two wire posts, also made from 304L stainless steel. The entire test apparatus is enclosed in a 90°C oven, except when samples are taken and observations made.

Details of the unsaturated test procedure are given elsewhere (Bates and Gerding, 1990; ANL, 1996). Each ongoing test series consists of three identically prepared WPAs, each in its own test vessel, and a blank (empty test vessel). Water drips down the sides of the glass and accumulates at the bottom of the WPA. Eventually the water drips from the WPA to the bottom of the vessel. When the drip tests are sampled (currently at 26-wk intervals), the WPA is examined visually to qualitatively ascertain the degree of reaction, including evidence of alteration-phase formation and possible spalling of the alteration phases and clay layer. After observation, the WPA is transferred to a fresh test vessel, the test solution is removed for analysis, and the just-used vessel is acid-stripped to determine sorbed species.

The compositions of the glasses used in the N2 and N3 tests are given in Table 2.2.2.2-1. The approximate composition, for the most concentrated elements, of the groundwater (EJ-13) used in the tests is given in Table 2.2.2.2-2.

Table 2.2.2.2-1 Compositions, in oxide-weight percentage, of glasses used in the N2 and N3 tests

Oxide	N2 Tests SRL 165 <sup>a</sup>	N3 Tests ATM-10 <sup>b</sup>
Al <sub>2</sub> O <sub>3</sub>	4.08	6.65
AmO <sub>2</sub>	0.00091	0.0064
B <sub>2</sub> O <sub>3</sub>	6.76	9.17
BaO	0.06	0.045
CaO	1.62	0.60
CeO <sub>2</sub>	<0.05	0.072
Cr <sub>2</sub> O <sub>3</sub>	<0.01	0.253
CsO <sub>2</sub>	0.072	0.062
Fe <sub>2</sub> O <sub>3</sub>	11.74	11.5
K <sub>2</sub> O	0.19	3.34
La <sub>2</sub> O <sub>3</sub>	<0.05	0.025
Li <sub>2</sub> O	4.18	2.88

Oxide	N2 Tests SRL 165 <sup>a</sup>	N3 Tests ATM-10 <sup>b</sup>
MgO	0.70	1.15
MnO <sub>2</sub>	2.79	1.29
Na <sub>2</sub> O	10.85	10.5
Nd <sub>2</sub> O <sub>3</sub>	<0.05	0.168
NiO	0.85	0.296
NpO <sub>2</sub>	0.0283	0.021
P <sub>2</sub> O <sub>5</sub>	0.29	2.34
PuO <sub>2</sub>	0.048	0.0081
RhO <sub>2</sub>	—	0.012
RuO <sub>2</sub>	—	0.061
SO <sub>3</sub>	—	0.31
SiO <sub>2</sub>	52.86	45.8
SrO	0.11	0.025
Tc <sub>2</sub> O <sub>7</sub>	0.02	0.0031
ThO <sub>2</sub>	—	3.29
TiO <sub>2</sub>	0.14	0.858
UO <sub>2</sub>	1.25	0.527
Y <sub>2</sub> O <sub>3</sub>	—	0.017
ZrO <sub>2</sub>	0.66	0.247

<sup>a</sup> From Bates and Gerding (1990), except as noted  
<sup>b</sup> From ANL (1996)

**Table 2.2.2.2-2 Typical composition of the EJ-13 water used in the N2 and N3 tests**

Element	Concentration (mg/L)
Al	0.7
B	0.2
Ca	6.6
Fe	<0.1
K	7
Mg	0.15
Li	0.04
Na	53
Si	40
F <sup>-</sup>	3
Cl <sup>-</sup>	10
NO <sub>2</sub> <sup>-</sup>	<1

Element	Concentration (mg/L)
NO <sub>3</sub> <sup>-</sup>	11
SO <sub>4</sub> <sup>-</sup>	23
HCO <sub>3</sub> <sup>2-</sup>	100
total carbon	25
organic carbon	7

The pH of EJ-13 water is ~8.6.  
Other cations are < 0.1mg/L

## 2.2.2.2.2 Results

### 2.2.2.2.2.1 Solution Cation Analyses

In the following discussion, the solution collected in the test vessel that had contacted the WP during the course of the test is designated as the vessel rinse, and the solution that results from soaking the vessel with acidified water is called the acid strip. As the glass reacts, material is released from the glass either truly dissolved in solution or as particulate material. The solution is also in contact with the pre-sensitized, 304L, stainless-steel retainer during the reaction process, so the analysis of the solution collected in the bottom of the test vessel represents all the material that is transported from the glass and the glass retainer. The solution is analyzed for its constituent parts, as described previously, but all the material analyzed in the test solution is considered to have been released from the glass/stainless-steel assembly.

A comparison of behaviors among elements present in widely different concentrations in the glass is best made by examination of the *normalized releases*. The normalized release rate is  $N_i = M_i / (\Delta t c_i A)$ , where  $M_i$  is the measured mass of element  $i$  in the leachate solution,  $c_i$  is its element fraction in the source glass,  $\Delta t$  is the time interval between tests, and  $A$  is the surface area of the glass monolith ( $1.36 \times 10^{-3} \text{ m}^2$ ). However, the use of such a normalization process in the drip tests averages the three types of water contact that occur: humid air, dripping water, and standing water.

### 2.2.2.2.2.2 Elements in the N2 Solution

Figure 2.2.2.2-1 shows the total cumulative mass release of lithium and boron in the vessel rinse from the N2 tests into solution as a function of time. The term "release" is used throughout this section to indicate elements that have left the WPA and are dissolved in solution, suspended as colloids, or sorbed onto the test vessel. The release of these elements is an important gauge of the glass corrosion because they are not expected to form secondary phases, are not major components of the EJ-13, and are not present in the steel.

Negligible amounts of lithium and boron are measured in the acid strip solutions. Normalized release rates for these elements appear in Figure 2.2.2.2-2. Note also the nearly identical behavior of these two elements, an indication that they are remaining in solution (dissolved) and are released from the glass congruently. Further note that, while the data from the three replicate samples in the test may differ, the N2-10 sample releases both lithium and boron at the fastest rate, while the N2-9 sample releases both elements at the slowest rate (not including N2-11, which was a blank test). The differences in measured reaction rate are real and are reflections of the reproducibility of this type of test over a 10-yr period. The composition of the unfiltered N2-10 vessel-rinse test solution from the June 17, 1996, sampling, which includes plutonium and americium contributions from colloids, appears in Table 2.2.2.2-3.

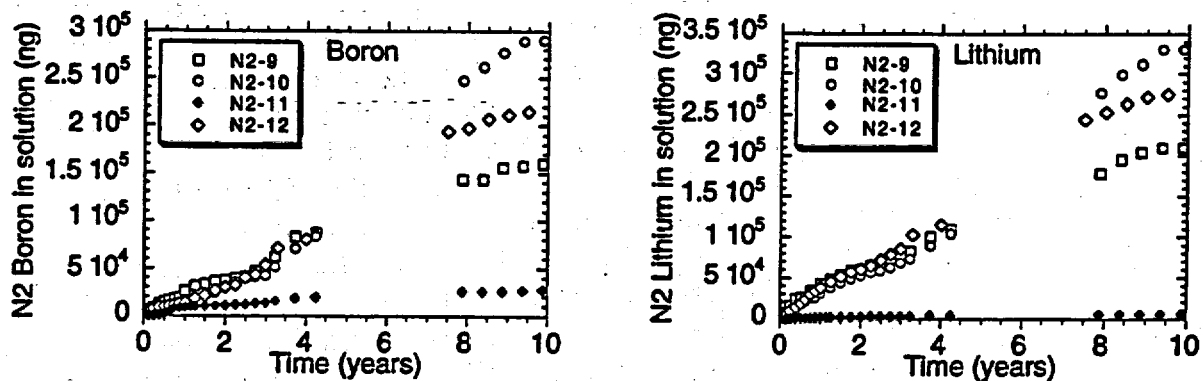


Figure 2.2.2.2-1 Cumulative release of boron and lithium from the N2 tests as a function of elapsed time. Note the increased release rate, relative to the other tests, from N2-10. The test N2-11 is a blank test, and the release data from the N2-11 test are upper bounds because of detection limits.

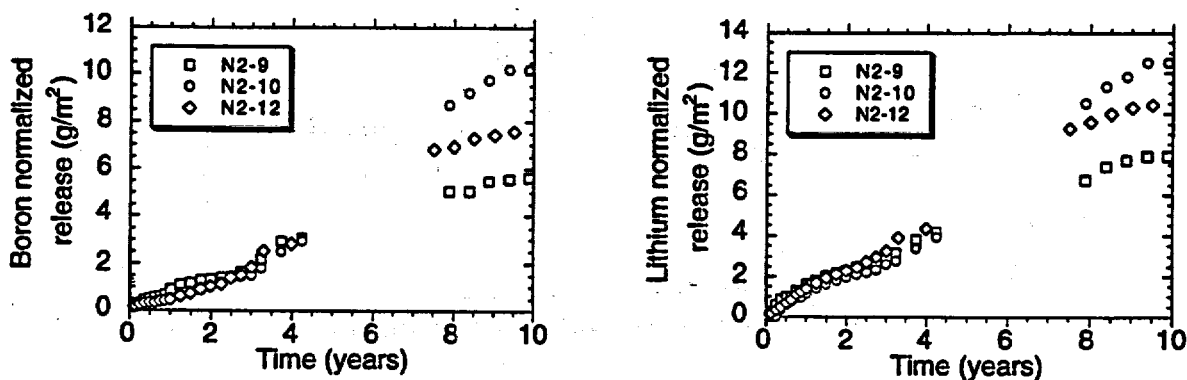
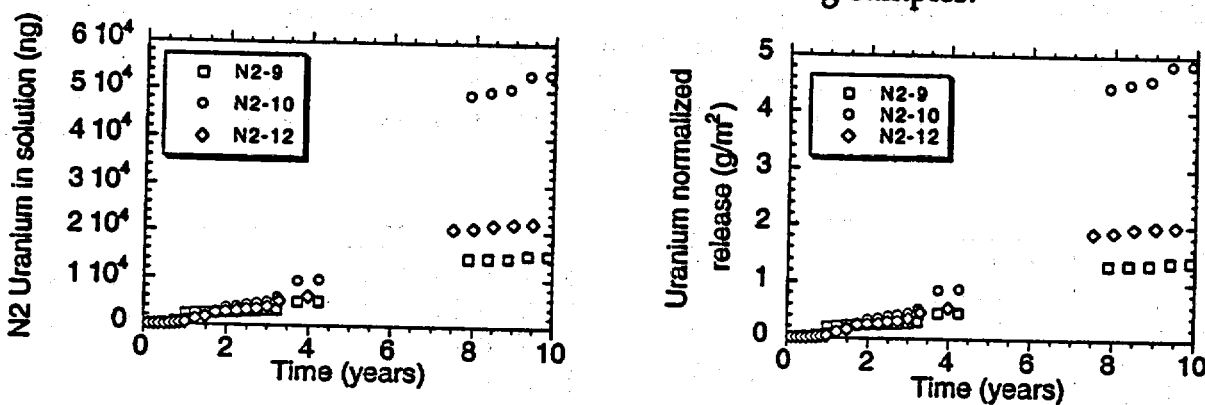


Figure 2.2.2.2-2 Normalized cumulative release of boron and lithium from the N2 tests as a function of elapsed time. Note the increased release rate, relative to the other tests, from N2-10. Note also that the normalized releases of these elements are in excellent agreement.

**Table 2.2.2.2-3** Composition of the unfiltered test solution collected from N2-10 on June 17, 1996. These values are typical of what has been observed in the N2 series over the past 3 yr.

Concentration ( $\mu\text{g/mL}$ )						
Li	B	Na	Al	Si	K	Ca
31200	6300	329000	10300	153000	54600	17500
Concentration ( $\mu\text{g/mL}$ )						
Cr	Fe	Ni	U	Np	Pu	Am
1800	30500	6500	2040	35	63	1.0

Uranium release from the N2 tests appears in Figure 2.2.2.2-3. Note that the uranium normalized release is about half (or less) that of lithium and boron (Figure 2.2.2.2-2) and that the N2-10 test appears to be releasing uranium at a much higher rate than did the other two. These plots do not include uranium from the acid strip of the test vessel, which has only been measured since the December 1993 sampling; extrapolating from present trends, the acid strip data would add about 30% to the observed release of uranium and are included in the normalized uranium release rates of Table 2.2.2.2-4. From Table 2.2.2.2-4, it is apparent that the normalized uranium release from N2-10 is approximately the same as the normalized lithium or boron release, whereas the N2-9 and 12 are releasing uranium somewhat more slowly. A release mechanism by solution-born colloids is proposed later in this section as a likely explanation of such variations among samples.



**Figure 2.2.2.2-3** Cumulative uranium release from the N2 tests as a function of time (left, total mass release; right, normalized release)

**Table 2.2.2.2-4 Normalized release rates over the latest 2.5-yr period for selected elements from the N2 tests series<sup>a</sup>**

Normalized Release Rates <sup>b</sup> (g m <sup>-2</sup> day <sup>-1</sup> )						
Test Series	Li	B	U	Np	Pu	Am
N2-9	1.6 x 10 <sup>-3</sup>	0.9 x 10 <sup>-3</sup>	4.0 x 10 <sup>-4</sup>	1.0 x 10 <sup>-4</sup>	3.0 x 10 <sup>-5</sup>	4.4 x 10 <sup>-5</sup>
N2-10	2.8 x 10 <sup>-3</sup>	2.2 x 10 <sup>-3</sup>	1.3 x 10 <sup>-3</sup>	3.4 x 10 <sup>-3</sup>	1.4 x 10 <sup>-3</sup>	1.4 x 10 <sup>-3</sup>
N2-12	1.7 x 10 <sup>-3</sup>	1.1 x 10 <sup>-3</sup>	3.2 x 10 <sup>-4</sup>	4.0 x 10 <sup>-4</sup>	0.8 x 10 <sup>-4</sup>	0.9 x 10 <sup>-5</sup>
Average	2.1 x 10 <sup>-3</sup>	1.4 x 10 <sup>-3</sup>	6.7 x 10 <sup>-4</sup>	1.6 x 10 <sup>-3</sup>	4.8 x 10 <sup>-4</sup>	5.0 x 10 <sup>-4</sup>

- <sup>a</sup> The rates include data from the period December 1993 through December 1995. The above rates are for vessel rinse only, except for the rates for U, Pu, and Am, which include the acid strip.
- <sup>b</sup> Error is approximately ±30% for each of the above rates. These rates reflect the latest glass composition analysis by ICP-MS (Table 2.2.2.2-1).

The elements in the acid strip solution (except for the actinides plus iron, nickel, and chromium from the stainless-steel test vessel itself) are present at very low amounts relative to the vessel rinse solution. Neptunium, plutonium, and americium in the acid strip have been monitored by high-resolution alpha spectroscopy since the tests were initiated. Uranium levels in the acid strip were not measurable by the alpha spectroscopy procedure and have only recently become available with the inductively coupled plasma-mass spectroscopy ICP-MS data.

The release of the transuranic elements Np, Pu, and AM into solution is plotted in Figures 2.2.2.2-4 and 2.2.2.2-5 for the N2 test series. Np is highly soluble and does not sorb substantially onto the stainless steel, a fact confirmed by measurements of the acid strip solutions. The reported values for Np, like those of Li and B, thus include only the vessel rinse. Pu and Am, on the other hand, are known to sorb onto the stainless steel (from which the test vessel is made) and may also be incorporated into the clay layer and alteration phases (Bates et al., 1992; Fortner et al., 1995; Fortner et al., 1997). The Pu and Am data in the figures represent a sum of the vessel rinse and acid strip results, where there are comparable contributions from each. Typically, 60 to 70% of the Pu and Am is from the vessel rinse, with the remaining 30 to 40% from the acid strip.

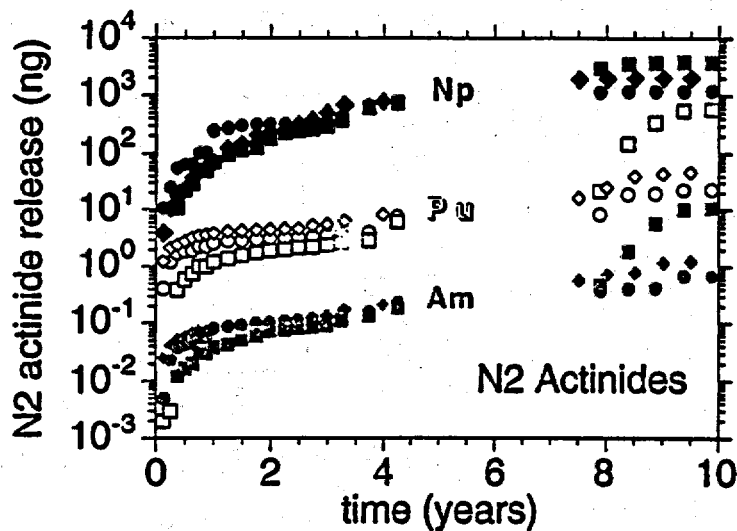


Figure 2.2.2.2-4 Cumulative mass releases for the transuranic elements neptunium, plutonium, and americium from the N2 Tests: N2-9 (circles), N2-10 (rectangles) and N2-12 (diamonds).

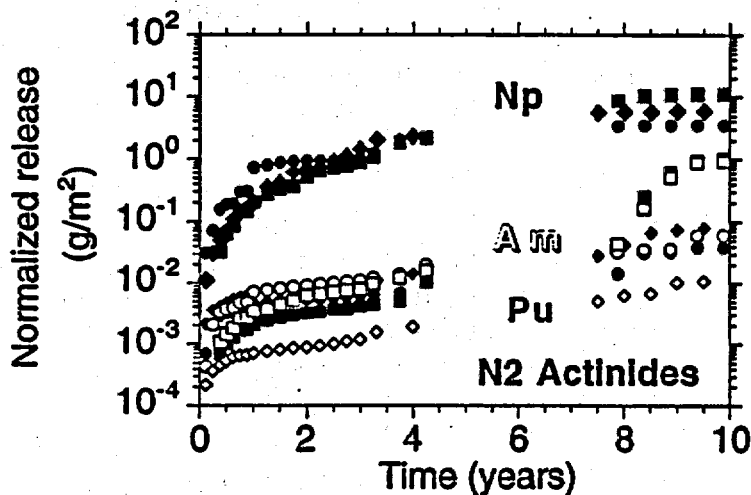
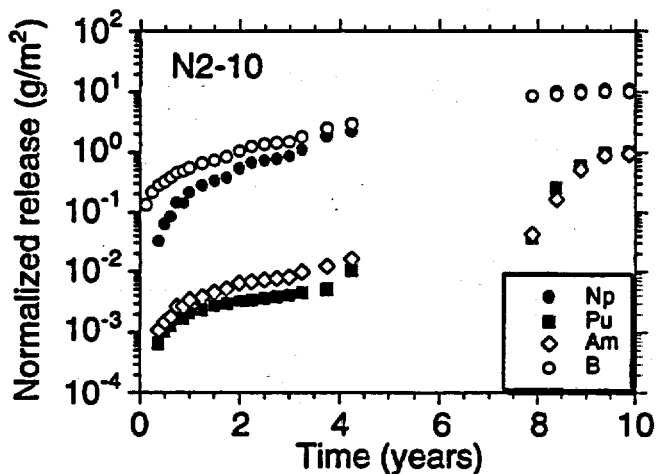


Figure 2.2.2.2-5 Normalized actinide release from the N2 tests: N2-9 (circles), N2-10 (rectangles), and N2-12 (diamonds). Note the retention of Am and Pu relative to Np.

The sharp increases in Pu and Am release rates seen in some of the latest data are a result of some actinide-bearing secondary phases spalling off the glass and appearing in the test solution. These increases are correlated with the visual observations, where the N2-10 test is observed to undergo the greatest (of the N2 series tests) corrosion of the metal and spalling of clay from the glass into the test solution. A comparison of the normalized releases of B, Np, Pu, and Am appears in Figure 2.2.2.2-6. For the first eight years, the release of the soluble B and Np was more than two orders of magnitude greater than that of the relatively insoluble Pu

and Am. During the latest two years, the release rate of the Pu and Am has nearly equaled that of the soluble elements (Table 2.2.2.2-4). Note that the Np release does not experience the recent jumps observed for Pu and Am, but continues smoothly as do the Li and B releases. This is consistent with the clay alteration layer being depleted in these elements; their release is thus unaffected by the spalling of the clay. Continued spalling of the clay may ultimately cause the normalized release of Pu and Am (as solution-born solid phases) to approach that of the Li and B. These lower rates are due to incorporation of elements into secondary phases, many of which remain attached to the WPA. The spalling off of these phases is then what controls the release of the incorporated elements from the glass. These spalled-off phases may become suspended in solution as colloids. The role of colloidal solids in solution is also reflected in the sequential filtering data, where substantial Pu and Am often appear on the filters and are removed from the filtered solution. Recent use of ultracentrifugation filtration has shown that nearly 100% of the Np is recovered in the filtered solution from the N2 tests, whereas less than 10% of the Pu and Am pass.

A more detailed analysis of the filtered solutions will be prepared as more data are compiled and analyzed. The masses of truly dissolved actinides from the N2-12 test sampled December 18, 1995, appear in Table 2.2.2.2-5. It is clear from these data (and others) that little of the Np in solution is associated with undissolved solids, whereas a majority of the Am and Pu are incorporated into particulates and colloids. Examples of solid phases observed from the N2 test components appear in Table 2.2.2.2-6.



**Figure 2.2.2.2-6** Normalized release of Np, B, Am, and Pu from a single test series, N2-10, which displayed evidence of excessive clay spallation. Note the sudden increase in release of the insoluble elements Pu and Am without an accompanying disruption in the release of the more soluble Np and B. This is likely due to the release of the Am and Pu as solids (colloids or larger particulates), potentially leading to near-congruent release of elements.

Table 2.2.2.2-5

Comparison of transuranic content in unfiltered and ultracentrifuge-filtered solutions from the N2-12 test sampled December 18, 1995 (the solution volume recovered was 1.42 mL)

Element in Solution (ng)					
Np (Unfiltered)	Np (Filtered)	Pu (Unfiltered)	Pu (Filtered)	Am (Unfiltered)	Am (Filtered)
5.1	5.2*	0.844	0.002	0.0115	0.0003

\* The recovery of more than 100% of the Np is an artifact of statistical error.

Table 2.2.2.2.1-6

Alteration phases identified on N2 solid components (from Bates and Gerding, 1990)

Phase	Nominal composition	comments
Ferrihydrate	$5Fe_2O_3 \cdot 9H_2O$	
Iron oxyhydroxide	$FeOOH$	
Sodium feldspar	$NaAlSi_3O_8$	Precipitate
Cristoballite	$SiO_2$	Precipitate
Orthoclase	$KAlSi_3O_8$	Precipitate
Smectite clay	Layered aluminosilicate with interlayer Fe and Mg	Variable composition

2.2.2.2.2.3 Elements in the N3 solution

The cumulative release of B and Li from the N3 tests appears in Figure 2.2.2.2-7, with normalized release plotted in Figure 2.2.2.2-8. As with the N2 tests, the normalized release of these elements is nearly identical with each test in the N3 series, consistent with congruent dissolution of the glass and complete solubility of the Li and B under the test conditions.

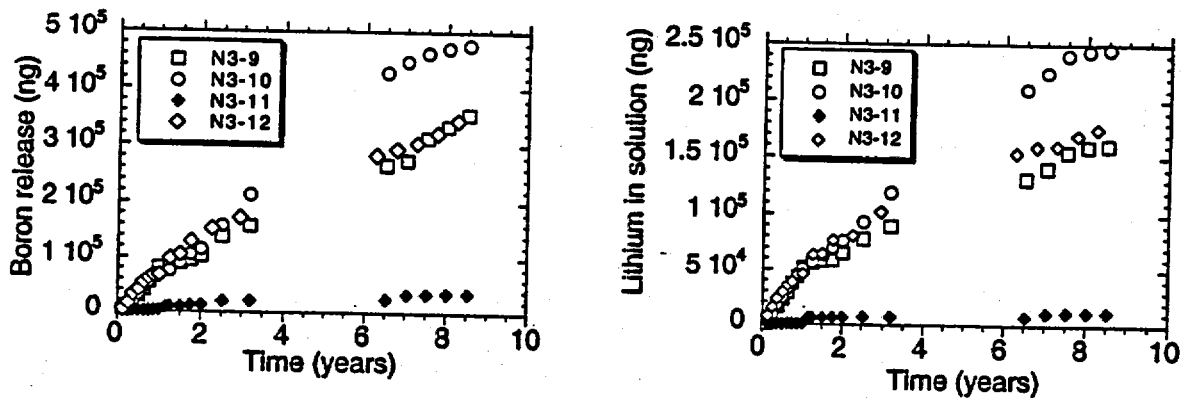
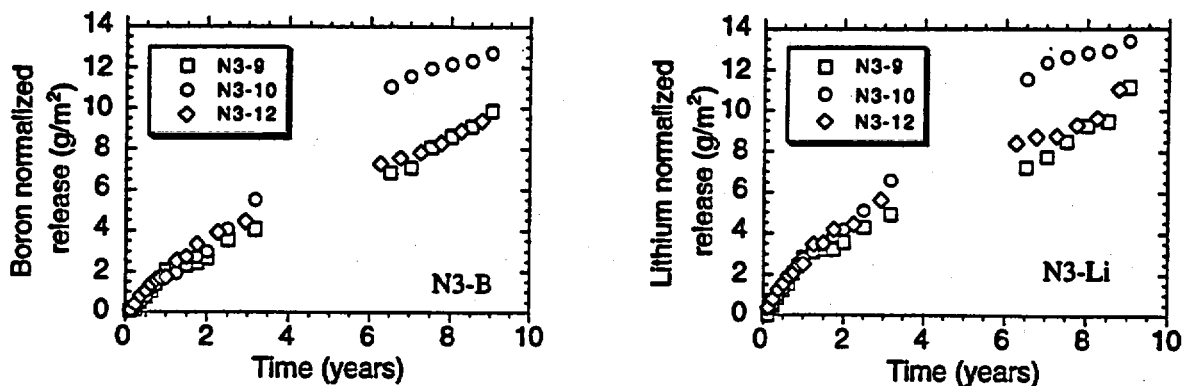


Figure 2.2.2.2-7

Cumulative release of B and Li from the N3 tests as a function of elapsed time. The test N3-11 is a blank test, and the release data from the N3-11 test are upper bounds due to detection limits.



**Figure 2.2.2.2-8** Normalized cumulative release of B and Li from the N3 tests as a function of elapsed time. Note also that the normalized releases of these elements are in excellent agreement with one another.

Transuranic release appears in Figures 2.2.2.2-9 and 2.2.2.2-10 as total mass release and normalized release, respectively. From these figures, it is apparent that the release rate for Pu and Am has increased by a factor of nearly two during the past two years, but still remains well below the release for the soluble elements (Table 2.2.2.2-7), rather than jumping by an order of magnitude, as was observed in the N2-10 test.

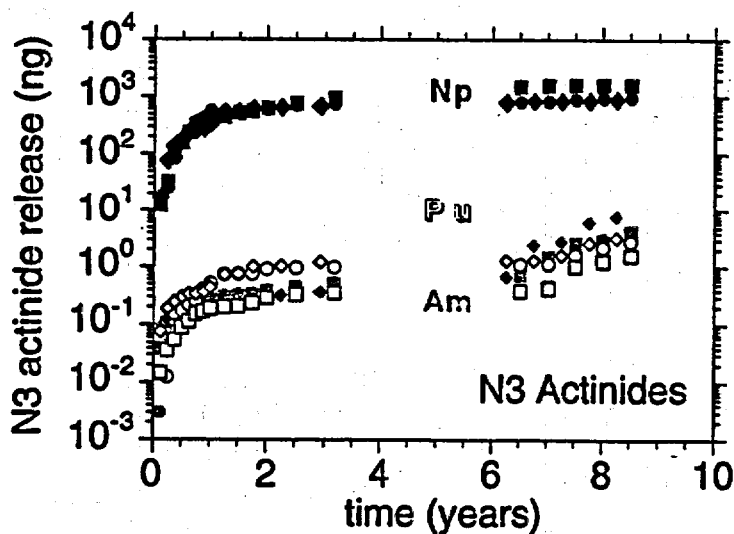


**Figure 2.2.2.2-9** Cumulative mass releases for the transuranic elements Np, Pu, and Am from the N3 Tests: N3-9 (circles), N3-10 (rectangles), and N3-12 (diamonds).

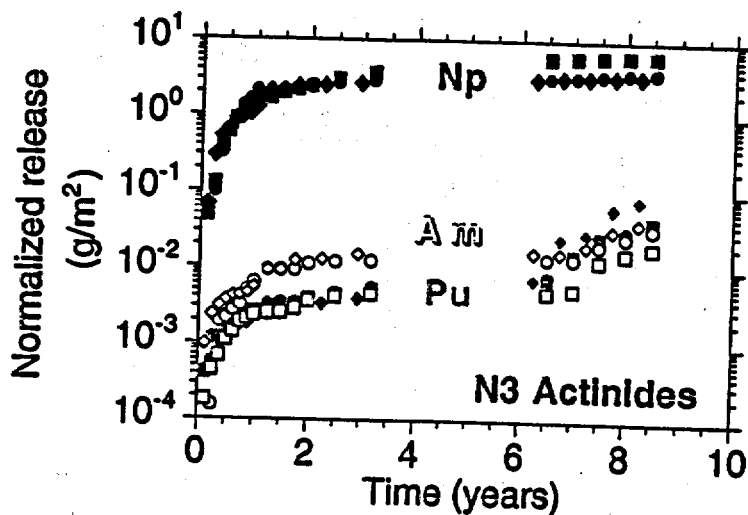


Figure 2.2.2.2-10 Normalized actinide release from the N3 tests: N3-9 (circles), N3-10 (rectangles), and N3-12 (diamonds). Note the retention of Am and Pu relative to Np.

Table 2.2.2.2-7 Normalized release rates over the latest 2.5-yr period for selected elements from the N3 tests series<sup>a</sup>

Normalized Release Rates <sup>b</sup> (g m <sup>-2</sup> day <sup>-1</sup> )							
Test Series	Li	B	Th	U	Np	Pu	Am
N3-9	4.0 x 10 <sup>-3</sup>	3.4 x 10 <sup>-3</sup>	1.3 x 10 <sup>-5</sup>	2.6 x 10 <sup>-4</sup>	9.6 x 10 <sup>-4</sup>	4.7 x 10 <sup>-5</sup>	3.0 x 10 <sup>-5</sup>
N3-10	1.8 x 10 <sup>-3</sup>	1.7 x 10 <sup>-3</sup>	2.1 x 10 <sup>-5</sup>	4.3 x 10 <sup>-4</sup>	6.6 x 10 <sup>-4</sup>	4.7 x 10 <sup>-5</sup>	2.2 x 10 <sup>-5</sup>
N3-12	2.6 x 10 <sup>-3</sup>	2.3 x 10 <sup>-3</sup>	1.1 x 10 <sup>-5</sup>	3.7 x 10 <sup>-4</sup>	4.9 x 10 <sup>-4</sup>	1.0 x 10 <sup>-4</sup>	3.6 x 10 <sup>-5</sup>
Average	2.8 x 10 <sup>-3</sup>	2.5 x 10 <sup>-3</sup>	1.5 x 10 <sup>-5</sup>	3.5 x 10 <sup>-4</sup>	7.0 x 10 <sup>-4</sup>	6.5 x 10 <sup>-5</sup>	3.0 x 10 <sup>-5</sup>

<sup>a</sup> The rates include data from the period January 1994 through July 1996. The rates are for vessel rinse only, except the rates for Th, U, Pu, and Am, which include the acid strip.

<sup>b</sup> Error is approximately ±30% for each of the rates.

The West Valley-type glass used in the N3 tests is unusual in that it contains a large amount, relative to most other waste glasses, of the actinide element Th. This element is found to concentrate in alteration phases (Fortner and Bates, 1996; Bates et al., 1992, Fortner et al., 1995). The N3 tests continue to release Th at the relatively low rate of  $1.5 (\pm 0.5) \times 10^{-5}$  g/(m<sup>2</sup> day), about 100 time less than the normalized release rates for B and Li (Table 2.2.2.2-7). This low release rate suggests that the Th alteration phases are mostly remaining with the test WPA, although they have been observed in colloidal particles from the test solution phases (Fortner and Bates, 1996; Bates et al., 1992). Alteration phases observed on components from the N3 test series are summarized in Table 2.2.2.2-8.

Table 2.2.2-8

Summary of alteration phases noted on the N3 surfaces (Fortner et al., 1997)

Phase	Location	Identification	Comments
Smectite clays	A layer on all glass surfaces. Spalled fragments located sporadically on 304L retainer components	Energy-dispersive spectroscopy (EDS), electron diffraction, lattice imaging	A ubiquitous layer that grew with test duration. The more advanced growths displayed a "backbone" structure.
Brockite (CaThPO <sub>4</sub> )	Copious amounts found on most glass surfaces. Clusters found on most 304L retainer surfaces, except those of shortest test duration.	EDS, electron diffraction, electron-energy-loss spectroscopy (EELS)	Appeared to form as separate crystallites in or on outer layer of clay. Entrained rare earth elements, U, and probably transuranics. This phase was amorphous or partly amorphized.
Uranium silicates	Very sparsely located on glass and 304L retainer surfaces. Were possibly more likely to be observed where 304L retainer interacted with glass.	EDS	Positive phase identification of these rarely encountered crystallites was not possible; they did not appear in any Auger electron microscopy (AEM) samples.
Iron silicates, iron silicate hydrates, and iron oxyhydrates	In some cases, iron-rich layers grew on glass where it contacted 304L retainer. Separate material and crystals found on most glass and 304L retainer surfaces.	EDS, electron diffraction	Electron diffraction generally found these materials to be amorphous. Fayalite was identified in one instance by electron diffraction.
Thorium titanium iron silicate	Appeared to precipitate colloiddally between glass and clay layer or in other regions of restricted water flow	EDS, EELS	This material was amorphous and grew as wisps that were usually mixed with the clay. The clay appeared to serve as a barrier, trapping this material between the glass and the clay "backbone."
Zeolites	Rarely encountered (possibly artifacts).	EDS, electron diffraction	Only two instances observed; once in the scanning electron microscopy (SEM) (N3#8 glass top) and once in the AEM (N3#3 glass bottom). Electron diffraction identified the later as a member of the heulandite subgroup.
Amorphous silica	Occasional white surface particulates	EDS, EELS, electron diffraction (as diffuse rings)	The conditions that, for silica rather than clay formation, are unknown

### 2.2.2.2.3 References

- ANL (1996). *NNWSI Unsaturated Test Procedure*. (NNWSI-05-011, Rev. 4) Argonne IL: Argonne National Laboratory, Chemical Technology Division.
- Bates, J. K., and T. J. Gerding (1990). *Application of the NNWSI Unsaturated Test Method to Actinide Doped SRL 165 Type Glass*. (ANL-89/24) Argonne, IL: Argonne National Laboratory Report.
- Bates, J. K., J. P. Bradley, A. Teetsov, C. R. Bradley, and M. Buchholtz ten-Brink (1992). "Colloid formation during waste form reaction: Implications for nuclear waste-disposal. *Science* 256(5057):649-651.
- Fortner, J. A., and J. K. Bates (1996). "Long-Term Results from Unsaturated Durability Testing of Actinide-Doped DWPF and WVDP Waste Glasses." In proceedings from *Mat. Res. Soc.* 412:205-211.
- Fortner J. A., T. J. Gerding, and J. K. Bates (1995). "Long-Term Test Results from a West Valley Actinide-Doped Reference Glass," in "Environmental Issues and Waste Management Technologies in the Ceramic and Nuclear Industries." V. Jain and R. Palmer (Eds.). *Ceramic Trans.* 61: 45-462.
- Fortner J. A., J. K. Bates, and T. J. Gerding (1997). *Analysis of Components from Drip Tests with ATM-10 Glass*. (ANL-96/16) Argonne, IL: Argonne National Laboratory.

## Section 2.2.2.3 Contents

2.2.2.3	Soluble-Precipitated/Colloidal Species .....	2.2.2.3-1
2.2.2.3.1	Colloidal Particle Analysis of Unsaturated Tests.....	2.2.2.3-1
2.2.2.3.1.1	Colloidal Particle Analyses .....	2.2.2.3-1
2.2.2.3.1.2	Summary.....	2.2.2.3-1
2.2.2.3.1.3	Ongoing Work.....	2.2.2.3-2
2.2.2.3.2	References.....	2.2.2.3-2

### **2.2.2.3: Soluble-Precipitated/Colloidal Species**

**Version 1.3  
July 23, 1998**

#### **2.2.2.3.1 Colloidal Particle Analysis of Unsaturated Tests**

##### **2.2.2.3.1.1 Colloidal Particle Analyses**

Small samples (~5 $\mu$ l) of the N2 and N3 unsaturated-drip-test fluids have been wicked through a porous or "holey" carbon-transmission electron-microscope grid to allow Auger electron microscopy (AEM) examination of suspended particles. In both the N2 and N3 tests, the majority of colloidal particles observed by AEM have been either a smectite-type clay or a variety of iron-silicates. Both clays and iron silicates can sorb actinides, and thus these colloids represent potential transport mechanisms for insoluble elements.

As stated in Sections 2.2.2.2.1 and 2.2.2.2-2, more than 90% of the Pu and Am in solution from the N2 and N3 tests appears to be associated with particulate matter that will not pass through a 1- $\mu$ m filter. In the N2 tests, both the clay and iron-silicate colloids are sometimes observed to contain small amounts of U. U is also observed on occasion in the clays and iron-silicates from the N3 tests; Th is generally detected only in an alteration phase such as brockite (Fortner and Bates, 1996; Bates et al., 1992; Fortner et al., 1995) and not in the clay itself (see Table 2.2.2.2-8 and discussion).

##### **2.2.2.3.1.2 Summary**

Drip tests designed to replicate the synergistic interactions among waste glass, repository groundwater, water vapor, and sensitized 304L stainless steel in the proposed Yucca Mountain repository have been in progress for with actinide-doped glasses more than 10 yr. The N2 test series on defense waste-processing facility (DWPF) -type glass has clearly demonstrated the importance of alteration phases in controlling actinide release from the corroding waste glass. These alteration phases may be spalled from the glass surface, releasing the actinides as solution-borne colloids and particulates. Unusual actinide-containing phases, several of which have been identified, formed on waste glass from the West Valley Demonstration Project (WVDP) in the N3 tests. As with the N2 tests, actinides in the N3 tests were initially retained in the alteration phases; they were later released by layer spallation as glass corrosion progressed. This alteration/spallation process effectively results in near-congruent release of elements from the glass, irrespective of their solubilities.

### 2.2.2.3.1.3 Ongoing Work

The N2 and N3 tests will continue, and updates of data and interpretations will be made in reports and publications in refereed journals. Detailed analysis of the sequentially filtered solution data and AEM examination of colloids will be performed. Because it appears from recent data that the spallation rate is increasing for actinide-bearing phases from the waste package test assembly, the role of colloidal particles in controlling release rates is expected to become correspondingly more important. An example of data now available but previously unpublished include Tc release, which is available for sample periods since 1993. Total mass-release rates for Tc from the N2 and N3 tests appear in Table 2.2.2.3-1.

Table 2.2.2.3-1 Release rates over the latest 2.5-yr period for Tc from the N2 and N3 tests series

Test Series	Tc Release Rate (ng year <sup>-1</sup> )
N2-9	2.9
N2-10	25
N2-12	15
N3-9	15
N3-10	3.3
N3-12	16

### 2.2.2.3.2 References

Bates, J. K., J. P. Bradley, A. Teetsov, C. R. Bradley, and M. Buchholtz ten-Brink (1992). "Colloid formation during waste from reaction: Implications for nuclear waster-disposal." *Science* 256(5057):649-651.

Fortner, J. A., and J. K. Bates (1996). "Long-Term Results from Unsaturated Durability Testing of Actinide-Doped DWPF and WVDP Waste Glasses." In proceedings from *Mat. Res. Soc.* 412:205-211.

Fortner J. A., T. J. Gerding, and J. K. Bates (1995). "Long-Term Test Results from a West Valley Actinide-Doped Reference Glass," in "Environmental Issues and Waste Management Technologies in the Ceramic and Nuclear Industries." V. Jain and R. Palmer (Eds.). *Ceramic Trans.* 61: 455-462.

## Contents for Section 3.2.2

3.2.2	Oxidation Models.....	3.2.2-1
3.2.2.1	Summary.....	3.2.2-1
3.2.2.2	Introduction.....	3.2.2-2
3.2.2.3	Oxidation Response of $\text{UO}_2$ to $\text{U}_4\text{O}_9$ .....	3.2.2-4
3.2.2.4	Oxidation Response of $\text{U}_4\text{O}_9$ to $\text{U}_3\text{O}_8$ .....	3.2.2-15
3.2.2.5	Comparison of Model Response to Oven Drybath Data .....	3.2.2-25
3.2.2.6	Model Predictions of Spent-Fuel Oxidation in a Constant 100°C Temperature Environment.....	3.2.2-30
3.2.2.7	Chemical and Physical Alteration of Spent Fuel.....	3.2.2-32
3.2.2.8	Oxidation Studies of Spent Fuel.....	3.2.2-34
3.2.2.9	Model Enhancements.....	3.2.2-37
3.2.2.10	Model Predictions of $\text{U}_4\text{O}_9 \rightarrow \text{U}_3\text{O}_8$ with TGA Experiments ....	3.2.2-39
3.2.2.11	Model Predictions of $\text{U}_4\text{O}_9 \rightarrow \text{U}_3\text{O}_8$ with Oven Drybath Experiments .....	3.2.2-49
3.2.2.12	Discussion of Modeling Comparisons with Experimental $\text{U}_4\text{O}_9 \rightarrow \text{U}_3\text{O}_8$ Histories.....	3.2.2-60
3.2.2.13	Environmental Impacts of Oxidation of $\text{UO}_2$ .....	3.2.2-60
3.2.2.14	References.....	3.2.2-63

## Section 3.2.2: Oxidation Models

Version 1.3

July 23, 1998

### 3.2.2.1 Summary

This version (1.3) of the *Waste Form Characteristics Report (WFCR)* presents a review of the oxidation-response model that was developed for the two phase transitions:  $\text{UO}_2 \rightarrow \text{U}_4\text{O}_9$  and  $\text{U}_4\text{O}_9 \rightarrow \text{U}_3\text{O}_8$ , and its predictions for the geological repository. Because of the higher potential risk associated with the  $\text{U}_3\text{O}_8$  phase, modeling its phase transformation is emphasized.

In WFCR Version 1.2, the Arrhenius kinetic parameters for both phase transformations were obtained from a set of thermogravimetric-analysis (TGA) experiments of small (200 mg) ATM-105 spent-fuel samples (burnup 27 MWd/kgU). These TGA experiments were conducted at temperatures ranging from 283 to 325°C. That the two phase formation models gave reasonable responses was verified by comparing the model to an independent set of experimental data.

The oven drybath (ODB) experiments used a wide variety of pulverized and spent-fuel fragment sample (5 g); these experiments were conducted at 255°C. It was shown that the oxidation history could be explained by an envelope of various sizes of  $\text{UO}_2$  grains. This review of the kinetic-phase-transformation models and the predictions are presented in Sections 3.2.2.1 through 3.2.2.5.

Sections 3.2.2.6 through 3.2.2.11 presents new material whose focus is the formation of  $\text{U}_3\text{O}_8$ . Although Stout et al. (1993a, 1993b) predicted burnup would be a very important property in spent-fuel oxidation, only recently has Hanson (1998) obtained experimental evidence verifying this theoretical prediction. He showed that the activation energy for the phase transformation  $\text{U}_4\text{O}_9 \rightarrow \text{U}_3\text{O}_8$  varies linearly with burnup. Independent experimental evidence shows that, for burnups greater than 40 MWd/kgU, the  $\text{UO}_2$  grains undergo major restructuring to a much finer and more porous structure.

Several pieces of experimental information were combined in the new theoretical study. First, as  $\text{U}_4\text{O}_9$  forms, the relatively large, unoxidized  $\text{UO}_2$  grains undergo shrinkage cracking, yielding a log normal distribution of  $\text{U}_4\text{O}_9$  grains. Second, the linear activation-energy relation with burnup was also used. Using this approach, half of the TGA and ODB experiment histories were very closely matched. The other set of experiments could not be matched without using unrealistically small  $\text{U}_4\text{O}_9$  grains. Examination (by scanning electron microscopy [SEM] and X-ray fluorescence [XRF]) of some of these questionable samples revealed that a thin layer of what appears to be dehydrated schoepite had formed on the spent fuel. By adjusting

the activation energy of some grain fractions downward, all TGA- and ODB-model history curves were within a 5% error of the experimental histories. Such close agreement of the model histories with experimental histories validates the model.

Using reasonable average grain sizes for  $U_4O_9$ , the model predicted the volume fractions of  $U_3O_8$  formed at 100 and 200°C at burnups of 25, 50, and 75 MWd/kgU. Even though the higher burnup fuels had smaller average grain sizes, the increased activation energy with burnup suppressed  $U_3O_8$  formation, even at a higher constant temperature.

### 3.2.2.2 Introduction

$UO_2$  spent fuels oxidize to higher uranium oxide phases in an oxygen atmosphere. The oxidation response of spent fuels impacts the radionuclide-release performance in potential repository environments because of two independent functional properties of the higher oxides:

1. Due to geometrical surface area and volume changes that occur as the higher oxides form
2. Due to chemical changes that yield higher dissolution rates of the  $U_3O_8$  oxide and the  $UO_3$  oxide hydrates

To include these known impacts from  $UO_2$  spent-fuel oxidation for performance assessment (PA) analyses, a model for fuel-oxidation response has been developed.

Model development depends strongly on experimental data obtained from TGA and ODB oxidation testing methods. The modeling approach derives functional forms and uses functional relations consistent with the observed spent-fuel oxidation processes. These functional relations have parametric constants (e.g., the activation energy in the Arrhenius rate expression) that are evaluated by using subsets of the experimental data. The models for spent-fuel oxidation described in the following subsection provide response functions for the elapsed time to higher oxidation phases. These response functions depend on temperature, nominal grain size, and time.

Recent experimental studies have shown that the Arrhenius kinetics are burnup-dependent. The literature shows that, as the concentration of fission products (especially the rare earth isotopes) and the generated actinide products increase with burnup,  $UO_2$  becomes progressively more difficult to oxidize. Oxidation of the  $UO_2 \rightarrow U_4O_9$  has also shown to be controlled by diffusion of oxygen through the increasingly thicker layer of  $U_4O_9$ , with smaller-grained fuels oxidizing faster in accordance to a larger surface area to volume (SA/V) ratio. Thus, the rate of oxidation to higher uranium-oxide forms depends on burnup and the distribution of grain half-sizes. Although idealized, the model development is considered representative of the observed experimental processes that occur in spent-fuel oxidation. With the idealizations, the oxidation-response models for the different phase transformations can be easily applied to provide bounding evaluations and

best-estimate values for oxidation impacts of spent-fuel performance in potential repository environments. The two spent-fuel oxidation-phase responses discussed in the following subsections are the  $\text{UO}_2 \rightarrow \text{U}_4\text{O}_9$  phase transformation and the  $\text{U}_4\text{O}_9 \rightarrow \text{U}_3\text{O}_8$  phase transformation.

The  $\text{U}_4\text{O}_9 \rightarrow \text{U}_3\text{O}_8$  phase transformation model used TGA oxidation data to evaluate kinetic parameters as a function of burnup. To partially substantiate the model, the oxidation data were compared to the predictions of the  $\text{U}_4\text{O}_9 \rightarrow \text{U}_3\text{O}_8$  oxidation model. This comparison with ODB data provided preliminary confirmation of the oxidation modeling development that used kinetic parameters evaluated from TGA data.

The updated model discussed in this section has the following new features:

- Activation-energy-dependence on burnup
- Log-normal distributions of grain half-sizes to account for the grain-cracking observed during  $\text{U}_4\text{O}_9$  formation
- The effect of what appears to be dehydrated schoepite formation observed on some experimental samples

At burnups greater than 40 to 45 MWd/kgU, the pellet rim progressively changes physically: the grain sizes get smaller, and takes on a porous cauliflower structure. In the previous version of this report, the bounding calculations were based on Arrhenius kinetics of ATM-105 spent fuel having a burnup of 27 MWd/kgU and larger grain sizes. Using the new information, the new performance predictions are considered much more realistic.

Fuels of sufficiently high burnup that have experienced restructuring in the rim region have much smaller grains, compared to the low-to-intermediate-burnup spent fuels. However, the activation energy for the  $\text{U}_4\text{O}_9 \rightarrow \text{U}_3\text{O}_8$  phase transformation varies linearly with burnup. The exponential dependence of this activation energy is orders of magnitude more important in suppressing this phase transformation than is the inversely proportional grain-size dependence in accelerating it.

The improved models, which is based on more recent information that will be presented, yields excellent fits to the TGA and the ODB tests. This agreement gives an extra degree of confidence that predictions of long-term geological repository safety of low- and high-burnup spent fuel are warranted.

Sections 3.2.2.2 through 3.2.2.5 present a review of the previous work; Sections 3.2.2.6 through 3.2.2.11 present more recent information, model enhancements, comparisons with TGA and ODB experiments, and improved predictions for safety of the geological repository.

### 3.2.2.3 Oxidation Response of $\text{UO}_2$ to $\text{U}_4\text{O}_9$

The first oxidation-phase transition of  $\text{UO}_2$  spent fuel produces a  $\text{U}_4\text{O}_9$  lattice structure with a weight-gain "oxide" of  $\text{UO}_{-2.42}$ . Thus, the  $\text{U}_4\text{O}_9$  phase is not stoichiometric. This  $\text{U}_4\text{O}_9$  phase-transition time response has an Arrhenius temperature-dependence and a geometric dependence on grain size. At early times, the  $\text{U}_4\text{O}_9$  phase progresses very rapidly down the grain boundaries of the  $\text{UO}_2$  spent fuels. This elapsed time to oxidize grain boundaries is neglected in the following oxidation-response models. The rapid grain boundary oxidation is partly due to fission gas bubbles, which form on grain boundaries in spent fuels during reactor operation. These gas bubbles enhance porosity and decrease density of material in a grain boundary relative to material in an adjacent grain volume.

In addition, the  $\text{U}_4\text{O}_9$  lattice is more dense (has less specific volume) than that of the initial  $\text{UO}_2$  by about 1.5 to 2.0%. This higher density phase promotes grain-boundary cracking and opens grain-boundary pathways for oxygen transport to the surfaces of all the grain volumes in a spent-fuel fragment. The subsequent  $\text{U}_4\text{O}_9$  oxidation of grain volumes is observed to progress as a  $\text{U}_4\text{O}_9$  phase front that propagates into each  $\text{UO}_2$  grain. Behind this phase front is the  $\text{U}_4\text{O}_9$  crystal lattice structure with a weight-gain oxide of  $\text{UO}_{-2.42}$ . The rate of propagation of the  $\text{U}_4\text{O}_9$  front was conservatively evaluated as part of the ODB testing (Einziger, et al., 1992; Thomas, et al., 1992).

For a set of spent-fuel samples, experiments measured the position of the  $\text{U}_4\text{O}_9$ - $\text{UO}_2$  oxidation front relative to the grain boundary. Each sample in the set was oxidized for a different duration. These measurements of widths of  $\text{U}_4\text{O}_9$  oxidation front (relative to the grain boundary) versus oxidation time had an approximate square root time-dependence at constant temperature. The temperature-dependence was assumed to be an Arrhenius exponential function. Using this time- and temperature-dependence, the data in an upper bounding band were used to evaluate parameters  $k$  and  $Q$  in the following equations for the width  $W$  of the  $\text{U}_4\text{O}_9$  oxidation front

$$W = 2\sqrt{kt}$$

3.2.2-1

where

$t$  = time (hours, h)

$k$  =  $k_0 \exp(-Q_{49}/RT)$

$k_0$  =  $1.04 \times 10^8$  ( $\mu\text{m}^2/\text{h}$ )

$Q_{49}$  = 24.0 kcal/mole (Arrhenius activation energy for the reaction  $\text{UO}_2 \rightarrow \text{U}_4\text{O}_9$ )

$R$  = 1.986 cal/mole/ $^\circ\text{K}$  (gas constant)

$T$  = temperature (Kelvin)

The time derivative of Eq. 3.2.2-1 gives the rate that the  $U_4O_9$  propagates into a grain volume of  $UO_2$ , which, at constant temperature, is

$$\dot{W} = \sqrt{k/t} \quad 3.2.2-2$$

and which has an initial square root in time singularity. This is typical for surface-film formations that are rate-controlled by diffusion through a film of increasing thickness.

From Eq. 3.2.2-1, the elapsed time for oxidation of  $UO_2$  grains to  $U_4O_9$  can be evaluated by solving for time. Thus, the elapsed time  $t_{2,4}$  to fully oxidize a  $UO_2$  grain of nominal dimension  $2W_0$  to  $U_4O_9$  in atmospheric air at constant temperature  $T$  is

$$t_{2,4} = W_0^2 / (4k_0 \exp(-Q_{4,0}/RT)) \quad 3.2.2-3$$

Table 3.2.2-1 lists the values of  $t_{2,4}$  for different temperatures and different nominal grain sizes.

Table 3.2.2-1 Elapsed time  $t_{2,1}$  for  $U_4O_9$

Phase Transformation of UO <sub>2</sub> for Grain Size				T in C	250	200	150	100	75	50	25
2Wo And Constant Temperature.				T in K	523.2	473.2	423.2	373.2	348.2	323.2	298.2
Wo=Grainsize/2	DVU409/VUO2	DW/Wo	DW								
10E-6 meters			10E-6 m	2.4 Times in Hours, One Year = 24*365 = 8760 hours							
5	1	1	5	6.4558E+02	7.4109E+03	1.5144E+05	6.9461E+06	7.1027E+07	1.0407E+09	2.3916E+10	
10	1	1	10	2.5823E+03	2.9643E+04	6.0577E+05	2.7784E+07	2.8411E+08	4.1627E+09	9.5663E+10	
15	1	1	15	5.8102E+03	6.6698E+04	1.3630E+06	6.2515E+07	6.3924E+08	9.3660E+09	2.1524E+11	
20	1	1	20	1.0329E+04	1.1857E+05	2.4231E+06	1.1114E+08	1.1364E+09	1.6651E+10	3.8265E+11	
25	1	1	25	1.6139E+04	1.8527E+05	3.7860E+06	1.7385E+08	1.7757E+09	2.6017E+10	5.9789E+11	
30	1	1	30	2.3241E+04	2.6879E+05	5.4519E+06	2.5006E+08	2.5570E+09	3.7464E+10	8.6097E+11	
35	1	1	35	3.1633E+04	3.6313E+05	7.4206E+06	3.4036E+08	3.4803E+09	5.0993E+10	1.1719E+12	
				2.4 Times in Years							
				7.3696E-02	8.4599E-01	1.7288E+01	7.9293E+02	8.1081E+03	1.1880E+05	2.7301E+06	
				2.9478E-01	3.3840E+00	6.9151E+01	3.1717E+03	3.2433E+04	4.7519E+05	1.0920E+07	
				6.6326E-01	7.6139E+00	1.5559E+02	7.1364E+03	7.2973E+04	1.0692E+06	2.4571E+07	
				1.1791E+00	1.3536E+01	2.7661E+02	1.2687E+04	1.2973E+05	1.9008E+06	4.3682E+07	
				1.8424E+00	2.1150E+01	4.3220E+02	1.9823E+04	2.0270E+05	2.9699E+06	6.8253E+07	
				2.6530E+00	3.0456E+01	6.2236E+02	2.8546E+04	2.9189E+05	4.2767E+06	9.8284E+07	
				3.6111E+00	4.1453E+01	8.4710E+02	3.8854E+04	3.9730E+05	5.8211E+06	1.3378E+08	

Parameters: Q49 = 24,000 cal/mole, kD = 1.04E + 8 micron<sup>2</sup>/h, R = 1.986 cal/mole/K

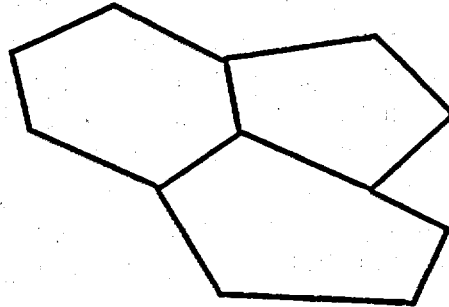
The use of constant temperature for elapsed times is an easy way to conservatively bound the time for full oxidation: pick the highest temperature value in the time interval. For repository evaluations, after the initial heat-up period, the temperatures are expected to be monotonically decreasing. Thus the temperature value when the spent fuel is initially exposed is conservatively high for the shortest elapsed time. To obtain a better approximation for the  $t_{2,4}$  elapsed time, the rate Eq. 3.2.2-2 can be assumed valid for quasi-steady temperature processes. Then the elapsed time  $t_{2,4}$  can be found by integration over the time-dependent temperature history such that  $W$  at  $t_{2,4}$  equals  $W_0$ .

The grain size is the other variable dependence in Eq. 3.2.2-3 used to calculate elapsed times for oxidation of  $UO_2 \rightarrow U_4O_9$ . Samples of spent fuels have a statistical distribution of grain sizes and geometrical shapes. Large samples for oxidation testing give better integration and averaging of grain-size distribution. This averaging process would tend to conceal second-order, or small, effects related to a detailed dependence on the statistical distribution attributes other than the mean, or average, grain size of a sample.

Similarly, the various geometric shapes, from six-sided cubic to many-sided approaching spherical, tend to be averaged over when testing with large samples. In the following, which is considered an effective or "macro" representation for oxidation response, grain-size distribution attributes are reduced to one, the nominal or average dimension of the grains. The nominal grain size will vary from sample to sample and does depend on the approved testing material (ATM) of the sample. Finally, to reduce modeling complexities, the geometric shape of the individual grains is assumed to be cubic; each grain is assumed to be subdivided into six pyramids with square bases. The cubes fill space contiguously and simplify the visualization of an idealized  $U_4O_9$  phase boundary propagating into a pyramidal subdivision of a cubical  $UO_2$  grain.

With the simplification of only nominal grain size and cubic-shaped grains, oxidation response for the volumetric quantity of  $U_4O_9$  at any time will be represented first as a rate and then as a time integral. Figures 3.2.2-1 through 3.2.2-3 provide sketches of the generic approach to create triangular (two-dimensional) spatial subsets and pyramidal (three-dimensional) spatial subsets of  $UO_2$  to  $U_4O_9$  oxidation fronts.

A set of grain volumes (In cross section)



Put a point at the center of each grain, and decompose into a set of pyramids (triangles in cross section).

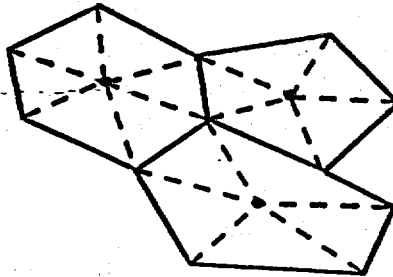


Figure 3.2.2-1 Grain set decomposed to pyramidal volume subsets

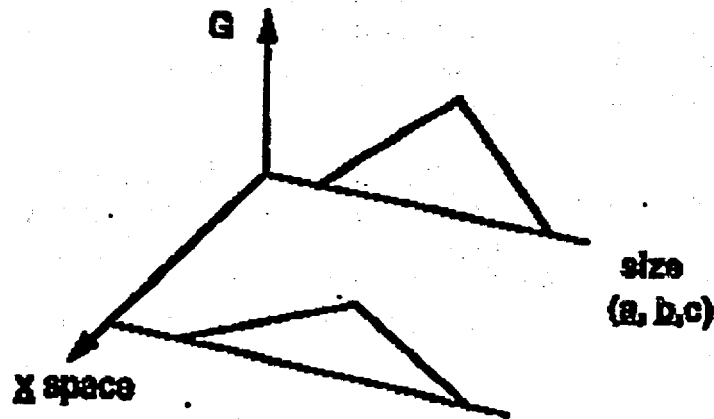


Figure 3.2.2-2 Density function: probable number of grain pyramids

Large numbers of grain pyramids exist, many of which are of the same size (compact domain set). A size can be identified by attributes  $(a, b, c)$ , as illustrated. Let  $G(x, t, a, b, c)$  denote the probable number of pyramids of size  $(a, b, c)$  in a unit spatial volume of grains about point  $x$  at time  $t$ .

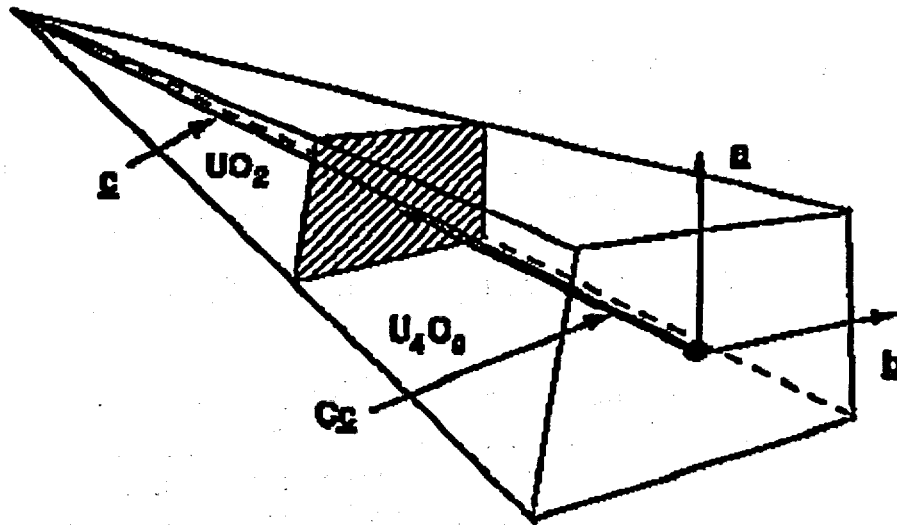


Figure 3.2.2-3 Grain volume oxidation front: pyramidal volume in an oxidizing grain and its associated physical attributes

The size attributes of the pyramids shown in Figure 3.2.2-3 are vector sets  $(\underline{a}, \underline{b}, \underline{c})$ . Vectors  $\underline{a}$  and  $\underline{b}$  are the bases vectors of the pyramid, and  $\underline{c}$  is the height vector from a base (face of a cube) to the center of the grain. There are six vector sets per cube. In the case of cubic grains, the length  $W_0$  of vector  $\underline{c}$  is one-half the length of vector  $\underline{a}$  or  $\underline{b}$ .

The rate of oxygen weight gain for a single pyramid is equal to the instantaneous area of the front moving at its frontal velocity along vector  $\underline{c} \times$  the weight of oxygen added to convert  $\text{UO}_2$  to  $\text{U}_4\text{O}_9$ , at oxide weight of  $\text{UO}_{2.4}$ . The instantaneous area is linearly reduced in vectors  $\underline{a}$  and  $\underline{b}$  as the front moves along vector  $\underline{c}$ . This area-reduction can be written in terms of a scalar function of time  $C(t)$ , which has a value between zero and one and scales the length of vector  $\underline{c}$  that has been converted to  $\text{U}_4\text{O}_9$ , from  $\text{UO}_2$ . When  $C$  equals zero, the pyramid is all  $\text{UO}_2$ ; when  $C$  equals one, the pyramid is all  $\text{U}_4\text{O}_9$ . Thus,  $\underline{c} \dot{C}(t)$  is the current width of the  $\text{U}_4\text{O}_9$  front. At width  $C(t)$ , the reduced length of  $\underline{a}$  and  $\underline{b}$  would be  $\underline{a}(1-C)$  and  $\underline{b}(1-C)$ , respectively. The  $\text{U}_4\text{O}_9$  frontal velocity would be  $\underline{c} \dot{C}(t)$ . From Eq. 3.2.2-2 for  $\dot{W}$ , the function of  $\dot{C}(t)$  is given by

$$\dot{C}(t) = \dot{W}/|\underline{c}| = \sqrt{k/t}/|\underline{c}| \quad 3.2.2-4$$

where  $|\underline{c}|$  is the scalar magnitude of vector  $\underline{c}$ , and  $k$  is a function of temperature. The amount of oxygen added per atom of uranium to form the  $\text{UO}_2$  oxide at the points on the  $\text{UO}_2$ -to- $\text{U}_4\text{O}_9$  phase front is chemically known to be



3.2.2-5

or 0.42 oxygen atoms per each uranium atom. Thus, when the phase boundary is at  $C_c$ , the rate that oxygen atoms are added per cubic grain of  $\text{UO}_2$  is

$$[\dot{O}] = 0.42[U]\dot{C}(t)c_i e_{ijk} a_j (1-C(t))b_k (1-C(t)) \quad 3.2.2-6$$

In Eq. 3.2.2-6,  $e_{ijk}$  is an alternating tensor used to form the vector dot product of  $\underline{c}$  with the vector cross product of vectors  $\underline{a}(1-C)$  and  $\underline{b}(1-C)$  for the six, pyramidal pieces of a cube;  $[U]$  is the number of uranium atoms per unit volume of the  $\text{UO}_2$  spent fuel. To find the change in  $[O]/[U]$  ratio for a partially oxidized sample of  $\text{UO}_2$  and  $\text{U}_4\text{O}_9$ , Eq. 3.2.2-6 must be multiplied by the number of grains in the sample and integrated over the time interval during which partial oxidation has occurred. This time interval is less than the value of  $t_{2.4}$  evaluated from Eq. 3.2.2-3. For  $G$  number of grains in the samples, this integration yields the following expression (Stout, et al., 1989).

$$[O]/[U](\text{UO}_2 \rightarrow \text{U}_{2.42}; t) = 0.42(6Gc_i e_{ijk} a_j b_k (3C(t) - 3C^2(t) + C^3(t))/3) \quad 3.2.2-7$$

For a sample of  $G$  (total number) cubical grains, this ratio is

$$[O]/[U]V_{\text{UO}_2}(G) = 0.42(3C(t) - 3C^2(t) + C^3(t)) \quad 3.2.2-8a$$

where the initial volume of  $\text{UO}_2$  is

$$V_{\text{UO}_2}(G) = 6Gc_i e_{ijk} a_j b_k / 3 \quad 3.2.2-8b$$

From Eq. 3.2.2-7, the volume amount of  $\text{UO}_{2.4}$ , formed for a sample of  $G$  grains at time  $t < t_{2.4}$  is

$$V_{\text{UO}_{2.4}}(G, t) = 6Gc_i e_{ijk} a_j b_k (3C(t) - 3C^2(t) + C^3(t))/3 \quad 3.2.2-9$$

which is also a parametric function of the temperature history and neglects the small volume decrease (~2%) from the phase transformation. The function  $C(t)$  is the time integration of Eq. 3.2.2-4, with  $C(t=0)$  equal to zero, which is

$$C(t) = 2\sqrt{kt}/|c| \quad \text{and } C(t) = 1 \text{ for } t \geq t_{2.4} \quad 3.2.2-10$$

where  $k$  is given as a function of temperature in Eq. 3.2.2-1, and  $|c|$  is one-half the nominal length of an effective cubic grain. From Eq. 3.2.2-8 and Eq. 3.2.2-9, the volume fraction of a sample of cubic grains that is  $UO_2$  at time  $t$  is given by

$$V_{UO_{2.4}}(G,t)/V_{UO_2}(G) = 3C(t) - 3C^2(t) + C^3(t) \quad 3.2.2-11$$

that, from Eq. 3.2.2-10, depends on grain size and temperature ( $k$  is temperature-dependent).

Eq. 3.2.2-11 can be inverted to find the elapsed time  $t_v$  during which a prescribed volume fraction of  $UO_{2.4}$  has transformed from  $UO_2$  at constant temperature. The inverse is found by adding one to the negative of equation 3.2.2-11 to obtain

$$(1 - C(t))^3 = (1 - V_{UO_{2.4}}/V_{UO_2}) \quad 3.2.2-12a$$

Then

$$C(t) = 1 - (1 - V_{UO_{2.4}}/V_{UO_2})^{1/3} \quad 3.2.2-12b$$

Using equation 3.2.2-1 and 3.2.2-10, the elapsed time  $t_{v,2.4}$  for a prescribed volume fraction of  $UO_{2.4}$  at constant temperature is

$$t_{v,2.4} = |c|^2 \left(1 - (1 - V_{UO_{2.4}}/V_{UO_2})^{1/3}\right)^2 / (4k_o \exp(-Q_{49}/RT)) \quad 3.2.2-13$$

Note that, as the volume fraction of  $UO_{2.4}$  approaches unity, Eq. 3.2.2-13 becomes the same as Eq. 3.2.2-3 because  $W_o$  equals  $|c|$ . Tables 3.2.2-2 through 3.2.2-4 have elapsed times  $t_{v,2.4}$  for 25%, 50%, and 75% volume fractions of  $U_4O_9$ .

Table 3.2.2-2 Elapsed time  $t_{2\sigma}$ , 25%  $U_4O_9$

Phase Transformation of UO2 for Grain Size				T in C	250	200	150	100	75	50	25
2 $\sigma$ And Constant Temperature.				T in K	523.2	473.2	423.2	373.2	348.2	323.2	298.2
W <sub>0</sub> =Grainsize/2	DVU4O9/VUO2	DW/W <sub>0</sub>	DW								
10E-6 meters			10E-6 m	tv24 Times in Hours, One Year = 24*365 = 8760 hours							
5	0.25	0.091439695	0.457198474	5.3978E+00	6.1964E+01	1.2682E+03	5.8078E+04	5.9387E+05	6.7012E+06	1.9997E+08	
10	0.25	0.091439695	0.914396949	2.1591E+01	2.4786E+02	5.0649E+03	2.3231E+05	2.3755E+06	3.4805E+07	7.9986E+08	
15	0.25	0.091439695	1.371595423	4.8580E+01	5.5767E+02	1.1396E+04	5.2270E+05	5.3449E+06	7.8311E+07	1.7997E+09	
20	0.25	0.091439695	1.828793897	8.6365E+01	9.9142E+02	2.0260E+04	9.2924E+05	9.5020E+06	1.3922E+08	3.1994E+09	
25	0.25	0.091439695	2.285992372	1.3494E+02	1.5491E+03	3.1656E+04	1.4519E+06	1.4847E+07	2.1753E+08	4.9991E+09	
30	0.25	0.091439695	2.743190846	1.9432E+02	2.2307E+03	4.5584E+04	2.0908E+06	2.1379E+07	3.1324E+08	7.1987E+09	
35	0.25	0.091439695	3.20038932	2.6449E+02	3.0362E+03	6.2046E+04	2.8458E+06	2.9100E+07	4.2636E+08	9.7983E+09	
				tv24 Times in Years							
				6.1619E-04	7.0735E-03	1.4455E-01	6.6299E+00	6.7794E+01	9.9329E+02	2.2827E+04	
				2.4647E-03	2.8294E-02	5.7819E-01	2.6519E+01	2.7118E+02	3.9732E+03	9.1308E+04	
				5.5457E-03	6.3681E-02	1.3009E+00	5.9669E+01	6.1014E+02	8.9396E+03	2.0544E+05	
				9.8590E-03	1.1318E-01	2.3128E+00	1.0608E+02	1.0847E+03	1.5893E+04	3.6523E+05	
				1.5405E-02	1.7684E-01	3.8137E+00	1.6575E+02	1.6948E+03	2.4832E+04	5.7068E+05	
				2.2183E-02	2.5465E-01	5.2037E+00	2.3868E+02	2.4406E+03	3.5758E+04	8.2177E+05	
				3.0193E-02	3.4660E-01	7.0828E+00	3.2486E+02	3.3219E+03	4.8671E+04	1.1185E+06	

Parameters: Q49 = 24,000 cal/mole, kD = 1.04E + 8 micron<sup>2</sup>/h, R = 1.986 cal/mole/K

Table 3.2.2-3 Elapsed time  $t_{2,}$ , 50%  $U_2O_5$

Phase Transformation of UO2 for Grain Size				T in C	250	200	150	100	75	50	25
2W <sub>o</sub> And Constant Temperature.				T in K	523.2	473.2	423.2	373.2	348.2	323.2	298.2
W <sub>o</sub> =Grainsize/2	DVU4O9/UO2	DW/W <sub>o</sub>	DW								
10E-6 meters			10E-6 m	t/2.4 Times in Hours, One Year = 24*365 = 8760 hours							
5	0.5	0.206299456	1.031497278	2.7475E+01	3.1540E+02	6.4453E+03	2.9562E+05	3.0229E+06	4.4290E+07	1.0178E+09	
10	0.5	0.206299456	2.062994557	1.0990E+02	1.2616E+03	2.5781E+04	1.1825E+06	1.2092E+07	1.7716E+08	4.0714E+09	
15	0.5	0.206299456	3.094491835	2.4728E+02	2.8386E+03	5.8007E+04	2.6606E+06	2.7206E+07	3.9861E+08	9.1606E+09	
20	0.5	0.206299456	4.125989114	4.3961E+02	5.0464E+03	1.0312E+05	4.7299E+06	4.8366E+07	7.0864E+08	1.6285E+10	
25	0.5	0.206299456	5.157486392	6.8688E+02	7.8851E+03	1.6113E+05	7.3905E+06	7.5572E+07	1.1073E+09	2.5446E+10	
30	0.5	0.206299456	6.18898367	9.8911E+02	1.1354E+04	2.3203E+05	1.0642E+07	1.0882E+08	1.5944E+09	3.6642E+10	
35	0.5	0.206299456	7.220480949	1.3463E+03	1.5455E+04	3.1582E+05	1.4485E+07	1.4812E+08	2.1702E+09	4.9874E+10	
				t/2.4 Times in Years							
				3.1385E-03	3.6005E-02	7.3576E-01	3.3747E+01	3.4508E+02	5.0560E+03	1.1619E+05	
				1.2546E-02	1.4402E-01	2.9430E+00	1.3499E+02	1.3803E+03	2.0224E+04	4.6477E+05	
				2.8228E-02	3.2404E-01	6.8219E+00	3.0372E+02	3.1057E+03	4.5504E+04	1.0457E+06	
				5.0183E-02	5.7608E-01	1.1772E+01	5.3995E+02	5.5212E+03	8.0895E+04	1.8591E+06	
				7.8411E-02	9.0012E-01	1.8394E+01	8.4367E+02	8.6269E+03	1.2640E+05	2.9048E+06	
				1.1291E-01	1.2962E+00	2.6487E+01	1.2149E+03	1.2423E+04	1.8201E+05	4.1829E+06	
				1.5369E-01	1.7642E+00	3.6052E+01	1.6536E+03	1.6909E+04	2.4774E+05	5.6934E+06	

Parameters: Q49 = 24,000 cal/mole, kD = 1.04E + 8 micron<sup>2</sup>/h, R = 1.986 cal/mole/K

Table 3.2.2-4 Elapsed time  $t_{2,4}$ , 75%  $U_4O_9$

Phase Transformation of UO <sub>2</sub> for Grain Size				T in C	250	200	150	100	75	50	25
2W <sub>0</sub> And Constant Temperature.				T in K	523.2	473.2	423.2	373.2	348.2	323.2	298.2
W <sub>0</sub> =Grainsize/2	DVU4O9/VUO2	DW/W <sub>0</sub>	DW								
10E-6 meters			10E-6 m	iv2.4 Times in Hours, One Year = 24*365 = 8760 hours							
5	0.75	0.370039446	1.85019723	8.8398E+01	1.0148E+03	2.0737E+04	9.5112E+05	9.7257E+06	1.4250E+08	3.2748E+09	
10	0.75	0.370039446	3.700394459	3.5359E+02	4.0591E+03	8.2947E+04	3.8045E+06	3.8903E+07	5.6999E+08	1.3099E+10	
15	0.75	0.370039446	5.550591689	7.9558E+02	9.1329E+03	1.8663E+05	8.5601E+06	8.7531E+07	1.2825E+09	2.9473E+10	
20	0.75	0.370039446	7.400788919	1.4144E+03	1.6236E+04	3.3179E+05	1.5218E+07	1.5561E+08	2.2800E+09	5.2396E+10	
25	0.75	0.370039446	9.250986149	2.2100E+03	2.5369E+04	5.1842E+05	2.3778E+07	2.4314E+08	3.5624E+09	8.1869E+10	
30	0.75	0.370039446	11.10118338	3.1823E+03	3.6531E+04	7.4652E+05	3.4240E+07	3.5013E+08	5.1299E+09	1.1789E+11	
35	0.75	0.370039446	12.95138061	4.3315E+03	4.9723E+04	1.0161E+06	4.6605E+07	4.7656E+08	6.9824E+09	1.6046E+11	
				iv2.4 Times in Years							
				1.0091E-02	1.1584E-01	2.3672E+00	1.0858E+02	1.1102E+03	1.6267E+04	3.7383E+05	
				4.0364E-02	4.6336E-01	9.4688E+00	4.3430E+02	4.4410E+03	6.5067E+04	1.4953E+06	
				9.0820E-02	1.0426E+00	2.1305E+01	9.7718E+02	9.9922E+03	1.4640E+05	3.3645E+06	
				1.6146E-01	1.8534E+00	3.7875E+01	1.7372E+03	1.7764E+04	2.6027E+05	5.9813E+06	
				2.5228E-01	2.8960E+00	5.9180E+01	2.7144E+03	2.7756E+04	4.0667E+05	9.3458E+06	
				3.6328E-01	4.1703E+00	8.5220E+01	3.9087E+03	3.9969E+04	5.8561E+05	1.3458E+07	
				4.9446E-01	5.6762E+00	1.1599E+02	5.3202E+03	5.4402E+04	7.9707E+05	1.8318E+07	

Parameters: Q<sub>49</sub> = 24,000 cal/mole, kD = 1.04E + 8 micron<sup>2</sup>, R = 1.986 cal/mole/K

In summarizing the above oxidation model for the phase transition of  $\text{UO}_2$  to  $\text{U}_4\text{O}_9$  (often written as  $\text{UO}_{2.4}$  or  $\text{UO}_{2.42}$ ), Eq. 3.2.2-3 can be evaluated for the elapsed time  $t_{2.4}$  for complete transformation of  $\text{UO}_2$  to  $\text{U}_4\text{O}_9$ . Eq. 3-2-2-10 [for  $C(t)$ ] and Eq. 3.2.2-11 can be evaluated for the volume fraction of  $\text{UO}_{2.4}$  relative to  $\text{UO}_2$  at times  $t$  less than  $t_{2.4}$ . Eq. 3.2.2-13 can be evaluated for the time  $t_{2.4}$  at which a prescribed fractional volume of  $\text{UO}_{2.4}$  relative to  $\text{UO}_2$  is attained. In each case, the results calculated from these equations depend on grain size  $|L|$  and temperature history  $T$ .

A full comparison of this model with future TGA and ODB oxidation weight-gain data will be provided as part of a model-validation process. Because grain size is a parameter of the model and has a distribution in any sample, a bounding model will most likely be proposed. For now, a nominal value for grain size is recommended to be an estimated average value of the particular spent fuel sample's grain size. The grain size is not a parameter readily known for all commercial spent fuels. A best estimate may be obtainable by a survey of nuclear fuel vendors. Otherwise, the range of grain size in the current ATM could be used as a sparse data set from which to stochastically evaluate the oxidation impact on spent fuel performance in a suitable repository.

#### 3.2.2.4 Oxidation Response of $\text{U}_4\text{O}_9$ to $\text{U}_3\text{O}_8$

Following the  $\text{UO}_2$ -to- $\text{U}_4\text{O}_9$ -phase transformation, the second oxidation-phase transition of spent fuels is from  $\text{U}_4\text{O}_9$  to a  $\text{U}_3\text{O}_8$  phase. The transition time to initiate the  $\text{U}_3\text{O}_8$ -phase change has a temperature-dependent delay time. The kinetics of this delay-time response is not understood in detail. It is believed to be related to the elapsed time for diffusion of oxygen into grain volumes and surface adsorption of oxygen onto grain surfaces of the  $\text{U}_4\text{O}_9$ . Hanson (1998) showed that the plateau and the oxidation to  $\text{U}_3\text{O}_8$  have the same activation energies and explained this observation as a restructuring of the crystal lattice. Until  $\text{UO}_2$  is fully converted to the  $\text{U}_4\text{O}_9$  phase, there will be no  $\text{U}_3\text{O}_8$  formation. During the delay-time interval, these diffusion and adsorption processes increase the local spatial concentration of oxygen atoms sufficiently for the  $\text{U}_3\text{O}_8$  oxidation transformation to occur. Early observations indicated that the delay time was relatively monotonic with respect to temperature. That is, the lower constant temperature tests showed longer elapsed times to initiate the transformations of  $\text{U}_3\text{O}_8$  (Einzig, et al., 1992, 1995). The duration of this elapsed time was estimated to be long at low temperatures ( $6 \times 10^7$  yr at  $100^\circ\text{C}$ ).

However, recent TGA test data show variations in the elapsed times for  $\text{U}_3\text{O}_8$  initiation at constant temperature. The elapsed-time duration is the length of time that a plateau exists in the oxygen-to-metal (O/M) weight-gain-time response plots of the test data. The variations in elapsed times are observed for a sequence of TGA tests, which are all at the same constant temperature, on small (~200 mg) spent-fuel fragments from the high-burnup region of the same fuel rod. This suggests that the variability is associated with small spatial differences of the spent-fuel test samples.

The current conjecture is that the radial location of a test sample influences the  $U_3O_8$  oxidation response. This radial dependence is linked to a well-known "rim" region on the circumference of the pellet where higher  $^{238}U$  resonance-capture of incoming neutrons occurs. This locally increases the density of plutonium isotopes and correspondingly enriches fissile isotopic density in the rim region ( $\sim 200 \mu\text{m}$ ). The consequences of this enriched fissile-density radial gradient is a radial burnup gradient with higher concentrations of fission products and actinides in the rim region relative to the central portion of a pellet. It is hypothesized that the sample-to-sample variations in observed  $U_3O_8$ -oxidation response are due to radial chemical compositional variations from the burnup gradient. Until these variations are understood, no credible model for the plateau delay time to initiate  $U_3O_8$ -oxidation response can be analytically represented. In terms of time-response models of oxidation, the neglect of this plateau delay time is conservative. This leads to a modeling assumption that the  $U_3O_8$ -oxidation response is initiated at the time the  $U_4O_9$  phase transformation is completed. This elapsed time is  $t_{2.4}$  evaluated from Eq. 3.2.2-3.

For times  $t$  greater than  $t_{2.4}$ , the following preliminary model of  $U_3O_8$  oxidation response is based on five assumptions:

1. The oxide that forms on the outer surfaces of the  $U_4O_9$  grains is essentially  $U_3O_8$  phase. ( $U_3O_8$  lattice has been identified in the TGA test samples; however, some powders found in the ODB 255°C test samples remain an enigma.)
2. The oxide surface is nonprotective; this follows for a  $U_3O_8$  phase because the large ( $\sim 30\%$ ) volume increase of  $U_3O_8$  relative to  $U_4O_9$ , causes the  $U_3O_8$  oxide surface to crack and spall, leaving the  $U_4O_9$  surface continuously exposed.
3. The  $U_3O_8$  boundary proceeds at constant speed into the  $U_4O_9$  grain volumes, which is really a consequence of the second assumption.
4. The high temperature data (250°C to 300°C) can be extrapolated to lower temperatures (25°C to 100°C).
5. The phase transition to  $U_4O_9$ , must be completed before the phase transition to  $U_3O_8$  is initiated.

Note that these assumptions make the  $U_3O_8$ -oxidation geometric response similar to that of  $U_4O_9$ , (i.e., an oxidation front that propagates into a grain volume). Thus, Figures 3.2.2-1 through 3.2.2-3 illustrate the frontal propagation, only now the  $U_3O_8$  replaces  $U_4O_9$ , and  $U_4O_9$  replaces  $UO_2$  of the figures.

Given these five assumptions, the TGA data can be used to provide preliminary estimates of the  $U_3O_8$  oxidation response. The data shown in Figure 3.2.2-4 (Einziger, et al., 1995) shows TGA oxidation data at five temperatures for spent-fuel samples from ATM-105. The three higher temperature curves (325°C, 305°C, and 283°C) show that the  $U_3O_8$ -oxidation response rate is less than the  $U_4O_9$ -oxidation response rate.

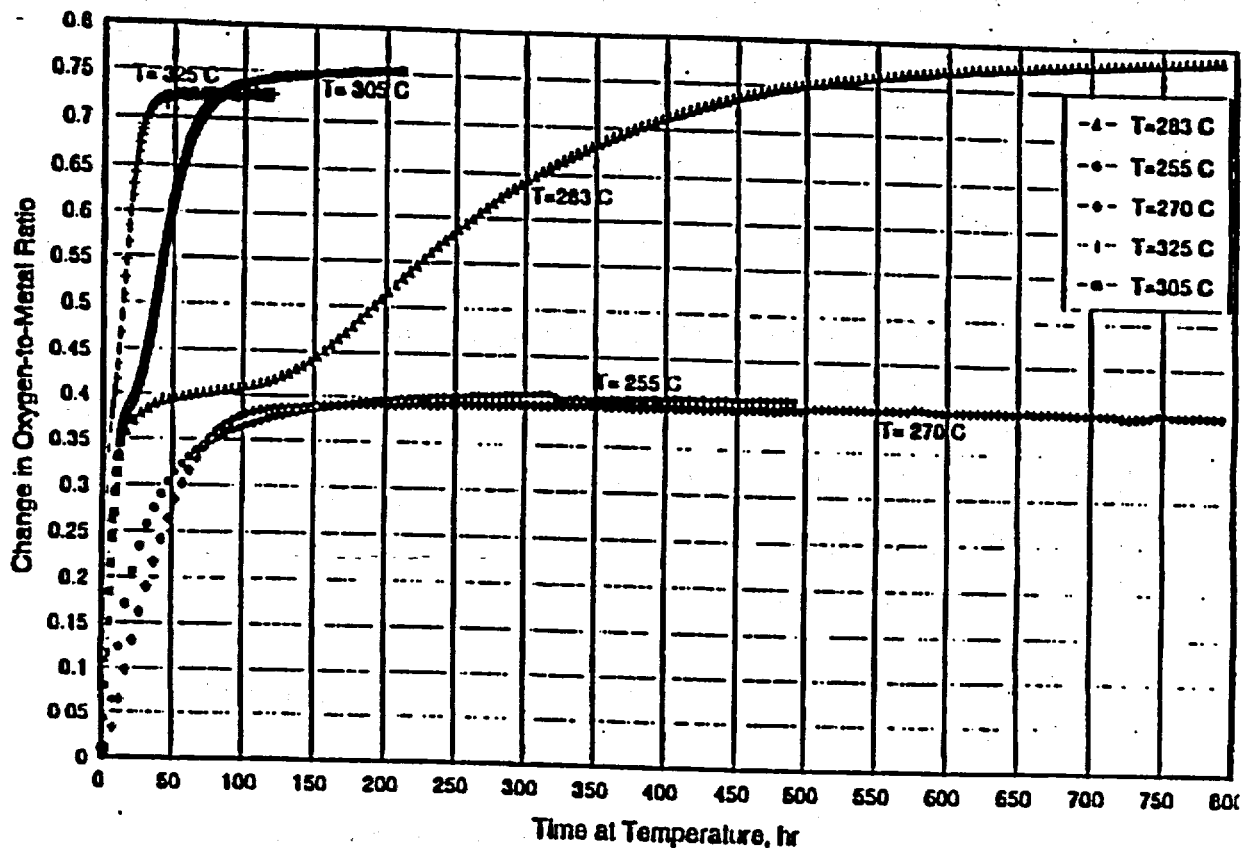


Figure 3.2.2-4 Oxidation of ATM-105 fuel at various temperatures

From these three curves, two methods exist to estimate the  $U_3O_8$ -oxidation rate response. One method is to graphically estimate the early time slopes of these curves as  $U_3O_8$  forms and to use these values to calculate an Arrhenius activation energy. With additional analysis, an estimate for the speed of the  $U_3O_8$  oxidation can be derived. The estimated slope and temperature values for the activation energy were  $(1.65 \times 10^{-2}/h, 598.2 K)$ ,  $(8.47 \times 10^{-3}/h, 578.2 K)$ , and  $(1.46 \times 10^{-3}/h, 556.2 K)$ . The activation energy estimate from these data was 38540 cal/mole.

For this reason, a second method was used to estimate the frontal speed of the  $U_3O_8$  oxidation process. This method used graphic estimates for the elapsed times to full oxidation from the  $U_4O_9$  plateau to a  $U_3O_8$  phase. The elapsed time is the time interval from estimated initiation of  $U_3O_8$  to estimated completion of  $U_3O_8$ , totally converted  $U_4O_9$ . This elapsed time neglects the delay elapsed time of the plateau and is a conservative estimate for the elapsed time to fully oxidize to  $U_3O_8$ . The three values for time intervals and temperatures were (33.33 h, 598.2 K), (106.25 h, 578.2 K), and (425.0 h, 556.2 K). The activation energy from these data was 40057 cal/mole, which is similar to the active energy of the previous method. The samples of spent

fuel for these test data were all from ATM-105, which has a nominal grain size of 13  $\mu\text{m}$ . For constant temperature histories, the speed of the  $\text{U}_3\text{O}_8$  oxidation front was previously assumed constant, hence the frontal speed  $\dot{W}_{38}$  or  $|\underline{c}|\dot{C}_{38}$  is given by an Arrhenius expression. The rate  $\dot{W}_{38}$  is given by

$$\dot{W}_{38} = k_{38} \exp(-Q_{38}/RT) \quad 3.2.2-14a$$

where  $Q_{38}$  and  $k_{38}$  can be estimated from the ATM-105:

$$Q_{38} = 40057 \text{ cal/mole (Arrhenius activation energy for the reaction } \text{U}_4\text{O}_9 \rightarrow \text{U}_3\text{O}_8)$$

$$k_{38} = 8.58 \times 10^{13} \mu\text{m/h using } |\underline{c}| = 6.5 \mu\text{m for ATM-105}$$

$$R = 1.986 \text{ cal/mole K}$$

$$T = \text{temperature Kelvin}$$

The  $\text{U}_3\text{O}_8$  frontal speed  $\dot{W}_{38}$  for any grain size is constant and  $\dot{C}_{38}$  is given by

$$\dot{C}_{38} = \dot{W}_{38}/|\underline{c}| \quad 3.2.2-14b$$

The preceding values for  $k_{38}$  and  $Q_{38}$  are preliminary and will be evaluated again as additional data become available. The preceding activation-energy value is higher than that of unirradiated fuel, but lower than expected when burnup-dependence is used.

The oxidation rate, in terms of  $[\dot{O}]$  to  $[M]$  response for  $\text{U}_3\text{O}_8$  is analogous to that of Eq. 3.2.2-6 for  $\text{U}_4\text{O}_9$ , except that the factor for the number of oxygen atoms added per uranium atom changes from 0.42. For the  $\text{U}_3\text{O}_8$ -oxidation response, which is also not stoichiometric, the oxidation curves plateau around  $\text{UO}_{2.75}$ , which chemically implies



Thus, each uranium atom will require, on the average, 0.33 of an oxygen atom to form a  $\text{U}_3\text{O}_8$  lattice cell at the  $\text{UO}_{2.42}$  oxidation front. With this value for oxygen atoms added per uranium atom for  $\text{U}_3\text{O}_8$ -phase transformation, and the frontal speed of Eq. 3.2.2-14, the rate of  $\text{U}_3\text{O}_8$  oxidation for a pyramidal section of a cubic grain follows analogously from Eq. 3.2.2-6 as

$$[\dot{O}]/[U](\text{U}_4\text{O}_9 \rightarrow \text{U}_3\text{O}_8; t) = 0.33 \dot{C}_{38} c_i e_{ijk} a_j (1 - C_{38}(t)) b_k (1 - C_{38}(t)) \quad 3.2.2-16$$

for times  $t \geq t_{2.4}$  of the  $\text{U}_4\text{O}_9$  oxidation.

In Eq. 3.2.2-16,  $\dot{C}_{38}$  is constant for a prescribed constant temperature and a nominal grain dimension  $|c|$  as given in Eq. 3.2.2-14; i.e.,

$$\dot{C}_{38} = (k_{38}/|c|) \exp(-Q_{38}/RT) \quad 3.2.2-17a$$

and  $C_{38}(t)$  is the time integration of  $\dot{C}_{38}$  for  $t > t_{2,4}$ , which, for constant temperature, is

$$C_{38}(t) = (t - t_{2,4}) \dot{C}_{38} \quad \text{for } t_{2,4} < t < tot_{3,8} \quad 3.2.2-17b$$

The time  $tot_{3,8}$  occurs at the time  $C_{38}$  equals unity. It is the total elapsed time from initial exposure of the  $UO_2$  at time  $t$  set to zero for the  $UO_2$  to change fully through the  $U_4O_9$  and  $U_3O_8$  phases. It does not include any estimate of the delay elapsed time of the plateau region thus, for a model response, it is conservative. Thus,  $tot_{3,8}$  consists of a  $t_{2,4}$  time and  $t_{3,8}$ ; the former given by Eq. 3.2.2-3 and the latter incremental time from Eq. 3.2.2-17a, when  $C_{38}$  is one, is given by

$$t_{3,8} = |c| / (k_{38} \exp(-Q_{38}/RT)) \quad 3.2.2-18a$$

Recall that  $|c|$  is  $W_o$ , half the grain size. Then  $tot_{3,8}$  is

$$tot_{3,8} = t_{2,4} + t_{3,8} \quad 3.2.2-18b$$

Values of elapsed time  $t_{3,8}$  are given in Table 3.2.2-5 for different constant temperature histories and nominal grain sizes.

Table 3.2.2-5

Elapsed time  $t_{3,8}$  for  $U_3O_8$

Table 3.2.2-5. Elapsed Time, $t_{3,8}$ , for $U_3O_8$					273.2	Parameters: Q38=40057 cal/mole, k38=8.58E+13 micron/h, R=1.986 cal/mole/K						
Phase Transformation of $UO_2$ for Grain Size					T in C	200	150	100	75	50	25	
2Wo And Constant Temperature.					T in K	523.2	473.2	423.2	373.2	348.2	323.2	298.2
4	Wo=Grainsize/2	DVU3O8/VUO2	DW/Wo	DW								
5	10E-6 meters			10E-6 m	3.8 Elapsed Times in Hours, One Year = 24*365 = 8760 hours							
6	5	1	1	5	3.2196E+03	1.8917E+05	2.9103E+07	1.7260E+10	8.3607E+11	7.3817E+13	1.3815E+16	
7	10	1	1	10	6.4393E+03	3.7835E+05	5.8205E+07	3.4520E+10	1.6721E+12	1.4763E+14	2.7630E+16	
8	15	1	1	15	9.6569E+03	5.6752E+05	8.7308E+07	5.1780E+10	2.5082E+12	2.2145E+14	4.1444E+16	
9	20	1	1	20	1.2879E+04	7.5669E+05	1.1641E+08	6.9039E+10	3.3443E+12	2.9527E+14	5.5259E+16	
10	25	1	1	25	1.6098E+04	9.4587E+05	1.4551E+08	8.6299E+10	4.1804E+12	3.6908E+14	6.9074E+16	
11	30	1	1	30	1.9318E+04	1.1350E+06	1.7462E+08	1.0356E+11	5.0164E+12	4.4290E+14	8.2889E+16	
12	35	1	1	35	2.2537E+04	1.3242E+06	2.0372E+08	1.2082E+11	5.8525E+12	5.1672E+14	9.6704E+16	
13												
14					3.8 Elapsed Times in Years							
15												
16					3.68E-01	2.16E+01	3.32E+03	1.97E+06	9.54E+07	8426597454	1.577E+12	
17					7.35E-01	4.32E+01	6.64E+03	3.94E+06	190883958	1.6853E+10	3.1541E+12	
18					1.10E+00	6.48E+01	9.97E+03	5.91E+06	286325937	2.528E+10	4.7311E+12	
19					1.47E+00	8.64E+01	1.33E+04	7.88E+06	381767916	3.3706E+10	6.3081E+12	
20					1.84E+00	1.08E+02	1.66E+04	9.85E+06	477209896	4.2133E+10	7.8852E+12	
21					2.21E+00	1.30E+02	1.99E+04	1.18E+07	572651875	5.056E+10	9.4622E+12	
22					2.57E+00	1.51E+02	2.33E+04	1.38E+07	668093854	5.8986E+10	1.1039E+13	

Parameters: Q38 = 40,057 cal/mole, k38 = 8.58E+13 micron/h, R = 1.986 cal/mole/K

Given the  $U_3O_8$  frontal speed Eq. 3.2.2-14 and the preceding Eq. 3.2.2-17b for  $C_{38}(t)$  the  $[O]/[U]$  ratio of a  $U_4O_9$  sample transforming to  $U_3O_8$  is the time integration of Eq. 3.2.2-16, and is analogous to that of Eq. 3.2.2-7, namely

$$[O]/[U](U_4O_9 \rightarrow UO_{2.75}; t) = 0.33(6Gc_i e_{ijk} a_j b_k (3C_{38}(t) - 3C_{38}^2(t) + C_{38}^3(t)/3)) \quad 3.2.2-19$$

for a sample containing  $G$  number of grains.

The  $UO_{2.4}$  volume expressions of Eq. 3.2.2-8b and Eq. 3.2.2-9 are analogs for the  $V_{U_3O_8}$  expressions, except that the function  $C(t)$  is replaced by  $C_{38}(t)$ . Thus, the volume of  $UO_2$  converted to  $U_3O_8$  for times  $t$  greater than  $t_{2.4}$  is

$$V_{U_3O_8}(G, t) = 6Gc_i e_{ijk} a_j b_k (3C_{38}(t) - 3C_{38}^2(t) + C_{38}^3(t))/3 \quad 3.2.2-20$$

where the dimensional lengths of grains for vectors  $\underline{c}$ ,  $\underline{a}$ , and  $\underline{b}$  are those of the  $UO_2$  phase. Thus, the volume of  $U_3O_8$  that exists at time  $t$  would be approximately 1.30 times larger than  $V_{U_3O_8}$  evaluated from Eq. 3.2.2-20.

Finally, the volume ratio relative to the  $UO_2$  phase transformed to  $U_3O_8$  is an analog of Eq. 2.2.2-11, namely

$$V_{U_3O_8}(G, t)/V_{UO_2}(G) = 3C_{38}(t) - 3C_{38}^2(t) + C_{38}^3(t) \quad \text{for } t_{2.4} \leq t \leq t_{3.8} \quad 3.2.2-21$$

and depends on grain size and temperature history of  $\dot{C}_{38}$  and  $C_{38}$  given in Eq. 3.2.2-17a and Eq. 3.2.2-17b.

In a manner similar to that of the elapsed time  $t_{v2.4}$  for a prescribed volume fraction of  $UO_{2.4}$ , Eq. 3.2.2-21 can be inverted to find the elapsed time,  $t_{v3.8}$ , after  $U_3O_8$  initiation to attain a prescribed volume fraction of  $U_3O_8$ . The expression is analogous to that of Eq. 3.2.2-13, except that the speed of the  $U_3O_8$  front is constant, rather than depending on the square root in time. Thus, the expression is

$$t_{v3.8} = |\underline{c}| \left( 1 - \left( 1 - V_{U_3O_8}/V_{UO_2} \right)^{1/3} \right) / \left( k_{38} \exp(-Q_{38}/RT) \right) \quad 3.2.2-22$$

Values for  $t_{v3.8}$  fractional volumes of  $U_3O_8$  at 25%, 50%, and 75%, at different constant temperatures and grain sizes, are given in Tables 3.2.2-6 to 3.2.2-8.

**Table 3.2.2-6 Elapsed time  $t_{3.8}$ , 25%  $U_3O_8$**

Phase Transformation of UO2 for Grain Size				TinC	250	200	150	100	75	50	25
2Wo And Constant Temperature.				TinK	523.2	473.2	423.2	373.2	348.2	323.2	298.2
Wo=Grainsize/2	DVU3O8/VUO2	DW/Wo	DW								
10E-6 meters			10E-6 m	tv3.8 Times in Hours, One Year = 24*365 = 8760 hours							
5	0.25	0.091439695	0.457198474	2.9440E+02	1.7298E+04	2.6611E+06	1.5782E+09	7.6450E+10	6.7498E+12	1.2632E+15	
10	0.25	0.091439695	0.914396949	5.8881E+02	3.4596E+04	5.3223E+06	3.1565E+09	1.5290E+11	1.3500E+13	2.5264E+15	
15	0.25	0.091439695	1.371595423	8.8321E+02	5.1894E+04	7.9834E+06	4.7347E+09	2.2935E+11	2.0249E+13	3.7897E+15	
20	0.25	0.091439695	1.828793897	1.1776E+03	6.9192E+04	1.0645E+07	6.3129E+09	3.0580E+11	2.6999E+13	5.0529E+15	
25	0.25	0.091439695	2.285992372	1.4720E+03	8.6490E+04	1.3306E+07	7.8912E+09	3.8225E+11	3.3749E+13	6.3161E+15	
30	0.25	0.091439695	2.743190846	1.7664E+03	1.0379E+05	1.5967E+07	9.4694E+09	4.5870E+11	4.0499E+13	7.5793E+15	
35	0.25	0.091439695	3.20038932	2.0608E+03	1.2109E+05	1.8628E+07	1.1048E+10	5.3515E+11	4.7249E+13	8.8426E+15	
				tv3.8 Times in Years							
				3.3608E-02	1.9747E+00	3.0378E+02	1.8016E+05	8.7272E+06	7.7053E+08	1.4420E+11	
				6.7215E-02	3.9493E+00	6.0757E+02	3.6033E+05	1.7454E+07	1.5411E+09	2.8841E+11	
				1.0082E-01	5.9240E+00	9.1135E+02	5.4049E+05	2.6182E+07	2.3116E+09	4.3261E+11	
				1.3443E-01	7.8986E+00	1.2151E+03	7.2066E+05	3.4909E+07	3.0821E+09	5.7681E+11	
				1.6804E-01	9.8733E+00	1.5189E+03	9.0082E+05	4.3636E+07	3.8526E+09	7.2102E+11	
				2.0165E-01	1.1848E+01	1.8227E+03	1.0810E+06	5.2363E+07	4.6232E+09	8.6522E+11	
				2.3525E-01	1.3823E+01	2.1265E+03	1.2611E+06	6.1090E+07	5.3937E+09	1.0094E+12	

Parameters: Q38 = 40,057 cal/mole, k38 = 8.58E+13 micron/h, R = 1.986 cal/mole/K

Table 3.2.2-7 Elapsed time  $t_{3.8}$ , 50%  $U_3O_8$

Phase Transformation of UO2 for Grain Size				TlnC	250	200	150	100	75	50	25
2Wo And Constant Temperature.				TlnK	523.2	473.2	423.2	373.2	348.2	323.2	298.2
Wo=Grainsize/2	DVU3O8/VUO2	DW/Wo	DW								
10E-6 meters			10E-6 m		tv3.8 Times in Hours, One Year = 24*365 = 8760 hours						
5	0.5	0.206299456	1.031497278		6.6421E+02	3.9026E+04	6.0039E+06	3.5607E+09	1.7248E+11	1.5228E+13	2.8500E+15
10	0.5	0.206299456	2.062994557		1.3284E+03	7.8053E+04	1.2008E+07	7.1214E+09	3.4496E+11	3.0457E+13	5.7000E+15
15	0.5	0.206299456	3.094491835		1.9926E+03	1.1708E+05	1.8012E+07	1.0682E+10	5.1744E+11	4.5685E+13	8.5500E+15
20	0.5	0.206299456	4.125989114		2.6568E+03	1.5611E+05	2.4015E+07	1.4243E+10	6.8992E+11	6.0914E+13	1.1400E+16
25	0.5	0.206299456	5.157486392		3.3210E+03	1.9513E+05	3.0019E+07	1.7803E+10	8.6241E+11	7.6142E+13	1.4250E+16
30	0.5	0.206299456	6.18898367		3.9853E+03	2.3416E+05	3.6023E+07	2.1364E+10	1.0349E+12	9.1370E+13	1.7100E+16
35	0.5	0.206299456	7.220480949		4.6495E+03	2.7319E+05	4.2027E+07	2.4925E+10	1.2074E+12	1.0660E+14	1.9950E+16
					tv3.8 Times in Years						
					7.5823E-02	4.4551E+00	6.8537E+02	4.0647E+05	1.9690E+07	1.7384E+09	3.2534E+11
					1.5165E-01	8.9101E+00	1.3707E+03	8.1294E+05	3.9379E+07	3.4768E+09	6.5068E+11
					2.2747E-01	1.3365E+01	2.0561E+03	1.2194E+06	5.9069E+07	5.2152E+09	9.7602E+11
					3.0329E-01	1.7820E+01	2.7415E+03	1.6259E+06	7.8759E+07	6.9538E+09	1.3014E+12
					3.7912E-01	2.2275E+01	3.4269E+03	2.0324E+06	9.8448E+07	8.6920E+09	1.6267E+12
					4.5494E-01	2.6730E+01	4.1122E+03	2.4388E+06	1.1814E+08	1.0430E+10	1.9520E+12
					5.3076E-01	3.1186E+01	4.7976E+03	2.8453E+06	1.3783E+08	1.2169E+10	2.2774E+12

Parameters: Q38 = 40,057 cal/mole, k38 = 8.58E+13 micron/h, R = 1.986 cal/mole/K

Table 3.2.2-8 Elapsed time <sub>13.8</sub> 75% U<sub>3</sub>O<sub>8</sub>

Phase Transformation of UO <sub>2</sub> for Grain Size				T in C	250	200	150	100	75	50	25
2W <sub>0</sub> And Constant Temperature.				T in K	523.2	473.2	423.2	373.2	348.2	323.2	298.2
W <sub>0</sub> -Grainsize/2	DVU3O8/VUO2	DW/W <sub>0</sub>	DW								
10E-6 meters			10E-6 m	1/3.8 Times in Hours, One Year = 24*365 = 8760 hours							
5	0.75	0.370039446	1.85019723	1.1914E+03	7.0002E+04	1.0769E+07	6.3868E+09	3.0938E+11	2.7315E+13	5.1120E+15	
10	0.75	0.370039446	3.700394459	2.3828E+03	1.4000E+05	2.1538E+07	1.2774E+10	6.1876E+11	5.4630E+13	1.0224E+16	
15	0.75	0.370039446	5.550591689	3.5742E+03	2.1001E+05	3.2307E+07	1.9160E+10	9.2814E+11	8.1946E+13	1.5336E+16	
20	0.75	0.370039446	7.400788919	4.7656E+03	2.8001E+05	4.3077E+07	2.5547E+10	1.2375E+12	1.0926E+14	2.0448E+16	
25	0.75	0.370039446	9.250986149	5.9570E+03	3.5001E+05	5.3846E+07	3.1934E+10	1.5469E+12	1.3658E+14	2.5560E+16	
30	0.75	0.370039446	11.10118338	7.1484E+03	4.2001E+05	6.4615E+07	3.8321E+10	1.8563E+12	1.6389E+14	3.0672E+16	
35	0.75	0.370039446	12.95138061	8.3398E+03	4.9001E+05	7.5384E+07	4.4708E+10	2.1657E+12	1.9121E+14	3.5784E+16	
				1/3.8 Times in Years							
				1.3600E-01	7.9911E+00	1.2294E+03	7.2909E+05	3.5317E+07	3.1182E+09	5.8357E+11	
				2.7201E-01	1.5982E+01	2.4587E+03	1.4582E+06	7.0635E+07	6.2363E+09	1.1671E+12	
				4.0801E-01	2.3973E+01	3.6881E+03	2.1873E+06	1.0595E+08	9.3545E+09	1.7507E+12	
				5.4402E-01	3.1964E+01	4.9174E+03	2.9164E+06	1.4127E+08	1.2473E+10	2.3343E+12	
				6.8002E-01	3.9955E+01	6.1468E+03	3.6454E+06	1.7659E+08	1.5591E+10	2.9178E+12	
				8.1602E-01	4.7946E+01	7.3761E+03	4.3745E+06	2.1190E+08	1.8709E+10	3.5014E+12	
				9.5203E-01	5.5937E+01	8.6055E+03	5.1036E+06	2.4722E+08	2.1827E+10	4.0850E+12	

Parameters: Q<sub>38</sub> = 40,057 cal/mole, k<sub>38</sub> = 8.58E+13 micron/h, R = 1.986 cal/mole/K

The comparison of the elapsed times for full oxidation of  $\text{UO}_2$  to the  $\text{U}_4\text{O}_9$  and  $\text{U}_3\text{O}_8$  phases are presented for  $t_{2,4}$  values in Table 3.2.2-1 and for  $t_{3,8}$  values in Table 3.2.2-5. At lower temperatures ( $T$  less  $100^\circ\text{C}$ ), the  $t_{3,8}$  values are significantly greater than the  $t_{2,4}$  values. It appears that large amounts of  $\text{U}_4\text{O}_9$  will form within thousands of years of exposure at  $\sim 100^\circ\text{C}$  temperatures, whereas it will take hundreds of thousands of years for large amounts of  $\text{U}_3\text{O}_8$  to form at the same temperatures ( $\sim 100^\circ\text{C}$ ).

### 3.2.2.5 Comparison of Model Response to Oven Drybath Data

The confirmation of a model depends primarily on how well it explains existing data and on its potential to explain future experiments. In this case, the  $\text{U}_4\text{O}_9$  and  $\text{U}_3\text{O}_8$  oxidation models based on the kinetic data from the small-sample TGA experiments successfully bounded the ODB data obtained over a larger scale and variety of spent-fuel sample sizes. This comparison confirms the "bounding approximations" of the oxidation-response model.

The kinetic parameters for the reaction  $\text{U}_4\text{O}_9 \rightarrow \text{U}_3\text{O}_8$  obtained from higher-temperature (greater than  $283^\circ\text{C}$ ) TGA measurements were applied to the lower-temperature ( $255^\circ\text{C}$ ) ODB experiments. The TGA tests used very small samples, approximately 200 mg of spent fuel. Compared to the TGA experiments, the ODB experiments accommodated much larger spent-fuel samples that must likely include both edge and center spent-fuel fragments. Thus, the ODB experiments are more representative of integral or averaged spent fuel.

The amounts of  $\text{U}_4\text{O}_9$  to  $\text{U}_3\text{O}_8$  ODB data are limited because these were obtained at  $255^\circ\text{C}$ , at which point the time response of  $\text{UO}_2$  conversion to  $\text{U}_3\text{O}_8$  is much slower. The ODB data have been provided by for the following fuels:

- Turkey Point PWR fuel
- ATM-104
- ATM-105
- ATM-106

These ODB data are additional, independent, experimental measurements for the oxidation of  $\text{U}_4\text{O}_9$  to  $\text{U}_3\text{O}_8$ . The ODB samples had initial  $\Delta(\text{O}/\text{M})$  ratios of 0.0 or 0.42 relative to  $\text{UO}_2$  because some of the samples had been previously oxidized at lower temperatures. Some of the spent-fuel samples used were as-removed fragments, while others were pulverized fragments. The majority of these ODB samples had nominal, grain half-sizes primarily in the range of 3 to 15 microns. When comparing ODB data to the model response that used kinetic parameters from TGA data, it is important to note that there was a wider spectrum of grain half sizes in the ODB samples.

In Figure 3.2.2-5 through Figure 3.2.2-8, the change in the oxygen-to-metal ratio  $\Delta(O/M)$  is plotted against time (thousands of hours). The  $\Delta(O/M)$ -versus-time curves represent the cumulative effect of the consecutive reactions:  $UO_2 \rightarrow U_4O_9 \rightarrow U_3O_8$ . At the ODB temperature  $T = 255^\circ C$  (528.2 K), the reaction rate  $k_{v4.9}$  for  $UO_2 \rightarrow U_4O_9$  is  $k_{v4.9} = 1.205 \times 10^{-2} \mu m^2/hr$ , and the reaction rate  $k_{v3.8}$  for  $U_4O_9 \rightarrow U_3O_8$  is  $k_{v3.8} = 3.4414 \times 10^{-4} \mu m/hr$ . The front propagation speeds for the respective reactions are given by Eq. 3.2.2-4 and Eq. 3.2.2-14a and Eq. 3.2.2-14b, respectively. A  $\Delta(O/M)$  of 0.42 represents the complete conversion of  $UO_2 \rightarrow U_4O_9$  (no  $UO_2$  or  $U_4O_9$  assumed to be present), and the time to achieve complete conversion is represented by  $t_{total 4.9}$ . A  $\Delta(O/M)$  of 0.75 represents the complete conversion of  $U_4O_9 \rightarrow U_3O_8$  (no  $UO_2$  or  $U_3O_8$  assumed to be present). Using Eq. 3.2.2-13 and Eq. 3.2.2-22, the cumulative elapsed time for any  $\Delta(O/M) > 0.42$  is given by Eq. 3.2.2-18b.

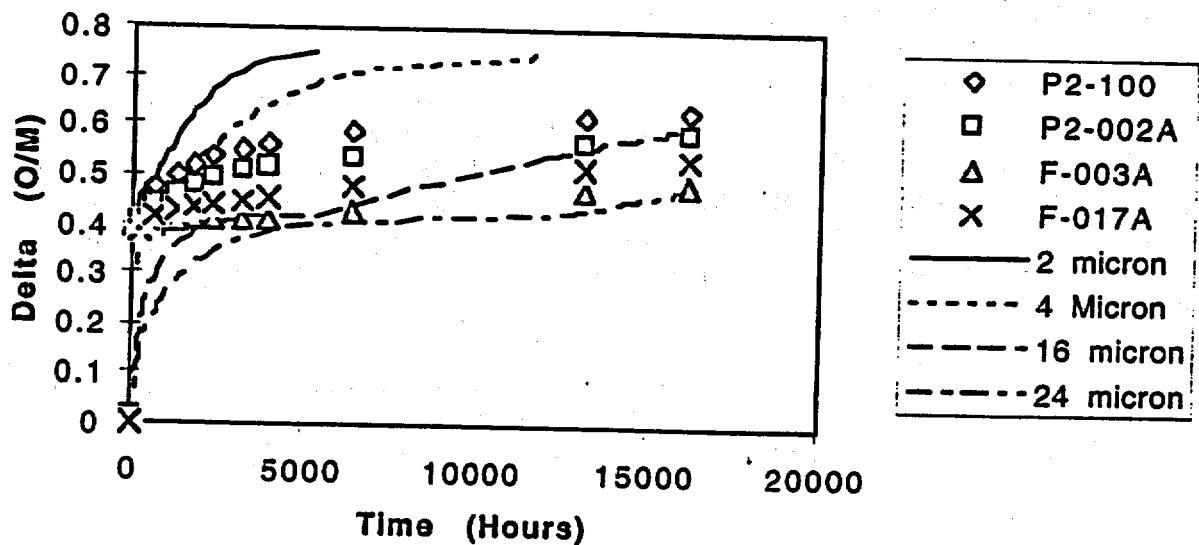


Figure 3.2.2-5  $\Delta(O/M)$  versus time for  $UO_2 \rightarrow U_4O_9 \rightarrow U_3O_8$ : model response and experimental data corresponding to Figure 10 (Turkey Point SNF sample) of Einziger and Hanson (1996) ODB tests conducted at  $255^\circ C$ .

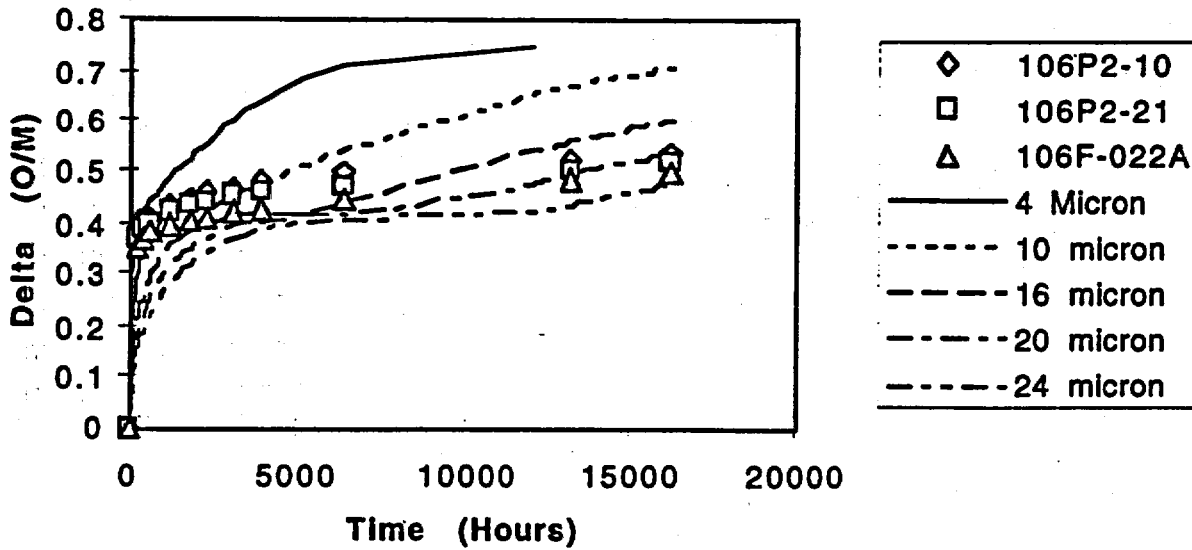


Figure 3.2.2-6.  $\Delta(O/M)$  versus time for  $UO_2 \rightarrow U_4O_9 \rightarrow U_3O_8$ ; model response and experimental data corresponding to Figure 11 (ATM-106 SNF samples) of Einziger and Hanson (1996) ODB tests conducted at 255°C.

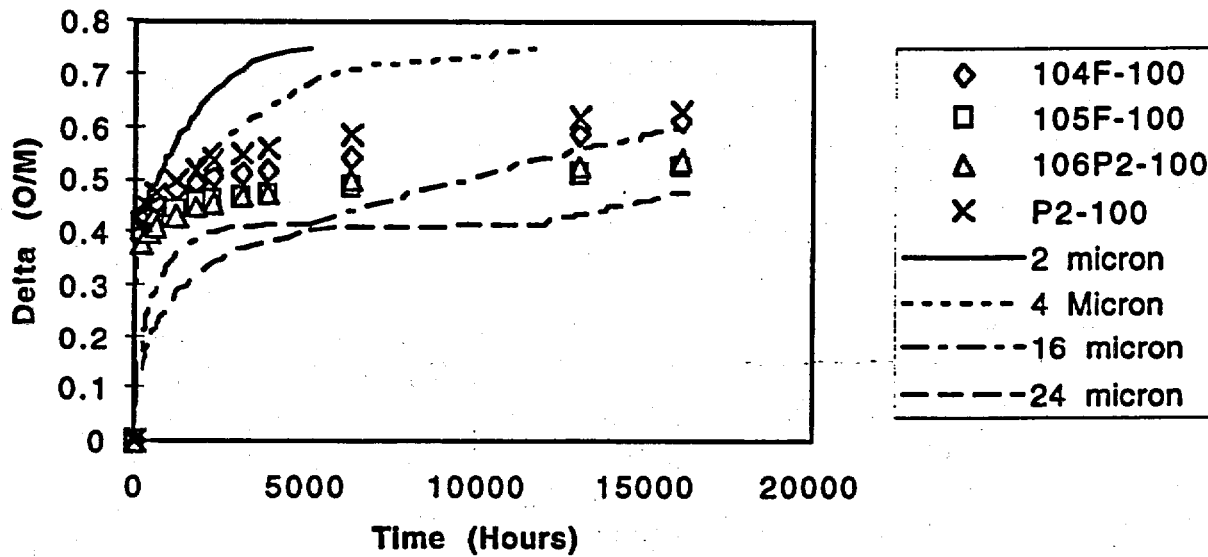


Figure 3.2.2-7.  $\Delta(O/M)$  versus time for  $UO_2 \rightarrow U_4O_9 \rightarrow U_3O_8$ ; model response and experimental data corresponding to Figure 14 (SNF samples) of Einziger and Hanson (1996) ODB tests conducted at 255°C.

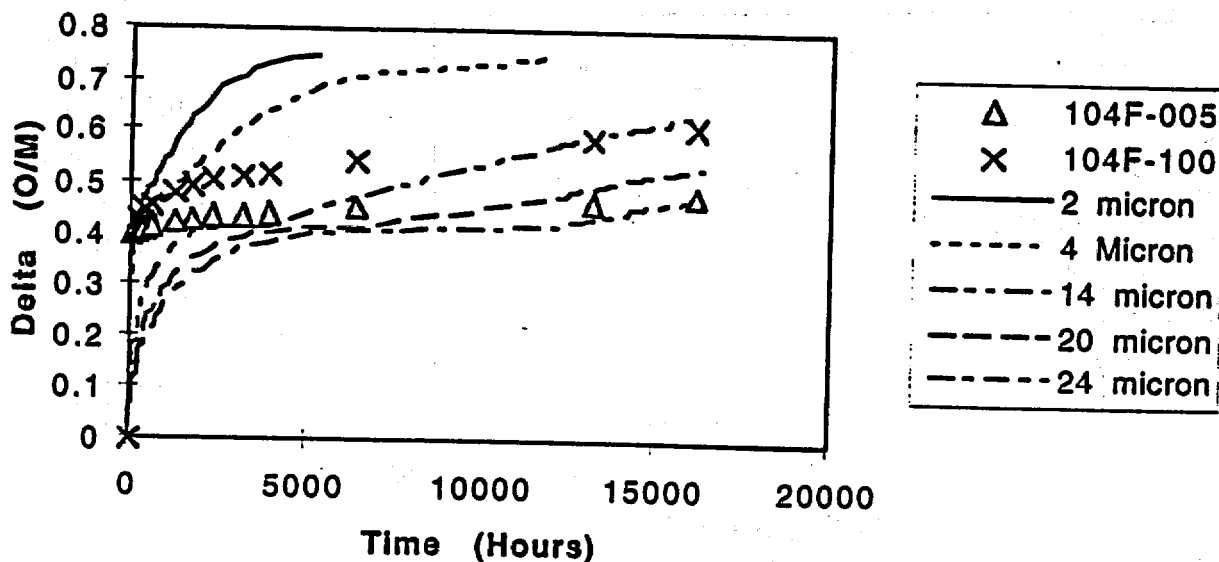


Figure 3.2.2-8  $\Delta(O/M)$  versus time for  $UO_2 \rightarrow U_4O_9 \rightarrow U_3O_8$ : model response and experimental data corresponding to Figure 15 (SNF samples, initial  $\Delta(O/M)=0.4$ ) of Einziger and Hanson (1996) ODB tests conducted at 255°C.

In these figures, the experimental ODB  $\Delta(O/M)$ -versus-time results are represented as symbols without lines; the various monosized grain half size  $\Delta(O/M)$ -versus-time curves are represented as continuous lines (solid, dotted, dashed, dot-dash, etc.). At time  $t = 0.0$ , the data have samples that were initially  $UO_2$  or had been oxidized at lower temperatures to  $U_4O_9$ . Some of these figures have both types.

As pointed out previously, the initial  $UO_2$  grain size determines the time scale required for the complete transformation of  $UO_2$  to  $U_4O_9$ , and the subsequent transformation of  $U_4O_9$  to  $U_3O_8$ . The  $\Delta(O/M)$ -versus-time curves show that the completion of the  $UO_2 \rightarrow U_4O_9$  reaction and the initiation of the  $U_4O_9 \rightarrow U_3O_8$  reaction require progressively longer times for larger grain half sizes. This model dependence on grain half size becomes quite pronounced for grain half sizes larger than 16 microns.

Figure 3.2.2-5 shows the plots of  $\Delta(O/M)$  versus time for the experimental samples (P2-100, P2-002A, F-003A, and F-017A) from Turkey Point spent fuel. Figure 3.2.2-6 shows the plots of  $\Delta(O/M)$  versus time for the ATM 106 samples (106F-022A, 106P2-100, and 106P2-21A). Figure 3.2.2-7 shows similar plots for the spent-fuel samples (104F-100, 106P2-100, 105F-100, P2-100, 106F-022A, and 106P2-21A). These figures show that the ODB experimental data are bounded by an envelope of model  $\Delta(O/M)$ -versus-time curves for grain half sizes of 2 microns to 24 microns. The grains of the various samples of  $U_4O_9$  are distributed over a spectrum of grain sizes,

with the very small grains of  $U_4O_9$ , oxidizing relatively rapidly to form  $U_3O_8$ , and the larger grains requiring longer times. Three different sets of  $\Delta(O/M)$ -versus-time plots of oxidizing spent-fuel samples are bounded by the envelope of model curves ranging from 2 microns to 24 microns.

Figure 3.2.2-8 shows the plots of  $\Delta(O/M)$  versus time for SNF samples (104F-100, 104F-005, and F-003A). Samples 104F-005 and F-003A had an initial  $\Delta(O/M) = 0.395$ ; sample 104F-100 had an initial  $\Delta(O/M) = 0.0$ . These ODB data are bounded by the envelope of model curves having grain half sizes from 2 microns to 24 microns. The distribution of grain half sizes varies from sample to sample. It appears that most of the ODB data at 255°C can be bounded by an envelope of monosized model-response  $\Delta(O/M)$ -versus-time curves for grain half sizes of 2 microns to 24 microns.

The kinetics used for the comparison of ODB data with model results were obtained independently from the higher temperature TGA experiments. The ODB experiments used various spent-fuel samples that were obtained from different types of reactors under different operating conditions. All the available ODB data, however, were bounded within a model-response envelope of grain half sizes ranging 2.0 to 24 microns. The results of the model comparison with the ODB data give confidence that the model accounts for the essential features of spent-fuel oxidation (i.e., the response history depends on both the temperature history and initial grain half-sizes).

Table 3.2.2-9 shows the time required, for various grain half sizes, to reach different volume fractions  $V_{U_3O_8}/V_{UO_2} = 0.00, 0.20, 0.40, 0.60, 0.80,$  and 1.00, for a ODB temperature held at 255°C. The time for the volume fraction  $V_{U_3O_8}/V_{UO_2} = 0.00$  represents the time required for the different grain half sizes to undergo the complete conversion of  $UO_2$  to  $U_4O_9$ , given by Eq. 3.2.2-13 for  $V_{U_4O_9}/V_{UO_2} = 1.0$ . The time required for a 5-micron grain half size of  $UO_2$  to form  $U_4O_9$  is 519 hr; the time to convert  $U_4O_9$  to  $U_3O_8$  is 15,048 hr. However, the time required for a 30-micron grain half size of  $UO_2$  to form  $U_4O_9$  is 18,676 hr; the time to convert  $U_4O_9$  to  $U_3O_8$  is 105,850 hr.

Table 3.2.2-9 Total elapsed time (hr) as a function of grain half size to convert  $UO_2$  to various volume fractions of  $U_3O_8$ , assuming temperature of 255°C (528.2 K)

Grain Size/2 (microns)	$V_{U_3O_8}/V_{UO_2} = 0.0$	$V_{U_3O_8}/V_{UO_2} = 0.2$	$V_{U_3O_8}/V_{UO_2} = 0.4$	$V_{U_3O_8}/V_{UO_2} = 0.6$	$V_{U_3O_8}/V_{UO_2} = 0.8$	$V_{U_3O_8}/V_{UO_2} = 1.0$
3.0	187	812	1552	2481	3806	8904
4.0	332	1165	2152	3391	5158	11955
5.0	519	1560	2794	4343	6551	15048
6.0	747	1997	3477	5336	7986	18182
7.0	1017	2475	4201	6370	9462	21357

Grain Size/2 (microns)	$V_{U_3O_8}/V_{UO_2} = 0.0$	$V_{U_3O_8}/V_{UO_2} = 0.2$	$V_{U_3O_8}/V_{UO_2} = 0.4$	$V_{U_3O_8}/V_{UO_2} = 0.6$	$V_{U_3O_8}/V_{UO_2} = 0.8$	$V_{U_3O_8}/V_{UO_2} = 1.0$
8.0	1328	2994	5968	7446	10980	24574
9.0	1681	3556	5775	8564	12539	27833
10.0	2075	4158	6625	9723	14140	31133
15.0	4669	7794	11493	16141	22766	48256
20.0	8301	12467	17400	23596	32430	66416
30.0	18676	24925	32325	41620	54871	105850

In the next sections, new information will be used to extend the bounding approximations to fitting TGA and drybath experiments by using log-normal grain-size distributions and burnup-dependent activation energies. The primary focus will be the oxidation of  $U_4O_9 \rightarrow U_3O_8$ .

### 3.2.2.6 Model Predictions of Spent-Fuel Oxidation in a Constant 100°C Temperature Environment

The rates of conversion of  $UO_2$  to  $U_4O_9$  and  $U_4O_9$  to  $U_3O_8$  depend exponentially on the inverse absolute temperature ( $1/T$  °K<sup>-1</sup>). Consequently, the rates of conversion are considerably more reduced when the temperature is held fixed at 100°C than they are when the temperature is held at 255°C. At 100 °C, the reaction rate for  $UO_2$  to  $U_4O_9$ ,  $k_{v,4.9} = 8.9979E-07$  mm<sup>2</sup>/hr; the reaction rate for  $U_4O_9$  to  $U_3O_8$ ,  $k_{v,3.8} = 4.4568E-11$  mm/hr.

Table 3.2.2-10 compares the time required, for various grain half sizes, to reach different volume fractions of  $U_4O_9$  and  $UO_2$ . In contrast, Table 3.2.2-9 shows the results for grain half sizes for which the temperature was held constant at 255°C. Consider the time required to convert  $UO_2$  to  $U_4O_9$  for grain half size of 5 microns: at 100°C, the total conversion time required to convert  $UO_2$  completely to  $U_4O_9$  is 6.9E+06 hr; at 255°C, the conversion time is 519 hr. Consider the time required to convert  $UO_2$  to  $U_4O_9$  for grain half-size of 10 microns: at 100°C, the total conversion time is 3.8E+07 hr; at 255°C the conversion time is 2075 hr.

Table 3.2.2-10 Total elapsed time (hr) as a function of grain half size to convert  $UO_2$  to various volume fractions of  $U_4O_9$ , assuming temperature of 100°C (373.2K)

Grain Size/2 (microns)	$V_{U_3O_8}/V_{UO_2} = 0.0$	$V_{U_3O_8}/V_{UO_2} = 0.2$	$V_{U_3O_8}/V_{UO_2} = 0.4$	$V_{U_3O_8}/V_{UO_2} = 0.6$	$V_{U_3O_8}/V_{UO_2} = 0.8$	$V_{U_3O_8}/V_{UO_2} = 1.0$
3.0	0	1.3E+04	6.1 E+04	1.7E+05	4.3E+05	2.5E+06
4.0	0	2.3E+04	1. 1E+05	3.1E+05	7.7E+05	4.4E+06
5.0	0	3.6E+04	1.7E+05	4.8E+05	1.2E+06	6.9E+06

Grain Size/2 (microns)	$V_{U_3O_8}/V_{UO_2} = 0.0$	$V_{U_3O_8}/V_{UO_2} = 0.2$	$V_{U_3O_8}/V_{UO_2} = 0.4$	$V_{U_3O_8}/V_{UO_2} = 0.6$	$V_{U_3O_8}/V_{UO_2} = 0.8$	$V_{U_3O_8}/V_{UO_2} = 1.0$
6.0	0	5.1E+04	2.5E+05	6.9E+05	2.7E+06	2.0E+07
7.0	0	7.0E+04	3.3E+05	9.4E+05	2.3E+06	1.4E+07
8.0	0	9.1E+04	4.4E+05	1.2E+06	3.1 E+06	1.8E+07
9.0	0	1.2E+05	5.5E+05	1.6E+06	3.9E+06	2.3E+07
10.0	0	1.4E+05	6.8E+05	1.9E+06	4.8E+06	3.8E+07
15.0	0	3.2E+05	1.5E+06	4.3E+06	1.1 E+07	6.3E+07
20.0	0	5.7E+05	2.7E+06	7.7E+06	1.9E+07	1.1E+08

Table 3.2.2-11 shows the total elapsed time as a function of grain half-size to convert  $UO_2$  to  $U_3O_8$  at  $100^\circ C$ . The conversion time to 100%  $U_3O_8$  is significantly longer for the  $100^\circ C$  as compared to the  $255^\circ C$  (Table. 3.2.2-9). Consider a grain half-size of 5 microns: the complete conversion time at  $255^\circ C$  is 15,048 hr., but the time  $100^\circ C$  is  $1.1E10$  hr. Consider a grain half-size of 10 microns: the conversion time at  $255^\circ C$  is 31,113 hr., but the conversion time at  $100^\circ C$  is  $2.2E11$  hr.

**Table 3.2.2-11** Total elapsed time (hr) as a function of grain half size to convert  $UO_2$  to various volume fractions of  $U_3O_8$ , assuming a constant temperature of  $100^\circ C$  (373.2K)

Grain Size/2 (microns)	$V_{U_3O_8}/V_{UO_2} = 0.0$	$V_{U_3O_8}/V_{UO_2} = 0.25$	$V_{U_3O_8}/V_{UO_2} = 0.50$	$V_{U_3O_8}/V_{UO_2} = 0.75$	$V_{U_3O_8}/V_{UO_2} = 1.0$
4.0	4.445E+06	8.211E+09	1.852E+10	3.322E+10	8.976E+10
5.0	6.946E+06	1.027E+10	2.315E+10	4.152E+10	1.122E+11
6.0	1.000E+07	1.232E+10	2.778E+10	4.983E+10	1.346E+11
7.0	1.361E+07	1.438E+10	3.242E+10	5.813E+10	1.571E+11
8.0	1.778E+07	1.643E+10	3.705E+10	6.644E+10	1.795E+11
9.0	2.251E+07	1.849E+10	4.168E+10	7.475E+10	2.020E+11
10.0	2.778E+07	2.054E+10	4.632E+10	8.306E+10	2.244E+11
11.0	3.362E+07	2.260E+10	5.095E+10	9.137E+10	2.468E+11
12.0	4.001E+07	2.466E+10	5.559E+10	9.967E+10	2.693E+11
13.0	4.696E+07	2.672E+10	6.022E+10	1.080E+11	2.917E+11
14.0	5.446E+07	2.878E+10	6.486E+10	1.163E+11	3.142E+11
15.0	6.251E+07	3.084E+10	6.950E+10	1.246E+11	3.366E+11
16.0	7.113E+07	3.290E+10	7.413E+10	1.329E+11	3.591E+11
17.0	8.030E+07	3.496E+10	7.877E+10	1.412E+11	3.815E+11
18.0	9.002E+07	3.702E+10	8.341E+10	1.495E+11	4.040E+11
19.0	1.003E+08	3.908E+10	8.805E+10	1.579E+11	4.264E+11
20.0	1.111E+08	4.115E+10	9.269E+10	1.662E+11	4.489E+11

### 3.2.2.7 Chemical and Physical Alteration of Spent Fuel

Depending on the burnup, spent fuel is always chemically, and sometimes physically, altered. Park and Olander (1992) show that the fission products in spent  $\text{UO}_2$  can be considered as dopants. The rare earth fission products from the lanthanide series are typically trivalent and form the compound  $(\text{U}_{1-z}\text{Ln}_z)\text{O}_{2+x}$ .  $\text{Gd}^{3+}$  does not form extended defects with oxygen interstitial, and it reduces the number of sites that can be occupied by oxygen interstitials. Consequently, as the number of oxygen vacancies increases, the stability occurs by the formation of Gd-vacancy clusters. In contrast,  $\text{Eu}^{3+}$  forms anion-vacancy clusters. The Gd-like dopants are isolated defects and tend to remain as such until the oxygen interstitial concentration becomes high enough to form a complex dopant cluster. But Eu forms clusters with anions. Eu exists as clusters of 6 other  $\text{Eu}^{3+}$  ions/anion vacancies and is stable at all stoichiometries. These authors believe that the lanthanide dopants whose concentrations are directly proportional to burnup are the major reason why spent fuel is more resistant to oxidation than unirradiated  $\text{UO}_2$ .

Walker et al (1992) point out that the burnup experienced in the rim tends to be about double the average burnup of the pellet itself. They studied five different fuels with average burnups (31.5 to 75 MWd/kgU) and  $^{235}\text{U}$  enrichment ranging from 1.5 to 7.0%. They noted structural changes such as markedly increased porosity with threshold burnups greater or equal to 40-45 MWd/kgU. While the altered shell or rim appeared to be small, it still accounted for 4 to 8% of the total volume. At high burnup, the grain volumes can experience anywhere from 1,000- to 10,000-fold reduction. The irradiated grain sizes can range from 0.4 to 1.0  $\mu\text{m}$ , compared to the unirradiated grains that range from 7 to 30  $\mu\text{m}$ . It appears that, if high burnup were maintained for a long time, the entire fuel cross-section could be affected. At high burnups, Xe and Kr bubbles are formed near the pellet surface and yield a sharp reduction in  $\text{UO}_2$  grain sizes. Near the surface, the local burnup is approximately double that of the average burnup; this region can experience very high temperatures ( $> 1100\text{-}1200^\circ\text{C}$ ) in which the thermally active Xe forms micro-bubbles over considerable distances and micro-structural changes. The formation of Pu from neutron absorption of  $^{238}\text{U}$  does not appear to account for the micro-structural changes. Walker et al observed a high concentration of gas bubbles (pores) forming in the rim due to the fission gas products, namely Xe and Kr. Similar observations on the high burnup structure were noted by Lassmann et al. (1995).

Matzke (1992) found that, in the region from the pellet surface to a depth  $d$ , the radial Pu, Np, and Xe concentrations vary exponentially. Pu, U-metal activity, and the Nd/Zr ratio also vary exponentially from approximately 200 mm from the interior to the pellet surface. The altered shell region, of width  $d$  for high burnups 40-60 MWd/kgU, represents 4 to 8% of the total pellet volume. This zone is characterized by very small grains (0.3 to 1.0  $\mu\text{m}$ ) and about 30% porosity. It is also Pu-rich. Matzke postulates that the burnup-dependent fission-gas content is the driving force for the structural changes. At high burnup, the gas pressure from fission gases can be approximately 10,000 bars.  $\text{UO}_2$  is not expected to be subject to

radiation-induced amorphism. However, depending on the fuel temperature during burnup, the stresses and deformations on a unit cell can cause grain subdivision. The pores that form will contain Re, As, I, Te, etc., that facilitate rounding the sharp edges of the smaller pieces. Radiation-induced thermal plasticity is known to occur in  $\text{UO}_2$  during fission. This plasticity is proportional to the fission rate. Pronounced plasticity prevents a buildup of very high pressure bubbles; instead, it produces swelling. Because the plasticity is proportional to the fission rate, radiation induced-plasticity is small in light-water reactors (LWRs). Neutron capture of  $^{238}\text{U}$  produces  $^{239}\text{Np}$  and  $^{239}\text{Pu}$ . The fission of  $^{239}\text{Pu}$  results in relatively high yields Pd, Ru, Rh, etc., that do not readily bind with oxygen. The burnup of 40 MWd/kgU appears to be the critical point at which small grains of  $\text{UO}_2$  are formed. At even higher burnups (70 to 80 MWd/kgU), the rim appears to be depleted of Xe and Kr, and the altered  $\text{UO}_2$  structure can extend 1.2 to 2.0 mm into the pellet. Of interest is the fact that the cauliflower structure from high burnup is not observed in the fast-breeder (U,Pu) $\text{O}_2$  reactor because most of the fission gas is readily released.

In a more recent study, Ray et al. (1997) examined the rim effect in very high-burnup spent fuel. The average burnup was 74 MWd/kgU; but, at the pellet surface, the local burnup was approximately 210 MWd/kgU. The original grain sizes that had been 10 to 20  $\mu\text{m}$  were now subdivided into grains ranging from 0.15 to 0.30  $\mu\text{m}$  in the irradiated rim region. The high burnup structure extended 1.65 mm below the surface.

Paraschiv et al. (1997) developed a mathematical formalism for fission-gas release. As for the cases of irradiated spent fuels, long-range diffusion can be required for the cases in which impurities segregate to the moving boundary. In the dissolved state, impurities will retard grain growth through elastic attraction toward the open structure of the grain boundary. It has long been observed that unirradiated  $\text{UO}_2$ , when annealed at high temperatures, has far larger grain sizes than does irradiated  $\text{UO}_2$  annealed at high temperatures (such as those occurring during burnup), apparently because, due to solute segregation, small amounts of metal oxide impurities dominate grain growth.

In summary, when the average burnup exceeds 40-45 MWd/kgU, the region at or near the pellet surface can undergo a drastic physical change. The effective burnup at the rim can be two to three times that of the average burnup. The rim is characterized by a radial distribution of fission and actinide products concentrations that decreases exponentially as one moves toward the center of the pellet. Furthermore, the rim has a very porous, cauliflower structure whose  $\text{UO}_2$  grains undergo significant grain-size reductions. Grains in the unirradiated  $\text{UO}_2$  that had originally been 10 to 20  $\mu\text{m}$  were now subdivided into grains ranging from 0.15 to 0.30  $\mu\text{m}$  in the high burnup rim region.

### 3.2.2.8 Oxidation Studies of Spent Fuel

UO<sub>2</sub>, which has a cubic fluorite crystalline structure, oxidizes initially by accommodating excess oxygen interstitially. There is some controversy about whether spent fuel "oxidizes" to U<sub>3</sub>O<sub>7</sub>. Boase and Vandergraf (1977) show that UO<sub>2</sub> rapidly oxidizes to form a thin film of U<sub>3</sub>O<sub>7</sub>, whose thickness is 22 nm. U<sub>3</sub>O<sub>7</sub> is found on very fine samples of spent fuel with large surface areas greater than 0.3 m<sup>2</sup>/g. Further oxidation proceeds by oxygen diffusion through the U<sub>3</sub>O<sub>7</sub> layer to form U<sub>4</sub>O<sub>9</sub>. The sequence is thought to be as follows:



U<sub>4</sub>O<sub>9</sub> and U<sub>3</sub>O<sub>8</sub> phases are essentially cubic fluorite crystalline structures, but the U<sub>4</sub>O<sub>9</sub> phase lattice is about 0.4% smaller than the UO<sub>2</sub> crystal. On the other hand, U<sub>3</sub>O<sub>8</sub> phase is quite different from the basic UO<sub>2</sub> because there is an increase in volume, as noted by the 30 to 36% decrease in density. Not only can U<sub>3</sub>O<sub>8</sub> disrupt cladding and spall, but its dissolution rate, as shown by Gray et al. (1993), is two to four times greater than that of UO<sub>2</sub> and U<sub>3</sub>O<sub>7</sub>, when the rates are normalized to the grain-surface areas.

Choi et al. (1996) argued that various studies in the burnup range 11.7 to 26.7 MWd/kgU reveal much scatter and uncertainty in the induction time and U<sub>3</sub>O<sub>8</sub> formation. To understand better the oxidation process, they examined SIMFUEL that is UO<sub>2</sub> and that had been doped with nonradioactive, simulated fission products such as Gd. They doped different SIMFUEL samples to simulate 0, 1.5, 3.0, 4.0, 6.0, or 8.0 atom% burnup. They found that the fraction of UO<sub>2</sub> oxidized to U<sub>3</sub>O<sub>8</sub> at a constant temperature of 250°C required progressively larger amounts of time as the dopant concentration increased. These authors postulate that the dissolved solid dopants significantly alter the kinetics of oxidation-to-U<sub>3</sub>O<sub>8</sub> formation. They believe that, for similar UO<sub>2</sub> grain sizes, the activation energy required for the reaction, U<sub>4</sub>O<sub>9</sub> → U<sub>3</sub>O<sub>8</sub>, would depend directly on burnup.

Hanson (1998) has shown that the fission product and actinide dopants appear to suppress the onset of oxidation of U<sub>4</sub>O<sub>9</sub> to U<sub>3</sub>O<sub>8</sub>. The higher concentration of fission products gives a more stable crystalline structure for the fluorite UO<sub>2</sub> and delays the formation of U<sub>3</sub>O<sub>8</sub>. Irradiated UO<sub>2</sub> resists oxidation, as evident from the O/M histories. Moderate burnup UO<sub>2</sub> (27 to 30 MWd/kgU) has a very long plateau at which U<sub>4</sub>O<sub>9</sub> resists further oxidation to U<sub>3</sub>O<sub>8</sub>. This plateau has both a burnup dependency and a grain-size dependency. Lower temperatures and higher burnup fuels resist this transformation to U<sub>3</sub>O<sub>8</sub>, whereas unirradiated and low-burnup fuel oxidize to U<sub>3</sub>O<sub>8</sub> more rapidly. The formation of U<sub>3</sub>O<sub>8</sub> from U<sub>4</sub>O<sub>9</sub> in irradiated fuels proceeds very slowly if the temperature is less than 250°C because of the high activation-energy barrier.

McEachern et al. (1997) performed a critical evaluation of the various techniques to measure the kinetics of  $U_3O_8$  formation and to understand the reason behind the considerable disparities in the results. Instead of using the weight-gain experiments, they used X-ray powder diffraction (XRD) to measure the rate of formation of  $U_3O_8$  on the  $UO_2$  surface. Involved are at least two different reactions, seemingly at different temperature ranges:

- $U_3O_8$ -spallation reaction
- Powder-formation reaction

McEachern et al. state there is no theoretical justification for the assumption of linearity in the kinetic reactions when it has been repeatedly shown the oxidation reactions are really sigmoidal. They obtained an average value for the activation energy of approximately 146.5 kJ/mole (35 kcal/mole) for the formation of  $U_3O_8$ , which is the range measured by other investigators.

Harrison et al. (1967) argue that the oxidation of  $UO_2 \rightarrow U_3O_7 / U_4O_9 \rightarrow U_3O_8$  is at least a two-stage kinetic reaction. In their experiments, they considered the oxidation of spheres of both natural uranium oxide (mean diameter of 120  $\mu\text{m}$ ) and enriched 93v (93%  $^{235}\text{UO}_2$ ) spheres with mean diameters of 150  $\mu\text{m}$ . The thickness of the  $U_3O_7$  layer was estimated to be less than 100 nm, and the  $U_4O_9$  formation appeared to follow behind the propagating  $U_3O_7$  front. They observed that, based on first-order kinetics, the two-stage kinetic reaction had discontinuous slopes. They found it very difficult to ascribe an exact meaning to the "order" of the reaction. They subjected the 93v pellets to different burnups and observed a dependence on the second-stage activation energies.

Thomas et al. (1993) studied the oxidation of LWR fuel in the burnup range 27-48 MWd/kgU. In this burnup range, 3 to 4.5% of the initial U atoms are involved in fission. At approximately 30 MWd/kgU, there are about 1% Pu and 3% fission products that exist in solid solution. Table 3.2.2-12 is reproduced from the paper by Thomas et al. (1993).

Table 3.2.2-12 Physical properties of some spent fuels

Fuel Reactor	ATM-105 Cooper	TP Turkey Point	ATM-104 Calvert Cliffs	ATM-106 Calvert Cliffs
Fuel Type	BWR 7x7	PWR 15x15	PWR 14x14	PWR 14x14
Burnup (MWd/kgU)	28	27	43	48
Fission Gas Release	0.6%	0.3%	1.1%	1.8%
Post Grain Size ( $\mu\text{m}$ )	11-15	20-30	10-13	7-15

Oxidation of spent fuel at 175 and 195°C showed  $\text{UO}_2$  oxidized to  $\text{U}_4\text{O}_9$  along grain boundaries and saturated at the O/M levels of 2.40. Thomas et al. (1989) studied 27 MWd/kgU spent fuel by transmission electron microscopy (TEM) and found very small 2-nm gas bubbles and 30-nm solid particles deposited within the  $\text{UO}_2$  and apparent cracks from oxidation of  $\text{UO}_2$  to  $\text{U}_4\text{O}_9$ . Whereas unirradiated  $\text{UO}_2$  oxidized uniformly, the irradiated  $\text{UO}_2$  with the gas bubbles appeared to oxidize preferentially, causing a short circuit in favor of bulk oxygen diffusion. In spent fuel,  $\text{U}_4\text{O}_9$  forms preferentially along grain boundaries, and sharp oxidation fronts were observed.

Einzigler et al. (1991) argued that, thermodynamically,  $\text{UO}_2$  should oxidize completely to  $\text{UO}_3$ . The basic uncertainty is the kinetics of such oxidation. They found that, because the grain-boundary-surface-area-to-volume ratio is inversely proportional to grain size, the 11 to 15 mm Cooper BWR fuel oxidized more rapidly than the larger, 20 to 30  $\mu\text{m}$  Turkey Point PWR fuel. In 12 comparisons with experimental data, the oxidation model by Stout et al. (1989, 1991, 1993a, 1993b, and version 1.2 of this document) clearly show this grain-size dependency on the O/M histories for the consecutive reactions:  $\text{UO}_2 \rightarrow \text{U}_4\text{O}_9$  and  $\text{U}_4\text{O}_9 \rightarrow \text{U}_3\text{O}_8$ . Stout et al. (1993a and 1993b) showed that the stress state for  $\text{UO}_2 \rightarrow \text{U}_4\text{O}_9$  transformation is sufficient to form microcracks; this is even more so the case for the  $\text{U}_4\text{O}_9 \rightarrow \text{U}_3\text{O}_8$  transformation in which  $\text{U}_3\text{O}_8$  spalls.

Experimentally, it is nearly impossible to obtain a monosized distribution of spent-fuel grain sizes. Stout et al. (version 1.2 of this document) showed that the experimental results were bounded in an envelope of monosized particles whose grain half sizes ranged from 4-24  $\mu\text{m}$ . The larger-sized particles oxidized considerably more slowly, and the transformation from  $\text{U}_4\text{O}_9$  to  $\text{U}_3\text{O}_8$  would exhibit a plateau.

With this brief background, it is possible to extend the previous work of Stout et al. (version 1.2 of this document). Previously, a set of monosized  $\text{UO}_2$  grains formed a bounding envelope for the ODB experimental measurements of  $\text{UO}_2 \rightarrow \text{U}_4\text{O}_9 \rightarrow \text{U}_3\text{O}_8$ . This envelope of grain half sizes is appropriate for the phase transformation  $\text{UO}_2 \rightarrow \text{U}_4\text{O}_9$ , but not for the next phase transformation,  $\text{U}_4\text{O}_9 \rightarrow \text{U}_3\text{O}_8$ .

The initial grain-size distribution for the phase transformation  $\text{UO}_2 \rightarrow \text{U}_4\text{O}_9$  is not appropriate for the subsequent phase transformation  $\text{U}_4\text{O}_9 \rightarrow \text{U}_3\text{O}_8$  because shrinkage cracks in the  $\text{U}_4\text{O}_9$  alter the original  $\text{UO}_2$  grain-size distribution. Thomas et al. (1991) presented optical micrographs of LWR (ATM-101) spent-fuel fragments showing the pellet rim and the fracture edge of the partial oxidation of  $\text{UO}_2 \rightarrow \text{U}_4\text{O}_9$ . The nominal burnup was 28.4 MWd/kgU, and the initial  $\text{UO}_2$  grain sizes were typically about 15 to 25  $\mu\text{m}$ . However, the micrographs of the  $\text{U}_4\text{O}_9/\text{UO}_2$  (see Thomas et al, 1991, Figure 2) showed a multitude of grain boundary and transverse cracks with a grain-size distribution ranging from 1.5 to 11  $\mu\text{m}$ , with a preponderance of

fine grain sizes, and relatively few larger grains (on the order of 8 to 11  $\mu\text{m}$ ). Grain-boundary cracking in the  $\text{U}_4\text{O}_9$  phase is a result, rather than the cause, of the oxidation.

Similarly, Thomas and Einziger (1992) studied ATM-103 PWR spent-fuel oxidation. The nominal burnup was 30 MWd/kgU, and the post-irradiation average grain size of the  $\text{UO}_2$  was 18.5  $\mu\text{m}$ . They oxidized the spent fuel at a constant temperature of 195°C. In Figure 1 of their report, they presented a series of micrographs taken at 24, 48, 118, and 355 hr. That boundary and transverse cracks yielded progressively finer grains is clearly evident from their micrographs. At 355 hr [ $\Delta(\text{O}/\text{M}) = 0.16$ ], there were grain sizes ranging from 3 to 22  $\mu\text{m}$ . The American Society for Testing and Materials (ASTM) grain size was determined to be 9.6  $\mu\text{m}$ .

### 3.2.2.9 Model Enhancements

The model enhancements for the reaction  $\text{U}_4\text{O}_9 \rightarrow \text{U}_3\text{O}_8$  are three-fold:

1. A log-normal distribution for grain sizes are assumed for the  $\text{U}_4\text{O}_9$ .
2. The activation energy  $Q_{38}$  for the phase transformation  $\text{U}_4\text{O}_9 \rightarrow \text{U}_3\text{O}_8$  varies linearly with burnup.
3. Spent-fuel  $\text{U}_4\text{O}_9$  samples contaminated with what appears to be a dehydrated schoepite film have a lower  $Q_{38}$  than does unhydrated  $\text{U}_4\text{O}_9$ . (This issue of dehydrated schoepite will be discussed subsequently.)

The basic formulation of the grain and fragment size statistical dependence for the oxidation response model has been presented by Stout et al. (1989, 1991, 1993a, 1993b, and version 1.2 of this document). Fragments are assumed to be composed of pyramidal shapes of varying sizes, in accordance with some probabilistic density function. The integrated response for the oxidation or weight gain history of a heterogeneous sample having some probabilistic density function of grain size distribution was formulated.

A heterogeneous sample of  $\text{U}_4\text{O}_9$  grains can be viewed as an ensemble of various numbers of monosized grains. For each monosized grain of half size  $c_i$ , assume there are  $N_i$  grains. Let  $P(c_i)$  be the normalized fractional distribution of grains with half-size,  $c_i$ . Let the response history of a monosized  $\text{U}_4\text{O}_9$  grain of size  $c_i$  be denoted by  $h(t|c_i)$ . Then the average, or expected, value of the history of a heterogeneous sample undergoing oxidation ( $\text{U}_4\text{O}_9 \rightarrow \text{U}_3\text{O}_8$ ) is given by

$$h(t) = \sum_i h(t|c_i)P(c_i).$$

3.2.2-23

Remenyi (1974, pp 78-81) showed that, in most circumstances, the grain-size distribution is a log normal with the mean value shifted toward fine grain sizes. This type of distribution will be assumed throughout the remaining portions of Section 3.2.2.

The Arrhenius chemical kinetics are very temperature-sensitive. The rate of  $U_3O_8$  formation is the primary concern in a repository environment. The frontal speed  $\dot{W}_{38}$  (see Eq. 3.2.2-14a) depends on temperature, activation energy, and the distribution of grain half sizes.

By using nonequilibrium thermodynamics, Stout et al (1993b) showed that the phase-transformation, front-rate tensors and mass-transport tensors are burnup-dependent. That is, oxidation rate is suppressed monotonically with increasing concentrations of fission products and actinides. They predicted that the thermodynamic models have a linear burnup dependence. After considerable analyses of numerous TGA and ODB experiments, Hanson (1998) confirmed the conjecture that there is indeed a linear burnup dependence on the activation energy for the reaction  $U_4O_9 \rightarrow U_3O_8$ . He found that, because the dopant fission products are directly proportional to burnup, the activation energy varies approximately as

$$Q_{38} = (Q_{38}^0 + \alpha \cdot BU) \text{kJ/mole-}^\circ\text{K} \quad 3.2.2-25$$

where  $Q_{38}^0 = 155 \text{ kJ/mole-}^\circ\text{K}$ ,

and  $\alpha = 1.2 \text{ kJ/(mole-}^\circ\text{K- MWd/kgU)}$ .

The uncertainty in  $Q_{38}$  is at least 10 to 15 kJ/mole (2.4-3.6 kcal/mole). Larger uncertainties in the fit can be attributed to the radial distribution in the fission and actinide concentrations; the quantity of actinides produced by neutron absorption can vary even for samples of nearly identical burnup. For more details, see Hanson (1998).

Thin films of what appears to be dehydrated schoepite have been found on some TGA and ODB samples. Before conducting the experiments, the spent-fuel samples had been stored at room temperature for a couple of years, and these samples reacted with the water vapor in the air to form thin schoepite films. Those samples with such schoepite films gained weight much more rapidly than did the unhydrated samples. The most plausible explanation is that the schoepite having a fine needle-like structure has a greatly increased effective surface area for oxygen adsorption and thus raises the oxygen potential available to the adjacent grains. These grains behaved as if their respective activation energies were lower than were those of the unhydrated grains.

The model presented in Section, 3.2.2.4, with the modification introduced in Section 3.2.2.9, is sufficiently robust to handle  $U_4O_9$  distributions, burnup-dependent

activation energies, and schoepite-modified activation energies.

The enhanced model is compared with experiments from two distinct experiments:

1. Thermogravimetric analysis (TGA), in which small samples (200 mg) were oxidized
2. Oven drybath (ODB) oxidation, in which larger samples (5 g) were used

In the next two subsections, model comparisons with the various experiments will be presented. Because  $U_3O_8$  has a potential, disruptive effect on depository performance, these studies will focus on the conversion of  $U_4O_9 \rightarrow U_3O_8$ .

### 3.2.2.10 Model Predictions of $U_4O_9 \rightarrow U_3O_8$ with TGA Experiments

It is advantageous to focus on the TGA oxidation experiments because there ought to be much less variability among individual samples (200 mg) than there is with the much larger ODB samples (5g). The present focus is on ATM-105-sample experiments conducted at different temperatures. The ATM-105 samples were stored in hot cells at room temperature for a number of years, and some of them appear to have formed a hydrated phase of dehydrated schoepite on the  $UO_2$ . Using SEM, clear photographic evidence of this hydrated film was found on several samples for both the TGA and the ODB oxidation experiments. The hydrated-surface formation was observed on the TGA samples ATM-105-01 and ATM-105-02 and on the ODB samples TP-P2-100 and 104F-100. This formation was identified on the fines of ATM-105 stored under identical conditions in the same hot cell. It is highly probable that the hydrated formation exists on other samples as well, especially on those that have been stored for extended periods at ambient temperature before being oxidized. While not all the suspected samples were analyzed by SEM, Hanson inferred that those samples that experienced very rapid initial weight gains had this dehydrated schoepite contamination, and the model results appear to have confirmed this hypothesis.

It is assumed that, in the process of forming  $U_4O_9$ , stress cracks will subdivide the original, larger grain-sized  $UO_2$ . Theoretically, the grain sizes have a log-normal grain-size distribution. This distribution was approximated by four grain half-size bins. Four grain half-size bins were chosen to limit the number of adjustable free parameters. An initial set of four representative grain half-size bins and their corresponding fractions were selected, and iteratively improved to give the best fit with the experimental  $\Delta(O/M)$  histories. Note that the  $\Delta(O/M)$  histories of this set of experiments exhibit a linear relation.

Hanson (1998) recorded the axial location in the fuel rod from which the sample came. He performed analyses on these samples to estimate the individual burnup. Even though the ATM-105 samples had a reported average burnup of 31 MWd/kgU in the high-burnup region, Hanson found significant variations in burnup with the ATM-105 samples. These variations in burnup are presented in Table 3.2.2-13. Because of these variations, it was decided to verify the model against the TGA experiments, taking into account the burnup variation with  $Q_{38}$ .

**Table 3.2.2-13** Burnup estimates of the TGA-104 and TAG-105 200-mg samples

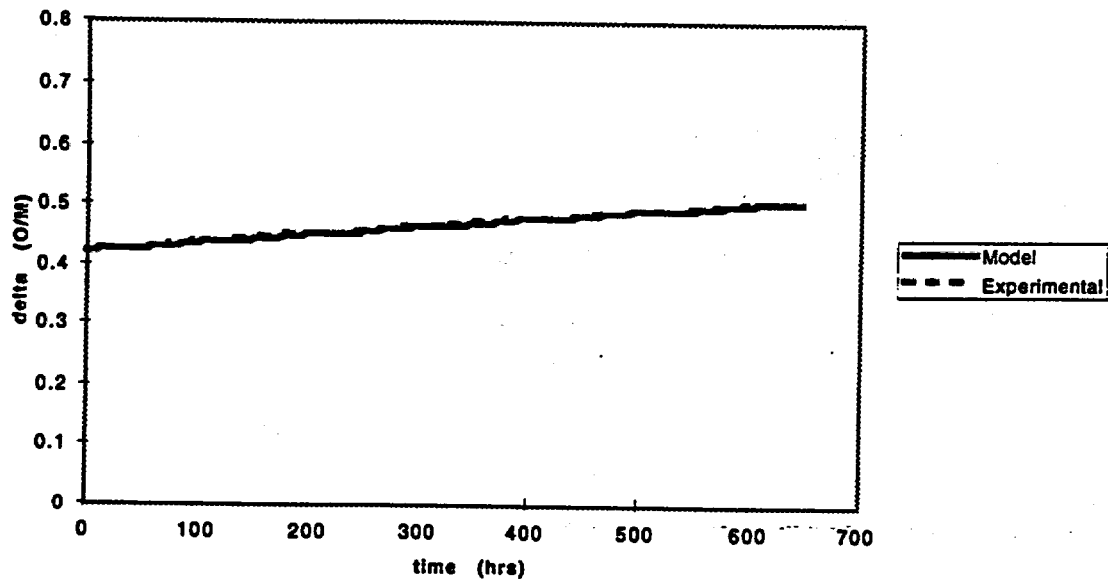
Sample Identifier	Sample Burnup (MWd/kgU)
105-01	unknown
105-02	unknown
105-03	28.1
105-04	27.5
105-06	31.5
105-10	29.8
105-11	29.6
105-14	28.1
105-15	18.6
105-17	16.7
105-18	16.8
104-01	42.3

Table 3.2.2-14 lists the sample specimen for samples ATM-105-04 through ATM-105-10, the optimized activation energy  $Q_{38}$ , the four grain half-sizes bins, and their respective fractions. Figures 3.2.2-9 through 3.2.2-12 show the fit of the theoretical histories (solid lines) and the experimental histories (dotted lines). The experimental measurements of  $\Delta(O/M)$  are accurate to 0.01; except for the experimental data scatter, the agreement is excellent. None of the ODB data that was used was regressed or smoothed. The TGA data shown in the figures are averages over a one-hour period; no other smoothing was performed.

**Table 3.2.2-14** TGA nonhydrated samples listing the temperatures at which the experiment was conducted, the optimized  $Q_{33}$ , and the grain half sizes and corresponding fractions

Sample	T (°C)	$Q_{33}$	$c_1$	$F_1$	$c_2$	$F_2$	$c_3$	$F_3$	$c_4$	$F_4$
105-04	270	182	1.05	0.45	2.00	0.40	5.00	0.10	7.00	0.05
105-06	283	189	1.00	0.39	2.00	0.36	4.00	0.13	7.00	0.12
105-10	305	183	0.90	0.61	2.00	0.29	3.50	0.09	6.40	0.01
105-11	305	185	0.90	0.33	1.70	0.36	4.10	0.15	7.50	0.16
105-14	305	183	1.00	0.35	1.80	0.43	3.30	0.14	6.00	0.08
105-17	305	174	0.35	0.60	0.70	0.25	3.50	0.10	7.00	0.05
104-01	305	194	1.00	0.48	2.00	0.33	4.00	0.13	7.00	0.06

TGA 104-01 (305 C)



**Figure 3.2.2-9**  $\Delta$  (O/M) versus time (hr) for the TGA sample ATM-104-01 (305°C)

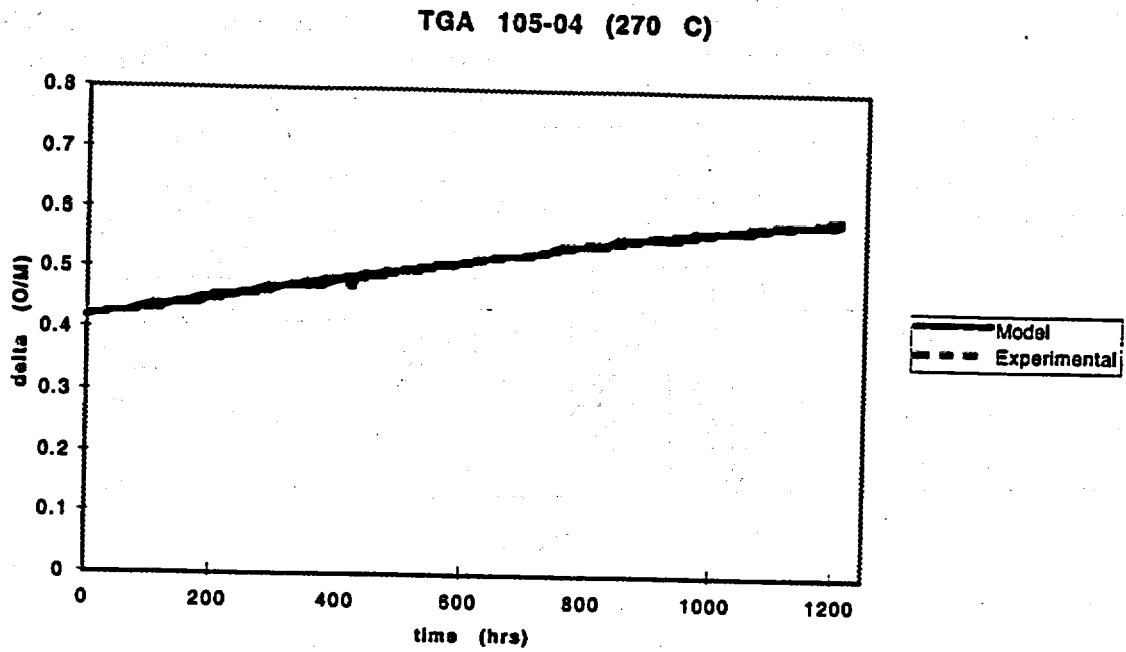


**Figure 3.2.2-10**  $\Delta$  (O/M) versus time (hr) for the TGA sample ATM-105-04 (270°C)

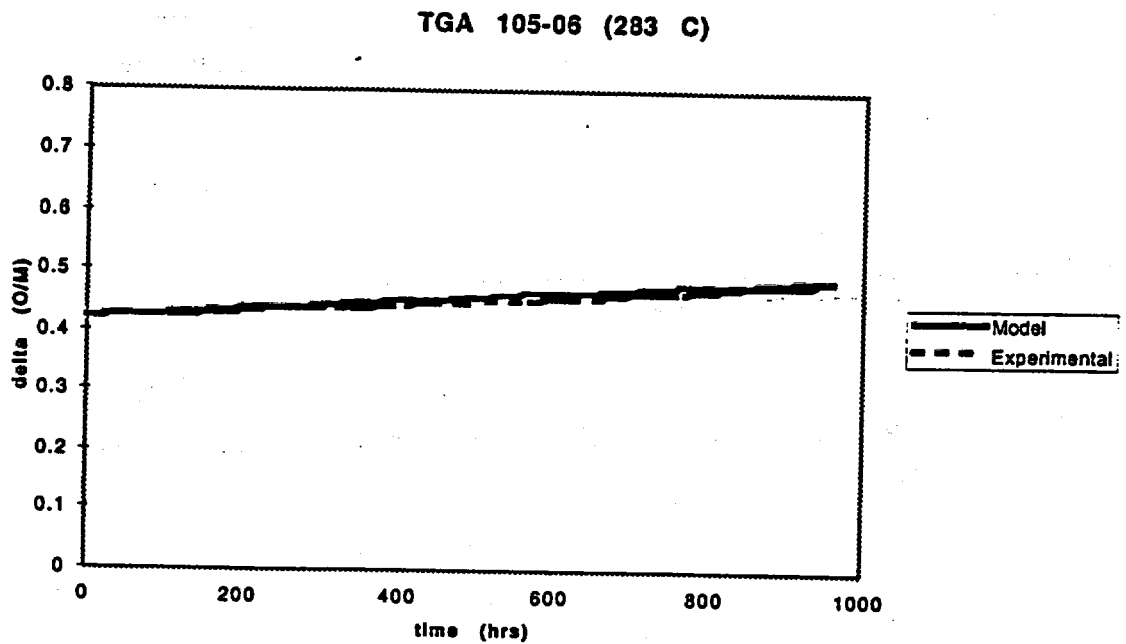


**Figure 3.2.2-11**  $\Delta$  (O/M) versus time (hr) for the TGA sample ATM-105-06 (283°C)

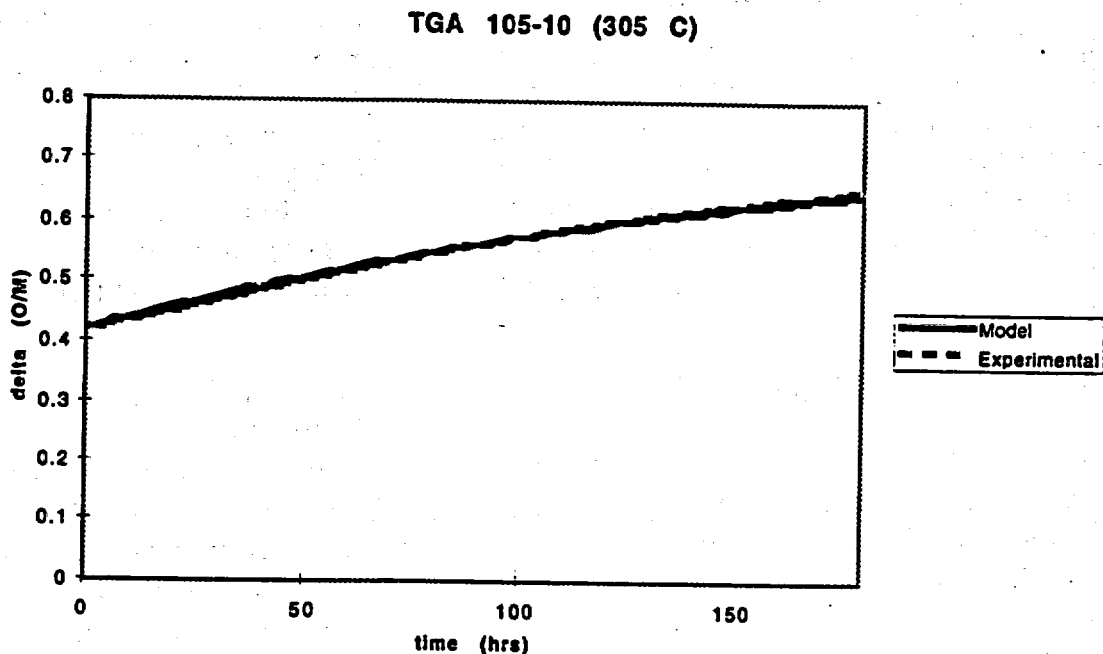


**Figure 3.2.2-12**  $\Delta$  (O/M) versus time (hr) for the TGA sample ATM-105-10 (305°C)

Other TGA samples (ATM-105-01, ATM-105-02, ATM-105-03, ATM-105-11, ATM-105-14, ATM-105-15, 105-17, and ATM-105-18) appear to exhibit anomalous behavior. These TGA samples did not exhibit a linear relation of  $\Delta$ (O/M) with respect to time. On closer inspection using SEM, Hanson observed that samples ATM-105-01 and ATM-105-02 had formed a thin layer of what appears to be dehydrated schoepite. (It is possible that samples ATM-105-03, ATM-105-11, and ATM-105-14 had some hydrated-phase formation, but this has not been confirmed.) Such samples exhibited a nonlinear weight-gain relation early in the experiment but asymptotically leveled off to a more linear relation with time. This behavior could be explained by either of two explanations:

- Somehow the samples had a distribution of very fine grain sizes, some of which could be smaller than  $0.07 \mu\text{m}$ . This explanation was dismissed because the shrinkage stresses that would occur in the formation of  $\text{U}_4\text{O}_9$  were not believed sufficient to form such small grains.
- The dehydrated schoepite, having a pronounced needle-like structure that greatly increases the effective surface area (the same effect as having smaller grain sizes), acts as a conduit for rapid oxygen transfer initially. After a sufficient amount of  $\text{U}_4\text{O}_9$  had formed and spalled, the remaining unhydrated  $\text{U}_4\text{O}_9$  oxidized more slowly with a nearly linear relation with time. This explanation seems to be the more reasonable scenario, and there is sufficient evidence that this is most plausible.

Samples ATM-105-15, ATM-105-17, and ATM-105-18 all came from the low-burnup (15-20 MWd/kgU), upper end of the same fuel rod as did the other ATM-105 samples. These samples are expected to have experienced very little grain growth because of the lower temperatures corresponding to the lower fission density. It is not clear whether  $U_3O_8$  formed concurrently with the  $U_4O_9$  phase or if  $U_3O_7$  formed instead. Further work on the low-burnup fuels is necessary to determine the cause for the observed difference in oxidation behavior. These samples came from a freshly cut segment of clad fuel, so the presence of the hydrated phase is not expected.

Tables 3.2.2-15 through 3.2.2-18 list the optimized  $Q_{38}$ , grain half sizes and fractions for the four bins for the TGA samples: ATM-105-01, ATM-105-02, ATM-105-03, ATM-105-11, ATM-105-14, ATM-105-17, and ATM-105-18. Figures 3.2.2-13 through 3.2.2-20 show the experimental and model  $\Delta(O/M)$  histories. The TGA model time histories are in excellent agreement with the experimental measurements for those samples with a thin layer of schoepite. It appears that the  $U_4O_9 \rightarrow U_3O_8$  kinetic model can indeed account for the presence of schoepite if the activation energies and effective grain sizes were adjusted downward for those bins influenced by the hydrated phase.

**Table 3.2.2-15** TGA-105-01 hydrated sample listing the optimized  $Q_{38}$  for each bin and the corresponding grain half sizes and fractions

$Q_{38}$	$c_1$	$F_1$	$c_2$	$F_2$	$c_3$	$F_3$	$c_4$	$F_4$
178.5	0.70	0.18						
178.0			1.50	0.30				
169.6					3.70	0.515		
169.6							7.00	0.005

**Table 3.2.2-16** TGA-105-02 hydrated sample listing the optimized  $Q_{38}$  for each bin and the corresponding grain half sizes and fractions

$Q_{38}$	$c_1$	$F_1$	$c_2$	$F_2$	$c_3$	$F_3$	$c_4$	$F_4$
178.5	0.7	0.18						
178.5			1.50	0.30				
170.0					4.00	0.47		
170.0							6.00	0.05

**Table 3.2.2-17** TGA-105-03 hydrated sample listing the optimized  $Q_{38}$  for each bin and the corresponding grain half sizes and fractions

$Q_{38}$	$c_1$	$F_1$	$c_2$	$F_2$	$c_3$	$F_3$	$c_4$	$F_4$
159.6	1.00	0.45						
159.6			2.00	0.35				
154.8					4.00	0.15		
154.8							7.00	0.05

**Table 3.2.2-18** TGA-105-18 hydrated sample listing the optimized  $Q_{38}$  for each bin and the corresponding grain half sizes and fractions

$Q_{38}$	$c_1$	$F_1$	$c_2$	$F_2$	$c_3$	$F_3$	$c_4$	$F_4$
150.4	1.15	0.45						
150.4			2.30	0.35				
160.6					4.00	0.15		
160.6							7.00	0.05

TGA 105- 11 ( 305

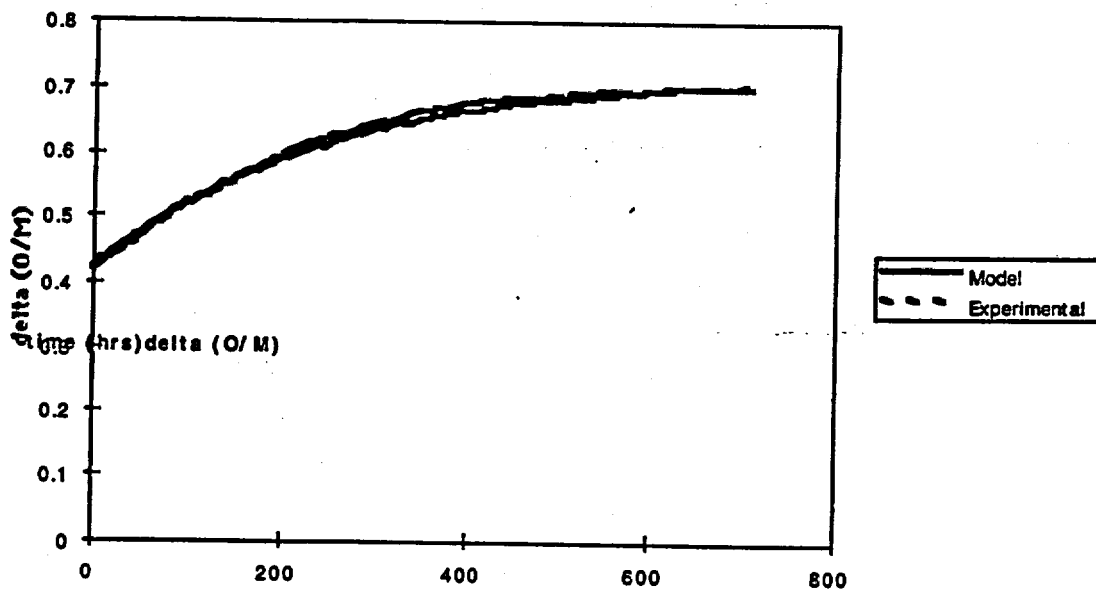


**Figure 3.2.2-13**  $\Delta$  (O/M) versus time (hr) for the TGA sample ATM-105-11 (305°C); some shoeelite present

TGA 105-14 (305 C)

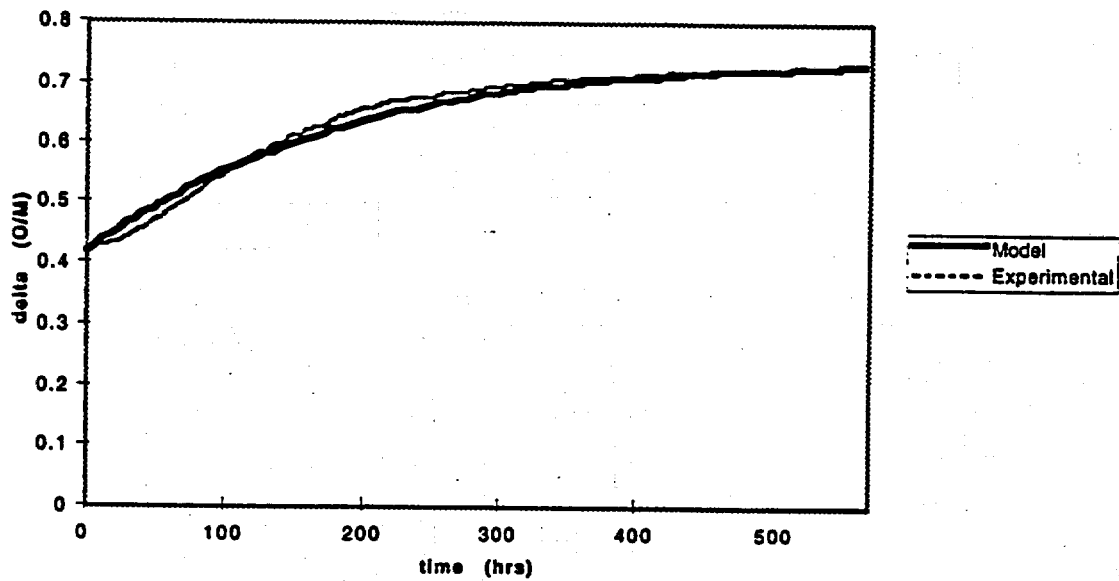


Figure 3.2.2-14  $\Delta$  (O/M) versus time (hr) for the TGA sample ATM-105-14 (305°C); some shoepite present

TGA 105-01 (305 C)

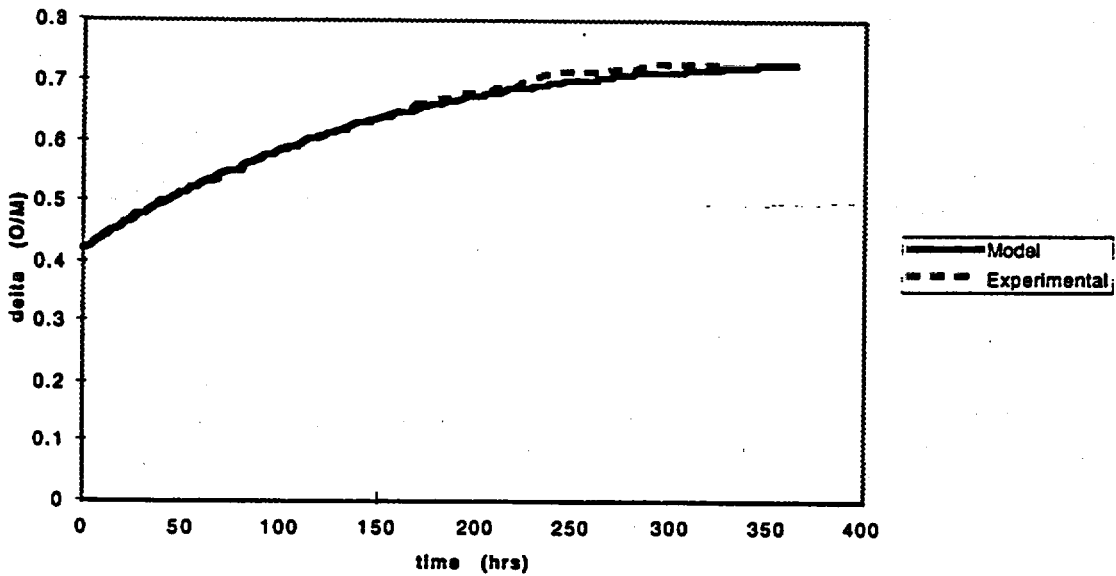


Figure 3.2.2-15  $\Delta$  (O/M) versus time (hr) for the TGA sample ATM-105-01 (305°C); shoepite present

TGA 105-02 (325 C)

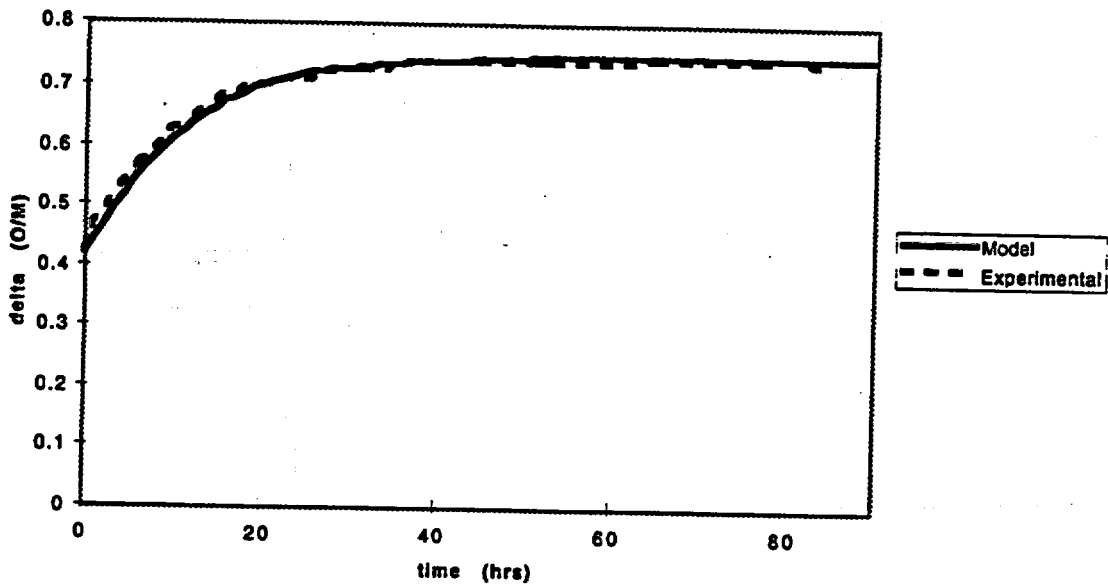


Figure 3.2.2-16  $\Delta$  (O/M) versus time (hr) for the TGA sample ATM-105-02 (325°C); shoepite present

TGA 105-03 (305 C)

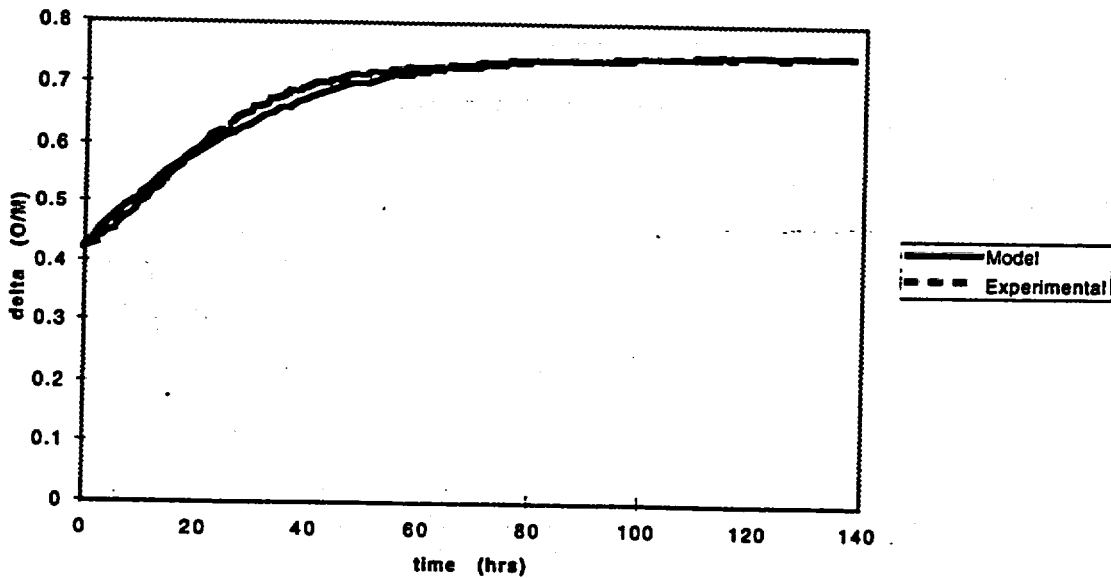
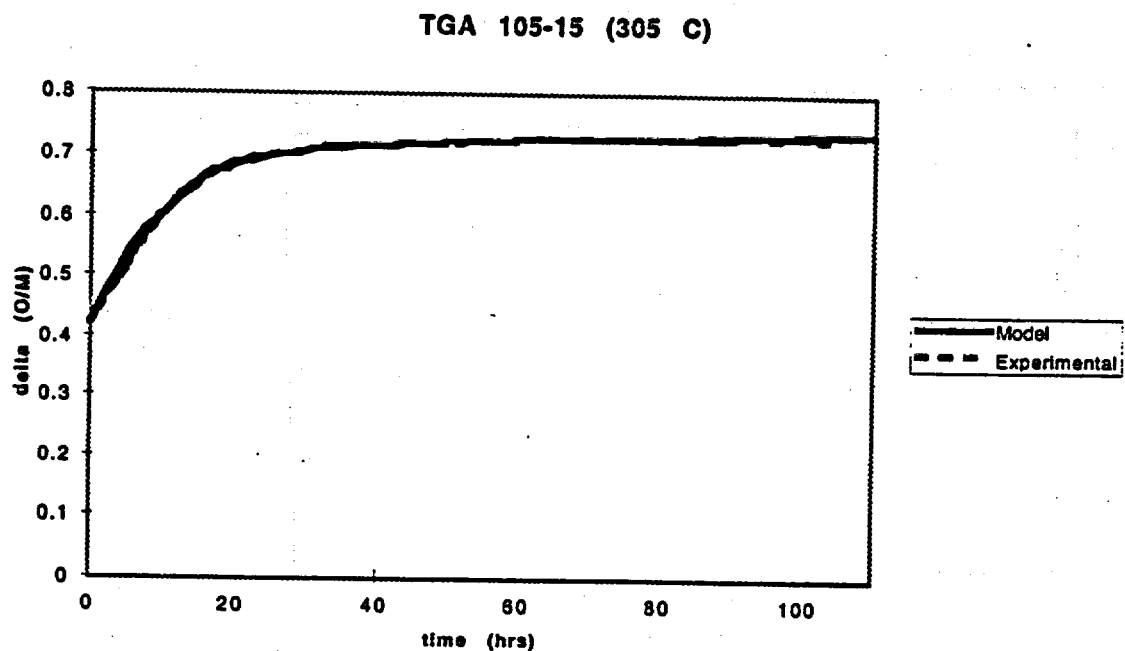
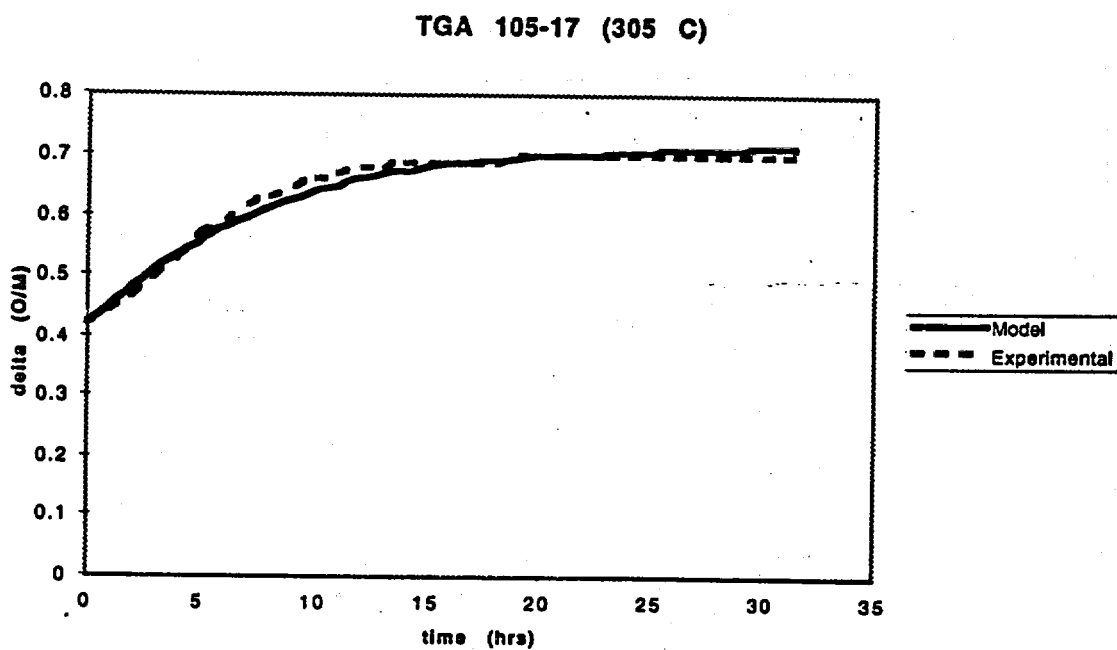


Figure 3.2.2-17  $\Delta$  (O/M) versus time (hr) for the TGA sample ATM-105-03 (305°C); shoepite present



**Figure 3.2.2-18**  $\Delta$  (O/M) versus time (hr) for the TGA sample ATM-105-15 (305°C); shoepite present



**Figure 3.2.2-19**  $\Delta$  (O/M) versus time (hr) for the TGA sample ATM-105-17 (305°C); shoepite present

### TGA 105-18 (305 C)

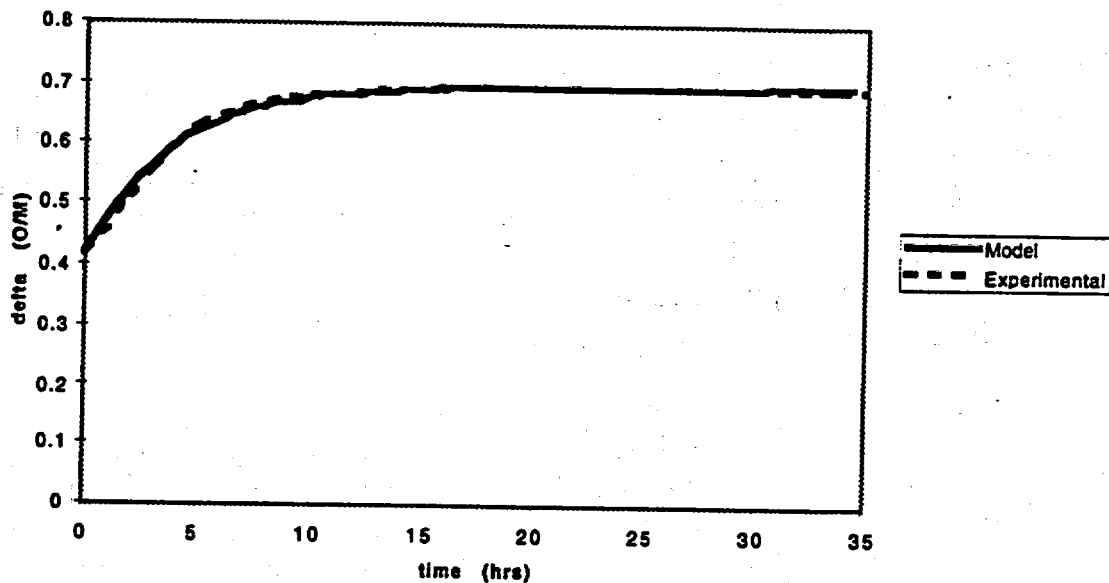


Figure 3.2.2-20  $\Delta$  (O/M) versus time (hr) for the TGA sample ATM-105-18 (305°C); shoebite present

#### 3.2.2.11 Model Predictions of $U_4O_9 \rightarrow U_3O_8$ with Oven Drybath Experiments

The experimental data against which the model was fit were based on the work of Einziger et al. (1995 and 1996) on LWR spent fuel at various burnups and initial  $UO_2$  grain sizes. The test consisted of 11 samples: 7 samples consisted of 5 g of spent-fuel fragments, and the remaining 4 samples consisted of 5 g of crushed fuel fragments.

Two of the seven samples of the uncrushed fragments were prepared from one of each ATM-104 and ATM-105 as-irradiated fuel fragments with no prior oxidation. The third sample was the Turkey Point fuel that had been oxidized at 110°C for 28,868 hr to an O/M of ~2.004. The fourth sample was ATM-106 fragments that had been oxidized at 110°C for 525 hr to an O/M = 2.000. Another set of samples included Turkey Point fuel that had been slightly oxidized at 175°C for 43,945 hr to an O/M = 2.395, an ATM-105 fuel that had been oxidized at 175°C for 34,430 hr to an O/M = 2.422, and an ATM-104 sample that had been oxidized at 175°C for 15,671 hr to an O/M = 2.395. For more details, see Hanson (1998).

For a specific ATM, the pulverized samples (denoted by the suffix P) gained weight more rapidly than did the samples of fragments (denoted by the suffix F). All samples with a -100 designation had been stored at ambient temperature in the hot cell longer than the other samples of the same ATM. These -100 samples were

expected to have a greater amount of hydrated-phase formation. This assumption is partially verified by the known presence of the hydrated phase on two of these samples (P2-100 and 104F-100).

Because the starting point for the various samples varied from unoxidized  $\text{UO}_2$ , mixtures of  $\text{UO}_2$  and  $\text{U}_4\text{O}_9$ , and completely converted  $\text{U}_4\text{O}_9$ , all the  $\text{U}_4\text{O}_9 \rightarrow \text{U}_3\text{O}_8$  modeling studies presented here adjusted the time when the reaction  $\text{UO}_2 \rightarrow \text{U}_4\text{O}_9$  was complete. Using the O/M measurement at various times, the time for complete conversion of  $\text{UO}_2 \rightarrow \text{U}_4\text{O}_9$  was linearly extrapolated to the estimated time at which  $\Delta(\text{O}/\text{M}) = 0.42$ . With these caveats, the modeling and experimental studies focused on studying the reaction,  $\text{U}_4\text{O}_9 \rightarrow \text{U}_3\text{O}_8$  as a function of time.

The linear relation between activation energy and burnup (Eq. 3.2.2-23) was used for the ODB Turkey Point, ATM-105, ATM-104, and ATM-106 samples in a manner similar to the previously described study with the TGA samples. The optimized fractions and grain half sizes obtained from the TGA fits were used to start the iteration scheme. In the TGA experiments, the O/M histories were obtained at different temperatures; all the ODB samples used for this analysis were conducted at a constant 255°C.

As was the case with the TGA experiments, the ODB data set was fitted in two categories:

- Those experimental samples that each had a nearly uniformly linear weight-gain history
- Those experimental samples that each had a rapid nonlinear initial weight-gain history that tended asymptotically to a linear weight-gain history

The ODB experiments that did exhibit a linear weight-gain history were lumped into two classes:

1. The Turkey Point and ATM-105 experiments had nearly similar burnups (28 and 27 MWd/kgU) and were expected to have similar grain half-size distributions and activation energies.
2. The ATM-104 and ATM-106 fuels had burnups of 43 and 48 MWd/kgU, respectively. These higher-burnup spent fuels had smaller starting  $\text{U}_4\text{O}_9$  grain half sizes because their starting  $\text{UO}_2$  grain half sizes were smaller. The ATM-106 fuel is known, however, to have a small amount of a restructured rim.

The optimized grain-size distributions for the nonhydrated Turkey Point and ATM-105 ODB samples are presented in 3.2.2-19, and the resulting comparison of the model fit and the experimental  $\Delta(\text{O}/\text{M})$  histories are presented in Figures 3.2.2-21 through 3.2.2-23. The grain-size fractions of the  $\text{U}_4\text{O}_9$  are reasonable with the photographs published by Thomas et al. (1991).

Table 3.2.2-19

ODB nonhydrated Turkey Point and ATM-105 samples listing the optimized  $Q_{38}$  for all bins and the corresponding grain half sizes and fractions

Fuel Sample	$Q_{38}$	Fraction (0.75,2.0) $\mu\text{m}$	Fraction (2.0,8.0) $\mu\text{m}$	Fraction (8.0,14.0) $\mu\text{m}$	Fraction >(14.0) $\mu\text{m}$
TP-F-003A	188.6	0.61	0.28	0.095	0.025
TP-F-017A	188.6	0.26	0.23	0.16	0.14
105F-13A	190.5	0.00	0.20	0.40	0.40

TP-F-003A

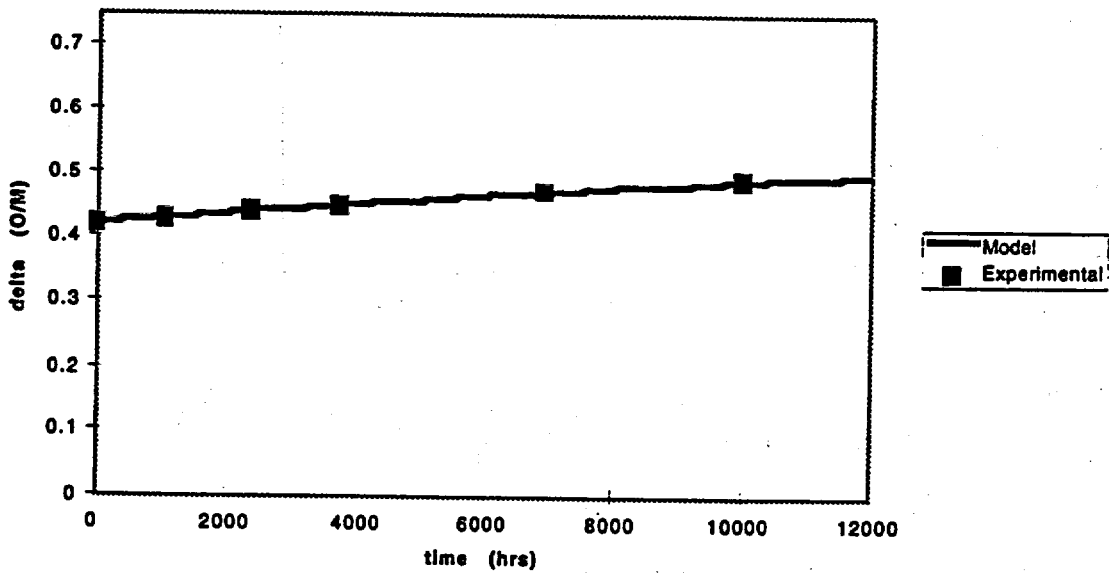


Figure 3.2.2-21  $\Delta$  (O/M) versus time (hr) for the ODB sample TP-F-003A; nominal burnup, 27 MWd/kgU

TP-F-017A

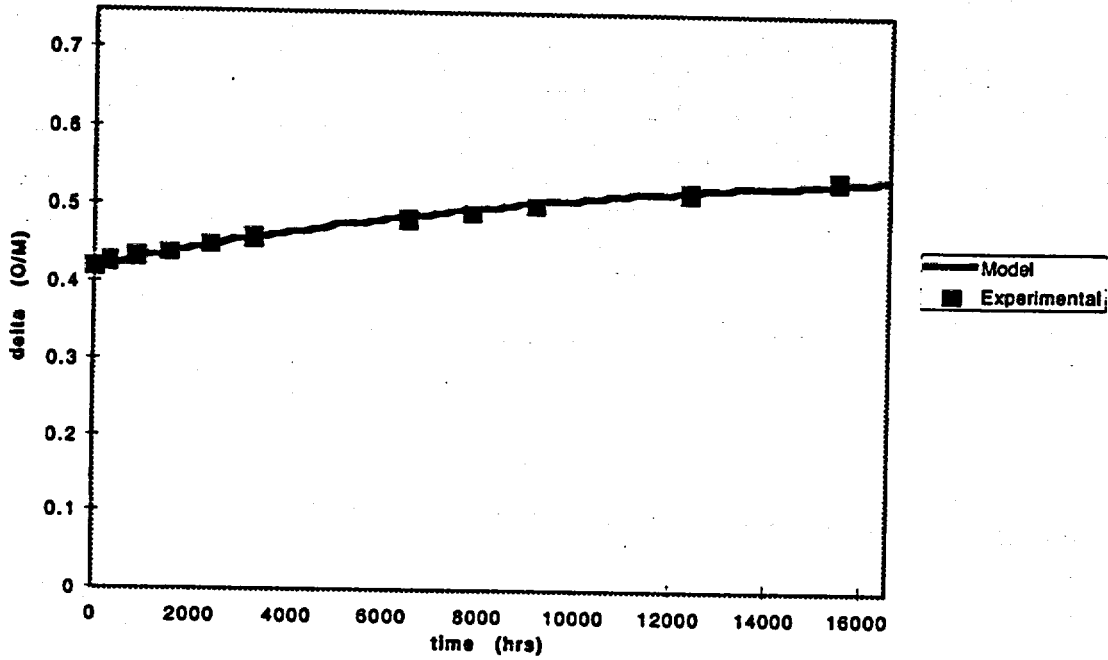


Figure 3.2.2-22  $\Delta$  (O/M) versus time (hr) for the ODB sample TP-F-017A; nominal burnup, 27 MWd/kgU

ATM 105F-013A

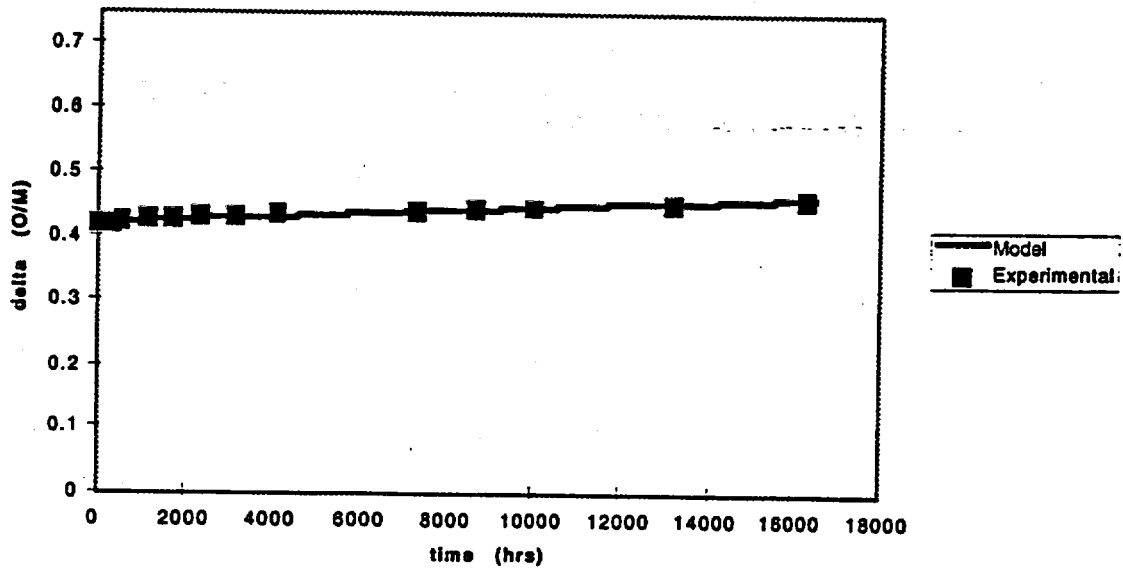


Figure 3.2.2-23  $\Delta$  (O/M) versus time (hr) for the ODB sample ATM-105F-013A; nominal burnup, 28 MWd/kgU

The higher burnup ATM-104 and ATM-106 fuel samples were an interesting set of experiments to fit. First, if nominal activation energy of 167.4 kJ/mole (40 kcal/mole) were used to fit these samples, the grain half sizes required would have ranged from 2-24  $\mu\text{m}$ . However, as shown in Table 3.2.2-12, which is taken from Thomas et al. (1991), the ATM-104 and ATM-106 spent fuels had unoxidized grain half sizes in the range of 5 to 6.5  $\mu\text{m}$  and 3.5 to 7.5  $\mu\text{m}$ , respectively. Not only do such large grain half sizes exceed that of the unoxidized  $\text{UO}_2$ , but also it would require that no grain subdivision occur in the formation of  $\text{U}_4\text{O}_9$ . This assumption was rejected as unphysical for these two reasons. It is not valid to use a  $Q_{38}$  that was optimized for a spent fuel having a burnup of 27 MWd/kgU for higher burnup spent fuels. The more reasonable approach was to use a burnup-dependent activation energy to account for the differences among the ATM fuels used in the ODB experiments.

The optimization for these higher burnup fuels was constrained to have grain sizes no smaller than 0.1 to 0.25  $\mu\text{m}$ , the size obtained when the rim region undergoes restructuring. Thus, the free parameters of the oxidation reaction  $\text{U}_4\text{O}_9 \rightarrow \text{U}_3\text{O}_8$  are the distribution of the grain half sizes in the bins and the activation energy. It was assumed that these higher burnup fuels with no obvious evidence of hydrated layers could be assigned a uniform activation energy throughout the sample. As pointed out by Hanson (1998), the activation energy has an uncertainty of at least 10 to 15 kJ/mole for the  $\text{U}_4\text{O}_9 \rightarrow \text{U}_3\text{O}_8$  reaction. The optimized grain half-size distributions and activation energies are presented in Table 3.2.2-20 for the ATM-104F-005A, ATM-106F-022A, and ATM-106F-13A samples. The comparison of the model fits and the experimental data are presented in Figures 3.2.2-24 through 3.2.2-26. The extremely fine-grain structure obtained for these samples is not realistic. The samples would have to contain virtually all restructured rim and/or there must be more cracking of the  $\text{U}_4\text{O}_9$  grains. Because all the ODB samples were at 255°C,  $\text{U}_4\text{O}_9$  would be expected to yield similarly sized cracked-grain sizes. An alternative explanation is that these samples contained, at most, 20% restructured rim and also hydrated phase. This would shift the effective grain sizes toward smaller values. At present, much more experimental study is required to confirm such speculations.

**Table 3.2.2-20 ODB nonhydrated ATM-104 and ATM-106 samples listing the optimized  $Q_{38}$  for all bins and the corresponding grain half sizes and fractions**

Fuel Sample	$Q_{38}$	Fraction (0.1–0.25) mm	Fraction (0.25–0.5) mm	Fraction (0.5–1.0) mm
104F-00F5A	201.1	0.74	0.11	0.05
106F-022A	203.2	0.74	0.11	0.05
106F-13A	204.6	0.74	0.11	0.05

ATM 104F-005A

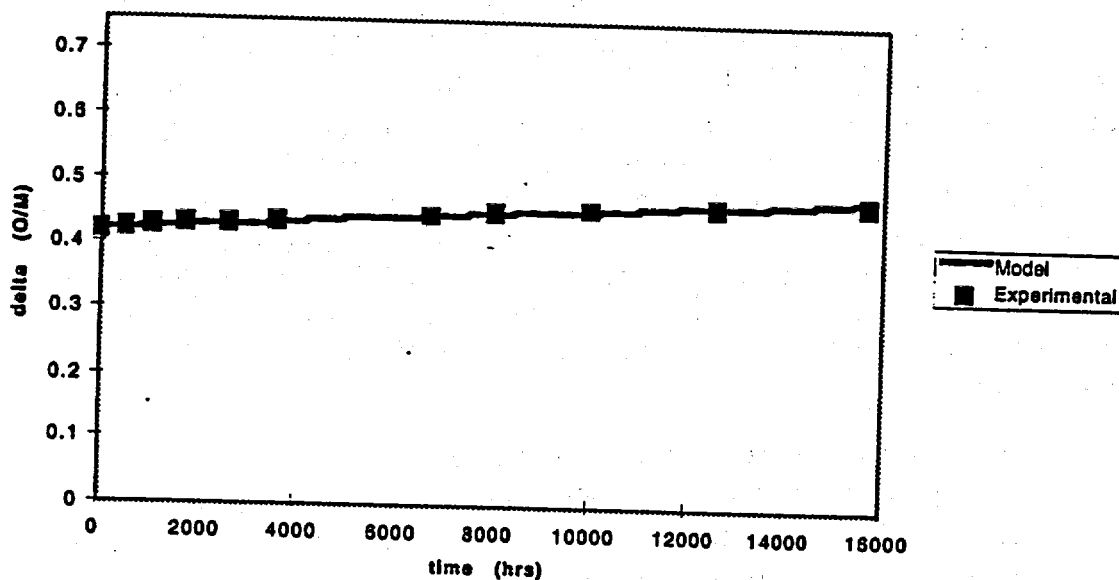


Figure 3.2.2-24  $\Delta$  (O/M) versus time (hr) for the ODB sample ATM-104F-005A; nominal burnup, 43 MWd/kgU

ATM 106F-013A

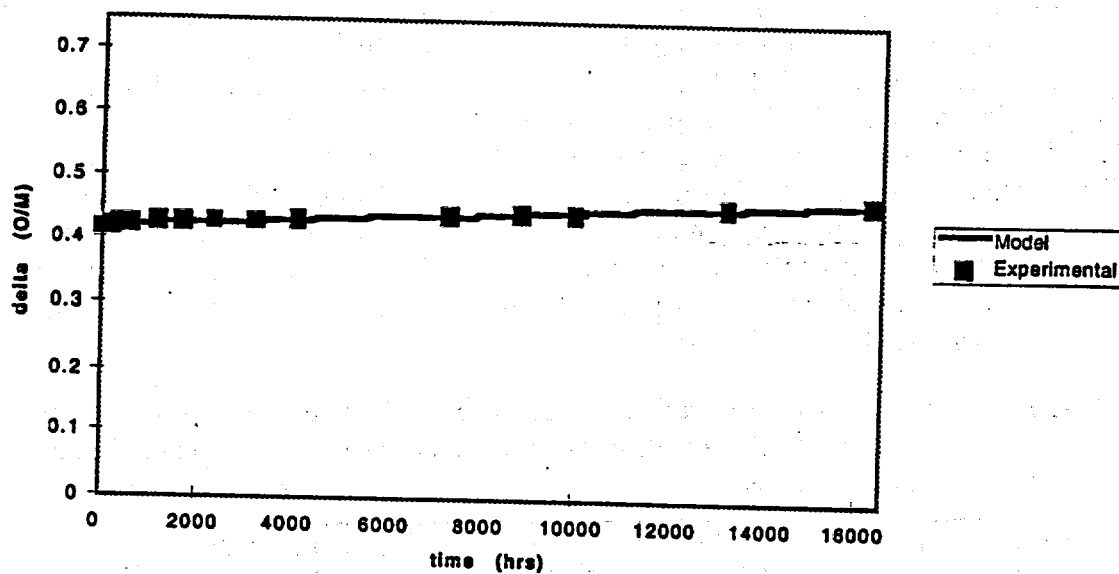


Figure 3.2.2-25  $\Delta$  (O/M) versus time (hr) for the ODB sample ATM-106F-013A; nominal burnup, 48 MWd/kgU

ATM 106F-022A

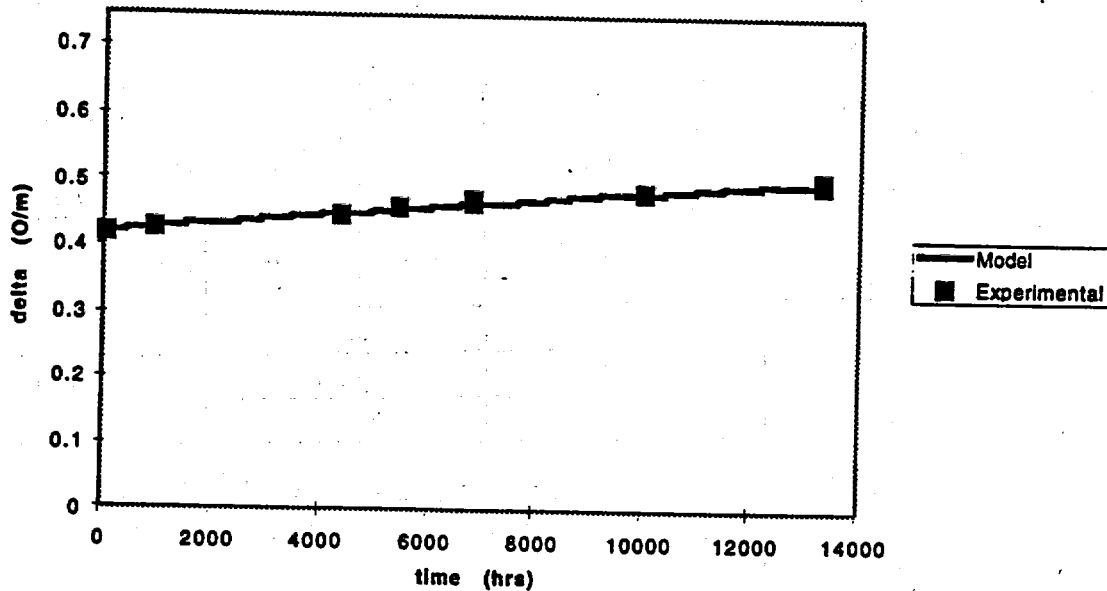


Figure 3.2.2-26  $\Delta$  (O/M) versus time (hr) for the ODB sample ATM-106F-002A; nominal burnup, 48 MWd/kgU

Some ODB experiments involved samples in which schoepite formed a thin layer on the surface of the unoxidized spent fuel and accelerated the weight gain by raising the oxygen potential, giving those grains with schoepite an apparent lower activation energy. As with the TGA experiments that involved hydrated spent fuel, it was assumed that the true sample is a mixture of hydrated  $U_4O_9$  and nonhydrated  $U_4O_9$ .

Table 3.2.2-21 and Table 3.2.2-22 present the results for the ODB experiments with those samples that exhibited a schoepite layer. Table 3.2.2-21 shows the activation energies and grain half-size distributions for the Turkey Point and ATM-105 fuel samples. The comparison of the experimental and model histories for the hydrated Turkey Point and ATM-105 samples is presented in Figures 3.2.2-27 through 3.2.2-29. Table 3.2.2-22 presents the activation energies and grain half-size distributions for the ATM 104 and ATM-106 fuel samples. The comparison of the experimental data and the model fits for the hydrated ATM-104 and ATM-106 fuels is presented in Figures 3.2.2-30 through 3.2.2-32. It must be reiterated that only the TP-P2-100 and 104F-100 samples were examined by SEM and are known to have the dehydrated schoepite. Because of their weight-gain histories, it was conjectured that the ATM-105F-100 and ATM-106-P2-100 samples also have schoepite. The same is true for the samples TP-P2-003A and 106-P2-021A. More study is required to confirm this conjecture.

**Table 3.2.2-21**

**ODB hydrated Turkey Point and ATM-105 samples listing the optimized  $Q_{38}$  for each bin and the corresponding grain half sizes and fractions**

Sample	Fraction (0.5-1.0) $\mu\text{m}$	Fraction (1.0-2.0) $\mu\text{m}$	Fraction (2.0-4.0) $\mu\text{m}$	Fraction (4.0-8.0) $\mu\text{m}$
TP-P2-003a	0.25	0.30	0.25	0.20
Bin $Q_{38}$	182.4	186.0	196.1	196.1
TP-P2-100	0.25	0.30	0.25	0.20
Bin $Q_{38}$	178.8	181.3	183.4	191.1
105F-100	0.25	0.25	0.25	0.25
Bin $Q_{38}$	182.1	190.4	198.0	202.8

**Table 3.2.2-22**

**ODB hydrated ATM-104 and ATM-106 samples listing the optimized  $Q_{38}$  for each bin and the corresponding grain half sizes and fractions**

Sample	Fraction (0.15-0.30) $\mu\text{m}$	Fraction (0.30-0.60) $\mu\text{m}$	Fraction (0.60-1.20) $\mu\text{m}$	Fraction (1.20-2.40) $\mu\text{m}$
104F-100	0.30	0.23	0.25	0.22
Bin $Q_{38}$	188.1	195.2	202.1	180.0
106-P2-021A	0.42	0.35	0.10	0.08
Bin $Q_{38}$	186.9	197.1	206.8	224.7
106-P2-100	0.42	0.35	0.10	0.08
Bin $Q_{38}$	182.1	197.1	205.8	218.7

ATM 105F-100

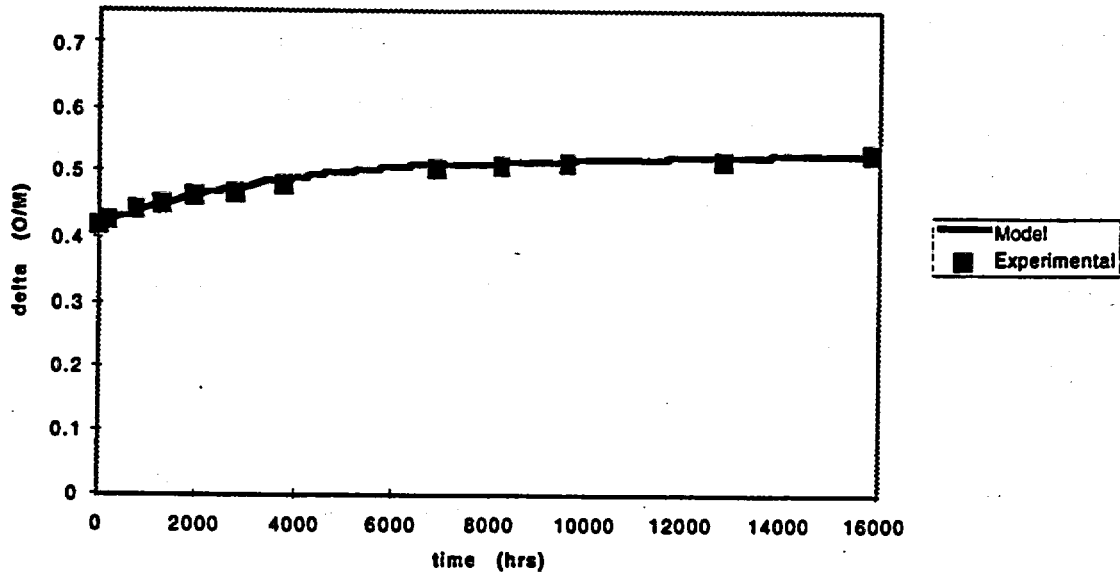


Figure 3.2.2-27  $\Delta$  (O/M) versus time (hr) for the ODB sample ATM-105F-100; nominal burnup, 27 MWd/kgU; shoepite present

TP-P2-003A

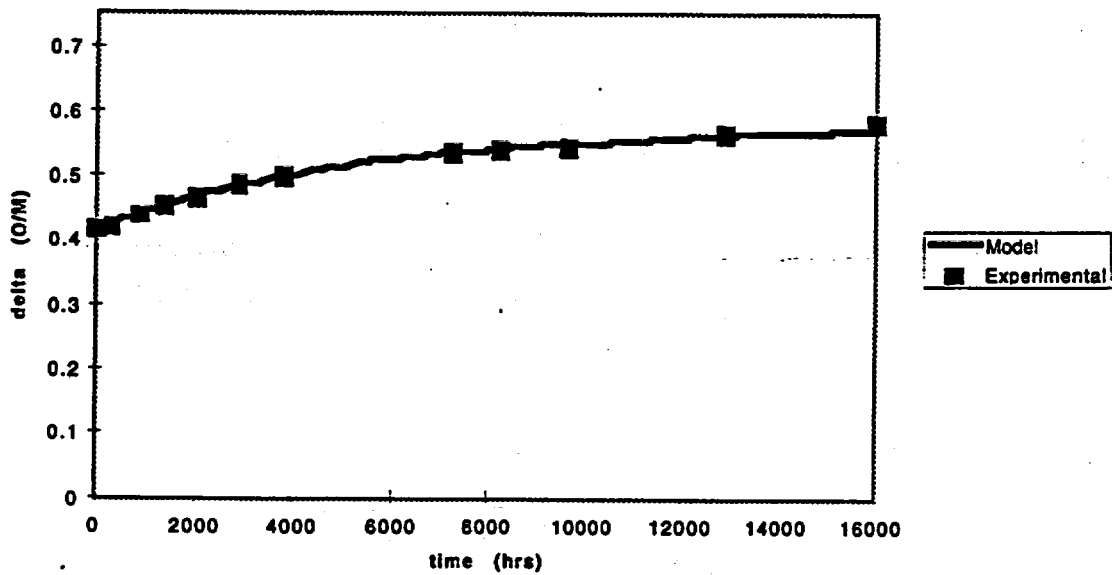


Figure 3.2.2-28  $\Delta$  (O/M) versus time (hr) for the ODB sample TP-P2-003A; nominal burnup, 28 MWd/kgU; shoepite present

TP-P2-100

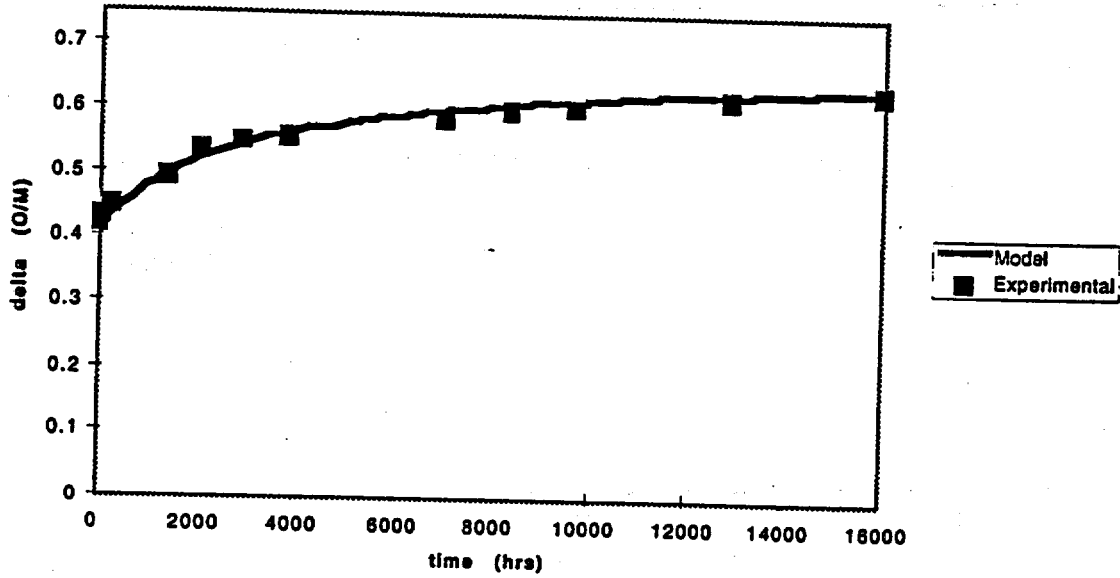


Figure 3.2.2-29  $\Delta$  (O/M) versus time (hr) for the ODB sample TP-P2-100; nominal burnup, 28 MWd/kgU; shoeelite present

ATM 104F-100

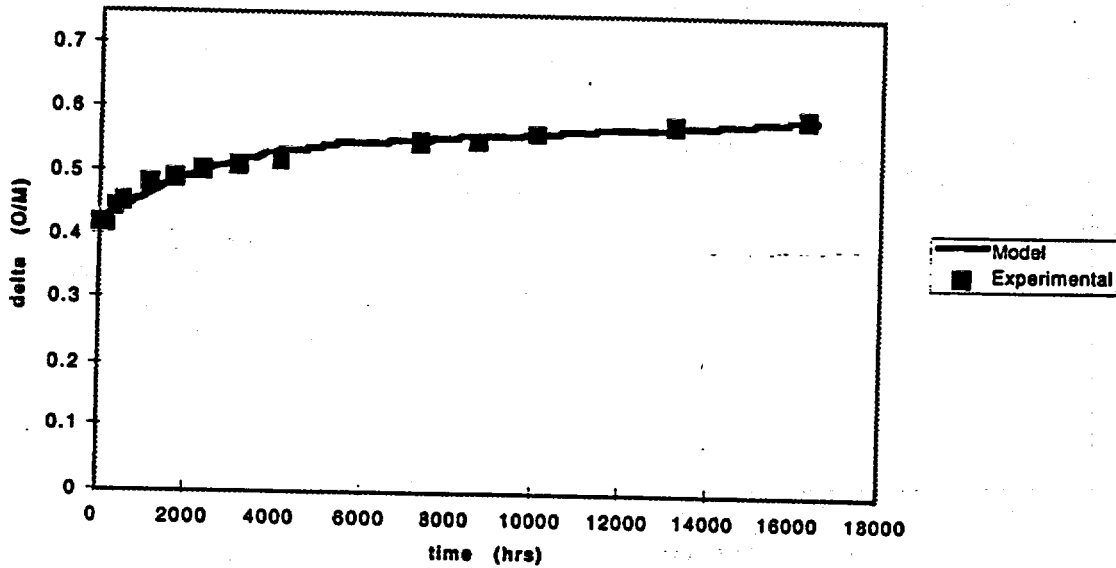


Figure 3.2.2-30  $\Delta$  (O/M) versus time (hr) for the ODB sample ATM-104F-100; nominal burnup, 43 MWd/kgU; shoeelite present

ATM 106-P2-100

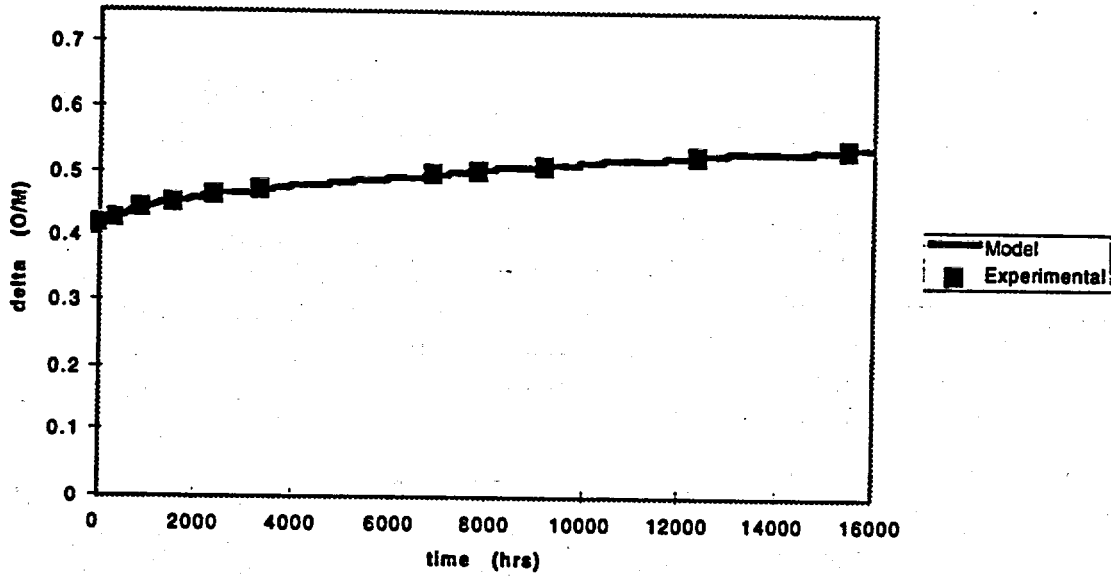


Figure 3.2.2-31  $\Delta$  (O/M) versus time (hr) for the ODB sample ATM-106-P2--100; nominal burnup, 48 MWd/kgU; shoepite present

ATM 106-P2-021A

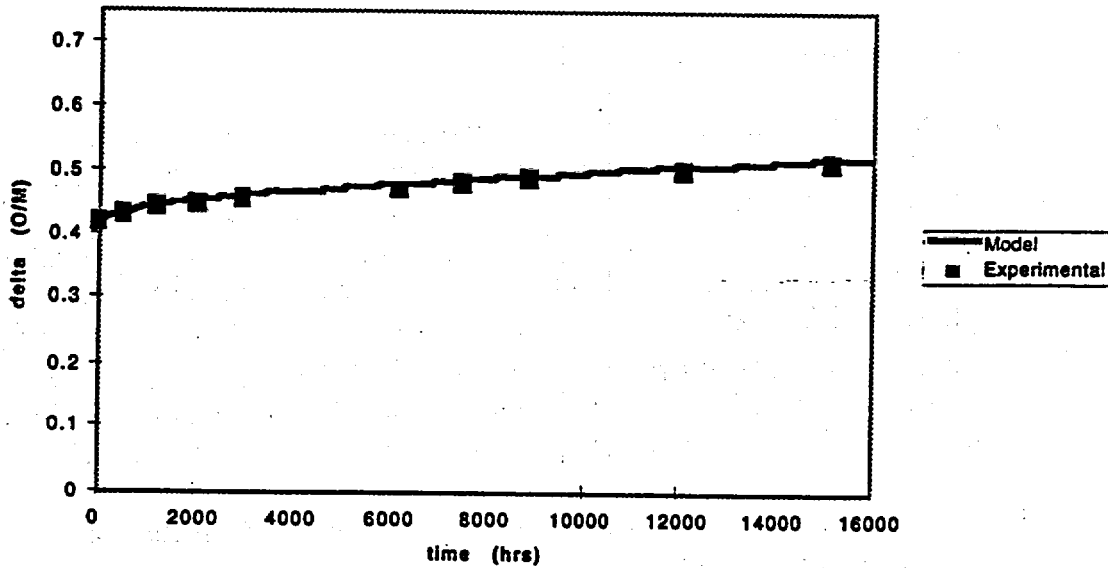


Figure 3.2.2-32  $\Delta$  (O/M) versus time (hr) for the ODB sample ATM-106-P2-021A; nominal burnup, 48 MWd/kgU; shoepite present

### 3.2.2.12 Discussion of Modeling Comparisons with Experimental $U_4O_9 \rightarrow U_3O_8$ Histories

The frontal speed at which  $U_4O_9 \rightarrow U_3O_8$  is given by Eq. 3.2.2-14a and Eq. 3.2.2-14b. This frontal speed depends inversely on the grain half size and exponentially on the activation energy  $Q_{38}$ .

These model calculations had been performed with the uncertainties arising from the grain-size distributions of totally converted  $U_4O_9$ . It was assumed that the grain-size distribution of the cracked  $U_4O_9$ , estimated from the paper of Thomas et al. (1991) is valid for totally converted  $U_4O_9$ . This assumption can be verified easily by SEM measurement. A question remains regarding the grain-size distribution at higher burnup that can be easily found by similar experimental techniques.

Hanson (1998) stated there can easily be a 10 to 15-kJ/mole uncertainty in the activation energy  $Q_{38}$ . This activation energy is sensitive to the isotopic composition of the fuel and to the position in the fuel rod because local burnup is not identical to the average burnup.

While some of the fine points of the modeling studies can be debated (with regard to the totally converted  $U_4O_9$  grain-size distribution or to the suitable activation energy), the uncertainties assumed in fitting the model can be easily overcome by additional experimental measurements.

### 3.2.2.13 Environmental Impacts of Oxidation of $UO_2$

Arrhenius chemical kinetics are very temperature-sensitive. Because  $U_3O_8$  formation is the primary concern in a repository environment, the frontal speed depends on temperature and on activation energy. According to Hanson (1998), the activation energy for the reaction  $U_4O_9 \rightarrow U_3O_8$  varies with burnup (see Eq. 3.2.2-25). To obtain a sense of the temperature and activation-energy dependence on the frontal speed  $\dot{w}_s$  (see Eq. 3.2.2-14a), Table 3.2.2-23 is presented. Instead of expressing the frontal velocities in the units of  $\mu\text{m}/\text{h}$ , these values will be expressed as  $\mu\text{m}/\text{yr}$ . The frontal speed for the very high activation energy 640 kJ/mole was not included because the frontal speed is essentially zero for the temperatures considered.

Table 3.2.2-23 Frontal speed  $\dot{W}_{38}$  ( $\mu\text{m}/\text{yr}$ ) dependence on temperature and activation energy

T °K	167.4 (kJ/(mole—°K))	314 (kJ/(mole—°K))	469 (kJ/(mole—°K))
323.2	8.44E-18	1.72E-41	1.62E-66
373.2	3.57E-14	1.09E-34	2.31E-56
528.2	2.69E-07	8.71E-22	4.1880E-37

Rather than using the  $\Delta(O/M)$  as a dependent variable, using the volume fraction of  $U_3O_8$  is more meaningful in a long-term repository for spent fuel. Figure 3.2.2-33 shows the volume-fraction histories for constant temperature  $100^\circ\text{C}$  for the phase transformation  $U_4O_9 \rightarrow U_3O_8$  for three different burnups. It was assumed that a 25-MWd/kgU spent fuel had an average  $U_4O_9$  half-grain size of  $4.0 \mu\text{m}$ , the 50 MWd/kgU had an average  $U_4O_9$  half-grain size of  $0.75 \mu\text{m}$ , and the 75 MWd/kgU  $U_4O_9$  had a half-grain size of  $0.25 \mu\text{m}$ . Figure 3.2.2-37 shows the volume fraction of  $U_3O_8$  on a log-time plot in years. Note that, even with progressively smaller average grain half-sizes, the 50 and 75 MWd/kgU burnup fuels require times on the order of  $1\text{E}+12$  and  $1\text{E}+15$  years for complete conversion, even though the average grain sizes become progressively smaller.

Volume fraction of  $U_3O_8$  formed at  $100^\circ\text{C}$  vs time

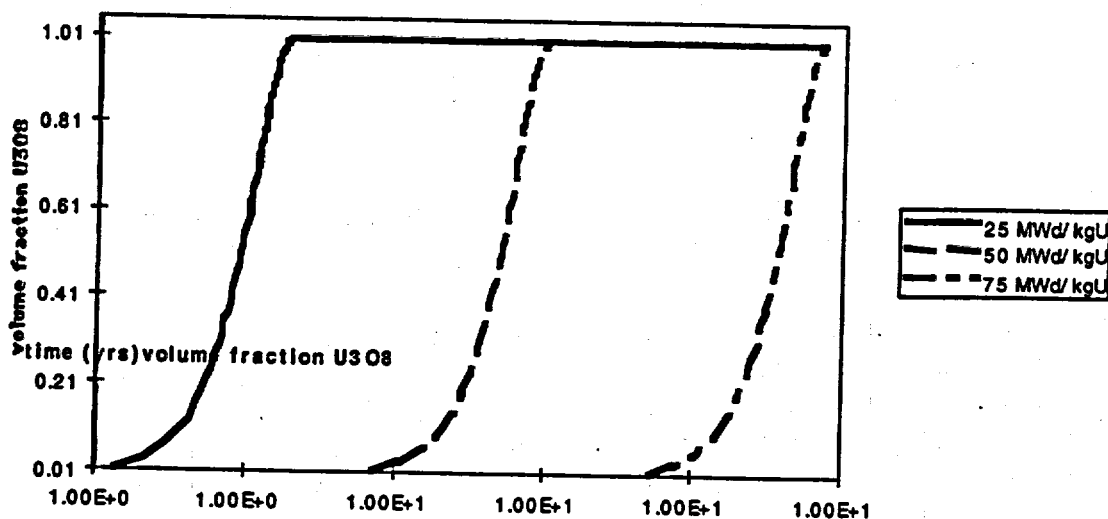


Figure 3.2.2-33 Volume fraction of  $U_3O_8$  formed vs time (yr) at a constant temperature of  $100^\circ\text{C}$  at burnups of 25, 50, and 75 MWd/kgU

Figure 3.2.2-34 shows the volume-fraction histories for constant temperature  $200^\circ\text{C}$  for the phase transformation  $U_4O_9 \rightarrow U_3O_8$  for three different burnups. It was assumed that a 25 MWd/kgU spent fuel had an average  $U_4O_9$  half-grain size of  $4.0 \mu\text{m}$ , the 50 MWd/kgU had an average  $U_4O_9$  half-grain size of  $0.75 \mu\text{m}$ , and the 75 MWd/kgU  $U_4O_9$  had a half-grain size of  $0.25 \mu\text{m}$ . The lower burnup 25 MWd/kgU fuel oxidizes completely to  $U_3O_8$  in 1300 yr; the 50 and 75 MWd/kgU oxidize completely in 500,000 yr and 300 million yr, respectively. However, a simple calculation shows that the low-burnup 25 MWd/kgU burnup fuel would oxidize completely in 335,000 yr if the temperature were at a constant  $150^\circ\text{C}$ .

### Volume Fraction of U<sub>3</sub>O<sub>8</sub> formed in time at 200 C

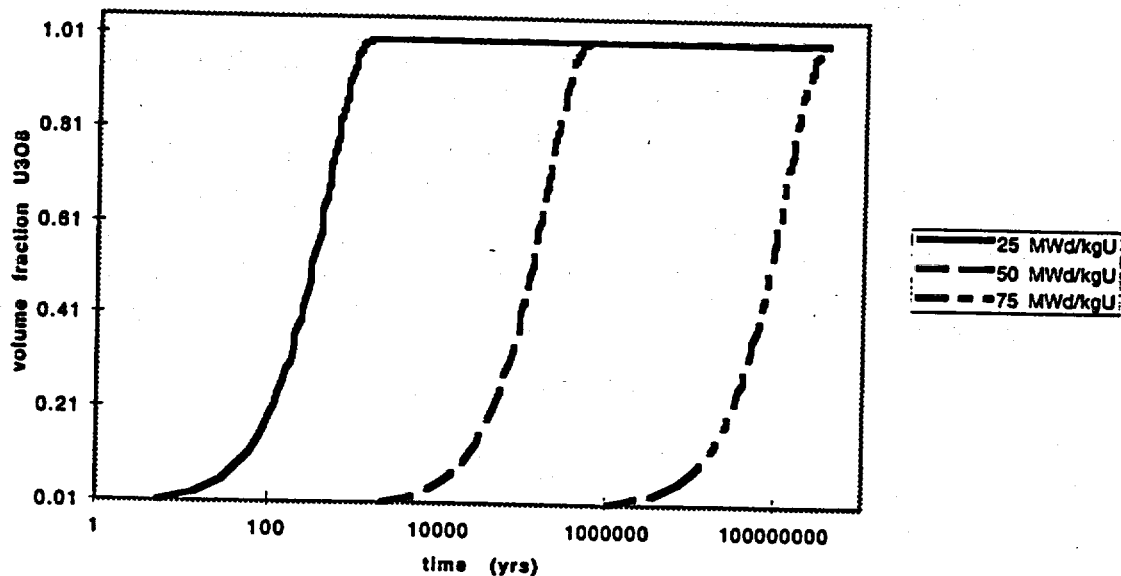


Figure 3.2.2-34 Volume fraction of U<sub>3</sub>O<sub>8</sub> formed vs time (yr) at a constant temperature of 200°C at burnups of 25, 50, and 75 MWd/kgU

Given the presently limited data on the dissolution rates, the dissolution of UO<sub>2</sub> and U<sub>4</sub>O<sub>9</sub> appear similar. However, an increase in exposed surface area for potential wetting and dissolution will occur from U<sub>4</sub>O<sub>9</sub> oxidation. The impact of surface area or grain size on dissolution remains to be evaluated in a release-rate model. Interpretation of dissolution-rate data from flow testing (Gray and Wilson, 1995) indicated that 3 to 14 grain depths may be possible. For pellet fragments having reasonably large grain sizes, the penetration depth is increased by a factor of approximately six times the nominal exterior surface area per grain layer. For unsaturated dissolution/release-rate response, this may not be a conservative estimate of spent-fuel degradation impacts from grain boundary effects.

The impacts of U<sub>3</sub>O<sub>8</sub> phase are as follows:

- Increased surface area for dissolution is proportional to grain size.
- There is about 30% increase in volume from UO<sub>2</sub> to U<sub>3</sub>O<sub>8</sub>.
- U<sub>3</sub>O<sub>8</sub> does not form a protective film on the U<sub>4</sub>O<sub>9</sub>.

Of these impacts, the first two are considered more significant. The U<sub>3</sub>O<sub>8</sub> volume increase of ~30% will create significantly larger openings in failed cladding and will, therefore, increase the amount of spent-fuel surface potentially exposed to wetting, compared to that which remains protectively covered by small flaw failures. The small flaw failures of the cladding are due to pressurized creep and/or zirconium hydride mechanisms. The U<sub>3</sub>O<sub>8</sub> sub-grain particle sizes that result from

the  $U_3O_8$  spalling and surface fracturing at the  $U_3O_8 \rightarrow U_4O_9$  oxidation front create several-orders-of-magnitude increases in surface area relative to the nominal grain-sized surface area of  $U_4O_9$ . As shown in Tables 3.2.2-5 through 3.2.2-8, the extent of  $U_3O_8$  is significantly delayed for temperature histories less than 100°C. Clearly, it is important to maintain spent-fuel containment for time periods until the local repository temperatures are less than 100°C.

The oxidation-response models discussed in this section provide equations that calculate conservative time estimates for the  $U_4O_9$  and  $U_3O_8$  oxidation-phase transformations. These models are simplistic in form and based on limited experimental data, but are useful for the current stage of design and performance assessment analyses. Updates, refinements, and impacts of these oxidation models will be completed as additional TGA and ODB data become available.

#### 3.2.2.14 References

- Boase, D. G., and T. T. Vandergraf (1977). "The Canadian spent fuel storage canister: some material aspects." *Nucl. Tech.* 32:60-71.
- Choi, J-W, R. J. McEachern, P. Taylor, and D. D. Wood (1996). "The effects of fission products on the rate of  $U_3O_8$  formation in SIMFUEL oxidized in air at 250°C." *J. Nucl. Mater.* 230:250-258.
- Einzigler, R. E., L. E. Thomas, and B. D. Hanson (1995). *Oxidation of Spent LWR Fuel, FY95 Year-End Report.* (MOL212 and MOL213) Richland, WA: Pacific Northwest National Laboratory. [MOL.19960611.0215]
- Einzigler, R. E., L. E. Thomas, H. C. Buchanan, and R. B. Stout (1992). "Oxidation of spent fuel in air at 175 to 195°C." *J. Nucl. Mater.* 190:53. [MOL.19980213.0585]
- Gray, W. J., and C. N. Wilson (1995). *Spent Fuel Dissolution Studies FY1991 to 1994.* (PNL-10540) Richland, WA: Pacific Northwest Laboratory. [MOL.19960802.0035]
- Gray, W. J., L. E. Thomas, and R. E. Einzigler (1993). "Effects of air oxidation on the dissolution rate of LWR spent fuel." In proceedings from Materials Research Society Symposium: Scientific Basis for Nuclear Waste Management XVI. C. G. Interrante and R. T. Pabalan (Eds.) 294:47. [236035]
- Hanson, B. D. (1998a). "The burnup dependence of light water spent fuel oxidation." Ph.D. Dissertation. Berkeley, CA: University of California at Berkeley.
- Harrison, K. T., C. Padgett, and K. T. Scott (1967). "The kinetics of the oxidation of irradiated uranium oxide spheres in dry air." *J. Nucl. Mater.* 23:121-138.

- Lassmann, K, C. T. Walker, K. van der Laar, and L. Lindstrom (1995). "Modeling the high burnup  $\text{UO}_2$  structure in LWR fuel." *J. Nucl. Mater.* 226:1-8.
- Matzke, H. (1992). "On the rim effect in high burnup  $\text{UO}_2$  LWR fuels." *J. Nucl. Mater.* 189:141-148.
- McEachern, R. J., J. W. Choi, M. Kolar, W. Long, P. Taylor, and D. D. Wood (1997). "Determination of the activation energy for the formation of  $\text{U}_3\text{O}_8$  on  $\text{UO}_2$ ." *J. Nucl. Mater.* 249:58-69.
- Paraschiv, M. C, A. Paraschiv, and F. Glodeanu (1997). "On the fission gas release from oxide fuels during normal grain growth." *J. Nucl. Mater.* 246:223-231.
- Park, K., and D. R. Olander (1992). "Defect models for the oxygen potential of gadolinium and europium doped uranium." *J. Nucl. Mater.* 187: 89-96.
- Ray, I. L. F., H. Matzke, H. A. Thiele, and M. Kinoshita (1997). "An electron microscopy study of the RIM structure of a  $\text{UO}_2$  fuel with a high burnup of 7.9% FIMA." *J. Nucl. Mater.* 245:115-123.
- Remenyi, K. (1974). *The theory of Grindability and the comminution of binary mixtures*. Budapest, Hungary: Akademiai Kiado.
- Stout, R. B., H. F. Shaw, and R. E. Einziger (1989). *Statistical model for grain boundary and grain volume oxidation kinetics in  $\text{UO}_2$  spent fuel*. (UCRL-100859) Livermore, CA: Lawrence Livermore National Laboratory. [NNA.19891031.0015]
- Stout, R. B, E. J. Kansa, R. E. Einziger, H. C. Buchanan, and L. E. Thomas (1991). "Spent fuel waste form characteristics: Grain and fragment size statistical dependence for oxidation response." In proceedings of Second International Conference on High-Level Radioactive Waste Management. La Grange Park, IL: American Nuclear Society and American Society of Civil Engineers. 1:103-111. [MOL.19980505.0016]
- Stout, R. B., E. J. Kansa, and A. M. Wijesinghe (1993a). *Kinematics and thermodynamics of non-stoichiometric oxidation phase transitions in spent fuel*. (UCRL-JC-110678) Livermore, CA: Lawrence Livermore National Laboratory. [NNA.19930224.0014]
- Stout, R. B, E. J. Kansa, and A. M. Wijesinghe (1993b). *Kinematics and thermodynamics across a propagating non-stoichiometric oxidation phase front in spent fuel grains*. (UCRL-JC-112823) Livermore, CA: Lawrence Livermore National Laboratory. [NNA.19931029.0077]
- Thomas, L. E., and R. E. Einziger (1992). "Grain Boundary Oxidation of Pressurized-Water Reactor Spent Fuel in Air." *Material Charact.* 28:149-156.

Thomas, L. E., R. E. Einziger, and R. Woodley (1989). "Microstructural Examination of Oxidized Spent PWR Fuel by Transmission Electron Microscopy." *J. Nucl. Mat.* 166:243-251. [NML.880707.0043; NNA.19900709.0482]

Thomas, L. E., C. E. Beyer, and L. A. Charlot (1992). "Microstructural analysis of LWR spent fuels at high burnup." *J. Nucl. Mat.* 188:80-89.

Thomas, L. E., R. E. Einziger, and H. C. Buchannan (1993). "Effect of fission products on air-oxidation of LWR spent fuel." *J. Nucl. Mat.* 201:310-319.

Walker, C. T., T. Kamesama, S. Kitajima, and M. Kinoshita (1992). "Concerning the microstructural changes that occur at the surface of  $UO_2$  pellets on irradiation to high burnup." *J. Nucl. Mater.* 188: 3-79.

## Section 3.4.2 Contents

3.4.2	Spent-Fuel Dissolution Models.....	3.4.2.1-1
3.4.2.1	Introduction .....	3.4.2.1-1
3.4.2.2	Nonequilibrium, Thermodynamic Dissolution-Rate Function Forms.....	3.4.2.2-2
3.4.2.3	Regression Fit of Data to Models.....	3.4.2.3-13
3.4.2.3.1	UO <sub>2</sub> and Spent-Fuel Data.....	3.4.2.3-13
3.4.2.3.2	U <sub>3</sub> O <sub>8</sub> Data.....	3.4.2.3-18
3.4.2.4	Aqueous-Release-Rate Response for Spent Fuels.....	3.4.2.4-19
3.4.2.5	Release-Rate Model and Preliminary Analysis of Radionuclide Release in Unsaturated Drip Tests.....	3.4.2.5-30
3.4.2.5.1	Introduction .....	3.4.2.5-30
3.4.2.5.1.1	Physical Transport Phenomena .....	3.4.2.5-30
3.4.2.5.2	Interpretive Mathematical Model.....	3.4.2.5-33
3.4.2.5.3	The Mass-Balance Equations .....	3.4.2.5-34
3.4.2.5.4	Limiting Solutions.....	3.4.2.5-37
3.4.2.5.5	Pseudo-Steady-State Conditions.....	3.4.2.5-37
3.4.2.5.6	Transport-Limited, Pseudo-Steady Conditions.....	3.4.2.5-38
3.4.2.5.7	Dissolution and Colloidal Particle Release-Limited, Pseudo-Steady Conditions.....	3.4.2.5-39
3.4.2.5.8	Total Mass Release Rate for Separate Drip and Vapor Zones.....	3.4.2.5-40
3.4.2.5.9	Total Mass Release Under Advective Transport-Limited Conditions .....	3.4.2.5-41
3.4.2.5.10	Mass Release Under Reaction-Rate-Limited Drip Zone and Advective Transport-Limited Vapor Zone.....	3.4.2.5-41
3.4.2.5.11	Numerical Methodology for Determining Release-Rate Model Parameters from Unsaturated Drip-Test Data ....	3.4.2.5-42
3.4.2.5.12	Release-Rate Model Parameters for Unsaturated, Low-Flow-Rate Conditions with Secondary Phase Formation.....	3.4.2.5-44
3.4.2.5.13	Comparison of Equilibrium Mass Concentrations Against TSPA Recommended Solubility Limits.....	3.4.2.5-47
3.4.2.6	References.....	3.4.2.6-48

## Section 3.4.2: Spent Fuel Dissolution Models

Version 1.3  
July 23, 1998

### 3.4.2.1 Introduction

This section discusses modeling of the aqueous dissolution and release-rate responses of uranium oxide spent-fuel waste forms. Section 3.4.2.2 describes the development of dissolution-rate function forms. The previous nonequilibrium thermodynamic model for dissolution rate, described in Version 1.2 of the *Waste Form Characterization Report (WFCR V1.2)*, has been extended to include surface chemisorption effects. The surface chemisorption phenomenon is represented by the well-known Tempkin isotherm. This extension provides the theoretical basis for function forms used to regress the existing experimental data. A brief discussion is provided for a different function form that would effectively represent radiolysis effects. Additional model development for radiolysis effects is in progress, but is not included in this revision.

In Section 3.4.2.3, numerical regression analyses, using various dissolution-rate functions are discussed. The incorporation of available new data has not changed the previous model significantly. The regression of the existing data to a dissolution-rate model suggested by outside experts has a small R-square value ( $R^2$ ) measure relative to the  $R^2$  of the nonequilibrium thermodynamic model. In Section 3.4.2.4, the development of the aqueous-release-rate model has not been changed; however, it has been used to evaluate film concentrations of radionuclides in the alteration layers based on data from the unsaturated drip tests. This film analysis and values of the film concentrations are discussed in Section 3.4.2.5.

The approach for developing a dissolution-rate model uses concepts from nonequilibrium thermodynamics. The objective is to derive function forms for the dissolution rate that are consistent with quasi-static thermodynamic processes. These function forms will contain thermodynamic chemical potentials of both the solid (spent fuels) and the solution (water chemistries) along with a set of coefficients and parameters that can be evaluated by numerical regression of dissolution-test data. Currently, detailed knowledge is not available for the atomic (mechanistic) steps and the sequence of chemical/electrochemical-reaction steps to describe the dissolution process over the range of spent-fuel inventory, potential water chemistries, and temperatures. The existing approach is to obtain an experimental database (flow-through tests) of dissolution rates for a subset of specific spent fuels approved test material (ATM) over a range of controlled, aggressive water chemistries and temperatures. With a numerical regression algorithm, these data are used to evaluate empirical parameters in a rate law for each specific spent fuel ATM (Gray et al., 1992; Steward and Gray, 1994). The function form of this rate law is a product polynomial of

the bulk water chemistry concentrations and temperature (Stumm and Morgan, 1981). This function form has been extended to have an explicit dependence on the thermodynamic properties of the uranium oxide waste form by using fuel-reaction burnup as an aggregate variable for fission product and actinide concentrations.

In addition, the use of bulk concentrations of water chemistry and spent-fuel burnup in the function form for the regression analysis of the dissolution data do not explicitly account for a dependence from possible surface-to-bulk concentration differences due to radiolysis, surface adsorption, and dipole layers. However, some of these shortcomings are effectively addressed, in Section 3.4.2.2, by the phenomena due to surface chemisorption. Several simplifying assumptions are made there.

The following thermodynamic model uses analysis methods and physical concepts taken primarily from classical mechanics. (Jackson, 1962; Eringen, 1967; Bikerman, 1970; Sedov and Radok, 1972), colloidal foundations (Hunter, 1993), thermodynamics (Gibbs, 1961; Lewis and Randall, 1961; deGroot and Mazur, 1962; Denbigh, 1968; Lupis, 1983), electrochemistry (Bikerman, 1970; Bockris and Reddy, 1970; Antropov, 1972; Pourbaix, 1973), geochemistry (Stumm and Morgan, 1981; Lasaga et al., 1981; Hochella and White, 1990); and surface chemistry (Hayward and Trapnell, 1964; Adamson, 1976; Jaycock and Parfitt, 1981)

The development of a release-rate model is more complex than the development of a dissolution-rate model. The release model includes dissolution rates, precipitation rates, colloidal kinetics, and adsorption rates. At this time, the approach is semi-empirical and depends strongly on the unsaturated testing experiments to provide data and chemical-process models.

The spent-fuel-waste-form dissolution/release-rate responses impact design and performance assessment evaluations and consequences of the substantially complete containment time period (SCCTP) [NRC 10CFR60.113] and the controlled release time period (CTRP) (NRC 10CFR60.113). These two regulatory requirements are coupled because waste-package failures during the SCCTP will potentially expose spent-fuel waste forms to atmospheric conditions in a repository. During this time period, the waste forms may be altered by oxidation and/or water vapor adsorbed to the spent-fuel surface and by dissolution and release of radionuclides from the waste form as a result of wetting by water. In these cases, alteration, hydration and dissolution of the spent-fuel-waste-form lattice-structure will take place. The development of a thermodynamically based dissolution and release model relates to the design requirements, to the subsystem release, and to total system performance assessment (TSPA) model-development needs.

#### 3.4.2.2 Nonequilibrium, Thermodynamic Dissolution-Rate Function Forms

In the following text, thermodynamic internal energy functionals are used to represent the energy responses for a generic solid and a generic liquid. The solid and liquid are assumed to be in contact at an idealized wetted surface. The analysis will assume that the wetted surface has a solid-surface side and liquid-surface side. The

wetted surface is a material discontinuity. This surface is also a dissolution front that propagates at an idealized dissolution velocity,  $\underline{V}$ , which, for assumed quasi-steady-state rate processes, will be taken as a constant.

The generic solid will have bulk constituents of typical  $\text{UO}_2$  spent fuel, namely minor concentrations of actinides, fission products, and defects in the bulk lattice structure. For purposes here, and as described elsewhere (Stout, 1996), the bulk lattice is assumed to be nominally that of the  $\text{UO}_2$  lattice structure; however, other oxide phases and adsorbed complexes may exist on and in spatial neighborhoods of the wetted surface. The generic liquid will be represented with a subset of arbitrary initial/bulk constituents, plus two subsets of dissolution products from the solid.

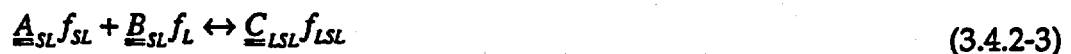
In particular, for the waste form solid with mass density  $\rho$ , let the  $(1 \times I)$  column matrix  $f_s = \{f_{s_i}\}$  denote the densities (number per unit volume) of the atomic lattices, other actinide atoms, fission product atoms, and conduction electrons; and, for now, neglect the possible defect structures. The column matrix  $f_s$  is an atomic fraction density, or equivalent to mass fraction densities for the solid. For the liquid, let the  $(1 \times I)$  column matrix  $f_L = \{f_{L_i}\}$  denote the densities (number per unit volume) of the aqueous state  $\text{H}_2\text{O}$ ,  $\text{H}_3\text{O}$ ,  $\text{OH}$  plus the added constituents. During dissolution, the solid constituents will react with the liquid constituents, although the exact details of these reactions are presently unknown. For purposes of a generic analysis, let the set of products on the solid side of the wetted surface be  $f_{sL}$ , which are created by reactions of general form



where  $\underline{A}_s$ ,  $\underline{B}_s$ , and  $\underline{C}_{sL}$  coefficient matrices of the reactions. The set  $\{f_{sL}\}$  represents complexes, compounds, and/or phase-change species on the solid side of the wetted surface. These will also be argument functions in the solid's internal energy functional. Similarly, on the liquid side of the wetted surface, let  $f_{sL}$  denote the set of liquid solution products that are created by reactions of the general form



where  $\underline{A}_s$ ,  $\underline{B}_s$ , and  $\underline{C}_s$  are coefficient matrices. In addition to the liquid-solid species set  $\{f_{sL}\}$  created directly from the solid constituents  $f_s$ , there also exists the solid surface constituent set  $\{f_{sL}\}$  that can react to create liquid species. These new species are denoted by a column matrix  $\{f_{sLL}\}$  and are created by reactions of the form



where  $\underline{A}_{sL}$ ,  $\underline{B}_{sL}$ , and  $\underline{C}_{sLL}$  are coefficient matrices. Thus, the dissolution process creates two species subsets  $\{f_{LS}\}$  and  $\{f_{LSL}\}$  in the liquid, and these concentrations will be included as function arguments of the liquid's internal energy functional.

Each of the constituent densities of the solid and the liquid will be assumed to move with the particle velocity of its spatial neighborhood  $\underline{y}$  plus its intrinsic diffusional velocity  $\underline{v}$  relative to the particle velocity. Thus, the argument variables of the constituent functions  $f_s, f_{SL}, f_L$ , and  $f_{LSL}$  are the spatial point  $\underline{x}$ , at time  $t$ , and the species associated diffusional velocities  $\underline{v}_s, \underline{v}_{SL}, \underline{v}_L, \underline{v}_{LS}$ , and  $\underline{v}_{LSL}$ , respectively. Finally, the thermodynamic internal energy functional also has argument functions for the entropy and the elastic (recoverable) strain tensor. The entropy functions are denoted by  $\eta_s(\underline{x}, t)$  and  $\eta_L(\underline{x}, t)$ , and the strain tensors are denoted by  $\gamma_s(\underline{x}, t)$  and  $\gamma_L(\underline{x}, t)$ , for points  $\underline{x}$  at time  $t$  of the solid and liquid, respectively. Note that entropy and strain are material particle potential functions and do not have diffusional velocities relative to this material particle located at point  $\underline{x}$  with velocity  $\underline{v}(\underline{x}, t)$ . These can be added; however, a later assumption will consider the dissolution process as a chemical reaction that is rate-controlled at the wetted solid-liquid-surface front. Therefore, the diffusion flux terms will be removed for the final dissolution rate model.

In the following, the effect of nonrecoverable deformations with finite, discontinuous strain tensor effects will be neglected. These deformation/strain effects produce stress work at the dissolution front and can be added when their potential import is better understood, as in the oxidation phase change deformation model (Stout et al, 1993a; 1993b).

Using the preceding notation and definitions of functions, the internal energy functional for the solid is defined as

$$\varepsilon_s(\eta_s, \gamma_s, \{f_s\}) \equiv \varepsilon_s(\eta_s, \gamma_s, f_s, f_{SL}) \quad (3.4.2-4)$$

and it is assumed that functional derivatives of  $\varepsilon_s$  exist with respect to each of its argument functions for all times  $t$  and at all points  $\underline{x}$  of the solid body  $\bar{R}_s$  plus its surface  $\partial\bar{R}_s$ . Similarly, the internal energy functional for the liquid is defined as

$$\varepsilon_L(\eta_L, \gamma_L, \{f_L\}) \equiv \varepsilon_L(\eta_L, \gamma_L, f_L, f_{LS}, f_{LSL}) \quad (3.4.2-5)$$

and also that functional derivatives exist for all times  $t$  and at all points  $\underline{x}$  of the liquid body  $\bar{R}_L$  plus its surface  $\partial\bar{R}_L$ . The idealized dissolution front, namely the wetted surface, is simultaneously adjacent to surfaces  $\partial\bar{R}_s$  and  $\partial\bar{R}_L$ , and is notationally written with a single square bracket  $\partial\bar{R}$  that denotes a surface of possible spatial discontinuity for kinematic, mass transport, momentum, stress, and energy relations. The following analysis will provide some details for only the energy conditions across an arbitrary segment  $\partial R$  of  $\partial\bar{R}$  for quasi-static conditions, surrounded by arbitrary subsets  $R_s + \partial R_s$  and  $R_L + \partial R_L$  and  $R_L + \partial R_L$  of the solid and liquid, respectively.

The textbook conservation equation for the rate of energy change of the combined solid and liquid system describes the rate of internal energy change of  $R_s + \partial R$  and  $R_L + \partial R_L$  as equal to the mechanical traction (body force work is neglected)

rates. The current–electric rate, plus the heat/flux rates, where the sets of points  $\{\underline{x}\}_S$  on  $\partial R_S$  and points  $\{\underline{x}\}_L$  on  $\partial R_L$  enclose the idealized surface  $\partial R$ , which propagates with the dissolution front velocity,  $\underline{V}$ . In equation form, the energy equation can be written with some shorthand notation as

$$\int_{R_S} d_t \varepsilon_S + \int_{\partial R_S} (\varepsilon_S \underline{n}_S \cdot (\underline{v}_S - \underline{V}) + \Delta_{f_S} \varepsilon_S \underline{n}_S \cdot \{f_S \underline{v}_S\}) + \int_{R_L} d_t \varepsilon_L + \int_{\partial R_L} (\varepsilon_L \underline{n}_L \cdot (\underline{v}_L - \underline{V}) + \Delta_{f_L} \varepsilon_L \underline{n}_L \cdot \{f_L \underline{v}_L\})$$

$$= \int_{\partial R_S} (\underline{\sigma}_S \cdot \underline{v}_S \cdot \underline{n}_S + \underline{h}_S \cdot \underline{n}_S) + \int_{R_S} \underline{J}_S \cdot \underline{E}_S + \dot{H}_S + \int_{\partial R_L} (\underline{\sigma}_L \cdot \underline{v}_L \cdot \underline{n}_L + \underline{h}_L \cdot \underline{n}_L) + \int_{R_L} \underline{J}_L \cdot \underline{E}_L + \dot{H}_L \quad (3.4.2-6)$$

where the new function symbols are  $\underline{n}_S$  and  $\underline{n}_L$  for the outward normal unit vectors of surfaces  $\partial R_S$  and  $\partial R_L$ , respectively;  $d_t \varepsilon$  denotes total time derivatives;  $\Delta_{f} \varepsilon$  denotes functional derivatives;  $\{f \underline{v}\}$  denotes the diffusional mass fluxes of constituents of the solid (subscript S) and of liquid (subscript L);  $\underline{\sigma}$  is the stress tensor;  $\underline{h}$  is the heat flux vector;  $H$  is heat generation rate;  $\underline{J}$  is the current vector (flux of charged constituents); and  $\underline{E}$  is the electric field vector, which will have a moving idealized dipole surface due to charges concentrated on  $\partial R_S$  and  $\partial R_L$ . For points  $\underline{x}$  in  $R_S$  and  $R_L$ , the rate and flux volume integrals are regular. However, across moving surfaces  $\partial R_S$  and  $\partial R_L$ , discontinuity conditions may exist for quasi-static internal energy rate changes because of entropy, strain, constituent masses, stress, heat flux, and current–electric–field energy contributions (Jackson, 1962; Eringen, 1967). This is written, again with shorthand notation, for the discontinuity across the surface  $\partial R$  between surfaces  $\partial R_S$  and  $\partial R_L$  as

$$\int_{\partial R} \left( (\Delta_{\eta} \varepsilon \eta + \Delta_{\gamma} \varepsilon \gamma + \Delta_{f} \varepsilon f) (\underline{v} - \underline{V}) \cdot \underline{n} \Big|_S^L + \Delta_{f} \varepsilon \{f \underline{v}\} \cdot \underline{n} \Big|_S^L - \underline{\sigma} \cdot \underline{v} \cdot \underline{n} \Big|_S^L - \underline{h} \cdot \underline{n} \Big|_S^L + \underline{J} \phi \cdot \underline{n} \Big|_S^L \right) = 0 \quad (3.4.2-7)$$

where terms for internal energy discontinuities with particle velocity  $\underline{v}$  minus front velocity  $\underline{V}$  contributions are separated from the diffusional flux velocity  $\underline{v}$  terms and from the energy rate terms from stress, heat flux, and the quasi-static electric current/field work term. The current/field work term is simplified by replacing the electric field vector  $\underline{E}$  with  $-\underline{\nabla} \phi$ , the gradient of the scalar potential for the charge density, and by assuming that there is no rate or charge changes on the surfaces  $\partial R_S$  and  $\partial R_L$  as the dissolution front  $\partial R$  propagates. This quasi-steady rate assumption for transient-current and charge-rate changes means that any dissolution-rate data measured over short times (seconds to days) may have transient errors and not be true steady-state rates for the imposed, controlled variables. Eq. 3.4.2-7 can be further reduced by assuming that the heat flux vector is continuous across  $\partial R$  and that the internal energy change due to elastic strain is equal to the traction work at the surfaces  $\partial R_S$  and  $\partial R_L$ . Finally the current  $\underline{J}$  is equal to the flux of charged particles transported across  $\partial R_S$  and  $\partial R_L$ , which can be written as

$$\underline{J}_S = e\{z\}{}_S(\underline{v}_S - \underline{V}) + e\{z\}{}_S \underline{v}_S \quad (3.4.2-8)$$

or

$$= e(z_S f_S + z_{SL} f_{SL})(\underline{v}_S - \underline{V}) + e(z_S f_S \underline{v}_S + z_{SL} f_{SL} \underline{v}_{SL})$$

and

$$\underline{J}_L = e\{z\}{}_L(\underline{v}_L - \underline{V}) + e\{z\}{}_L \underline{v}_L \quad (3.4.2-9)$$

or

$$= e(z_L f_L + z_{LS} f_{LS} + z_{LSL} f_{LSL})(\underline{v}_L - \underline{V}) + e(z_L f_L \underline{v}_L + z_{LS} f_{LS} \underline{v}_{LS} + z_{LSL} f_{LSL} \underline{v}_{LSL})$$

where the subsets  $\{z\}_S$  and  $\{z\}_L$  are the number of unit charges of magnitude  $e$  (+ for cations and - for electrons and anions) of the associated species subsets  $\{f\}_S$ ,  $\{f\}_L$ , and  $\{f\}_L$ . Using these assumptions and the shorthand notation of Eq. 3.4.2-8 and Eq. 3.4.2-9, Eq. 3.4.2-7 can be written as an entropy rate expression across an arbitrary subset  $\partial R^*$  of surface  $\partial R$ .

$$\int_{\partial R^*} \Delta_\eta \varepsilon \eta (\underline{v} - \underline{V}) \cdot \underline{n} \Big|_S^L = - \int_{\partial R^*} (\Delta_f \varepsilon f - e\{z\} \phi) (\underline{v} - \underline{V}) \cdot \underline{n} \Big|_S^L \quad (3.4.2-10)$$

$$- \int_{\partial R^*} (\Delta_f \varepsilon \{f\} \underline{v} - e\{z\} \underline{v} \phi) \cdot \underline{n} \Big|_S^L$$

Equation 3.4.2-10 has an entropy production/dissipation energy term given by the dissolution reaction term moving with essentially nominal velocity  $\underline{V}$  of surface  $\partial R$  and a diffusional mass flux of dissolution product and supply species across surface  $\partial R$ . There are two approaches for developing kinetic (rate) models from Eq. 3.4.2-10: One is the classical Onsager approach that couples rate terms to thermodynamic forces (this is the first regression modeling approach); the second approach is to use the entropy production term across the dissolution surface as the thermodynamic measure for the dissolution propagation velocity. This latter approach results in the classical Butler-Volmer equation, when the Boltzmann configuration form for entropy is used. Both will be formulated in the following. For reasons discussed subsequently, the Butler-Volmer equation provided the better model.

For an Onsager-type model, the kinetics of the surface propagation velocity  $\underline{V}$  and the diffusional flux velocities  $\{f\}$  are thus coupled thermo-electrochemical rate processes, yet are independent kinematic (motion) variables that provide independent contributions to entropy production. Therefore, a general, nonequilibrium, thermodynamic formulation of dissolution would take the function rate forms

$\{\rho\}(\underline{v}-\underline{V})\cdot\underline{n}$  and  $\{f\underline{v}\}\cdot\underline{n}$ , which are specific mass-dissolution front-velocity terms and diffusion-flux velocity terms as nonequilibrium thermodynamic rate functions for entropy production/dissipation. Corresponding to the rates, there exist the nonequilibrium thermodynamic forces driving the thermo-electrochemical processes toward an equilibrium thermodynamic state. These thermodynamic forces are functional multipliers of the rate functions given in Eq. 3.4.2-10; namely  $(\Delta_f \varepsilon - e\{z\}\phi)$ . In terms of the shorthand notation, the coefficients appear to be the same for both rate terms. However, when the stoichiometric equation forms for the reactions of Eq. 3.4.2-1, Eq. 3.4.2-2, and Eq. 3.4.2-3 are formally incorporated, the thermodynamic force functionals describe an independent energy change for chemical reaction kinetics and an independent energy change for diffusional mass-transport kinetics. Using Onsager's concepts to describe nonequilibrium or irreversible thermodynamic processes, the two rate functions are coupled by function or functional coefficients to the two thermodynamic forces of energy kinetics and diffusion mass transport kinetics. Formally these are

$$\{\rho\}(\underline{v}-\underline{V})\cdot\underline{n} = L_{ff} \left[ (\Delta_f \varepsilon - e\{z\}\phi) \{f\} \right]_{energy} + L_{fv} \left[ \Delta_f \varepsilon - e\{z\}\phi \right]_{diffusion} \quad (3.4.2-11a)$$

$$\{f\underline{v}\}\cdot\underline{n} = L_{vf} \left[ (\Delta_f \varepsilon - e\{z\}\phi) \{f\} \right]_{energy} + L_{vv} \left[ \Delta_f \varepsilon - e\{z\}\phi \right]_{diffusion} \quad (3.4.2-11b)$$

where the four coefficients  $L_{ff}$ ,  $L_{fv}$ ,  $L_{vf}$ , and  $L_{vv}$  (which can be functions of the atomic fraction  $\{f\}$ ) couple the rate functions to the thermodynamic forces. For strictly non-negative entropy production, the Onsager coupling coefficients have symmetry such that, formally,  $L_{vf}$  is equal to  $L_{fv}$ .

Eq. 3.4.2-11a provides an Onsager-type thermodynamic function form that should be evaluated at the dissolution front for the dissolution rate function, which is essentially the dissolution front velocity when the details of the surface particle velocities are neglected. These function forms have internal energy thermodynamic chemical potential functions  $\Delta_f \varepsilon_s$  for the solid constituents ( $f = \{f_s, f_{sl}\}$ ) and  $\Delta_f \varepsilon_L$  for the waste form liquid constituents ( $f = \{f_s, f_{sl}, f_{lsl}\}$ ) and have parameters related to the surface dipole potential of the dissolution front. For numerical regression analyses in the simplest, ideal cases, particular chemical reactions with some regression parameters could be assumed, and the regression parameters could be evaluated based on the available thermodynamic values and dissolution data sets. For the complex case of spent-fuel waste form dissolution, Eq. 3.4.2-11a was reduced to the following for regression analysis

$$\rho V = L_{ff} \left[ \Delta_f \varepsilon_f - e\{z\}\phi \right]_L^2 \quad (3.4.2-12)$$

which represents the dissolution rate as proportional to the chemical potential energy change of the waste-form solid relative to the liquid; and the Onsager coefficient function  $L_{ff}$  can be represented as a general function of the densities functions ( $f_s$ ) and ( $f_L$ ) of the spent-fuel waste form and the liquid.

The second approach also assumes that only the energy-change term of Eq. 3.4.2-10 has the significant contribution to the production of entropy as waste-form solid dissolves into a liquid. Then, from Eq. 3.4.2-10, the entropy term propagating at velocity  $(\underline{v}-\underline{V})$  is set equal to only the energy term propagating also at velocity  $(\underline{v}-\underline{V})$  (as follows at any arbitrary point on the surface R):

$$\Delta_{\eta} \epsilon \eta (\underline{v}-\underline{V}) \cdot \underline{n}]_s^L = -(\Delta_f \epsilon f - e\{zf\}\phi)(\underline{v}-\underline{V}) \cdot \underline{n}]_s^L \quad (3.4.2-13)$$

The velocity term  $(\underline{v}-\underline{V}) \cdot \underline{n}$  is common to both sides of Eq. 3.4.2-13; therefore, the entropy energy change from liquid to solid in Eq. 3.4.2-13 is set equal to the negative chemical potential changes (defined from internal energy) as constituents of the solids that react with and dissolve into the liquid. Thus,

$$\Delta_{\eta} \epsilon \eta]_s^L = -(\Delta_f \epsilon f - e\{zf\}\phi)]_s^L \quad (3.4.2-14)$$

Using Boltzmann's definition of entropy (Denbigh, 1968), the thermodynamic entropy  $\eta$  can be expressed in terms of a configurational or thermodynamic state probability function  $\Omega$

$$\eta = k \ln \Omega \quad (3.4.2-15)$$

where  $k$  is Boltzmann's constant. Then, Eq. 3.4.2-14 can be rewritten in terms of  $\Omega$  as

$$\Delta_{\eta} \epsilon k \ln \Omega]_s^L = -(\Delta_f \epsilon f - e\{zf\}\phi)]_s^L \quad (3.4.2-16)$$

If the dissolution process is considered far from equilibrium, the dissolution rate given by the propagation velocity of wetted surface is assumed to be functionally related to the change in the configurational entropy as the solid dissolves into the liquid. From Eq. 3.4.2-16, the ratio of configurational entropy is

$$\Omega_L / \Omega_S = \exp\left[-(\Delta_f \epsilon f - e\{zf\}\phi) / \Delta_{\eta} \epsilon k\right]_s^L \quad (3.4.2-17)$$

The simplest form for the quasi-static dissolution response is to assume that the dissolution front velocity is linearly dependent on this configurational entropy ratio. This is the same as assuming that the rate of changing configurational entropy states of a solid into a liquid is related to the dissolution rate. Then, the dissolution rate, in terms of normal velocity and waste-form mass density, is assumed to be of form

$$\begin{aligned} \rho \underline{V} \cdot \underline{n} &= c \Omega_L / \Omega_S \\ &= c \exp \left[ \left( -(\Delta_f \varepsilon_f - e\{zf\}\phi) / kT \right) \right]_S^L \end{aligned} \quad (3.4.2-18)$$

where the temperature function  $T$  of classical thermodynamics is substituted for the change of internal energy with respect to changes in entropy, and  $c$  is a parametric constant of the dissolution rate response. Eq. 3.4.2-18 is a form of the Butler-Volmer model (Bockris and Reddy, 1970) used in electrochemical studies of corrosion rates.

In Eq. 3.4.2-12 and Eq. 3.4.2-17, the functional argument of the Onsager model and the Butler-Volmer model is that the internal energy change as a solid surface reacts and dissolves into an adjacent solution. The functional argument includes the chemical potential and electrochemical potential energy contributions for the solid-to-liquid surface reactions. The chemical potential terms are defined relative to the internal energy  $\Delta_f \varepsilon_f$ , where  $\Delta_f \varepsilon_f$  is the energy change per unit (atomic or molar) of reacted species in set  $\{f\}$ , and  $f$  denotes the relative amounts of reacted species for members in the set  $\{f\}$ . The relative ratios for the amounts are, in theory, established by the chemical reaction Eq. 3.4.2-1 through Eq. 3.4.2-3. In practice, the chemical reactions are often not stoichiometrically ideal nor well-known (Aagaard and Helgeson, 1982). Furthermore, even the functional forms for the chemical potentials  $\Delta_f \varepsilon_f$  are not explicitly available in many situations. Similar uncertainties exist for the electrochemical potential term  $e\{zf\}\phi$ , which represents the electric field work at the solid-liquid dipole surface. The magnitude of the dipole charge between the liquid and solid  $\phi]_S^L = \phi_L - \phi_S$  is the effective surface charge of the liquid minus the effective surface charge of the solid. Both of these charge fields are complex and depend on the ionic and electronic charges distributions in the liquid and solid, respectively. In particular, the charge distribution in the liquid is nonlinearly dependent on the ionic species in the liquid set  $\{f_L\}$ . These changes can also be spatially distributed in the liquid and adjacent to the solid surface (Antropov, 1972). Thus, selecting chemical and electrochemical functional forms for data regressions is somewhat arbitrary. However, the function variables of the functional forms used in the regression analysis are constrained to be the controlled variables of the experiments performed for dissolution-rate data. These variables are temperature, pH, carbonate, oxygen, and spent-fuel burnup.

Thus, the simplest forms for regression analysis are polynomials in the bulk-controlled concentration variables of the liquid and the spent fuel, and the temperature. Quadratic functions are well known to approximate physical data adequately. They are also easy to differentiate and integrate (Box et. al., 1978; Davies, 1956). Thus, a quadratic

function, including cross terms, with parametric coefficients was selected to represent the chemical potential and electrochemical energy functional terms for an Onsager model and an initial or first Butler-Volmer model. In addition to this first Butler-Volmer model (see 3.4.2 Appendix, Eq. A3.4.2-1), a second Butler-Volmer model was selected that had the concentration-dependent chemical-potential terms represented as logarithmic functions of concentrations, which, for small concentrations, is represented in classical thermodynamic texts as

$$\Delta_f \varepsilon \equiv \mu_f = \mu_{of} + kT \ln[f] \quad (3.4.2-19)$$

where  $\mu_{of}$  is the chemical potential at standard state conditions and  $[f]$  is species concentration in the aqueous solution or solid.

The logarithmic functions correspond to accepted function representations for both ideal and nonideal solutions often used for both liquids and solids (Antropov, 1972; Lewis and Randall, 1961; Stumm and Morgan, 1981; Lupis, 1983). Because the logarithmic dependence is an exponential argument, the second Butler-Volmer model reduces to a product of concentrations, each raised to a regression parametric power. Thus, Eq. 3.4.2-18 combined with Eq. 3.4.2-19 becomes

$$\rho \underline{V} \cdot \underline{n} = c \exp(-((\mu_{of} + kT \ln[f])f - e\{zf\}\phi)/kT) \frac{L}{S} \quad (3.4.2-20)$$

Because  $\exp(\ln[f])=[f]$ , Eq. 3.4.2-2, when combined with the ideal mass balance Eq. 3.4.2-1 through Eq. 3.4.2-3, can be written as

$$\rho \underline{V} \cdot \underline{n} = c(\Pi [f]^N) \exp(-(\mu_{of}f - e\{zf\}\phi)/kT) \frac{L}{S} \quad (3.4.2-21)$$

where  $\Pi [f]^N$  is the product of liquid-solid concentrations raised to the power N. This equation can be written in terms of liquid concentration of the water chemistry variables, which, in the current studies, are the hydrogen ion ( $H^+$ ), total carbonate ( $CO_3$ ), and oxygen ( $O_2$ ), with spent fuel burnup (Bu) as an aggregate variable that represents the concentration effects of fission products and actinides. This approach yields the following regression expression for dissolution rate in terms of controlled variables:

$$\rho \underline{V} \cdot \underline{n} = A[H^+]^{N_H} [CO_3]^{N_C} [O_2]^{N_O} [Bu]^{N_B} \exp(-Q/kT) \quad (3.4.2-22)$$

where Q represents an effective activation energy parameter for the temperature-dependence of dissolution. Eq. 3.4.2-22 has the general character of simple rate laws given in textbooks (e.g., see Stumm and Morgan, 1981, p.90); as discussed in these textbooks, these rate laws are useful in evaluating rate constants and reaction order from given sets of experimental data. In many cases, the dissolution-rate response of a material may not be simple. In this case, a simple rate law with assumed constant parameter values for Q,  $N_H$ ,  $N_C$ ,  $N_O$ , and  $N_B$  that are evaluated by a numerical regression analysis over a set of experimental data would provide a predictive model, but the

model would have large error. The measure of relatively large regression model error occurs for small ( $<0.5$ )  $R^2$  values. In these cases, based on analysis of variance, more complex models with cross-term variables and higher-order polynomials are commonly used in numerical regression analysis to obtain larger  $R^2$  values.

As discussed in Section 3.4.2.3, this has been the situation for numerical regression analysis performed over the sets of unirradiated  $UO_2$  and spent-fuel  $UO_2$  dissolution-rate data. One of the simple regression models of Section 3.4.2.3 starts with the familiar form of Eq. 3.4.2-22 and takes the logarithm of each side. For this case, when the parameters  $Q$ ,  $N_H$ ,  $N_C$ ,  $N_O$ , and  $N_B$  are assumed constants to be evaluated by regression analysis, a linear dissolution model follows with their coefficients being data values from the variable set  $\{1/T, \ln[H^+], \ln[CO_3], \ln[O_2], \ln[Bu]\}$ , which is of the form

$$\ln(\rho V \cdot \dot{n}) = \ln A + Q/KT + N_H \ln[H^+] + N_C \ln[CO_3] + N_O \ln[O_2] + N_B \ln[BU] \quad (3.4.2-23)$$

This regression model resulted in low  $R^2$  values when  $Q$ ,  $N_H$ ,  $N_C$ ,  $N_O$ , and  $N_B$  are evaluated. The  $R^2$  value is significantly increased when the regression parameters are assumed functions of the variable set and product cross-terms and higher-order terms of the variable set are included in the regression model. For example, suppose the exponent parameter  $N_C$  of Eq. 3.4.2-22 is represented by the following function form

$$N_C = N_{C_0} + N_{CT}/T + N_{CH} \ln[H^+] + N_{CC} \ln[CO_3] + N_{CO} \ln[O_2] + N_{CB} \ln[BU] \quad (3.4.2-24)$$

Similar function expressions can be written for exponent parameters  $N_H$ ,  $N_O$ , and  $N_B$ . Substitution of those expressions in Eq. 3.4.2-23 will clearly provide cross-terms (e.g.,  $\ln[CO_3] \cdot \ln[BU]$ ) for a more complex regression model to fit the sets of dissolution-rate data. As discussed in Section 3.4.2.3, this more-complex regression model results in an improved fit with respect to a larger  $R^2$  value (see Eq. 3.4.2-27).

If development of the dissolution model were left at this point, it could be considered semi-empirical in that cross-terms were included without addressing their physical significance. In addressing this point, it is important to realize that dissolution-model development for a multicomponent solid (spent fuel) in a multicomponent, water-chemistry environment will be more complex than for a single-component solid in a single- or dual-component water-chemistry environment. Certainly, if a simple physical model with some purported mechanistic basis "fits" the range of data sets available (has a large  $R^2$  value), that simple model should be acceptable. However, if the simple model has a low  $R^2$  value for the available data set, the simple model is normally rejected, irrespective of the purported physical significance, by statisticians as unsuitable for predicting response.

Put concisely, a simple regression model that does not "explain" the available data sets (has small  $R^2$  values) is not generally accepted as a predictive model, any more than is a regression model without some physical basis. Thus, in the ideal situation, development of a model must address both physical basis issues and predictive issues.

At present, the simple model of Eq. 3.4.2-22 has a strong physical basis from nonequilibrium thermodynamics and is similar to function forms proposed in the literature for chemical reactions. However, it does not have high predictive merit unless the exponent parameters are expressed as more general functions, as given by Eq. 3.4.2-24. Thus, physical-basis issues can be addressed by identifying chemical processes or mechanisms that are functionally described by exponent function forms, as given in Eq. 3.4.2-24. One such chemical process or mechanism exists in the form of chemical adsorption on the solid-liquid interface. The surface adsorption mechanism was identified in uraninite dissolution experiments performed by Grandstaff (1976). Grandstaff proposed that the uraninite dissolution-rate dependence on aqueous carbonate concentrations could be explained by using a Langmuir adsorption isotherm. According to Grandstaff, the Langmuir isotherm described the surface coverage as a function of carbonate solution concentration. Grandstaff linearized the Langmuir isotherm at low carbonate concentrations and proposed a linear relationship between surface coverage and concentration. However, at intermediate aqueous concentrations, the Tempkin adsorption isotherm is considered more descriptive of surface adsorption because it is expressed in terms of the thermodynamic chemical potential function (Hayward and Trapnell, 1964, pp. 165 and 176).

The form of the Tempkin adsorption isotherm is very similar to that given in Eq. 3.4.2-24. However, the Tempkin-isotherm-dependent function is the number of active surface sites  $\Theta_i$  for a reaction "i" involving a chemical species subset of [f] concentrations. An analysis to incorporate the number of active sites  $\Theta_i$  for multicomponent and the multireaction processes has been completed for fixed concentrations [f] reactions (see Aagaard and Helgeson, 1982). Aagaard and Helgeson showed that it is not expected, nor reasonable to expect, that stoichiometric coefficients in proposed chemical-reaction equations appear in regression analysis of data. The analysis steps to use Eq. 3.4.2-24 as a concentration-dependent exponent in Eq. 3.4.2-23 requires that the derivation of Eq. 3.4.2-14 through Eq. 3.4.2-18 be performed for the case with surface area subsets remaining as a functional dependence. Then the exponents  $N_H$ ,  $N_C$ ,  $N_O$ , and  $N_B$  of Eq. 3.4.2-22 and Eq. 3.4.2-23 would have an explicit linear dependence on the active site number density function  $\Theta_i$ .

For this linear  $\Theta_i$  dependence, the function form for  $N_H$ ,  $N_C$ ,  $N_O$ , and  $N_B$  would have a generalized form of the Tempkin isotherm given by Eq. 3.4.2-24. By substituting these forms into Eq. 3.4.2-23, cross-terms in the logarithmic functions (e.g.,  $\ln[O] \cdot \ln[BU]$ ) appear from the nonequilibrium thermodynamic model and the chemisorption model. Certainly other chemisorption isotherms could be used to derive function forms for regression models of available data. Presently, the use of a generalized Tempkin isotherm is considered consistent with surface complexation of carbonate and hydrogen ionic species of the aqueous solutions to form a charge double layer at the surface of a  $UO_2$  solid. In the case of spent fuel, because the  $UO_2$  solid has fission products and actinides, both the number of active sites on the solid and the concentrations of radiolytic aqueous species are functionally dependent on an aggregate variable such as

spent fuel burnup. The problem is sufficiently complex that the explicit dependence of bulk aqueous concentrations and spent-fuel burnup can only be quantified by well-planned and -controlled experiment methods.

The results of regression analysis using these four models—the quadratic-concentration polynomial Onsager model, the first Butler–Volmer model with a quadratic-concentration polynomial, the second Butler–Volmer model (chemisorption-modified) with logarithmic-dependent concentrations, and the simplified chemisorption-modified Butler–Volmer model (Stumm–Morgan form; see Eq. 3.4.2-22) are discussed in Section 3.4.2.3. Each of these models is consistent with nonequilibrium thermodynamics concepts and provides function forms for regression analyses. These models do not contain an explicit dependence on radiolysis effects. Radiolysis effects from spent-fuel radionuclide decay will alter the concentrations of bulk-controlled concentrations in a boundary layer at the liquid–solid interface because of the deposition energy of radiation. The effects of this bulk to boundary-layer concentration are contained in the dissolution-rate data; however, no functional dependence because of radiolysis and these altered concentrations has been completed. Hence, this radiolysis problem remains to be explicitly represented in a functional model. However, because the dissolution data are obtained with radioactive spent fuel, a radiolysis dependence is implicitly contained as the burnup variable in the regression fits of data for each model.

### 3.4.2.3 Regression Fit of Data to Models

#### 3.4.2.3.1 UO<sub>2</sub> and Spent-Fuel Data

Using nonequilibrium thermodynamics, two different function forms were developed to describe the dissolution response of spent-fuel waste forms. Eq. 3.4.2-12 provides a classic Onsager relation for dissolution rate that is linearly related to the energy change of the solid dissolving into a liquid. This is expected to be descriptive of dissolution response close to thermodynamic equilibrium. Eq. 3.4.2-18 provides a classic Butler–Volmer relation for the dissolution rate that is exponentially related to the energy change of the solid dissolving into a liquid. Eq. 3.4.2-12 and Eq. 3.4.2-18 provide a consistent thermodynamic basis for the function forms of dissolution-rate models. Function forms based on both Eq. 3.4.2-12 and Eq. 3.4.2-18 were used for multilinear regression analyses (Davies and Goldsmith, 1972, Chapter 8; Draper and Smith, 1981) over subsets of unirradiated UO<sub>2</sub> and spent-fuel UO<sub>2</sub> dissolution-rate data. Several forms of these models have been examined, and some were included in previous updates and revision of this WFCR and are discussed in Appendix A of this section (Section 3.4.2 Appendix).

The current model has the Butler–Volmer form. By substituting the traditional chemical potentials that include a logarithmic dependence on activities or concentrations for the chemical potential changes in Eq. 3.4.2-18 (also see Eq. 3.4.2-22), the classic chemical kinetic rate law was derived:

$$\text{Rate} = k[A]^a[B]^b[C]^c \dots \exp(E_a/RT) \quad (3.4.2-25)$$

Burnup was also represented as a concentration term, because it is proportional to the aggregated production and concentration of fission products. For regression purposes, Eq. 3.4.2-25 was transformed by taking logarithms of each term and fitting that equation and allowing interaction and quadratic terms indicated by the data to improve the fit. The negative logarithms of the water-chemistry variables were used to be consistent with the standard definition of pH:  $-\log_{10}[H^+]$ .

A modest refinement of model 3.4.2.20b in WFCR V1.2 (see Equation A3.4.2-3 in Appendix A) derives from an extensive analysis for performance assessment (PA) (Lawrence Livermore National Laboratory memorandum "Regression Fit of the  $UO_2$  and  $UO_2$  Spent-Fuel Matrix Dissolution Data for Use in the PA Model," William O'Connell to Ray Stout, LLYMP9805049, July 31, 1997). This refinement is the accepted intrinsic dissolution model for TSPA-VA at the time Version 1.3 of this report was published and is listed also in Appendix A. This model form includes a linear term of all variables, including the inverse temperature instead of its square and the linear LBU term with minimal loss in the correlation coefficient and adjusted for number of terms in the equation. The linear portion of the model is equivalent to the classic chemical rate law (Eq. 3.4.2-25). Eq. 3.4.2-26 (note base-10 logarithms) represents this current model:

$$\log_{10}(\text{Rate } UO_2) = a_0 + a_1 \cdot IT + a_2 \cdot PCO3 + a_3 \cdot PO2 + a_4 \cdot PH + a_5 \cdot LBU + a_6 \cdot PO2 \cdot IT + a_7 \cdot LBU \cdot IT + a_8 \cdot LBU \cdot PCO3 + a_9 \cdot LBU \cdot PO2 + a_{10} \cdot LBU \cdot PH + a_{11} \cdot PCO3^2 \quad (3.4.2.3-2)$$

Table 3.4.2.3-1 lists the coefficients (and their definitions) and the fitting statistics.<sup>1</sup> They are slightly different than those given for the TSPA-VA model in Appendix A because the four additional spent-fuel dissolution data for ATM-106 (30 MWd/kgU) are included. The new ATM-106 data were not available before the TSPA-VA model-acceptance deadline.

<sup>1</sup> For the regression fit to this model, all 53 runs from Tables 2.1.3.5-4 and 4a in Section 2.1.3.5 were used. Because unirradiated  $UO_2$  represents zero or no burnup, logarithmic values of zero  $UO_2$  burnup used in this model would produce infinitely negative values for the terms in the regression fit of such data, and could not be allowed. For this reason, a value of 1 MWd/kgM ( $\log_{10}(1)=0$ ) was substituted for the burnup of  $UO_2$  in the regression data set for this model. Nominal initial pH values were used for the  $UO_2$  data, following the same approach used for the tabulated pHs of the spent-fuel data.

**Table 3.4.2-1 Coefficients and fitting statistics for current model**

Term	Coeff. (a <sub>i</sub> )	Standard Error	T-Value	Significance	Term Description
0 1	5.419896	1.253984	4.32	0.0001	Regression Constant
1 IT	-2464.539023	334.080576	-7.38	0.0001	Inverse Temperature (K <sup>-1</sup> )
2 PCO3	1.543336	0.415766	3.71	0.0006	[-Log10] of Total Carbonate Conc. (mol/L)
3 PO2	-1.706529	0.530258	-3.22	0.0025	[-Log10] of Oxygen Partial Pressure (atm)
4 PH	0.238402	0.056131	4.25	0.0001	[-Log10] of Hydrogen Ion Conc. (mol/L)
5 LBU	-0.591871	0.744152	-0.80	0.4310	[+Log10] of Burnup (MWd/kgM)
6 IT*PO2	395.742290	168.814229	2.34	0.0240	
7 IT*LBU	713.604985	186.289045	3.83	0.0004	
8 PCO3*LBU	0.158012	0.047410	3.33	0.0018	->2nd Order Interactions
9 PO2*LBU	0.163853	0.053389	3.07	0.0038	
10 PH*LBU	-0.264657	0.049583	-5.34	0.0001	
11 PCO3**2	-0.346206	0.076765	-4.51	0.0001	->Quadratic

No. cases = 53      R<sup>2</sup> = 0.8687      RMS Error = 0.2223  
 Resid. df = 41      R<sup>2</sup>-adj. = 0.8335      Cond. No. = 199.3

The standard error provides, in the same units as the estimate, a measure of the uncertainty of the coefficient estimate. The fourth and fifth columns provide statistics related to the test of the hypothesis that the coefficient being estimated is zero. A high significance value indicates there is reason to believe that the coefficient is zero; thus, the term can be dropped from the model. Conversely, the closer to zero the significance value in the fifth column, the more important the term.

The table footnotes provide statistics to help assess the fit:

- The number of cases or runs are given.
- The residual degrees of freedom (cases less the number of terms in the model) are provided.
- The correlation coefficients R<sup>2</sup> and adjusted R<sup>2</sup> are numbers that indicate how well the fitted values produced by the model are correlated with the actual response values. An R<sup>2</sup> value is always between zero and one. An adjusted R<sup>2</sup> value (which is adjusted for the number of terms in the model) is less than R<sup>2</sup>,

but it is the better of the two for selecting the model with the most significant terms. The closer a value is to one, the better the fit. The best model is usually the one that maximizes both the  $R^2$  and adjusted  $R^2$  values.

- The root mean square (RMS) error is a measure, in the units of the fit, of the response variability that is not explained by the fit.
- The condition number can vary from one, which indicates a perfectly mathematical orthogonal experimental design, to infinity, which indicates a model containing singularities.

This model is the best representation of the existing data for PA purposes. It has a relatively high correlation coefficient; it is based on chemical and physical principles; and it is stable when used to extrapolate to variable values outside the original data space. This model, like the others, should be used only at alkaline conditions and not be used at acidic conditions (i.e., less than  $\text{pH} = 7$ , which is a chemically different regime).

Figure 3.4.2-1, Figure 3.4.2-2, and Figure 3.4.2-3 show the model (Eq. 3.4.2-20) calculations at aggressive conditions, using the coefficients in Table 3.4.2-1. Each of these three figures depicts conditions at a different pH, at 0.02 M total carbonate; the data are extrapolated beyond the currently available dissolution data to a burnup of 70 MWd/kgM and  $100^\circ\text{C}$ . Figure 3.4.2-1 is at a pH of 7. Figure 3.4.2-2 and Figure 3.4.2-3 are similar, but at  $\text{pH} = 8$  and  $\text{pH} = 10$ , respectively. All figures are at atmospheric oxygen partial pressure. Figure 3.4.2-4 shows model results at aggressive "J-13-like" conditions, which means a pH of 7.7, total carbonate of 0.002 M, but including no calcium or silicate precipitating components. Calculations at even 0.30 atm oxygen, imitating radiolysis effects, show only a modest increase in dissolution rates.

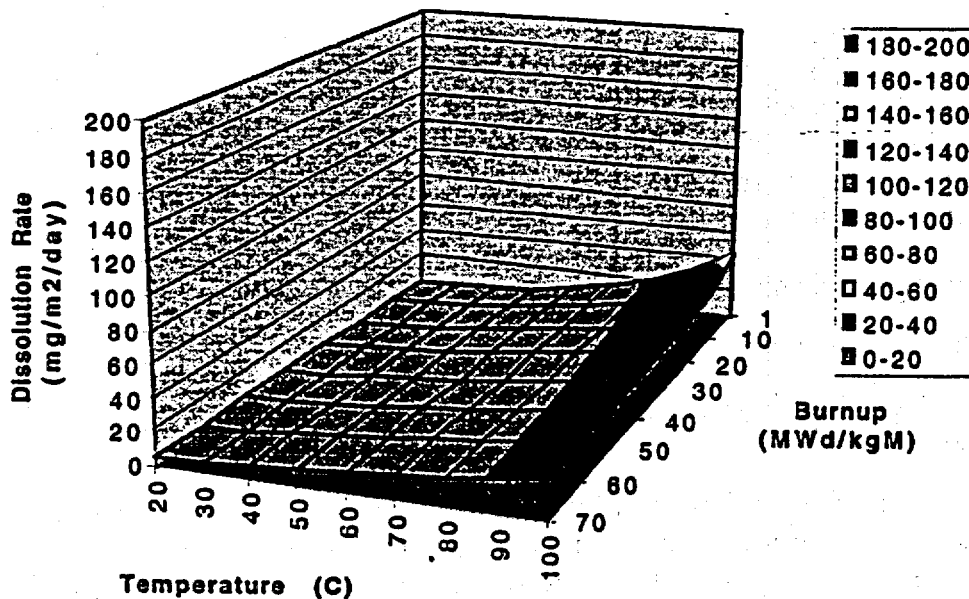


Figure 3.4.2-1 Dissolution rate at  $\text{pH} = 7$ , atmospheric oxygen, and 0.02M total carbonate

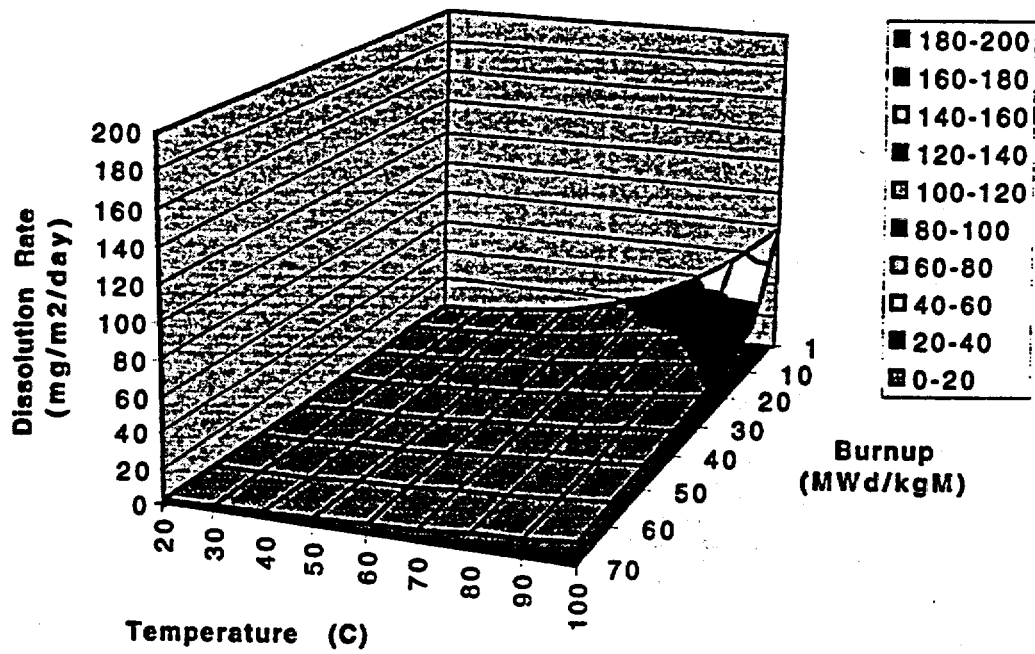


Figure 3.4.2-2 Dissolution rate at pH = 8, atmospheric oxygen, and 0.02M total carbonate

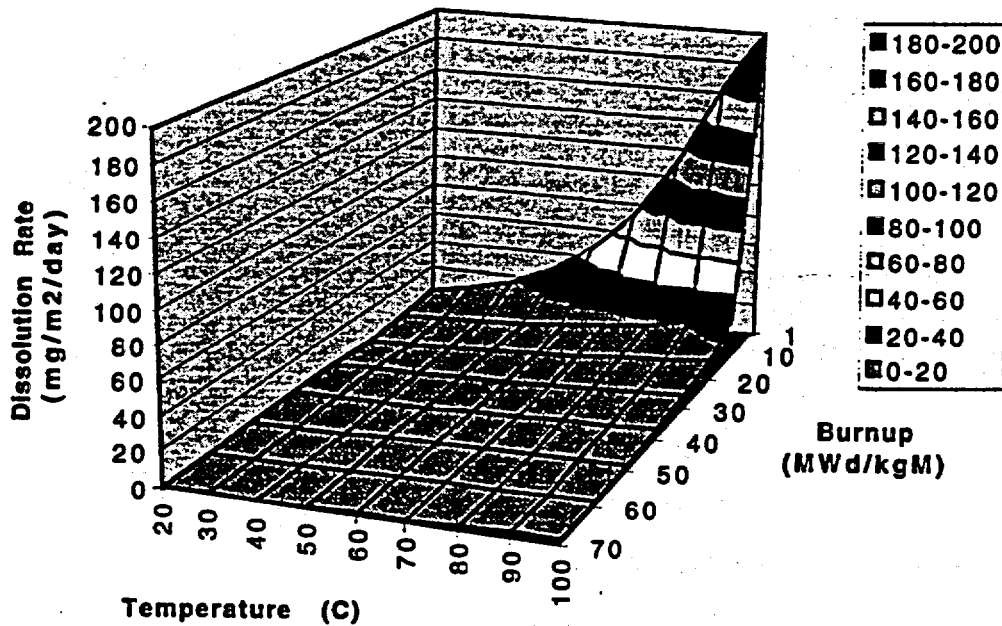


Figure 3.4.2-3 Dissolution rate at pH = 10, atmospheric oxygen, and 0.02M total carbonate

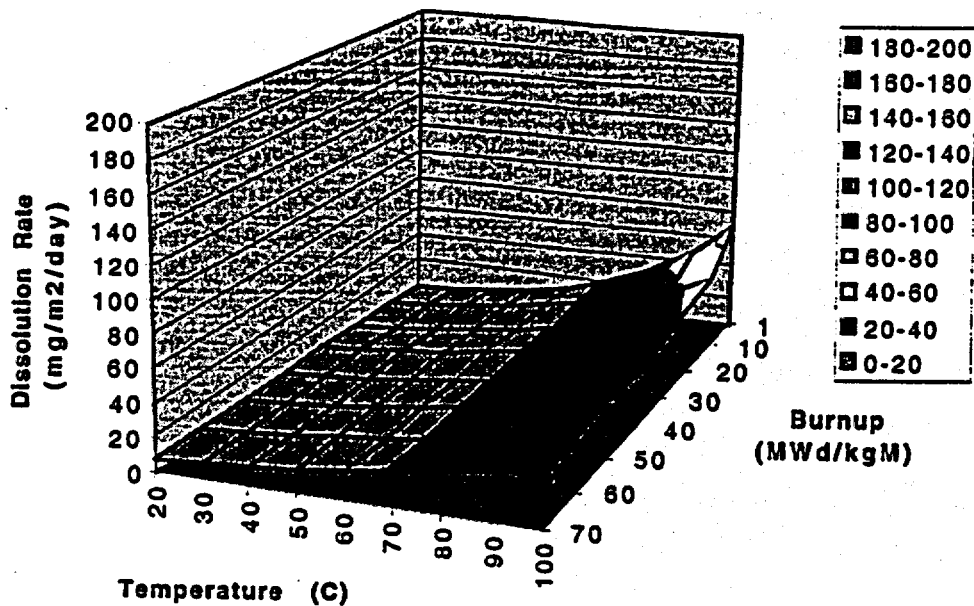


Figure 3.4.2-4 Dissolution rate at J-13 conditions of pH = 7.7 and 0.002M carbonate

### 3.4.2.3.2 U<sub>3</sub>O<sub>8</sub> Data

For the higher oxide data shown in Table 2.1.3.5-5, only the 14 U<sub>3</sub>O<sub>8</sub> dissolution rate data were modeled. Because the UO<sub>3</sub>·H<sub>2</sub>O dissolved so rapidly, their dissolution rates are estimates or minima and not appropriate for modeling. As with the UO<sub>2</sub> and spent-fuel dissolution data, different approaches to U<sub>3</sub>O<sub>8</sub> dissolution modeling are being explored. Here the classic, observed chemical kinetic rate law was used (Eq. 3.4.2-25).

Model parameters are presented, based on the pHs of the original carbonate solutions before contact with the samples, as used previously for the UO<sub>2</sub> and spent-fuel data. The pHs of the fresh-carbonate-leaching solutions are probably more representative of the pH at the sample than the pH of the leachate-analysis sample that has been exposed to dissolved CO<sub>2</sub> from the air.

Using the pHs of the prepared carbonate solutions given in the Table 2.1.3.5-5, the following equation is obtained from regression analysis: U<sub>3</sub>O<sub>8</sub> (carbonate soln. pHs):

$$\log_{10}(\text{Rate})\{\text{mgU}/\text{m}^2\cdot\text{day}\} = a_0 + a_1 \cdot \text{PCO}_3 + a_2 \cdot \text{PHC} - a_3 \cdot \text{IT} \quad (3.4.2-27)$$

with the coefficients and regression statistics shown in Table 3.4.2-2.

**Table 3.4.2-2 Linear-dissolution model for U<sub>3</sub>O<sub>8</sub> at atmospheric oxygen**

	Term	1. Coefficient (a <sub>i</sub> )	2. Standard Error	3. T-Value	4. Significance
0	1	7.950863	1.433419	—	—
1	IT	-1333.106149	337.537767	-3.95	0.0027
2	PCO3	-0.649162	0.084716	-7.66	0.0001
3	PHC	-0.106466	0.094032	-1.13	0.2840

No. cases = 14      R<sup>2</sup> = 0.8757      RMS Error = 0.2924  
 Resid. df = 10      R<sup>2</sup>-adj. = 0.8384      Cond. No. = 44.47

As with the earlier UO<sub>2</sub> and spent-fuel dissolution data, the pH did not have much effect on the model; however, carbonate concentration—not temperature—had the strongest effect on the U<sub>3</sub>O<sub>8</sub> dissolution rate. The temperature had half the effect of carbonate concentration on the uranium-dissolution rate. The pH was only about one-sixth as effective as carbonate concentration in explaining the changes in U<sub>3</sub>O<sub>8</sub> dissolution rates. Leaving out the pH term had a negligible effect on the other regression coefficients and was absorbed in the constant: U<sub>3</sub>O<sub>8</sub> (carbonate soln. pHs):

$$\log_{10}(\text{Rate})\{\text{mgU}/\text{m}^2\cdot\text{day}\} = a_0 + a_1 \cdot \log_{10}[\text{CO}_3] - a_2 \cdot \text{IT} \quad (3.4.2-28)$$

with the coefficients and regression statistics shown in Table 3.4.2-3.

**Table 3.4.2-3 Linear-dissolution model for U<sub>3</sub>O<sub>8</sub> at atmospheric oxygen without pH**

	Term	1. Coefficient (a <sub>i</sub> )	2. Standard Error	3. T-Value	4. Significance
0	1	6.925056	1.124932	—	—
1	IT	-1307.384093	341.061156	-3.83	0.0028
2	PCO3	-0.648615	0.085794	-7.56	0.0001

No. cases = 14      R<sup>2</sup> = 0.8598      RMS Error = 0.2961  
 Resid. df = 11      R<sup>2</sup>-adj. = 0.8343      Cond. No. = 33.53

All three variables (i.e., temperature, pH, and carbonate concentration) show significant interaction. A five-term equation, with a correlation coefficient of 0.95, that includes a constant, the three possible interaction terms, and a quadratic pH term (all nonlinear) improves the fit significantly. However, this equation is not suitable as a model because of its high degree of nonlinearity and its propensity to predict unrealistic dissolution rates outside the existing data space.

#### 3.4.2.4 Aqueous-Release-Rate Response for Spent Fuels

This subsection discusses models for the aqueous release of radionuclides from spent fuel. In the following text, the modeling will address quasi-steady-rate responses only and, for the most part, will provide bounding estimates for the concentrations of radionuclides in the quantity of water flowing past the wetted spent-fuel surface. For

purposes here, the release rate for a particular radionuclide species is defined as the aqueous concentration of the radionuclide (mass/volume of liquid) multiplied by the flow rate of the liquid (volume of liquid/unit time). The concentration will have additive components of "in-solution" and colloidal masses.

The release-rate response of radionuclides from spent fuels is complex. The release rate depends functionally on the following:

- Volume flow rate of the contacting water
- Intrinsic dissolution rate due to the chemistry of the water wetting the spent fuel
- History and current values of environmental variables surrounding and adjacent to the spent fuel
- Precipitation and colloidal kinetics of dissolved spent fuel in the adjacent water
- Adsorption kinetics of radionuclides on available surfaces
- Existing oxidation phase/alteration state of the spent fuel

Relating to these functional dependencies, Section 3.4.2.3 described a model for the intrinsic dissolution rate for a prescribed subset of aggressive water chemistries, environmental variables of explicit temperature and implicit spent-fuel radiation field, and a limited subset of different  $\text{UO}_2$  spent fuels. This dissolution model had function forms derived from nonequilibrium thermodynamics, and parameters of the function forms were evaluated by regression analyses over subsets of experimental dissolution-rate data. The dissolution rate is a fundamental component of the release rate because the dissolution rate provides a bounding estimate for the concentrations of the high-soluble radionuclides for a thick-film quantity of water flowing past a wetted spent-fuel surface. This statement will be substantiated in subsequent discussion. The other functional dependencies of the release-rate response are not well represented or isolated by available models or available experimental data. It is for this reason that a bounding approach is being used to develop a model of release-rate response.

The mass-balance equation is the basis of the following release-rate model for radionuclides being transported in water from a mass (or volume) of wetted spent fuel. The mass-balance equation, as written here, will initially contain expressions for all the functional dependencies discussed previously. However, because detailed models for each of these functional dependencies are not known, bounding approximations will be assumed to simplify and uncouple expressions in the mass-balance equations for the restricted conditions of quasi-steady-rate responses. This approach to model development will provide equations with parameters that can be evaluated from the available, but limited, experimental data obtained from the fully saturated testing and from the unsaturated testing performed on spent fuels.

The mass-balance equation, as written below, describes the time rate of change of a generic radionuclide in an arbitrary volume of fluid  $V_F$  with fluid-flow surface  $A_F$ . The fluid has an arbitrary (space  $\underline{x}$  and time  $t$  dependent) velocity field  $\underline{v}(\underline{x}, t)$  in contact with spent-fuel surfaces  $A_S$  and adsorption surfaces  $A_A$ . The concentration of a generic "in-solution" radionuclide is denoted by a density distribution function  $C(\underline{x}, t, \underline{v}_C)$ , where  $\underline{x}$ ,  $t$ , and  $\underline{v}_C$  are space, time, and diffusional velocity variables. The units of  $C$  are mass per unit fluid volume per unit diffusional velocity. The in-solution radionuclide denotes ionic, atomic, or molecular components with dimensions less than a few nanometers. If a particular in-solution concentration is to be denoted, the elemental symbol (or isotope symbol) will be enclosed in square brackets (e.g., the in-solution concentration of uranium is [U]).

The colloidal radionuclide concentration is more complex and is generically denoted by  $K(\underline{x}, t, \underline{v}_K, \underline{a}, r)$ , where  $K$  is the density-distribution function for the number of colloids at point  $\underline{x}$  and time  $t$  with diffusional velocity  $\underline{v}_K$ , effective area and orientation  $\underline{a}$ , and effective areal radionuclide density per unit area on area  $\underline{a}$  of radionuclide  $r$ . For reasons of notational simplicity, it is assumed that only radionuclide colloids form and that each colloidal species comprises only one radionuclide elemental species. Thus, by assumption, no pseudo-colloidal kinetics are represented in the following analyses, and colloids with multiple radionuclide species on area  $\underline{a}$  are assumed not to form. These assumptions of no pseudo-colloids and no multispecies colloids are consistent with the limited test data. If additional data or new interpretations of existing data are advanced, these modeling assumptions can be readily revisited. The use of subspecies variables  $\underline{v}_C$ ,  $\underline{v}_K$ ,  $\underline{a}$ , and  $r$  to denote physical attributes of a particular subset for diffusion velocities and for generic colloids is notationally cumbersome. However, the notational scheme will be simplified as the model development progresses to reflect experimentally measured concentrations by integration over the domains of attributes variables  $\underline{v}_C$ ,  $\underline{v}_K$ ,  $\underline{a}$ , and  $r$ . These domains are considered broad number sets and are denoted by curly brackets (i.e.,  $\{\underline{v}_C\}$ ,  $\{\underline{v}_K\}$ ,  $\{\underline{a}\}$ , and  $\{r\}$ ). For example, the colloidal concentration of a generic radionuclide at a given diffusion velocity  $\underline{v}_K$  is given by the integration of the density distribution  $K$  times the two attributes variables over their attribute domains. This is denoted in different ways, depending on the context of the discussion:

$$K_v(\underline{x}, t, \underline{v}_K) \equiv \overline{a r K} \equiv \int_{\{\underline{a}\}} \int_{\{r\}} \underline{a} r K(\underline{x}, t, \underline{v}_K, \underline{a}, r) d\underline{a} dr \quad (3.4.2-29)$$

Similarly, the in-solution concentration of a generic species for all diffusional velocities is given by the integration of density distribution  $C$  times the diffusional velocity attribute over its domain

$$\overline{C}(\underline{x}, t) \equiv \int_{\{\underline{v}_C\}} C(\underline{x}, t, \underline{v}_C) d\underline{v}_C \quad (3.4.2-30)$$

Likewise, the colloidal concentration of a generic species for all generic diffusional species is given by the integration

$$\bar{K}(\underline{x}, t) \equiv \int_{\{\underline{v}_K\}} K_v(\underline{x}, t, \underline{v}_K) d\underline{v}_K \quad (3.4.2-31)$$

From the last two equations, the averaged diffusional velocities for in-solution and colloidal concentrations  $\bar{v}_C$  and  $\bar{v}_K$  are defined from the following expressions

$$\bar{v}_C \bar{C} \equiv \overline{v_C C} \equiv \int_{\{\underline{v}_C\}} \underline{v}_C C(\underline{x}, t, \underline{v}_C) d\underline{v}_C \quad (3.4.2-32)$$

and

$$\bar{v}_K \bar{K} \equiv \overline{v_K K} \equiv \int_{\{\underline{v}_K\}} \underline{v}_K K_v(\underline{x}, t, \underline{v}_K) d\underline{v}_K \quad (3.4.2-33)$$

In the preceding, the radionuclide-decay/growth, exponential-time responses are implicitly imbedded in the inventory terms. For short-term analysis of experiments, these decay/growth responses can be neglected in the following.

Using the preceding notation for concentrations, the aggregate, mass-balance equation for an arbitrary generic radionuclide can be written as

$$\begin{aligned} & \int_{V_F} \partial_t \bar{C} + \partial_i \bar{K} dV_F + \int_{A_F} (\underline{v}_F + \bar{v}_C) \cdot \underline{n}_F \bar{C} + (\underline{v}_F + \bar{v}_K) \cdot \underline{n}_F \bar{K} dA_F \\ & = \int_{A_S} \rho_c \underline{v}_S \cdot \underline{n}_S + \bar{v}_K \cdot \underline{n}_S \bar{K} dA_S - \int_{A_P} \bar{v}_C \cdot \underline{n}_P \bar{C} + \bar{v}_K \cdot \underline{n}_P \bar{K} dA_P \\ & - \int_{A_K} \bar{v}_C \cdot \underline{n}_K \bar{C} + \bar{v}_K \cdot \underline{n}_K \bar{K} dA_K - \int_{A_A} \bar{v}_C \cdot \underline{n}_A \bar{C} + \bar{v}_K \cdot \underline{n}_A \bar{K} dA_A \end{aligned} \quad (3.4.2-34)$$

which is a statement that the time rate of change for the total concentration in fluid volume  $V_F$  occurs from fluid concentrations transported through a fluid-flow boundary  $A_F$  with outward directed normal  $\underline{n}_F$ , from the congruent dissolution at velocity  $\underline{v}_S$  of spent-fuel surface  $A_S$  with inward directed normal  $\underline{n}_S$  for generic species  $C$  where the solid has fractional mass density  $\rho_c$  for species  $C$ , from aggregated colloidal spallation and formation  $\bar{K}$  at the spent fuel surface area  $A_S$ , from precipitation kinetics of the in-solution and colloidal concentrations transported to all accessible precipitate surfaces  $A_P$  with outward directed normal  $\underline{n}_P$ , from interchange colloidal kinetics of the in-solution and colloidal concentrations transported to all accessible colloidal surfaces  $A_K$  with outward directed normal  $\underline{n}_K$ , and, finally, from all adsorption kinetics for both in-solution and colloidal concentrations transported to all accessible adsorption surfaces  $A_A$  with outward directed normal  $\underline{n}_A$ .

In the aggregate measure of total concentration, the interchange kinetics terms would determine the relative components rate values for the in-solution concentration  $\bar{C}$  and the colloidal concentration  $\bar{K}$ . However, the value of the total concentration, in-solution plus colloidal, would remain invariant with respect to all models for interchange kinetics. Thus, only the dissolution rate, the precipitation rate, and the adsorption rate integral terms add and/or subtract mass from the total concentration when represented as an aggregate measure of in-solution and colloidal components.

When spent fuel is present and dissolving into solution under quasi-steady conditions, it is reasonable to assume that any precipitation- and adsorption-rate processes will be positive in the sense these processes will be subtracting mass from the solution. Given this assumption, it can be seen from Eq. 3.4.2-34 that a bounding model for the total concentration of a radionuclide in solution is provided by neglecting the precipitation and adsorption kinetic terms because these would subtract mass from the total concentration. Of course, for the highly soluble fission-product radionuclides and for cases of significantly high fluid-flow rates, the precipitation integral would be zero. Furthermore, the highly soluble radionuclides, for a bounding model, is assumed not to form colloidal species. Thus, Eq. 3.4.2-34 for a quasi-static-rate state will have bounding release-rate terms that depend on the areas of fluid flow  $A_F$  and spent fuel dissolution  $A_S$  only and would reduce to

$$\int_{A_F} (\bar{v}_F + \bar{v}_C) \cdot \underline{n}_F \bar{C} dA_F = \int_{A_S} \rho_C \underline{v}_S \cdot \underline{n}_S dA_S \quad (3.4.2-35)$$

Eq. 3.4.2-35 can be area-integrated over an inlet-fluid boundary  $A_F$  in and an outlet fluid boundary  $A_F$  out and for flows that have fluid velocities significantly greater than the diffusional velocities. The quasi-steady change in concentration between the inlet and outlet fluid boundaries becomes

$$\bar{C}_{out} - \bar{C}_{in} = 1/Q_F \int_{A_S} \rho_C \underline{v}_S \cdot \underline{n}_S dA_S \quad (3.4.2-36)$$

where the volumetric flow rate  $Q_F$  is defined as

$$Q_F \equiv \int_{A_F} \underline{v}_F \cdot \underline{n}_F dA_F \quad (3.4.2-37)$$

For quasi-steady flows,  $Q_F$  has the same value at the inlet and outlet areas.

Eq. 3.4.2-36 is used to evaluate the dissolution rate and/or the dissolution velocity  $\underline{v}_S$  for the flow-through testing experiments when solid area  $A_S$  is assumed not to evolve in time. In these tests, the flow rate  $Q_F$  is controlled, the dissolution area is measured, and the water chemistry is prescribed at the inlet surface. Thus,  $\underline{v}_S$  can be evaluated for the prescribed set of testing conditions for which the precipitation, colloidal, and adsorption terms do not have contributions.

For these same conditions, the release-rate concentration for fluid flowing over exposed spent fuel in a waste package can be modeled by integrating Eq. 3.4.2-35 in a slightly different manner. For this integration, consider a uniformity thick film of fluid flowing on an arbitrary wetted path  $\ell(\underline{x})$  of exposed spent-fuel surface in a waste package. For a film thickness of  $h$  and an arbitrary film width  $w$  that also wets a width of fuel  $w$ , the change in averaged concentration of the film as the fluids flows from a point  $\underline{x}$  to neighboring point  $\underline{x} + d\underline{x}$  on wetted path  $\ell(\underline{x})$  is

$$\frac{\partial}{\partial \underline{x}} \bar{C}(\underline{x}) \underline{v}_F \cdot \underline{n}_F hw d\underline{x} = \rho_C \underline{v}_S \cdot \underline{n}_S w d\underline{\ell} \quad (3.4.2-38)$$

In Eq. 3.4.2-38, the area  $A_F$  of the fluid flow is film thickness  $\times$  film width ( $hw$ ), and the dissolution area  $A_S$  is film width  $w \times$  the wetted path length ( $w d\underline{\ell}$ ). This is ideally valid; however, from observation of dissolution samples and in interpretation of flow-through samples, it has been conjectured that the exposed surface is enhanced by the rapid dissolution along grain boundaries up to a depth of three to five grain boundaries. Therefore, an empirical factor multiplied by the dissolution area should be applied. This factor would have a dependence on grain size; based on flow-through tests (Gray and Wilson, 1995), a value of four is recommended. A generic parameter  $\delta_S$  will be used for a value of this empirical factor in the following. The integration of Eq. 3.4.2-38 between arbitrary points  $\underline{x}_{in}$  to  $\underline{x}_{out}$  with a corresponding path length of  $\ell(\underline{x}_{out}) - \ell(\underline{x}_{in})$  is

$$\bar{C}(\underline{x}_{out}) - \bar{C}(\underline{x}_{in}) = ((\rho_C \underline{v}_S \cdot \underline{n}_S \delta_S w) / (\underline{v}_F \cdot \underline{n}_F hw)) (\ell(\underline{x}_{out}) - \ell(\underline{x}_{in})) \quad (3.4.2-39)$$

Equation 3.4.2-39 evaluates the change in concentration as fluid flows past and dissolves spent fuel with a wetted contact length of  $\ell(\underline{x}_{out}) - \ell(\underline{x}_{in})$ . For waste packages with horizontally emplaced fuel rods, the contact length would be the crack opening of the failed rods in a radial direction. For those cases that may be conjectured in which the generic radionuclide concentration evaluated by Eq. 3.4.2-39 exceeds a solubility limit, it is recommended that the outlet concentration be limited such that

$$\bar{C}(\underline{x}_{out}) \leq C_{\text{solubility limit}} \quad (3.4.2-40)$$

A colloidal-release-concentration expression that is an analog to Eq. 3.4.2-39 exists for the case of colloidal spallation and formation adjacent to the surface  $A_S$ . It is given by

$$\bar{K}(\underline{x}_{out}) - \bar{K}(\underline{x}_{in}) = ((\underline{v}_K \cdot \underline{n}_S \bar{K} w) / (\underline{v}_F \cdot \underline{n}_F hw)) (\ell(\underline{x}_{out}) - \ell(\underline{x}_{in})) \quad (3.4.2-41)$$

In some conjectured situations, there is a potential for a fixed volume  $V_F$  of fluid to be in constant contact with spent fuel. This situation corresponds to the fully saturated tests on spent fuels performed by Wilson (1990) and possibly in the alteration layer of the unsaturated tests (Finn et al., 1997). In these Wilson tests, the highly soluble fission-product radionuclides did not appear to exceed solubility limits. However, the actinide radionuclides did attain constant total concentration values, which, for release rate modeling purposes, will be taken as effective release concentrations and generically denoted as  $C_{erc}$  obtained from fully saturated test by Wilson (1990) are for in-solution plus colloidal concentration. For most cases, the colloidal components were small. For a quasi-steady-rate analysis of these tests, Eq. 3.4.2-34 reduces to

$$\int_{V_F} \partial_t \bar{C} + \partial_t \bar{K} dV_F = \int_{A_S} \rho_C \bar{v}_S \cdot \bar{n}_S + \bar{v}_K \bar{n}_S \bar{K} dA_S - \int_{A_P} \bar{v}_C \cdot \bar{n}_P \bar{C} dA_P + \bar{v}_K \cdot \bar{n}_P \bar{K} dA_P - \int_{A_K} \bar{v}_K \cdot \bar{n}_K \bar{C} + \bar{v}_K \cdot \bar{n}_K \bar{K} dA_K \quad (3.4.2-42)$$

where surface adsorption is assumed to be zero for this quasi-steady rate analysis. For highly soluble fission products, no colloidal and no precipitation kinetic is assumed, and for constant area of spent fuel  $A_S$  the rate of change in radionuclide concentration is a constant that depends proportionally on the dissolution rate; thus,

$$\bar{C}(t) = \frac{1}{V_F} \int \bar{C}(\underline{x}, t) dV_F = (\rho_C \bar{v}_S \cdot \bar{n}_S A_S / V_F) t \quad (3.4.2-43)$$

where the initial concentration at time zero is taken as zero. In applications, the surface area  $A_S$  should be multiplied by the empirical  $\delta_s$  parameter to have a bounding model.

For actinide radionuclides, where precipitation and some colloidal kinetics are occurring, Eq. 3.4.2-42 requires additional assumptions to constrain and formulate a model. From the experimental data (Wilson, 1990), the total concentration of  $(\bar{C} + \bar{K})$  attains an effective release concentration  $C_{erc}$ ; thus, the value of the concentration-rate integral over fluid volume  $V_F$  (first integral expression in Eq. 3.4.2-42) after this time is zero, and

$$\bar{C}(t) + \bar{K}(t) = C_{erc} \text{ for } t \geq t_{erc} \quad (3.4.2-44)$$

where  $t_{erc}$  is the time determined from experimental data when the total concentration  $(\bar{C} + \bar{K})$  is less than  $C_{erc}$ . Based on results of experiments (Wilson, 1990), the time interval  $(0, t_{erc})$  is on the order of days or weeks for these fuel-area-to-water-volume ratios; thus, the value of  $t_{erc}$  can, for most cases, be set to zero. This is bounding because, for times  $t$  less than  $t_{erc}$ , the total concentrations  $\bar{C} + \bar{K}$  is less than  $C_{erc}$ .

From Eq. 3.4.2-42, the preceding experimentally based assumption that the left-side term for concentration changes is zero means that the sum of terms on the right is also zero. Thus, for quasi-steady rates and fixed fluid volumes, the rate of spent-fuel dissolution and colloidal spalling is equal to the rate of precipitation and colloidal kinetics. Although it has not been explicitly stated previously, it will be assumed that the dissolution process is such that the spent-fuel radionuclides of the spent fuel dissolve directly to in-solution concentrations and add to only  $\bar{C}$  at the surface of the spent fuel. To maintain quasi-steady constant  $\bar{C}$ , the precipitation and colloidal kinetic terms on neighboring surfaces  $A_p$  and  $A_k$  must balance this dissolution rate; thus

$$\int_{A_p} \bar{v}_C \cdot \bar{n}_p \bar{C} dA_p + \int_{A_k} \bar{v}_K \cdot \bar{n}_K \bar{C} dA_K = \int_{A_s} \rho_C \bar{v}_S dA_S \quad (3.4.2-45)$$

Similarly, the rate of aggregated colloidal interchanges to surfaces  $A_p$  and  $A_k$  must balance the spallation and formation rate of aggregated colloidal increase. Thus,

$$\int_{A_p} \bar{v}_K \cdot \bar{n}_p \bar{K} dA_p + \int_{A_k} \bar{v}_K \cdot \bar{n}_K \bar{K} dA_K = \int_{A_s} \bar{v}_K \cdot \bar{n}_S \bar{K} dA_S \quad (3.4.2-46)$$

Without additional microscopic details, the precipitation and colloidal surface kinetic rates on surfaces  $A_p$  and  $A_k$  in Eq. 3.4.2-45 and Eq. 3.4.2-46 cannot be partitioned into separate components of the dissolution-rate concentration from surface  $A_s$ . Nonetheless, for quasi-steady state release-rate processes, these equations, these equations do show that, for fixed fluid-volume processes, the concentrations of both in-solution species  $\bar{C}$  and aggregated colloidal species  $\bar{K}$  are constants for quasi-static rate processes. Quasi-static rate processes are attainable in a short period of elapsed time when the fluid volume  $V_f$  wetting the spent-fuel surface is small in thickness relative to a length-scale metric of the spent-fuel surface. Hence, for thin film flows or stagnated thin-wetting films, dissolution on surface  $A_s$  potentially would be immediately followed by precipitation and colloidal kinetic processes in the wetted film adjacent to a spent-fuel surface  $A_s$ . This will be assumed case for the analysis in the following paragraphs. This analysis will result in a bounding model for the release-rate measurements performed in the unsaturated/drip testing on spent fuels that are briefly discussed in the following paragraph.

The unsaturated/drip test is a closed-vessel, 100% humidity experiment. The closed vessel contains fragments of spent fuel placed in a Zircaloy™ tube; an equilibrated, J-13 water is dripped onto the spent-fuel surface. During the first couple of years, the drips flowed over a visually unaltered spent-fuel surface. Release rates were measured for the total in-solution and colloidal concentrations that were transported to an outlet basin of the vessel. These concentrations also include the mass contribution that was adsorbed onto the surface of the outlet vessel. This total concentration is the measured release rate for the drips flowing past the mass of spent fuel in the Zircaloy™ tube. The concentrations are being measured approximately every two to three months for the high-drip-rate tests and slightly less often for the low-drip-rate tests. After

approximately a year and a half to two years, a visible layer of alteration products was observed on the spent-fuel surface. These alteration products were precipitates containing fission products and actinide isotopes, not all of which have been fully identified. The alteration layer is highly porous and appears somewhat as a fibrous mat of precipitation species that adhere to the wetted spent-fuel surface.

The following simplified analysis and model of these unsaturated/drip tests has several assumptions. For the first assumption, which covers the transient time period of approximately two years during which the surface visually appears unaltered, the release-rate concentration will be assumed to be given by Eq. 3.4.2-11 and Eq. 3.4.2-13 for the in-solution and colloidal concentrations, respectively. This is considered a transient period. However, a two-year time increment is small when compared to many thousands of years for a repository time period. Thus, the averaging of experimental release data for this time period would be an approximate way to provide nominal data for this initial, short-period, transient time period before the alteration layers form on the spent-fuel surface. The detailed analysis to evaluate the path length  $\ell(\underline{x}_{out}) - \ell(\underline{x}_{in})$  and to estimate consistent rate parameters from the high- and low-drip-rate tests has not been completed. This data evaluation requires some additional assumptions. For example, it appears that the high-drip-rate test had sufficient flow rate to pool around the spent-fuel surface in the Zircaloy™ tube. Thus, the high-drip-rate water remained in contact with the spent fuel longer (had a long residence-time interval) than did the low-drip-rate water. Concentrations estimated from the high-drip-rate would then be the bounding concentrations for release rates, independent of the path length and the flow rate. However, for lower drip rates, estimates of the path length and fluid-flow rates can be used to reduce the release concentrations. For example, it can be seen from Eq. 3.4.2-39 that, for high-flow rates ( $\underline{v}_f \cdot \underline{n}_f \cdot hw$ ), the release concentration is reduced. Note, however, that the release rate, which is concentration multiplied by flow rate, depends only on the dissolution rate and the path length. This initial unaltered surface-dissolution/release rate is also enhanced due to rapid release from gap- and grain-boundary radionuclide inventories. The use of the high-drip release data thus would incorporate approximately some nonhomogeneous spatial radionuclide densities into this transient release rate.

Following the transient-release-rate period, the spent-fuel surface is assumed to be altered, and a dense mat of precipitated products is assumed to be adhered to the spent-fuel surface. The porosity of this altered layer is assumed to be fully saturated with water, and the dissolution process is assumed to be actively reacting at the spent fuel surface  $A_s$ . This dissolution process beneath the alteration layer is assumed to be a quasi-steady-rate process in a stagnate (nonflowing) thin film of water. Thus, the concentrations of the in-solution and colloidal components are assumed to attain constant values within the alteration layer. Therefore, Eq. 3.4.2-44 for the total concentrations  $C_{erc}$  is assumed to be valid for the radionuclides in the water of the porous altered layer.

Next, the dripping water is assumed to flow on the exterior surface of the alteration layer, and transport of in-solution and colloidal radionuclides is assumed to occur by mass transport from the alteration layer into the moving drip of water flowing over the alteration layer. In the linear case of intersurface mass transfer, the rate of diffusion exchange (or with slight surface-to-surface fluid mixing) is represented as proportional to the difference between the concentration of the water in the alteration layer and the concentration of the water in the flowing film (or drip, in this case). The equation for this transport process is similar to that of Eq. 3.4.2-38, except that the right side is replaced with the diffusional exchange term, resulting in

$$\frac{\partial}{\partial x} \bar{C}(x) v_F \cdot n_F h w d x = \lambda_C (\bar{C}_{\text{film}} - \bar{C}(x)) w d \ell \quad (3.4.2-47)$$

where  $\lambda_C$  is a mass-transfer coefficient to be evaluated from data of the high- and low-flow-rate saturated-drip tests. For quasi-steady rates, Eq. 3.4.2-47 can be integrated to

$$\bar{C}(x_{\text{out}}) = \bar{C}_{\text{film}} (1 - \exp(-\Lambda_C (\ell(x_{\text{out}}) - \ell(x_{\text{in}})))) \quad (3.4.2-48)$$

where  $\Lambda_C$  is  $\lambda_C w / (v_F \cdot n_F h w)$ , and the concentration at the inlet point  $x_{\text{in}}$  is assumed to be zero. Similarly, Eq. 3.4.2-41 for colloidal concentrations can be reformulated analogously, and the aggregated colloidal concentration transferred from the altered surface to the fluid is

$$\bar{K}(x)_{\text{out}} = \bar{K}_{\text{film}} (1 - \exp(-\Lambda_K (\ell(x_{\text{out}}) - \ell(x_{\text{in}})))) \quad (3.4.2-49)$$

where  $\bar{K}_{\text{film}}$  is the aggregate concentration of colloidal species in the water of the porous altered layer, and  $\Lambda_K$  is a transfer coefficient to be evaluated from the high- and low-saturated-drip data. The term  $\Lambda_K$  has the parameter  $\lambda_K$  and flow rate incorporated into it as  $\lambda_K w / (v_F \cdot n_F h w)$  and is similar to  $\Lambda_C$ .

The parameters  $\bar{C}_{\text{film}}$  and  $\bar{K}_{\text{film}}$  in Eq. 3.4.2-48 and Eq. 3.4.2-49 will be estimated with release-concentration data from the high-drip-rate tests. In the high-drip-rate tests, the water was observed to remain in contact with the altered layer on the fragments and to pool around the spent-fuel surface. Therefore, the residence-time interval of the water contact on the porous alteration layer is assumed to be sufficiently long that the concentrations of  $\bar{C}$  and  $\bar{K}$  of the water become equal to the concentrations  $\bar{C}_{\text{film}}$  and  $\bar{K}_{\text{film}}$  in the porous layer. A long residence-time interval is functionally equivalent to a long path-length interval in terms of the water concentrations becoming equal to the film concentrations, as expressed in Eq. 3.4.2-48 and Eq. 3.4.2-49. To defensibly evaluate the film concentration values, this assumption needs to be substantiated. Future experiments are planned to provide better estimates of the in-

solution and colloidal concentrations parameters. For now, the available data of the high-drip-rate tests can be used to provide preliminary estimates of release concentrations.

For cases where the flow is in contact with the altered layer for shorter time intervals or, equivalently, shorter path lengths, then the concentration at the outlet point  $x_{out}$  will be reduced. To calculate the reductions in concentrations with Eq. 3.4.2-48 and Eq. 3.4.2-49, values for parameters  $\Lambda_c$  and  $\Lambda_k$  are required. In some cases, the release-concentration data from the low-drip-rate test can be used to estimate values of  $\Lambda_c$  and  $\Lambda_k$  for different radionuclides. This approach uses experimental data to provide release-concentration estimates for cases in which, in a horizontally emplaced waste package, the path-length interval is conjectured to be short (e.g., when cladding failure flaws are expected to be represented as narrow cracks along the axis of spent fuel rods).

The preceding, simplified release models for in-solution and colloidal concentrations have parameters that can be estimated from the limited data now becoming available from the unsaturated test methods. The observations and measurements of colloidal concentrations have greatly added to the complexity of developing waste-form release concentrations and release rates. The colloidal contributions to total concentration means that the release-concentration constraint imposed by idealized solubility limits is not strictly conservative. Of course, once the areal-size classes of colloids are established and validated, it may be possible to design filtration beds or adsorption materials to reduce the colloidal concentration near the waste package; solubility limits would then be applicable. This remains to be evaluated.

Finally, the alteration rate of spent fuel, in the preceding model of an altered layer, is assumed to progress at the rate of the dissolution velocity  $v_d$ . Thus, the alteration life time of a spent-fuel fragment is roughly its half-size dimension divided by the magnitude of  $v_d$ . Hence, the altered layer is assumed to continue to increase in thickness until all of the fuel particle is transformed into precipitation and colloidal alteration products. Subsequent to this alteration life-time interval, it will be assumed that the release concentrations from the fully altered spent-fuel fragments will be long path-length limited to the  $\bar{C}_{film}$  and  $\bar{K}_{film}$  concentrations for a time interval whose span is limited by the inventory of the radionuclide. For short path lengths of fluid flow, the release concentrations would be reduced with values calculated from Eq. 3.4.2-48 and Eq. 3.4.2-49. This means that, although the dissolution-rate process is assumed to be essentially congruent, the release concentrations and release-rate concentrations are not necessarily a congruent process with respect to the initial inventory of the radionuclides. This should pose no problem for the fission-product releases. The releases of fissile isotopes, released and remaining in the altered spent fuel, should be evaluated with respect to the history of their concentration over time.

### 3.4.2.5 Release-Rate Model and Preliminary Analysis of Radionuclide Release in Unsaturated Drip Tests

#### 3.4.2.5.1 Introduction

The focus of this modeling work is on the combined processes of oxidation, dissolution, and redeposition that take place when spent fuel is simultaneously exposed to air and to small amounts of groundwater. The concurrent incorporation of all of these processes distinguishes the *spent-fuel-release models for unsaturated conditions* presented in Section 3.4.2.5 from the *forward-dissolution-rate models for spent fuel* presented in Section 3.4.2.3 (Steward and Gray, 1994)

In the forward-dissolution rate models, the amount of oxygen is limited to that dissolved in water, the amount of flowing water is substantial, and the dissolved products become unavailable for participation in subsequent processes because of the high water-flow rates that rapidly transport dissolved products away from the site of reaction. The parameters of the unsaturated-release-rate models presented here are obtained by analyzing laboratory data from unsaturated, spent-fuel-release drip tests conducted at Argonne National Laboratory (Finn et al., 1994a, 1994b, 1995; Bates et al., 1995; personal correspondence, "Yucca Mountain Nuclear Waste Management Program Project Data Transmittal from the Unsaturated Spent Fuel Testing Task at the Argonne National Laboratory to the Waste Form Characterization Task at the Lawrence Livermore National Laboratory," P.A. Finn, Argonne National Laboratory, to Ananda Wijesinghe, Lawrence Livermore National Laboratory, July 1997).

In contrast, the basic kinetic-dissolution-rate parameter of the spent-fuel forward-dissolution-rate model is obtained from laboratory flow-through tests conducted under dissolution-rate-limited saturate-flow conditions at high water-flow rates (Steward and Gray, 1994). The unsaturated-release-rate models presented here have been developed to analyze and extract the minimum number of parameters that could represent the experimentally observed releases in drip tests. No attempt has been made to provide a detailed predictive capability based on more fundamental thermodynamic and kinetic properties of the underlying chemical species and reactions. Because the unsaturated-release-rate models incorporate dissolution as one of the active processes, detailed prediction of release rates from fundamental considerations will require, as one of the many required thermodynamic and kinetic parameters, use of the forward-dissolution rate of spent fuel obtained from saturated flow through dissolution tests. Furthermore, because secondary mineral phases are formed and redeposited from solution during spent fuel dissolution under unsaturated conditions at low flow rates, the release rates under these conditions are generally smaller by orders of magnitude than the release rates predicted by a forward-dissolution-rate model for saturated high flow-rate conditions.

#### 3.4.2.5.1.1 Physical Transport Phenomena

The conceptual model for spent-fuel release under unsaturated low-flow-rate conditions divides the region occupied by the fuel fragments into two parts: a drip-water contact zone and a condensed vapor-water contact zone. In the drip-water zone, droplets of water intermittently drip onto the fuel fragments. When the small droplets contact the fuel fragments, they collect in patches of water on the surface and spread out into a thin film of water covering the fuel surface. In addition, localized patches grow in thickness as attached droplets until capillary forces are exceeded, at which point they drain along the surfaces of the fuel fragments in intermittent rivulets. Thus, most of this water quickly flows away from the collection of fuel fragments in rivulets while a small part of the water remains trapped by surface tension at the surfaces of contact between fuel fragments. The void space between fuel fragments that is not occupied by the flowing and/or trapped drip water at any instant is assumed to be occupied by air saturated with water vapor. Thus, the surface of the fuel fragment in this region is contacted by a film of condensed water vapor when it is not in contact with drip water.

In the vapor zone, which is not directly contacted by the dripping water, the fuel fragments exist in an atmosphere saturated by water vapor. The water vapor is assumed to condense on the surface of the fuel fragments to form a thin film of water that covers the entire external surface of each fuel fragment. Surface patches of water may also grow in thickness and coalesce into larger droplets on the surfaces of the fuel fragments that drain away as rivulets, in the same manner as in the drip zone but at a much slower rate.

The liquid film in the vapor-contact regions is assumed to flow under gravity along the surfaces of the fuel fragments. The rate of solution drainage will depend on the film thickness and drop size and on the combined action of surface tension, viscous, and gravitational forces. A pool of drained water is always assumed to exist in the neighborhood of the fuel fragments; thus, there is always sufficient water to saturate the void spaces. Consequently, the rate of condensation of water on the fuel fragments is assumed to be exactly equal to the rate of drainage of water from the condensed vapor film, and the process is in a steady state with respect to the evaporation and condensation of water vapor and drainage of liquid water.

In the areas contacted by the drip water, the rapidity of drainage of the drops will not permit sufficient time for the chemical reactions of dissolution to act to any significant extent with the intermittent falling droplets. Instead, the significant processes will be the mixing of the drip water with the existing vapor-film water and the mechanical entrainment of colloidal particles from the contacted surface into the droplets as they drain away from the fuel fragments (Finn et al., 1994b). The degree of entrainment of the colloidal particles is likely to be much more significant in the drip region than in the vapor region because the drip water volume is locally much greater and faster flowing than is the water vapor-water film. When each drop has rapidly drained away, the dissolution process reverts to that of a vapor test. In essence, the

drip-region behaves in a manner similar to that of the vapor region with the addition of short periods of rapid transport and liquid mixing that coincide with the release of a drop onto the fuel fragments. In this model of release under unsaturated-drip conditions, the differences in chemistry will become evident primarily in the change in chemistry of the residual liquid film along the path of passage of the drip water.

In both regions, the water in the films will react with the fuel fragments and will diffuse into their interiors. However, unlike the surfaces exposed only to water vapor, the surfaces contacted by the dripping water will also be affected by reactions with chemical components dissolved in the original groundwater. Some of the reactants will dissolve and diffuse back into the water film so that the film will consist of a solution of water and dissolution products.

### *Chemical Transformation Phenomena*

The chemical reactions between the fuel and the water contacting the fuel fragments transform the fuel-fragment surfaces through a sequence of chemical transformations involving the following:

1. Oxidation to more soluble phases
2. Dissolution and removal of the oxidized phases
3. Precipitation of secondary mineral phases from solution
4. Sorption of colloidal matter in the solution phase
5. Redissolution of the secondary mineral phases
6. Reprecipitation as other alteration mineral phases

These complex transformations occur not only at the nominal exposed surface of the altering fuel fragment, but also to some distance into the interior of fuel fragment along grain boundaries that dissolve preferentially. The paragenetic sequences observed in both natural and experimental systems follow the general trend of uranium dioxide  $\Rightarrow$  uranyl oxide hydrates  $\Rightarrow$  alkali- and alkali-earth uranyl oxide hydrates  $\Rightarrow$  uranyl silicates  $\Rightarrow$  alkali- and alkaline-earth uranyl silicates + palygorskite clay. The specific mineral-phase sequence usually observed is uranium dioxide  $\Rightarrow$  dehydrated schoepite  $\Rightarrow$  compregnacite + becquerelite  $\Rightarrow$  soddyite  $\Rightarrow$  boltwoodite + uranophane + palygorskite clay (Wronkiewicz, 1977).

Observation of the mineral transformations that take place in the drip tests indicate that the dissolved minerals in the incoming groundwater would affect only the surfaces directly contacted by the drip water; this effect is significant only at relatively high flow rates that bring substantial amounts of these dissolved minerals. The dominant mineral phases observed in these tests over approximately 3.5 yr are given in the order in which they form in Table 3.4.2.5-1 (Finn et al., 1995; Bates et al., 1995; personal correspondence, "Yucca Mountain Nuclear Waste Management Program Project Data Transmittal from the Unsaturated Spent Fuel Testing Task at the Argonne National Laboratory to the

Waste Form Characterization Task at the Lawrence Livermore National Laboratory," P.A. Finn, Argonne National Laboratory, to Ananda Wijesinghe, Lawrence Livermore National Laboratory, July 1997). The alkali- and alkaline-earth uranyl silicates represent the long-term solubility-limiting phases for uranium in these tests and in natural uranium deposits in natural oxidizing systems. From this table, one can see that the mineral transformations that occur under vapor test (condensed vapor-water flow only) and low-drip test (condensed vapor-water and low-drip water-flow rate) conditions are similar over the entire time period; however, they are significantly different from those of the high-drip test (condensed vapor-water and high-drip water-flow rate), particularly at late times. Accordingly, the assumption that the same mineral phases form over the entire time period in vapor and low-drip conditions may be used to simplify and consolidate the analysis models for these two conditions.

**Table 3.4.2-4 Spent-fuel transformation mineral phases in vapor and drip tests**

Dominant Mineral Phases in Vapor and Drip Tests			
	Vapor Test	Low-Drip Test	High-Drip Test
1	Spent fuel (UO <sub>2</sub> )	Spent fuel (UO <sub>2</sub> )	Spent fuel (UO <sub>2</sub> )
2	Higher oxides	Higher oxides	Higher oxides
3	Schoepite	Schoepite	Schoepite
4			Compreignacite bequerelite
5			Soddyite
6			Boltwoodite

### 3.4.2.5.2 Interpretive Mathematical Model

A mathematical model was developed by the Argonne National Laboratory to analyze the laboratory vapor and drip tests conducted on two standard spent fuels (ATM-103, ATM-106). The water used for these tests was J-13 well water equilibrated with tuffaceous rock from the Yucca Mountain potential repository site. As previously stated, this model is not intended to enable detailed predictions of the radionuclide releases as a function of the chemistry of the groundwater and the temperature of the environment. Instead, it was developed for the limited purpose of extracting the radionuclide concentrations released as a function of the drip-water rate for the given groundwater composition and temperature, while allowing for the formation of secondary minerals under unsaturated low-flow-rate conditions.

The experimental configuration adopted in the drip tests for evaluating radionuclide release from spent fuels under unsaturated hydrologic conditions is shown in Figure 3.4.2-5. In these tests, the experimental test condition was the same for the drip test and the vapor test except that, in the drip test, the drip groundwater had a different chemical composition than did the initial water used in the vapor test. The interpretation of the drip tests is more complicated than the interpretation of the vapor tests because of the uncertainty regarding the spatial distribution of the drop water and

the area of contact between the drop water with the spent-fuel fragments. A similar uncertainty would exist in application to a repository, in that the spatial extent of the drip water contact zone would have to be estimated.

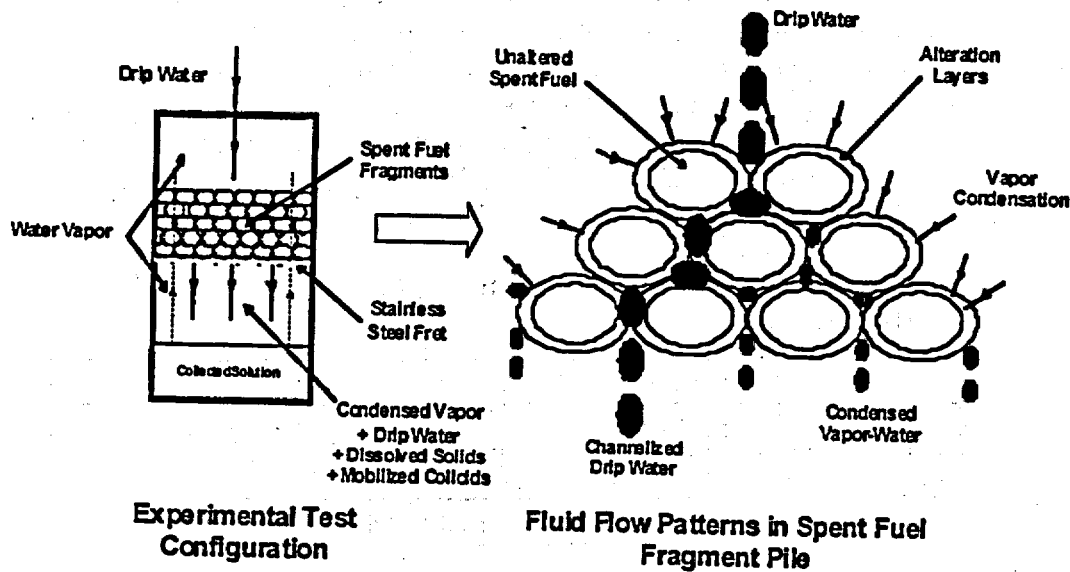


Figure 3.4.2-5 Experimental conditions for unsaturated drip tests

### 3.4.2.5.3 The Mass-Balance Equations

Using the notation developed in Section 3.4.2.4, the mass-balance equation for an arbitrary generic radionuclide in-solution species can be written as

$$\int_{V_F} \frac{\partial \bar{C}}{\partial t} dV_F + \int_{A_F} (\underline{v}_F + \underline{v}_{CF}) \cdot \underline{n}_F \bar{C} dA_F = \int_{A_S} \rho_{CS} \underline{v}_{CS} \cdot \underline{n}_S dA_S - \int_{A_P} \underline{v}_{CP} \cdot \underline{n}_P \bar{C} dA_P + \int_{V_F} \mu_{CK} dV_F - \int_{A_A} \underline{v}_{CA} \cdot \underline{n}_A \bar{C} dA_A, \quad (3.4.2-50)$$

where, the first term represents the rate of species mass accumulation in the fluid phase, the second term represents the net rate of efflux of the species across the transport surface  $A_F$ , the third term is the rate of species mass dissolving into the fluid phase, the fourth term is the rate of precipitation of species mass, the fifth term is the rate of transfer of mass between the in-solution dissolved species and the suspended-colloid phase expressed as an integral over the volume of the fluid phase, and the sixth term is the rate of adsorption of species mass on the solid surfaces exposed to the fluid phase. Likewise, the mass balance equation for the suspended-colloid species is given by the equation

$$\int_{V_f} \frac{\partial \bar{K}}{\partial t} dV_f + \int_{A_f} (\nu_f + \nu_{KF}) \cdot \underline{n}_f \bar{K} dA_f = \int_{A_s} \rho_{CS} \nu_{KS} \cdot \underline{n}_s dA_s$$

$$\int_{A_p} \nu_{KP} \cdot \underline{n}_p \bar{K} dA_p - \int_{V_f} \underline{\mu}_{CK} dV_f - \int_{A_A} \nu_{KA} \cdot \underline{n}_A \bar{K} dA_A, \quad (3.4.2-51)$$

where, the terms are directly analogous to the corresponding terms in the mass-balance equation for the dissolved in-solution species in the fluid phase. The third term is now interpreted to be the mass of colloidal particles released by the solid surfaces, while the precipitation and adsorption terms retain the conventional interpretations. Because the mass transfers between the in-solution and suspended-colloid species are equal, the fifth term is represented as the negative of the corresponding term in the in-solution species mass-balance equation. This mass transfer is the result of precipitation and adsorption of material from the in-solution material in the fluid phase onto the solid surfaces of the suspended colloid" and the dissolution and release of the material from the suspended colloids into the fluid phase. This term will be a sink of mass for the in-solution material if precipitation and adsorption exceed the rate of material dissolution and desorption from the suspended-colloidal particles; the term will be a source of mass if the reverse is true. Accordingly, a constitutive relation that reflects this two-way mass transfer may be written for the specific mass transfer term as

$$\mu_{CK}(t) \equiv \lambda_K \bar{K} - \lambda_C \bar{K} \frac{\bar{C}}{\rho_{CS}} \quad (3.4.2-52a)$$

$$= \lambda_K \bar{K} \left( 1 - \frac{\bar{C}}{C_{Km}} \right) \quad (3.4.2-52b)$$

where

$$C_{Km}(t) \equiv \frac{\lambda_K}{\lambda_C} \rho_{CS} \quad (3.4.2-53)$$

and  $\lambda_C$  and  $\lambda_K$  are the kinetic rate coefficients (1/day) for mass transfer from the fluid phase to the suspended colloids (due to precipitation and sorption) and from the suspended colloids to the fluid phase (due to dissolution and desorption), respectively.

The magnitude of the concentration  $C_{Km}$ , a parameter defined for convenience, may or may not exceed the in-solution species concentration  $\bar{C}$ . Therefore, this constitutive equation accommodates net mass transfer in either direction between the solution and colloidal phases. All of these material properties vary with changes in the materials' chemical compositions with time. Because the total surface area of the colloidal particles on which precipitation and sorption occur from solution is proportional to the number density of colloidal particles, and hence to the colloid mass concentration, the second term on the left side of Eq. 3.4.2-52a contains the product of the colloid mass

concentration  $\bar{K}$  and the in-solution species concentration  $\bar{C}$ . Therefore, at low in-solution and colloid concentrations, this term will be small compared to the first term on the left side. Also, if the in-solution concentration  $\bar{C}$  is equal to  $C_{km}$ , the left side of Eq. 3.4.2-52a/b will be zero, and there will be no net mass transfer between the in-solution and the suspended-colloid phases.

Eq. 3.4.2-50 and Eq. 3.4.2-51 can be expressed in the following, simpler lumped-parameter form by assuming that the variables are spatially uniform and that diffusive transport in the fluid phase can be neglected

$$V_F \frac{\partial \bar{C}}{\partial t} + v_F A_F \bar{C} = r_C A_S \left( 1 - \frac{\bar{C}}{C_{\max}} \right) + V_F \lambda_F \bar{K} \left( 1 - \frac{\bar{C}}{C_{km}} \right), \quad (3.4.2-54)$$

$$V_F \frac{\partial \bar{K}}{\partial t} + v_F A_F \bar{K} = r_K A_S \left( 1 - \frac{\bar{K}}{K_{\max}} \right) - V_F \lambda_F \bar{K} \left( 1 - \frac{\bar{C}}{C_{km}} \right). \quad (3.4.2-55)$$

In the two preceding equations, it has been assumed that no radioactive species existing in the spent-fuel are present in the incoming groundwater. Furthermore, the rate of mass dissolution from noncolloidal solid surfaces for in-solution species and the rate of colloid mass release from no-colloidal solid surfaces for the suspended-colloids have been defined by the expressions

$$r_C(t) = \rho_{CS} v_{CS}, \quad (3.4.2-56)$$

$$r_K(t) = \rho_{KS} v_{KS}. \quad (3.4.2-57)$$

In addition, equilibrium mass concentrations in the absence of convective and diffusive mass transport and mass transfer between in-solution and suspended-colloid species has been defined by

$$C_{\max}(t) \equiv \frac{r_C A_S}{v_{CP} A_P + v_{CA} A_A}, \quad (3.4.2-58)$$

$$K_{\max}(t) \equiv \frac{r_K A_S}{v_{KP} A_P + v_{KA} A_A}, \quad (3.4.2-59)$$

where the time dependence of these two parameters is explicitly shown to emphasize that all parameters appearing in these definitions vary as the chemical compositions of the materials change with time. Upon solving Eq. 3.4.2-54 and Eq. 3.4.2-55 for the in-solution and suspended-colloid mass concentrations, the total mass released  $\Delta M$  in an increment of time  $\Delta t$  can be computed from the general expression

$$\Delta M \equiv v_F A_F \bar{C}_T \Delta t. \quad (3.4.2-60)$$

where the total concentration  $\bar{C}_T$  of both in-solution and suspended colloidal species is defined by

$$\bar{C}_T \equiv (\bar{C} + \bar{K}). \quad (3.4.2-61)$$

#### 3.4.2.5.4 Limiting Solutions

Useful limiting solutions can be derived from the preceding equations for certain limiting conditions that may be realized in experimental and field conditions. Several limiting solutions applicable to the unsaturated drip tests are developed in the following text. The first approximation made is to neglect the term that represents the precipitation and sorption of in-solution species mass on the colloid particles because this is a term of second-order of smallness in magnitude and is dominated by precipitation and sorption on the spent-fuel surfaces. Accordingly, Eq. 3.4.2-54 and Eq. 3.4.2-55 reduce to

$$V_F \frac{\partial \bar{C}}{\partial t} + v_F A_F \bar{C} = r_C A_S \left( 1 - \frac{\bar{C}}{C_{\max}} \right) + V_F \lambda_F \bar{K}, \quad (3.4.2-62)$$

$$V_F \frac{\partial \bar{K}}{\partial t} + v_F A_F \bar{K} = r_K A_S \left( 1 - \frac{\bar{K}}{K_{\max}} \right) - V_F \lambda_K \bar{K}. \quad (3.4.2-63)$$

#### 3.4.2.5.5 Pseudo-Steady-State Conditions

Very useful and tractable pseudo-steady solutions to these equations can be obtained if the convective velocities are sufficiently large for the transport terms (second terms) on the right sides of Eq. 3.4.2-62 and Eq. 3.4.2-63 to be much larger than the mass accumulation terms (first term) given by the time derivatives of the concentrations. Neglecting the time derivatives and solving the resulting two simultaneous algebraic equations for the in-solution and colloid-species mass concentrations gives the results

$$\bar{C} = \frac{r_C A_S + V_F \lambda_K \bar{K}}{[r_C A_S + v_F A_F C_{\max}]} C_{\max}, \quad (3.4.2-64)$$

and

$$\bar{K} = \frac{r_K A_S}{[r_K A_S + (v_F A_F + V_F \lambda_K) K_{\max}]} K_{\max}. \quad (3.4.2-65)$$

It important to recognize that, although subject to the pseudo-steady assumption, these expressions are valid for arbitrary in-solution and suspended colloid species mass concentrations in the fluid phase that may be sufficiently high for secondary phases to form and precipitate out of solution.

#### 3.4.2.5.6 Transport-Limited, Pseudo-Steady Conditions

The pseudo-steady solutions given by Eq. 3.4.2-64 and Eq. 3.4.2-65 can be further specialized for two limiting conditions with respect to the flow rate. For low water-flow rates, such as those encountered in certain *unsaturated drip tests*, Eq. 3.4.2-64 yields, for the suspended colloid concentration,

$$\bar{K} \approx K_{\max} , \quad (3.4.2-66a)$$

provided that the water flow rates are sufficiently small to satisfy

$$v_F A_F K_{\max} \ll r_K A_S , \quad (3.4.2-66b)$$

and the kinetic coefficient  $\lambda_K$  for mass transfer between the in-solution species and the suspended colloid satisfies

$$V_F \lambda_K K_{\max} \ll r_K A_S . \quad (3.4.2-66c)$$

Similarly, Eq. 3.4.2-65 yields, for the in-solution species mass concentration,

$$\bar{C} \approx C_{\max} , \quad (3.4.2-67a)$$

provided that the water-flow rates are sufficiently small to satisfy

$$v_F A_F C_{\max} \ll r_C A_S , \quad (3.4.2-67b)$$

and the kinetic coefficient  $\lambda_K$  for mass transfer between the in-solution species and the suspended colloid satisfies Eq. 3.4.2-66c.

The incremental mass released in a time  $\Delta t$  is now obtained by substituting the above results in Eq. 3.4.2-60

$$\Delta M \approx v_F A_F (C_{\max} + K_{\max}) \Delta t . \quad (3.4.2-68)$$

Under these very slow flow-rate *transport-limited conditions*, the colloid and in-solution-species concentrations are approximately equal to their equilibrium-mass concentrations  $K_{\max}$  and  $C_{\max}$  that are attained for equilibrium between the processes of dissolution/colloidal-mass release from the spent-fuel surfaces and precipitation/adsorption of the in-solution and suspended colloids from solution. These equilibrium-

mass concentrations include the effects of all chemical interactions with the spent fuel and the water and, therefore, can be directly compared with the elemental solubilities previously used in total system performance assessment to bound the radioactive species mass releases.

### 3.4.2.5.7 Dissolution and Colloidal Particle Release-Limited, Pseudo-Steady Conditions

For the opposite limit of high flow-rate *dissolution and colloid release-rate limited conditions*, Eq. 3.4.2-64 and Eq. 3.4.2-65 give

$$\bar{K} \approx \frac{r_K A_S}{v_F A_F}, \quad (3.4.2-69a)$$

provided that the water flow rates are sufficiently small to satisfy

$$v_F A_F K_{\max} \gg r_K A_S, \quad (3.4.2-69b)$$

and the kinetic coefficient  $\lambda_K$  for mass transfer between the in-solution species and the suspended colloid satisfies

$$v_F A_F K_{\max} \gg V_F \lambda_K K_{\max}. \quad (3.4.2-69c)$$

Similarly, for this limiting condition, Eq. 3.4.2-65 yields for the in-solution species mass concentration

$$\bar{C} \approx \frac{r_C A_S}{v_F A_F}, \quad (3.4.2-70a)$$

provided that the water flow rates are large to satisfy

$$v_F A_F C_{\max} \gg r_C A_S, \quad (3.4.2-70b)$$

and the kinetic coefficient  $\lambda_K$  for mass transfer between the in-solution species and the suspended colloid satisfies Eq. 3.4.2-69c. The incremental mass  $\Delta M$  released in a time  $\Delta t$  given by Eq. 3.4.2-60 reduces to the form

$$\Delta M = (r_C + r_K) A_S \Delta t. \quad (3.4.2-71)$$

Because  $C_{\max}$  and  $K_{\max}$  are absent in these equations for  $\bar{C}$  and  $\bar{K}$ , no phenomena associated with the precipitation and sorption of secondary minerals are represented by these equations. These results are applicable to high flow-rate *flow-through dissolution tests*.

### 3.4.2.5.8 Total Mass Release Rate for Separate Drip and Vapor Zones

The expressions developed in the preceding text for the in-solution and suspended-colloid species-mass concentrations under low-flow-rate and high-flow-rate conditions can be applied to repository and laboratory release-rate tests by separately identifying the drip-water contact and the condensed vapor-water contact zones in each case and applying the appropriate limiting equations to each zone. If the drip-water-contact-zone volume (and area) fraction is defined by  $f_d$ , the total mass  $\Delta M$  released from the vapor and drip zones in a given time increment  $\Delta t$  is given by

$$\Delta M \equiv (1 - f_d) A_F v_{Fv} (\bar{C}_v + \bar{K}_v) \Delta t + f_d A_F v_{Fd} (\bar{C}_d + \bar{K}_d) \Delta t \quad (3.4.2-72)$$

where the vapor-zone concentrations and drip-zone concentrations, separately identified by the subscripts  $v$  and  $d$ . They are given by Eq. 3.4.2-64 and Eq. 3.4.2-65, respectively, in the general case, provided the parameters are separately labeled with these subscripts and are evaluated separately for each zone.

The general expression for mass release given by Eq. 3.4.2-72 may be applied to unsaturated and saturated tests (by appropriately choosing the volume/area fraction  $f_d$ ) and to low flow-rate and high flow-rate conditions. For interpreting the drip tests, the drip-zone liquid-flow velocity can be expressed more conveniently in terms of the condensed vapor-water flow velocity  $v_{Fv}$  and the drip-water-volume flow rate  $q_d$  the equation

$$v_{Fd} \equiv v_{Fv} + q_d / (A_F f_d) . \quad (3.4.2-73)$$

In summary, for conditions in which advective transport is sufficiently large for the advective mass transport to dominate the rate of mass accumulation in the liquid phase, the general expressions Eq. 3.4.2-64 and Eq. 3.4.2-65 give the variation of the in-solution and suspended-colloid film-mass concentrations with fluid flow rate while including the dissolution of spent fuel, formation of alteration products, and dissolution of the alteration products. Only two time-varying constitutive properties appear in each equation for each of the in-solution and colloidal film-mass concentrations of a particular chemical element (i.e., the effective rate of dissolution/colloid release and the equilibrium film-mass concentration). Therefore, in interpreting mass-release data from drip tests using this interpretive model, the task is to determine the condensed vapor-water circulation rate  $v_{Fv}$ , the effective dissolution rates  $r_{Cd}$ ,  $r_{Cv}$  and  $r_K$ ,  $r_{Kv}$ , and the equilibrium film-mass concentrations  $C_{maxd}$ ,  $C_{maxv}$ , and  $K_{maxd}$ ,  $K_{maxv}$  given the drip-water flow rate  $q$ , the incremental mass released  $M$  in the time increment  $t$ , the total transport surface area  $A_F$  (i.e., the total fuel-fragment surface area), and the drip-zone area fraction  $f_d$ . For an experiment that involves as many as 10 measured chemical elements, this is a feasible, but formidable, challenge.

### 3.4.2.5.9 Total Mass Release Under Advective Transport-Limited Conditions

If the water flow rate is sufficiently low for the advective transport of mass to be the mechanism limiting mass release, Eq. 3.4.2-72 for the mass released simplifies to the form

$$\Delta M \equiv (1 - f_d) A_F v_{Fv} (C_{\max v} + K_{\max v}) \Delta t + f_d A_F v_{Fd} (C_{\max d} + K_{\max d}) \Delta t \quad (3.4.2-74)$$

that is independent of the effective rates of dissolution and is a function only of the equilibrium film-mass concentrations. This approximation is valid if the flow velocities is sufficiently small that Eq. 3.4.2-66b, Eq. 3.4.2-66c, and Eq. 3.4.2-67b are satisfied.

The mass released can be expressed in an even more convenient form if it is assumed that, for the flow rates satisfying Eq. 3.4.2-66b, Eq. 3.4.2-66c, and Eq. 3.4.2-67b, *the alteration products being formed are essentially the same in the vapor zone and in the drip zone*. Under this assumption, the equilibrium in-solution and colloidal film-mass concentrations would be the same in the drip zone and in the vapor zone, and Eq. 3.4.2-74 simplifies to the form

$$\Delta M \equiv (A_F v_{Fv} + q_d) (C_{\max} + K_{\max}) \Delta t \quad (3.4.2-75)$$

where, the separate subscripts for the drip and vapor zones have been dropped from the symbols for the equilibrium in-solution and colloidal film-mass concentrations.

Therefore, in interpreting mass-release data from drip tests using this advective, transport-limited, approximate model, the task is to determine the condensed vapor-water circulation rate  $v_{Fv}$ , the total equilibrium in-solution and colloidal film-mass concentration  $C_{T\max} \equiv (C_{\max} + K_{\max})$ , given the drip-water flow rate  $q_d$ , the incremental mass releases  $M$  in the time increment  $t$ , and the transport surface area  $A_F$  (i.e., the total fuel-fragment surface area). Note that, in this approximation, *it is not necessary to independently specify the transport surface-area fraction  $f_d$*  because of the assumption that the same chemical transformations occur in the drip and vapor zones. When compared to the full interpretive model for mass release given by Eq. 3.4.2-73, the number of parameters that must be determined from the drip-test data is much smaller in this approximate model. These parameters are the single value of the condensed vapor-water circulation rate  $v_{Fv}$  and the total equilibrium film-mass concentration  $C_{T\max}$  for each radionuclide at each measurement time.

### 3.4.2.5.10 Mass Release Under Reaction-Rate-Limited Drip Zone and Advective Transport-Limited Vapor Zone

If the water drip rate is sufficiently high, and mass release is reaction-rate limited in the drip zone and advective transport-limited in the vapor zone, Eq. 3.4.2-72 for the mass released simplifies to the form

$$\Delta M \cong (1 - f_d) A_F v_{Fv} (C_{\max v} + K_{\max v}) \Delta t + f_d A_F (r_{Cd} + r_{Kd}) \Delta t \quad (3.4.2-76)$$

that is independent of the equilibrium film-mass concentrations in the drip zone and the effective rates of dissolution and colloid release in the vapor zone. It is a function only of the total effective rate of dissolution and colloid release

$r_{Td} \cong (r_{Cd} + r_{Kd})$  in the drip zone and of the total equilibrium in-solution and colloid mass concentration  $C_{T\max v} \cong (C_{\max v} + K_{\max v})$  in the vapor zone. This approximation is valid if the flow velocities in the drip and vapor zones are such that conditions in Eq. 3.4.2-69b, Eq. 3.4.2-69c, and Eq. 3.4.2-50b are satisfied in the drip zone while conditions in Eq. 3.4.2-66b, Eq. 3.4.2-66c, and Eq. 3.4.2-67b are satisfied in the vapor zone. Further, if the flow domain is completely saturated, by setting  $f_d=1$ , one can eliminate the first term on the left side of Eq. 3.4.2-76 and recover the expression applicable to saturated high flow-rate flow-through dissolution tests. Under these circumstances, it is also likely that no alteration products would be formed, and the effective dissolution rate is the dissolution rate for the spent fuel itself.

#### 3.4.2.5.11 Numerical Methodology for Determining Release-Rate Model Parameters from Unsaturated Drip-Test Data

The release rate model presented in the preceding section (Section 3.4.2.4) was used to extract data from the unsaturated drip tests performed at the Argonne National Laboratory. In these tests, two standard fuel types (ATM-103 and ATM-106) were tested at three levels of drip rate in zero-drip, low-drip, and high-drip -rate drip tests. The method adopted to fit the data was to assume that the effective dissolution rates and equilibrium film-mass concentrations defined as model parameters in the unsaturated release-rate model varied with fuel type, released chemical element, experimental time, and drip rate. Even though the effect of drip rate on mass transport was explicitly represented in the model, additional dependence of these two constitutive parameters on drip rate (through effects of dissolved chemicals present in the incoming drip water) was recognized because different types of alteration minerals were formed in the later stages of these experiments. As shown in Table 3.4.2-4, the high drip-rate tests, in particular, showed the formation of boltwoodite as the dominant mineral at long times, whereas schoepite was the predominant mineral formed in the vapor and low-drip tests. These differences in long time response were particularly important because the response at long times, and possible emergence of these minerals as stable end states, are of greater relevance to repository performance than the responses at short times.

By substituting for the in-solution and colloidal-mass concentrations from Eq. 3.4.2-64 and Eq. 3.4.2-65 in the general expression for total incremental mass release given by Eq. 3.4.2-72, one obtains an expression for the incremental mass release  $\Delta M_i^{\alpha\beta}$  of a chemical element  $\alpha$  in flow-rate test (where  $\beta=1$  for a vapor test,  $\beta=2$  for a low-flow-rate drip test, and  $\beta=3$  for a high-flow-rate drip test) during the time interval  $\Delta t_i^\beta$ . Because the same secondary phases were observed during the measurement period in the vapor and low-drip tests and estimates showed that the flow rates were sufficiently small, these two sets of data were analyzed together using Eq. 3.4.2-75 for the incremental

mass release. Because the high-drip test exhibited secondary mineral phases that were different from those observed in the vapor and low-drip tests, it was analyzed separately using only the condensed vapor-water flow rate derived from the combined vapor- and low-drip-test analysis. For the high-drip-rate analysis, Eq. 3.4.2-72 was used. Furthermore, because the void spaces were observed to be fully saturated with water in the high-drip test,  $f_d = 1$  was assumed. Therefore, for these test conditions,

$$\Delta M_i^{\alpha\beta} \approx (A_F^\beta v_{Fv}^\beta + q_{di}^\beta) C_{T \max i}^\alpha \Delta t_i \quad (3.4.2-77)$$

for the vapor (=1) and low-drip (=2) tests and

$$\Delta M_i^{\alpha\beta} = \left( \frac{r_{Ci}^\alpha A_{Sdi} C_{\max di}^\alpha}{[r_{Ci}^\alpha A_{Sdi} + (A_F v_{Fv} + q_{di}) C_{\max di}]} + \frac{r_{Ki}^\alpha A_{Sdi} K_{\max di}^\alpha}{[r_{Ki}^\alpha A_{Sdi} + (A_F v_{Fv} + q_{di}) K_{\max di}]} \right) (A_F v_{Fv} + q_{di}) \Delta t_i \quad (3.4.2-78)$$

for the high-drip ( $\beta=3$ ) test. In the high-drip test, estimates do not clearly indicate that the low-flow-rate assumptions can be invoked to simplify the preceding expression. If the low-flow-rate assumptions can be invoked, Eq. 3.4.2-78 simplifies to the same form as Eq. 3.4.2-77.

The data-fitting task is to find, given the measured values of the previously identified known parameters, the set of unknown parameters. The general method adopted was to minimize, with respect to the values of the unknown parameters, the square error between the experimentally measured mass release and the mass release predicted by the preceding expression summed over all chemical elements, measurement times, and tests. That is, minimize the error  $E$  defined by

$$E(Z) \equiv \frac{1}{2} \sum_{\beta} \sum_{\alpha} \sum_i (\Delta M_i^{\alpha\beta} |_{\text{predicted}} - \Delta M_i^{\alpha\beta} |_{\text{measured}})^2 \quad (3.4.2-79)$$

with respect to each member  $Z_n$  of the set of unknown parameters by setting

$$\frac{dE}{dZ_n} = \left\{ \sum_{\beta} \sum_{\alpha} \sum_i (\Delta M_i^{\alpha\beta} |_{\text{predicted}} - \Delta M_i^{\alpha\beta} |_{\text{measured}}) \frac{d(\Delta M_i^{\alpha\beta} |_{\text{predicted}})}{dZ_n} \right\} = 0. \quad (3.4.2-80)$$

This procedure yields a set of  $n$  coupled, nonlinear algebraic equations that were solved for the  $n$  unknowns by a suitable iterative method (e.g., Newton-Raphson, sub-space projection/iteration methods). A computer program was developed within the Microsoft Excel 97 spreadsheet program for this purpose.

Generally, the number of distinct measurements must equal or exceed the number of unknown parameters for a solution to the problem to be obtained. If the effective rates of dissolution/release and the equilibrium in-solution and colloidal film-mass concentrations were allowed to vary with time and remain different in the vapor, low-drip, and high-drip tests, the number of measurements available was not sufficient to

determine all of the unknown parameters. Furthermore, the greater the number of measurements above the minimum required, the more reliable and accurate are the fitted parameters. For these reasons, it was decided to verify the applicability and adopt the approximate model (given by Eq. 3.4.2-77 for advective transport-limited conditions) and the additional assumption of equal-equilibrium film-mass transfer concentrations in the vapor and low-drip tests. The high-drip test, in which the alteration products were different from those observed in the vapor and low-drip tests, was excluded from this first step of the parameter-fitting procedure. That is, the vapor test and low-drip test data were used to determine the vapor-water circulation rate and the time-varying equilibrium film-mass coefficients for each chemical element at each experimental measurement time. The equations solved for the total equilibrium film-mass concentrations, obtained by substituting Eq. 3.4.2-77 in Eq. 3.4.2-80, are given by

$$\sum_{\beta} (\Delta M_i^{\alpha\beta} |_{predicted} - \Delta M_i^{\alpha\beta} |_{measured}) A_{di}^{\beta} \Delta t_i^{\beta} = 0. \quad (3.4.2-81)$$

Similarly, the equation for the vapor-water recirculation rate  $v_{Fv}$  is given by

$$\sum_{\beta} \sum_{\alpha} \sum_i (\Delta M_i^{\alpha\beta} |_{predicted} - \Delta M_i^{\alpha\beta} |_{measured}) A_F^{\beta} C_{max,i}^{\alpha} \Delta t_i^{\beta} = 0. \quad (3.4.2-82)$$

These nonlinear algebraic equations were simultaneously solved for the constant value of the condensed vapor-water recirculation rate and the unknown total equilibrium film-mass concentrations at each measurement time.

#### 3.4.2.5.12 Release-Rate Model Parameters for Unsaturated, Low-Flow-Rate Conditions with Secondary Phase Formation

This subsection presents the constitutive parameters fitted to the release rate model for unsaturated, low-flow conditions that accounts for the formation of alteration mineral products. The approximate model for mass release given by Eq. 3.4.2-75 was used to analyze the vapor and low-drip test data. This model is valid when the release rate is limited by advective transport and the alteration minerals formed in the vapor and drip zones are of the same composition and have the same equilibrium film-mass concentrations. The condensed vapor-water flow rate determined from this analysis was then used to determine the total film concentrations in the high-drip test because the condensed vapor-water flow rate is primarily a function of the temperature at which the test is performed.

The equilibrium-mass concentrations and vapor-recirculation velocities that were fitted to the vapor and low-drip test data are given in Table 3.4.2-5 and Table 3.4.26. These values are plotted against time in Figure 3.4.2-6 and Figure 3.4.2-7 for ATM-103 and ATM-106 fuels, respectively. The first important aspect of these results is that all equilibrium film-mass concentrations decrease in value with increasing time by many orders of magnitude. This is important because it implies that the formation of alteration products reduces radionuclide release far below initial levels. The second

important feature is that the equilibrium film-mass concentrations appear to approach constant values at long times. This is important because constant long-term values would imply that stable alteration minerals are being formed. The calculated equilibrium film-mass concentrations indicate that the mass releases are not congruent, although dissolution of spent fuel itself may be congruent. Finally, the differences in the relative magnitudes of the equilibrium film-mass concentrations for different chemical elements cannot be explained solely on the basis of their pure element solubilities, further underscoring the importance of preferential substitutional incorporation of elements in alteration minerals.

**Table 3.4.2-5** Equilibrium film-mass concentrations fitted to ATM-103 spent-fuel vapor and low-drip test data using the advective transport-limited approximate model; fitted vapor-water recirculation velocity = 2.666E-06 cm/d

All ATM-103 Tests: Fitted Equilibrium Total Mass Concentrations g/mL									
Time Interval	Pu	U	Cs	Tc	Sr	Mo	Am	Np	I
	0.00E+00								
1	5.343E-07	1.599E-05	5.349E-08	1.700E-07	2.899E-13	1.317E-07	1.216E-06	8.333E-08	2.117E-04
2	1.201E-08	1.499E-06	4.263E-09	1.171E-08	4.701E-09	2.899E-08	2.279E-09	6.481E-10	1.560E-07
3	7.979E-10	1.397E-07	1.920E-10	2.514E-09	3.032E-10	1.853E-09	3.873E-10	8.059E-11	1.168E-07
4	1.531E-11	2.937E-07	5.126E-10	3.969E-08	6.121E-10	4.832E-10	9.704E-11	3.835E-12	6.983E-08
5	4.456E-12	1.814E-09	2.463E-11	8.203E-10	8.284E-10	1.464E-09	3.030E-12	1.054E-12	1.262E-08
6	2.605E-11	5.536E-09	2.219E-10	1.112E-08	2.160E-09	2.704E-10	7.932E-12	6.361E-12	7.155E-09
7	3.365E-12	4.963E-09	3.132E-10	3.407E-09	6.617E-10	8.341E-11	1.579E-11	2.692E-12	2.201E-09

**ATM103: Fitted Film Mass Concentrations**

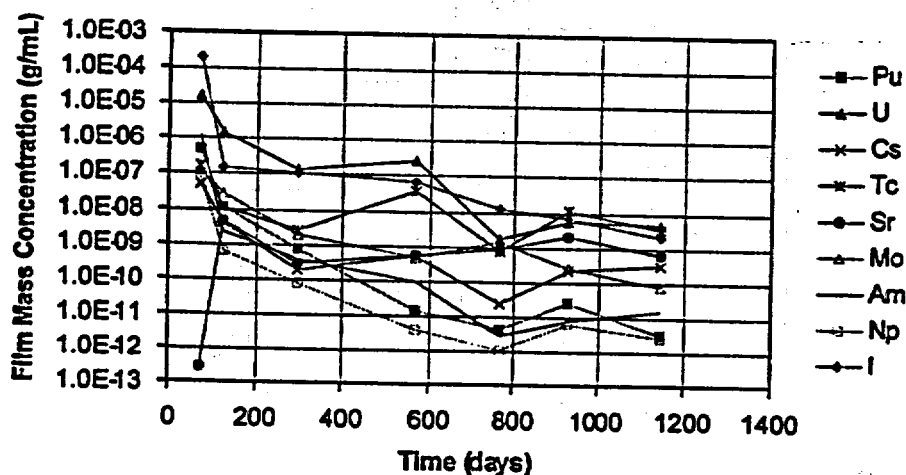


**Figure 3.4.2-6** Equilibrium total film-mass concentration fitted to ATM-103 spent-fuel-vapor test and low-drip-test data using the advective transport-limited approximate model

Table 3.4.2-6

Equilibrium film-mass concentrations fitted to ATM-106 spent-fuel vapor and low-drip-test data using the advective transport-limited approximate model; fitted vapor-water recirculation velocity = 2.014E-5 cm/d

All ATM-106 Tests: Fitted Equilibrium Total Mass Concentrations g/mL									
Time Interval	Pu	U	Cs	Tc	Sr	Mo	Am	Np	I
	0.00E+00								
1	4.366E-07	6.025E-05	1.515E-10	2.662E-07	1.445E-10	2.330E-07	3.632E-07	1.067E-07	6.026E-04
2	4.969E-09	1.014E-08	1.822E-09	2.901E-09	1.245E-08	1.705E-07	6.001E-10	5.934E-10	1.585E-06
3	7.444E-11	3.065E-08	4.400E-10	6.844E-10	5.952E-10	2.421E-08	8.322E-11	1.950E-11	1.826E-06
4	2.992E-11	4.625E-08	8.306E-10	1.771E-08	7.612E-09	1.888E-09	5.797E-12	3.734E-11	4.080E-07
5	5.811E-12	4.886E-10	1.454E-10	7.647E-10	1.140E-09	2.181E-09	1.190E-12	1.104E-12	3.349E-08
6	3.758E-12	9.465E-10	1.097E-09	5.164E-09	3.411E-10	1.373E-10	2.504E-12	3.514E-13	4.013E-08
7	1.915E-07	2.704E-05	1.128E-07	2.024E-09	1.334E-10	5.248E-11	4.468E-08	1.349E-08	1.508E-08

ATM106: Fitted Film Mass Concentrations

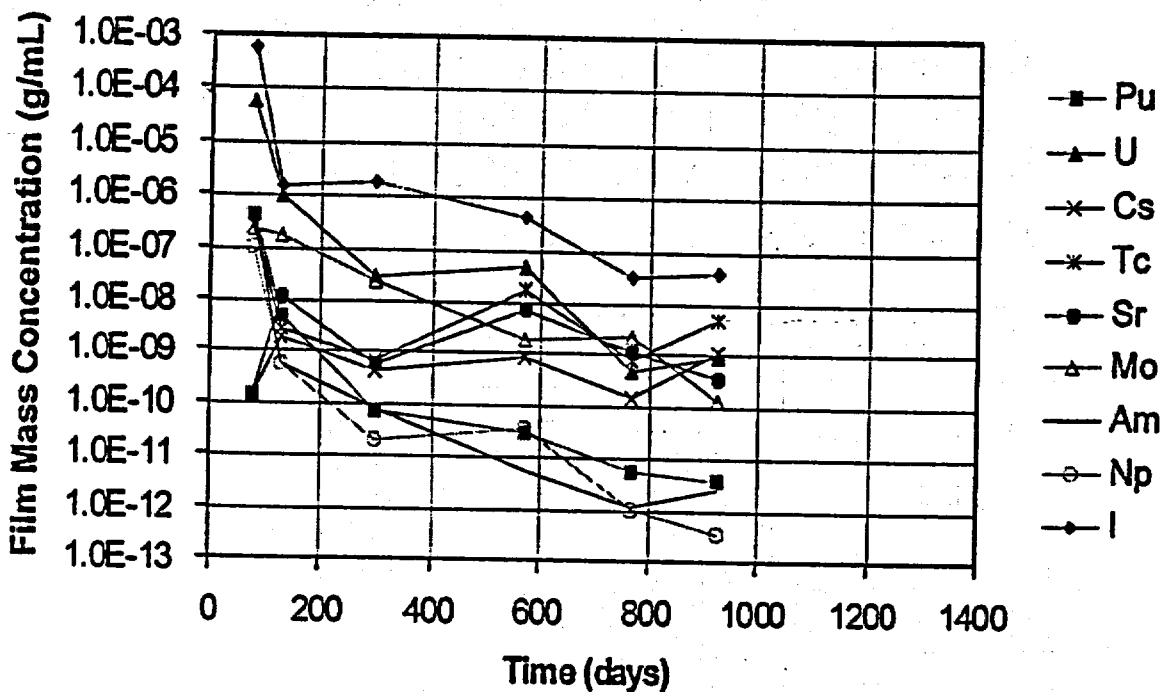


Figure 3.4.2-7

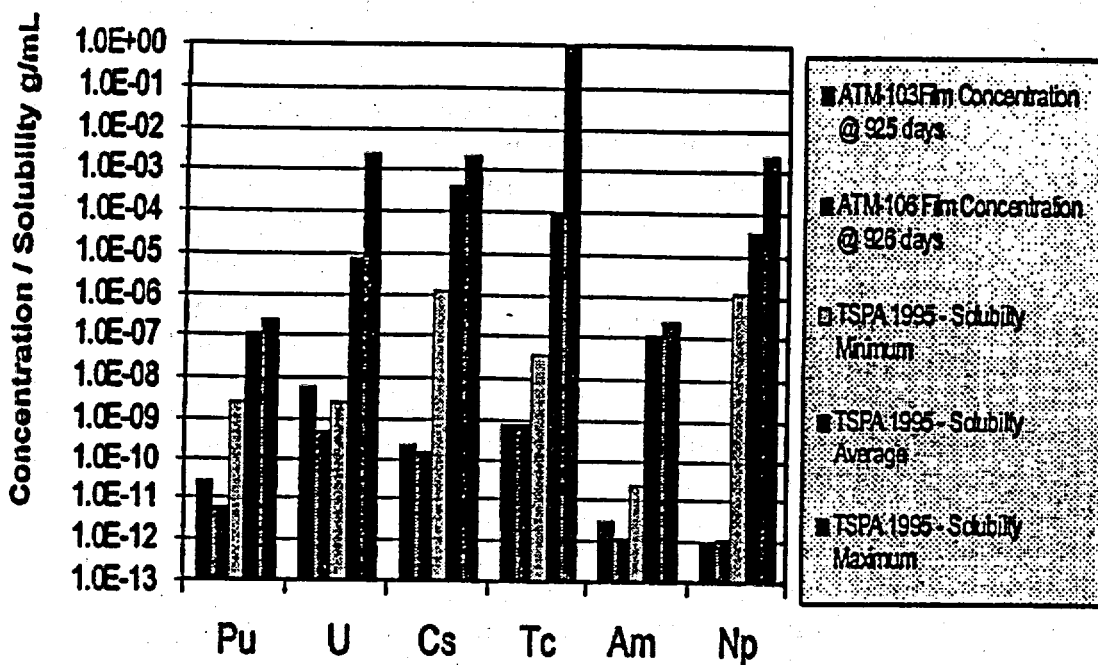
Equilibrium total film-mass concentration fitted to ATM-103 spent-fuel vapor test and low-drip test data using the advective transport-limited approximate model

### 3.4.2.5.13 Comparison of Equilibrium Mass Concentrations Against TSPA Recommended Solubility Limits

An important aspect of the equilibrium film-mass concentrations presented here is that, in the advective transport-limited analysis model, they are the actual film-mass concentrations of the chemical elements and, therefore, can be compared directly against the pure-element solubilities previously recommended in *Total System Performance Assessment—1995: An Evaluation of the Potential Yucca Mountain Repository* (TSPA—1995; CRWMS M&O, 1995) for bounding the radionuclide mass releases from spent fuel. The long-term equilibrium film-mass concentrations and the TSPA-1995 recommended average, minimum, and maximum solubilities are given in Table 3.4.2-7 and are plotted in Figure 3.4.2-8 for comparison. It can be seen immediately that the equilibrium film-mass concentrations are many orders of magnitude smaller than the average recommended TSPA-1995 values and are often many orders of magnitude smaller than the minimum solubilities recommended in TSPA-1995. Thus, the formation of alteration minerals under unsaturated, slow-flow conditions appears to reduce the release of radionuclides into the flowing groundwater by many orders of magnitude. If these preliminary results from analyzing the unsaturated drip test data can be confirmed, on detailed examination, as correct, they hold highly significant, favorable implications for repository performance.

**Table 3.4.2-7 Comparison of long-term equilibrium film-mass concentrations fitted to spent-fuel vapor and low-drip test data against TSPA (1995) recommended solubility limits.**

Equilibrium Concentration or Solubility Limit (g/mL)	Pu	U	Cs	Tc	Am	Np
ATM-103 Equilib.Conc@ 925 days	2.605E-11	5.536E-09	2.219E-10	8.203E-10	3.030E-12	1.054E-12
ATM-106 Equilib.Conc@ 926 days	5.811E-12	4.886E-10	1.454E-10	7.647E-10	1.190E-12	1.104E-12
TSPA 1995 - Solubility Average	1.200E-07	7.600E-06	3.900E-04	1.000E-04	1.200E-07	3.400E-05
TSPA 1995 - Solubility Minimum	2.400E-09	2.400E-09	1.200E-06	3.500E-08	2.400E-11	1.200E-06
TSPA 1995 - Solubility Maximum	2.400E-07	2.400E-03	2.100E-03	9.900E-01	2.400E-07	2.400E-03



3.4.2.6 Figure 3.4.2-8 Comparison of long-term equilibrium film-mass concentrations fitted to spent-fuel vapor and low-drip test data against TSPA (1995) recommended solubility limits (Neptunium solubility reduced by two orders of magnitude in TSPA-VA (1997).)

### 3.4.2.7 References

- Aagaard, P., and H. C. Helgeson (1982). "Thermodynamic and Kinetic Constraints on Reaction Rates Among Minerals and Aqueous Solutions. I. Theoretical Considerations." *Am. J. Sci.* 282:237-285. [HQS.19880517.2373]
- Adamson, A. (1976). *Physical Chemistry of Surfaces, 3rd Ed.* New York, NY: John Wiley & Sons.
- Antropov, L. I. (1972). *Theoretical Electrochemistry.* Moscow, Russia: Mir Publishers, Moscow.
- Bates, J. K., Bourcier, W. L., Finn, P. A., Stout, R. B. (1995). "Reaction Progress Pathways for Glass and Spent Fuel Under Unsaturated Conditions," In proceedings of Sixth Annual International Conference on High-Level Radioactive Waste Management. Las Vegas, NV: April 30-May 5, 1995. pp. 600-602. [MOL.19951219.0074]
- Bikerman, J. J. (1970). *Physical Surfaces.* New York, NY: Academic Press.
- Bockris, J. O., and A. K. Reddy (1970). *Modern Electrochemistry, Vols. 1 & 2.* New York, NY: Plenum Press.

- Box, G. E. P., W. G. Hunter, and J. S. Hunter (1978). *Statistics for Experimenters: An Introduction to Design, Data Analysis, and Model Building*. New York, NY: John Wiley & Sons.
- CRWMS M&O (1995). *Total System Performance Assessment—1995: An Evaluation of the Potential Yucca Mountain Repository*. (B00000000-01717-2200-00136, Rev. 01) Las Vegas, NV: Civilian Radioactive Waste Management System Management and Operating Contractor: TRW Environmental Safety Systems, Inc.
- Davies, O. L. (Ed.) (1956). *The Design and Analysis of Industrial Experiments*. London, UK: ICI by Longman.
- Davies, O. L. and P. L. Goldsmith (Eds.) (1972). *Statistical Methods in Research and Production*. New York, NY: Hafner.
- deGroot, S. R., and P. Mazur (1962). *Non-equilibrium Thermodynamics*. Amsterdam, The Netherlands: North Holland, Amsterdam.
- Denbigh, K. (1968). *The Principles of Chemical Equilibrium*. Cambridge, UK: University Press.
- Draper, N., and H. Smith (1981). *Applied Regression Analysis*, 2nd Ed. New York, NY: John Wiley & Sons. [231231]
- Eringen, A. C. (1967). *Mechanics of Continua*. New York, NY: John Wiley & Sons.
- Finn, P. A., J. C. Hoh, S. F. Wolf, M. Surchik, E. C. Buck, and J. K. Bates (1997). Spent Fuel Reaction: The Behavior of the  $\epsilon$ -phase Over 3.1 Years." In proceedings from Materials Research Society Symposium II. 465:527–534.
- Finn, P. A., J. C. Hoh, S. F. Wolf, S. A. Slater, and J. K. Bates (1995). "The Release of Uranium, Plutonium, Cesium, Strontium, Technetium, and Iodine from Spent Fuel Under Unsaturated Conditions." In proceedings from Migration '95: Fifth International Conference on Chemistry and Migration Behavior of Actinides and Fission Products in the Geosphere. Saint-Malo, France: September 10–15, 1995.
- Finn, P. A., J. K. Bates, J. C. Hoh, J. W. Emery, L. D. Hafenrichter, E. C. Buck, and M. Gong (1994a). "Elements Present in Leach Solutions From Unsaturated Spent Fuel Tests." In proceedings from Materials Research Society Symposia. 333:399–407.
- Finn, P. A., E. C. Buck, M. Gong, J. C. Hoh, J. W. Emery, L. D. Hafenrichter, and J. K. Bates (1994b). "Colloidal Products and Actinide Species in Leachate from Spent Nuclear Fuel." *Radiochim. Acta*. 66/67:189–195.
- Gibbs, J. W. (1961). *The Scientific Papers of J. Willard Gibbs*. Vols. 1 & 2. New York, NY: Dover Pub.
- Grandstaff, D. E. (1976). "A Kinetic Study of the Dissolution of Uraninite." *Econ. Geo.* 71:1493.
- Gray, W. J., H. R. Leider, and S. A. Steward (1992). "Parametric study of LWR spent fuel dissolution kinetics." *J. Nucl. Mater.* 190:46–52. [MOL.19960613.0037]

- Gray, W. J., and C. N. Wilson (1995). *Spent Fuel Dissolution Studies, FY1991 to 1994*. (PNL-10540) Richland, WA: Pacific Northwest National Laboratory. [MOL.19960802.0045]
- Hayward, D. O., and B. M. W. Trapnell (1964). *Chemisorption* (2nd Ed.). London, UK: Butterworths.
- Hochella, M. F., and A. F. White (Eds.) (1990). *Reviews in Mineralogy*, Vol. 23. Mineral-Water Interface Geochemistry, Mineral. Soc. of America. Washington, DC.
- Hunter, R. J. (1993). *Foundations of Colloid Science*. Oxford, UK: Clarendon Press.
- Jackson, J. D. (1962). *Classical Electrodynamics*. New York, NY: John Wiley & Sons.
- Jaycock, M. J., and G. D. Parfitt (1981). *Chemistry of Interfaces*. New York, NY: Halsted.
- Lasaga, A. C., R. A. Berner, G. W. Fisher, D. E. Anderson, and R. J. Kirkpatrick (1981). *Kinetics of Geo-chemical Processes*, Vol. 8. A. C. Lasaga and R. J. Kirkpatrick (Eds.). Washington, DC: Mineral. Soc. of America.
- Lewis, G. N., and M. Randall (1961). *Thermodynamics*. New York, NY: McGraw-Hill.
- Lupis, C. H. P. (1983). *Chemical Thermodynamics of Materials*. New York, NY: North-Holland.
- Pourbaix, M. (1973). *Lectures on Electrochemical Corrosion*. New York, NY: Plenum Press.
- Sedov, L. I., and J. R. M. Radok (1972). *A Course in Continuum Mechanics, Vol. II Physical Foundations and Formulations of Problems*. Gröningen, The Netherlands: Wolters-Noordhoff Pub.
- Steward, S. A., and W. J. Gray (1994). "Comparison of Uranium Dissolution Rates from Spent Fuel and Uranium Dioxide," In proceedings of the Fifth Annual International High-Level Radioactive Waste Management (IHLRWM) Conference. Las Vegas, NV: May 22-26, 1994. 4:2602-2608. (Also UCRL-JC-115355 for Lawrence Livermore National Laboratory, Livermore, CA.) [NNA.19940524.0024]
- Stout, R. B. (1996). "Nonequilibrium Thermodynamical Model for Spent Fuel Dissolution Rate." In proceedings for Seventh Annual International High-Level Radioactive Waste Management (IHLRWM) Conference. Las Vegas, NV: April 1996. pp. 393-396. (Also UCRL-JC-122737 for Lawrence Livermore National Laboratory, Livermore, CA.) [233230]
- Stout, R. B., E. J. Kansa, and A. M. Wijesinghe (1993a). *Kinematics and Thermodynamics of Non-stoichiometric Oxidation Phase Transformation in Spent Fuel*. (UCRL-JC-110678) Livermore, CA: Lawrence Livermore National Laboratory. [NNA.19930224.0014]

Stout, R. B., E. J. Kansa, and A. M. Wijesinghe (1993b). *Kinematics and Thermodynamics Across a Propagating Non-stoichiometric Oxidation Phase Front in Spent Fuel Grains*. (UCRL-JC-112821) Livermore, CA: Lawrence Livermore National Laboratory. [NNA.19930323.0053]

Stumm, W., and J. J. Morgan (1981). *Aquatic Chemistry: An Introduction Emphasizing Chemical Equilibria in Natural Waters*. New York, NY: John Wiley & Sons. [208448]

Wilson, C. N. (1990). *Results from NNWSI Series 3 Spent Fuel Dissolution Tests*. (PNL-7170) Richland, WA: Pacific Northwest National Laboratory. [200816]

Wronkiewicz, D. J., E. C. Buck, and J. K. Bates (1997). "Grain Boundary Corrosion and Alteration Phase Formation During the Oxidative Dissolution of  $UO_2$  pellets." In proceedings from Material Research Society Symposium. 465:519.

**Contents for Section 3.4.2 Appendix**

**A.3.4.2.1 Previous Significant Models .....3.4.2-1A**  
**A.3.4.2.2 Proposed Model from Expert Elicitation.....3.4.2-5A**  
**A.3.4.2.3 References.....3.4.2-6A**

## Section 3.4.2 Appendix

### Description of Previous or Alternative Intrinsic Dissolution Models

#### A.3.4.2.1 Previous Significant Models

The initial data-modeling efforts to represent available  $\text{UO}_2$  and spent-fuel dissolution data used simplified equations based on the Onsager-type thermodynamic function forms of Equations 3.4.2-11 and 3.4.2-12. The data sets consisted of macroscopic measurements of dissolution rates and the controlled, independent variables, temperature, and bulk solution chemistry, which consisted of total carbonate, dissolved oxygen, and hydrogen ion concentrations. Therefore,  $L_{ff}$  was initially represented by a product of solution chemical concentrations  $\times$  an exponential energy term,  $\exp(-Q/RT)$ , to include the temperature dependence. The solid potential energy  $\mu_s$  was represented by a constant and a coefficient  $\times$  the burnup. The liquid or solid chemical potential energy for a concentration  $C_i$ ,  $\mu(C_i)$  was represented by  $\mu_0 + RT\ln(\gamma C_i)$ . The solid-liquid chemical potential energy-change term  $\mu_s - \mu_l$  was the difference of these representations. Thus, the dissolution rate was represented essentially as  $L_{ff}(\mu_s - \mu_l)$ .

Several polynomial variations for the forms of  $L_{ff}$ ,  $\mu_s$ , and  $\mu_l$  were explored. Nonlinear regression analysis was used with these forms. These models all produced substantial differences compared with the measured dissolution rates. Because these models consisted of many products of the polynomial terms from  $L_{ff}(\mu_s - \mu_l)$ , a simple quadratic polynomial was selected as a close approximation of the model. A polynomial is much easier to analyze using multilinear regression. All of the regression fits of these polynomial, Onsager-type models resulted in low correlation coefficients. Furthermore, these dissolution models often predicted negative dissolution rates. For these reasons, only results with the regression analyses with the two Butler-Volmer expressions are provided as representative dissolution rate models over the available data sets.

The test data for dissolution response is best represented by Equation 3.4.2-18, which has the form of the Butler-Volmer equation used in the correlation of corrosion and electrochemical-rate data. The normal derivation of the Butler-Volmer equation assumes that the electrochemical processes are near thermodynamic equilibrium. In the preceding approach, thermodynamic nonequilibrium was assumed for the dissolution process. Also, the functional form to relate the dissolution velocity to the ratio of nonequilibrium configurational entropy was assumed.

Rather than regress on the exponential function in the Butler-Volmer equation, the natural logarithm of the dissolution rate [ $\text{mg}/(\text{m}^2\text{-day})$ ] was used as the fitted response. The chemical and electrochemical potentials of the exponential function of the first Butler-Volmer model were represented as a polynomial in the bulk concentration and burnup variables. Burnup was also represented as a

concentration term because it is proportional to the aggregated production and concentration of fission products. This approach also eliminated the possibility of a model yielding negative dissolution rates. The initial regressions used a full, 21-term quadratic polynomial of 5 variables.<sup>1</sup> A third-order term with burnup, oxygen concentration, and inverse temperature was included to better represent the apparent effects of radiolysis. The equation with the smallest root-mean-square error and largest correlation coefficient ( $r^2 = 0.91$ ) was a 13-term model:

$$\ln(\text{Rate } \text{UO}_2) = a_0 + a_1 \cdot \text{BU} + a_2 \cdot \text{IT} + a_3 \cdot \text{CO3} + a_4 \cdot \text{O2} + a_5 \cdot \text{H} + a_6 \cdot \text{BU} \cdot \text{IT} + a_7 \cdot \text{BU} \cdot \text{O2} + a_8 \cdot \text{BU} \cdot \text{H} + a_9 \cdot \text{CO3} \cdot \text{O2} + a_{10} \cdot \text{CO3}^2 + a_{11} \cdot \text{O2}^2 + a_{12} \cdot \text{BU} \cdot \text{O2} \cdot \text{IT} \quad (\text{A3.4.2-1})$$

with the following:

**Table A3.4.2-1** Coefficients, term descriptions, and regression statistics for 13-term model

Term	Coefficient (a <sub>i</sub> )	Std. Error	T-Value	Significance	Term Description
01	13.848639	1.534127	9.03	0.0001	Regression Constant
1 BU	-0.479226	0.082894	-5.78	0.0001	Burnup (MWd/kg)
2 IT	-4536.815865	480.481755	-9.44	0.0001	Inverse Temperature (K <sup>-1</sup> )
3 CO3	823.431331	132.396019	6.22	0.0001	Total Carbonate Concentration (mol/L)
4 O2	50.158103	12.594141	3.98	0.0004	Oxygen Partial Pressure (atm)
5 H	-1.148737E+08	2.398216E+07	-4.79	0.0001	Hydrogen Ion Concentration (mol/L)
6 BU*IT	147.090980	26.299886	5.59	0.0001	1->2nd Order Interaction
7 BU*O2	1.794648	0.550020	3.28	0.0028	
8 BU*H	6.120887E+06	1.12358E+06	5.45	0.0001	
9 CO3*O2	204.202747	86.865356	2.35	0.0255	
10 CO3**2	-38928.713074	6393.94265	-6.09	0.0001	1->Quadratic
11 O2**2	-206.190757	59.419902	-3.47	0.0016	
12 BU*O2*IT	-614.563609	172.992767	-3.55	0.0013	-->3rd Order Interaction

No. cases = 43    R-sq. = 0.9114    RMS Error = 0.4787  
 Resid. df = 30    R-sq-adj. = 0.8759    Cond. No. = 118.3

This first Butler-Volmer-type model describes some features of the chemical dissolution processes far from thermodynamic equilibrium and provides a reasonably good fit to the available data. However, the model is nonlinear because

<sup>1</sup> The dissolution data used for this regression analysis with the first Butler-Volmer model were the 42 combined flow-through tests of UO<sub>2</sub> and spent fuel (ATM-103) in Table 2.1.3.5-4 of Section 2.1.3.5 plus the one dissolution rate of 7 mg·m<sup>-2</sup>·d<sup>-1</sup> for ATM-105 (burnup of 31 MWd/kgM also reported in that section).

the Butler-Volmer model's energy change term is in the exponent and contains quadratic terms. Depending on the terms and coefficients in the model, extrapolation outside the measured, independent variable space could cause large prediction errors and should be used with caution.

A second Butler-Volmer model also was examined. By substituting the traditional chemical potentials that include a logarithmic dependence on activities or concentrations for the chemical potential changes in equation 3.4.2.2-18, the classic chemical kinetic rate law was derived:

$$\text{Rate} = k[A]^a[B]^b[C]^c \dots \exp(E_a/RT) \quad (\text{A3.4.2-2})$$

Because it is proportional to the aggregated production and concentration of fission products, burnup was also represented as a concentration term. For regression purposes, Eq. A3.4.2-2 was transformed by taking logarithms of each term and fitting that equation. That approach was used here, but allowing interaction and quadratic terms to improve the fit. The resulting model was (note base-10 logarithms)

$$\log_{10}(\text{Rate } \text{UO}_2) = a_2 + a_1 \cdot \text{PCO3} + a_2 \cdot \text{PO2} + a_3 \cdot \text{PH} + a_4 \cdot \text{PO2} \cdot \text{IT} + a_5 \cdot \text{LBU} \cdot \text{IT} + a_6 \cdot \text{LBU} \cdot \text{PCO3} + a_7 \cdot \text{LBU} \cdot \text{PO2} + a_8 \cdot \text{LBU} \cdot \text{PH} + a_9 \cdot \text{IT}^2 + a_{10} \cdot \text{PCO3}^2 \quad (\text{A3.4.2-3})$$

with the coefficients and regression statistics given in Table A3.4.2-2.

A modest refinement of model 3.4.2.20b in Version 1.2 of the *Waste Form Characterization Report* (WFCR V1.2) (see Eq. A3.4.2-3) derives from an extensive analysis of by William O'Connell (Lawrence Livermore National Laboratory memorandum "Regression Fit of the  $\text{UO}_2$  and  $\text{UO}_2$  Spent-Fuel Matrix Dissolution Data for Use in the PA Model," William O'Connell to Ray Stout, LLYMP9805049, July 31, 1997). This refinement was the currently accepted intrinsic dissolution model for total system performance assessment—viability assessment (TSPA-VA) at the time this version of this report was published. This model form includes a linear term of all variables, including the inverse temperature instead of its square and the linear LBU term with minimal loss in the correlation coefficient and adjusted for the number of terms in the equation. The linear portion of the model is equivalent to the classic chemical rate law (Eq. A3.4.2-2). Equation A3.4.2-4 (note base-10 logarithms) represents this current model:

$$\log_{10}(\text{Rate } \text{UO}_2) = a_0 + a_1 \cdot \text{IT} + a_2 \cdot \text{PCO3} + a_3 \cdot \text{PO2} + a_4 \cdot \text{PH} + a_5 \cdot \text{LBU} + a_6 \cdot \text{PO2} \cdot \text{IT} + a_7 \cdot \text{LBU} \cdot \text{IT} + a_8 \cdot \text{LBU} \cdot \text{PCO3} + a_9 \cdot \text{LBU} \cdot \text{PO2} + a_{10} \cdot \text{LBU} \cdot \text{PH} + a_{11} \cdot \text{PCO3}^2 \quad (\text{A3.4.2-4})$$

The coefficients and fitting statistics are in Table A3.4.2-3.

Table A3.4.2-2 Coefficients and regression statistics for Eq. A3.4.2-2

Term	Coefficient (a <sub>i</sub> )	Std. Error	T-Value	Significance	Term Description
01	1.161868	0.803471	1.45	0.1584	Regression Constant
1 PC03	1.547418	0.434866	3.56	0.0010	[-Log10] of Total Carbonate Conc. (mol/L)
2 PO2	-1.672304	0.565034	-2.96	0.0053	[-Log10] of Oxygen Partial Pressure (atm)
3 PH	0.260294	0.053553	4.86	0.0001	[-Log10] of Hydrogen Ion Conc. (mol/L)
4 IT*PO2	384.146973	179.898661	2.14	0.0392	Inverse Temperature (K <sup>-1</sup> ) I->2nd Order Interaction
5 IT*LBU	584.818339	123.912588	4.72	0.0001	[Log10] of Burnup (MWd/kgM) I->2nd Order Interaction
6 PCO3*LBU	0.147972	0.050678	2.92	0.0059	I->2nd Order Interaction
7 PO2*LBU	0.174971	0.056308	3.11	0.0036	I
8 PH*LBU	-0.285106	0.043195	-8.60	0.0001	I
9 IT**2	-3.727218E+05	52092.019943	-7.16	0.0001	I->Quadratic
10 PCO3**2	-0.345209	0.080324	-4.30	0.0001	I

No. cases = 49  
Resid. df = 38

R-sq. = 0.8649  
R-sq-adj. = 0.8293

RMS Error = 0.2309  
Cond. No. = 147.9

Table A3.4.2-3 Coefficients and fitting statistics for Eq. A3.4.2-4

Term	Coefficient (a)	Std. Error	T-Value	Significance	Term Description
01	5.299561	1.321560	4.01	0.0003	Regression Constant
1 IT	-2441.512949	352.342615	-6.93	0.0001	Inverse Temperature (K <sup>-1</sup> )
2 PCO3	1.588315	0.437626	3.63	0.0010	[-Log10] of Total Carbonate Conc. (mol/L)
3 PO2	-1.649281	0.567653	-2.91	0.0053	[-Log10] of Oxygen Partial Pressure (atm)
4 PH	0.237613	0.058783	4.04	0.0001	[-Log10] of Hydrogen Ion Conc. (mol/L)
5 LBU	-0.756673	0.808096	-0.94	0.3552	[+Log10] of Burnup (MWd/kgM)
6 IT*PO2	377.413900	180.831077	2.09	0.0438	
7 IT*LBU	731.867389	202.871969	3.61	0.0009	
8 PCO3*LBU	0.157908	0.052016	3.04	0.0044	I->2nd Order Interactions
9 PO2*LBU	0.172391	0.056724	3.04	0.0043	I
10 PH*LBU	-0.255023	0.053269	-4.79	0.0001	I
11 PCO3**2	-0.354358	0.080776	-4.39	0.0001	I->Quadratic

No. cases = 49    R-sq. = 0.8668    RMS Error = 0.2323  
 Resid. df = 37    R-sq-adj. = 0.8272    Cond. No. = 193.5

The simple form of the rate law corresponding to Eq. 3.4.2.2-22 and Eq. 3.4.2.2-23 and to Eq. A3.4.2-2 in this appendix is:

$$\text{Rate (mg/(m}^2\text{-day))} = 7.269 \cdot 10^4 \cdot [\text{O}_2]^{0.38} \cdot [\text{CO}_3]^{0.16} \cdot [\text{H}]^{-0.04} \cdot [\text{BU}]^{-0.13} \cdot \exp(-5382/\text{RT})$$

$$R^2 = 0.61 \quad (\text{A3.4.2-5})$$

The combined effects of spent-fuel burnup with the water chemistry variables is clear from a comparison of the R-squares of Eq. A3.4.2-4 and Eq. A3.4.2-5. The interaction of temperature and oxygen concentration may be caused by radiolysis. The quadratic carbonate term may result from surface coverage effects of carbonate species.

#### A.3.4.2.2 Proposed Model from Expert Elicitation

During the first series of expert-panel-elicitation meetings, an alternative spent-fuel intrinsic-dissolution model was proposed (Geomatrix, 1998). The proposed model was

$$\text{Rate} = k \cdot [\text{O}_2]^{0.7} \cdot [\text{CO}_3]^{0.45} \cdot \exp(-Q/\text{RT}) \quad (\text{A3.4.2-6})$$

The exponents of the oxygen and carbonate concentrations were fixed and based on a compilation (Tait, 1997) of single variable experiments by authors at several laboratories. Spent fuel and  $UO_2$  were considered to have similar dissolution rates (i.e., burnup is not a factor).

This model was fit to the same 49 data points given in Tables 2.1.3.5-4 and 2.1.3.5-4a and used in the earlier models discussed Section A.3.4.2.1 of this appendix. The results are

$$\text{Rate (mg/(m}^2\cdot\text{day))} = 4.3172 \cdot 10^6 \cdot [O_2]^{0.7} \cdot [CO_3]^{0.45} \cdot \exp(-5760.9/RT) \quad R^2 = 0.23 \quad (\text{A3.4.2-7})$$

This is a poor result, and the correlation coefficient is very similar to using only the most significant variable, temperature, in the fit

$$\text{Rate (mg/(m}^2\cdot\text{day))} = 2.0497 \cdot 10^4 \cdot \exp(-5541.3/RT) \quad R^2 = 0.24 \quad (\text{A3.4.2-8})$$

By determining the coefficient and exponents directly from a regression fit of the data with the same terms as in equation A3.4.2-6, the following equation was obtained:

$$\text{Rate (mg/(m}^2\cdot\text{day))} = 1.928 \cdot 10^5 \cdot [O_2]^{0.35} \cdot [CO_3]^{0.15} \cdot \exp(-5627/RT) \quad R^2 = 0.57, \quad (\text{A3.4.2-9})$$

which provides a much better fit but significantly different exponents on the oxygen and carbonate terms. The R-square of Eq. A3.4.2-9 is only slightly less than the full simple-rate law in Eq. A3.4.2-5 because of the small effect of pH and the fact that burnup exhibits its importance in the interaction or cross-terms.

#### A.3.4.2.3 References

Geomatrix Consultants, Inc. (1998). *Waste Form Degradation and Radionuclide Mobilization Expert Elicitation Project*. K. J. Coppersmith and R.C. Perlman (Eds.) San Francisco, CA: produced under DE-AC O8-91RW00134 for U. S. Department of Energy.

Tait, J. C., and J. L. Luht (1997). *Dissolution Rates of Uranium from Unirradiated  $UO_2$  and Uranium and Radionuclides from Used CANDU Fuel Using the Single-Pass Flow-Through Apparatus*. (06819-REP-01200-0006 R00) Atomic Energy of Canada, Limited, Whiteshell Laboratories, and Ontario Hydro.

## Section 3.5.1 Contents

3.5.1	Experimental Parameters for Glass Dissolution.....	3.5.1-1
3.5.1.1	Introduction .....	3.5.1-1
3.5.1.2	Rate Equation for Simplified Glass-Dissolution Model .....	3.5.1-1
3.5.1.3	Parameters for Simplified Glass Dissolution Model.....	3.5.1-2
3.5.1.4	Example Calculation.....	3.5.1-7
3.5.1.5	Limitations of the Simplified Model .....	3.5.1-8
3.5.1.6	Incorporation of Simplified Glass Model into Performance Assessment Models.....	3.5.1-8
3.5.1.6.1	Silica Distribution Between Alteration Phases and Solution....	3.5.1-9
3.5.1.6.2	pH versus Extent of Reaction.....	3.5.1-10
3.5.1.6.3	Estimate of Long-Term Reaction Rate.....	3.5.1-12
3.5.1.6.4	Glass Release from a Waste Package.....	3.5.1-15
3.5.1.6.5	Flow-Through Mode.....	3.5.1-16
3.5.1.6.6	Bathtub Mode .....	3.5.1-18
3.5.1.7	Solubility-Limited Radionuclide Release from Glass .....	3.5.1-20
3.5.1.8	Comparison With Laboratory Results .....	3.5.1-26
3.5.1.9	Effect of Dissolved Iron on Borosilicate Glass Dissolution.....	3.5.1-27
3.5.1.9.1	Introduction .....	3.5.1-27
3.5.1.9.2	Experimental Methods.....	3.5.1-29
3.5.1.9.3	Results and Discussion.....	3.5.1-29
3.5.1.10	References.....	3.5.1-31

## **Section 3.5.1: Experimental Parameters for Glass Dissolution**

**Version 1.3  
June 23, 1998**

### **3.5.1.1 Introduction**

The goal of the Yucca Mountain Site Characterization Project (YMP) glass task has been to develop a mechanistic model that predicts an alteration/dissolution rate for a glass under localized conditions (i.e., for any spot on the glass, a packet of water with some composition and temperature will cause the glass to react at some rate and to produce some set of alteration products). Integration of this localized process would provide the overall behavior of the glass waste form on a repository scale. For the glass-reaction model, parameters such as surface area/volume (SA/V) ratio and  $f$  (fraction of Si in precipitates discussed subsequently) are not input parameters but derived parameters based on the fundamental mechanisms incorporated in the model. However, this amount of detail will not be appropriate for YMP performance assessment (PA) models. Simplification of the model is necessary for it to be interfaced into present PA codes. The simplified model described here is meant to be a first step in making this connection.

The topic of this section is experimental parameters; however, to provide a context in which to place the parameters, this section also includes a succinct summary of the fundamental rate equations in the model. With this discussion, the proper use and the effective limitations of the present model and model parameters can be understood.

### **3.5.1.2 Rate Equation for Simplified Glass-Dissolution Model**

Because the glass-alteration rate changes as the solution composition changes, it is necessary to closely couple the evolving solution composition with glass dissolution. The rate of glass dissolution depends on the concentrations of all the elements in solution that are present in the surface gel layer of the dissolving glass and on the solution pH. However, some simplifications can be made. Experimental and modeling work on borosilicate glass to date show that the two most important solution compositional parameters to be considered for predicting radionuclide release rates from glass are pH and dissolved silica concentration (temperature and reactive glass surface area must also be known). Thus, the feedback of solution composition to glass dissolution rate can be restricted by regressing experimental rate data of these two parameters. Following are the equations and parameters needed to calculate conservative release rates of radionuclides from glass with this simplified model. Also included are suggestions on further simplifying the model to make it appropriate for input into a first-cut, comprehensive PA model of a repository.

Long-term dissolution models for borosilicate glass employ a rate equation consistent with transition state theory. A simplified rate equation is given as

$$R = s k \left[ 1 - \left( \frac{Q}{K} \right)^\sigma \right] + s r_l \quad (3.5.1-1)$$

where

R = alteration rate of glass (g/yr)

s = surface area of reactive glass (m<sup>2</sup>)

k = glass surface alteration rate constant (g/m<sup>2</sup>/yr), a function of temperature and pH of the solution

Q = concentration of dissolved silica (g/m<sup>3</sup> water)

K = solubility constant for borosilicate glass; here it equals the solubility of amorphous silica (g/m<sup>3</sup> water)

σ = experimentally determined constant

r<sub>l</sub> = long-term dissolution rate (under "silica saturated" conditions in units of g/m<sup>2</sup>/yr)

To calculate radionuclide release rates from glass, each of these parameters must be known or estimated. At present, the value of σ is not well determined, based on the available experimental data. The value of σ is therefore set to one in this model. Suggested values for each of the other parameters are discussed in subsequent text.

### 3.5.1.3 Parameters for Simplified Glass Dissolution Model

#### Surface Area, s

As the molten glass cools in the melter, it undergoes fracturing. Estimates for the increase in glass surface area due to fracturing range from 2 to 100 times the uncracked surface area. A reasonable average value to use for the extent of fracturing is 25 (Baxter, 1983). The initial total glass surface area per waste package A<sub>o</sub> comprises a nominal area per glass log, the number of glass logs per package n and a cracking factor, which is a multiplier on the nominal area (≥1, typically around 25).

$$A_o = 25 \cdot n \cdot 2\pi r_o^2 \left( 1 + \frac{L_o}{r_o} \right) \quad (3.5.1-2)$$

where

- $A_o =$  total glass surface area ( $m^2$ )
- $r_o =$  radius of the glass log
- $L_o =$  length of the glass log
- $n =$  number of glass logs per waste package

The glass log is assumed to be the same cylindrical shape with a constant length to radius ratio  $L_o/r_o$  during the dissolution process. Assuming the glass retains a constant density throughout alteration, then

$$A_1 = A_o \left( \frac{M_1}{M_o} \right)^{\frac{2}{3}} \quad (3.5.1-3)$$

where

- $A_1 =$  surface area after dissolution,  $m^2$
- $A_o =$  initial surface area,  $m^2$
- $M_1 =$  glass mass after dissolution, kg
- $M_o =$  initial glass mass, kg

In the bathtub-water-contact mode, the total surface area of the glass log is in contact with water when the container is filled. For the flow-through mode, only a fraction of surface contacts water. The wetted area depends on the groundwater flow rate. It is assumed the wetted area remains the same for a given water influx  $q$  until the total glass surface area decreases to less than the initial wetted area because of glass dissolution. Then the wetted area equals the total area until the glass completely dissolved.

*Rate Constant, k*

The rate constant  $k$  has been measured over a range of pH and temperature conditions. Table 3.5.1-1 and Figure 3.5.1-1 show the values of  $k$  in units of  $g/m^2/day$  from flow-through experiments by Knauss et al. (1990) for an analog, SRL-165 glass composition. The data are plotted in Figure 3.5.1-1, and the following regression relations are obtained:

$$k = 365 \times 10^m (g/m^2/yr) \quad (3.5.1-4a)$$

where  $m$  is the higher value of the following two equations:

$$m = 8.632 - \frac{2600}{T + 273} - 0.65pH \quad (3.5.1-4b)$$

$$m = 7.268 - \frac{4550}{T + 273} + 0.50pH \quad (3.5.1-4c)$$

and where  $T$  = solution temperature ( $^{\circ}\text{C}$ ).

**Table 3.5.1-1**  $\text{Log}_{10}$  glass dissolution rate in  $\text{g}/\text{m}^2/\text{day}$   
(from Knauss et al., 1990)

pH	T = 25°C	T = 50°C	T = 70°C
1	-1.25	0.02	0.51
2	-1.73	-0.68	-0.18
3	-2.21	-1.38	-0.87
4	-2.69	-2.08	-1.56
5	-3.17	-2.78	-2.25
6	—	—	-2.94
7	-4.53	-3.43	-2.30
8	-4.02	-2.92	-1.90
9	-3.51	-2.41	-1.50
10	-3.00	-1.90	-1.10
12	-1.98	-0.88	-0.30

#### *Solution Chemistry, Q and K*

The major effect of groundwater chemistry on the glass-dissolution rate (other than pH) is the concentration of dissolved silica. In this simple model,  $Q$  equals the concentration of dissolved silica in the water contacting the glass. The chemistry of the groundwater in the vicinity of the potential repository will likely be dominated by the host rocks (Wilder, 1997); the silica concentration is therefore expected to be close to cristobalite saturation at the ambient temperature. Cristobalite is a common constituent of the host rocks at Yucca Mountain. Table 3.5.1-2 lists concentrations of silica in equilibrium with cristobalite at temperatures from 0 to 150°C from the thermodynamic database SUPCRT92 (Johnson et al., 1992)

" $K$ " in Eq. 3.5.1-1 for the waste glass is assumed equal to the equilibrium constant for amorphous silica in this simple model.  $K$  actually varies as a function of glass composition; for most waste glass compositions, the experimentally determined value of  $K$  is of the same general magnitude but less than the value of  $K$  for amorphous silica.

This simplification therefore gives conservative estimates. Table 3.5.1-2 lists values of  $\log_{10} K$  (in molality) for temperatures from 0 to 150°C. As an example, at 60°C,  $Q/K = 10^{-3.02}/10^{-2.43} = 0.26$ . The term  $(1-Q/K) = (1-0.26)$  or 0.74. Thus, the glass reaction rate is about 74% of the rate under silica-free conditions.

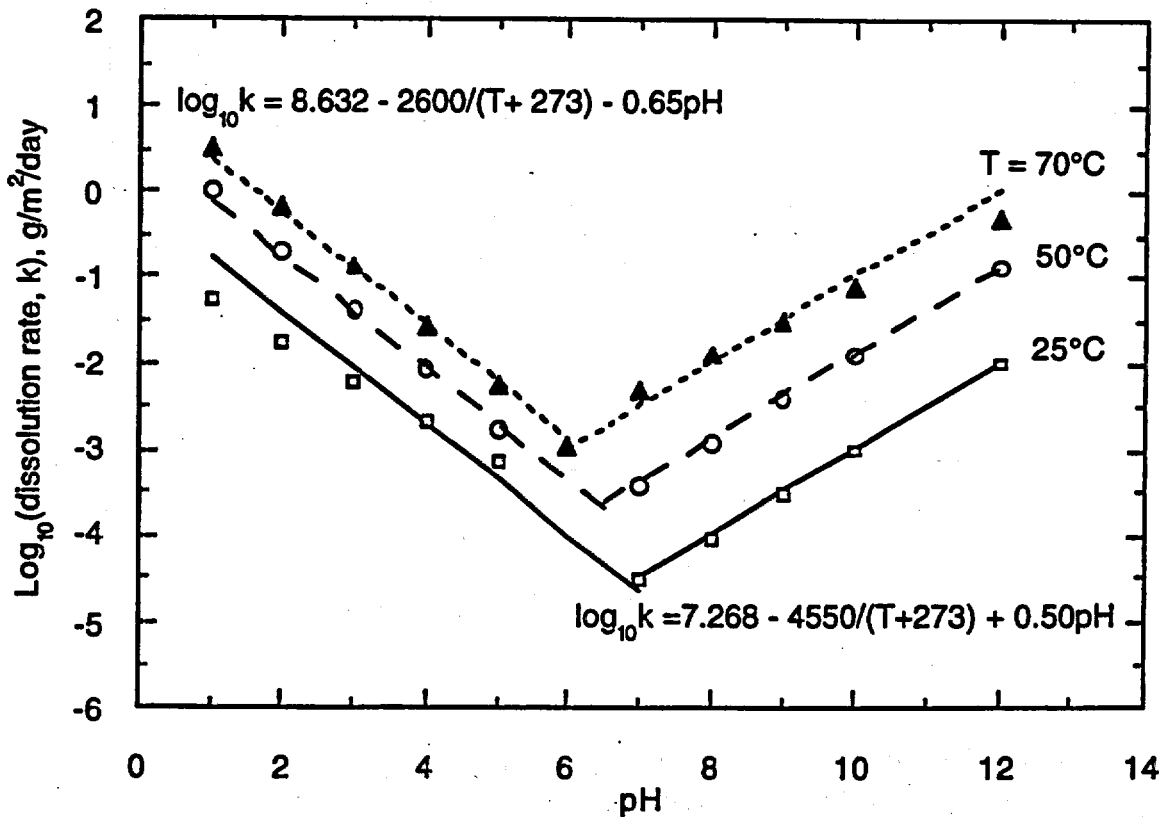


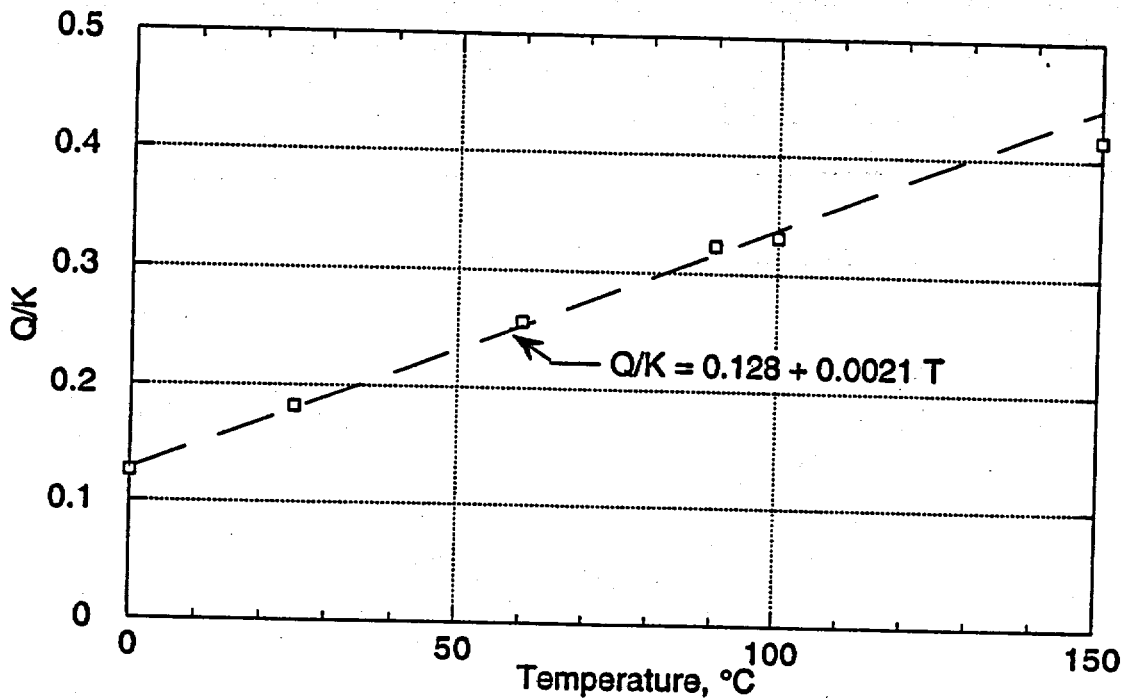
Figure 3.5.1-1  $\log_{10}$  (dissolution rate,  $g/m^2/day$ ) versus solution pH from Knauss et al. (1990).

Figure 3.5.1-2 shows the relation between  $Q/K$  and temperature. For a temperature between 0 and 100°C, the relation can be expressed as:

$$\frac{Q}{K} = 0.128 + 0.0021T \quad (3.5.1-5)$$

Table 3.5.1-2 Cristobalite and amorphous silica solubilities (from Johnson et al., 1992) ( $\log_{10}$  [molality])

T°C =	0	25	60	90	100	150
Cristobalite	-3.89	-3.45	-3.02	-2.75	-2.68	-2.36
Amorphous Silica	-2.99	-2.71	-2.43	-2.26	-2.20	-1.98



**Figure 3.5.1-2** Relation between Q/K and temperature

*Solution pH*

Experimental studies of tuff-water interactions have shown that reacted J-13 water maintains a pH slightly higher than neutral (Knauss et al., 1987). For anticipated repository conditions, a slightly alkaline pH of about 8 is recommended as a substitute for the lack of a more rigorous calculation of groundwater chemistry. This pH value should be used to estimate rate constants for glass dissolution from Table 3.5.1-1 (it should also be consistent with any data for solubility-limited radionuclide concentrations that are also highly dependent on pH). Note, however, that glass-dissolution rates and radionuclide-release rates are very sensitive to pH, and nothing more than a qualitative estimate of release rates is possible without a more rigorous treatment of solution chemistry in the repository performance assessment model.

*Temperature Dependence of Glass Dissolution Rate*

Experiments have shown that glass-dissolution rates follow the Arrhenius relation  $\text{rate} \propto e^{-E/RT}$ , where R is the gas constant, T is temperature (Kelvin) and the activation energy (E) is about 20 kcal/mole. This corresponds roughly to dissolution rate increasing by a factor of 2 for a 10° rise in temperature. This simple rule can be used to describe the effect of temperature on glass-dissolution rate if the data in Table 3.5.1-1 cannot be explicitly used.

## Radionuclide Content of Glass

Table 3.5.1-3 lists anticipated radionuclide contents for SRL glasses. More information on glass compositions is provided in Section 2.2.1 of this report. Conservative estimates for release rates for radionuclides from the glass waste form are given by multiplying the glass-dissolution rate (R) by the weight fraction of radionuclide in the glass from Table 3.5.1-3.

**Table 3.5.1-3 Radioisotope content per high-level waste (HLW) container for borosilicate glass from the Savannah River Site (from Table 6.14 of Version 1.2 of the Waste Form Characteristics Report)**

Isotope	g/canister	Isotope	g/canister
U-234	.549e1	Tc-99	.182e3
U-235	.727e2	Pd-107	.286e2
U-236	.174e2	Sn-126	.156e2
U-238	.312e5	Cs-135	.863e2
Np-237	.126e2	Cs-137	.499e3
Pu-238	.867e2	Ce-143	.401e3
Pu-239	.208e3	Ce-144	.309e1
Pu-240	.381e2	Nd-144	.411e3
Pu-241	.162e2	Pm-147	.261e2
Pu-242	.321e1	Sm-147	.877e2
Am-241	.321e1	Sm-148	.192e2
Cm-244	.132e1	Sm-149	.742e1
Se-79	.243e1	Sm-151	.941e1
Rb-87	.996e1	Eu-154	.229e1
Sr-90	.343e3	Eu-155	.102e1
Zr-93	.444e3		

Contents in grams of each isotope  
 Mass of glass in each canister is 1682 kilograms.  
 Only elements with more than 1 gram per canister are reported here.

### 3.5.1.4 Example Calculation

What is the rate of release of  $^{235}\text{U}$  from one canister of glass at  $70^\circ\text{C}$  in cristobalite-saturated groundwater of  $\text{pH} = 8$ ? The rate constant for glass dissolution at  $70^\circ\text{C}$  and  $\text{pH} = 8$  is  $10^{-19} \text{ g/m}^2/\text{day}$ . The affinity term  $(1-Q/K)$  has a value of  $(1-10^{-293}/10^{-237})$  or 0.72. The bulk dissolution rate of glass is therefore  $0.0091 \text{ g/m}^2/\text{day}$ . Surface area for one canister is  $125 \text{ m}^2$ ; thus, the total rate of glass dissolution is  $1.13 \text{ g/day/canister}$ . Predicted  $^{235}\text{U}$  content of SRL waste glass is  $72.78 \text{ g/canister}$ . Total weight of glass in a canister is  $1682 \text{ kg}$ ; thus, the weight fraction of  $^{235}\text{U}$  is  $4.3 \times 10^{-5}$ . Release rate of  $^{235}\text{U}$  is therefore  $1.13 \times 4.3 \times 10^{-5} = 4.89 \times 10^{-5} \text{ g/day}$  or  $.018 \text{ g/year}$ .

Further simplification of the model can be achieved by the following:

- Assume constant pH of 8 and cristobalite saturation of the groundwater.
- Use Table 3.5.1-1 to provide the rate constant as a function of temperature at pH = 8.
- Use Table 3.5.1-2 to provide the factor that accounts for the lowering of glass-dissolution rate due to dissolved silica. (This provides a simple function of glass-dissolution rate with temperature and no other variables need to be considered.)

### 3.5.1.5 Limitations of the Simplified Model

This simplified treatment of estimating glass-dissolution rates provides conservative estimates for release rates of radionuclides. It ignores solubility limits of some radioactive species (such as the actinides) and instead uses the conservative assumption that the radionuclides will be released no faster than the breakdown of the glass structure. This is consistent with the measured rates of diffusion of actinides in the glass, which are negligible under repository temperatures. Experiments have shown that, during glass corrosion, the actinides are commonly included in alteration phases at the surface of the glass either as minor components of other phases or as phases made up predominantly of actinides. No credit for this process is taken in this simple glass-dissolution model. To perform accurate estimates of solubility-limited release rates, one needs detailed information on water chemistry (e.g., pH, Eh), which demands a much more complex PA model that explicitly accounts for coupled chemical interactions among all the repository materials (e.g., spent fuel, glass, metals).

This simple model also ignores all solution chemistry other than pH and silica concentration of the leachate. It is known from a variety of experiments that species such as dissolved Mg and Fe can change glass-dissolution rates by as many as several orders of magnitude. Mg decreases the rate; Fe increases the rate. Effects such as these are not accounted for in this model. Because these effects have not yet been quantified, it is currently impossible to include them in PA models of any level of complexity.

Also ignored is vapor-phase alteration of the glass. If a canister containing glass is breached, and humid air reaches the glass, the glass will react and form a thick alteration rind composed of hydrated glass and secondary phases. The durability of this material with respect to later contact with liquid water may be much greater or much less than the durability of unaltered glass. This effect is not accounted for here.

### 3.5.1.6 Incorporation of Simplified Glass Model into Performance Assessment Models

Much of the information presented in this section was developed by O'Connell et al. (1997). That document includes a more complete derivation of the equations used to predict borosilicate glass dissolution in the performance assessment code.

Three more pieces of information are needed to incorporate a simple glass-dissolution model into the current PA model:

1. A functional relation between the amount of silica released into solution and the amount that remains in solid alteration phases and layers
2. A functional relation between the pH and the amount of glass dissolved
3. Estimates of long-term rates determined from experimental data

This information is necessary to apply the glass model to the range of hydrologic conditions, from bathtub to flow-through mode, using a single model. The fraction of silica released to solution is needed to compute the silica concentration in the evolving leachate. The pH is needed to compute the reaction-rate constant for the glass during reaction progress.

#### 3.5.1.6.1 Silica Distribution Between Alteration Phases and Solution

The relation between the amount of silica released to solution and the amount tied up in secondary phases depends on the composition of the glass, the temperature, the pH, the composition of the starting solution, and probably other factors.

As the glass dissolves, secondary phases begin to precipitate. The types of phases that form depend on the glass composition. These phases lower the concentration of dissolved silica. The exact phases that will precipitate for a given glass in a given fluid composition cannot presently be predicted. Data from experiments is used to identify the phases.

In spite of these complexities, it is generally true that, given enough time, the solution in any closed-system test approaches the condition in which the amount of silica released from the glass equals the amount taken up in alteration phases. This is referred to as the "silica-saturated" or "long-term" dissolution rate. This is the slowest rate at which glasses are known to react. Because high SA/V test conditions act to accelerate the test, high SA/V conditions generally show behavior where "f" (the ratio of total released silica in the alteration phases to silica in solution) approaches one (silica is almost entirely in the alteration phases). Under these conditions, the PA model should predict that the glass will react at the long-term rate (see discussion of long-term rates in Section 3.5.1.6.3).

The plot in Figure 3.5.1-3 (from Delage et al., 1992) shows the silica fraction trapped in alteration layers versus silica concentration in solution. The relation is one that shows an increasing fraction of silica trapped in the alteration layer with increasing SA/V ratio. In terms of the extent of reaction, this is consistent with the higher SA/V tests being more advanced and, therefore, having both higher silica concentrations in solution and higher values of "f" as the tests approach silica saturation. Unfortunately, the test conditions and raw data from which this plot was made were not provided in Delage et al., so no more interpretation is possible.

The simple linear trend reported in the paper by Delage et al. should not be overinterpreted. The tests are for a very restricted range of experimental conditions, in distilled water, and over a very narrow range of SA/V conditions. This simple trend cannot be reliably extrapolated to more complex conditions where fluid composition depends on materials other than glass, and the history of glass reaction is not known because most of the initial pH increase is due to ion exchange of the outermost few microns of glass surface. After this zone is depleted of alkali, there will be a reduction in the rate of pH increase. In a repository with variable hydrologic regimes, evolving input fluid composition, variable temperature, and other more complex conditions, a simple linear trend between Si concentration in solution and "f" is not expected.

Some data on the value of "f" for Savannah River glasses are available. For example, data for the SRL-202 glass based on closed system tests at SA/V ratios of 10, 2000, and 20,000 m<sup>-1</sup> give "f" values of 0.42, 0.54, and 0.98, respectively, after about 1 to 2 yr reaction. SRL-202 is currently the target glass composition to be produced by the defense waste-processing facility (DWPF).

Based on the preceding discussion, it is recommended that the current PA model use a simple relationship between SA/V and "f" for the SRL-202 glass using the data in the preceding paragraph (or Figure 3.5.1-3). However, the numerous conditions and limitations discussed indicate that, although the relation provides what is a correct trend, the absolute magnitude of the value of "f" at a particular value of SA/V is only an estimate. This is perhaps an adequate approximation for this initial glass-dissolution model. If the application is limited to an SRL-202 glass at near-neutral to weakly alkaline pHs, the results are probably correct in a semi-quantitative sense. More experimental work and analysis of existing data are needed to better define whether any simple relation exists between SA/V and "f."

#### 3.5.1.6.2 pH versus Extent of Reaction

As glasses dissolve in closed-system tests, the pH of the leachant solution increases because of two effects:

1. Ion exchange between cations in the glass and H<sup>+</sup> in solution
2. Bulk glass dissolution

Precipitation of secondary phases tends to lower the pH. For most glasses, a near-neutral, unbuffered pH solution will quickly rise to pHs of between 9 and 11, depending on the alkali content of the glass (Na, Li, K) and the SA/V ratio of the test. The higher the SA/V ratio, the higher the pH. The pH of the leachant quickly reaches a limiting (steady state) and nearly constant value. For tests at approximately 100°C, this plateau is reached in a few days to a few weeks.

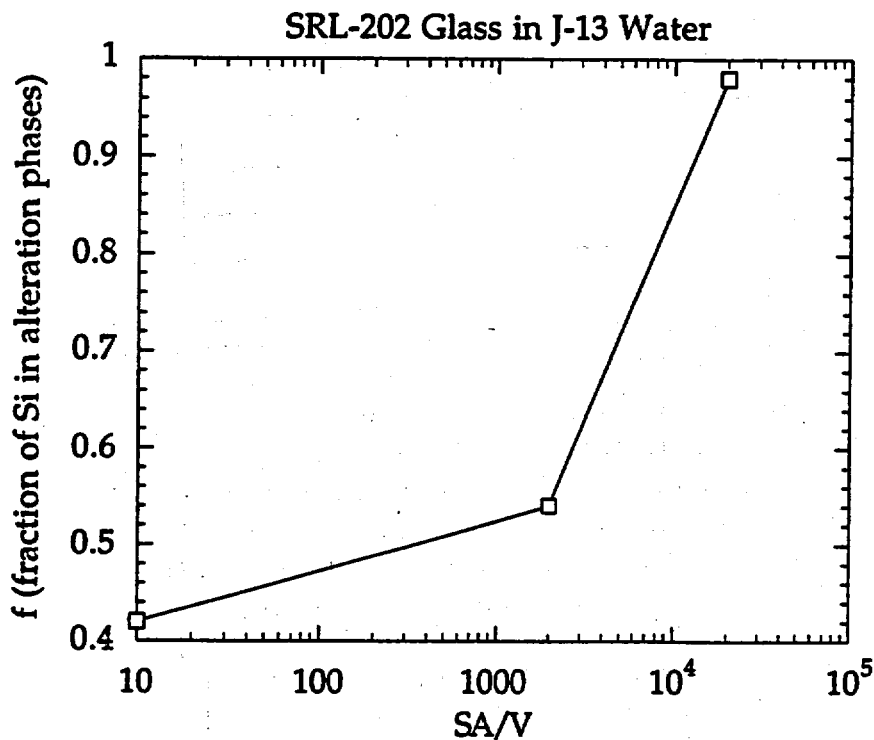


**Figure 3.5.1-3** Experimental data for fraction of silica released from glass that is incorporated into alteration layer, as a function of SA/V ratio of the test

This pH effect is not important in flow-through tests. The very low effective SA/V ratios of these tests cause the ion-exchange effect to be much less effective in modifying the solution pH.

An additional factor to be considered is that the solution entering the glass canister will have some initial pH and pH-buffering capacity that will be greater than the buffering capacity of the distilled water used in most of the test results. This buffer capacity will oppose pH changes because of glass dissolution and ion exchange. The change in pH will be a complex function of the flow rate, buffer capacity of the fluid, and alkali content of the glass; there is also no simple relation obvious from test results.

The dominant effect in this complex situation will most likely be the ion-exchange capacity of the glass. If one assumes the other factors are negligible, the pH that the solution will reach can be interpreted as a simple function of SA/V ratio. At high SA/V, the pH will increase to some higher constant value; at low SA/V (below about  $0.01\text{m}^{-3}$ ), the pH will not change at all.

It is impossible to consider all these effects in the current PA model. Therefore, the following simplified approach is recommended. Data for the steady-state pH for closed system tests of SRL-202 glass at  $90^{\circ}\text{C}$  are as shown in Table 3.5.1-4 (see also Figure 3.5.1-4).

**Table 3.5.1-4 Steady state pH vs. SA/V ratio of test**

Surface-Area-to-Volume Ratio (m <sup>-1</sup> )	Steady-State pH
10	9.0
2000	10.5
20,000	12.0

For bathtub-type hydrologic scenarios, a reasonable value for the solution pH can be estimated directly from the relation between pH and SA/V in Table 3.5.1-4. For flow-through and intermediate hydrologic scenarios, the situation is more difficult because the ion-exchange process, which is the dominant mechanism causing the pH to rise, takes place early in the glass-water reaction. The initial packets of reacting fluids will carry away the alkalis as high pH solutions. Later fluids will contact alkali-depleted glass, which will not have nearly as great an effect on the pH of the solution. Again, because a rigorous analysis is not possible in the PA code (although it is currently something that can be done in the glass submodel), the extension of the SA/V vs. pH relationship to the extreme end member of essentially SA/V=0 for flow-through conditions, where the pH will be equal to the initial pH, is recommended. A curve regressed to these data will provide a reasonable value of the pH of the reacting fluid for any given effective SA/V ratio of the system.

#### **3.5.1.6.3 Estimate of Long-Term Reaction Rate**

Experimental data show that, even when the solution is saturated with silica after a long period of time, there is still a long-term dissolution rate for several glass compositions. Because a mechanistic model does not exist that can predict the variation of the long-term rates with environmental parameters, an averaged experimental value must be used.

Table 3.5.1-5 lists measured long-term (silica saturation) dissolution rates for several glass compositions. The SRL-202 glass is the current, most likely composition for glasses to be produced at DWPF and should be used for estimating glass behavior at the YMP site. Based on the data in this table, a value of 0.002 g glass/m<sup>2</sup>/day for the long-term (silica saturated) rate for SRL-202 glass is recommended for a temperature of 30°C.

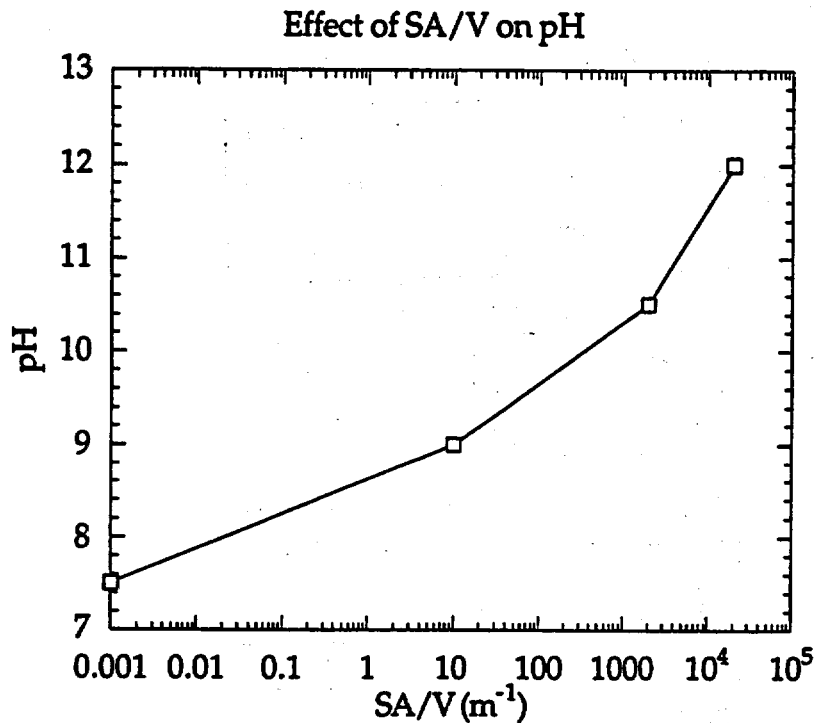


**Figure 3.5.1-4 Steady state pH vs. SA/V ratio of test**

For other temperatures, the same temperature-dependency relation for the long-term rate is assumed for the saturation rate. That is,

$$k_{long} \cong 2.5 \times 10^5 \text{ g/m}^2/\text{yr} \quad (3.5.1-6a)$$

$$\delta = 12 - \frac{4550}{T + 273} \quad (3.5.1-6b)$$

Note that here,  $k_{long}$  is identical to  $r_1$  in Eq. 3.5.1-1. More experimental data are needed to improve these numbers.

Clearly, a simplified model of glass dissolution will have numerous conditions and limitations that will make it unable to predict accurate behavior outside a clearly defined and restricted set of conditions. A single mechanistic model that covers the range of hydrologic conditions, from flow-through to bathtub-type scenarios, does not currently exist. However, by making several simplifying assumptions, a simple model based on mechanistic glass-dissolution reaction has been developed and can be used to predict closed-system (bathtub) type conditions and flow-through test conditions with some ability to model hydrologic conditions between those two end-member scenarios.

**Table 3.5.1-5 Forward and saturation rates for HLW glasses**

Glass/Leachant	SAV (m <sup>-1</sup> )	Forward Rate	Saturation Rate	Reference
<b>Static Tests</b>				
PNL 76-68/DIW	2,000	1.6	0.08 <sup>a</sup>	A
SRL 165/DIW	2,000	0.80	0.024 <sup>a</sup>	A
EMS-11/DIW	2,000	0.083	0.0016 <sup>a</sup>	A
JSS-A/DIW	10 <sup>b</sup>	1.5	0.0025	B
PNL 76-68/DIW	10 <sup>b</sup>	1.8	0.0075	B
SRL 131/DIW	10 <sup>b</sup>	3.0	0.033	B
SRL 131/J-13 <sup>c</sup>	10	0.14	—	C
SRL 131/J-13	2,000	0.24	0.021	C
SRL 131/J-13	20,000	0.84	0.053	C
SRL 202/J-13	10	0.10		C
SRL 202/J-13	2,000	0.025	0.0016	C
SRL 202/J-13	20,000	0.04	0.0025	C
R7T7/DIW	5	4.9 (100°C)	—	D
R7T7/DIW	50		0.0083	E
R7T7/Volvic <sup>d</sup>	50		0.0133	E
R7T7/DIW	400		0.0045	E
R7T7/Volvic	400		0.025	E
R7T7/Volvic	2,000		0.0006	E
R7T7/Volvic	8,000		0.0006	E
R7T7/Volvic	20,000		<0.0001	E
MW/DIW	1,320	1.1	0.01	F
<b>Dynamic Tests</b>				
SRL 202/pH 7 Buffer		0.28 (80°C)		G
SRL 165 <sup>e</sup> /pH 10.5 Buffer		0.05 <sup>a</sup>		H
SRL 165 <sup>e</sup> /pH 10 Buffer		0.08 (70°C)		I
R7T7/DIW		1.03		J
SRL 131/DIW		2.5		K

<sup>a</sup> Estimated

<sup>b</sup> Values determined from results of both static and dynamic tests

<sup>c</sup> Tuff groundwater: major components are Si(45), Na(55), HCO<sub>3</sub>-(120) in ppm

<sup>d</sup> Granite groundwater: major components are Si(11), Ca(9.8), Na(9.2) HCO<sub>3</sub>-(66) in ppm.

<sup>e</sup> Analog glass without iron

See Cunnane (1993), Volume 2, page 75, for references.

### 3.5.1.6.4 Glass Release from a Waste Package

Adapting data from batch and flow-through tests, two water-contact modes (flow-through and bathtub) are modeled here. In the flow-through mode, as shown in Fig. 3.5.1-5, it is assumed that the water is flowing down the side of a waste glass log without mixing, and keeping a surface area ( $s$ ) wet. In the bathtub mode, the waste package develops a breach, and water flows in and fills up over time, eventually overflowing, as illustrated in Fig. 3.5.1-6. The water inside the container is assumed to be well mixed.

The units used in the PA model are meters, grams, years, and degrees Celsius ( $^{\circ}\text{C}$ ).

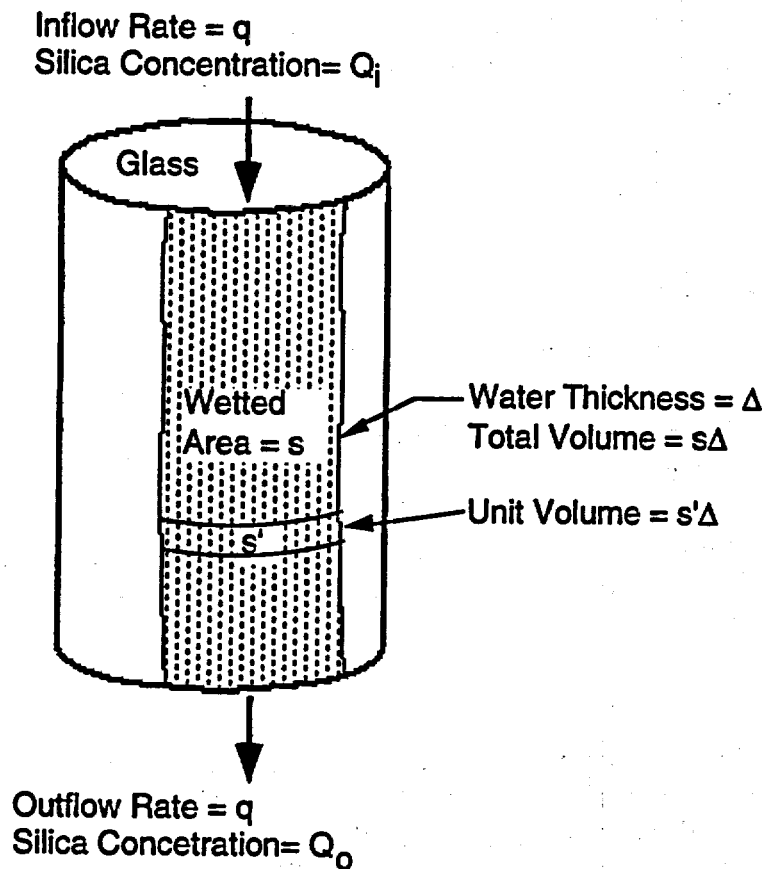


Figure 3.5.1-5 Flow-through water-contact mode

Eq. 3.5.1-1 predicts that the dissolution rate will slow down as the dissolution adds to the silica in solution. Silica ( $\text{SiO}_2$ ) is one of the components of glass waste. For example, the DWPF glass contains about 50 wt% of silica (Cunnane, 1993). After water flows inside the waste package, the change of silica concentration in the solution comes from the dissolution of silica released from the glass during alteration process. As the glass dissolves, secondary phases begin to precipitate. A fraction of the silica  $f_p$  contained in the glass will be trapped in the secondary phases—i.e., only  $(1 - f_p)$  of silica

in altered glass actually dissolves in the solution. The value of  $f_p$  increases with increasing SA/V ratio and silica concentration in solution. Because there is not sufficient data for consideration of the change of  $f_p$ , a constant intermediate value of  $f_p$  is assumed in this model.

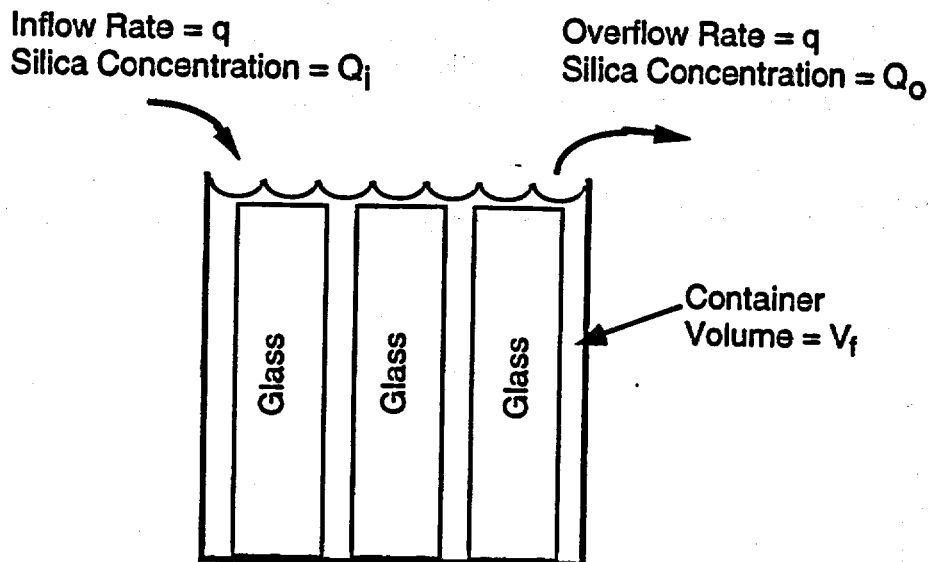


Figure 3.5.1-6 Bathtub water-contact mode

On the other hand, the dissolution rate will change because of changes of pH in the solution. The change in pH will be a complex function of the flow rate, buffer capacity of the fluid, and alkali content of the glass. There is insufficient data to obtain a relation for the change of pH due to the dissolution of glass, and only the initial pH value of the inflow groundwater is used in the calculation. This is probably true for the flow-through mode with a high flow rate.

#### 3.5.1.6.5 Flow-Through Mode

The area of the glass log wetted by water ( $s$ ) is usually unknown in the flow-through, water-contact mode. It is to be determined within the model for in-package hydrology. A larger wetted area generally produces a larger release. For glass, the larger area produces a slowdown of alteration rate because of the silica in solution nearing saturation. The two effects oppose each other. Also there is a minimum long-term alteration rate for the rate. The net release rate resulting from these three factors must be evaluated with the numerical model; it cannot be predicted in a simple way.

With a thickness of the water film on the glass of  $\Delta$ , the volume of water covering the glass is  $s\Delta$ . When groundwater of a flow rate of  $q$  covers a portion of surface area as shown in Fig. 3.5.1-5, the time for the water to flow in and out of the package is  $t_{in} = s\Delta/q$ . As the water proceeds downward, the silica increases, and the reaction rate slows.

For a steady-state flow condition, the glass-dissolution condition can be considered as a unit volume of water ( $s'\Delta$ ) contacting the glass for a duration of  $t_{in}$ . The increase of silica concentration during a time interval  $dt$

$$dQ = \frac{s'kf_{si}(1-f_p)}{s'\Delta} \left(1 - \frac{Q}{K}\right) dt \quad (3.5.1-7)$$

where  $f_{si}$  = fraction of silica in glass. Therefore,

$$-\ln\left(1 - \frac{Q}{K}\right) = \frac{kf_{si}(1-f_p)t}{K\Delta} + C \quad (3.5.1-8)$$

where  $C$  is a constant depending on the initial conditions. If the silica concentration of incoming groundwater is  $Q_i$  and that of outgoing is  $Q_o$  after a duration of  $t_{in}$ , then

$$Q_o - Q_i = K \left(1 - \frac{Q_i}{K}\right) [1 - \exp(-\alpha)] \quad (3.5.1-9)$$

$$\text{where } \alpha = f_{si}(1-f_p) \frac{ks}{Kq}$$

If  $\beta = ks/Kq$ , one can see that a high water-refresh rate gives a low value of  $\beta$ . When  $\beta$  is high, the system approaches a saturated condition. Also  $f_p$  starts changing toward high values, but there are not very precise data for  $f_p$ . The intermediate value of 0.5 is used.

Because only a fraction of silica  $f_{si}(1-f_p)$  in the waste glass dissolves in the solution, the total mass of dissolved glass per unit volume of outgoing water should be

$$G_o = \frac{Q_o - Q_i}{f_{si}(1-f_p)} \quad (3.5.1-10)$$

The dissolution rate (g/yr) from the whole waste glass in the waste package for the flow-through, water-contact mode is

$$R = qG_o = \frac{q(Q_o - Q_i)}{f_{si}(1-f_p)} = \frac{qK}{f_{si}(1-f_p)} \left(1 - \frac{Q_i}{K}\right) [1 - \exp(-\alpha)] \quad (3.5.1-11)$$

According to data in Table 3.5.1-2,  $K$  (g/m<sup>3</sup>) can be expressed as a function of  $T$  (°C):

$$K = 6.0 \times 10^{-5} + 1.90 \times 10^{-6} T + 1.25 \times 10^{-8} T^2 \quad (3.5.1-12)$$

When the silica concentration is very near its saturation limit, a long-term rate applies. The mass of glass dissolved in a unit volume of water in a time interval  $dt$  is

$$dG = \frac{s k_{long}}{s \Delta} dt \quad (3.5.1-13)$$

The dissolved glass mass per unit volume of water exiting the waste package is

$$G_o = \frac{k_{long} t_{in}}{\Delta} = \frac{s k_{long}}{q} \quad (3.5.1-14)$$

Thus,

$$R = q G_o = s k_{long} \quad (3.5.1-15)$$

### 3.5.1.6.6 Bathtub Mode

During filling of the container, it is assumed that the fraction of wetted area increases in proportion to the fraction of the filled volume in the container, as shown in Fig. 3.5.1-6. That is,

$$\frac{A(t)}{V(t)} = \frac{s}{V_f} \quad (3.5.1-16)$$

where

$A(t)$  = wetted surface area of glass at time  $t$

$V(t)$  = volume of water in the container at time  $t$  equal to  $q t$

$s$  = total surface area of glass in the waste package

$V_f$  = water volume of bathtub when filled

The increment of silica concentration during a time interval before overflowing is

$$dQ = \frac{A(t)}{V(t)} k f_{si} (1 - f_p) \left(1 - \frac{Q}{K}\right) dt = \frac{s}{V_f} k f_{si} (1 - f_p) \left(1 - \frac{Q}{K}\right) dt \quad (3.5.1-17)$$

The surface area of the glass logs decreases as the glass dissolves. Conservatively, it can be assumed the surface area remains at the initial value during the filling period. Then,

$$-\ln\left(1 - \frac{Q}{K}\right) = \frac{s}{K V_f} k f_{si} (1 - f_p) t + C_1 \quad (3.5.1-18)$$

where  $C_1$  is a constant depending on the initial conditions. The time for filling the container is  $t_f = V_f/q$ . If the silica concentration of incoming groundwater is  $Q_i$ , and that, at the time of overflow, is  $Q_f$ , then

$$Q_f - Q_i = K \left(1 - \frac{Q_i}{K}\right) \left[1 - \exp\left(-\frac{skf_{si}(1-f_p)t_f}{KV_f}\right)\right] = K \left(1 - \frac{Q_i}{K}\right) [1 - \exp(-\alpha)] \quad (3.5.1-19)$$

where 
$$\alpha = f_{si}(1-f_p) \frac{ks}{Kq}$$

To estimate the mass of glass dissolved during filling, one considers the possible maximum increase of silica concentration of the solution inside the container:

$$(Q_f - Q_i)_{\max} = K \left(1 - \frac{Q_i}{K}\right) \quad (3.5.1-20)$$

According to Table 3.5.1-2, the silica concentration increase at 90°C is 0.000225 g/m<sup>3</sup>. For 4 glass logs with 0.3 m radius and 2.2 m length inside a container with a radius of 0.80 m and a length of 3.76 m, the bathtub volume,  $V_f$ , is 5.072 m<sup>3</sup>. Assuming  $f_{si} = 0.45$  and  $f_p = 0.5$ , one obtains the mass of dissolved glass during filling =  $0.000225 \times 5.072 / (0.45 \times 0.5) = 0.0051$  g. This loss of mass is negligible compared with the initial mass of the 4 glass logs at 6720 kg. Therefore, the assumption of constant surface area of glass is appropriate during the filling period.

After filling (i.e.,  $t > t_f$ ) the change of silica in the water inside the container will be

$$V_f dQ = \left[ skf_{si}(1-f_p) \left(1 - \frac{Q}{K}\right) - (Q - Q_i)q \right] dt = [(\alpha K + Q_i) - (\alpha + 1)Q] q dt \quad (3.5.1-21)$$

The loss of mass of glass over a long period after filling can be significant. To deal with changes of surface area resulting from the dissolved mass of the glass logs, calculations can be performed with time steps. Again, the surface area can be conservatively assumed constant as the initial value. Solving the differential equation with the boundary conditions at the time of overfilling, one obtains

$$Q_o - Q_i = \frac{\alpha K}{\alpha + 1} \left(1 + \frac{Q_i}{K}\right) [1 - \exp(-\tau)] + (Q_f - Q_i) \exp(-\tau) \quad (3.5.1-22)$$

where

$$\tau = \frac{(1 + \alpha)(t - t_f)}{t_f}$$

For a steady state, when  $t \rightarrow \infty$ ,  $\exp(-\tau) \rightarrow 0$ ,

$$Q_o - Q_i = \frac{\alpha K}{\alpha + 1} \left( 1 - \frac{Q_i}{K} \right) \quad (3.5.1-23)$$

The release rate (g/yr) of the waste glass from the waste package for the bathtub mode is

$$R = \frac{q(Q_o - Q_i)}{f_{Si}(1 - f_p)} \quad (3.5.1-24)$$

For the long-term silica-saturated condition

$$R = s k_{long} \quad (3.5.1-25)$$

### 3.5.1.7 Solubility-Limited Radionuclide Release from Glass

The following data provide radionuclide solubility limits for the elements U, Pu, Np, Am, Sr, and Cs calculated for SRL-202-type HLW glasses reacting in J-13 water. The data from the calculations are compared with radionuclide concentrations measured in laboratory glass dissolution.

Radionuclide concentrations are calculated for four scenarios. Two are closed systems in which the redox state and total carbon were controlled entirely through reactions between J-13 water and the glass reactant. The other two scenarios are for open conditions in which the total carbon and redox state of the fluid are controlled by atmospheric gases assumed to be present in the proposed underground repository at Yucca Mountain. For the open-system simulations, the pressures of carbon dioxide and oxygen gases are assumed to be 0.00032 bars and 0.20 bars, respectively, their average atmospheric values. The compositions of J-13 water and the SRL-202 glass used in the simulations are given in Table 3.5.1-6 and Table 3.5.1-7, respectively.

Table 3.5.1-6

**Composition of J-13 well water used in the simulation  
(Delaney, 1985)**

Component	Concentration (mg/L)	Component	Concentration (mg/L)
Li	0.042	Si	27.0
Na	43.9	NO <sub>3</sub>	9.6
K	5.1	F	2.2
Ca	12.5	Cl	6.9
Mg	1.9	HCO <sub>3</sub>	125.3
Sr	0.035	SO <sub>4</sub>	18.7
Al	0.012	pH	7.6
Fe	0.006		

Table 3.5.1-7

**Composition of SRL-202 glass used in simulation**

Glass SRL-202 Reduced Component Set						
Oxide	Element	Oxide (wt %)	Oxide (mole %)	Element (wt %)	Element (mole %)	Cation (mole %)
SiO <sub>2</sub>	Si	48.9500	56.53	22.88	17.21	40.72
Al <sub>2</sub> O <sub>3</sub>	Al	3.8400	2.61	2.03	1.59	3.76
B <sub>2</sub> O <sub>3</sub>	B	7.9700	7.94	2.48	4.84	11.44
Mn <sub>2</sub> O <sub>3</sub>	Mn	1.0033	0.44	0.70	0.27	0.64
Fe <sub>2</sub> O <sub>3</sub>	Fe	11.4100	4.96	7.98	3.02	7.14
Na <sub>2</sub> O	Na	8.9200	9.99	6.62	6.08	14.39
K <sub>2</sub> O	K	3.7100	2.73	3.08	1.66	3.94
Li <sub>2</sub> O	Li	4.2300	9.82	1.97	5.98	14.15
Cs <sub>2</sub> O	Cs	0.0720	0.02	0.07	0.01	0.03
CaO	Ca	1.2000	1.48	0.86	0.45	1.07
MgO	Mg	1.3200	2.27	0.80	0.69	1.64
SrO	Sr	0.1100	0.07	0.09	0.02	0.05
MnO	Mn	0.9016	0.88	0.70	0.27	0.64
U <sub>3</sub> O <sub>8</sub>	U	1.9300	0.16	1.64	0.15	0.34
NpO <sub>2</sub>	Np	0.0080	0.00	0.01	0.00	0.00
PuO <sub>2</sub>	Pu	0.0220	0.01	0.02	0.00	0.00
Am <sub>2</sub> O <sub>3</sub>	Am	0.0004	0.00	0.00	0.00	0.00
ThO <sub>2</sub>	Th	0.2600	0.07	0.23	0.02	0.05
<b>Totals</b>		<b>95.8573</b>	<b>100.00</b>	<b>95.86</b>	<b>100.00</b>	<b>100.00</b>

Two types of calculations were carried out for both the closed and open systems. In the first, all possible mineral phases that can form were allowed to precipitate as alteration minerals. This included mineral phases that, for kinetic reasons, generally do not form at low temperatures or over short time periods. In the second simulation, phases (see Table 3.5.1-8) that are known or that are suspected not to precipitate rapidly at low temperatures were suppressed. Note that list in Table 3.5.1-8 includes some highly insoluble actinide oxide phases ( $\text{PuO}_2$ ,  $\text{NpO}_2$ , and  $\text{Am}_2\text{O}_3$ ), which results in predictions of much higher actinide solubilities for the second case than for the first case. The list also includes phases, such as quartz and andradite, that do not contain radionuclides, but which are known, from observations of natural analogs, not to form readily at low temperatures. One consequence of suppressing these phases is that the solution concentrations of some elements, such as Si and Al, increase to higher values during the simulation than is the case for simulations when the phases are not suppressed. This affects the solubility limits for the radionuclides by changing the amounts of ligands available for complexation, the solution pH, and the concentrations of competing metals. The ultimate effect of the suppression of these phases on radionuclide solubilities is therefore complex, as discussed subsequently.

**Table 3.5.1-8 Phases suppressed in glass dissolution simulation in "metastable" calculation**

Name	Formula	Name	Formula
	$\text{Am}_2\text{C}_3$		$\text{Pu}_2\text{O}_7$
	$\text{Am}_2\text{O}_3$		$\text{NpO}_2$
	$\text{AmO}_2$	Quartz	$\text{SiO}_2$
Andradite	$\text{Ca}_3\text{Fe}_2(\text{SiO}_4)_3$	Rhodonite	$\text{MnSiO}_3$
Dolomite	$\text{CaMg}(\text{CO}_3)_2$	Talc	$\text{Mg}_3\text{Si}_4\text{O}_{10}(\text{OH})_2$
K-Feldspar	$\text{KAISi}_3\text{O}_8$	Tephroite	$\text{Mn}_2\text{SiO}_4$
	$\text{Np}_2\text{O}_5$	Thorianite	$\text{ThO}_2$
Petalite	$\text{LiAlSi}_4\text{O}_{10}$	Tridymite	$\text{SiO}_2$

Each simulation begins with one liter of J-13 water and one gram of SRL-202 glass. All calculations were performed using the GEMBOCHS version EQ3/6 (Wolery, 1992) V8-R6 composite data file. The glass and water were allowed to react at a fixed rate until the one gram of glass has completely reacted. The system was then composed of a modified water composition in equilibrium with a set of alteration minerals that formed during the reaction. The choice of one gram of glass per liter fluid was arbitrary. Simulations using a smaller amount of glass show that the pH and Eh of the system are not yet dominated by the glass; the system is relatively insensitive to reacting to greater amounts of glass. The results provide an approximation of "bathtub-type" repository situations in which water has breached the glass containment and sits in contact with

the glass for extended periods of time under relatively stagnant conditions. A more precise time of reaction is impossible to estimate without including more details (e.g., flow rates) of hydrologic conditions.

Table 3.5.1-9 shows the results of the four simulations: the first part shows the closed system results, and the second part shows the open system results. The line labeled "Total" gives the total amount of radionuclide in the one gram of glass. For each element, this is the conservative maximum available for colloidal transport. The next four lines provide the solubility of each radionuclide (if solubility-limited), the stable phase containing that element that controls the solubility, and the dominant aqueous complex of that element. The first case is for control by metastable solids (as discussed previously), and the second case allows all potential precipitates to form. Note that, because the systems are constrained differently (closed versus open), the solutions for the two cases are at much different values of pH,  $f_{O_2}$ , and  $f_{CO_2}$  (see Table 3.5.1-9 caption). The radionuclide solubilities are being compared under much different conditions, and the difference in values can provide an indication of the sort of variability in solution concentrations that can be expected for differing repository conditions.

**Table 3.5.1-9 Radionuclide concentrations and equilibrium phases calculated for SRL-202 glass reaction with J-13 water**

Element	U	Np	Pu	Am	Cs	Sr
<b>Closed System (pH = 10.8, log <math>f_{O_2}</math> = -45, log <math>f_{CO_2}</math> = -6.6)</b>						
Total (mg)	16.4	0.07	0.19	0.003	0.68	0.93
Soluble (metastable)	0.5E-3	0.5E-3	0.4E-3	0.7E-4	0.68	0.5E-2
Stable Phase	haiweeite	Np(OH) <sub>4</sub>	Pu(OH) <sub>4</sub>	Am(OH) <sub>3</sub>	—	SrCO <sub>3</sub>
Dominant Complex	UO <sub>2</sub> (OH) <sub>3</sub> <sup>-</sup>	Np(OH) <sub>4</sub> (aq)	Pu(OH) <sub>4</sub> (aq)	Am(OH) <sub>2</sub> <sup>+</sup>	Cs <sup>+</sup>	Sr <sup>2+</sup>
Solubility-Limited	yes	yes	yes	yes	no	yes
Soluble (xtal)	0.8E-3	0.2E-11	0.3E-11	0.6E-4	0.68	0.5E-2
Stable Phase	CaUO <sub>4</sub>	NpO <sub>2</sub>	PuO <sub>2</sub>	Am(OH) <sub>3</sub>	—	SrCO <sub>3</sub>
Dominant Complex	UO <sub>2</sub> (OH) <sub>3</sub> <sup>-</sup>	Np(OH) <sub>4</sub> (aq)	Pu(OH) <sub>4</sub> (aq)	Am(OH) <sub>2</sub> <sup>+</sup>	Cs <sup>+</sup>	Sr <sup>2+</sup>
Solubility-Limited?	yes	yes	yes	yes	no	yes
<b>Open System (pH = 8.9, log <math>f_{O_2}</math> = -0.7, log <math>f_{CO_2}</math> = -3.5)</b>						
Total (mg)	16.4	0.07	0.19	0.003	0.68	0.93
Soluble (metastable)	0.24	0.07	0.03	0.001	0.68	0.02
Stable phase	haiweeite	—	PuO <sub>2</sub> (OH) <sub>2</sub>	AmPO <sub>4</sub> (am)	—	SrCO <sub>3</sub>
Dominant Complex	UO <sub>2</sub> (CO <sub>3</sub> ) <sub>3</sub> <sup>4-</sup>	NpO <sub>2</sub> CO <sub>3</sub> <sup>-</sup>	PuO <sub>2</sub> (CO <sub>3</sub> ) <sub>2</sub> <sup>2-</sup>	Am(CO <sub>3</sub> ) <sub>2</sub> <sup>-</sup>	Cs <sup>+</sup>	Sr <sup>2+</sup>
Solubility-Limited	yes	no	yes	yes	no	yes

Element	U	Np	Pu	Am	Cs	Sr
<b>Open System (pH = 8.9, log <math>f_{O_2}</math> = -0.7, log <math>f_{CO_2}</math> = -3.5)</b>						
Soluble (xtal)	1.6	0.07	0.9E-6	0.001	0.68	0.02
Stable Phase	Haiweeite	—	PuO <sub>2</sub>	AmPO <sub>4</sub> (am)	—	SrCO <sub>3</sub>
Dominant Complex	UO <sub>2</sub> (CO <sub>3</sub> ) <sub>3</sub> <sup>4-</sup>	NpO <sub>2</sub> CO <sub>3</sub> <sup>-</sup>	PuO <sub>2</sub> (CO <sub>3</sub> ) <sub>2</sub> <sup>2-</sup>	Am(CO <sub>3</sub> ) <sub>2</sub> <sup>-</sup>	Cs <sup>+</sup>	Sr <sup>2+</sup>
Solubility-Limited?	yes	no	yes	yes	no	yes

All radionuclide amounts in milligrams (mg).

"Total" indicates total amount of radionuclide released from reaction of one gram of SRL-202 glass.

"Soluble (meta)" is amount of radionuclide in one liter of solution (mg/L) in equilibrium with more soluble (metastable) phase indicated as "stable phase."

"Dominant complex" is dominant aqueous species for given element.

"Soluble (xtal)" is amount of radionuclide in one liter of solution (mg/L) in equilibrium with most stable (crystalline) phase labeled "stable phase."

For all four simulations, U, Pu, Am, and Sr were always solubility-controlled, generally to a much lower value than the total element available. Of the actinides, only Np was found not to be solubility-controlled. Under open system conditions, the relatively high solubility of oxidized Np combined with high carbonate concentrations due to additions of CO<sub>2</sub> from air stabilized the NpO<sub>2</sub>CO<sub>3</sub><sup>-</sup> complex to where the least soluble Np phase, NpO<sub>2</sub>, was still a half log unit undersaturated at 0.07 mg/L aqueous Np concentration. Under reducing conditions (closed system), the Np was always solubility-controlled.

An important conclusion from Table 3.5.1-9 is that actinide solubilities are extremely sensitive to whether highly ordered anhydrous crystalline phases (i.e., PuO<sub>2</sub>) or metastable phases such as Pu(OH)<sub>4</sub> control actinide solubilities. These differences can be as high as 7 log units for Pu and Np.

Notice that, unlike the other actinides, uranium solubilities actually decreased when the metastable phases were used to control solubilities. This is true for uranium mainly because of the increased silica concentrations in the metastable-phase-alteration simulations because of suppression of quartz. Greater silica in solution increased the stability of uranium silicate phases such as Haiweeite, which lowered uranium solubility.

Figure 3.5.1-7 graphically depicts the information Table 3.5.1-9. The soluble fraction of total radionuclide inventory available from one gram of glass is plotted for the metastable solids assemblage and for the stable solids assemblage. If the element is not solubility-controlled (i.e., Cs), the entire inventory is available and no bar is shown.

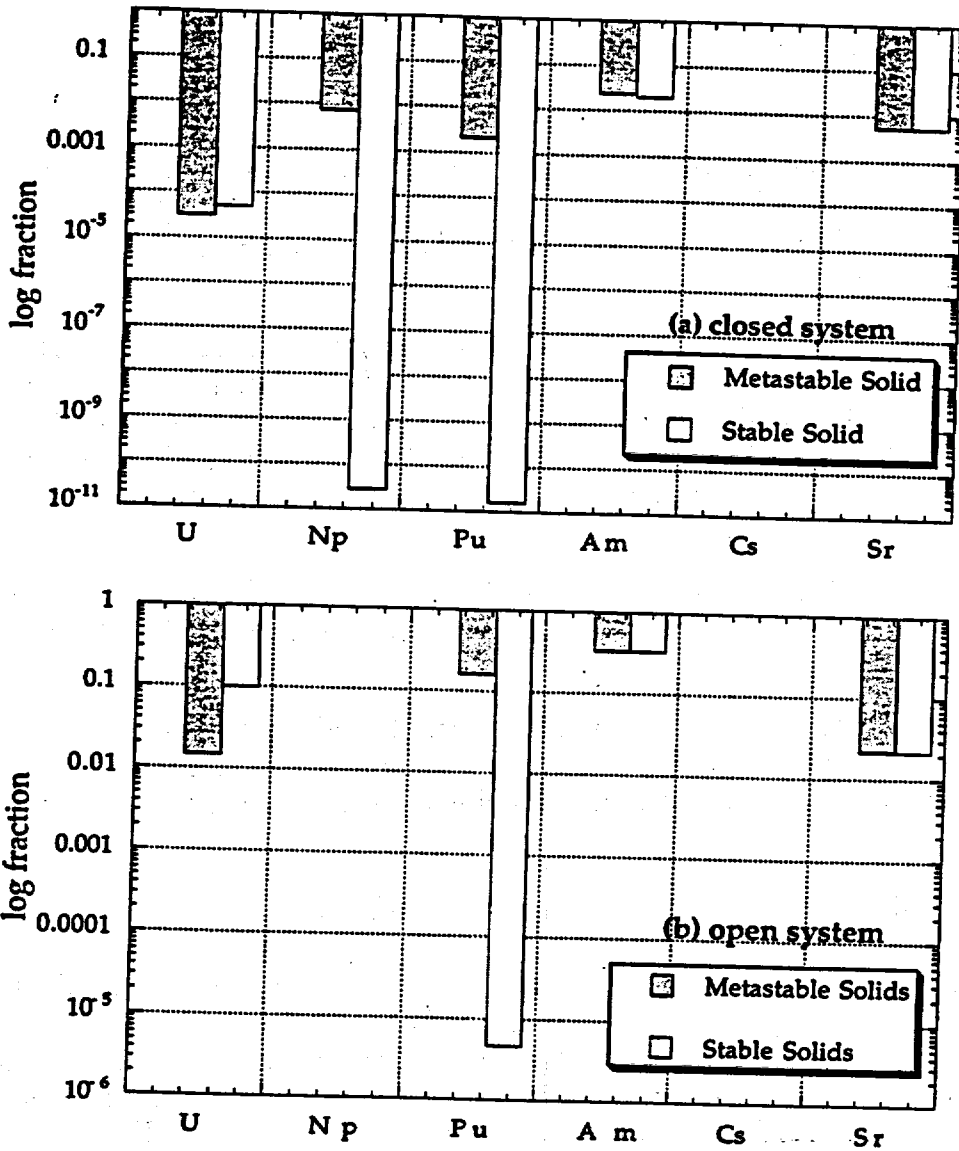


Figure 3.5.1-7

Histograms showing fractions of radionuclide inventory in glass available for transport for (a) closed-system simulation and (b) open-system simulation. Three cases are shown for each element: (1) no solubility control (all values = 1), (2) solubility control by metastable solids (3) solubility control by stable solids. Data are from Table 3.5.1-9.

### 3.5.1.8 Comparison With Laboratory Results

Measured actinide releases from long-term drip tests of HLW glasses have been reported by Fortner and Bates (1995). Data from their N2-10 test are shown in Figure 3.5.1-8. These were unsaturated (drip) tests of EJ-13 water onto SRL-165 glass. Unfortunately, for several reasons, these experimental data cannot be directly compared to the model calculations:

- The tests report the entire released inventory of actinides, including soluble, colloidal, and adsorbed masses. The EQ3/6 model calculated only the soluble amounts. Precipitated actinide solids are included in the masses of precipitated secondary phases. EQ3/6 cannot predict the relative amounts of these solids that remain on the glass monolith versus those that flake off and fall to the bottom of the test vessel.
- The tests are of older formulation SRL-165 glasses and cannot be compared directly with the model calculations, which are for the current SRL-202 glass composition.
- The data reported do not include the amounts of fluid in which the total masses of actinides were measured, so they cannot be converted to concentration units needed to determine the relative saturation states of the actinides.

These apparent shortfalls are a consequence of the defined purpose of these tests, which were intended to simulate, as closely as possible, anticipated repository conditions and which were, therefore, not optimum for validating modeling studies. It is still useful to compare trends and relative solubilities of actinides between the experiments and these simulations. The drip-test procedure calls for periodic refreshing of the test vessel with air. The drip-test methodology correlates best with the model's open-system simulations, in which the system stays equilibrated with air. The Fortner and Bates results show that Np is the most soluble actinide; this is in agreement with the simulation results. There is no indication of solubility control of Np release in these tests, which is consistent with the model's calculated results. Am and Pu are generally released at rates 3 to 4 log units slower than Np is released. Their release is probably solubility-controlled. This is consistent with Pu solubility control by some metastable solid somewhat less stable than pure crystalline PuO<sub>2</sub>. The amount of released uranium is intermediate between Np and Pu; this is also in agreement with the modeling results.

The increased release of Pu and Am occurring after about 8 yr, shown in Figure 3.5.1-8, is thought to be due to spallation of the actinide-containing rinds of alteration minerals to the bottom of the test vessel. The spalled material is potentially available for colloidal transport.

More exact comparison of the model results with the experiments depends on the better characterization of the alteration products that control actinide solubilities (work that is in progress) and on a better estimate of the effective oxidation state and pH of the

fluid inside the test vessel. Actinide solubilities are highly dependent on Eh and pH. Overall, the model results are in qualitative agreement with the experimental observations.

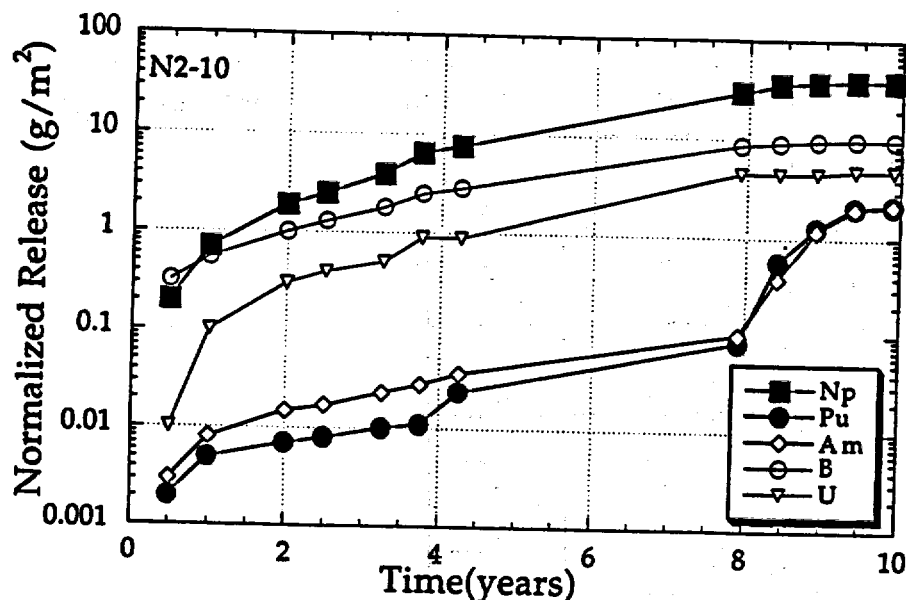


Figure 3.5.1-8 Experimental data modified from Figure I-7 in Fortner and Bates (1995) showing the normalized release of actinides from SRL-165 glass in an unsaturated (drip) test. Release values shown include cumulative soluble, sorbed, and colloidal release.

### 3.5.1.9 Effect of Dissolved Iron on Borosilicate Glass Dissolution

Flow-through borosilicate glass-dissolution experiments were performed in pH-buffered solutions ranging in pH from 6 to 12 and doped with dissolved ferric iron ( $Fe^{3+}$ ) at 70°C. The iron concentrations were at saturation with amorphous ferric hydroxide ( $Fe(OH)_3$ ) at each pH. No difference in dissolution rate was found for iron-doped versus iron-free solutions at any pH. This result suggests there will be no deleterious effect of dissolved iron on glass-dissolution rates in a repository for the range of dissolved iron concentrations used in these experiments. However, ferric iron colloids may affect glass-dissolution rates if they cause the removal of dissolved silica from solutions. No iron colloids were present in these tests.

#### 3.5.1.9.1 Introduction

Although solution composition apparently has an important effect on the dissolution rate of borosilicate glasses, there has been little experimental data obtained that can be used to quantify this effect for different elements in solution. Flow-through dissolution tests have been performed on the simple analog SRL-202 glass composition (Table 3.5.1-10) in pH-buffered solutions that have been doped with small amounts of

dissolved iron to provide quantification of the effect of dissolved iron on glass dissolution rates. The solution compositions, iron concentrations, and pH buffers used are given in Table 3.5.1-11.

**Table 3.5.1-10** Compositions of glass tested in mole percent oxide and cation mole percent (S-202 glass is a simple analog of SRL-202 glass.)

Oxide/Cation	Mole % Oxide		Cation Mole %	
	SRL-202	S-202	SRL-202	S-202
SiO <sub>2</sub>	55.44	55.6	40.1	40.9
Al <sub>2</sub> O <sub>3</sub>	2.56	8.1	3.7	11.5
Fe <sub>2</sub> O <sub>3</sub>	4.86	—	7.0	—
B <sub>2</sub> O <sub>3</sub>	7.79	8.0	11.3	11.3
Na <sub>2</sub> O	9.79	22.7	14.2	32.3
Li <sub>2</sub> O	9.63	—	13.9	—
CaO	1.46	5.7	1.2	4.1
MgO	2.23	—	1.6	—
MnO	1.10	—	0.6	—
SrO	0.02	—	0.01	—
BaO	0.10	—	0.07	—
NiO	0.75	—	0.5	—
U <sub>3</sub> O <sub>8</sub>	0.16	—	0.3	—

**Table 3.5.1-11** Composition of solutions used in flow-through dissolution tests

pH	Buffer	Iron Concentration
6	0.005 molal Ortho-phthalic acid + KOH	$3.3 \times 10^{-7}$ molal FeCl <sub>3</sub>
8	0.005 molal Boric Acid + KOH	$7.8 \times 10^{-8}$ molal FeCl <sub>3</sub>
10	0.005 molal Boric Acid + KOH	$2.6 \times 10^{-7}$ molal FeCl <sub>3</sub>
12	0.013 molal KOH	$2.2 \times 10^{-5}$ molal FeCl <sub>3</sub>

The effect of solution composition on glass-dissolution rates is incorporated into a kinetic model for glass dissolution with a rate equation of the form shown in Eq. 3.5.2-1. The effects of dissolved species in solution are included in the product term (P). Eq. 3.5.2-1 shows that the solution composition can affect the glass dissolution rate in two ways: through the affinity term or directly on the value of the rate constant. These experiments can be used to determine the coefficients of the product term. They are designed to exclude saturation effects because the solution composition is chosen to be far from glass (silica) saturation.

### 3.5.1.9.2 Experimental Methods

The glass was dissolved in single-path, flow-through (SPFT) cells using pH buffers of ortho-phthalic acid, borate, and KOH-KCl at ionic strengths of 0.005 molal. Powdered glasses (surface area = 450 cm<sup>2</sup>/g) in 3-ml cells react with buffer solutions at flow rates of 50 to 100 ml/day. Experimental data typically show steady-state dissolution rates after a few days. No change in steady-state dissolution rates was found when flow rates were doubled, indicating the systems behaved as continuously stirred reactors in that the dissolution rates were not rate-limited by transport away from the glass reaction surface.

The pH buffers were doped with Fe<sup>3+</sup> (added as FeCl<sub>3</sub>) with the concentrations fixed at amorphous Fe(OH)<sub>3</sub> saturation at each pH. This is likely to be the maximum dissolved iron concentration in repository waters because ferric hydroxide readily precipitates from supersaturated solutions.

A five-component analog of the SRL-202 glass composition, rather than SRL-202 glass, was used in the test. The analog was prepared by adjusting the mole fraction of each component in the analog glass to equal the sum of the mole fractions of the components in the actual glass that were judged to occupy similar structural sites in the glass. This determination was based on crystal chemical principles, including primarily ion size and radius. For example, the sodium content of the S-202 glass was determined by adding the molar concentrations of all the alkalis in the SRL-202 glass. Similar calculations were performed for Ca, Al, and Si in the analog glass. The mole fraction of B was kept equal to that of the waste glass. The simple glasses avoid the problems in data interpretation due to redox reactions during dissolution and precipitation of insoluble secondary phases in real waste glasses. Iron and manganese are particular problems.

### 3.5.1.9.3 Results and Discussion

The effects on the glass-dissolution rate of doping the buffers with Fe can be seen in Fig. 3.5.1-9, which shows the release rate of silica from the glass as a function of pH for both undoped and doped buffers. Apparently, dissolved iron has little effect on glass-dissolution rates over the pH range and iron concentration range tested. The data points for the iron-doped and undoped buffers lie essentially on top of each other, and their differences in all cases are less than the precision of the experimental method.

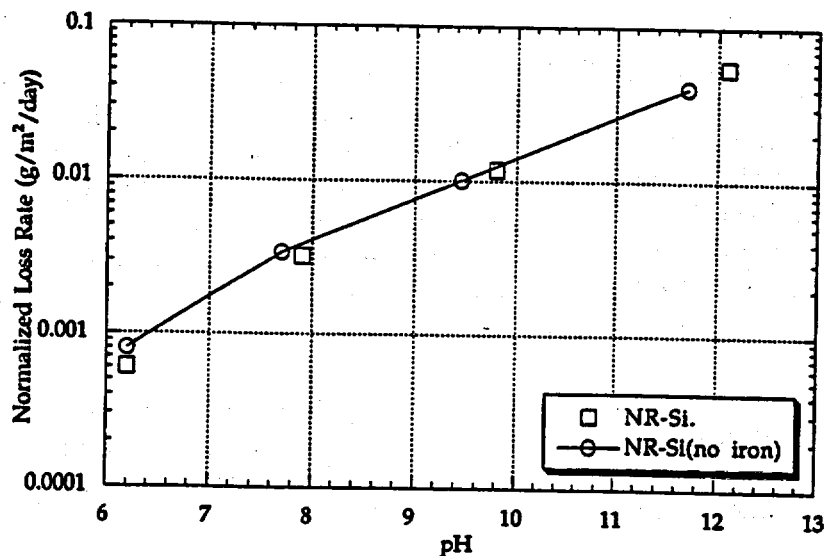


**Figure 3.5.1-9** Normalized loss rate (dissolution rates) for SRL-202 analog glass in pH buffer with and without aqueous Fe present at  $\text{Fe}(\text{OH})_3$  saturation. There appears to be little effect of the dissolved iron on glass dissolution rates.

These results are consistent with several previous studies of the effect of iron on borosilicate glass dissolution in which borosilicate glass was leached in the presence of various metal phases, including 304L stainless steel, the pour canister material (Bates et al., 1988; Bibler and Jantzen, 1987; Burns et al., 1986). In all of these studies, the iron had little or no effect on the glass-dissolution rate.

Other studies have noted an enhancement of glass-dissolution rates, presumably due to the presence of iron-containing materials in the system (Bart et al., 1987; Inagaki et al., 1996; McVay and Buckwalter, 1982). It is concluded in each of these studies that it is the sorption of silica onto iron colloids, or the sorption of silica onto iron-containing solids, that causes the glass to dissolve more quickly by lowering the silica concentration in solution. The system is therefore farther from silica saturation, and the glass dissolves more quickly under those conditions. Presumably, these later experiments contained iron solids with higher surface areas than did tests where no iron effect was noticed. In some cases, the iron-containing material was much more reactive than 304L stainless steel (i.e., McVay and Buckwalter [1982] used ductile iron, which corrodes much more rapidly and evidently gave rise to iron colloids).

It is concluded that the presence of iron in a waste repository can have a significant negative impact on borosilicate glass performance only if it either leads to the development of colloids that sorb silica or presents a large amount of surface area for silica sorption. In both cases, the amount of colloids or surface area must be sufficient to significantly decrease the concentration of dissolved silica due to sorption. The presence of dissolved iron alone apparently has little effect on the glass dissolution rate.

### 3.5.1.10 References

- Bart G., H. U. Zwicky, E. T. Aerne, T. Graber, D. Z'Berg, and M. Tokiwai (1987). "Borosilicate glass corrosion in the presence of steel corrosion products." In proceedings from Materials Research Society Symposium. 84:459-470.
- Bates J. K., W. L. Ebert, D. F. Fisher, and T. J. Gerding (1988). "The reaction of reference commercial waste glasses during gamma irradiation in a saturated tuff environment." *J. Mat. Res. Soc.* 3:576-597. [NNA.19900125.0073]
- Baxter, R. G. (1983). *Description of defense waste processing facility reference waste form and container.* (Dp-1606). Aiken, SC: Savannah River Site. [NNA.19890327.0057]
- Bibler N. E., and Jantzen, C. M. (1987). "Materials interactions relating to long-term geologic disposal of nuclear waste glass." In proceedings from Materials Research Society Symposium. 84:47-66.
- Burns D. B., B. H. Upton, and G. G Wicks (1986). "Interactions of SRP waste glass with potential overpack materials." *J. Non-Crys. Sol.* 84:258-267.
- Cunnane, J. C. (1993). *High-level waste borosilicate glass: a compendium of corrosion characteristics.* (DOE-EM-0177) Washington, DC: U.S. Department of Energy, Office of Waste Management.
- Delage, F., D. Ghaleb, J. L. Dussosoy, O. Chevallier, and E. Vernaz (1992). "A mechanistic model for understanding nuclear waste." *J. Nucl. Mat.* 190:191-197.
- Delaney, J. M. (1985). *Reaction of Topopah Spring Tuff with J-13 water: a geochemical modeling approach using the EQ3/6 reaction path code.* (UCRL-53631) Livermore, CA: Lawrence Livermore National laboratory. [HQS.19980517.2419]
- Fortner, J. A., and J. K. Bates (1995). *Long-term results from unsaturated testing of actinide-doped DWPF and WVDP waste glasses.* (UCRL-CR-122614; DE960072159; B-291561) Livermore, CA: Lawrence Livermore National Laboratory, and Argonne, IL: Argonne National Laboratory.
- Inagaki Y., A. Ogata, H. Furuya, K. Idemitsu, T. Banba, and T. Maeda (1996). "Effects of redox condition on waste glass corrosion in the presence of magnetite." In proceedings from Materials Research Society Symposium. 412:257-264.
- Johnson, J. W., E. H. Oelkers, and H. C Helgeson (1992). "SUPCRT92: A software package for calculating the standard molal thermodynamic properties of minerals, gases, aqueous species, and reactions from 1 to 5000 bars and 0 to 1000°C." *Computers and Geosciences.* 18:890-947.
- Knauss, K. G., W. J. Beiringer, and D. W. Peifer (1987). *Hydrothermal interaction of solid wafers of Topopah Spring Tuff with J-13 water at 90 and 150°C using Dickson-type gold bag rocking autoclaves: Long-term experiments.* (UCRL-53722) Livermore, CA: Lawrence Livermore National Laboratory. [NNA.19870713.0081]

Knauss, K. G., W. L. Bourcier, K. D. McKeegan, C. I. Merzbacher, S. N. Nguyen, F. J. Ryerson, D. K. Smith, H. C. Weed, and L. Newton, L. (1990). "Dissolution kinetics of a simple nuclear waste glass as a function of pH, time, and temperature." In proceedings from Mat. Res. Soc. Symp. 176:371-381. [NNA.19891206.0279]

McVay, G. L., and C. Q. Buckwalter (1982). "Effect of iron on waste-glass leaching." *J. Amer. Cer. Soc.* 66(3):170-174. [NNA.19900306.0097]

O'Connell, W. J., W. L. Bourcier, J. Gansemer, T. S. Ueng (1997). Performance Assessment Modeling for Savannah River Glass HLW Disposal in a Potential Repository at Yucca Mountain. (UCRL-JC-127352) Livermore, CA: Lawrence Livermore National Laboratory. (Presented at the American Chemical Society National Meeting/Symposium on Science and Technology for Disposal of Radioactive Tank Wastes, Las Vegas, NV, September 8-11, 1997) [MOL.19980211.0541]

Wilder, D. G. (1997). *Near-Field and Altered-Zone Environment Report, Volume I: Technical Basis for EBS design.* (UCRL-LR-124998, Vol. 1) Livermore, CA: Lawrence Livermore National Laboratory. [MOL.19980127.0120]

Wolery, T. J. (1992). *EQ3/6, A software package for geochemical modeling of aqueous systems: Package overview and installation guide.* (UCRL-MA-110662) Livermore, CA: Lawrence Livermore National Laboratory. [NNA.19921023.0028]

## Contents for Section 3.5.2

3.5.2	Glass Dissolution Models.....	3.5.2-1
3.5.2.1	Overview of Glass Dissolution.....	3.5.2-1
3.5.2.2	Modeling of Glass Corrosion.....	3.5.2-4
3.5.2.2.1	The Rate Law .....	3.5.2-5
3.5.2.2.2	Secondary Phases .....	3.5.2-6
3.5.2.2.3	Ion Exchange.....	3.5.2-7
3.5.2.2.4	Transport-Limited Corrosion.....	3.5.2-7
3.5.2.2.5	Surface Interactions.....	3.5.2-8
3.5.2.2.6	Effect of Glass Composition.....	3.5.2-11
3.5.2.2.7	Deviant Glass Dissolution Behavior.....	3.5.2-13
3.5.2.3	Limitations of Current Models.....	3.5.2-13
3.5.2.4	Conclusions.....	3.5.2-14
3.5.2.5	Assessment of Current Methods for Estimating Glass-Dissolution Rates under Silica-Saturated Conditions....	3.5.2-15
3.5.2.5.1	Current Models of Glass Dissolution under Silica-Saturated Conditions.....	3.5.2-16
3.5.2.5.2	Needed Improvement in the Current Models.....	3.5.2-18
3.5.2.5.3	Glasses Versus Crystalline Silicates .....	3.5.2-20
3.5.2.5.4	Dissolution Models for Silicate Minerals.....	3.5.2-21
3.5.2.5.5	Conclusions.....	3.5.2-21
3.5.2.6	References.....	3.5.2-22

## Section 3.5.2: Glass Dissolution Models

Version 1.3

July 23, 1998

### 3.5.2.1 Overview of Glass Dissolution

A chemical model of glass corrosion will be used to predict the rates of release of radionuclides from borosilicate glass waste forms in high-level waste (HLW) repositories. The model will be used to calculate the rate of degradation of the glass and to predict the effects of chemical interactions between the glass and repository materials such as spent fuel, canister and container materials, backfill, cements, and grouts. Coupling between the degradation processes affecting all these materials is expected. The glass-corrosion model must therefore be mechanistic and not a simple empirical extrapolation of experimental glass-degradation rates.

This overview is concerned with dissolution behavior of borosilicate glass compositions currently anticipated for use as waste forms under repository-relevant conditions. The models described here cannot be expected to predict glass-corrosion rates under conditions significantly different from these.

Figure 3.5.2-1 illustrates the major processes taking place during glass corrosion. The reaction begins with water diffusion into the glass and alkali ion exchange. Evidence for water diffusion comes from secondary ion mass spectroscopy (SIMS) and ion-probe profiling of reacted glasses that show diffusion profiles for water in a surface zone generally less than 1 micron thick (Abrajano and Bates, 1987; Oversby and Phinney, 1992). Ion exchange is indicated by the early rapid release of alkalis relative to other glass components, which is commonly observed in glass-dissolution tests (Mendel, 1984). Hydration and ion exchange result in the formation of two layers on the glass surface: an inner diffusion layer where concentration gradients for alkalis and water are observed and an outer, hydrated "gel layer" where network hydrolysis (breakage of Si-O-Si) bonds takes place. The gel layer is depleted in alkalis and boron and enriched in insoluble elements such as Al, Ca, Mg, and heavy metals (e.g., actinides).

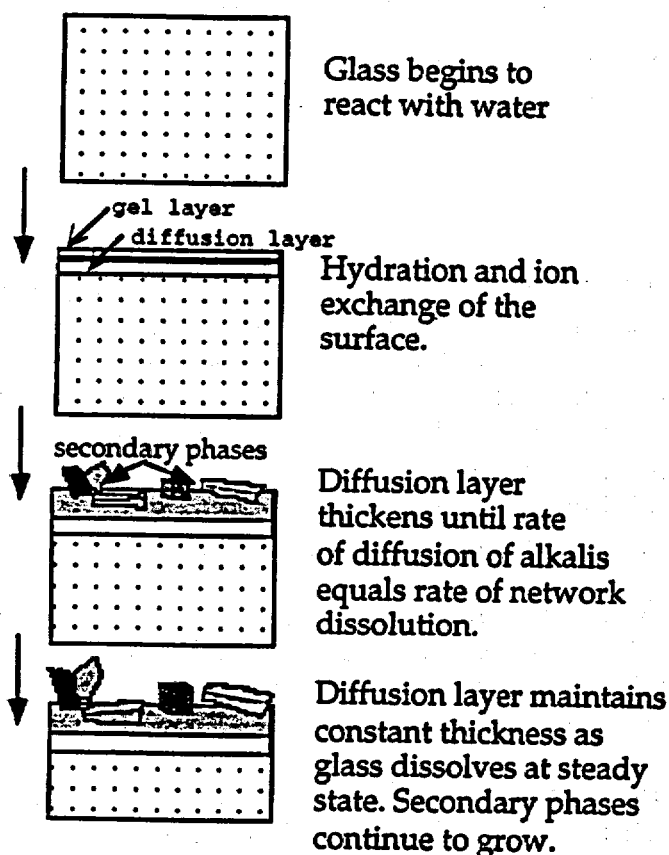


**Figure 3.5.2.1 Glass-dissolution mechanism**

With time, some elements released into solution reprecipitate on the hydrated glass surface and elsewhere as a variety of secondary phases. These phases are commonly clays, zeolites, and metal oxides/hydroxides. The reaction of glass to form secondary phases is driven by the thermodynamically unstable nature of glasses. Water allows glass to react and transform into a set of crystalline phases that are thermodynamically more stable. Water acts as a flux and allows the glass to react at a measurable rate. Under anhydrous conditions, even glass compositions that are relatively nondurable in water are stable for billions of years (Klein, 1986, 1986; Palmer et al., 1988).

Steady-state conditions are commonly observed during glass dissolution in which the rates of water diffusion and ion exchange are equal to the rate at which the glass network dissolves. Steady-state conditions are evidenced by the tendency for the glass diffusion layer to remain constant in thickness while the glass dissolves away and the mass of secondary phases increases with time (Abrajano et al., 1986).

In open-system experiments, the rate of release of most elements is approximately constant or slowly decreasing with time. In closed-system experiments, the release rates slow down more rapidly with time because of "saturation" effects (i.e., the buildup of dissolved glass species in solution)

(Fig. 3.5.2-2). Increased silica concentrations are the primary reason for decreased dissolution rates (Chick and Pederson, 1984), although other elements also have effects (Bourcier et al., 1992). Elemental releases from glasses in closed-system tests also show nonstoichiometric behavior: some elements are released much more rapidly than others (Fig. 3.5.2-2). Most of this nonstoichiometry is due to the precipitation of the less soluble glass components as secondary mineral phases, although a small amount is accounted for in the formation of leached layers.

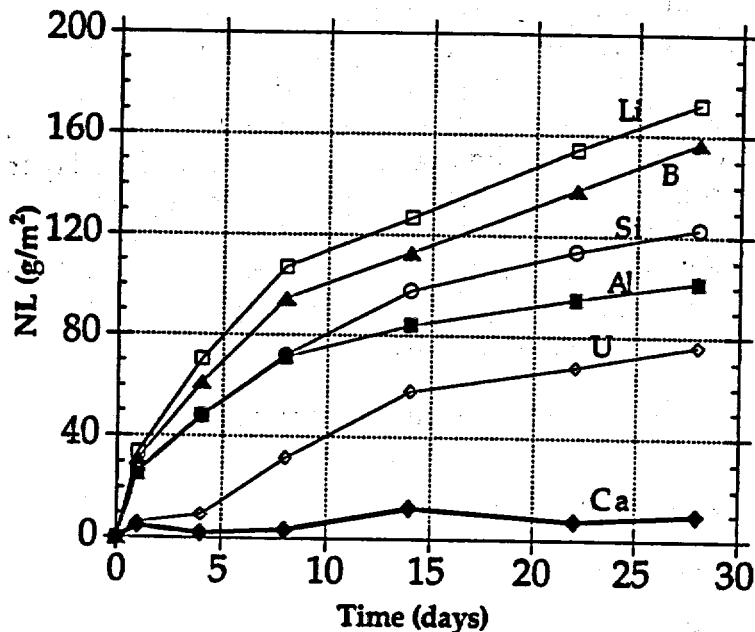


Figure 3.5.2.2 Normalized elemental release from SRL-165 glass reacted in 0.003m NaHCO<sub>3</sub> at 150°C, surface area to volume (SA/V) ratio 0.01cm<sup>-1</sup> (Bourcier, 1990)

Nuclear magnetic resonance (NMR) spectroscopy shows that network dissolution reactions taking place in the gel layer are complex. Experiments that are doped with <sup>17</sup>O show that both breakage and reformation of Si-O-Si linkages are taking place (Bunker et al., 1988). Hydrolysis of the highly stressed glass structure allows relaxation and removal of incompatible elements. The original glass is transformed into a hydrous silica-rich phase plus local areas enriched in transition and other heavy metals such as actinides. This alteration layer eventually crystallize into a variety of solid phases.

In some flow-through glass-dissolution tests, the gel layer appears to serve as a transport barrier that limits the overall dissolution rate (Grambow, 1987). In most closed-system experiments, however, elemental release data and electron microscopic examination of the surface layers show that the overall reaction rate is not controlled by diffusion of elements through the alteration layers (Abrajano et al., 1990; Chick and Pederson, 1984; Murakami et al., 1988).

Recent NMR data have also shown that boron in waste glasses is clustered into boron-rich regions (Phillips, 1993). Boron occurs in both three- and four-fold coordination with alkalis in a sodium-di-borate-type structure. The high reactivity and solubility of these zones gives rise to the relatively rapid release of boron from borosilicate glasses in waste glass leach tests.

Rates of glass dissolution may also be strongly affected by certain dissolved elements. For example, dissolution rates of silicate glasses are strongly decreased in the presence of dissolved Mg, Pb, and Zn and strongly enhanced, under some conditions, by dissolved Fe. Likewise, anions such as phosphate and sulfide are known to affect mineral-dissolution rates and may likewise affect glass-dissolution rates. Depending on the specific metal, these effects may be attributable to several processes: the formation of surface complexes, the precipitation of a surface layer providing a transport barrier, or the reaction of dissolved glass species with the dissolved metals causing the precipitation of colloids or secondary phases that affect the glass dissolution affinity (McVay and Buckwalter, 1983). These types of effects are potentially important in repository environments where a variety of dissolved species will be present from other repository materials.

In summary, a model for borosilicate glass dissolution must account for the following processes:

- Kinetically-controlled network dissolution
- Precipitation of secondary phases
- Ion exchange of selected elements
- Rate-limiting diffusive transport through a hydrous surface reaction layer (in some cases)
- Specific glass-surface interactions with dissolved cations and anions

This set of coupled processes should be able to quantitatively predict observations of glass dissolution that include the saturation effect (glass-dissolution rates slows down as dissolved glass species build up in solution), the increase in pH that accompanies glass dissolution in closed-system tests, the variability of glass-dissolution rate as a function of glass composition, and rate-affecting interactions of the glass surface with dissolved cations and anions. First one must look at examples of how the five processes are incorporated into current models and then critically review modeling results using a representative set of examples for modeling of experimental data.

### 3.5.2.2 Modeling of Glass Corrosion

Current long-term corrosion models for borosilicate glass employ a rate equation consistent with transition-state theory embodied in a geochemical reaction-path modeling program that calculates aqueous-phase speciation and

mineral precipitation/dissolution. These models ignore early diffusion-controlled dissolution behavior that is more important for less durable glass compositions such as alkali-silicates and is important only in the very early stages of reaction of borosilicate waste glasses. Diffusion in this case refers to solid-state diffusion of ions through the partially hydrated glass surface layer rather than to diffusion of aqueous species through the more hydrated and restructured gel layer. Therefore, there is no discussion of the many studies that solve the equations for the formation of a moving and thickening transport-limiting surface layer.

### 3.5.2.2.1 The Rate Law

The rate law commonly used to model network hydrolysis, assumed to be rate-controlling during glass dissolution, has the general form (Aagaard and Helgeson, 1982; Lasaga, 1984):

$$\frac{dn_i}{dt} = Sv_i k \prod_j a_j^{-N_j} \left( 1 - e^{\left( \frac{-A}{RT} \right)} \right) \quad (3.5.2-1)$$

where  $n_i$  is the number of moles of species  $i$  in solution released from the glass,  $t$  is time,  $S$  is the reactive surface area of glass,  $v_i$  is the concentration of species  $i$  in the glass,  $k$  is the rate coefficient for the glass,  $\prod_j a_j^{-N_j}$  is the product of the activities (concentrations) raised to the power of  $N_j$  of dissolved aqueous species that make up the activated complex of the rate-limiting microscopic dissolution reaction,  $A$  is the reaction affinity defined as  $RT \ln(Q/K)$  where  $Q$  is the activity product and  $K$  the equilibrium constant for the rate-determining glass dissolution reaction,  $s$  is a stoichiometric factor that relates the rate-controlling microscopic reaction to the overall solid dissolution reaction (usually it is assumed  $s=1$ ),  $R$  is the gas constant, and  $T$  is the temperature in Kelvin.

The form of Eq. 3.5.2-1 predicts that the dissolution rates of solids have the following characteristics:

- The amount of solid dissolved is proportional to exposed surface area.
- The dissolution rate slows down as the solid approaches saturation.
- The dissolution rate is constant under conditions far from saturation ( $Q/K \ll 1$ ).

An expression having this general form is used in all of the major glass modeling computer codes at this time (e.g., PHREEQE/GLASSOL [Grambow, 1987], EQ3/6 [Bourcier, 1990], DISSOL [Advocat et al., 1990], REACT, [Bourcier et al., 1993a], LIXIVER [Delage et al., 1992]).

This rate law implies that, at equilibrium, there is a *reversible* microscopic dissolution reaction that is rate-limiting. However, because glass is thermodynamically unstable and cannot reach saturation, the overall glass-dissolution reaction is clearly not reversible. Therefore, when this rate law is applied to glass dissolution, it must be applied not to the overall reaction, but to some rate-limiting microscopic reversible reaction.

Many of the parameters in Eq. 3.5.2-1 are not known either from theory or from experiments, so that in practice the equation is simplified to

$$\frac{dn_i}{dt} = A v_i k(pH) \left( 1 - \left( \frac{Q}{K} \right)^r \right)^s \quad (3.5.2-2)$$

where the product term  $\prod a_j^{-\nu_j}$  is reduced to include only the pH dependence of the rate coefficient, and the affinity expression is simplified and re-expressed in terms of the saturation index (Q/K) of the dissolving solid. This form of rate law is commonly used as an expression to which experimental elemental release data are fitted (i.e., values of k, K, r, and s are determined by regression of experimental data).

Current modeling codes may further simplify Eq. 3.5.2-2. GLASSOL assumes no solution compositional dependence of k, which is assumed to vary only with temperature. DISSOL, EQ3/6, LIXIVER, and REACT treat k as a function of both pH and T. No models account for any further dependencies of k on solution composition as indicated in Eq. 3.5.2-1.

To use Eq. 3.5.2-2 to predict glass-dissolution rates, one must assume what phase becomes saturated in order to evaluate the Q/K term. Several phases have been tried, ranging from the initial, unreacted glass composition (Bourcier, 1990; Advocat et al., 1990) to the composition of the alkali-depleted surface layer (Bourcier et al., 1990) to simple hypothetical silica (Grambow, 1987; Advocat et al., 1991; Vernaz and Dussossoy, 1992; Michaux et al., 1992). It is clear from these modeling studies that using the unreacted glass composition gives results that deviate from experimental observations (see subsequent text). However, the other two approaches give comparable agreement with experiments.

### 3.5.2.2.2 Secondary Phases

Precipitation of secondary phases takes place as glasses dissolve and the concentrations of species build up in solution. Geochemical modeling codes used to model glass dissolution incorporate algorithms that track saturation states for these possible mineral phases and predict, based on mineral thermodynamic data, the most stable phase assemblage. The types and amounts of phases are continually adjusted during the reaction path calculation to maintain the most stable phase assemblage. While this approach works well for simulations of high-temperature-hydrothermal systems, experience has shown that this approach often leads to

incorrect phase-assemblage predictions for the lower temperature (<150°C) glass-dissolution tests (Bruton, 1988; Bourcier, 1990). Thermodynamically less stable phases tend to precipitate instead.

Alternative methods of predicting secondary phases have therefore been used in the simulations. One method, termed "inverse modeling," uses the measured-solution composition to identify which phases are near saturation (Grambow and Strachan, 1988). These phases are assumed to be those actively precipitating and controlling the solution composition, and only these phases are allowed to precipitate during the glass reaction. Another approach is to simply restrict the database of mineral phases allowed to precipitate to those actually observed experimentally. Obviously, neither approach has any predictive capability for secondary phases, but no reliable theory is currently available to enable predictions of the most likely secondary phases in these complex systems (see Steefel and Van Cappellen [1990] for a new approach).

### 3.5.2.2.3 Ion Exchange

The formation of secondary phases is the primary cause for the observed nonstoichiometric release of elements during glass dissolution. The formation of an alkali-depleted surface layer also contributes to nonstoichiometric release and affects the pH of the solution through ion-exchange reactions:



Similar reactions take place for other alkalis, including lithium, potassium, and cesium. The ion-exchanged zone has variable thickness depending on the glass composition and test conditions but is generally 1 to 10 microns thick. The net effect of the ion-exchange reaction is to raise the pH of the surrounding solution. The pH effect is larger as the surface area to volume (SA/V) ratio of the test increases.

Although the ion-exchange process is complex and involves diffusion of ions and water through a partially hydrated and inhomogeneous medium, the chemical effect of the process can be modeled simply. Unless the ion-exchange process is rate-limiting, only the chemical effects need to be incorporated into the model. A simple method for incorporating this effect first suggested a few years ago (Strachan et al., 1990) was recently reported (Bourcier et al., 1993a). In this approach, an ion-exchange reactant is used in addition to the glass reactant in the simulation. This ion-exchange reactant is composed only of the elements released during ion exchange. The mass of this reactant is fixed by the experimentally measured thickness of the ion-exchanged zone. The reactant is allowed to react rapidly at first to simulate the rapid, initial formation of an ion-exchanged zone. The predicted pH and elemental concentration of species using this method agree fairly well with experimental results. The results also show that inclusion of ion-exchange effects is only necessary for simulations of fairly high SA/V ratio.

#### 3.5.2.2.4 Transport-Limited Corrosion

Experimental evidence suggests that, under certain flow-through test conditions, the dissolution rate of some glasses is controlled by transport. Grambow (1987) has hypothesized that it is the transport of silica through the surface alteration layers that is rate-limiting. The transport-limited rate is modeled by a simple diffusion law:

$$r_t = \frac{D}{L}(a_s - a_b) + r_{fin} \quad (3.5.2-4)$$

where ( $r_t$ ) is the dissolution rate,  $D$  and  $L$  are the diffusion constant and thickness of the hydrous alteration layer, ( $a_s - a_b$ ) is the dissolved silica concentration gradient across the layer from the surface ( $s$ ) to the bulk solution ( $b$ ).  $r_{fin}$  is the "final rate," an experimentally estimated empirical parameter to account for the observed finite rate of glass reaction even at "saturation" where using Eq. 3.5.2-1 would predict zero reaction rate.

The affinity-based rate control (Eq. 3.5.2-2) is combined with this simple diffusion-rate control in the GLASSOL (Grambow, 1987). The model tests whether the rate is controlled by transport or surface reaction and makes the appropriate calculation. The LXIVER code (Delage et al., 1992) has also combined transport and affinity-based rate control. In the LXIVER model, the thickness and rate of silica diffusion through the gel layer control the concentration of silica at the gel layer/solution interface, and this ion concentration is used to evaluate  $Q$  in Eq. 3.5.2-2. This approach assumes that silica diffusion through the gel layer affects the concentration of dissolved silica at the gel/solution interface, thereby coupling the effects of silica transport and affinity rate control.

#### 3.5.2.2.5 Surface Interactions

Dissolved ions present in solution are known to affect glass-dissolution rates. For example, Mg and Zn are known to decrease glass dissolution rates (Barkatt et al., 1989; Tait and Jensen, 1982), while dissolved iron is known to increase it (Lee and Clark, 1986). Current glass-dissolution models account for the effect of dissolved silica on glass dissolution, but do not account for the effects of other ions. Although silica effects are important, and in most cases dominate over the effects of other ions, this is not always the case; it is necessary to provide for these other ions if the model is to be generally applicable. This is especially important in repositories where the effects of species produced from corrosion of other repository materials, such as metals and cements, are available to interact with the dissolving waste forms.

Three general mechanisms by which dissolved species affect glass alteration rates have been proposed:

1. Ions sorb onto the dissolving glass surface and affect the strength of the Si-O bonds at the glass surface (see Figure 3.5.2-3). It is the hydrolysis of these bonds that controls the overall rate of glass dissolution and radionuclide release. This effect is particularly significant for long-term performance, where the rate at "near-saturation" conditions is likely to be strongly affected by the nature of the glass-solution interface, and therefore the types and concentrations of sorbed species, and the surface charge. Some attempts have been made to understand and model deviations in dissolution behavior believed to be due to surface complex formation (Lee and Clark, 1986; McVay and Buckwalter, 1983; Bart et al., 1987; Grambow et al., 1986; Andriambololona et al., 1992)
2. Dissolved species react with the glass surface to form a protective layer. The protective layer armors the glass surface and reduces the rate of further attack. The overall dissolution process then becomes rate-limited by transport through the protective layer. It is believed that magnesium affects glass dissolution through this process (Barkatt, 1989).
3. Colloids are formed by reaction with the dissolved ion in question and species dissolving from the glass. An example of this is iron. Dissolved iron reacts with silica from the dissolving glass to form iron-silica colloids. The silica-containing colloids act as a sink for silica and maintain a low dissolved-silica concentration in solution. This effectively reduces the glass saturation state and causes the glass-dissolution rate to remain high (see Eq. 3.5.2-1). Note that these colloids will also tend to sorb actinide species and pose a potential migration pathway for otherwise insoluble actinide species.

Qualitative data for the effects of several dissolved metals on glass durability are listed in Table 3.5.2-1. This table summarizes a broad variety of data from experiments that, in many cases, are difficult to interpret because supporting data are lacking. Many of the studies, for example, do not report pH. In some cases, the data conflict; the same dissolved species may cause the dissolution rate to increase in one type of test and decrease in another. In other cases, the glass-dissolution rate may change with time. An aqueous component that first decreases glass-reaction rate may later on enhance it (i.e., the case of lead reported by Zwicky et al. [1992]; see table 3.5.2-1 notes). Another complication is that species may only have an effect if at a sufficiently high concentration to cause precipitation of an armoring surface solid, as is apparently the case for magnesium. At low dissolved Mg concentration, Mg has no noticeable effect (Bourcier et al., 1992); at higher concentrations, where the magnesium-silicate phase sepiolite is supersaturated, Mg greatly decreases the glass-reaction rate, presumably because of precipitation of a surficial Mg-silicate phase such as sepiolite.

Note in Table 3.5.2-1 that there is a lack of data for many metals likely to be present in the repository (i.e., alloying metal in stainless steels such as Cr, Mn, Ni, and Mo).

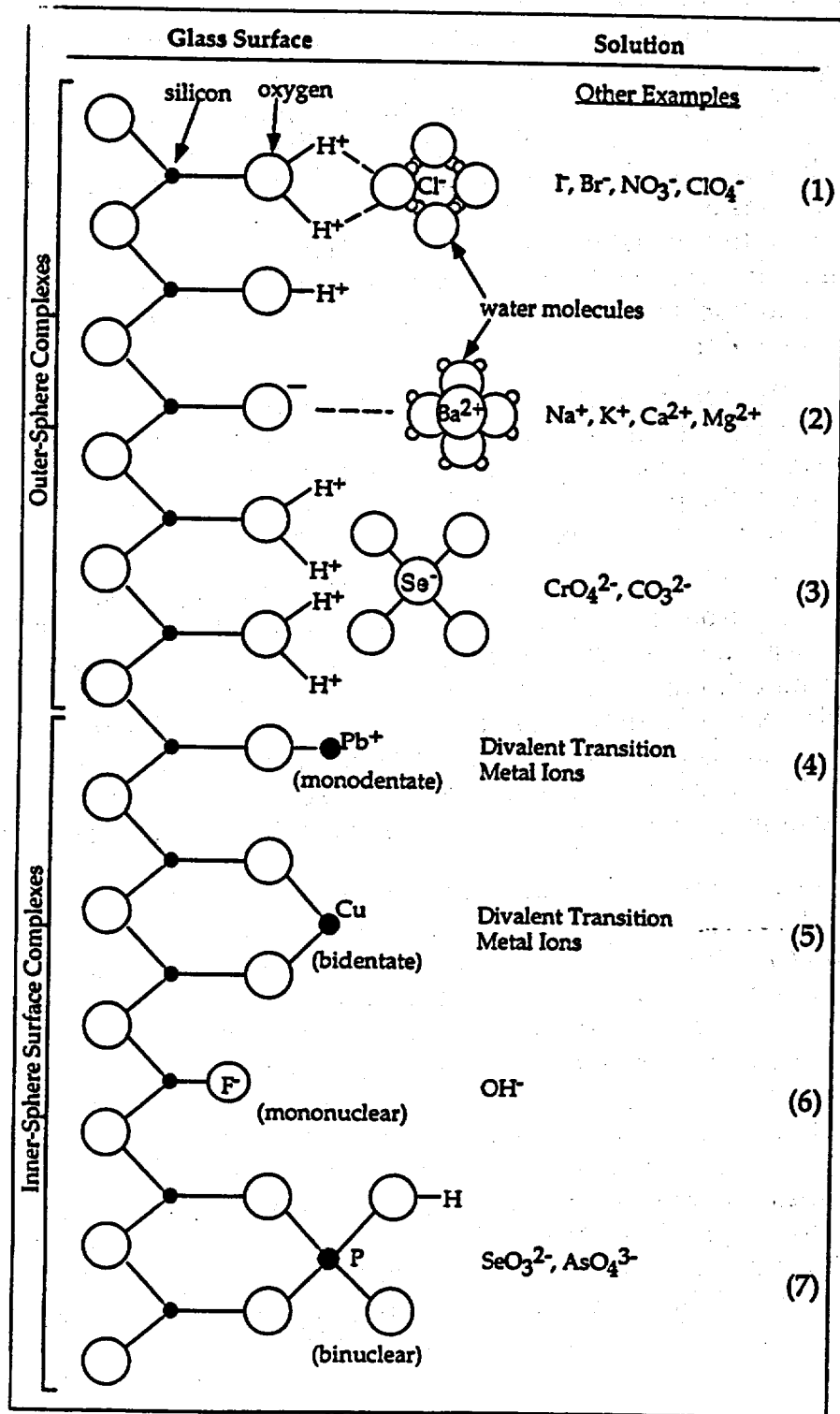


Figure 3.5.2-3 Types of metal complexes on oxide surfaces (Hayes, 1987)

Although this qualitative information is available, it alone is not sufficient for incorporation of these effects into models of glass dissolution. Experiments are needed to identify the mechanisms through which dissolved species affect dissolution rates and to provide the parameters needed to quantify these effects in the glass-dissolution models. Explicit provision for surface interactions will be especially critical to account for coupled effects of glass with other repository materials in performance assessment (PA) calculations.

**Table 3.5.2-1 Effects of dissolved ions on glass-dissolution rate**

Metal	Low pH	Near-Neutral pH	High pH	Reference
B	none	none	unknown	Bourcier et al., 1992
Mg	none	major -	major -	Bourcier et al., 1992; Barkatt et al., 1989; Lee and Clark, 1986; Sang et al., 1994
Ca	none	none	minor -	Bourcier et al., 1992; Lee and Clark, 1986; Oka et al., 1979
Si	none	major -	major -	Bourcier et al., 1992; Lanza et al., 1988
Al	major -	minor -	none/minor +	Bourcier et al., 1992; Lee and Clark, 1986; Zwicky et al., 1992; Buckwalter and Pederson, 1982
Na	unknown	minor -	minor -	Lee and Clark, 1986
Zn	unknown	minor +	major -	Lee and Clark, 1986; Zwicky et al., 1992; Tait and Jensen, 1982
Li	unknown	unknown	minor +	Feng and Barkatt, 1987
Fe	unknown	major/minor +	major +	Bunker and Arnold, 1983; McVay and Buckwalter, 1983; Bart et al., 1987; Bibler and Jantzen, 1987; Burns et al., 1986; Hermansson et al., 1985; Inagaki et al., 1996
Pb	unknown	major -	major -	Bart et al., 1987; Lehman and Kuchinski, 1985; Burns et al., 1986; Zwicky et al., 1992; Buckwalter and Pederson, 1982
Cu	unknown	unknown	none	Buckwalter and Pederson, 1982
Sn	unknown	unknown	none	Buckwalter and Pederson, 1982
Ti	unknown	unknown	none	Buckwalter and Pederson, 1982

Minor = less than factor of 10 effect; major = greater than factor of 10 effect; + means glass dissolution rate is increased, - means rate is decreased; none = no effect observed; unknown = no data or data uninterpretable

### 3.5.2.2.6 Effect of Glass Composition

In current models, the effect of glass composition on glass-dissolution rates is accounted for in two ways. Glass has an intrinsic durability related to its composition and structure; quantification of this property affects the rate parameter,  $k$ , in Eq. 3.5.2-1. The glass composition also affects the value of the equilibrium constant  $K$  in the affinity term of the rate equation. The value of  $K$  used in the model depends on which dissolution reaction is rate-controlling.

Several approaches have been used to try to account for the effect of glass composition on glass-corrosion rate. These include using "hydration theory" (Plodinec et al., 1984; Jantzen and Plodinec, 1984) to calculate both the rate coefficient and the equilibrium constant  $K$  (Grambow, 1984); calculating  $K$  from estimated thermodynamic properties of the surface layer (Bourcier et al., 1990); determining experimentally the rate coefficient from flow-through tests (Knauss et al., 1990); and by empirical fitting to experimental data to determine both  $k$  and  $K$  (Grambow, 1987).

Although the success of hydration theory in correlating glass durability with glass thermodynamic properties has been documented (Jantzen, 1992), the theory has been less successful in making quantitative predictions in glass-corrosion models (Advocat et al., 1990; Bourcier, 1990). When incorporated into glass-corrosion models, the free energies of formation of glasses (which determine the value of  $K$  in Eq. 3.5.2-2) calculated using hydration theory do not predict any slowing of glass-dissolution rate as saturation is approached. The value of  $K$  is predicted to be too large.

Alternatively, Grambow used hydration theory to estimate the rate coefficient in the rate equation (Grambow, 1984) using the expression

$$k_f = X e^{(-E_a/RT)} e^{(-\Delta G_r(\xi)/RT)} \quad (3.5.2-5)$$

where  $E_a$  is the activation energy for dissolution (determined experimentally), and  $\Delta G_r$  is the hydration free energy for the glass-dissolution reaction. The first term in the equation [ $X \exp(-E_a/RT)$ ] is an Arrhenius term that accounts for the effect of temperature on the rate constant. The second term [ $\exp(-\Delta G_r(\xi)/RT)$ ] corrects the rate constant for the effect of glass composition. This approach has had limited success when dealing with the compositional range of real waste glasses. It was eventually dropped from the Grambow model and replaced with experimentally determined values for specific glass compositions.

Another way to apply the hydration free-energy model to glass dissolution is to assume that the rate-limiting step in glass dissolution is the dissolution of the surface, alkali-depleted, hydrous layer. The thermodynamic properties of this layer can be approximated by assuming it is a solid solution of amorphous components

(Bourcier et al., 1990). In this method, the hydration free energy is applied to the surface-alteration layer rather than to the unreacted glass, and the components are chosen to be amorphous rather than crystalline to be structurally and energetically more similar to the amorphous surface layer. This model better predicts the experimental glass-dissolution rates than does the hydration free-energy model applied to the unaltered glass. However, the relation between starting glass composition and glass-dissolution rate in this model is complex. The composition of the alteration layer (which is used to calculate the glass-dissolution affinity and the dissolution rate) is affected by the glass composition and by solution composition. No attempt has yet been made to quantify this effect in the glass-dissolution model. The composition of the alteration layer is determined by analysis of reacted glasses.

#### **3.5.2.2.7 Deviant Glass Dissolution Behavior**

Several studies have shown that glass-dissolution rates may abruptly increase in rate after showing normal behavior over extended periods of time at what appeared to be nearly constant "final" dissolution rates (Barkatt et al., 1991; Ebert et al., 1993; Patyn et al., 1990; Van Iseghem et al., 1992). These rate changes may be accompanied by abrupt changes in pH and the onset of precipitation of new secondary phases. The rate changes are not well understood, but may be related to physical changes in the surface layers (Sang et al., 1993), secondary phase precipitation (Ebert et al., 1993), or as-yet-unidentified processes.

#### **3.5.2.3 Limitations of Current Models**

The most important problems of current models fall into three categories:

1. Most model parameters are obtained from the same experiments as those being modeled.
2. The concept of "silica saturation" lacks precise definition.
3. The long-term release rate is poorly defined and quantified.

These areas need to be addressed with additional experimental and modeling work.

Although the GLASSOL approach has successfully predicted glass-corrosion tests results, some questions have been raised about its suitability for long-term predictions. Curti (1991) used the GLASSOL code to model the dissolution of the French COGEMA and British MW borosilicate glasses (glass produced at British Nuclear Fuel Laboratory) to assess whether GLASSOL can be applied to safety analysis of the Swiss HLW repository. Curti found three areas where improvement was needed before GLASSOL could be suitable for safety analysis:

1. Better accounting for the effects of silica sorption on bentonite backfill
2. Inclusion of provisions for partitioning radionuclides into alteration phases (currently stoichiometric release is assumed)

3. The problem that the final rate of corrosion is poorly defined and has no mechanistic basis

Curti also notes that "a significant drawback of the modeling exercises reported . . . is that the relevant parameters ( $k$ ,  $R_{fin}$ ,  $K$ ) are derived *ad hoc* from the experiment to be modeled."

The most serious limitation of these three is that of estimating, both in terms of providing a mechanism controlling this rate and a numerical value to be used in modeling, the long-term or "final" reaction rate. More recent work by Grambow et al. (1992) illustrates this problem using data from dissolution tests in saline fluids and suggests that the rate control may switch from surface-reaction control to water-diffusion control over long time periods. Clearly, the exact mechanism that controls dissolution rates over long time periods is not yet known.

Godon et al. (1989) have observed that R7T7 glass dissolution in contact with 11 different materials shows no systematic "silica-saturation" level. Although the dissolved silica concentration reaches a nearly constant value in each test, that value varies greatly from test to test depending on the type of additional material present. The silica-saturation level, therefore, is not a parameter related to glass composition only, but also depends on test conditions. The silica-saturation level for a particular test probably results from a balance between the rate of formation of silica-containing secondary phases (including colloids) and the rate of release of silica from the glass. The silica-saturation value ( $K$ ) from Eq. 3.5.2-2 is not a constant for a given glass composition, but will change as a function of test conditions. Thus, long-term predictions based on a constant value of  $K$  in the rate equation are of questionable reliability.

#### 3.5.2.4 Conclusions

It is clear that further progress in developing quantitative, predictive models for glass dissolution depends on obtaining results from systematic, interpretable experiments that confirm and quantify the postulated glass reaction mechanisms. Some work has been done in this area (Trotignon, 1990; Knauss et al., 1990), but much remains to be done. Some specific suggestions for future work are given in Strachan et al. (1994) and include the following:

- Flow-through tests of glasses in continuously stirred reactors with controlled pHs that are designed to measure the rate constant for glass dissolution over a matrix of temperatures, pHs, and glass compositions— Similar tests should be performed in pH-buffer solutions doped with relevant cations and anions to systematically determine the effects of dissolved species on dissolution rate. These tests should be combined with surface titrations to characterize glass-surface speciation.

- **Closed-system tests of a matrix of glass compositions with controlled pH (pH stat) to investigate the effect of glass composition on glass-dissolution rate under conditions in which secondary phases form (unlike the flow-through tests)—These tests should be combined with NMR analysis of unreacted glasses to correlate glass structure and coordination with glass durability, as measured in both the flow-through and the closed-system tests.**
- **Additional closed-system tests where stable secondary phases such as calcite, quartz, and clays are added to control solution composition—The data from these tests should help define and quantify the affinity term in the rate expression.**
- **Molecular orbital calculations of glass-surface speciation and molecular-dynamics simulations of glass-dissolution behavior—These would help constrain macroscopic glass-dissolution models and support validation of proposed dissolution mechanisms.**

In all cases, experiments should include as complete an analysis of both solid and aqueous phases as possible. Too many experiments have been performed in which incomplete characterization of either solids or solution phases have made interpretation of the results ambiguous, both for mechanistic interpretation of the results and for use of results in model validation attempts.

The results of these experimental investigations should be combined with additional model development to produce a workable and sufficiently comprehensive glass-dissolution model for use in repository PA simulations.

### **3.5.2.5 Assessment of Current Methods for Estimating Glass-Dissolution Rates under Silica-Saturated Conditions**

Glass-dissolution rates decrease dramatically as glasses approach saturation with respect to the leachate solution. This effect may lower the dissolution rate to 1/100 to 1/1000 of the unsaturated rate. Although rate controls on glass dissolution are best understood for conditions far from saturation, most repository sites are chosen where water fluxes are minimal; thus, the waste glass is most likely to dissolve under conditions close to saturation. Understanding controls on dissolution rates close to saturation is of greater significance for assessing release rates of radionuclides from repositories than understanding controls on dissolution rates far from saturation.

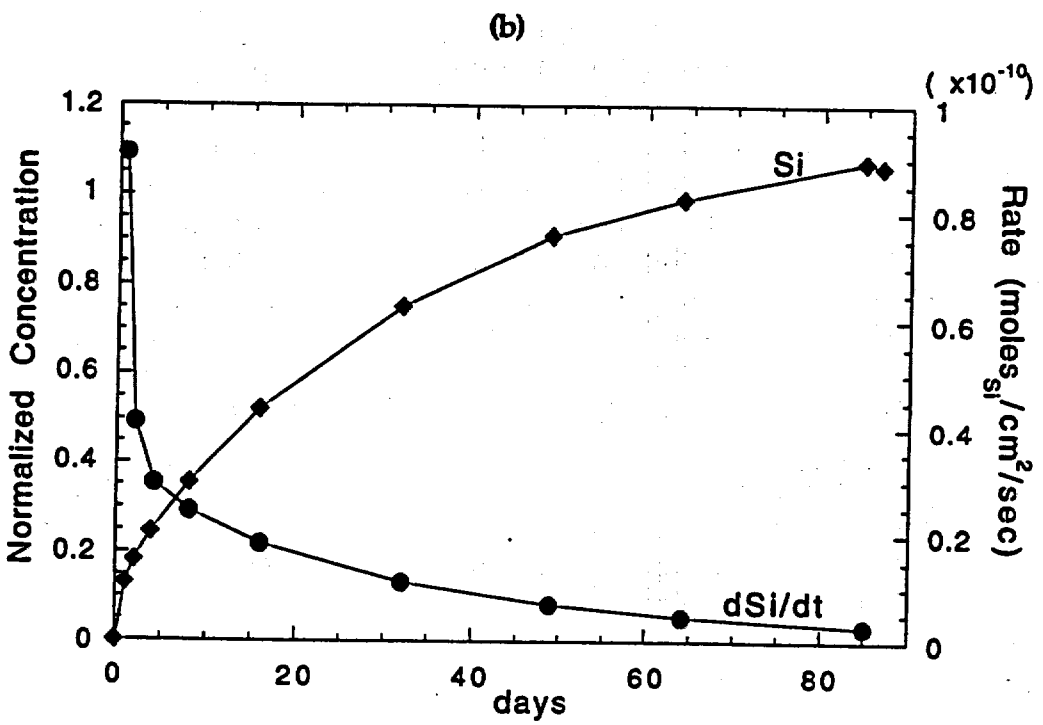
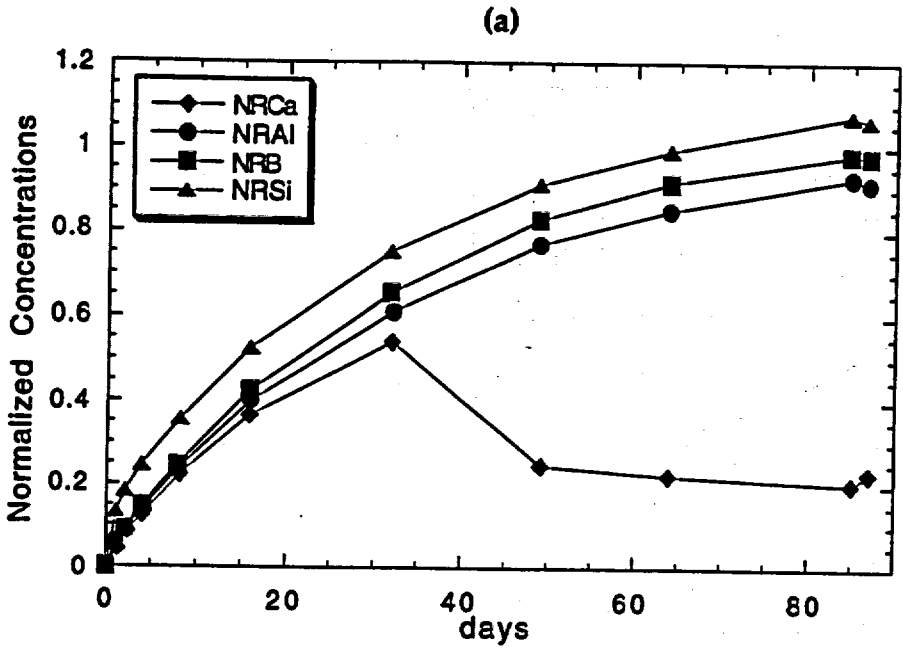
The key term in the rate expression used to predict glass-dissolution rates close to saturation is the affinity term, which accounts for saturation effects on dissolution rates. The form of the affinity term and parameters used to model glass dissolution are clearly critical for accurate estimates of glass performance in a repository.

The concept of saturation with respect to glass dissolution is problematic because of the thermodynamically unstable nature of glass. Saturation implies similar rates of forward (dissolution) and back (precipitation) reactions, but glasses cannot precipitate from aqueous solutions; there can be no back reaction to form glass. However, experiments have shown that, when dissolving, glasses do exhibit saturation effects analogous to saturation effects observed for thermodynamically stable materials. Thus, attempts to model the glass-dissolution process have employed theories and rate equations more commonly used to model dissolution of crystalline solids.

### 3.5.2.5.1 Current Models of Glass Dissolution under Silica-Saturated Conditions

Because glasses are thermodynamically unstable and Eq. 3.5.2-1 is derived for a solid that dissolves reversibly, a factor called the residual rate is sometimes added to the equation to account for observed, slow long-term rates. This gave rise to the concept of "residual affinity" (Grambow and Strachan, 1983) and some attempts to provide a mechanistic basis to predicting long-term rates under near-saturation conditions (Petit et al., 1990; Advocat et al., 1990). These attempts have been unsuccessful. No mechanistically based model for predicting long-term rates based only on dissolved silica concentration or silica diffusion through a surface-alteration layer has been developed that is consistent with all experimental observations. As shown subsequently, the effects of dissolved species such as Al greatly affect mineral-dissolution rates, in some cases changing them by orders of magnitude. The effects of Al would swamp the observed correlation of long-term glass-dissolution rates with silica content in solution.

In addition, the value of  $\sigma$  in Eq. 3.5.2-1 is assumed to equal one. Analysis of the dissolution rate of a simple borosilicate glass as a function of silica concentration depicted in Figure 3.5.2-4 shows that a value of  $\sigma=0.1$  better fits the experimental data. This value is in the range of values of  $\sigma$  reported for kaolinite  $\text{Al}_2\text{Si}_2\text{O}_5(\text{OH})_4$  (Devidal et al., 1992) and amorphous silica (Jørgensen, 1968). This range of values of  $\sigma$  will clearly make a large difference in the calculated value of the dissolution rate close to saturation. Note, however, that the data from Bourcier et al. (1993b), from which a value of  $\sigma=0.1$  was obtained, could be reinterpreted in terms of the effects of increasing Al in solution, using an approach similar to the model of Schott and Oelkers (1995) described subsequently.



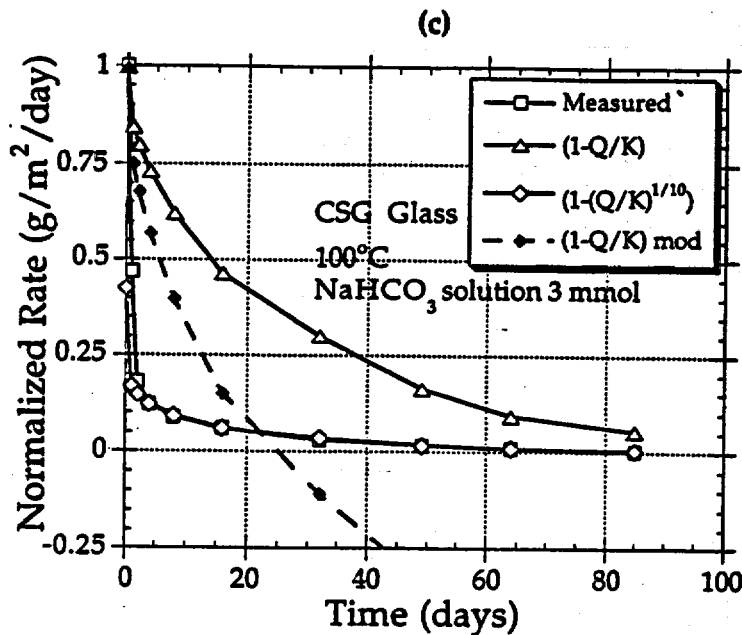


Figure 3.5.2.4

Experimental data for simple SRL-165 glass analog ( $\text{Na}_2\text{O}$  19 mol%,  $\text{CaO}$  7 mol%,  $\text{B}_2\text{O}_3$  8 mol%,  $\text{Al}_2\text{O}_3$  7 mol%,  $\text{SiO}_2$  59 mol%) dissolving in 3 mmol  $\text{NaHCO}_3$  solution at  $100^\circ\text{C}$  in closed system: Plot (a) shows release data for all elements; (b) shows rate of silica release from slope of silica curve in (a) after release data corrected for pH effect on rate constant and solution volume changes due to sampling. Plot (c) shows attempted fit to data using various affinity functions where both  $\sigma$  and  $K$  were allowed to vary. Best fit is obtained when  $\sigma = 0.1$  ( $n = 10$ ) and  $\log K$  is  $-3.1$  (data are open boxes; calculated values are open diamonds). Open triangles show curve for  $\sigma = 1$ .

Much recent experimental work on silicate mineral-dissolution rates close to saturation are also inconsistent, with simple affinity control following Eq. 3.5.2-1 (Nagy et al., 1991; Burch et al., 1992; Dove and Elston, 1992; Gin, 1996; Schott and Oelkers, 1995; Berger et al., 1994a, 1994b; Oelkers et al., 1994). In fact, only quartz dissolution has been successfully modeled with this approach. It is clear that the glass-dissolution process is more complicated than any model based entirely on Eq. 3.5.2-1.

### 3.5.2.5.2 Needed Improvement in the Current Models

Although the current, simple models can predict glass-dissolution rates reasonably well in dilute, weakly alkaline solutions typical of groundwaters in repositories, the models fail badly under conditions that deviate significantly from those in the site-specific tests where rate measurements were made. Recent experimental data for glasses (Gin, 1996; Berger et al., 1994b; Bourcier et al., 1992) and analogous aluminosilicate minerals (Devidal et al., 1992; Oelkers et al., 1994;

(Berger et al., 1994a; Burch et al., 1992) show rate dependencies that cannot be explained entirely by changing silica concentration, or even as functions of reaction affinity. Numerous papers show the importance of species other than dissolved silica affecting the dissolution rates of silicate minerals. Alkalis such as sodium and dissolved lead increase the rate of quartz dissolution (Dove and Elston, 1992; Berger et al., 1994a). Aluminum dramatically affects dissolution rates of borosilicate waste glass (Gin, 1996), kaolinite (Devidal et al., 1992), and albite (Oelkers et al., 1994). Flow-through tests of simulated radioactive waste glasses and simple analog composition glasses (Bourcier et al., 1992) show that dissolved aluminum decreases glass-dissolution rates, with the effect being larger at lower pHs (Figure 3.5.2-5). In the same tests, dissolved silica lowered glass dissolution rates above pH 7, but had little effect below pH 7. Dissolved Mg and Ca had no effect at any pH tested when present at 2.5 mmolal concentrations. Clearly the effects of other dissolved species need to be included in the glass-dissolution model.

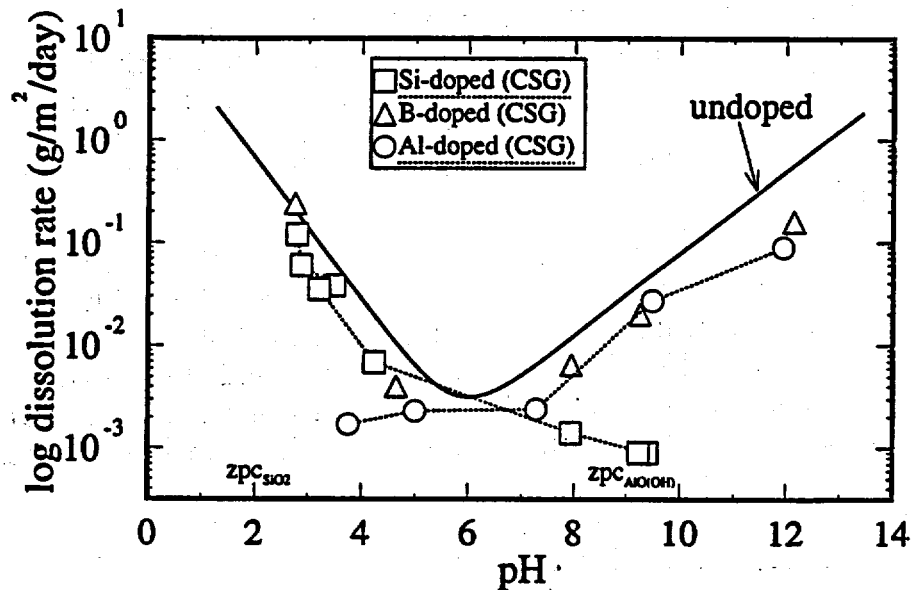


**Figure 3.5.2-5** Dissolution rates of a simplified five-component analog of SRL-165 glass measured in flow-through reactors in pH-buffered solutions doped with 2.5 mM  $\text{Al}(\text{ClO}_4)_3$ , 2.5 mM  $\text{B}(\text{OH})_3$ , and 2.5 mM  $\text{K}_2\text{SiO}_3$ . V-shaped line is regression to data for this glass in undoped buffers. Dissolution rates are decreased by dissolved Si at high pHs, and rates are lowered due to the presence of dissolved Al at low pHs (Bourcier et al., 1992).

For glasses, some observed deviations from simple rate control by  $\text{SiO}_2(\text{aq})$  were explained by assuming rate control by silica concentrations at the glass-water contact inside a surface gel layer (Grambow, 1987). Silica diffusion through this gel layer controlled the silica concentration at the contact, and the silica concentration at the contact controlled the glass-dissolution rate. By combining this mechanism with the

rate law of Eq. 3.5.2-1, Grambow was able to explain observed maxima in flow-through glass-dissolution tests and regress physically reasonable values for the diffusion constant for  $\text{SiO}_2$  in this gel layer. But even with this added term, the model still cannot predict results of recent experiments, particularly experiments that show significant effects of dissolved aluminum (Gin, 1996).

### 3.5.2.5.3 Glasses Versus Crystalline Silicates

Many similarities and parallels between the dissolution behavior of silicate glasses and the dissolution behavior of silicate minerals suggest that recent developments in surface-complexation models for crystalline silicates can be applied to silicate glasses as well. Figure 3.5.2-6 shows dissolution rates versus pH for albite glass versus albite mineral at  $70^\circ\text{C}$ . For both crystalline albite and albite glass, the pH dependence of the rate is identical. However, the glass dissolves one to one-and-one-half orders of magnitude faster than the mineral. As noted previously, the dissolving solid that is rate-limiting for glass-water reactions is an alkali-depleted, partially repolymerized hydrous material. A similar type of material exists on the surface of dissolving minerals such as albite, where several surface techniques have consistently shown a sodium-depleted, partially hydrated layer at the albite-water interface (Hellmann et al., 1990; Casey et al., 1988). The observed layer thickness for albite at near-neutral pHs is 1 to 90 nm, whereas for typical borosilicate waste glasses it is a thicker 10 to 200 nm.

Similar hydrous layers are likely present on other reacting silicate minerals; if they are not observed, it is likely the same mechanisms are operating with both glasses and minerals but at different rates (Petit et al., 1989). For both glasses and minerals, the water contacts an alkali-depleted, partially hydrated surface where the rate-limiting hydrolysis reaction takes place. For all these reasons, it is clear that the basic framework for understanding dissolution-rate control for both silicate glasses and silicate minerals is the same.

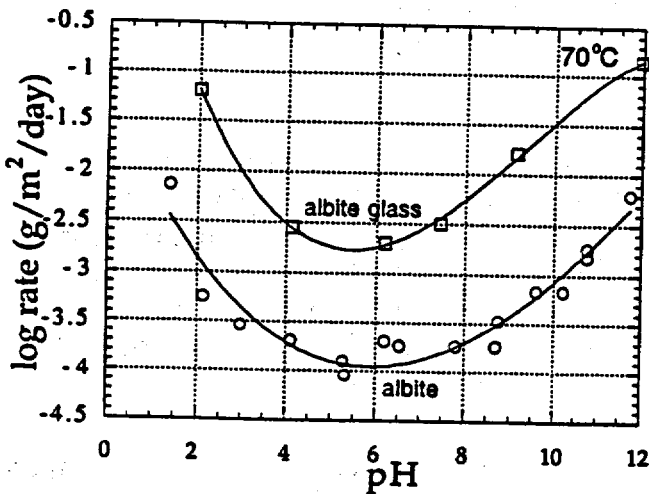


Figure 3.5.2-6 Comparison of dissolution rates of crystalline albite vs. albite glass in flow-through reactor at  $70^\circ\text{C}$  (unpublished data) (Bourcier, 1997)

#### 3.5.2.5.4 Dissolution Models for Silicate Minerals

Recent work in developing a mechanistic understanding of silicate mineral dissolution has generated dissolution models with specific provisions for the effects of adsorbed surface species on activated complex. From their data on albite dissolution kinetics, Schott and Oelkers (1995) have proposed a model for aluminosilicate mineral dissolution that includes a functional dependency of dissolved Al on dissolution rates of silicate and aluminosilicate minerals. They propose that the dissolution rate for most silicate minerals is rate-limited by a silica-rich, precursor complex. The dissolution rate is proportional to its concentration. An increase in Al in solution increases the number of Al-rich complexes on the surface of aluminosilicate minerals, thereby lowering the dissolution rate by decreasing the concentration of the silica-rich precursors. Their rate equation, which incorporates this effect, can successfully predict a wide variety of data from several silicate and aluminosilicate minerals.

A similar modeling approach was developed previously by Berger et al. (1994a) for quartz dissolution in solutions containing dissolved lead and sodium. They proposed a surface-complexation model in which changes in dissolution rates are caused by changes induced in the surface structure due to ionic adsorption. Inner sphere complexes generally decrease rate, outer sphere ionic complexes do the opposite, but both effects change in magnitude in response to pH and reaction affinity. The effects become less significant close to saturation because of competition between electrolyte and silica adsorption on the surface.

It is clear that no comprehensive and generally accepted model exists that explains the existing dissolution data for silicates. But the models that have been proposed are converging on a modified rate law formulation that includes the effects of adsorbed species and accounts for their effects on some rate-limiting, precursor complex. Future experimental studies on glass dissolution should focus on experiments that are explicitly designed to test these models (i.e., Gin [1996] and Berger et al. [1994b]).

#### 3.5.2.5.5 Conclusions

Interpretations of experimental data on the dissolution behavior of silicate glasses and silicate minerals indicate the following:

- Simple affinity control (Eq. 3.5.2-1) does not explain the observed dissolution-rate data for silicate minerals or glasses.
- Dissolution rates can be significantly modified by dissolved cations even under conditions far from saturation where the affinity term is near unity.
- The effects of dissolved species such as Al and Si on the dissolution rate vary with pH, temperature, and saturation state.

- As temperature is increased, the effect of pH and temperature on glass and mineral-dissolution rates decrease, which strongly suggests a switch in rate control from surface, reaction-based (affinity control) to diffusion control (Guy and Schott, 1989; Berger et al., 1994b; Vernaz et al., 1988); this is also consistent with the relative magnitudes of their activation energies ( $E_{diff} < E_{affinity}$ ).

Borosilicate glass-dissolution models need to be upgraded to account for these recent experimental observations. Most important of these are the effects of dissolved species that can sorb on the glass surface and either increase or decrease the dissolution rate. The glass model should be based on current dissolution models for aluminosilicate minerals that are based on a modified transition-state theory rate equation, which specifically accounts for the existence and stoichiometry of a rate-limiting precursor complex. The effects of ionic strength and inner and outer sphere surface complexes must be included in a robust model to predict glass-dissolution rates under repository conditions.

The model for glass dissolution must eventually be incorporated into waste form PA codes. These codes do not generally calculate values for all the parameters that will be needed by any rigorous glass-dissolution submodel. Thus, to simplify submodels of these complex models are needed for inclusion in the PA codes.

### 3.5.2.6 References

- Aagaard, P., and H. C. Helgeson (1982). "Thermodynamic and kinetic constraints on reaction rates among minerals and aqueous solutions I. Theoretical considerations." *Am. J. Sci.* 282:237-285. [HQS.19880517.2373]
- Abrajano, T., J. K. Bates, W. L. Ebert, and T. Gerding (1986). *The effect of gamma radiation on groundwater chemistry and glass leaching as related to the NNWSI repository site.* (SANL-510-001) Argonne, IL: Argonne National Laboratory. [202939]
- Abrajano, T. A., and J. K. Bates (1987). "Transport and reaction kinetics at the glass:solution interface region: results of repository-oriented leaching experiments." In proceedings from Materials Research Society Symposium. 84:533-546. [NNA.19900620.0006]
- Abrajano, T. A., J. K. Bates, A. K. Woodland, J. K. Bradley, and W. L. Bourcier (1990). "Secondary phase formation during nuclear waste-glass dissolution." *Clays and Clay Min.* 38(5):537-548. [NNA.19910903.0114]
- Advocat, T., J. L. Crovisier, B. Fritz, and E. Vernaz (1990). "Thermokinetic model of borosilicate glass dissolution: contextual affinity." In proceedings from Materials Research Society Symposium. 176:241-248.
- Advocat, T., J. L. Crovisier, E. Vernaz, G. Ehret, and H. Charpertier (1991). "Hydrolysis of R7T7 nuclear waste glass in dilute media: Mechanisms and rate as a function of pH." In proceedings from Materials Research Society Symposium. 212:57-64.

- Andriambololona, Z., N. Godon, and E. Vernaz (1992). "R7T7 glass alteration in the presence of mortar: Effect of the cement grade." In proceedings from Materials Research Society Symposium. 257:151-158.
- Barkatt, A., A. Olszowka, W. Sousanpour, M. A. Adel-Hadadi, R. Adiga, A. Barkatt, G. S. Marbury, and S. Li (1991). "Leach rate excursions in borosilicate glasses: effects of glass and leachant composition." In proceedings from Materials Research Society Symposium. 212:65-76.
- Barkatt, A., E. E. Saad, R. Adiga, W. Sousanpour, A. Barkatt, and M. A. Adel-Hadadi (1989). "Leaching of natural and nuclear waste glasses in sea water." *Appl. Geochem.* 4:593-603. [NNA.19910424.0078]
- Bart, G., H. U. Zwicky, E. T. Aerne, T. Graber, D. Z'Berg, and M. Tokiwai (1987). "Borosilicate glass corrosion in the presence of steel corrosion products." In proceedings from Materials Research Society Symposium. 84:459-470.
- Berger, G., E. Cadore, J. Schott, and P. Dove (1994a). "Dissolution of quartz in lead and sodium chloride solutions between 25 and 300°C: Effect of the nature of surface complexes and reaction affinity." *Geochim. Cosmochim. Acta* 58(2):541-551.
- Berger, G., C. Claparols, C. Guy, and V. Daux (1994b). "Dissolution of a basalt in silica-rich solutions: Implications for long-term alteration." *Geochim. Cosmochim. Acta* 58(22):4875-4886.
- Bibler, N. E., and C. M. Jantzen (1987). "Materials interactions relating to long-term geologic disposal of nuclear waste glass." In proceeding from Materials Research Society Symposia. 84:47-66.
- Bourcier, W. L. (1990) *Geochemical modeling of radioactive waste glass dissolution using EQ3/6: Preliminary results and data needs.* (UCID-21869) Livermore, CA: Lawrence Livermore National Laboratory. [NNA.19900501.0161]
- Bourcier, W. L. (1997). "Affinity Functions for Modeling Glass Dissolution Rates." In proceedings from CEA-Valrho Summer Workshop. Méjannes-le-Clap, France: August 31-September 7, 1997. Also UCRL-JC-131186 for Lawrence Livermore National Laboratory, Livermore, CA.
- Bourcier, W. L., W. L. Ebert, and X. Feng (1993a). "Modeling surface area to volume effects on borosilicate glass dissolution." In proceedings from Materials Research Society Symposium. 294:577-582.
- Bourcier, W. L., S. A. Carroll, B. L. and Phillips (1993b). "Constraints on the affinity term for modeling long-term glass-dissolution rates." In proceedings from Materials Research Society Symposium. Boston, MA: November 29-December 3, 1993. Also UCRL-JC-116132 for Lawrence Livermore National Laboratory. [NNA.19940516.0093]

Bourcier, W. L., D. Peiffer, K. Knauss, K. McKeegan, and D. Smith (1990). "A kinetic model for borosilicate glass dissolution based on the dissolution affinity of a surface reaction layer." In proceedings from Scientific Basis for Nuclear Waste Management XIII. Materials Research Society. 176:209-216. [NNA.19900522.0148]

Bourcier, W. L., H. C. Weed, S. N. Nguyen, J. K. Nielsen, L. Morgan, L. Newton, and K. G. Knauss (1992). "Solution compositional effects on dissolution kinetics of borosilicate glass." In proceedings from Seventh Annual Water-Rock Conference. p. 81-84.

Bruton, C. J. (1988). "Geochemical simulation of dissolution of West Valley and DWPF glasses in J-13 water at 90°C." In proceedings from Materials Research Society Symposium. 112:607-619. Also UCRL-96703 for Lawrence Livermore National Laboratory, Livermore, CA. [NNA.19891026.0021]

Buckwalter, C. Q., and L. R. Pederson (1982). "Inhibition of nuclear waste glass leaching by chemisorption." *J. Am. Cer. Soc.* 65:431-436.

Bunker, B. C., and G. W. Arnold (1983). "The effect of solution pH and ion concentrations on leaching of silicate glass." In proceedings from Materials Research Society Symposium. 15:151-158.

Bunker, B. C., D. R. Tallant, T. J. Headley, G. L. Turner, and R. J. Kirkpatrick (1988). "The structure of leached sodium borosilicate glass." *Phys. Chem. of Glasses* 29:106-120. [NNA.19900215.0017]

Burch, T. E., K. L. Nagy, and A. C. Lasaga (1992). "Free energy dependence of albite dissolution kinetics at 80°C, pH 8.8." *Chem. Geol.* 105:137-162.

Burns, D. B., B. H. Upton, G. G. Wicks (1986). "Interactions of SRP waste glass with potential canister and overpack metals." *J. Noncryst. Solids.* 84:258-267.

Casey W. H., H. R. Westrich, and G. W. Arnold (1988). "Surface chemistry of labradorite feldspar reacted with aqueous solution at pH=2, 3 and 12." *Geochim. Cosmochim Acta* 52:2795-2807.

Chick, L. A., and L. R. Pederson (1984). "The relationship between layer thickness and leach rate for nuclear waste glasses." In proceedings from Materials Research Society Symposium. 26:635-642. [HQZ.19870131.6438]

Curti, E. (1991). *Modelling the dissolution of borosilicate glasses for radioactive waste disposal with the PHREEQE/GLASSOL code: theory and practice.* Würenlingen, Germany: Paul Scherrer Institute.

Delage, F., D. Ghaleb, J. L. Dussossoy, O. Chevallier, and E. Vernaz (1992). "A mechanistic model for understanding nuclear waste." *J. Nucl. Mat.* 90:191-197.

Devidal, J. L., J. L. Dandurand, and J. Schott (1992). "Dissolution and precipitation kinetics of kaolinite as a function of chemical affinity (T = 150°C, pH = 2 and 7.8)." *Water-Rock Interaction.* Y. K. Kharaka and A. S. Maest (Eds.) Rotterdam, The Netherlands: Balkema. p. 93-96.

- Dove, P. M., and S. F. Elston (1992). "Dissolution kinetics of quartz in sodium chloride solutions: Analysis of existing data and a rate model for 25°C." *Geochim. Cosmochim. Acta* 56:4147-4156. [235345]
- Ebert, W. L., J. K. Bates, E. C. Buck, and C. R. Bradley (1993). "Accelerated glass reaction under PCT conditions." In proceedings from Materials Research Society Symposium. 294:569-576.
- Feng, X., and A. Barkatt (1987). "Effects of aqueous phase composition on the leach behavior of nuclear waste glasses." In proceedings from Materials Research Society Symposia. 84:519-531.
- Gin, S. (1996). "Control of R7T7 nuclear glass alteration kinetics under saturation conditions." In proceedings from Materials Research Society Symposium. 412:189-196.
- Godon, N., E. Vernaz, J. H. Thomassin., and J. C. Touray (1989). "Effect of environmental materials on aqueous corrosion of R7T7 glass." In proceedings from Materials Research Society Symposium. 127:97-104.
- Grambow, B. (1984). "Ein physikalische-chemisches Modell für den Mechanismus der Laskorrosion—unetr besonderer Berücksichtigung simulierter radioaktiver Abfallgläser." Ph.D. thesis. Berlin, Germany: Freien Universität Berlin. [225985]
- Grambow, B. (1987). Nuclear waste glass dissolution: Mechanism, model and application. (87-02) Stockholm, Sweden: JSS Project, Swedish Nuclear Fuel and Waste Management Co. [NNA.19900215.0035]
- Grambow, B., W. Lutze, and R. Müller (1992). "Empirical dissolution rate law for the glass R7T7 contacting halite- and silica-saturated brines." In proceedings from Materials Research Society Symposium. 257:143-150.
- Grambow, B., and D. Strachan (1983). "Leach testing of waste glasses under near-saturation conditions." In proceedings from Materials Research Society Symposium. 26:623-634. [NNA.19870406.0329]
- Grambow, B., and D. M. Strachan (1988). *A comparison of the performance of nuclear waste glasses by modeling.* (PNL-6698) Richland, WA: Pacific Northwest Laboratory. [NNA.199000215.0036]
- Grambow, B., H. U. Zwicky, G. Bart, I. K. Björner, and L. O. Werme (1986). "Modeling the effect of iron corrosion products on nuclear glass performance." In proceedings from Materials Research Society Symposium. 84:471-481. [HWS.19880517.2449]
- Guy, C., and J. Schott (1989). "Multisite surface reaction versus transport control during hydrolysis of a complex oxide." *Chem. Geol.* 78:181-204.
- Hayes, K. F. (1987). "Equilibrium, spectroscopic, and kinetic studies of ion adsorption at the oxide/aqueous interface." Ph.D. thesis. Stanford, CA: Stanford University. [223485]

- Hellmann, R., C. M. Eggleston, M. F. Hochella, and D. A. Crerar (1990). "The formation of leached layers on albite surfaces during dissolution under hydrothermal conditions." *Geochim. Cosmochim. Acta* 54:1267-1281.
- Hermansson H. P., H. Christensen, I. K. Björner, L. Werme, and D. E. Clark (1985). "Variables affecting the leaching of Swedish nuclear waste glasses." *Nucl. Chem. Waste Manag.* 5:315-332.
- Inagaki Y., A. Ogata, H. Furuya, K. Idemitsu, T. Banba, and T. Maeda (1996). "Effects of redox condition on waste glass corrosion in the presence of magnetite." In proceedings from Materials Research Society Symposium. 412:257-264.
- Jantzen, C. M. (1992). "Thermodynamic approach to glass corrosion." *Corrosion of Glass, Ceramics, and Ceramic Superconductors*. D. E. Clark and B. K. Zaitos (Eds.) Park Ridge, NJ: Noyes Publications. p. 153-215.
- Jantzen, C. M., and M. J. Plodinec (1984). "Thermodynamic model of natural, medieval, and nuclear waste glass durability." *J. Non-Crys. Solids*. 67:207-223. [NNA.19900215.0045]
- Jørgensen, S. S. (1968). "Solubility and dissolution kinetics of precipitated amorphous silica in 1 M NaClO<sub>4</sub> at 25°C." *Acta Chem. Scand.* 22:335-341.
- Klein, L. C. (1986). "Natural glasses in Howardites and Chondrites (Meteorites)." *Advances in Ceramics*, Vol. 20. Westerville, OH: American Ceramic Society. p. 693-698.
- Knauss, K. G., W. L. Bourcier, K. D. McKeegan, C. I. Merzbacher, S. N. Nguyen, F. J. Ryerson, D. K. Smith, H. C. Weed, and L. Newton (1990). Dissolution kinetics of a simple analogue nuclear waste glass as a function of pH, time, and temperature. In proceedings from Materials Research Society Symposium. 176:371-381. Also UCRL-101112 for Lawrence Livermore National Laboratory, Livermore, CA. [NNA.19900320.0195]
- Lanza, F., A. Manara, L. Mammarella, P. Blasi, and G. Ceccone (1988). "Borosilicate HLW glass leaching in silica-saturated solution. In proceedings from Materials Research Society Symposium. 112:685-691.
- Lasaga, A. C. (1984). "Chemical kinetics of water-rock interactions." *J. Geophys. Res.* 89(B6):4009-4025. [NNA.1990216.0060; NNA.19921103.0016]
- Lee, C. T., and D. E. Clark (1986). "Effects of solution cations on waste glass leaching." *Advances in Ceramics*, Volume 20. Westerville, OH: American Ceramic Society. p. 541-550.
- Lehman, R. L., and F. A. Kuchinski (1985). "The effect of various lead species on the leaching behavior of borosilicate waste glass." In proceedings from Materials Research Society Symposium. 44:179-186.
- McVay, G. L., and C. Q. Buckwalter (1983). "Effect of iron on waste-glass leaching." *J. Amer. Ceram. Soc.* 66(3):170-174. [NNA.19900306.0097]

- Mendel, J. E. (1984). *Final Report on the Defense High Level Waste Leaching Mechanisms Program.* (PNL-5157) Richland, WA: Pacific Northwest Laboratory. [HQS.19880517.2498]
- Michaux, L., E. Mouche, and J.-C. Petit. (1992). "Geochemical modeling of the long-term dissolution behavior of the French nuclear glass R7T7." *Appl. Geochem.* 1(Special Issue):41-54.
- Murakami, T., R. C. Ewing, and B. C. Bunke (1988). "Analytical electron microscopy of leached layers on synthetic basalt glass." In proceedings from Materials Research Society Symposium. 112:737-748. [NNA.19900306.0106]
- Nagy, K. L., A. E. Blum, and A. C. Lasaga (1991). "Dissolution and precipitation kinetics of kaolinite at 80°C and pH 3: the dependence on solution saturation state." *Amer. J. Sci.* 291:649-686. [MOL.19980429.0735]
- Oelkers, E. H., J. Schott, and J.-L. Devidal. (1994). "The effect of aluminum, pH, and chemical affinity on the rates of aluminosilicate dissolution reactions." *Geochim. Cosmochim. Acta* 58(9):2011-2024. [236030]
- Oka, Y., K. S. Ricker, and M. Tomozawa (1979). "Calcium deposition on glass surface as an inhibitor to alkaline attack." *J. Am. Cer. Soc.* 62:631-632.
- Oversby, V. M., and D. L. Phinney (1992). "The development of surface alteration layers on SRL-165 nuclear waste glasses." *J. Nucl. Mat.* 190:247-268.
- Palmer, H. C., K. Tazaki, W. S. Fyfe, and Z. Zhou (1988). "Precambrian Glass." *Geol.* 16:221-224. [NNA.19900215.0061]
- Patyn, J., P. Van Iseghem, and W. Timmermans (1990). "The long-term corrosion and modeling of two simulated Belgian reference high-level waste glasses—Part II." In proceedings from Materials Research Society Symposium. 176:299-307.
- Petit, J. C., J. C. Dran, G. Della Mea, and A. Paccagnella (1989). "Dissolution mechanisms of silicate minerals yielded by intercomparison with glasses and radiation damage studies." *Chem. Geol.* 78:219-227.
- Petit, J. C., M. C. Magonthier, J. C. Dran, and G. Della Mea (1990). "Long-term dissolution rate of nuclear glasses in confined environments: Does a residual chemical affinity exist?" *J. Mat. Sci.* 25:3048-3052.
- Phillips, B. L. (1993). "Preliminary NMR investigation of sodium borosilicate and analogue SRL waste glasses." *ANL Technical Support Program for DOE Environmental Restoration and Waste Management. Annual Report October 1991-September 1992.* (ANL-93/13) J. K. Bates (Ed.) Argonne, IL: Argonne National Laboratory. p. 153-164. [NNA.19930907.0056]
- Plodinec, M. J., C. M. Jantzen, and G. G. Wicks (1984). "Stability of radioactive waste glasses assessed from hydration thermodynamics." In proceedings from Materials Research Society Symposium. 26:755-762. [NNA.199090215.0065]

- Sang, J. C., A. Barkatt, I. G. Talmy, and M. K. Norr (1993). "Increases in leach rate due to possible cracking in silicate glasses." In proceedings from Materials Research Society Symposium. 294:583-589.
- Sang, J. C., Y. Guo, A. Barkatt, M. A. Adel-Hadadi, G. S. Marbury, and A. A. Barkatt (1994). "Dissolution mechanism of soda-lime silicate glass and of PNL 76-68 in the presence of dissolved Mg." In proceedings from Materials Research Society Symposium. 333:519-524.
- Schott, J., and E. H. Oelkers (1995). "Dissolution and crystallization rates of silicate minerals as a function of chemical affinity." *Pure and Appl. Chem.* 67(6):903-910.
- Steeffel, C. I., and P. Van Cappellen (1990). "A new kinetic approach to modeling water-rock interaction: The role of nucleation, precursors, and Ostwald ripening." *Geochim. Cosmochim. Acta* 54:2657-2677.
- Strachan, D. M., W. L. Bourcier, and B. P. McGrail (1994). Toward a consistent model for glass dissolution." *Radioactive Waste Management and Environmental Restoration* 19:129-145. [MOL.19960716.0118]
- Strachan, D. M., B. P. McGrail, M. J. Apted, D. W. Engel, and P. W. Eslinger (1990). *Preliminary assessment of the controlled release of radionuclides from waste packages containing borosilicate waste glass.* (PNL-7591) Richland, WA: Pacific Northwest Laboratory. [NNA.19900116.0029]
- Tait, J. C., and C. D. Jensen (1982). "The effect of Zn(II) ion adsorption on the durability of sodium borosilicate glasses." *J. Non-Cryst. Solids.* 49:363-377.
- Trotignon, L. (1990). "Aqueous corrosion of borosilicate glasses: Nature and properties of alteration layers." Ph.D. thesis. Toulouse, France: Paul Sabatier University.
- Van Iseghem, P., T. Amaya, Y. Suzuki, and H. Yamamoto (1992). "The role of Al<sub>2</sub>O<sub>3</sub> in the long-term corrosion stability of nuclear waste glasses." *J. Nucl. Mat.* 190:269-276.
- Vernaz, E. Y., J. L. and Dussossoy (1992). "Current state of knowledge of nuclear waste glass corrosion mechanisms: the case of R7T7 glass." *Appl. Geochem.* 1(Special Issue):13-22.
- Vernaz, E. Y., J. L. Dussossoy, and S. Fillet (1988). "Temperature dependence of R7T7 nuclear waste glass alteration mechanism." In proceedings from Materials Research Society Symposium. 112:555-563. [NNA.19900306.0125]
- Zwicky, H. U., T. Graber, R. Grauer, and R. Restani (1992). "Cationic corrosion inhibitors for alkali borosilicate glass." In proceedings from Materials Research Society Symposium. 257:83-90.

## **Appendix A**

### **Quality Assurance Information**

**Appendix A**  
**Quality Assurance Information**

**Version 1.3**  
**July 23, 1998**

The tables presented in this appendix address the acceptance criteria for the Level 3 deliverable *Waste Form Characteristics Report, Version 1.3*. Table A-1 is the required "roadmap" that indicates where the criteria are met in this report. Table A-2 is a list of the codes used for calculations discussed in this report, including the versions used and whether the codes are qualified.

Table A-3 lists the significant data used the sections included in this revision and the related data-tracking numbers (DTNs) from the Technical Data Management System (TDMS).

**Table A-1 "Roadmap" table identifying where the deliverable (WP20M3) acceptance criteria are met in the *Waste Form Characteristics Report, Version 1.3***

Criteria Description	Section	Comment
<p>Provide preliminary degradation process models and up-to-date supporting test data that describe the performance, consistent with applicable expected environmental conditions, of commercial spent fuel and high-level, radioactive waste (HLW) immobilized in borosilicate glass for each applicable performance parameter and identified in the <i>Waste Package Development Document (WPDD)</i> [BBA000000-01717-5705-00009 Rev. 1].</p> <p><b>WPDD Performance Parameters</b></p> <ul style="list-style-type: none"> <li>• Process models for cladding failure from strain failure, delayed hydride cracking, and mechanical failure</li> </ul> <p>Section also discusses cladding dry oxidation and chemical corrosion. Pit penetration/localized corrosion is not addressed.</p> <ul style="list-style-type: none"> <li>• Higher SNF oxide formation rate data</li> <li>• SNF dissolution/corrosion and release data</li> </ul> <p>Addresses RN concentrations in contacting water</p> <ul style="list-style-type: none"> <li>• Glass fracture data; radionuclide (RN) release from glass; and colloidal species</li> </ul> <p>Addresses RN concentrations in contacting water</p> <ul style="list-style-type: none"> <li>• Higher SNF oxide formation rate models</li> </ul>	<p style="text-align: center;">2.1.3.1</p> <p style="text-align: center;">2.1.3.2</p> <p style="text-align: center;">2.1.3.5</p> <p style="text-align: center;">2.2.1.5 2.2.2.2 2.2.2.3</p> <p style="text-align: center;">3.2.2</p>	<p>There are 10 sections in this update, version 1.3. Six of the sections include data and are in Chapter 2. Those revised sections are 2.1.3.1, 2.1.3.2, 2.1.3.5, 2.2.1.5, 2.2.2.2, and 2.2.2.3. The remaining four sections (3.2.2, 3.4.2, 3.5.1, and 3.5.2) are in Chapter 3 and contain material on model development for spent nuclear fuel (SNF) and HLW glass waste forms.</p>

Criteria Description	Section	Comment
<p><b>WPDD Performance Parameters (continued)</b></p> <ul style="list-style-type: none"> <li>• SNF dissolution/corrosion and release models</li> </ul> <p>Addresses RN concentrations in contacting water</p> <ul style="list-style-type: none"> <li>• Glass dissolution data/experimental parameters and glass dissolution models</li> </ul> <p>Addresses RN concentrations in contacting water.</p> <p>The HLW glass canister is stainless steel, which has a high corrosion rate. Consequently, no protective credit is taken for the canister.</p>	<p>3.4.2</p> <p>3.5.1</p> <p>3.5.2</p>	
<p>Provide available information related to the degradation behavior of additional spent fuel and waste forms proposed for disposal per the program baseline (e.g., DOE SNF, U.S. Navy fuel, and surplus weapons-usable fissile materials)</p>		<p>Information not currently available</p>
<p>Q and non-Q (NQA) data used and cited in this deliverable are appropriately noted and clearly identified.</p>	<p>Appendix A</p>	<p>Significant data are identified as Q or NQA in Table A-3.</p>
<p>Every effort has been made to ensure that qualified data are used in this deliverable.</p>	<p>2.1.3.1 through 3.5.2</p>	
<p>Technical data contained in the deliverable and not already incorporated in the GENISES will be submitted, if appropriate, for incorporation. Submittal compliance will be demonstrated by including in this report a copy of the technical data information form (TDIF) and the transmittal letter to the GENISES administrator.</p>	<p>Appendices A and B</p>	<p>Data actually used in this report are identified in Appendix A. Where these data are not incorporated in the automated data-tracking system, technical data information forms (TDIFs) are in the process of being submitted, as demonstrated (as far as possible) by the records included in Appendix B.</p>
<p>Record accession numbers and automated tracking numbers will be included, as appropriate, for all data used or cited in this deliverable.</p>	<p>Chapters 3 through 7; Appendix A</p>	<p>Accession numbers are provided in the reference lists for sources for which they are available. Data-tracking numbers are provided in Appendix A for data used.</p>

**Table A-2 Simulation codes and chemical databases used in the Waste Form Characteristics Report, Revision 1.3**

Section	Code	Version	Description	Application	Qualified?	Reference
2.1.3.5.3 3.5.1.7 3.5.1.9	EQ3/6	7.2b	Thermodynamic and reaction-path model	Equilibrium water composition and reaction-path modeling	Yes	Wolery 1992a; Wolery 1992b; Wolery and Daveler, 1992
3.5.1.7 3.5.1.9	GEMBOCHS	EQ3/6 V. 6	Thermodynamic database and maintenance software	Derive, enter, and test thermo-dynamic data files	No	Wolery 1992a; Wolery 1992b
3.4.2.3	RS/1 Explore	2.1	Data analysis software	Multiple regression analysis	No; commercial software	BBN Software Products, 1990

**Table A-3 Summary of significant data used in the Waste Form Characteristics Report, Revision 1.3**

Data Description	Reference	LLNL Data?	Related DTNs	Q/NQ
<b>Section 2.1.3.1 Cladding Degradation</b>				
Tables 2.1.3.1-1, 2.3.1-2, and 2.1.3-3 Figures 2.1.3.1 through Figure 2.3.1-5	Siegmann, 1998	No	In process of submission	NQ
<b>Section 2.1.3.2 UO<sub>2</sub> Oxidation in Fuel</b>				
Tables 2.1.3.2-1, 2.1.3.2-2, and 2.1.3.2-3 Figures 2.1.3.2-1 through Figure 2.1.3.2-13	Hanson, 1998	No	LL980608251021.045 (see Appendix B)	Q
<b>Section 2.1.3.5 Dissolution Radionuclide Release from UO<sub>2</sub> Fuel</b>				
Table 2.1.3.5-1	Wilson, 1984	No	In process of submission	Q
Table 2.1.3.5-2	Wilson, 1990	No	In process of submission	Q
Tables 2.1.3.5-3 and 2.1.3.5-6	Gray, 1998	No	In process of submission	Q
Table 2.1.3.5-4	Steward and Gray, 1994	Yes	LL980601551021.042	Q
Table 2.1.3.5-4a	Gray, 1996; 1998	No	LL980704251021.046 (see Appendix B)	Q
Table 2.1.3.5-5	Steward and Mones, 1997	Yes	LL961210151021.027	Q
Tables 2.1.3.5-7 and 2.1.3.5-8	Wronkiewicz et al., 1996	No	In process of submission	Q
Table 2.1.3.5-9	Finn et al., 1997	No	In process of submission	Q
Tables 2.1.3.5-10 through 2.1.3.5-22	Finn et al., 1997	No	In process of submission	Q

Data Description	Reference	LLNL Data?	Related DTNs	Q/NQ
<b>Section 2.2.2.2 Dissolution Radionuclide Release from Glass</b>				
Tables 2.2.2.2-1 through 2.2.2.2-5	This report	No	In process of submission	Q
Table 2.2.2.2-6	Bates and Gerding, 1990	No	In process of submission	
Table 2.2.2.2-7	This report	No	In process of submission	
Table 2.2.2.2-8	Fortner et al., 1997	No	In process of submission	Q
Figures 2.2.2.2-1 through 2.2.2.2-10	This report	No	In process of submission	Q
<b>Section 2.2.2.3 Soluble-Precipitated/Colloidal Species</b>				
Table 2.2.2.3-1	This report	No	In process of submission	Q
<b>Section 3.2.2 Oxidation Models</b>				
Models use data from Section 2.1.3.2	This report	Yes	In process of submission	Q
<b>3.4.2 Spent Fuel Dissolution Models</b>				
Models use data from Section 2.1.3.5	This report	Yes	In process of submission	Q
<b>Section 3.5.1 Experimental Parameters for Glass Dissolution</b>				
Table 3.5.1-1	Knauss et al., 1990	Yes	In process of submission	NQ
Table 3.5.1-2	Johnson et al., 1992	No	In process of submission	NQ
Table 3.5.1-3	This report	Yes	In process of submission	NQ
Table 3.5.1-4	This report	Yes	In process of submission	NQ
Table 3.5.1-5	This report	Yes	In process of submission	NQ
Table 3.5.1-6	Delaney, 1985	No	In process of submission	NQ
Tables 3.5.1-7 through 3.5.1-9	This report	Yes	In process of submission	NQ
Tables 3.5.1-10 and 3.5.1-11	This report	Yes	In process of submission	Q
Figure 3.5.1-3	Delage et al., 1992	No	In process of submission	NQ
Figure 3.5.1-8	Fortner and Bates, 1995	No	In process of submission	Q
Figure 3.5.1-9	This report	Yes	In process of submission	Q
<b>Section 3.5.2 Glass Dissolution Models</b>				
Table 3.5.2-1	This report	Yes	In process of submission	NQ
Figure 3.5.2-2	Bourcier, 1990	Yes	In process of submission	NQ
Figure 3.5.2-4	Bourcier, 1994	Yes	In process of submission	NQ
Figure 3.5.2-5	Bourcier, 1992	Yes	In process of submission	NQ
Figure 3.5.2-6	This report	Yes	In process of submission	NQ

## References

- Bates, J. K., and T. J. Gerding (1990). *Application of the NNWSI Unsaturated Test Method to Actinide Doped SRL 165 Type Glass*. (ANL-89/24) Argonne, IL: Argonne National Laboratory Report.
- BBN Software Products (1990). *RS/Explore* (Version 2.1). Cambridge, MA: BBN Software Products Corporation.
- Bourcier, W. L., S. A. Carroll, B. L. and Phillips (1993b). "Constraints on the affinity term for modeling long-term glass-dissolution rates." In proceedings from Materials Research Society Symposium. Boston, MA: November 29-December 3, 1993. Also UCRL-JC-116132 for Lawrence Livermore National Laboratory. [NNA.19940516.0093]
- Bourcier, W. L., H. C. Weed, S. N. Nguyen, J. K. Nielsen, L. Morgan, L. Newton, and K. G. Knauss (1992). "Solution compositional effects on dissolution kinetics of borosilicate glass." In proceedings from Seventh Annual Water-Rock Conference. p. 81-84.
- Bourcier, W. L. (1990) *Geochemical modeling of radioactive waste glass dissolution using EQ3/6: Preliminary results and data needs*. (UCID-21869) Livermore, CA: Lawrence Livermore National Laboratory. [NNA.19900501.0161]
- Delage, F., D. Ghaleb, J. L. Dussossoy, O. Chevallier, and E. Vernaz (1992). "A mechanistic model for understanding nuclear waste." *J. Nucl. Mat.* 190:191-197.
- Delaney, J. M. (1985). *Reaction of Topopah Spring Tuff with J-13 water: a geochemical modeling approach using the EQ3/6 reaction path code*. (UCRL-53631) Livermore, CA: Lawrence Livermore National laboratory. [HQS.19980517.2419]
- Finn, P. A., D. J. Wronkiewicz, R. J. Finch, J. C. Hoh, J. W. Emery, E. C. Buck, J. A. Fortner, S. F. Wolf, L. A. Neimark, and J. K. Bates (1997). *Yucca Mountain Project—Argonne National Laboratory, Annual Progress Report, FY 1997*. (ANL-98/12) Argonne, IL: Argonne National Laboratory.
- Fortner, J. A., and J. K. Bates (1995). *Long-term results from unsaturated testing of actinide-doped DWPF and WVDP waste glasses*. (UCRL-CR-122614; DE960072159; B-291561) Livermore, CA: Lawrence Livermore National Laboratory, and Argonne, IL: Argonne National Laboratory.
- Fortner J. A., J. K. Bates, and T. J. Gerding (1997). *Analysis of Components from Drip Tests with ATM-10 Glass*. (ANL-96/16) Argonne, IL: Argonne National Laboratory.
- Gray, W. J. (1996). *FY 1996 Letter Report on Spent Fuel Dissolution Studies*. (Informal YMP Status Report) Richland, WA: Pacific Northwest National Laboratory. [MOL.19970114.0282]

Gray, W. J. (1998). *Letter Report on Spent Fuel Dissolution Rates as a Function of Burnup and Water Chemistry*. (Informal YMP Status Report, PNNL-11895) Richland, WA: Pacific Northwest National Laboratory.

Johnson, J. W., E. H. Oelkers, and H. C Helgeson (1992). "SUPCRT92: A software package for calculating the standard molal thermodynamic properties of minerals, gases, aqueous species, and reactions from 1 to 5000 g-bars and 0 to 1000°C." *Computers and Geosciences*. 18:890-947.

Knauss, K. G., W. L. Bourcier, K. D. McKeegan, C. I. Merzbacher, S. N. Nguyen, F. J. Ryerson, D. K. Smith, H. C. Weed, and L. Newton, L. (1990). "Dissolution kinetics of a simple nuclear waste glass as a function of pH, time, and temperature." In proceedings from Mat. Res. Soc. Symp. 176:371-381. [NNA.19891206.0279]

Siegmann, E. (1998). *Waste Form Degradation and Radionuclide Mobilization Preliminary TSPA, Section 2.7*. Las Vegas, NV: Civilian Radioactive Waste Management System, Management and Operating Contractor. (B00000000-01717-2200-0199)

Steward, S. A., and W. J. Gray (1994). "Comparison of Uranium Dissolution Rates from Spent Fuel and Uranium Dioxide." In proceedings from Fifth Annual Intl. High-Level Radionuclide Waste Management Conference. Las Vegas, NV: May 22-26, 1994. 4:2602-2608. (Also UCRL-JC-115355 for Lawrence Livermore National Laboratory, Livermore, CA). [210933]

Steward, S. A., and E. T. Mones (1997). "Comparison and Modeling of Aqueous Dissolution Rates of Various Uranium Oxides." In proceedings from Materials Research Society Fall Meeting: Scientific Basis for Nuclear Waste Management XX. W. J. Gray and I. R. Triay (Eds.). Boston, MA: December 2-6, 1996. 465 557-564. Also UCRL-JC-124602 (1996) for Lawrence Livermore National Laboratory, Livermore, CA. [MOL.19971210.0278]

Wilson, C. N. (1984). *Results from NNWSI Series 1 Spent Fuel Leach Tests*. (HEDL-TME 84-30) Richland, WA: Hanford Engineering Development Laboratory. [NNA.900216.0070]

Wilson, C. N. (1990). *Results from NNWSI Series 3 Spent Fuel Dissolution Tests*. (PNL-7170) Richland, WA: Pacific Northwest National Laboratory. [NNA.199000814.0048]

Wolery, T. J. (1992a). *EQ3/6, A Software Package for Geochemical Modeling of Aqueous Systems: Package Overview and Installation Guide*. (UCRL-MA-110662) Livermore, CA: Lawrence Livermore National Laboratory. (part 1) [NNA.19921023.0028]

Wolery, T. J. (1992b). *EQ3NR, A Computer Program For Geochemical Aqueous Speciation-Solubility Calculations: Theoretical Manual, User's Guide, and Related Documentation*. (UCRL-MA-110662) Livermore, CA: Lawrence Livermore National Laboratory. (Version 7.0) [NNA.19921218.0010]

Wolery, T. J., and S. A. Daveler (1992). *EQ6, A Computer Program for Reaction Path Modeling of Aqueous Geochemical Systems: Theoretical Manual, User's Guide, and Related Documentation (Version 7.0)*. (UCRL-MA-110662) Livermore, CA: Lawrence Livermore National Laboratory. (part 4) [MOL.19980218.0570]

Wronkiewicz, D. J., J. K. Bates, S. F. Wolf, and E. C. Buck (1996). "Ten-Year Results From Unsaturated Drip Tests With UO<sub>2</sub> at 90°C: Implications for the Corrosion of Spent Nuclear Fuel." *J. Nucl. Mater.* 238: 78-95. [MOL.19971218.0965]

## **Appendix B**

### **Technical Data Submissions**



# Lawrence Livermore National Laboratory

LLYMP9807043  
July 17, 1998

QA: N

Phill Jones, Acting Administrator  
YMP Technical Database  
Yucca Mountain Site Characterization  
Project Office  
1180 Town Centre Drive  
Las Vegas, NV 89134

**SUBJECT: Five Tables of Developed Data Associated with report entitled "The Burnup Dependence of Light Water Reactor Spent Fuel" and Thesis for U. Calif. LL980608251021.046 (WBS 1.2.2.4.1)**

Enclosed is a hardcopy of the subject results. Also enclosed are a disk with the data in tab delimited form and a copy of the TDIF.

The data review package will be sent to the RPC in accordance with procedures. These data have been technically reviewed in accordance with 033-YMP-QP 3.6, "Collection, Review, and Submittal of Technical Data."

If there are any questions, please contact Herman Leider, (925) 423-3378.

A handwritten signature in black ink, appearing to read "James A. Blink".

James A. Blink  
CRWMS LLNL Manager

JAB/BB/tjr

cc (w/o enc):  
C. Newbury, DOE/YMP

YMP-023-R4  
05/08/96

# YUCCA MOUNTAIN SITE CHARACTERIZATION PROJECT TECHNICAL DATA INFORMATION

Page 1 of 1

(Check one):  ACQUIRED DATA (complete Parts I and II)  
 Data Tracking Number (DTN): LL980608251021.044

DEVELOPED DATA (complete Parts I, II and III)  
 Data Tracking Number (DTN): \_\_\_\_\_

### PART I Identification of Data

Title/Description of Data: THE BURNUP DEPENDENCE OF LIGHT WATER REACTOR SPENT FUEL AND THESIS FOR U CALIF. VA SUPPORTING DATA.

Principal Investigator (PI): HANSEN, B D  
Last Name First and Middle Initials

PI Organization: PACIFIC NORTHWEST LABORATORY

Are Data Qualified?:  Yes  No Governing Plan: SCP

SCPB Activity Number(s): 8.3.5.10.2.1

WBS Number(s): 1.2.2.4.1

### PART II Data Acquisition/Development Information

Method: CARRIED OUT UNDER ACTIVITY PLAN D 20-44. TGA THERMOGRAVIMETRIC STUDIES OF THE OXIDATION RESPONSE OF SPENT FUEL AT VARIOUS LEVELS OF BURNUP. DATA ACQUIRED FROM A SCIENTIFIC NOTEBOOK.

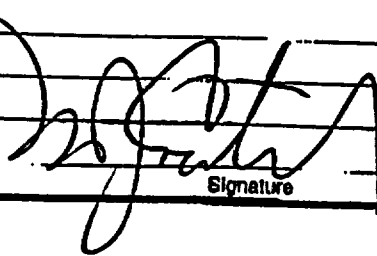
Location(s): PNL

Period(s): 3/1/93 to 12/31/97  
From: MM/DD/YY To: MM/DD/YY

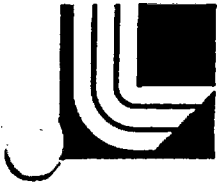
Sample ID Number(s): N/A

### PART III Source Data DTN(s)

### Comments

Checked by:   
Signature

7/17/98  
Date



# Lawrence Livermore National Laboratory

LLYMP9807045  
July 17, 1998

QA: N

Phill Jones, Acting Administrator  
YMP Technical Database  
Yucca Mountain Site Characterization  
Project Office  
1261 Town Centre Drive  
Las Vegas, NV 89134

**SUBJECT: Data Associated with "Additional Spent Fuel Flow-through Tests"  
LL980704251021.045 (WBS 1.2.2.4.1)**

Enclosed is a hardcopy of the subject results. Also enclosed are a disk with the data in tab delimited form and a copy of the TDIF.

The data review package will be sent to the RPC in accordance with procedures. These data have been technically reviewed in accordance with 033-YMP-QP 3.6, "Collection, Review, and Submittal of Technical Data."

If there are any questions, please contact Herman Leider, (925) 423-3378.

James A. Blink  
CRWMS LLNL Manager

JAB/BB/tjr

cc (w/o enc):  
C. Newbury, DOE/YMP

YMP-023-R4  
05/08/98

# YUCCA MOUNTAIN SITE CHARACTERIZATION PROJECT TECHNICAL DATA INFORMATION

Page 1 of 1

(Check one):  ACQUIRED DATA (complete Parts I and II)  
 Data Tracking Number (DTN): 11.980608251021.045

DEVELOPED DATA (complete Parts I, II and III)  
 Data Tracking Number (DTN): \_\_\_\_\_

### PART I Identification of Data

Title/Description of Data: ADDITIONAL SPENT FUEL FLOW-THROUGH TESTS. VA SUPPORTING DATA.

Principal Investigator (PI): GRAY, W \*  
Last Name First and Middle Initials

PI Organization: PACIFIC NORTHWEST LABORATORY

Are Data Qualified?:  Yes  No Governing Plan: SCP

SCPB Activity Number(s): 8.3.5.10.2.1.1

WBS Number(s): 1.2.2.4.1

### PART II Data Acquisition/Development Information

Method: CARRIED OUT UNDER ACTIVITY PLAN D-20-44. TGA THERMOGRAVIMETRIC STUDIES OF THE OXIDATION  
RESPONSE OF SPENT FUEL AT VARIOUS LEVELS OF BURNUP. DATA ACQUIRED FROM SCIENTIFIC NOTEBOOK.

Location(s): PNL

Period(s): 3/1/93 to 12/31/97  
From: MM/DD/YY To: MM/DD/YY

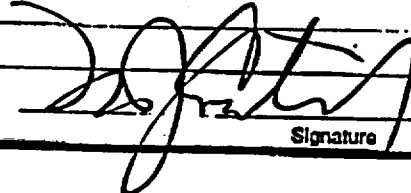
Sample ID Number(s): N/A

### PART III Source Data DTN(s)

_____	_____	_____	_____
_____	_____	_____	_____
_____	_____	_____	_____

### Comments

\_\_\_\_\_  
\_\_\_\_\_  
\_\_\_\_\_

Checked by:  Signature 7/18/98 Date

Aff: Organization: M&O  
Prep: - 17-NOV-97:12:14:27

Yucca Mountain Site Characterization Project  
Planning and Control System (PACS)  
Participant Planning Sheet (PPS)

DE-AC 1RW00134

Page - 1

Dollars in Thousands (Esc.)

PWBS Element: 1.2.2.4  
Product: 7030  
Control Account: 12247030

Waste Form Testing and Modeling  
WP122 - Long-Term Waste Form Testing & Modeling  
Waste Form Materials Testing & Modeling, 1.2.2.4

Start Date: 01-oct-1996  
Finish Date: 28-feb-2002  
QA - YES

Annual Budget	Fiscal Year Distribution										At Complete			
	Prior 1958	FY1998	FY1999	FY2000	FY2001	FY2002	FY2003	FY2004	FY2005	FY2006		FY2007		
	1958	4001	6384	5332	3881	300	0	0	0	0	0	0	0	21856

#### Statement of Work

The following work shall be controlled in accordance with approved implementing procedures identified on the current, OCRWM-accepted Requirements Traceability Network Matrix.

The work to be accomplished under this CA is to acquire data on the performance of candidate waste form (WF) materials under anticipated repository conditions; to prepare mathematical models describing the performance of candidate WF materials relative to performance parameters; provide documentation of the models and the acquired data; respond to comments from peer reviews, expert elicitations, the repository consulting board and requests for data from organizations within the M&O; prepare technical input to appropriate technical documents; provide reviews and comments of appropriate technical and management documents; as necessary provide updates to the Waste Package Development Technical Document, and provide technical management of the work.

Inputs to this work arise from test conditions and environmental parameters used in modeling material performance, from the anticipated repository conditions, from the identified and potential WFs, and as appropriate, from the description in the Waste Package Development Technical Document. Also, as appropriate, performance parameters which are to be evaluated or tested in the activities described in this CA are contained in the Waste Package Development Technical Document, Revision 01 dated May 29, 1996 Table 4-1, "Technical Approach to Engineered Barrier System Development."

Quality Affecting work shall be performed in accordance with the QARD and as appropriate, the guidance of the Waste Package Development Technical Document. Appropriate approved quality procedures shall be used in performing quality related work.

Acquired test data and modeling information shall be available for the WF materials selection for the VA and LA design, for the TSPA-VA, the TSPA-LA and for performance confirmation.

Work under this CA has been divided into related work packages. A general description of the work included in these packages follow:

**WF SNF and HLW Glass Testing:** Conduct short and long duration unsaturated drip-condition waste form testing on commercial and DOE spent nuclear fuel and high-level waste glass under anticipated repository conditions. Assemble data from both test suites, analyze data, report data in the Waste Form Characteristics Report (WFCR) updates and provide to other data users such as Performance Assessment (PA) and design to support the viability assessment (VA) and License Application (LA).

**Procure Approved Test Materials (ATMs):** Identify the existence, availability, and, if possible, acquire small sections of high burnup LWR spent fuels (burnup greater than 60,000 Mwd/MTU) that may become new ATMs. Perform ATM characterization and report characterization results.

**Perform Integrated Testing and Colloid Studies:** Initiate colloid modeling studies to provide bounding rates for colloidal concentrations and transport characteristics. The model development will require experimental data from testing activities for closure. Assemble data from all test suites, analyze data, report data in the WFCR updates and provide to other users such as PA and design to support VA and LA and performance confirmation testing.

**Spent Fuel Testing and Data Generation:** Perform temperature-time thermogravimetric (TGA) tests on available spent fuel ATM samples and flow through dissolution (FTD) tests for the range of available spent fuel inventory (burnup, PWR/BWR), degradation states (oxidation phases), temperatures, and water chemistries. Assemble data from all test suites, analyze data, report data in the WFCR updates and provide to other users such as PA and design to support VA and LA and performance confirmation testing.

**Perform Scoping Tests on C-14 Release:** Initiate dissolution rate tests on hardware components made of stainless steel and Inconel.

**Perform Scoping Tests on SF Hardware Release:** Initiate dissolution rate tests on new ATM cladding and fuel specimens to compare release of C-14 to that obtained for existing ATMs.

12247030 Waste Form Materials Testing & Modeling, 1.2.2.4 (continued)

**Dry Bath SF Oxidation Testing:** Rather than continue operations and examinations of existing dry bath oxidation test samples and initiating additional tests on additional ATM samples, this work has been deferred until further evaluation determines whether the test data are needed.

**WF Modeling and Technical Management:** Participate in the development of PA WF process models abstractions for the WF and other WF materials. Review the results of the TSPA to ensure the mechanistic models developed in the model development activities are appropriately captured. Participate with Systems Engineering as required in developing systems studies. Interface the testing program with results achieved from the site characterization program activities. Manage, integrate and coordinate WF materials testing activities at LLNL and other sites. Develop budgets, schedules and meet administrative, technical, safety, environmental and quality requirements. Provide reviews of testing documents, data packages, and plans for all testing activities in spent fuels and glass waste forms.

**Parameter Tests, Modeling and WFCR:** Perform flow through tests, closed system tests, and surface titration tests on borosilicate waste glass over a range of pH buffered solutions with variations in dissolved ferrous and ferric iron and magnesium or manganese silicate concentrations. Assemble and synthesize the data and develop process models from all of the waste form tasks for predicting waste form performance, including long term oxidation response, dissolution rate response and release rate of spent fuel for a range of potential environmental conditions, and glass waste form alteration, dissolution, and release rates. Prepare and distribute process model updates to the WFCR updates. Assemble data from all test suites, analyze data, report data in the WFCR updates and provide to other users such as PA and design to support VA and LA and performance confirmation testing. Prepare and distribute updates to the WFCR.

#### TECHNICAL BASELINE DOCUMENTS

Work is to be performed in accordance with the latest revision of the following technical documents:

Level 1 - Program:

Not Applicable

Level 2 - YMSCO:

Not Applicable

Level 3 - WAST:

Not Applicable

#### Work Packages

Work Package	Title
12247030M0	HIST. Waste Form Materials Testing & Modeling, 1.2
12247030M2	WF SNF and HLW Glass Testing
12247030M3	SF Testing and Data Generation
12247030M4	WF Modeling & Technical Management
12247030M5	Parameter Tests, Modeling and WFCR
12247030M6	FCF 1997 Modeling Deferred Work
12247030M7	SF Testing Deferred Work

12247030 Waste Form Materials Testing & Modeling, 1.2.2.4 (continued)

DELIVERABLES

Deliv ID	Description/Completion Criteria	Due Date
WP110M3	<p>Waste Form Charact Report Update for LA</p> <p>Criteria -            Description:</p> <p>The Waste Form Characteristics Report - update for LA (WFCR-LA) shall, at a minimum, provide preliminary degradation process models and up-to-date supporting test data that describe the performance of commercial spent fuel and high-level radioactive waste (HLW) immobilized in borosilicate glass collected and developed since the WFCR-VA update. As available, information related to the degradation behavior of additional spent fuel and waste forms proposed for disposal per the program baseline (e.g., DOE SNF, Naval fuel, and surplus weapons-useable fissile materials), shall also be provided. Degradation process models and supporting test data for commercial spent fuel and HLW, shall, at a minimum, be provided for each applicable performance parameter identified in the Waste Package Technical Document and be consistent with applicable expected environmental conditions. Q and non-Q data used and cited in this deliverable shall be appropriately noted and clearly identified. Every effort was made to assure that qualified data are used in this deliverable as specified in Section: Supplement III, 2.5 "Data Usage". Technical data contained within the deliverable and not already incorporated in the Geographic Nodal Information Study and Evaluation System (GENISES) is submitted, if appropriate, for incorporation into GENISES in accordance with YAP-SIII.3Q. Verification of technical data submittal compliance is demonstrated by including as part of the deliverable: 1) a copy of the Technical Data Information Form generated identifying the data in the Automated Technical Data Tracking System, and 2) a copy of the transmittal letter attached to the technical data transmittal to the GENISES Administrator. Record accession numbers and Automated Tracking numbers are included, as appropriate, for all data used and/or cited in this deliverable.</p> <p>Completion Criteria:</p> <p>The WFCR-LA shall have completed internal M&amp;O review utilizing appropriate approved quality assurance procedures implementing requirements of the QARD. The document need not complete a YAP-30.12 review for completion of the level 3 deliverable. The WFCR-LA update is scheduled to be submitted to YMSCO 31JUL00 for review and acceptance by 28AUG00. The deliverable is complete when it is submitted to DOE in accordance with YAP 5.1Q and logged into the TPM database.</p> <p>Acceptance Criteria:</p> <p>This deliverable shall include all information identified in the Deliverable Description on this PPS sheet unless specifically exempted in writing by the COR at least 60 days before the scheduled due date (30 days in special cases agreed to by the COR). This constitutes the "completion criteria" identified in section 5.4.3 (b) of YAP 5.1Q. The COR will review the deliverable and process in accordance with YAP 5.1Q.</p>	31-jul-2000
WP20BM3	<p>Waste Form Characteristics Report Update</p> <p>Criteria -            Description:</p> <p>The Waste Form Characteristics Report - update for VA (WFCR-VA) shall, at a minimum, provide preliminary degradation process models and up-to-date supporting test data that describe the performance of commercial spent fuel and high-level radioactive waste (HLW) immobilized in borosilicate glass. As available, information related to the degradation behavior of additional spent fuel and waste forms proposed for disposal per the program baseline (e.g., DOE SNF, Naval fuel, and surplus weapons-useable fissile materials), shall also be provided. Degradation process models and supporting test data for commercial spent fuel and HLW, shall, at a minimum, be provided for each applicable performance parameter identified</p>	31-jul-1998

12247030 Waste Form Materials Testing & Modeling, 1.2.2.4 (continued)

DELIVERABLES

Deliv ID	Description/Completion Criteria	Due Date
	<p>in the Waste Package Technical Document and be consistent with applicable expected environmental conditions. Q and non-Q data used and cited in this deliverable shall be appropriately noted and clearly identified. Every effort was made to assure that qualified data are used in this deliverable as specified in Section: Supplement III, 2.5 "Data Usage". Technical data contained within the deliverable and not already incorporated in the Geographic Nodal Information Study and Evaluation System (GENISES) is submitted, if appropriate, for incorporation into GENISES in accordance with YAP-SIII.3Q. Verification of technical data submittal compliance is demonstrated by including as part of the deliverable: 1) a copy of the Technical Data Information Form generated identifying the data in the Automated Technical Data Tracking System, and 2) a copy of the transmittal letter attached to the technical data transmittal to the GENISES Administrator. Record accession numbers and Automated Tracking numbers are included, as appropriate, for all data used and/or cited in this deliverable.</p> <p><b>Completion Criteria:</b></p> <p>The WFCR-VA shall have completed internal M&amp;O reviews utilizing appropriate approved quality assurance procedures implementing requirements of the QARD. The document need not complete a YAP-30.12 review for completion of the level 3 deliverable. The WFCR-VA update is scheduled to be submitted to YMSCO 31JUL98 for review and acceptance by 28AUG98. The deliverable is complete when it is submitted to DOE in accordance with YAP 5.1Q and logged into the TPM database.</p> <p><b>Acceptance Criteria:</b></p> <p>This deliverable shall include all information identified in the Deliverable Description on this PPS sheet unless specifically exempted in writing by the COR at least 60 days before the scheduled due date (30 days in special cases agreed to by the COR). This constitutes the "completion criteria" identified in section 5.4.3 (b) of YAP 5.1Q. The COR will review the deliverable and process in accordance with YAP 5.1Q.</p>	

Approvals

Preparer RD SWELL print name  
 Technical Reviewer DEWIS R. WILLIAMS print name  
 QA Reviewer R.D. HABBE print name  
 Preparer - signature [Signature] Date 11/17/97  
 Technical Reviewer - signature [Signature] Date 11/18/97  
 QA Reviewer - signature [Signature] Date 11-19-97